united nations
educational, scientific
and cultural
organization

international atomic
energy agency

the
abdus salam
international centre for theoretical physics

ICTP 40th Anniversary

SCHOOL ON SYNCHROTRON RADIATION AND APPLICATIONS
In memory of J.C. Fuggle & L. Fonda

19 April - 21 May 2004

Miramare - Trieste, Italy

1561/21

Multiplets, XMCD

F. De Groot

Multiplets in X-ray Spectroscopy
lectures ICTP 2004, by Frank de Groot

Multiplets in X-ray Spectroscopy

lectures ICTP 2004, by Frank de Groot

1. X-rays

X-rays are defined as the electromagnetic radiation with a wavelength between Ultraviolet radiation and gamma radiation. The border between Ultraviolet radiation and X-rays is not clearly defined but usually set around 10^{-8}meter, i.e. 10 nm. The upper limit of x-rays is usually set at 10^{-12} meter, i.e. 1 pm, although radiation with an energy above 10^{-11} meter is also called gamma radiation, in particular if it is created with a radioactive element. X-rays are sub-divided into soft x-rays, between 10 nm and 100 pm and hard x-rays between 100 pm and 1 pm. Soft x-rays are called 'soft' because they do not penetrate air and as such are relatively safe to work with. We will discuss the penetration length of x-rays below. Because of historical reasons, x-rays are often given in Angstroms, where 1 Å equals 10^{-10} meter or 100 pm.

The bottom two axes in the figure give the frequency and the energy of the electromagnetic radiation, using the inverse proportionality between frequency   and wavelength , i.e.   =c/ , where c is the speed of light $3 \cdot 10^{8}$ m/s. This yields x-ray frequencies between 10^{16} and 10^{21} Hertz. It is more common to indicate x-rays with their energies E, using E=h , with the energy given in electron volts (eV) or kilo electron volts (keV), where they range between 100 eV and 10^{6} eV.

Calculate the energy in electron volt for a x-ray with 1 Å wavelength.

Use: E= h   = hc/ , with c=$3 \cdot 10^{8}$ m/s, h=$6.6 \cdot 10^{-34}$ and 1 eV = $1.6 \cdot 10^{-19}$ J

E (1 Å)= $6.6 \cdot 10^{-34}$ $3 \cdot 10^{8}$ / 10-10 = $2 \cdot 10^{-15}$ J   /$1.6 \cdot 10^{-19}$ = $1.2 \cdot 10^{4}$ eV=12.4 keV

It can be checked in the figure that a wavelength of 10^{-10}meter corresponds to energy slightly above 10^{4} eV.

The wavelength of x-rays are of the same size as molecules, which range from 100 pm for small molecule such as water to 10 nm for macromolecules such as enzymes. In particular the distance of 1 Å is important in matter, because it corresponds to a typical interatomic distance. This makes diffraction with x-rays of approximately 1 Å an important technique to determine the interatomic distances and, in general, the structure of matter.

X-rays are traditionally produced using x-ray tubes. In a x-ray tube, electrons are accelerated between the anode and the cathode. When they hit the cathode with high energy, they are decelerated through inelastic collisions with atoms in the target material. If the energy of the electrons is high enough this produces a continuous spectrum of x-rays. In addition, the impinging high-energy electrons excite core electrons from the cathode material. Core holes decay, in part, via radiative processes in which a shallow core electron fills a deep core hole, thereby emitting x-rays. These x-rays are characteristic for the cathode material and are confined to only a few energies. This process will be discussed in detail below.

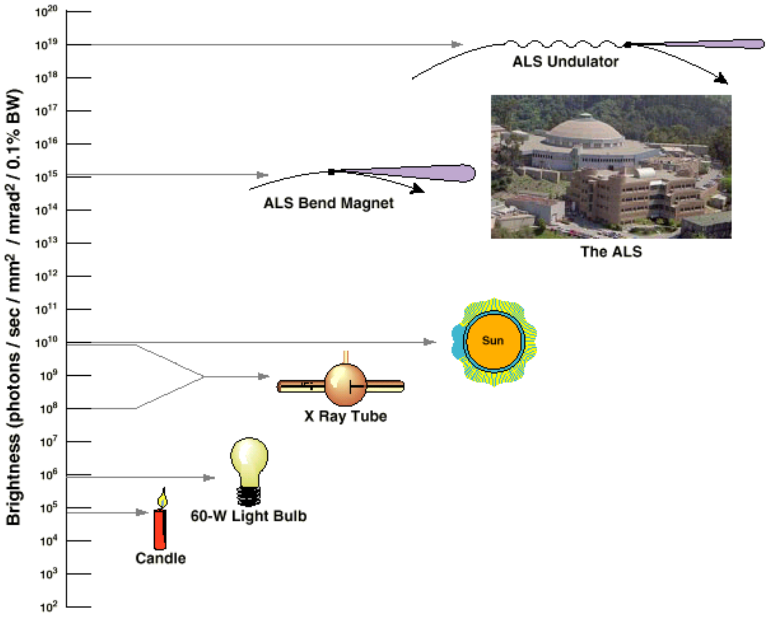

X-ray tubes are used in many x-ray applications; for example (almost) all medical x-ray images use x-ray tubes. In addition, laboratory x-ray sources used in x-ray photoemission and x-ray diffraction make use of x-ray tubes. In x-ray spectroscopy however the role of x-ray tubes has been declining over the last few decades. The reason is evident from the figure: X-ray tubes produce a maximum of 10^{10} 'photons per second', whereas x-rays produced with synchrotrons reached up to 10^{19} photons per second. These photon counts are usually given with the 'brightness'. The brightness is normalised to an area of 1 mm^2 and further normalised to the x-ray beam divergence and the energy (range). It is clear that with 10^9 times more photons per second, one can carry out much faster experiments. In addition, it allows a range of new experiments that have very low x-ray cross-sections. It should be noted that the x-rays produced with synchrotrons have very high intensity, but still they cannot be considered as x-ray lasers, because in general they have insufficient coherence.

1.1. Interaction of x-rays with matter

If an x-ray hits a solid material, the material starts to emit electrons. This is essentially the photoelectric effect that also occurs with ultraviolet radiation. In the case when a metal surface is exposed to ultraviolet or x-ray radiation, the following experimental observations can be made:

a. No electrons are ejected unless the radiation has a frequency above a certain threshold value characteristic of the metal.

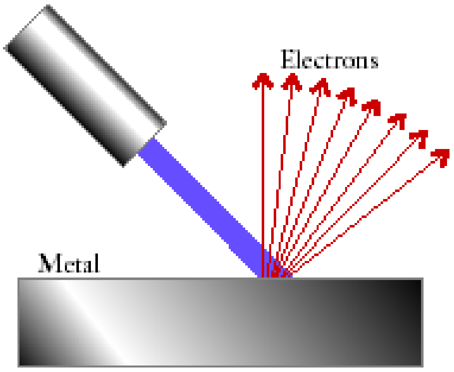

b. In case of x-rays, there is always some electron emission, but one observes intensity jumps in the emitted electrons at certain energies.

c. Electrons are ejected immediately, however low the intensity of the radiation.

d. The kinetic energy of the ejected electrons increases linearly with the frequency of the incident radiation.

These observations follow naturally from the quantum nature of electromagnetic radiation; in fact the photoelectric effect was used by Einstein to (re)define electromagnetism.

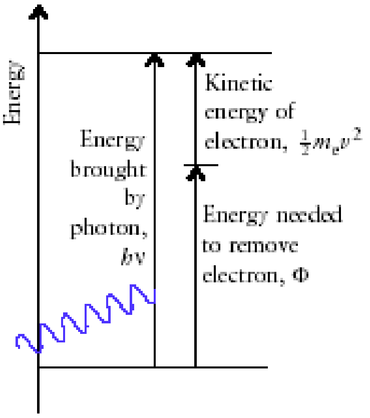

The characteristics of the photoelectric effect can be explained in terms of photons. If the incident radiation has frequency , it consists of a stream of photons of energy h . These particles collide with the electrons in the metal. If the energy of a photon is less than the energy required removing an electron from the metal, then an electron will not be ejected, regardless of the intensity of the radiation. The energy required to remove an electron from the surface of a metal is called the **work function** of the metal and denoted . However, if the energy of the photon is greater than , then an electron is ejected with a kinetic energy, $E=\frac{1}{2}mv^2$, equal to the difference between the energy of the incoming photon and the work function. In case of x-rays, the explanation is analogous, with the addition that a core electron is excited instead of a valence electron. The **binding energy** of the core electron must be added and the kinetic energy is given as:

$$\frac{1}{2}mv^2 = \hbar\upsilon - E_B - \Phi$$

In fact, this equation defines the binding energy of a core level and x-ray photoemission experiments are used to measure core level binding energies. The binding energy E_B is closely related to the **ionisation energy** that is defined as E_B+ .

Example: In an x-ray photoemission (XPS) experiment, NiO is excited with al K radiation with an energy of 1487 eV. One observes peaks in the XPS spectrum at respectively 607 eV and 637 eV. Assume that the work function of NiO is equal to 2 eV; calculate the binding energies of the core levels associated with the observed peaks.

Solution: rewrite the equation to: E_B = h - E_K -
1487- 607-2=878 eV
1487-632-2= 853 eV

Explanation: These core level energies are both related to the 2p core level of the nickel atoms in NiO. The 2p core level is split into two sub-peaks due to the 2p spin-orbit coupling that will be explained later.

Self-Test; calculate the ionisation energy of a rubidium atom, given that radiation of wavelength 58.4 nm produces electrons with a speed of 2450 km/s. The mass of an electron is 9.1 10^{-31}kg.

The photoelectric effect is not the only interaction of x-rays with matter. Another important interaction is the elastic scattering of x-rays due to electrons, which is the origin of x-ray diffraction experiments. Elastic scattering is also known as **Thompson scattering**. In a x-ray diffraction experiment one hits a sample with a x-ray and measures the diffracted x-rays. The diffraction angle can be correlated with the interatomic distances using Bragg's law.

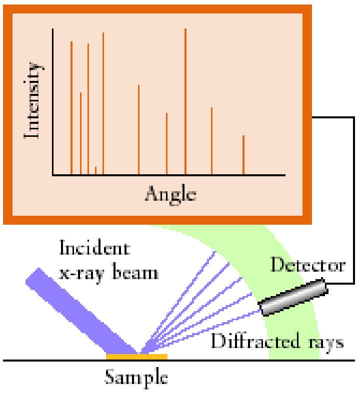

In this course we focus on spectroscopy and x-ray diffraction will not further be treated. With respect to spectroscopy, it is important to note that the amount of x-rays involved in x-ray diffraction is almost constant with respect to the photon energy. As such, it only gives an (almost constant) background upon which the photoelectric effect is superimposed.

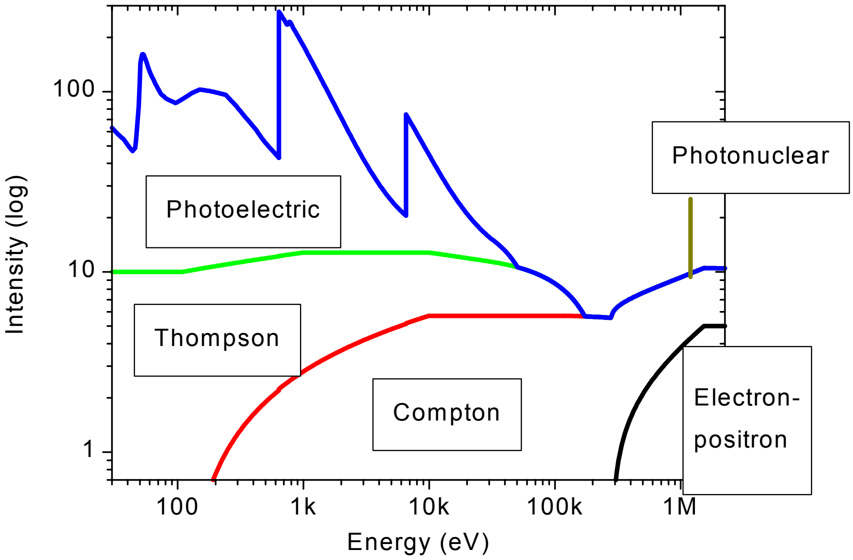

This figure gives all contributions to the x-ray absorption process for a manganese atom (in a gas or in a solid). The intensity axis is given on a logarithmic scale and it can be seen that the photoelectric effect dominates up to approximately 50 keV. At higher energies the photoelectric effect dies out and in addition to Thompson scattering, Compton scattering becomes important. Compton scattering refers to inelastic scattering. Around 1 MeV an additional x-ray process takes place, i.e. the photonuclear absorption, which refers to the absorption of a x-ray in a nuclear transition. This process is well known under the name of **Mössbauer effect**. At even higher energies the photon energy is high enough to cause the creation of electron-positron pairs, which is the inverse process of the electron-positron annihilation as used in positron emission tomography (PET) scans.

In the following we will consider x-ray energies up to 100 KeV and assume that only Thompson scattering and the photoelectric effect take place.

1.1.1 X-ray absorption spectroscopy

A straightforward experiment is to measure the transmission of an x-ray through a sample. A photon entering solid can be scattered or annihilated in the photo-electric effect. All other photons will be transmitted and will leave the sample. In x-ray absorption spectroscopy (XAS) the absorption of x-rays by a sample is measured. The intensity of the beam before the sample I_0 and the intensity of the transmitted beam I are measured.

Consider an infinitely thin layer, of thickness, dl, of the absorbing material. The intensity I_0 of the incident beam is reduced by dI on passing through dl. dI is proportional to dl and dI is also proportional to the total intensity I, i.e.:

$$dI = -\ \mu\ I \cdot dl$$

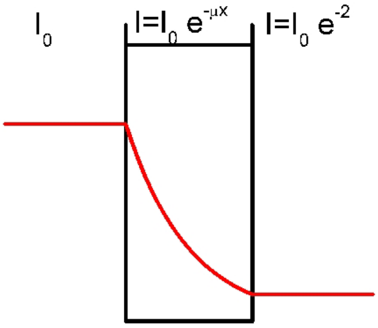

  is a proportionality constant called the **linear absorption coefficient**. It incorporates the combined effects of all photoelectric ( ) and scattering ( ) processes. One can rewrite the equation to:

$$\frac{1}{I}dI = -\mu \cdot dl$$

Integration over a finite thickness from 0 to x yields:

$$\ln I \Big|_{I_0}^{I_x} = -\mu \cdot l \Big|_{0}^{x}$$

$$\ln I_x - \ln I_0 = -\mu \cdot x$$

The linear absorption coefficient   is dependent on the x-ray energy (indicated with its frequency) and rewriting the equation yields:

$$I_x(\omega) = I_0(\omega) \cdot e^{\mu(\omega)\cdot x}$$

alternatively, the linear absorption coefficient   can be given as:

$$\mu(\omega) = \tfrac{1}{x} \cdot \ln \frac{I_0}{I_t}$$

The figure below indicates the intensity drop through sample of thickness x equal to 2/ . This reduces the intensity after the sample to $e^{-2}\cdot I_0$.

Multiplets in X-ray Spectroscopy

lectures ICTP 2004, by Frank de Groot

X-ray attenuation lengths

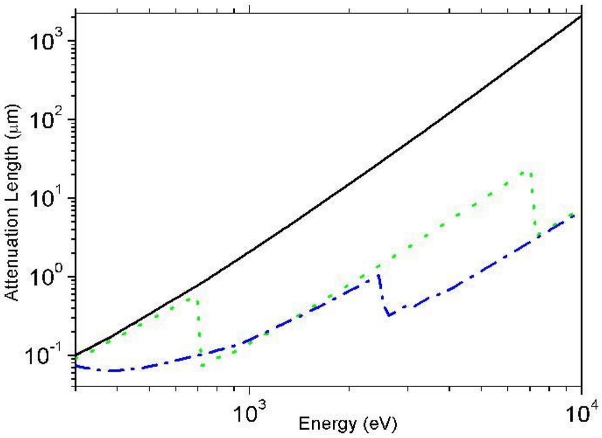

Figure: The attenuation length of x-rays through carbon (solid), iron (dotted) and lead (dash-dotted).

The figure gives the attenuation lengths of x-rays from 300 eV to 10 keV through C, Fe and Pb. X-rays with energies less than 1 keV have an attenuation length of less than ~1 m, implying that for soft x-rays the sample has to be thin. The figure below shows the transmission through 1 m and 10 m iron and it can be seen that soft x-rays (<1 keV) have little to no transmission through 1 m iron. At the iron K edge at 8 KeV the transmission through 10 m iron drops from ~0.65% to less than 0.10%. The extra absorption of the iron 1s core level takes away most of the x-rays in the first 10 m. In addition soft x-rays have a large absorption cross section with air, hence the experiments have to be performed in vacuum.

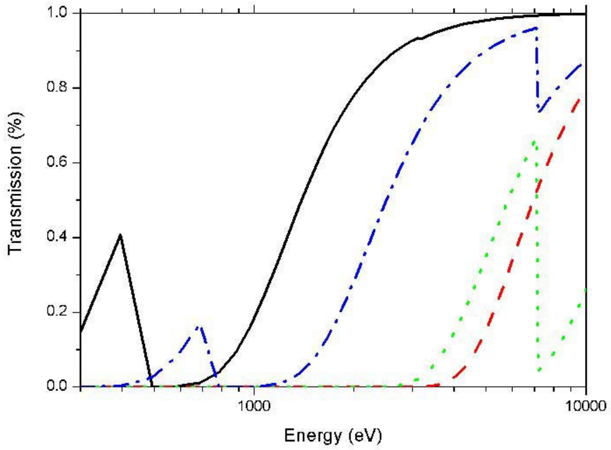

Figure: Transmission through air and bulk iron. Given are respectively 10 cm air (solid), 10 m air (dashed), 1 m iron (dash-dotted) and 10 m iron (dotted).

Multiplets in X-ray Spectroscopy

lectures ICTP 2004, by Frank de Groot

Questions:
- Why is lead the best element to be used to protect against the transmission of x-rays?
- A synchrotron that yields x-rays up to 2 KeV is not protected with lead shielding. Why is this not necessary?

Webpage:
- Go to the webpage of the Center for X-ray Optics (CXRO) in Berkeley and follow the link to http://www-cxro.lbl.gov/
- Check the attenuation lengths of copper and lead between 100 eV and the maximum energy possible. Modify each plot also to a logarithmic scale.
- Check the transmission of x-rays for Be and quartz (SiO_2) between 100 eV and the maximum energy possible. Use thicknesses of 1 m and 1 mm.

Questions:
- In Ultra-High-Vaccuum equipment one uses berylium windows. Why Be?
- To attenuate the synchrotron beams at energies above 3 KeV (for example for radiation sensitive experiments) one uses aluminum foils. Why is Al used and not for example Cu or Pb?

The next task is to determine the absorption cross section   as a function of the energy . We assume that the scattering is small and constant and limit ourselves to the photoelectric effect. An x-ray acts on charged particles such as electrons. As an x-ray passes an electron, its electric field pushes the electron first in one direction, then in the opposite direction, in other words the field oscillates in both direction and strength. In most descriptions of x-ray absorption one uses the vector field A to describe the electromagnetic wave. The vector field A is given in the form of a plane wave of electromagnetic radiation:

$$A = \hat{e}_q A_0 \cos(kx - \omega t) = \tfrac{1}{2}\hat{e}_q A_0 \, e^{i(kx-\omega t)}$$

The cosine plane wave function contains the wave vector k times the displacement x and the frequency   times the time t. The cosine function is rewritten to an exponential function, for which only the absorbing $e^{-i \ t}$ term has been retained. $\hat{e}_q$ is a unit vector for a polarisation q. (These polarisation effects will not be treated explicitly below.) The Hamiltonian describing the interaction of x-rays with electrons can be approximated in perturbation theory and its first term can be written as:

$$H_1 = \tfrac{e}{mc} p \cdot A$$

The first term of the interaction Hamiltonian H_1 describes the action of the vector field *A* on the momentum operator *p* of an electron. The electric field E is collinear to the vector field, in other words this term can also be understood as the electric field *E* acting on the electron moments. The proportionality factor contains the electron charge e, its mass m and the speed of light c.

Multiplets in X-ray Spectroscopy

lectures ICTP 2004, by Frank de Groot

The Golden Rule states that the transition probability W between a system in its initial state i and final state f is given by:

$$W_{fi} = \tfrac{2\pi}{\hbar}\left|\left\langle \Phi_f \middle| \mathrm{T} \middle| \Phi_i \right\rangle\right|^2 \delta_{E_f - E_i - \hbar\omega}$$

The initial and final state wave functions are built from an electron part and a photon part. The photon part of the wave function takes care of the annihilation of a photon in the x-ray absorption process. In the text below, it will not be included explicitly. The delta function takes care of the energy conservation and a transition takes place if the energy of the final state equals the energy of the initial state plus the x-ray energy. The squared matrix element gives the transition rate.

The transition operator T_1 describes one-photon transitions such as x-ray absorption. It is in first order equal to the first term of the interaction Hamiltonian, i.e. $T_1=H_1$. The transition rate W is found by calculating the matrix elements of the transition operator T_1. Two-photon phenomena, for example resonant x-ray scattering, are described with the transition operator in second order. The interaction Hamiltonian is found by inserting the vector field into H_1:

$$T_1 = \sum_q \sum_k \tfrac{e}{m}\sqrt{\tfrac{2\pi\hbar}{V\omega_k}}\left[a_k\left(\hat{e}_{kq}\cdot p\right)e^{ikr}\right]$$

This equation can be rewritten using a Taylor expansion of $e^{ikr}=1+ikr+\ldots$. Limiting the equation to the first two terms 1+ikr, the transition operator is:

$$T_1 = \sum_q \sum_k a_k \tfrac{e}{m}\sqrt{\tfrac{2\pi\hbar}{V\omega_k}}\left[\left(\hat{e}_{kq}\cdot p\right) + i(\hat{e}_{kq}\cdot p)(k\cdot r)\right]$$

T_1 contains the electric dipole transition ($\hat{e}_{kq}\cdot p$). The electric quadrupole transition originates from the second term. The value of k r can be calculated from the edge energy in eV and the atomic number Z.

$$k\cdot r \approx \sqrt{\hbar\omega(edge)}(eV)/80Z$$

In case of the 1s core levels (called K edges) from carbon (Z=6, $\hbar$ edge = 284 eV) to zinc (Z=30, $\hbar$ edge = 9659 eV), the value of k r lies between 0.03 and 0.04. The transition probability is equal to the matrix element squared, hence the electric quadrupole dipole transition is smaller by approximately 1.5 10^{-3} than the dipole transition and can be neglected, which defines the well-known dipole approximation. The transition operator in the dipole approximation is given by:

$$T_1 = \sum_q \sum_k a_k \tfrac{e}{m}\sqrt{\tfrac{2\pi\hbar}{V\omega_k}}\left[\left(\hat{e}_{kq}\cdot p\right)\right]$$

Omitting the summation over k and using the commutation law between the position operator r and the atomic Hamiltonian ($p=m/i\hbar[r,H]$) one obtains the familiar form of the x-ray absorption transition operator:

$$T_1 = \sum_q e\sqrt{\frac{2\pi\hbar\omega}{V}}\,\hat{e}_q\cdot r \quad \propto \quad \sum_q \hat{e}_q\cdot r$$

1.1.2 Basics of XAFS Spectroscopy

Including this operator into the Fermi golden rule gives:

$$W_{fi} \propto \sum_{q} \left| \left\langle \Phi_f \middle| \hat{e}_q \cdot r \middle| \Phi_i \right\rangle \right|^2 \delta_{E_f - E_i - \hbar\omega}$$

This equation will form the basis for the rest of the lectures. It is a rather theoretical and formal description. What happens in practice? If an assembly of atoms is exposed to x-rays it will absorb part of the incoming photons. At a certain energy (depending on the atoms present) a sharp rise in the absorption will be observed (Figure 1.2). This sharp rise in absorption is called the absorption edge.

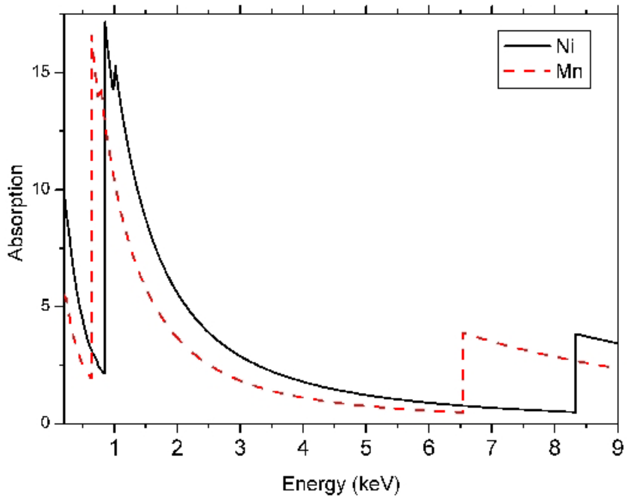

Figure**:** ***The x-ray absorption cross sections of manganese and nickel. Visible are the*** $L_{2,3}$ ***edges at respectively 680 and 830 eV and the K edges at respectively 6500 eV and 8500 eV.***

The energy of the absorption edge is determined by the binding energy of a core level. Exactly at the edge the photon energy is equal to the binding energy, or more precisely the edge identifies transitions from the ground state to the lowest empty state. The figure shows the x-ray absorption spectra of manganese and nickel. The $L_{2,3}$ edges relate to a 2p core level and the K edge relates to a 1s core level binding energy. Many complicating aspects do play a role here and we will come back to this issue later.

In the case of solids, when other atoms surround the absorbing atom, a typical XAFS spectrum is shown below.

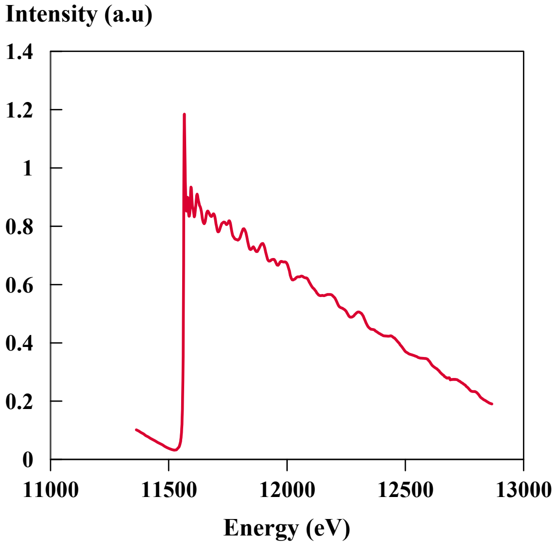

Figure: *The L_3 XAFS spectrum of platinum metal. The edge jump is seen at 11564 eV and above one observes a decaying background modulated by oscillations.*

Instead of a smooth background we see here changes in the intensity of the absorption. Oscillations as function of the energy of the incoming x-rays are visible. The question, which rises immediately, is what causes these oscillations?

An answer can be found by assuming that the electron excitation process is a one electron process. This makes it possible to rewrite the initial state wave function as a core wave function and the final state wave function as a free electron wave function ( ). One implicitly assumes that all other electrons do not participate in the x-ray induced transition. We will come back to this approximation below.

$$\left|\left\langle \Phi_f \middle| \hat{e}_q \cdot r \middle| \Phi_i \right\rangle\right|^2 = \left|\left\langle \Phi_i \underline{c}\varepsilon \middle| \hat{e}_q \cdot r \middle| \Phi_i \right\rangle\right|^2 = \left|\left\langle \varepsilon \middle| \hat{e}_q \cdot r \middle| c \right\rangle\right|^2 = M^2$$

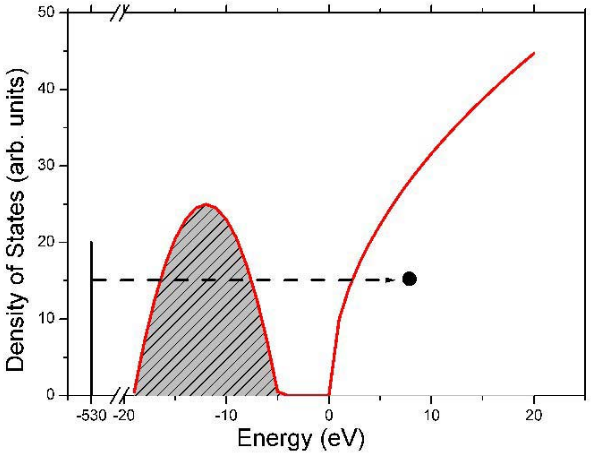

Figure: *The schematic density of states of an oxide. The 1s core electron at 530 eV binding energy is excited to an empty state: the oxygen p-projected density of states.*

The squared matrix element M^2 is in many cases a number that is only little varying with energy and one can often assume that it is a constant. The delta function of the Golden Rule implies that one effectively observes the density of empty states ( ).

$$I_{XAS} \sim \quad M^2 \rho$$

The x-ray absorption selection rules determine that the dipole matrix element M is non-zero if the orbital quantum number of the final state differs by 1 from the one of the initial state (L = 1, i.e. *s* *p, p* *s or d* , etc.) and the spin is conserved (S = 0). The quadrupole transitions imply final states that differ by 2 from the initial state (L = 2, i.e. *s* *d, p* *f* or (L = 0, i.e. *s* *s, p* *p*). They are some hundred times weaker than the dipole transitions and can be neglected in most cases. It will be shown below that they are visible though as pre-edge structures in the K edges of 3d-metals and the $L_{2,3}$ edges of the rare earths.

In the dipole approximation, the shape of the absorption spectrum should look like the partial density of the (L = 1) empty states projected on the absorbing site, convoluted with a Lorentzian. This Lorentzian broadening is due to the finite lifetime of the core-hole, leading to an uncertainty in its energy according to Heisenberg's principle. A more accurate approximation can be obtained if the unperturbed density of states is replaced by the density of states in presence of the core-hole. This approximation gives a relatively adequate simulation of the XAS spectral shape, at least in those cases where the interaction between the electrons in the final state is relatively weak. This is often the case for 1*s* 4*p* transitions (K-edges) of the 3*d* metals.

1.2. The Electronic Structure of Solids

Before we will discuss XANES spectra and their comparison to the density of states, we will first introduce the concept of density of states and the ways to calculate it.

1.2.1. Orbitals in One dimension

Much of the physics and chemistry of solids is already present in one dimension. We begin with a chain of equally spaced hydrogen atoms. A chemist would have an intuitive feeling for what that model chain of atoms would do if released from the prison of its theoretical construction. At ambient pressure, it would form a chain of hydrogen molecules. This simple bond-forming process can be analysed by calculating a band, then seeing that it is subject to instability. One would conclude that the initially equally spaced hydrogen polymer would form a chain of hydrogen molecules.

It turns out to be computationally convenient to think of a chain of hydrogen atoms as a bent segment of a large ring. The orbitals of medium-sized rings on the way to that very large one are quite well known. They are shown in figure 1. For a hydrogen molecule there is bonding $_g$ below an antibonding $_u^*$ state. For cyclic H_3 we have one orbital below two degenerate ones; for H_4 the familiar one below two below one, and so on. Except for the lowest (and occasionally the highest) level, the orbitals come in degenerate pairs. The number of nodes increases as one rises in energy. We would expect the same for an infinite hydrogen chain: the lowest level nodeless, the highest with the maximum number of nodes. In between the levels should come in pairs, with a growing number of nodes.

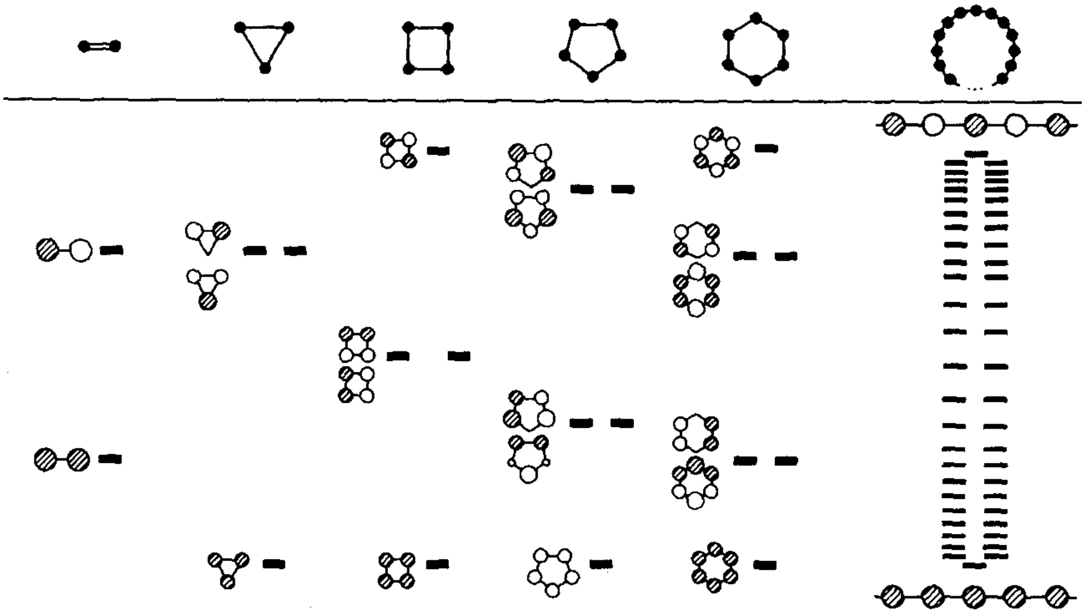

Figure 1: Bonding and anti-bonding orbitals of ring-shaped structures.

1.2.2. Bloch Functions, Band Structures and k

One can describe the orbitals quantitatively by making use of the translation symmetry. We have a lattice whose points are labelled by an index n = 0, 1, 2, 3, etc., and on each lattice point there is a basis function (an H ls orbital), $_0$, $_1$, $_2$, etc. The appropriate symmetry-adapted linear combinations are given as:

$$\Psi_k = \sum e^{ikna}\chi_n \qquad \begin{matrix} 0 & \xleftrightarrow{a} & 1 & \xleftrightarrow{a} & 2 & \xleftrightarrow{a} & 3 \\ \chi_0 & & \chi_1 & & \chi_2 & & \chi_3 \end{matrix}$$

Here *a* is the lattice spacing, the unit cell in one dimension, and *k* is an index that labels the irreducible representation of the translation group. The process of symmetry adaptation is called 'forming Bloch functions.' To reassure that one is getting what one expects, let's see what combinations are generated for two specific values of *k: 0* and /a:

$$\Psi_0 = \sum_n e^0\chi_n = \sum_n \chi_n = \chi_0 + \chi_1 + \chi_2 + \chi_3 +$$

$$\Psi_{\pi/a} = \sum_n e^{i\pi n}\chi_n = \sum_n (-1)^n\chi_n = \chi_0 - \chi_1 + \chi_2 - \chi_3 +$$

The wave function corresponding to k=0 is the most bonding one, the one for k= /a the top of the band. For other values of k, we get the other levels in the band. Therefore, k counts nodes: The larger the absolute value of k, the more nodes there are in the wave function. But one has to be careful; there is a range of k and if one goes outside of it, one does not get a new wave function, but rather repeats an old one. The unique values of *k* are in the interval /a.

How many values of *k* are there? As many as the number of translations in the crystal or, alternatively, as many as there are microscopic unit cells in the macroscopic crystal. So let us say Avogadro's number. There is an energy level for each value of k (actually a degenerate pair of levels for each pair of positive and negative k values. There is an theorem that states that E(k)=E(-k). Most representations of E(k) do not give the redundant E(-k), but plot E(|k|) and label it as E(k). In addition, the allowed values of k are equally spaced in the space of k, which is called reciprocal or momentum space. Remarkably, *k* is not only a symmetry label and a node counter, but it is also a wave vector, and so measures momentum. The range of allowed k is called 'the Brillouin zone'.

The band of the infinite chain is repeated at left in the figure below. Alternatively it can be drawn as an *E(k) vs. k* diagram at the right. Graphs of *E(k) vs. k* are called band structures. They can be much more complicated than this simple one. *k* is quantized, and there is a finite but large number of levels in the diagram at right. The reason it looks continuous is that this is a fine dot matrix printer; there are Avogadro's number of points and so it's no wonder we see a line.

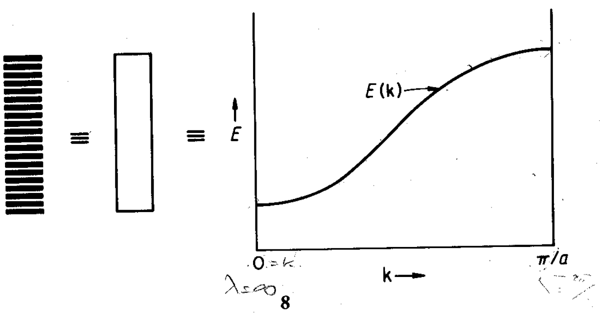

Figure: Band structure of a one-dimensional infinite chain of s orbitals

Band Widths

One very important feature of a band is its *dispersion,* or *bandwidth,* the difference in energy between the highest and lowest levels in the band. What determines the width of bands? The same thing that determines the splitting of levels in H_2, namely the overlap between the interacting orbitals. The greater the overlap between neighbours, the greater the bandwidth. The figure below illustrates this in detail for a chain of H atoms spaced 3, 2, and 1 Å apart. That the bands extend unsymmetrical around their origin, the energy of a free H atom at -13.6 eV, is consequence of the inclusion of overlap in the calculations:

$$E_{\pm} = \frac{H_{AA} \pm H_{AB}}{1 \pm S_{AB}}$$

The bonding E_+ combination is less stabilised than the antibonding one E_- is destabilised. There are nontrivial consequences, for this is the source of four-electron repulsions and steric effects in one-electron theories.

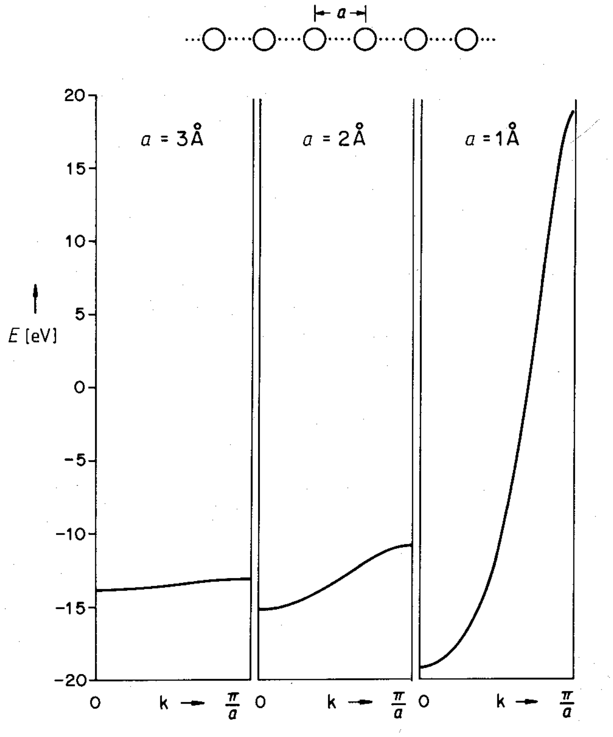

Figure: the band structure of a chain of hydrogen atoms spaced 3, 2 and 1 A apart. The energy of an isolated H atom is - 13.6 eV.

Another interesting feature of bands is how they run. $_k$= e^{ikna} $_n$ applies in general; it does not say anything about the energy of the orbitals at the centre of the zone *(k=0)* relative to those at the edges *(k=* /a). For a chain of H atoms it is clear that *E(k=0)*

< *E(k=* /a). However, consider a chain of p functions as sketched below. The same combinations as for the H case are given to us by the translation symmetry, but now it is clearly *k=0* that is the most antibonding way to put together a chain of p orbitals. The band of s functions for the hydrogen chain runs up, the band p orbitals runs down (from zone centre to zone edge). In general, the topology of orbital interactions determines which way bands run. To summarise: the bandwidth is set by inter-unit-cell overlap, and the way bands run is determined by the topology of that overlap.

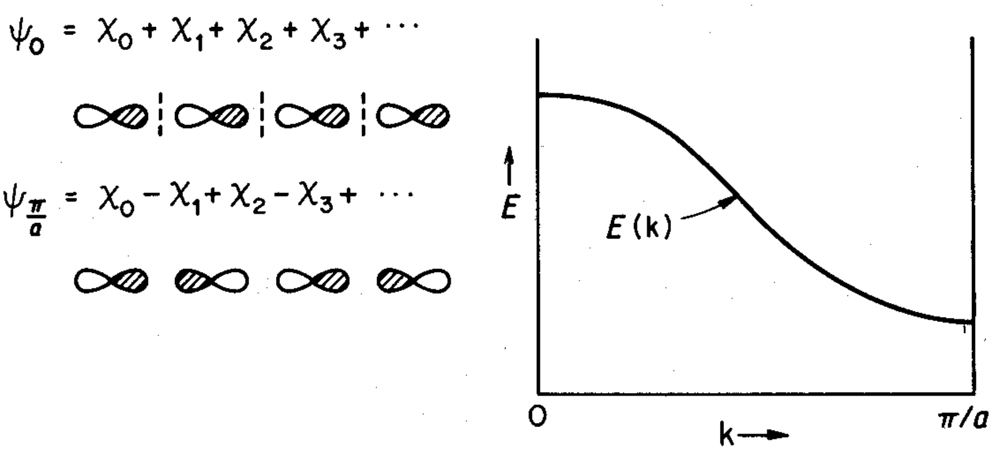

Figure: Band structure of a one-dimensional infinite chain of p orbitals

The Fermi Level

If there are Avogadro's number of unit cells, there will be Avogadro's number of levels in each bond. And each level has a place for two electrons. The Fermi level is the highest occupied molecular orbital (HOMO). There are materials that have their Fermi level in a band, i.e. there is a zero band gap between filled and empty levels and these systems are metals. Other materials have a substantial gap: they are semiconductors or insulators. In general, conductivity is not a simple phenomenon to explain, and the Fermi level cuts one or more bands. One must beware, however, of (1) distortions that open gaps at the Fermi level and (2) very narrow bands cut by the Fermi level because these will lead to localised states, not to good conductivity.

1.2.3. Electronic states in two dimensions

Nothing much new happens if one moves from one to two dimensions, except that we must treat **k** as a vector with components in reciprocal space. To introduce some of these ideas, let's begin with a square lattice, defined by the translation vectors $\boldsymbol{a_1}$ and $\boldsymbol{a_2}$. Suppose there is an H 1s orbital on each lattice site. It turns out that the Schrödinger equation in the crystal factors into separate wave equations along the x and y axes, each of them identical to the one-dimensional equation for a linear chain. The range of both k_x and a k_y is between 0 and /***a***, ***a*** being the absolute value of $\boldsymbol{a_1}$. Some typical solutions are shown below.

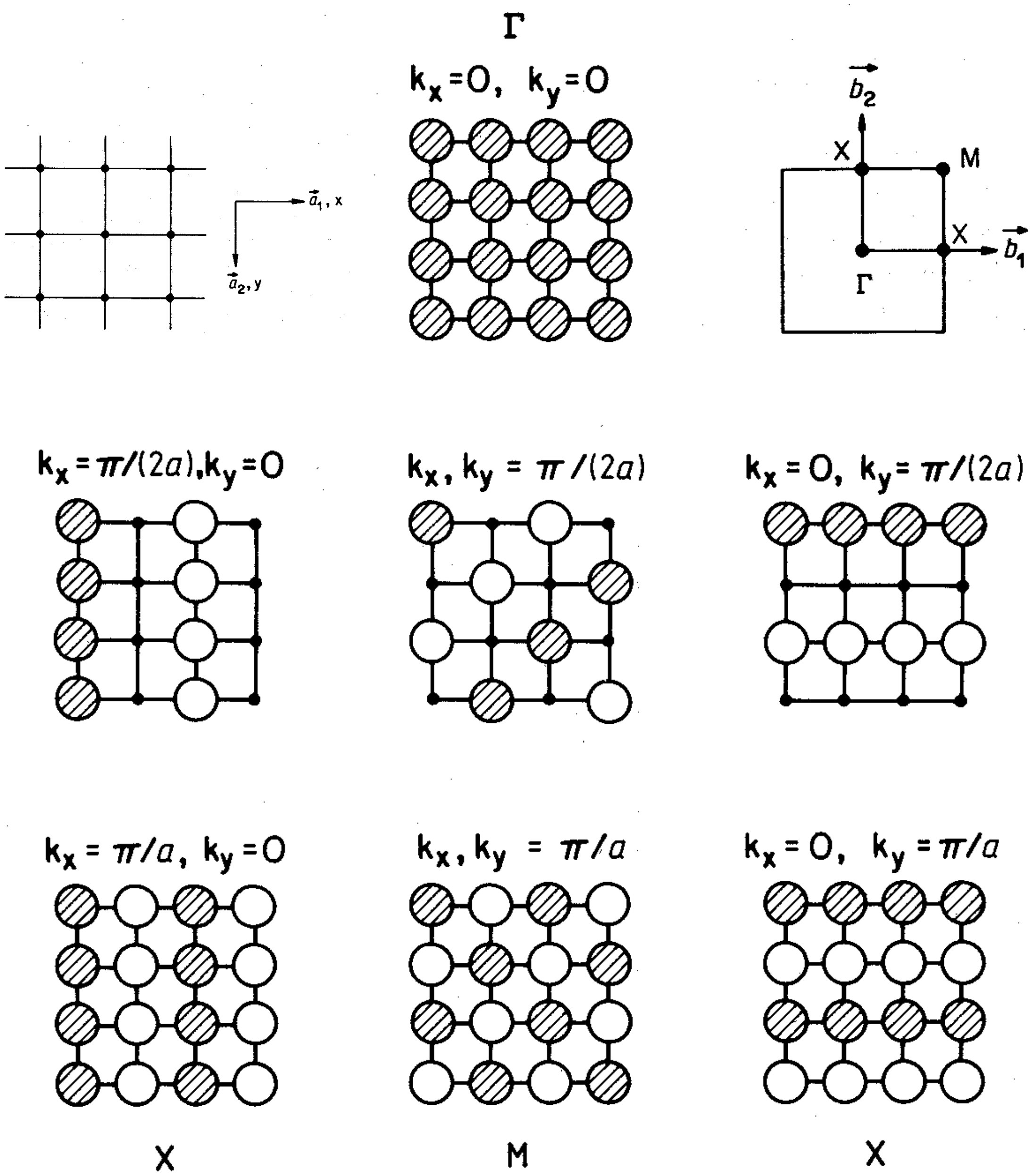

Figure: The s-orbitals overlap in two dimensions. At the top-left the translation vectors; at the top-right the vectors in reciprocal space.

What the construction shows is the vector nature of **k**. Consider the (k_x, k_y) = (/2a, /2a) and (/a, /a) solutions. A look at them reveals that they are waves running along a direction that is the vector sum of k_x and k_y, i.e., on a diagonal. The wavelength is inversely proportional to the magnitude of that vector. The space of k here is defined by two vectors **b**$_1$ and **b**$_2$, and the range of allowed k, the Brillouin zone, is a square. Certain special values of k are given names: =(0,0) is the zone centre, =(/a ,0)=(0, /a) and = (/a, /a) These are at the top-right of the figure. It is difficult to show the energy levels *E(r)* for all r. So what one typically does is to illustrate the evolution of *E* along certain lines in the Brillouin zone. Some obvious ones are from to , from to and from M back to . From the figure it is clear that *M* is the highest energy wave function, and that X is pretty much nonbonding, since it has as many bonding interactions (along y) as it does antibonding ones (along x). So we would expect the band structure to look like the figure below. In fact this is a computed band structure for a hydrogen lattice with *a=2.0.*

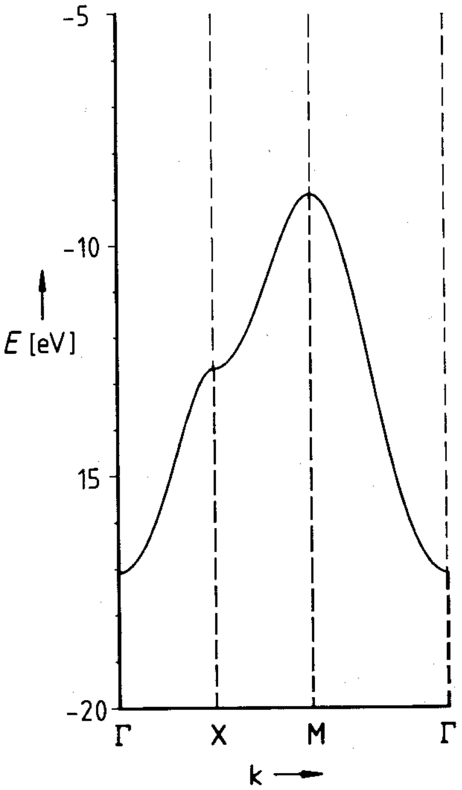

Figure: The band structure of a square lattice of H atoms at a separation of 2 Å.

Let's now put some p orbitals on the square lattice, with the direction perpendicular to the lattice taken as z. The 2p$_z$ orbitals are separated from 2p$_y$ and 2p$_x$ by their symmetry. They will give a band structure similar to that of the s orbital, since the topology of the interaction of these orbitals is similar. The 2p$_y$ and 2p$_x$ orbitals present a somewhat different problem. Shown below are the symmetry-adapted combinations of each at , X, Y, and M. Y is by symmetry equivalent to X; the difference is just in the propagation along x or y. At the x and y combinations are antibonding and bonding; at X they are and bonding (one of them), and and antibonding (the other). At M they are both bonding, antibonding. It is also clear that the x, y combinations are degenerate at and M and nondegenerate at X and Y.

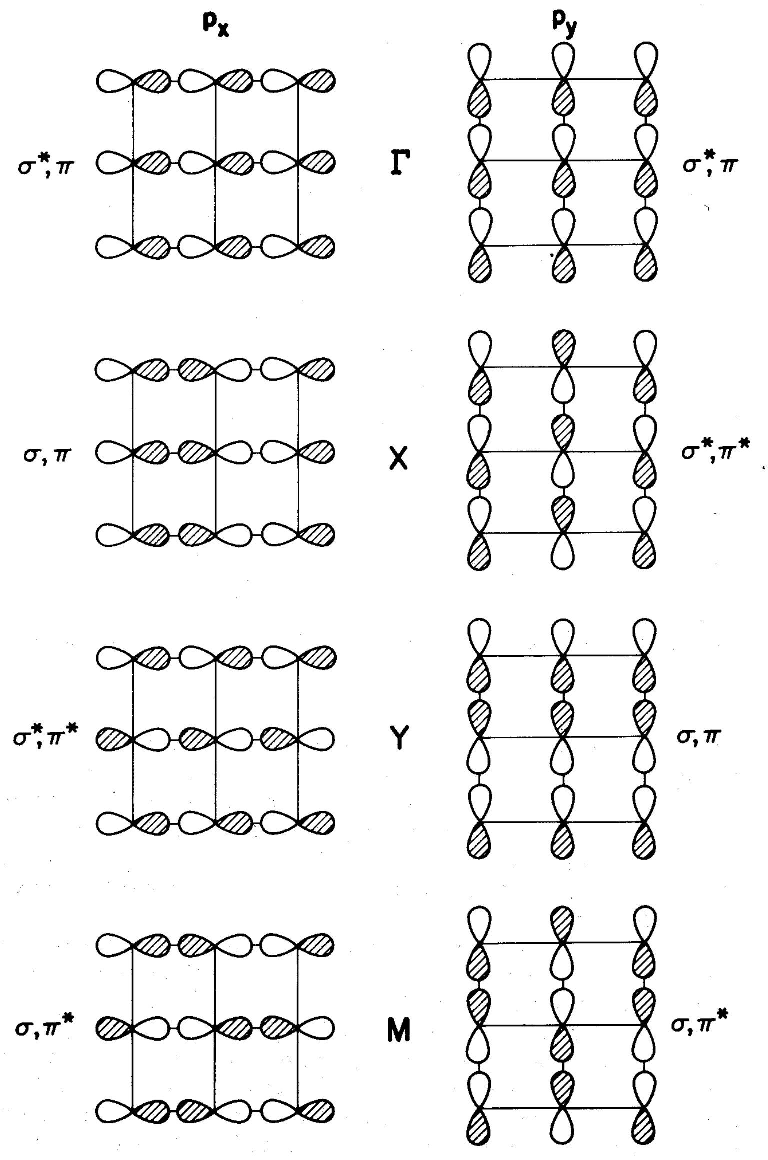

Figure: The p-orbitals overlap in two dimensions. On the left the bonding in the x-direction is shown, on the right the bonding in the y-direction.

Putting in the estimate that bonding is more important than bonding, one can order these special symmetry points of the Brillouin zone in energy and draw a qualitative band structure as given in the figure below. The actual appearance of any real band structure will depend on the lattice spacing. Band dispersions will increase with short contacts, and complications due to s, p mixing will arise. Roughly, however, *any* square lattice, for example a square overlayer of atoms or molecules absorbed on Ni(100), will have these orbitals. The right of the figure gives the actual calculation of a square lattice of CO molecules on Ni(100).

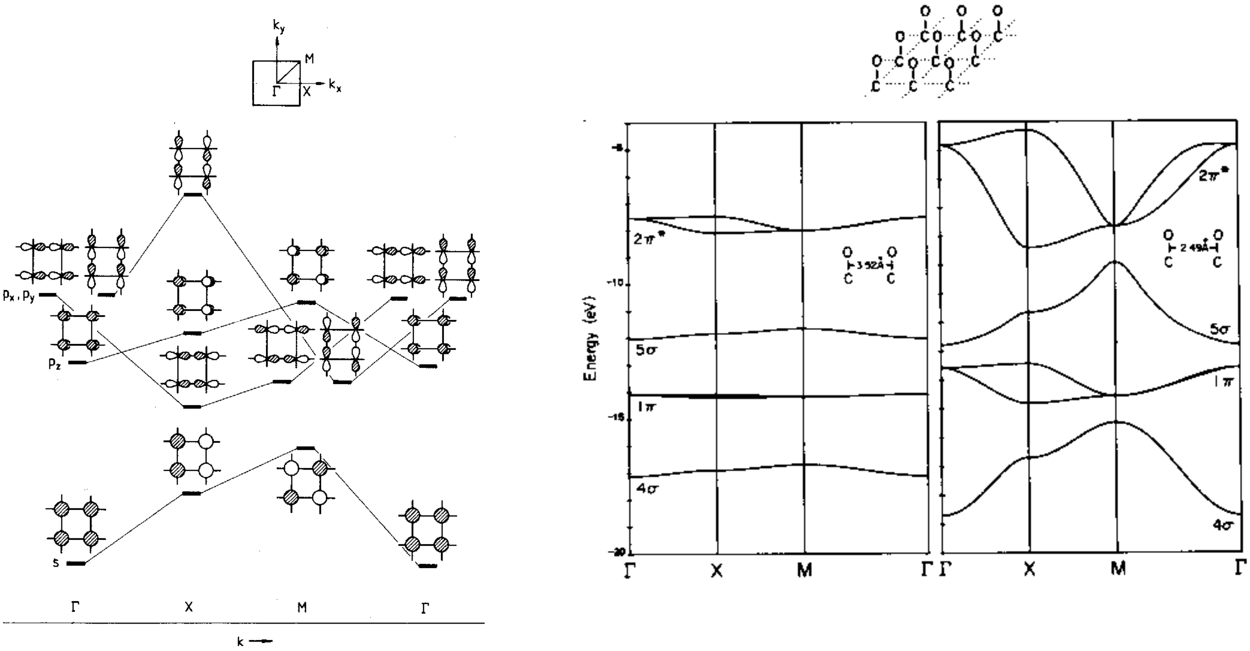

Figure : Left: Schematic band structure of a planar square lattice of atoms bearing s and p orbitals. The s and p levels are assumed to have a large enough separation that they do not overlap; Right: Band structures of square monolayers of CO at two separations, corresponding to 1/2 and full coverage of a Ni(100) surface.

Exercise: Consider a one-dimensional chain of copper atoms that runs in the z-direction.
Each copper atom contains its five 3d-orbitals given below.
Draw the band structure for each 3d sub-band.
What kind of bonding occurs for each of the sub-bands?
How does this affect the dispersion of the bands?

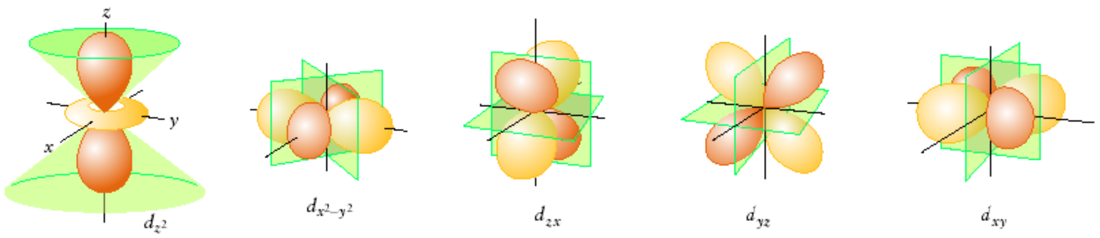

1.2.4. Density of States

In the solid, or on a surface, one has to deal with a very large number of levels or states. If there are *n* atomic orbitals (basis functions) in the unit cell, generating n molecular orbitals, and if in our macroscopic crystal there are *N* unit cells *(N* is a number that approaches Avogadro's number), then we will have N*n* crystal levels. Many of these are occupied and, roughly speaking, they are jammed into the same energy interval in which we find the molecular or unit cell levels. In a discrete molecule, we are able to single out one orbital or a small subgroup of orbitals as being the frontier, or valence orbitals of the molecules, responsible for its geometry, reactivity, etc. There is no way in the world that a single level among the myriad *Nn* orbitals of the crystal will have the power to direct a geometry or reactivity.

There is, however, a way to retrieve a frontier orbital in the solid state. We cannot think about a single level, but instead we can talk about bunches of levels. There are many ways to group levels, but one pretty obvious way is to look at all the levels in a given energy interval. The density of states *(DOS)* is the number of levels between E and E+dE.

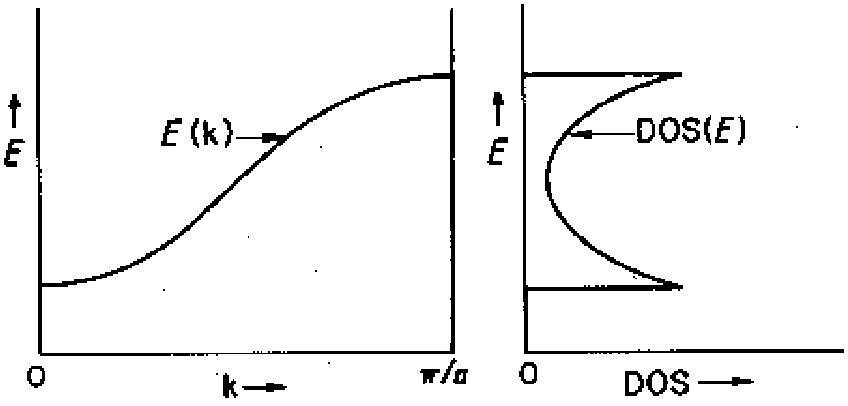

Figure: Band structure and Density of States of a chain of hydrogen atoms.

For a simple band of a chain of hydrogen atoms, the *DOS* curve takes on the shape as indicated above. Note that because the levels are equally spaced along the *k* axis and because the *E(k)* curve has a simple cosine shape, there are more states in a given energy interval at the top and bottom of this band. In general, DOS*(E)* is proportional to the inverse of the slope of *E(k) vs. k,* in other words the flatter the band, the greater the density of states at that energy.

The shapes of DOS curves are predictable from the band structures. In general, the detailed construction of these is a job best left to computers. The DOS curve counts levels. The integral of DOS up to the Fermi level is the total number of occupied MOs. Multiplied by two; it's the total number of electrons, so that the DOS curves plot the distribution of electrons in energy. One important aspect of the DOS curves is that they represent a return from reciprocal space to real space. The DOS is an average over the Brillouin zone, i.e., over all k that might give molecular orbitals at the specified energy. There is another aspect of the return to real space that is significant: one can sketch the approximate DOS of any material 'intuitively'. All that is involved is knowledge of the atoms, their approximate ionisation potentials and electronegativities, and some judgements as to the extent of inter-unit-cell overlap, often deducible from the structure.

1.2.5. Density Functional Theory and the local spin density approximation

Since the establishment of the density functional theorem (DFT), stating that the ground state energy can be expressed as a function of the electron density [Hohenberg and Kohn, 1964], and the practical implementation of this theorem in the local density approximation (LDA) [Kohn and Sham, 1965], solid state calculations based on this formalism have become important. This not only to determine the total energy but also to obtain a picture of the electronic structure in terms of the density of states, which in turn is used to analyse spectra. As in Hartree-Fock, the kinetic, nuclear and Hartree potentials are used. The difference is that exchange and correlation effects are described by a combined potential V_{xc}. All potentials are local functions of the electron density *n*. All complications are collected in the exchange-correlation potential, for which it is assumed that in a solid its value is equal to that of a homogeneous electron gas for a particular n. Thus for the spin-polarised version the potential is given as:

$$H = \sum_N \frac{p_{i(}^2}{2m} + \sum_N \frac{-Ze^2}{r_i} + \sum_j \int dx'\phi_j(x')\phi_j^*\ (x')\frac{1}{r-r'} + V_{xc}[n] \qquad \textbf{(2.1)}$$

It contains respectively the kinetic energy, the electrostatic interaction of the electrons with the nucleus of charge, the Hartree potential and the exchange-correlation potential. For V_{xc} several alternative formulations are used and the electronic structure and properties of solids are described with a number of alternative realisations of LDA. These methods vary in the use of plane waves or spherical waves, the use of fixed basis sets such as the linear combination of atomic orbitals (LCAO) and the use of the electron scattering formulation, such as real space multiple scattering. For each of these methods in general several computer codes exist. Some methods exist in versions for spin-polarised calculations, the inclusion of spin-orbit coupling and fully relativistic codes.

Web-exercise: A very useful web-page can be found at **the Electronic Structures Database:** http://cst-www.nrl.navy.mil/es-access.html
This database includes a large set of common systems, in particular the pure metals, some alloys, simple oxides, etc, from which the band structure and the density of states curves can be viewed and downloaded.
Example: Search for the density of states and the band structure of Cu (in the fcc structure).

Exercise: Search for the density of states and the band structure of TiO (in the NaCl structure).

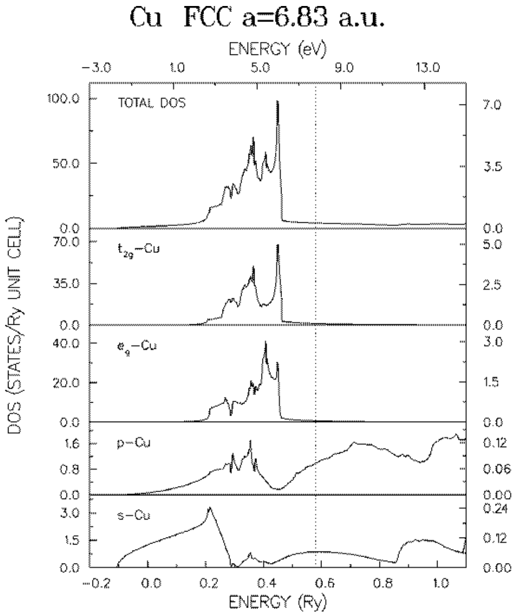

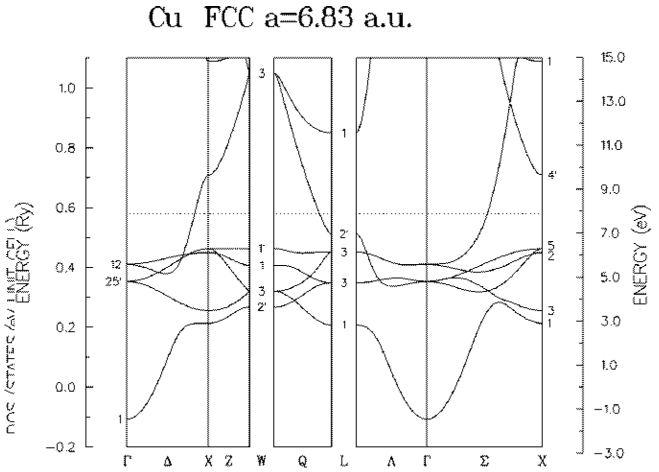

1.3. XANES

The single electron approximation as stated in section 1.3 gives an adequate simulation of the XANES spectral shape if the interactions between the electrons in the final state are relatively weak. This is the case for all K edges and to a very good degree also for all other edges with binding energies above 3 keV (with a few exceptions). We will assume this is correct and use the equivalence of I_{XAS} and the density of states (I_{XAS}~M^2) as a starting point.

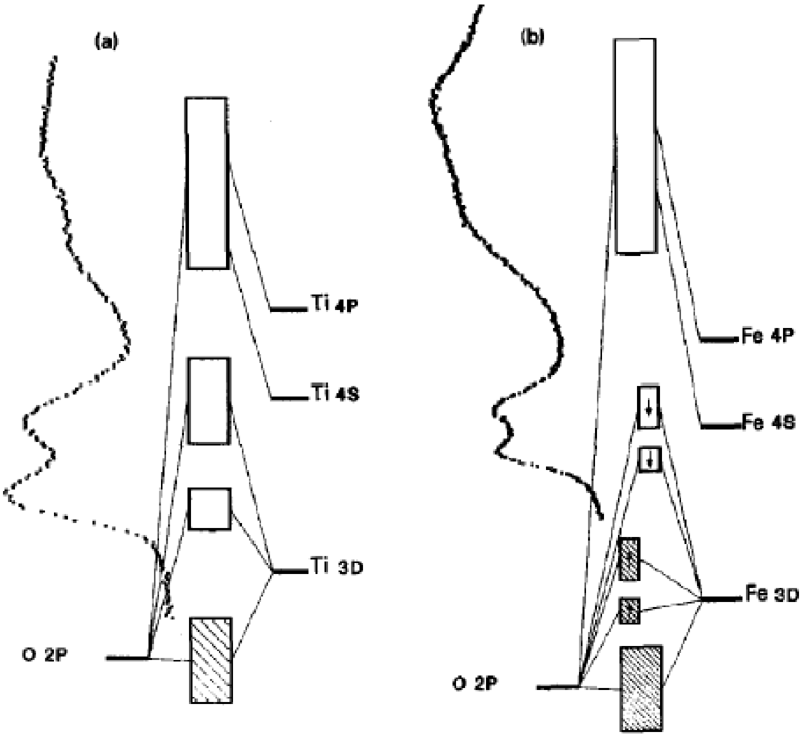

Figure: Schematic band picture of (a) a TiO_6*- cluster and (b) a* FeO_6*- cluster.* Ti^{4+} *in* TiO_2 *has an empty 3d band and* Fe^{3+} *in* Fe_2O_3 *contains a half filled 3d band.*

A usual picture to visualise the electronic structure of a transition metal compound, such as oxides and halides, is to describe the chemical bonding mainly as a bonding between the metal 4sp states and the ligand p states, forming a bonding combination, the valence band and empty antibonding combinations. The 3d states also contribute to the chemical bonding with the valence band that causes them to be antibonding in nature. This bonding, taking place in a (distorted) cubic crystal-line surrounding, causes the 3d states to be split into the so-called t_{2g} and e_g manifolds. This situation is visualised for a $Ti^{IV}O_6$ cluster in the figure above. For comparison the oxygen 1s X-ray absorption spectrum is given. On the right this picture is modified for a partly filled 3d band in a $Fe^{III}O_6$ cluster. The 3d band is split by the crystal field splitting and a large exchange splitting. This qualitative description of the electronics structure of transition metal compounds can be worked out quantitatively within DFT.

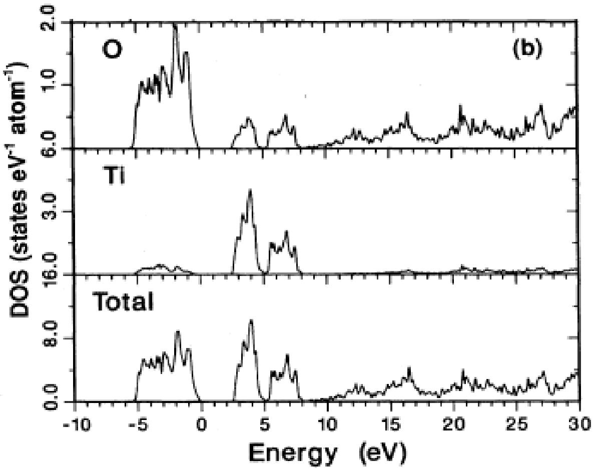

The picture of the left is a DFT calculation of the density of states of TiO_2. The total DOS is projected to oxygen (O) and titanium (Ti) respectively. The picture below shows the broadened oxygen DOS in comparison with the experimental spectrum. In line with the dipole selection rule only the oxygen p-projected DOS is used.

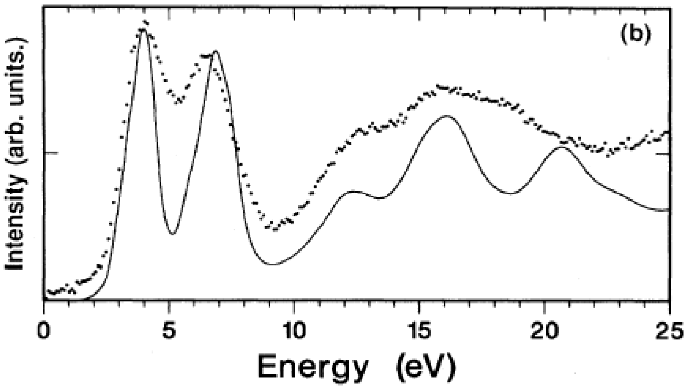

We assume that the density of states of complex systems is calculated using the DFT approximation. Programs to calculate the X-ray absorption spectral shape include FEFF, GNXAS and Wien2k. These and other software packages can be found at http://www.esrf.fr/computing/scientific/exafs/intro.html. In these programs, a number of approximations and assumptions are made. Below we will, in short, sketch some of the important conceptual issues. We will respectively discuss, (1.3.1) many body effects in the ground state, (1.3.2.) core hole effects, (1.3.3) multiplet effects, (1.3.4) the influence of the matrix element, (1.3.5) calculations over a large energy range, (1.3.6) approximations in the potential and (1.3.7) real space versus reciprocal space calculations.

1.3.1. Many Body Effects in the ground state

The use of the LDA to calculate the density of states is a rather poor approximation and a large number of improvements upon LDA exist. In particular, we would like to mention the generalized gradient approximation (GGA). The GW approach, the inclusion of the Coulomb interaction U into LDA, the inclusion of self-interaction corrections and the inclusion of orbital polarization effects. Essentially all these methods try to improve the LDA approximation towards the determination of the correct initial state and final state wave functions. Within the context of these lectures, we will not go into detail on these improvements that essentially deal with so-called many body effects. We would like to indicate that most XANES-programs use LDA as starting model. This implies that many body effects in the ground state are not treated properly. In case of correlated electron states, such as the 3d-band in transition metal systems, this can introduce errors in the edge region. A special type of final-state many-body effect is the multiplet effect as discussed in section 1.3.3.

1.3.2 Core hole effects

Following the final state rule, one has to calculate the distribution of empty states in the final state of the absorption process. The final state includes a core hole on the absorbing site. The inclusion of the core hole introduces a significantly larger unit cell in case of reciprocal space calculations. In case of real-space calculations, the inclusion of a core hole is straightforward and only the potential of the central atom is modified. It has been shown for many examples that the inclusion of the core hole improves the agreement with experiment.

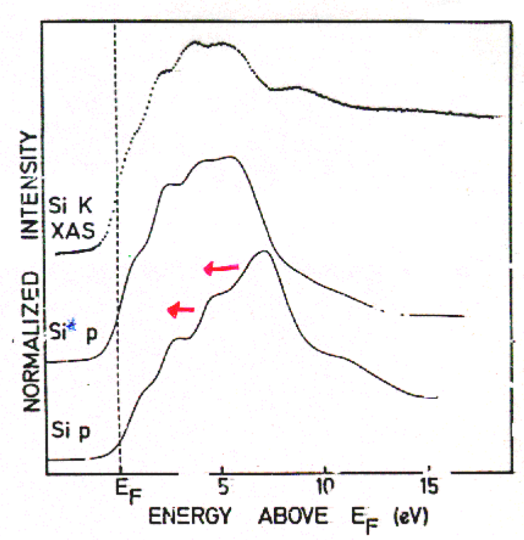

The figure on the left shows the silicon K edge of $TiSi_2$ (points at top). The Fermi level is indicated with the dashed line and set to 0 eV. The bottom curve is the silicon p-projected DOS as calculated from a DFT program. It can be seen that some agreement is obtained, but differences are also clear.

The middle spectrum also shows the silicon p-projected DOS, but in this case the core hole has been explicitly included into the calculations. One can observe a shift of the intensity to lower energy (due to the additional potential of the core hole) and the agreement with experiment is clearly improved. This example confirms the Final state rule. Note that in addition to the final state rule, there is also an initial state rule, which is a formal rule and states that the integrated intensity of an edge is given by the initial state. We will use this rule in the examples below.

1.3.3. *Multiplet effects*

The core hole that is part of the XANES final state does not only have an influence on the potential, but the core state also has a wave function. In case of a 1s core state, this wave function is spherically symmetric (caries no orbital momentum) and sits close to the nucleus, hence far from the valence electrons. This implies that for 1s core holes one can neglect the effects of the core wave function overlap. In case of 2s and 3s wave functions the overlap is larger but the only effect that plays a role is the spin-up or spin-down character of the core hole. The spin-moment of the core hole interacts with the valence electrons (or holes) giving rise to an exchange splitting in 2s and 3s XANES. The same exchange interaction plays a role in 2s and 3s XPS spectra, which are more often studied than their XANES counterparts.

Things become dramatically more complex in those cases where a core hole carries an orbital momentum. Very well known is the core hole spin-orbit coupling that separates the 2p spectra into their $2p_{3/2}$ (L_3) and $2p_{1/2}$ (L_2) parts. But this is not all: the 2p wave function can have significant overlap with the valence electrons. In case of 5d-systems, the 2p5d overlap is small and can, in first approximation, be neglected. However in case of 3d-systems, the 2p3d overlap is significant and in fact completely modifies the spectral shape. The term 'Multiplet effect' is used to indicate this overlap. The largest effect of core-valence overlap occurs for relatively shallow core states and multiplet effects do play a much larger role for soft X-ray absorption than for hard X-ray absorption. A detailed discussion of their inclusion into XANES simulations is therefore given in chapter 3.

1.3.4. *The influence of the Matrix element*

The Golden Rule states that XANES is given by the squared matrix element (M^2) multiplied by the density of states. In many cases, the matrix element is (assumed to be) constant over the XANES energy range and the density of states is directly compared with the XANES spectrum. If one uses the element and orbital momentum projected DOS the agreement between DOS and XANES is often very good, but this is not a general result. It is therefore preferable to include the matrix elements into the calculation of the XANES spectral shapes. At this moment, most XANES codes include the matrix elements explicitly.

1.3.5. *Calculations over a large energy range*

Multiple scattering is particularly appropriate for the calculation of the empty states, because they can be easily calculated for arbitrary large energies. Multiple scattering calculations are usually performed with the Green function approach, where the Green function describes the propagation of the electron in the solid, which is scattered by the atoms surrounding the absorbing atom. Band structure codes are used to calculate the optimized structure and as such need only to calculate the occupied electron states, i.e. the electron distribution and the accompanying potential. Most of these band structure codes are not easily applicable to the calculation of large energy ranges of unoccupied states. In particular, codes that make use of limited basis sets can be accurate for the occupied states, but inaccurate for unoccupied states, in particular at energies more than 10-20 eV above the Fermi level. Recently some elegant codes have been written that circumvent this problem and are able to combine accurate band structure codes to optimize the structure and special projection operators to calculate the empty states at all energies.

1.3.6. Approximations in the potential

The approximations made to the electronic potential that is used in the calculations play an important role in their development and improvements. Some fifteen years ago, most DFT codes used various approximations to the potential, such as the atomic-sphere-approximation in LMTO and the muffin-tin approximation in many other codes. For example, the FEFF code still operates under the muffin-tin approximation.

1.3.7. Real Space versus Reciprocal space calculations

Particularly for hard X-rays, the absorption spectra are calculated with a real space multiple scattering formalism. It has been shown that the real space multiple scattering result is identical to the result obtained from band structure. Because the calculation is performed in real space, the calculations can relatively easily be carried out for disordered systems. The core hole potential on the absorbing atom can be added directly and one can carry out the multiple scattering in steps of growing cluster size. These advantages make FEFF the most popular code for XANES calculations, despite the limitations in the accuracy of the potential. For comparison to experiment, both band structure calculations and multiple scattering results can be treated on the same footing, using the 'density of states' picture as guide.

An important program to analyse XAFS spectra is FEFF. You can find a course on FEFF on the following webpages: http://leonardo.phys.washington.edu/~ravel/course/

1.4. XANES spectral shape analysis

We have seen that the oxygen K edge x-ray absorption spectrum of TiO_2 can be simulated with the oxygen p-projected DOS as calculated by DFT. (Actually in case of the oxygen K edge of TiO_2, the core hole effect is small and can be neglected). The similarity between x-ray absorption and the projected DOS allows a qualitative analysis of the spectral shapes without the actual inclusion of calculations.

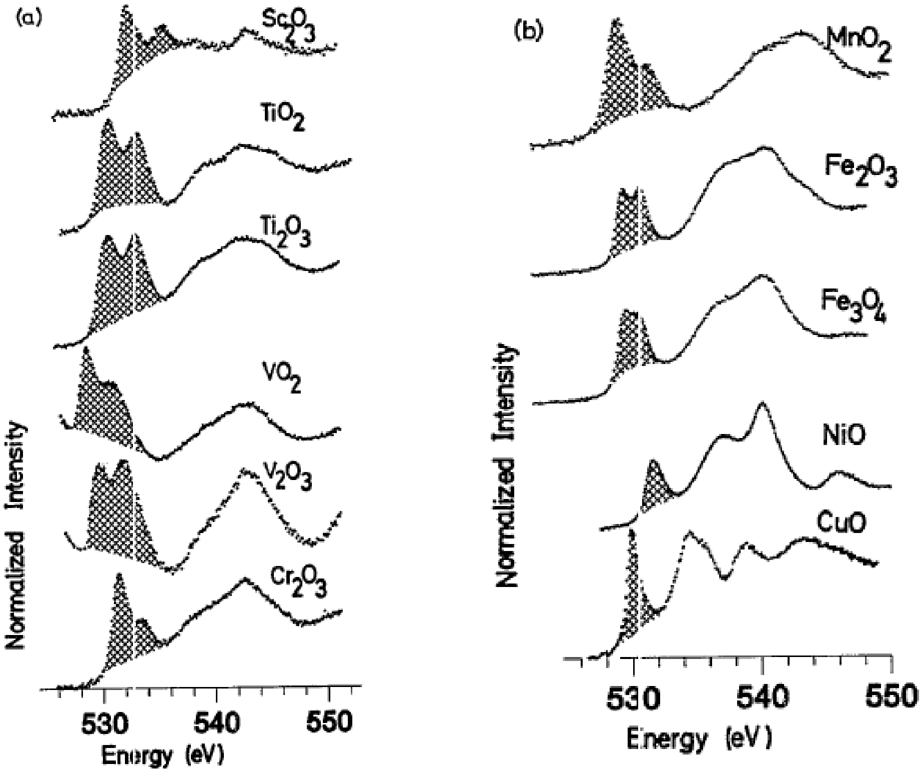

Above we give the oxygen K edges of a series of transition metal oxides, ranging from Sc_2O_3 to CuO. Sc_2O_3 contains Sc^{III} and is formally a $3d^0$ compound, i.e. it has all ten 3d states empty. CuO is a $3d^{10}$ compound and has all ten 3d-states occupied. One can distinguish two regions in the spectrum: the dashed region is related to the empty 3d-band, actually to the oxygen p-projected DOS inside this 3d-band. The structure at 540 eV is related to the empty 4s and 4p states of copper. The dashed region is split by the cubic crystal field splitting and, in first approximation, one observes two peaks that are respectively related to the t_{2g} (xy, xz, yz) and eg (z^2, x^2-y^2) orbitals.

Using the initial state rule, one can determine the total intensity of the metal 4sp-band (or in fact the amount oxygen p-projected DOS to it). The integrated signal of the 3d-band gives the total amount oxygen p-projected DOS in the 3d-band. If one assumes that the bonding follows the same trend for the 4sp states than for the 3d-states, one can derive the number of empty 3d-states from the ratio of the 3d-peaks with respect to the 4sp-peaks.

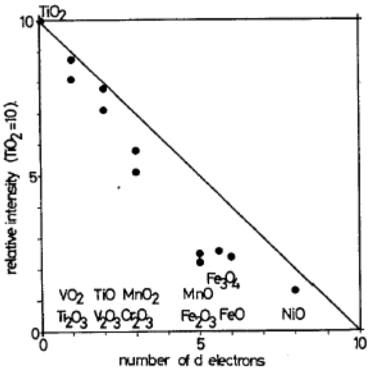

This is indicated in the figure. It can be observed that this trend is roughly confirmed, but one finds too low intensity in the middle of the 3d-series. This indicates that the 3d-electrons in the middle of the series do (relatively) show less hybridization with the oxygen 2p-bands.

An important set of XANES studies involves the 1s X-ray absorption spectra (K edges) of the 3d-metals. We will discuss respectively the shape, the energy position and the white line intensity of the 1s XANES spectra. The 1s edges of the 3d transition metals have energies ranging from about 4 to 9 keV. Self-consistent full potential multiple scattering calculations show that the complete spectral shape of TiO_2 is nicely reproduced and it can be concluded that the 1s XANES of 3d transition metals does indeed correspond to the metal p-projected density of state. In addition, the pre-edge region is found to be an addition of dipole and quadrupole transitions.

In many applications, the systems studied are amorphous or heterogeneous. The metal 1s edges do show fine structure and edge shifts that can be used without the explicit calculation of the density of states. For example, the Fe^{III} edges are shifted to higher energy with respect to the Fe^{II} edges. The shift to higher energies with higher valence is a general phenomenon that can be used to determine the valence of 3d transition metals in unknown systems.

1.4.1. The energy position of X-ray absorption edges

It is not a trivial task to determine the energy position of a XANES *edge*. There are, at least, three different methods to define the energy of the edge.

a. The inflection point
b. The energy where the intensity is 50% of the edge maximum
c. The average of the energies at 20% and 80% of the edge maximum

The inflection point is well defined and can be accurately determined from the maximum of the first derivative. In case of a single, non-structured edge the methods (a) to (c) all find exactly the same energy. The situation becomes more complicated with a spectrum for which a clear shoulder is visible on the leading edge. For example, iron metal has an edge on which a clear shoulder is visible. The inflection point might loose its meaning in such a case and, in fact, there can be two inflection points. Also the inflection point can be different from the 50% point, and from the average of the 20% and 80% point. There is no clear criterion to decide which procedure should be followed. Much depends on the spectral details of the observed spectra. The best procedure would perhaps be the use of two or three methods for the edge determination. Differences in the values from the three methods would immediately indicate the presence of additional structure. The edge position E_0 does not directly relate to a physical parameter. Fermi level E_F corresponds to the highest occupied (or lowest unoccupied) state and, formally, E_0 is related to the vacuum level, i.e. the energy at which the electron would have zero kinetic energy. The energy difference between E_F and E_0 is the work function. The main problem is the determination and use of E_0 in an experimental spectrum. Formally E_0 can be determined from a comparison to a theoretical density of states and correcting for the work function. Theoretical simulations are however not always available and one has to resort to a determination of E_0 from the experimental spectrum itself. This can lead to the following possible determinations of E_0:

a'. The energy of the Fermi level, corrected for the work function (from an alignment with theory)
b'. The onset or energy position of the lowest (pre)peak visible in the spectrum
c'. The onset of the edge
d'. The edge itself.
e'. The energy that is found from an EXAFS fitting procedure.

In many papers the value of E_0 is determined from an EXAFS fitting procedure (e'), in which case it is more often treated as a free fitting parameter, than as an energy that indicates the energy of zero kinetic energy. The use of pre-edges for the determination of E_0 is complicated by the fact that they could be affected by so-called 'excitonic effects', implying that these excitonic states are states that occur below the (ground state) Fermi level due to the core hole potential. Recent calculations of the K edges of the 3d transition metals show that most of the pre-edge intensity comes from dipole transitions to the 3d-band, i.e. these pre-edges are no excitons and the Fermi level is positioned below these pre-edges. The large variety in E_0 determinations makes it impossible to compare values blindly from one paper to another.

Despite the variety of procedures to determine the edge energy and E_0, the use of consistent procedures to determine energy positions can lead to clear trends of these energies with the formal valence of the system. It is found that a linear relation exists between the edge position and the formal oxidation state. In addition, a linear relation was found between the pre-edge energy and the formal oxidation state. The slope of the pre-edge and edge energies is however different, respectively about 2 eV/valence for the edge energy and 0.6 eV/valence for the pre-edge energy. This also implies that the energy difference between the pre-edge position and the edge position is linear with the formal oxidation state. An interesting question relates to the relative energy position of the edge and peak position of octahedral and tetrahedral sites. In the case of iron, equivalent energy positions are found, whereas for example in the case titanium, copper and aluminium a systematic shift is observed with the tetrahedral peak shifted by approximately 1 eV in the case of copper.

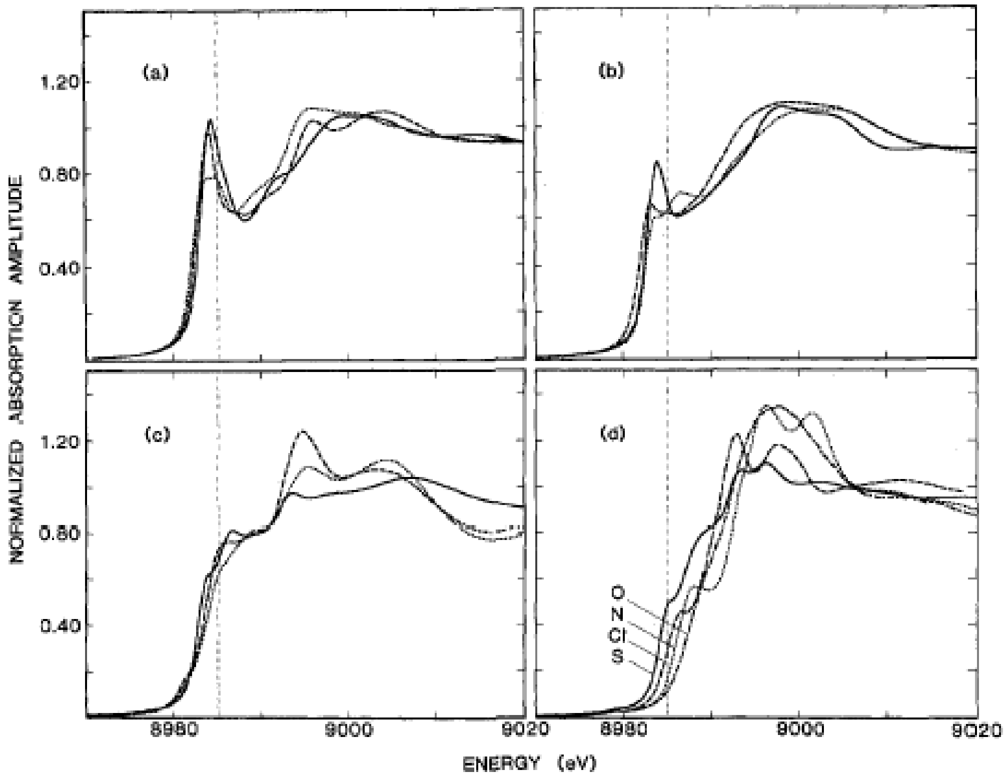

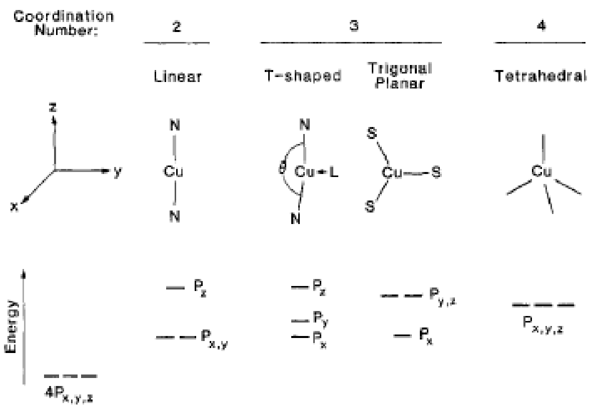

The spectra above give an overview of copper complexes. (a), (b) and (c) show Cu^I complexes in respectively 2-fold, 3-fold and 4-fold surroundings. Image (d) shows Cu^{II} spectra for various ligands. One observes a shift between the formal valences Cu^I and Cu^{II}, but it can be seen that a number of other variations play a crucial role. In particular the chemical nature of the neighbour atoms plays an important role as can be seen in figure d.

The large variation of spectral shapes as given above confirms the difficulty of determining a precise criterion for the edge position E_0. The authors of this figure did choose the inflection point of the first 'structure' as criterion (as can best be seen in the indicated trend in figure d) and for these spectra that indeed seems the most obvious choice.

1.4.2. *The intensity of the white line*

We have discussed that the XANES spectral shape reflects the density of empty states. An important question about the electronic state of a number of different problems (catalysis, electrochemistry, alloys, membranes, material science) is its number of occupied d-electrons. It would be very important if one could derive the number of occupied d-electrons from XANES. Using the dipole selection rule, this implies that one need to use 2p (or 3p) core states to probe the d-band. In the case of 3d-systems this poses a problem because the 2p core states occur at the soft X-ray range between 400 and 900 eV. It will be shown in chapter 3 that their spectral shape is completely dominated by multiplet effects, but that careful analysis still allows the determination of the occupation of the 3d-band. The 1s core states are excited into 4p and higher p-orbitals. As such, the K edges do not probe the occupation of the 3d-states. It will be shown below that the pre-edge intensity probes the 3d4p mixing and not the 3d occupation.

In the case of 4d and 5d systems, the L_3 and L_2 edges are separated by a relatively large energy that allows for the separate determination of the L_3 and L_2 white line intensity. One subtracts the edge jump, for example from a reference material with full d-band and as such one determines values for the L_3 and L_2 white line area that is related to the empty 3d-states. This allows one to determine a (relative) scale for the number of empty d-states. This technique has often been used, for example for the determination of the d-occupancy in binary alloys and to compare metals with compounds. In the case of catalysis research, it can be very useful to measure the white line intensity under reaction conditions or for example to study the effects of oxidation and reduction. In addition, it is one of the few probes to study the effect of hydrogen bonding.

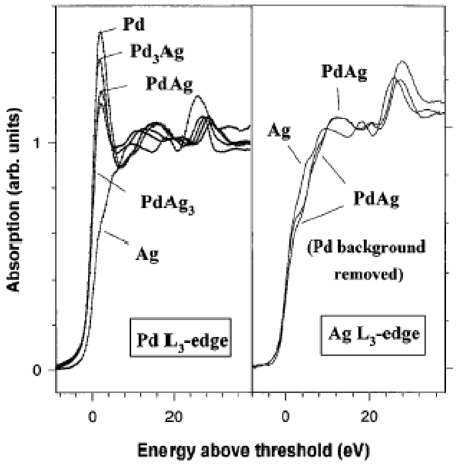

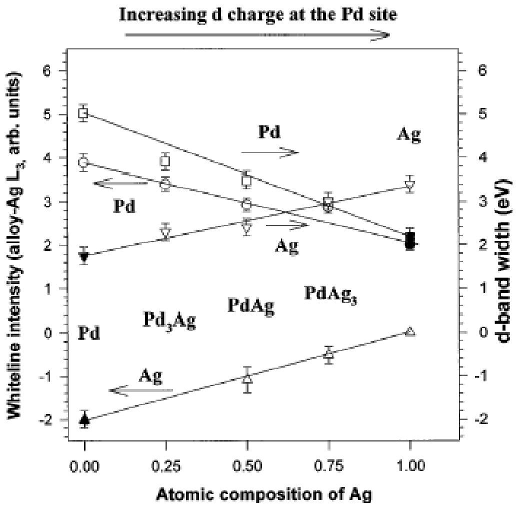

An example is given in the figure above. The Pd 2p3/2 edge is given for Pd and a number of PdAg alloys. One observes that the Pd white line decreases which indicates that the number of holes in the Pd 4d-band decreases. The white line intensity as given in the right figure decreases linearly with the silver content indicating that the 4d band is filling up. (In the same paper it was found that the amount of sp-character compensates the amount of 4d-character lost).

The fact that one can measure both the L_3 and the L_2 edge yields additional information. In principle the L_3 edge and the L_2 edge probe the same 5d (or 4d) density of states. One observes however that the L_3 edge usually has larger white line intensity than the L_2 edge. The reason can be found in relativistic effects. The 5d spin-orbit coupling splits the 5d-valence band into two sub-bands. Most papers that analyze the 2p edges of the 5d-elements assume that the $2p_{1/2}5d_{3/2}$, $2p_{3/2}5d_{5/2}$ and $2p_{3/2}5d_{3/2}$ transitions are possible. Following band structure results on Pt, a fixed ratio is assumed for these three transitions. The ratio between the $2p_{3/2}5d_{5/2}$ and $2p_{3/2}5d_{3/2}$ transitions is assumed to be 6:1. Detailed analysis shows that the $2p_{1/2}5d_{5/2}$ transition is not completely forbidden. This implies that even in case of a completely filled $5d_{3/2}$ band (for example Pt metal), there will be a non-zero white line intensity related to the $2p_{1/2}5d_{5/2}$ transition at the L_2 edge.

1.4.3. Peaks at higher energies in the XANES region

In most studies, only the pre-edge and edge region of the XANES spectrum are used. Some studies use in addition spectral features at higher energies. A well-known example is the use of the $1/R^2$ rule, which relates the energy of a peak in the XANES with the distance R between the absorbing atom and its neighbours. In a sense this is a scattering (EXAFS) feature in the XANES region. The scattering vector k is proportional to E_k. In the course on EXAFS (ASSSM lectures) it has been shown that within the single scattering approximation the distance R is inversely proportional to the scattering vector k, yielding as a result the $1/R^2$ rule. In fact, some additional approximations must be valid, such as small variations in the phase shifts. The $1/R^2$ rule has been applied successfully for the determination of bond lengths in (adsorbed) small molecules, but it has been demonstrated empirically that in general the rule is not very accurate.

1.4.4. The pre-edge region

The pre-edge region of the transition metal 1s edges has led to a number of debates regarding the quadrupole and/or dipole nature and possible excitonic effects. The pre-edge region is related to transitions to the 3d-bands. Both direct 1s3d-quadrupole transitions and dipole transitions to 4p-character hybridized with the 3d-band are possible. For the quadrupole transitions the matrix elements are less than 1% of the dipole transition, but on the other hand the amount of 3d-character is by far larger than the p-character. This can make, depending on the particular system, the contributions of quadrupole and dipole transitions equivalent in intensity. A direct manner to check the nature of the transitions is to measure the polarization dependence that is different for quadrupole respectively dipole transitions.

The intensity of the pre-edge region is much larger for compounds in which the metal site has tetrahedral symmetry than for octahedral systems. In tetrahedral systems the local mixing of p and d nature is symmetry allowed, while for a system with inversion symmetry such as octahedral symmetry it is 'forbidden'. This rule is relaxed in the solid and if the density of states is calculated one finds small admixtures of p-states into the 3d-band even for perfect octahedral systems. This admixture is less than for tetrahedral systems which explains the small pre-edge. p-character will be mixed into the 3d-band, if an octahedral metal site is distorted, the amount depending on the particular distortion For example, it has been shown that a roughly linear relationship exists between the bond angle variance (a measure of the distortion) and the pre-edge intensity relative to the step.

The figure below shows Fe K-edge XAS spectra, pre-edge fits, and theoretical analysis and simulation of octahedral high-spin Fe^{III} complexes. Fe K-edge spectra of (A) FeF_3 (solid), $FeCl_3$, $FeBr_3$, and a $FeCl_6$-complex and (B) other Fe-complexes. The insets are expansions of the pre-edge region with the normalized absorption scaled to 0.1 in each case. (C) gives a fit to the Fe K-edge pre-edge region and (D) a systematic analysis of the octahedral pre-edge features including the effect of the ligand field on the electric quadrupole intensity, the effects due to covalency. (E) gives a theoretical simulation of the pre-edge region. This analysis in fact uses multiplets that will be discussed in chapter 3, but in case of octahedral high-spin Fe^{III} complexes the multiplets results are similar to a DOS interpretation of the pre-edge and edge region.

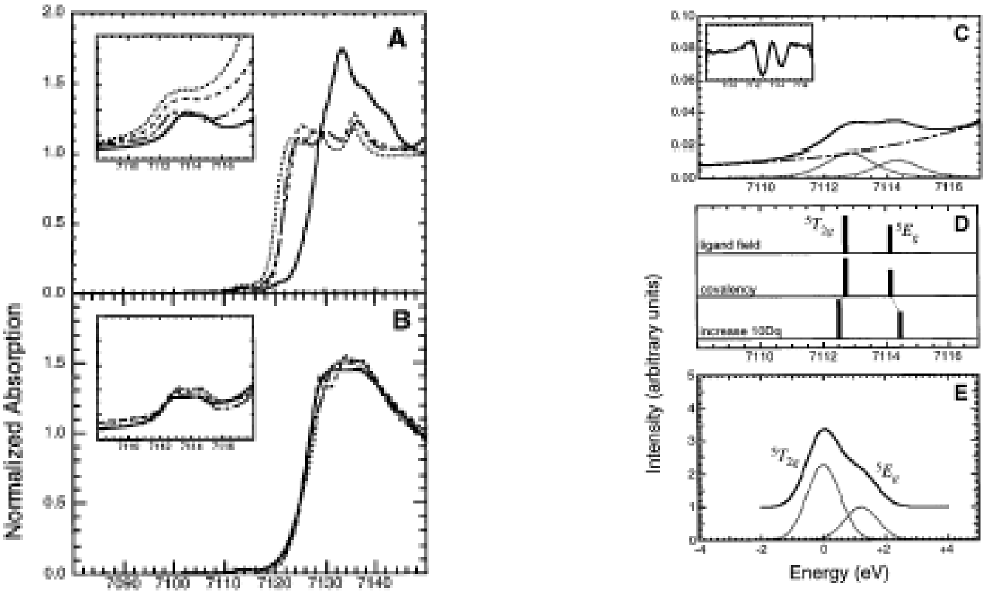

Multiplets in X-ray Spectroscopy

lectures ICTP 2004, by Frank de Groot

2. Multiplet effects

This chapter deals with atomic multiplet effects in x-ray spectroscopy. Some aspects of atomic multiplet theory has been discussed already in the lectures on theory (angular moment coupling) and on UV-VIS spectroscopy.

2.1. Why is multiplet theory needed?

In the case of an x-ray absorption transition to states where the interaction between the electrons is strong (strongly correlated or localised states), like the 3*d* states of transition metal ions or the 4*f* states of rare earths, the one-electron approximation, say DFT, does not hold. The interaction between the electrons, as well as the interaction of the electrons with the core-hole after the absorption process, has to be taken into account explicitly. Actually, all systems that contain a partly filled 3d shell in the final state of the x-ray absorption process have large interactions between the valence electrons and the 2p, 3s or 3p core hole. Even the 3d-metals for which the valence electrons can be described relatively well with mean field methods such as Density Functional Theory, the 2p3d multiplet interactions remain large and will significantly affect the 2p x-ray absorption spectral shapes.

1s	2s	2p	3s	3p	3d	4s	4p	4d	5s	5p	
0.07 -	**5** **-**	**8** **17**	**13** **-**	**17** **2**							28 Ni^{II} c3d^{9}
0.04 -	2 -	2 160	1 -	7 27	**10** **5**	**9** **-**	**13** **5**				46 Pd^{II} c4d^{9}
0.00 -	0.2 -	2 700	5 -	12 140	**10** **32**	**13** **-**	**18** **15**	**20** 7			64 Gd^{II} c4f^{7}
0.08 -	2 -	3 1710	1 -	5 380	5 90	3 -	10 90	**10** **17**	**14** **-**	**19** **12**	78 Pt^{II} c5d^{9}

Table: *The number in the first line for each element indicates the values of the maximum core-valence Slater-Condon parameter for the final states. The second line gives the spin-orbit coupling for each core level of* Ni^{II}, Pd^{II}, Pt^{II} *and* Gd^{II}. *The valence electrons are the 3d-states for nickel, 4d for palladium and 5d for platinum and the 4f-states for gadolinium.* Gd^{II} *is chosen instead of the common* Gd^{III} *ion for sake of comparison to the other divalent ions. Boldface values indicate clearly visible multiplet effects.*

The table shows the multiplet interactions between the various possible core holes and the partly filled valence band. The configurations calculated are respectively s^1d^9, p^5d^9 and d^9d^9 for the final states of Ni^{II}, Pd^{II} and Pt^{II}. In addition, the final state configurations are included for Gd^{II}, with $4f^7$ instead of d^9. The largest Slater integral (discussed below) is given in the first line and the core level spin-orbit coupling in the second line. The numbers in boldface indicate edges for which multiplet effects will be clearly visible. For multiplet effects to have a significant effect, the value of the Slater-Condon parameters must be larger than or of the same order of magnitude as the spin-orbit coupling separating the two edges. If spin-orbit coupling is very large there still will be an effect from the Slater-Condon parameters but it will be much less pronounced. For example, the 2p and 3p edges of the 4d elements have a large spin-orbit splitting and the multiplet effects are not able to mix states of both sub-edges. However, the effect of the Slater-Condon parameters will still be visible. If a multiplet effect will actually be visible in x-ray absorption further depends on the respective life time broadenings. Another clear conclusion is that all shallow core levels are strongly affected and the deeper core levels are less affected.

The situation for the 3d metals is clear: no visible multiplet effects for the 1s core level (K edge) and a significant influence on all other edges. In case of the 4d metals, the 3d, 4s, 4p edges show significant multiplet effects. The most commonly studied Pd edges are however the 1s and 2p edges that are not (1s) and only a little (2p) affected. The rare earth systems show large multiplet effects for the 3d, 4s, 4p and 4d core levels, hence all vuv and soft x-ray edges. The often-studied 2p core level is much less affected.

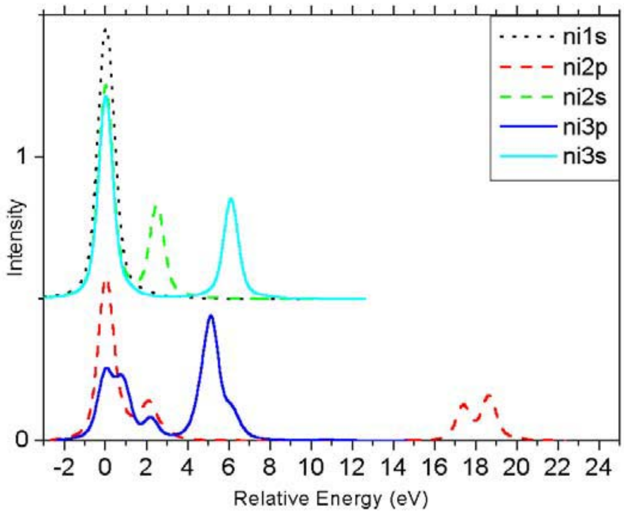

Figure: *All x-ray absorption spectra for Ni^{II}. The respective binding energies are 8333, 1008, 870, 110 and 68 eV for the first peak of the 1s, 2s, 2p, 3s and 3p edges.*

The figure shows the comparison of all edges for Ni^{II} with atomic multiplet effects included. A cubic crystal field of 1.0 eV splits the 3d states. The effects of crystal fields are further discussed in chapter 4. The top three spectra are respectively the 1s, 2s and 3s x-ray absorption spectrum calculated as the transition from $1s^2 3d^8 4p^0$ to $1s^1 3d^8 4p^1$. The lifetime broadening has been set to 0.2 eV half-width half-maximum. Its value is in fact larger in reality. One observes one peak for the 1s spectrum and two peaks for the 2s and 3s spectra. The reason for the two peaks is the 2s3d and 3s3d exchange interactions, which are directly related to the Slater-Condon parameters of respectively 5 and 13 eV. The splittings between the parallel and antiparallel states are respectively 2.5 and 6.5 eV, i.e. approximately half the respective Slater-Condon parameter. The 1s x-ray absorption spectrum of NiO looks in reality different than this single peak, because one essentially observes an edge jump and transitions from the 1s core state to all empty states of p-character. The complete spectral shape of K edge x-ray absorption is therefore better described with a multiple scattering formalism. This single peak reflects just the first white line or leading edge of the spectrum. The 2s and 3s x-ray absorption spectra are not often measured. The 2s spectrum is very broad and therefore adds little information. The 3s x-ray absorption spectrum is also not very popular. Instead the $3s^1 3d^N$ final states do play an important role in spectroscopies like 3s XPS, 2p3s resonant x-ray emission, and 2p3s3s resonant Auger. In those spectroscopies the role of the 3s3d exchange interaction plays an important role, as does the charge transfer effect that is further discussed in chapter 5.

The spectra at the bottom are the 2p (dashed) and 3p (solid) x-ray absorption spectral shapes. These are essentially the well-known 2p and 3p spectra of NiO and other divalent nickel compounds. The $2p^5 3d^9$ and $3p^5 3d^9$ final states contain one p hole and one 3d hole that interact very strongly. This gives rise to a multitude of final states. Because the lifetime broadening for 2p states is relatively low, these spectral shapes can actually be observed in experiment. This gives 2p x-ray absorption, and to a lesser extend 3p x-ray absorption, their great potential for the determination of the local electronic structure. In the next chapters we will explain in detail the three main ingredients that are necessary to explain the spectral shapes of x-ray absorption in those cases where multiplet effects are important.

A successful method to analyse these transitions is based on a charge transfer and ligand-field multiplet model. For its description, we start with an atomic model, where only the interactions within the absorbing atom are considered, without influence from the surrounding atoms. Effects of the surroundings are then introduced as a perturbation. In chapter 4 we introduce crystal field effects and in chpater 5 charge transfer effects. This approach can be justified if the intra-atomic interactions are much larger than the ones between the atoms.

Multiplets in X-ray Spectroscopy

lectures ICTP 2004, by Frank de Groot

2.2. Atomic Multiplets

In order to show how spectra in strongly correlated electron systems are calculated, we start with the example of a free atom, where there is no influence from the environment. The Schrödinger equation contains the kinetic energy of the N electrons ($\sum_N \frac{p_i^2}{2m}$), the electrostatic interaction of the N electrons with the nucleus of charge +Z ($\sum_N \frac{-Ze^2}{r_i}$), the electron-electron repulsion ($H_{ee}=\sum_{pairs} \frac{e^2}{r_{ij}}$) and the spin-orbit coupling of each electron ($H_{ls}=\sum_N \zeta(r_i)\, l_i \cdot s_i$). The total Hamiltonian is thus given by:

$$H = \sum_N \frac{p_i^2}{2m} + \sum_N \frac{-Ze^2}{r_i} + \sum_{pairs} \frac{e^2}{r_{ij}} + \sum_N \zeta(r_i)\, l_i \cdot s_i$$

The kinetic energy and the interaction with the nucleus are the same for all electrons in a given atomic configuration. They define the average energy of the configuration (H_{av}). The electron-electron repulsion and the spin-orbit coupling define the relative energy of the different terms within this configuration. The main difficulty when solving the Schrödinger equation is that H_{ee} is too large to be treated as a perturbation. A solution to this problem is given by the Central Field approximation, in which the spherical average of the electron-electron interaction is separated from the non-spherical part. The spherical average $<H_{ee}>$ is added to H_{av} to form the average energy of a configuration. In the modified electron-electron Hamiltonian H_{ee}, the spherical average has been subtracted.

$$H'_{ee} = H_{ee} - \left\langle H_{ee} \right\rangle = \sum_{pairs} \frac{e^2}{r_{ij}} - \left\langle \sum_{pairs} \frac{e^2}{r_{ij}} \right\rangle \tag{2.2}$$

The two interactions H_{ee} and H_{ls} determine therefore the energies of the different terms within the atomic configuration.

2.2.1. Term symbols

The terms of a configuration are indicated with their orbital moment L, spin moment S and total moment J, with $|L-S| \quad J \quad L+S$. In the absence of spin-orbit coupling, all terms with the same L and S have the same energy, giving an energy level which is (2L+1)(2S+1)-fold degenerate[i]. When spin-orbit coupling is important, the terms are split in energy according to their J-value with a degeneracy of 2J+1. A term is designed with a so-called term symbol $^{2S+1}X_J$, where X corresponds to a letter according to the value of L. X = S, P, D, F, etc. for L = 0, 1, 2, 3, etc. The quantity 2S+1 is called the spin multiplicity of the term, and the terms are called singlet, doublet, triplet, quartet, etc. according to S = 0, 1/2, 1, 3/2, etc.

A single 1s electron has an orbital moment L=0, a spin moment S=1/2 and a total moment J=1/2. There is only one term, with term symbol $^2S_{1/2}$. For one p electron, L=1, S=1/2, and J can be 1/2 or 3/2, corresponding to term symbols $^2P_{1/2}$ and $^2P_{3/2}$.

$m_{la}, m_{sa}>$	$m_{lb}, m_{sb}>$	$M_L, M_S>$	#	$m_{la}, m_{sa}>$	$m_{lb}, m_{sb}>$	$M_L, M_S>$	#

1, +>	1, >	2, 0>	1	1, >	-1, >	0, -1>	1
1, +>	0, +>	1, 1>	1	0, +>	0, >	0, 0>	3
1, +>	0, >	1, 0>	1	0, +>	-1, +>	-1, 1>	1
1, +>	-1, +>	0, 1>	1	0, +>	-1, >	-1, 0>	1
1, +>	-1, >	0, 0>	1	0, >	-1, +>	-1, 0>	2
1, >	0, +>	1, 0>	2	0, >	-1, >	-1, -1>	1
1, >	0, >	1, -1>	1	-1, +>	-1, >	-2, 0>	1
1, >	-1, +>	0, 0>	2				

Table: *The fifteen combinations of states m_{la}, m_{sa}> and m_{lb}, m_{sb}> of a $2p^2$ configuration. The fourth column counts the degeneracy of the total symmetry M_L, M_S> states.*

In case of a $2p^2$ configuration, the first electron has six quantum states available, the second electron only five. This is due to the Pauli exclusion principle that forbids two electrons to have the same quantum numbers n, M_L and M_S. Because the sequence of the two electrons is not important, one divides the number of combinations by two and obtains fifteen possible combinations. These fifteen combinations are indicated in the table. The presence of |2,0> and [1]|-2,0> states implies that there must be a ^{1}D term. This term contains five states with M_S = 0 and M_L = -2,-1,0,1,2, as indicated in table below. We are left with ten states, containing M_L =   1 and M_S =   1. So there also has to be a ^{3}P term, with nine states. One state is left, with M_S = M_L = 0, giving a ^{1}S-term. The $2p^2$ configuration contains therefore the terms ^{3}P , ^{1}D and ^{1}S . It can be checked that total degeneracy adds up to fifteen. Note also that the term symbols of a $2p^2$ configuration form a sub-set of the term symbols of the 2p3p configuration, which do not have to obey the Pauli principle. Including J in the discussion we have the values $^1D_2$, $^1S_0$ and $^3P_{210}$, a short-hand notation of $^3P_2$ plus $^3P_1$ plus $^3P_0$. Focusing on the J-values, we have two J=0, one J=1 and two J=2 values. This would imply that if a calculation would be carried out in intermediate coupling, the total calculation would split up in three separate parts, one for each J -value.

ALL	M_S=1	M_S=0	M_S=-1		**^{1}D**	M_S=1	M_S=0	M_S=-1
M_L=2	0	1	0		M_L=2	0	**1 0**	0
M_L=1	1	2	1		M_L=1	1	**2 1**	1
M_L=0	1	3	1		M_L=0	1	**3 2**	1
M_L=-1	1	2	1		M_L=-1	1	**2 1**	1
M_L=-2	0	1	0		M_L=-2	0	**1 0**	0
^{3}P	M_S=1	M_S=0	M_S=-1		**^{1}S**	M_S=1	M_S=0	M_S=-1
M_L=2	0	0	0		M_L=2	0	0	0
M_L=1	**1 0**	**1 0**	**1 0**		M_L=1	0	0	0

---

[1]

M_L=0	**1 0**	**2 1**	**1 0**		M_L=0	0	**1 0**	0
M_L=-1	**1 0**	**1 0**	**1 0**		M_L=-1	0	0	0
M_L=-2	0	0	0		M_L=-2	0	0	0

Table: *A schematic diagram of the separation of the fifteen total symmetry states of a* $2p^2$ *configuration into the three irreducible representations* ^1D, ^3P *and* ^1S.

Exercise:

- Write out all two-electron states of a 2p3p configuration.
- Why does the Pauli principle not apply?
- How many states are present?
- Select all states into their M_S and M_L quantum numbers and make a table as given above for a $2p^2$ configuration.
- Extract all term symbols from the table.
- Calculate the degeneracies of the term symbols and check if the total degeneracy is equal to the total number of states.
- If one compares the term symbols of a 2p3p configuration with those of a $2p^2$ configuration. What relation can be found?

In the case of a transition metal ion, the important configuration for the initial state of the absorption process is $3d^n$. In the final state with a 3s or a 3p core hole, the configurations are $3s^13d^{n+1}$ and $3p^53d^{n+1}$. The main quantum number has no influence on the coupling scheme, so the same term symbols can be found for 4d and 5d systems, or for 2p and 3p core holes. A $3d^1$ configuration has term symbols $^2D_{5/2}$ and $^2D_{3/2}$ with, respectively, six (5/2 times 2 plus 1) and four (3/2 x2 +1) states. The LS term symbols for a $3d^14d^1$ configuration can be found by "multiplying" the term symbols for the configurations $3d^1$ and $4d^1$. This multiplication consists of separately summing L and S of both terms. Multiplication of terms A and B is written as A B. Since both L and S are vectors, the resulting terms have possible values of $|L_A-L_B| \quad L \quad L_A+L_B$ and $|S_A-S_B| \quad S \quad S_A+ S_B$. For $^2D \quad ^2D$, this gives L = 0, 1, 2, 3 or 4 and S = 0 or 1. The ten LS term symbols of the $3d^14d^1$ configuration are given in Table 2.4, together with their degeneracy and possible J-values. The total degeneracy of the $3d^14d^1$ configuration is 100. In the presence of spin-orbit coupling, a total of eighteen term symbols is found.

$3d^14d^1$	**^{1}S**	^{1}P	**^{1}D**	^{1}F	**^{1}G**	^{3}S	**^{3}P**	^{3}D	**^{3}F**	^{3}G	
Deg.	**1**	3	**5**	7	**9**	3	**9**	15	**21**	27	100 **45**
J-values	**0**	1	**2**	3	**4**	1	**0** **1** **2**	1 2 3	**2** **3** **4**	3 4 5	

Table 1 *Possible term LS term symbols for a $3d^1 4d^1$ configuration, with their degeneracy and possible J values. The sub-set of LS term symbols for a $3d^2$ configuration is given in boldface.*

A $3d^2$ configuration does not have the same degeneracy as the $3d^1 4d^1$ configuration, due to the Pauli exclusion principle. In total there are 10 9/2 = 45 possible states. Following the same procedure as for the $2p^2$ configuration, one can write out all 45 combinations of a $3d^2$ configuration and sort them by their M_L and M_S quantum numbers. Analysis of the combinations of the allowed M_L and M_S quantum numbers yields the term symbols ^1G, ^3F, ^1D, ^3P and ^1S. This is a sub-set of the term symbols of a $3d^1 4d^1$ configuration. The term symbols can be divided into their J-quantum numbers as $^3F_2$, $^3F_3$, $^3F_4$, $^3P_0$, $^3P_1$, $^3P_2$, $^1G_4$, $^1D_2$ and $^1S_0$ as also indicated in table 4.

In case of a $3d^3$ configuration a similar approach shows that the possible spin-states are doublet and quartet. The quartet-states have all spins parallel and it turns out that there are two quartet term symbols, respectively ^4F and ^4P. The doublet states have two electrons parallel and for these two electrons the Pauli principle yields the combinations identical to the triplet states of the $3d^2$ configuration. To these two parallel electrons a third electron is added anti-parallel, where this third electron can have any value of its orbital quantum number m_l. Writing out all combinations and separating them into the total orbital moments M_l gives the doublet term symbols ^2H, ^2G, ^2F, ^2D, another ^2D and ^2P. By adding the degeneracies, it can be checked that a $3d^3$ configuration has 120 different states. The general formula to determine the degeneracy of a $3d^n$ configuration is:

$$\binom{10}{n} = \frac{10!}{(10-n)!n!}$$

Exercise:

- Check that adding the degeneracies of the term symbols of $3d^3$ indeed yields 120.
- Use the equation above to determine the overall degeneracy for $3d^3$.

We can show that the term symbols of a configuration $3d^n$ do also exist in a configuration $3d^{n+2}$, for n+2 5. Thus the term symbols of $3d^4$ contain all term symbols of $3d^2$ which contains the ^1S term symbol of $3d^0$. Similarly the term symbols of $3d^5$ contain all term symbols of $3d^3$ which contains the ^2D term symbol of $3d^1$. In addition there is a symmetry equivalence of holes and electrons, hence $3d^3$ and $3d^7$ have exactly the same term symbols.

The 2p x-ray absorption edge (2p 3d transition) is often studied for the 3d transition metal series, and it provides a wealth of information. Crucial for its understanding are the configurations of the $2p^5 3d^n$ final states. The term symbols of the $2p^5 3d^n$ states are found by multiplying the configurations of $3d^n$ with a ^2P term symbol. The total degeneracy of a $2p^5 3d^n$ state is given in the equation below. For example, a $2p^5 3d^5$ configuration has 1512 possible states. Analysis shows that these 1512 states are divided into 205 term symbols, implying in principle 205 possible final states. If all these final states have finite intensity depends on the selection rules.

$$6 \times \binom{10}{n} = 6 \times \frac{10!}{(10-n)!n!}$$

Exercise:

- The Ni^{II} ion in NiO can be approximated with a $3d^8$ ground state configuration. Which term symbols are found for a $3d^8$ configuration?
- In a 3p x-ray absorption process, a 3p core electron fills another 3d-hole. What is the final state configuration of this process?
- What are the term symbols of the final state?

2.2.2. *Matrix elements*

Using symmetry, we have found the number of states of a certain $3d^n$ configuration and their term symbols. The next task is to find the relative energies of the different terms, calculating the matrix elements of these states with the Hamiltonian H_{ATOM}. As discussed in the previous section, H_{ATOM} consists of the effective electron-electron interaction H'_{ee} and the spin-orbit coupling H_{ls}:

$$H_{ATOM} = \sum_{pairs} \frac{e^2}{r_{ij}} + \sum_{N} \zeta(r_i)\, l_i \cdot s_i$$

The electron-electron interaction commutes with L^2, S^2, L_z and S_z, which implies that all its off-diagonal elements are zero. The general formulation of the matrix elements of two-electron wave functions is given as:

$$\left\langle {}^{2S+1}L_J \left| \frac{e^2}{r_{12}} \right| {}^{2S+1}L_J \right\rangle = \sum_k f_k F^k + \sum_k g_k G^k$$

F^i *(f_i)* and G^i *(g_i)* are the Slater-Condon parameters for the radial (angular) part of the direct Coulomb repulsion and the Coulomb exchange interaction, respectively. f_i and g_i are non-zero only for certain values of i, depending on the configuration. Table 5 gives the possible i-values for some important configurations.

Conf.	f_i	g_i	**Conf.**	F_i	g_i	**Conf.**	f_i	g_i
$1s^2$	0	-	**1s2s**	0	0	**1s2p**	0	1
$2p^2$	0 2	-	**2p3p**	0 2	0 2	**2p3d**	0 2	1 3
$3d^2$	0 2 4	-	**3d4d**	0 2 4	0 2 4	**3d4f**	0 2 4	1 3 5

Table 2 *The possible values of f_i and g_i for simple configurations.*

It can be seen that the exchange interaction g_i is present only for electrons in different shells. f_0 is always present and the maximum value for i equals two times the lowest value of l. For g_k, *i* is even if l_1+l_2 is even, and *i* is odd if l_1+l_2 is odd. The maximum value of *i* equals l_1+l_2.

A simple example is a 1s2s configuration consisting of ^1S and ^3S term symbols. The value of both *f_0* and *g_0* is 1, and the respective energies are given by:

$$\left\langle {}^1S \,|\, \tfrac{e^2}{r_{12}} | {}^1S \right\rangle = F^0(1s2s) + G^0(1s2s) \qquad \left\langle {}^3S \,|\, \tfrac{e^2}{r_{12}} | {}^3S \right\rangle = F^0(1s2s) - G^0(1s2s)$$

This result can be stated as “the singlet and the triplet state are split by the exchange interaction”. This energy difference is $2G^0(1s2s)$. An analogous result is found for a 1s2p state for which the singlet and triplet states are split by $(2/3)G^0(1s2p)$. The 2/3 prefactor is determined by the degeneracy of the 2p-state.

For a $3d^2$ configuration, the two electrons are in the same shell hence there are no exchange interactions. There are five term symbols ^1S, ^3P, ^1D, ^3F and ^1G. Their energies are given in Table 6. f_0 is equal to the number of permutations (N(N-1)/2) of n electrons, i.e. equal to 1.0 for two electron configurations. The Slater-Condon parameters F^2 and F^4 have approximately a constant ratio: $F^4 = 0.62\ F^2$. The last column in table 6 gives the approximate energies of the five term symbols. In case of the 3d transition metal ions, F^2 is approximately equal to 10 eV. This gives for the five term symbols the energies respectively as ^3F at -1.8 eV, ^1D at -0.1 eV, ^3P at +0.2 eV, ^1G at +0.8 eV and ^1S at +4.6 eV. The ^3F-term symbol has lowest energy and is the ground state of a $3d^2$ system. This is in agreement with the Hunds rules, which will be discussed in the next section. The three states ^1D, ^3P and ^1G are close in energy some 1.7 eV to 2.5 eV above the ground state. The ^1S state has a high energy of 6.4 eV above the ground state, the reason being that two electrons in the same orbit strongly repel each other.

		Relative Energy	Relative Energy
^1S	$F^0 + 2/7\ F^2 + 2/7\ F^4$	$0.46F^2$	4.6 eV
^3P	$F^0 + 3/21\ F^2 - 4/21\ F^4$	$0.02F^2$	0.2 eV
^1D	$F^0 - 3/49\ F^2 + 4/49\ F^4$	$-0.01F^2$	-0.1 eV
^3F	$F^0 - 8/49\ F^2 - 1/49\ F^4$	$-0.18F^2$	-1.8 eV
^1G	$F^0 + 4/49\ F^2 + 1/441\ F^4$	$0.08F^2$	0.8 eV

Table 3 *The relative energies of the term symbols for a* $3d^2$ *configuration (see text).*

In literature one finds a number of slightly different notations and names for the Slater-Condon parameters. Table 7 gives three related notations that are used to indicate the radial integrals. The Slater-Condon parameters F^k, the normalised Slater-Condon parameters F_k and the Racah parameters A, B and C. The bottom half of table 7 uses the relationship between F^2 and F^4 and it further uses a typical F^2 value of 10 eV and a F^0 value of 8 eV.

Slater-Condon	**Normalised**	**Racah**
F^0	$F_0=F^0$	$A = F_0 - 49F_4$
F^2	$F_2 = F^2/49$	$B = F_2 - 5F_4$
F^4	$F_4 = F^4/441$	$C = 35F_4$
$F^0 = 8.0$	$F_0 = 8.0$	$A = 7.3$
$F^2 = 10.0$	$F_2 = 0.41$	$B = 0.13$
$F^4 = 6.2$	$F_4 = 0.014$	$C = 0.49$

Table 4 *A comparison of the Slater-Condon parameters* F^k*, with the normalised Slater-Condon parameters* F_k *and the Racah parameters.*

For three and more electrons the situation is considerably more complex. It is not straightforward to write down an anti-symmetrized three-electron wave function. It can be shown that the three-electron wave function can be build from two-electron wave functions with the use of the so-called coefficients of fractional parentage. This will not be further discussed here.

2.3. Atomic multiplet ground states of $3d^n$ systems

The term symbols for a partly filled d-band with the lowest energy, found after calculating the matrix elements, are given in table 5. They are in agreement with the so-called Hunds rules. Based on experimental information Hund formulated three rules to determine the ground state of a $3d^N$ configuration. The three Hunds rules are:

1. Term symbols with maximum spin S are lowest in energy,
2. Among these terms, the one with the maximum orbital moment L is lowest,
3. In the presence of spin-orbit coupling, the lowest term has J = |L-S| if the shell is less than half full and J = L+S if the shell is more than half full.

A configuration has the lowest energy if the electrons are as far apart as possible. The first Hunds rule 'maximum spin' can be understood from the Pauli principle: Electrons with parallel spins must be in different orbitals, which on overall implies larger separations, hence lower energies. This is for example evident for a $3d^5$ configuration, where the ^6S state has its five electrons divided over the five spin-up orbitals, which minimises their repulsion. In case of $3d^2$, the first Hunds rule implies that either the ^3P or the ^3F-term symbol must have lowest energy. From the previous section one finds that the ^3F term symbol is lower in energy than the ^3P-term symbol, because again the ^3F wave function tends to minimise electron repulsion. The effects of spin-orbit coupling are well known in case of core states. A 2p-core state has $^2P_{3/2}$ and $^2P_{1/2}$ states. The state with the lowest energy is $^2P_{3/2}$. Consider for example the 2p XAS or XPS spectrum of nickel. The $^2P_{3/2}$ peak is positioned at approximately 850 eV and the $^2P_{1/2}$ at about 880 eV. Note that the state with the lowest binding energy is related to the lowest energy of the final state configuration. This is in agreement with Hunds third rule: the configuration is $2p^5$, so more than half-full, implying that highest J-value has lowest energy. The third rule implies that the ground state of a $3d^8$ configuration is $^3F_4$, while it is $^3F_2$ in case of a $3d^2$ configuration.

2.3.1. jj coupling

Above, we have supposed that the perturbation due to spin-orbit coupling is small compared to the one due to electronic repulsions. The spins and orbital moments of the individual electrons are coupled to give the total S and L of the configuration, the spin-orbit coupling splits the resulting terms according to their J-value. This is known as the Russell-Saunders coupling scheme: spin-orbit coupling is considered as a small perturbation on the terms set up by electron repulsions. The Russell-Saunders coupling scheme is valid for most lighter elements, for which the spin-orbit coupling is small, like the 3d Transition Metals. For heavy elements, spin-orbit coupling becomes more important while electron repulsion starts to decrease (the radial extent of the orbitals becomes larger and the electrons are thus farther apart). This can lead to a breakdown of the Russell-Saunders coupling scheme.

When the spin-orbit coupling is much larger than the electron repulsions, the orbital moment l and spin moment s of each electron has to be coupled to give the total moment j, and the j-values of all the electrons are coupled to give the total J. A configuration is first split into levels according to their J-value and the electron repulsions are then treated as a perturbation on these spin-orbit coupling levels. This approach is known as the **j j** coupling scheme, and is the direct reverse of the Russell-Saunders scheme. Many heavier elements, like the rare earths, do not conform to either of the two limiting cases, and an intermediate coupling scheme has to be applied. This is also the case for the final state after $2p$ absorption in $3d$ transitions metals, since the spin-orbit coupling is strong for the $2p$ hole.

2.4. X-ray Absorption Spectra described with Atomic Multiplets.

2.4.1. 2p XAS of 3d transition metals

We start with the description of closed shell systems. The 2p x-ray absorption process excites a 2p core electron into the empty 3d shell and the transition can be described as $2p^63d^0$ $2p^53d^1$. The ground state has $^1S_0$ symmetry and we find that the term symbols of the final state are $^1P_1$, $^1D_2$, $^1F_3$, $^3P_{012}$, $^3D_{123}$ and $^3F_{234}$, where $^3F_{234}$ is a short-hand notation of $^3F_2 + {}^3F_3 + {}^3F_4$. The energies of the final states are affected by the 2p3d Slater-Condon parameters, the 2p spin-orbit coupling and the 3d spin-orbit coupling. The x-ray absorption transition matrix elements to be calculated are:

$$I_{XAS} \propto \left\langle 3d^0 \mid p \mid 2p^5 3d^1 \right\rangle^2$$

The symmetry aspects are:

$$I_{XAS} \propto \left\langle \left[{}^1S_0\right] \middle| \left[{}^1P_1\right] \middle| \left[{}^{1,3}PDF\right] \right\rangle^2$$

Table 8 contains the result of an atomic multiplet calculation for Ti^{IV} ($3d^0$) using the atomic parameters. The twelve states are built from the twelve term symbols according to the matrix given. The irreducible representations, i.e. the states with the same J-value block out in the calculation. It is found that the lowest energy state is the pure $^3P_0$ state. This state has zero intensity in an x-ray absorption process (because of the selection rule |J-1| J J+1), but it is possible that another state decays to this $^3P_0$ state via Coster-Kronig Auger decay.

	$^3P_0$	**$^3P_1$**	**$^3D_1$**	**$^1P_1$**	$^3P_2$	$^3D_2$	$^3F_2$	$^1D_2$	$^3D_3$	$^3F_3$	$^1F_3$	$^3F_4$
-3.281	1.0											
-2.954		**-0.94**	**0.30**	**0.08**								
0.213		**-0.19**	**-0.77**	**0.60**								
5.594		**0.24**	**0.55**	**0.79**								
-2.381					0.81	-0.46	0.01	0.34				
-1.597					-0.03	-0.50	0.56	-0.65				
3.451					0.04	-0.30	-0.82	-0.47				
3.643					-0.57	-0.65	-0.06	0.48				
-2.198									-0.21	0.77	0.59	
-1.369									0.81	-0.19	0.54	
3.777									-0.53	-0.60	0.59	
-2.481												1.0

Table 5 *The relative energies of an atomic multiplet calculation for Ti^{IV}. The J=1 states (which have finite intensity) are given in boldface.*

The symmetry of the dipole transition is given as $^1P_1$, according to the dipole selection rules, which state that J = + 1, 0, - 1 but not J = J = 0. Within LS coupling also S=0 and L=1. The dipole selection rule reduces the number of final states that can be reached from the ground state. The J-value in the ground state is zero. In this case, the dipole selection rule proclaims that the J-value in the final state must be one, thus only the three term symbols $^1P_1$, $^3P_1$ and $^3D_1$ can obtain finite intensity. They are indicated in table 8 in boldface. The problem of calculating the 2p absorption spectrum is effectively reduced to solving the three by three energy matrix of the final states with J=1. As discussed above the atomic energy matrix consists of terms related to the two-electron Slater integrals ($H_{ELECTRO}$) and the spin-orbit couplings of the 2p ($H_{LS\text{-}3d}$) and the 3d electrons ($H_{LS\text{-}3d}$):

$$H_{eff} = H_{ELECTRO} + H_{LS-2p} + H_{LS-3d}$$

$$H_{ELECTRO} = \left\langle 2p^5 3d^1 \,|\, \tfrac{e^2}{r_{12}} \,|\, 2p^5 3d^1 \right\rangle$$

$$H_{LS-2p} = \left\langle 2p \,|\, \varsigma_p l_p \cdot s_p \,|\, 2p \right\rangle$$

$$H_{LS-3d} = \left\langle 3d \,|\, \varsigma_d l_d \cdot s_d \,|\, 3d \right\rangle$$

To show the individual effects of these interactions they will be introduced one by one. A series of five calculations will be shown, in which respectively:

(a) All final state interactions are set to zero: H = 0
(b) The 2p spin-orbit coupling is included: $H = H_{LS\text{-}2p}$
(c) The Slater-Condon parameters are included: $H = H_{ELECTRO}$
(d) The 2p spin-orbit coupling and Slater-Condon parameters are included: $H = H_{ELECTRO} + H_{LS\text{-}2p}$
(e) The 3d spin-orbit coupling is included: $H = H_{ELECTRO} + H_{LS\text{-}2p} + H_{LS\text{-}3d}$.

We start by setting all final state interactions to zero. The results of the 2p x-ray absorption spectrum will be given with two 3x3 matrices. The energy levels are given below. They are labelled from top to bottom '^{3}P', '^{3}D' and '^{1}P' states, indicating the approximate term symbol related to the state. The original term symbols ^{3}P, ^{3}D and ^{1}P are given in respectively the first row, second row and bottom row of the eigenvector matrix. The intensity of the states is indicated on the right. With all interactions zero, the complete energy matrix is zero. The states all are the pure LSJ-states and because of the dipole selection rules all intensity goes to the $^1P_1$ state.

Energy Matrix $\begin{vmatrix} 0 & 0 & 0 \\ 0 & 0 & 0 \\ 0 & 0 & 0 \end{vmatrix}$		*Eigenvectors* $\begin{vmatrix} 1 & 0 & 0 \\ 0 & 1 & 0 \\ 0 & 0 & 1 \end{vmatrix}$
Energy Levels		**Intensities**
0.00	^{3}P	0.00
0.00	^{3}D	0.00
0.00	^{1}P	1.00

Table 6 *The energy matrix and eigenvectors of the 3x3 matrices of the $2p^5 3d^1$ final states with J=1. The bottom half of the table gives the resulting energies and intensities. All final state interactions are set to zero.*

Inclusion of the 2p spin-orbit coupling $H_{LS\text{-}2p}$ of 3.776 eV creates non-diagonal elements in the energy matrix. In other words the LS-character of the individual states is mixed. In case only 2p spin-orbit coupling is included the result is rather simple, with the triplet states at -1/2 $_p$ and the singlet state at + $_p$. The eigenvector matrix shows that the three states are mixtures of the three pure states, i.e. the first state is in fact: '^{3}P'= 0.5 $^3P_1$- 0.866 $^3D_1$. The intensities of the three states are directly given by the square of percentage of $^1P_1$ character. This gives the familiar result that the triplet states, or $2p_{3/2}$ states, have twice the intensity of the singlet, or $2p_{1/2}$, states. This has been indicated also in the figure.

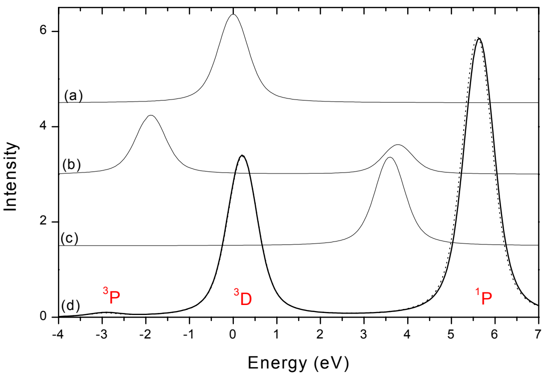

Figure: *The effects of the Slater-Condon parameters and the spin-orbit coupling on the atomic multiplet spectrum of a 3d^0 system. (a) no interactions, (b) only 2p spin-orbit, (c) only Slater-Condon, (d) both Slater-Condon and 2p spin-orbit (solid). The dashed line includes the 3d spin-orbit coupling.*

Energy Matrix $\begin{vmatrix} 0.944 & 1.635 & 2.312 \\ 1.635 & -0.944 & 1.335 \\ 2.312 & 1.335 & 0.000 \end{vmatrix}$		*Eigenvectors* $\begin{vmatrix} 0.5 & -0.5 & -0.707 \\ -0.866 & -0.288 & -0.408 \\ 0.0 & 0.816 & -0.577 \end{vmatrix}$
Energy Levels		**Intensities**
-1.888	^{3}P	0.00
-1.888	^{3}D	0.666
+3.776	^{1}P	0.333

Table 7 *The energy matrix and eigenvectors of the 3x3 matrices of the $2p^5 3d^1$ final states with J=1, after inclusion of the 2p spin-orbit coupling.*

Next we include only the pd Slater-Condon parameters, keeping the 2p spin-orbit coupling zero. The Slater-Condon parameters are reduced to 80% of their atomic Hartree-Fock values and F^2, G^1 and G^3 are respectively 5.042 eV, 3.702 eV and 2.106 eV. This gives the three states at respectively -1.345, 0.671 and 3.591 eV. Only the $^1P_1$ state has a finite intensity and its energy is shifted to an energy of 3.591 eV above the centre of gravity. The two other states have zero intensity. It can be seen that the pd Slater-Condon parameters are diagonal in the LS-terms, hence the three states are pure in character.

Energy Matrix $\begin{vmatrix} -1.345 & 0 & 0 \\ 0 & 0.671 & 0 \\ 0 & 0 & 3.591 \end{vmatrix}$		*Eigenvectors* $\begin{vmatrix} 1 & 0 & 0 \\ 0 & 1 & 0 \\ 0 & 0 & 1 \end{vmatrix}$
Energy Levels		**Intensities**

-1.345	^{3}P	0.00
+0.671	^{3}D	0.00
+3.591	^{1}P	1.00

Table 8 *The energy matrix and eigenvectors of the 3x3 matrices of the* $2p^5 3d^1$ *final states with J=1, after inclusion of the 2p3d Slater-Condon parameters.*

In part (b) we have seen that the non-diagonal terms of the 2p spin-orbit coupling makes that all three states are mixtures of the individual term symbols. 2p spin-orbit coupling further creates the 2:1 intensity ratio, thereby shifting most of the ^{1}P character to lower energy. In part (c) it was found that the Slater-Condon parameters shift the ^{1}P state to higher energy and that the triplet states have a considerably lower energy. If one includes both the 2p spin-orbit coupling and the pd Slater-Condon parameters, the result will depend on their relative values. In case of the 2p core hole of Ti^{IV}, the Slater-Condon parameters are relatively large and most intensity goes to the $2p_{1/2}$ state. The triplet states are separated by 3 eV and the lowest '^{3}P' energy state is extremely weak, gaining less then 1 % of the total intensity. The figure shows the typical spectral shape with three peaks. In the next section we compare four similar spectra with different ratios of Slater-Condon parameters and core hole spin-orbit couplings to show the variations in their spectral shapes.

Energy Matrix $\begin{vmatrix} 1.615 & 1.635 & 2.312 \\ 1.635 & -2.289 & 1.335 \\ 2.312 & 1.335 & 3.591 \end{vmatrix}$		*Eigenvectors* $\begin{vmatrix} 0.297 & -0.776 & 0.557 \\ -0.951 & -0.185 & 0.248 \\ 0.089 & 0.603 & 0.792 \end{vmatrix}$
Energy Levels		**Intensities**
-2.925	^{3}P	0.008
+0.207	^{3}D	0.364
+5.634	^{1}P	0.628

Table 9 *The energy matrix and eigenvectors of the 3x3 matrices of the* $2p^5 3d^1$ *final states with J=1, after inclusion of the 2p3d Slater-Condon parameters and the 2p spin-orbit coupling.*

For completeness we include in the final calculation also the 3d spin-orbit coupling. Because the 3d spin-orbit coupling is only 32 meV, its influence on the spectral shape is negligible in the present case. The energy position of the '^{1}P' state shifts by 40 meV and its intensity drops by 0.4% of the total intensity. The effects on the intensities and energies have been included as the extra number in Table 2.13. It is noted that the 3d spin-orbit coupling can have very significant effects on the spectral shape of 3d compounds if the 3d-shell is partly filled in the ground state.

Energy Matrix		*Eigenvectors*
$\begin{vmatrix} 1.575 & 1.649 & 2.293 \\ 1.649 & -2.313 & 1.301 \\ 2.293 & 1.301 & 3.591 \end{vmatrix}$		$\begin{vmatrix} 0.303 & -0.774 & 0.555 \\ -0.949 & -0.195 & 0.246 \\ 0.082 & 0.601 & 0.795 \end{vmatrix}$
Energy Levels		**Intensities**
2.954 0.029	^3P	0.007 0.001
+0.212 +0.005	^3D	0.361 0.003
+5.594 0.040	^1P	0.632 +0.004

Table 2.10 *The energy matrix and eigenvectors of the 3x3 matrices of the* $2p^5 3d^1$ *final states with J=1, after inclusion of the 2p3d Slater-Condon parameters, the 2p spin-orbit coupling and the 3d spin-orbit coupling. The second number indicates the change in energy level and intensity due to the 3d spin-orbit coupling.*

We compare a series of x-ray absorption spectra of tetravalent titanium 2p and 3p edges and the trivalent lanthanum 3d and 4d edges. The ground states of Ti^{IV} and La^{III} are respectively $3d^0$ and $4f^0$ and they share a ^1S ground state. The transitions at the four edges are respectively:

Ti^{IV} $L_{2,3}$ edge: $3d^0$ $2p^5 3d^1$
Ti^{IV} $M_{2,3}$ edge: $3d^0$ $3p^5 3d^1$
La^{III} $M_{4,5}$ edge: $4f^0$ $3d^9 4f^1$
La^{III} $N_{4,5}$ edge: $4f^0$ $4d^9 4f^1$

These four calculations are equivalent and all spectra consist of three peaks with J=1. What changes are the values of the atomic Slater-Condon parameters and core hole spin-orbit couplings. They are given in table 6 for the four situations. The G^1 and G^3 Slater-Condon parameters have an approximately constant ratio with respect to the F^2 value. The important factor for the spectral shape is the ratio of the core spin-orbit coupling and the F^2 value. Finite values of both the core spin-orbit and the Slater-Condon parameters cause the presence of the pre-peak. It can be seen in table 6 that the 3p and 4d spectra have small core spin-orbit couplings, implying small $p_{3/2}$ ($d_{5/2}$) edges and extremely small pre-peak intensities. The deeper 2p and 3d core levels have larger core spin-orbit splitting with the result of a $p_{3/2}$ ($d_{5/2}$) edge of almost the same intensity as the $p_{1/2}$ ($d_{3/2}$) edge and a larger pre-peak. Note that none of these systems comes close to the single-particle result of a 2:1 ratio of the p edges or the 3:2 ratio of the d edges. Figure 2.4 shows the x-ray absorption spectral shapes. They are given on a logarithmic scale to make the pre-edges visible.

Edge	Ti 2p	Ti 3p	La 3d	La 4d
Average Energy (eV)	464.00	37.00	841.00	103.00
Core spin-orbit (eV)	3.78	0.43	6.80	1.12
F^2 Slater-Condon (eV)	5.04	8.91	5.65	10.45

Intensities:				
Pre-peak	0.01	10^{-4}	0.01	10^{-3}
$p_{3/2}$ or $d_{5/2}$	0.72	10^{-3}	0.80	0.01
$p_{1/2}$ or $d_{3/2}$	1.26	1.99	1.19	1.99

Table 2.11 *The relative intensities, energy, core hole spin-orbit coupling and F^2 Slater-Condon parameters are compared for four different $^1S_0$ systems. The last two columns repeat the results of situation (b) and (c) as given above.*

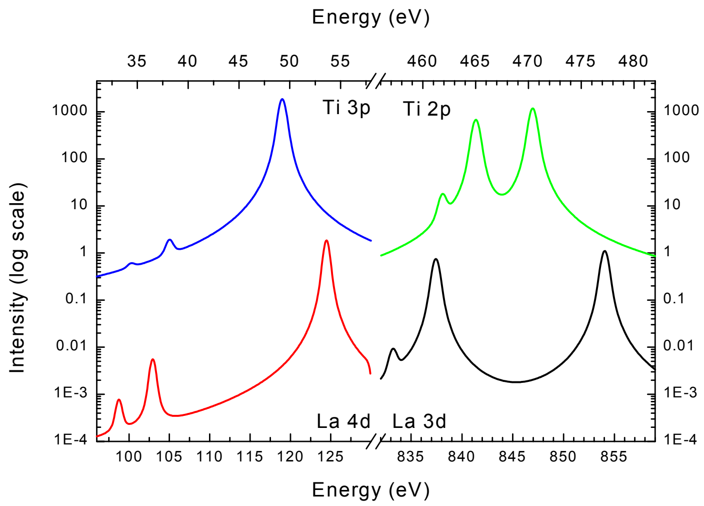

Figure 2.4 *The La^{III} 4d and 3d plus Ti^{IV} 3p and 2p x-ray absorption spectra as calculated for isolated ions. The intensity is given on a logarithmic scale to make the pre-edge peaks visible. The intensities of titanium have been multiplied by 1000.*

In table 2.15 the term symbols of all $3d^N$ systems are given. Together with the dipole selection rules this sets immediately strong limits to the number of final states which can be reached, similar to the case of a $3d^0$ ground state. Consider for example the $3d^3$ $2p^53d^4$ transition: The $3d^3$ ground state has J=3/2 and there are respectively 21, 35 and 39 states of $2p^53d^4$ with J'=1/2, J'=3/2 and J'=5/2. This implies a total of 95 allowed peaks out of the 180 final state term symbols. From table 5 some special cases can be discriminated: a $3d^9$ system makes a transition to a $2p^53d^{10}$ configuration, which has only two term symbols, out of which only the term symbol with J'=3/2 is allowed. In other words, the L_2 edge has zero intensity. $3d^0$ and $3d^8$ systems have only three respectively four peaks, because of the limited amount of states for the $2p^53d^1$ and $2p^53d^9$ configurations.

Transition	Ground	Transitions	Term Symbols

$3d^0$ $2p^53d^1$	$^1S_0$	3	12
$3d^1$ $2p^53d^2$	$^2D_{3/2}$	29	45
$3d^2$ $2p^53d^3$	$^3F_2$	68	110
$3d^3$ $2p^53d^4$	$^4F_{3/2}$	95	180
$3d^4$ $2p^53d^5$	$^5D_0$	32	205
$3d^5$ $2p^53d^6$	$^6S_{5/2}$	110	180
$3d^6$ $2p^53d^7$	$^5D_2$	68	110
$3d^7$ $2p^53d^8$	$^4F_{9/2}$	16	45
$3d^8$ $2p^53d^9$	$^3F_4$	4	12
$3d^9$ $2p^53d^{10}$	$^2D_{5/2}$	1	2

Table 2.12 *The 2p x-ray absorption transitions from the atomic ground state to all allowed final state symmetries, after applying the dipole selection rule:* $J = -1, 0$ *or* $+1$

Atomic multiplet theory is able to accurately describe the 3d and 4d x-ray absorption spectra of the rare earths. In case of the 3d metal ions, atomic multiplet theory can not simulate the x-ray absorption spectra accurately because the effects of the neighbours on the 3d-states are too large. It turns out that it is necessary to include both the symmetry effects and the configuration-interaction effects of the neighbours explicitly. Ligand field multiplet theory takes care of all symmetry effects, while charge transfer multiplet theory allows the use of more than one configuration.

2.4.2. 3d XAS of rare earths

The rare earths or Lanthanides are elements of the 6th row, with, in the atomic state, electronic configuration $4f^n5d^{0\,(1)}6s^2$. In the solid state, in most rare earths one 4f electron goes to the valence band and the configuration becomes $4f^N(5d6s)^3$. In calculations, usually the rare earth trivalent ions are considered, without the outermost (5d and 6s) electrons which do not influence the absorption spectra. The 4f electrons are very localised and have little interaction with the environment. They determine the magnetic properties, but do not participate in the chemical bonding. The X-ray Absorption edges implying the 4f electrons, like the $M_{4,5}$ edges (3d 4f transitions) or $N_{4,5}$ edges (4d 4f transitions) can therefore be described very well within the atomic multiplet theory(Vanderlaan and others 1986). The ground states for the different rare Earth ions are again given by Hunds rules, and are collected in Table 2.16.

RE	Ce	Pr	Nd	Sm	Eu	Gd	Tb	Dy	Ho	Er	Tm	Yb	Lu
Conf.	$4f^1$	$4f^2$	$4f^3$	$4f^5$	$4f^6$	$4f^7$	$4f^8$	$4f^9$	$4f^{10}$	$4f^{11}$	$4f^{12}$	$4f^{13}$	$4f^{14}$
Sym.	$^2F_{5/2}$	$^3H_4$	$^4I_{9/2}$	$^6H_{5/2}$	$^7F_0$	$^8S_{7/2}$	$^7F_6$	$^6H_{15/2}$	$^5I_8$	$^4I_{15/2}$	$^3H_6$	$^2F_{7/2}$	^1S

Table 2.16 *The* $4f^N$ *atomic ground states of the rare earths.*

The absorption process can be written as $4f^n$ $3d^9 4f^{n+1}$. The number of possible $3d^9 4f^{n+1}$ states can be very large, even though in the absorption spectrum only those reachable from the Hunds rule ground state satisfying the J = 0, 1 selection rules will be present. Still, the number of final states that can be reached increases from 3 in lanthanum to 53 in cerium, to 200 in praseodymium and to 1077 in gadolinium. In the end of the series, where the number of 4f holes is reduced, it decreases again to 4 in thulium and 1 for ytterbium.

The cases of Tm and Yb involve only configurations with a maximum of respectively one and two holes and can be readily calculated. They will be discussed in detail. The initial state for Yb^{III}, with thirteen 4f electrons has L=3 and S=1/2. Two J-values are possible J=7/2 and J=5/2 of which the first one, with term symbol $^2F_{7/2}$, is the ground state according to Hunds third rule. The $^2F_{5/2}$ has an energy difference with the ground state that is given by the 4f spin-orbit coupling and from atomic calculations one finds an energy difference of 1.3 eV. The final state, after 3d (or 4d) absorption, is given by $3d^9 4f^{14}$, with term symbols $^2D_{3/2}$ and $^2D_{5/2}$. The energy difference between these terms, corresponding to the 3d spin-orbit coupling is 49.0 eV. However, in the x-ray absorption spectrum only the $^2D_{5/2}$ line (corresponding to the M_5-edge) is present, since the $^2D_{3/2}$ term can not be reached from the $^2F_{7/2}$ ground state because of the J selection rules. Transitions to both final states are possible from the $^2F_{5/2}$ initial state. The relative intensities of these three transitions can be directly determined from a 2x2 matrix. The relative intensities of the $^2F_{5/2}$ state versus the $^2F_{7/2}$ are given by 2J+1 as 6 to 8. Because the relative intensities of $^2D_{3/2}$:$^2D_{5/2}$ is 4:6 and the transition $^2F_{7/2}$ $^2D_{3/2}$ is forbidden one can immediately determine the other three numbers in the matrix as given in table 2.17. As will be discussed in chapter 3, crystal field effects will modify these numbers and effectively mix the $^2F_{5/2}$ state into the $^2F_{7/2}$ ground state.

	$^2F_{5/2}$	$^2F_{7/2}$	
$^2D_{3/2}$	14	0	14
$^2D_{5/2}$	1	20	21
	15	20	

Table 2.17 *The relative intensities of the four transitions from a single d to a single f electron.*

For Tm, the transition is from the $4f^{12}$ ground state to the $3d^9 4f^{13}$ final state. The configurations that must be considered are respectively f^2 and df. An f^2 configuration contains all d^2 configurations as discussed above. Table 2.18 includes all configurations and ground states for the s^2, p^2, d^2 and f^2 configurations. The third Hunds rule gives a $^3H_4$ ground state for $4f^2$. In case of $4f^{12}$ the third Hunds rule yields the maximum J-value and the ground state is $^3H_6$.

	^{1}S	**^{3}P**	**^{1}D**	**^{3}F**	**^{1}G**	**^{3}H**	**^{1}I**		Ground State
Deg.	1	9	5	21	9	33	13		
s^2	1							1	$^1S_0$
p^2	1	9	5					15	$^3P_0$
d^2	1	9	5	21	9			45	$^3F_2$
f^2	1	9	5	21	9	33	13	91	$^3H_4$
J-values	**0**	**0** **1** **2**	**2**	**2** **3** **4**	**4**	**4** **5** **6**	**6**		

Table 2.18 *Possible term symbols for the $1s^2$, $2p^2$, $3d^2$ and $4f^2$ configurations, with their degeneracy and possible J values.*

Most discussions stop at this point, but if one looks more carefully into the problem, one notices that there is a second term symbol with J=6, i.e. the $^1I_6$ state. In intermediate coupling this state will mix with the $^3H_6$ state and the actual ground state will be a linear combination of both states. To discuss this point quantitatively, it is necessary to give the atomic parameters that are part of the calculation. The $4f^{12}$ configuration is set to an average energy of 0.0 and further contains three Slater-Condon parameters and the 4f spin-orbit coupling. The Slater-Condon parameters are respectively F^2=13.175 eV, F^4=8.264 eV and F^6=5.945 eV. The 4f spin-orbit coupling has a value of 0.333 eV. The Slater-Condon parameters determine the energies of the seven LS term symbols indicated in table 2.18. The LS term symbols are split by the 4f spin-orbit coupling to the total of thirteen tem symbols, where the lowest energy is found for the $^3H_6$ state. The $^3H_5$ state and the $^3H_4$ state are very close in energy though, being split only by the 4f spin-orbit coupling. This 4f spin-orbit coupling also mixes the $^1I_6$ state into the ground state according to table 2.19. With the atomic parameters used the energy of the $^3H_6$ state is -2.201 eV below the configuration average and the energy of the $^1I_6$ state lies at 2.064 eV. The small 4f spin-orbit coupling mixes in only a little bit of $^1I_6$ character and the ground state is approximately 99% pure in its $^3H_6$ character.

Energy Matrix		*Eigenvectors*
$\begin{vmatrix} -2.201 & -0.408 \\ -0.408 & 2.025 \end{vmatrix}$		$\begin{array}{c} {}^3H_6 \\ {}^1I_6 \end{array} \begin{vmatrix} 0.995 & -0.095 \\ 0.095 & 0.995 \end{vmatrix}$
Energy Levels		
-2.240	I ~$^3H_6$	
2.064	II ~$^1I_6$	

Table 2.19 *The energy matrix and eigenvectors of the 2x2 matrices of the* f^2 *initial states with* $J=6$*.*

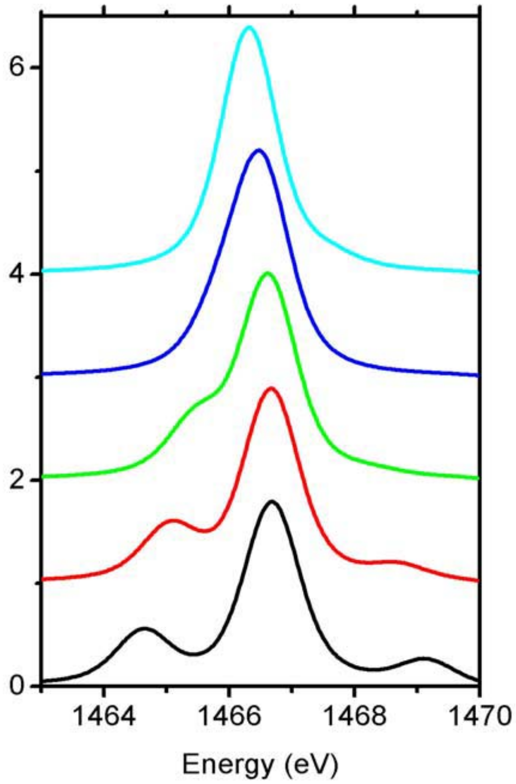

Figure 2.5: *The three peaks of the M5 edge of Tm3+ as a function of the Slater-Condon parameters. The bottom spectrum uses atomic Slater-Condon parameters, i.e. 80% of their Hartree-Fock value. The magnitude of the Slater-Condon parameters is respectively 80%, 60%, 40%, 20% and 0% from bottom to top.*

The $3d^9 4f^{13}$ state after absorption has symmetries that are found after multiplication of a d with a f symmetry state. $^2D \otimes ^2F$ implies that S is 0 or 1 and L is 1,2,3,4 or 5. This gives five singlet terms ($^1P_1$, $^1D_2$, $^1F_3$, $^1G_4$ and $^1H_5$) and fifteen triplet terms ($^3P_{0,1,2}$, $^3D_{1,2,3}$, $^3F_{2,3,4}$, $^3G_{3,4,5}$ and $^3H_{4,5,6}$), with an overall degeneracy of 10x14 is 140. The $^3H_6$ ground state has J=6 and the dipole selection rules states that the final state J must be respectively 5, 6 or 7. There are three states with J=5, respectively $^1H_5$, $^3G_5$ and $^3H_5$ plus one state with J=6, i.e. $^3H_6$. This implies that the $M_{4,5}$ edges of Tm exist of four transitions.

Figure 2.5 shows the three peaks at the M_5 edge. The peak at lowest energy is the Hunds rule $^3H_6$ at 1462.38 eV. This is the only term with J=6 and is therefore a pure $^3H_6$ peak also in **j j** and thus in intermediate coupling. The other peaks all have J=5, and are mixtures of the three term symbols with J=5 in intermediate coupling. One can determine the exact nature of these three states by solving a 3x3 matrix. The $3d94f^{13}$ configuration has an average energy of 1482.67 eV and further contains five Slater-Condon parameters, the 4f spin-orbit coupling and the 3d spin-orbit coupling. The Slater-Condon parameters are respectively F^2=9.09 eV, F^4=4.31 eV, G^1=6.68 eV, G^3=3.92 eV and G^5=2.71 eV. The

4f spin-orbit coupling has a value of 0.37 eV. The main difference with the initial state is the effect of the large 3d spin-orbit coupling of 18.05 eV that is able to strongly mix all states with equal J. This can be seen in table 2.20.

Energy Matrix $\begin{vmatrix} 1484.706 & 10.607 & -19.163 \\ 10.607 & 1469.995 & -10.088 \\ -19.163 & -10.088 & 1486.965 \end{vmatrix}$		*Eigenvectors* $\begin{array}{c\|ccc\|} {}^3H_5 & 0.455 & -0.609 & -0.649 \\ {}^3G_5 & -0.890 & -0.302 & -0.341 \\ {}^1H_5 & 0.116 & -0.733 & 0.680 \end{array}$
Energy Levels		**Intensities**
1464.44	I	4.11
1466.89	II	0.52
1510.33	III	0.23
1462.38	$^3H_6$	1.16

Table 2.20 *The energy matrix and eigenvectors of the 3x3 matrices of the* $3d^9 4f^{13}$ *final states with J=5, after inclusion of the Slater-Condon parameters and the 3d and 4f spin-orbit couplings. The bottom line includes the energy and intensity of the J=6 final state.*

State I has a wave function 0.455 $^3H_5$> - 0.890 $^3G_5$> + 0.116 $^1H_5$>. This state is thus approximately 80% pure $^3G_5$ character as also discussed by (Pompa and others 1997). The final result of the calculation are the four energies and their respective intensities. After broadening they are given in Figure 2.5.

The $3d$ $4f$ transitions have been calculated for all the rare earths *(Thole and others 1985)* using atomic multiplets in intermediate coupling. The electrostatic parameters F^i_f in the initial state and F^i_f and F^i_{fd} in the final state, as well as the exchange parameters G^i_{fd} in the final state, were calculated using an atomic Hartree-Fock program developed by Cowan (Cowan 1981). These values for scaled down to 80% to account for atomic CI effects. The resulting line spectra were then broadened by a Lorentzian to account for the finite lifetime, and an additional Gaussian to reproduce the experimental resolution. For $3d_{3/2}$-transitions, the lineshape is asymmetric due to interactions between the "discrete" $3d_{3/2}$ $4f$ transitions and the transitions from $3d_{3/2}$ into the continuum ($6p$, $7p$, $5f$, etc.). This has been taken into account using a Fano lineshape for the M_4-edge. The results of the calculations are in very good agreement with the experimental absorption edges.
Some general trends in the spectra are the presence of three distinct groups of lines in the calculated line spectra, giving rise to three peaks in the absorption edge. This is visible especially in the M_4-edge for the lighter rare earths and in the M_5-edge for the heavier ones. This splitting into three groups is due to the spin-orbit coupling, which, in intermediate coupling, tends to group lines with the same J together. Another trend is the M_5:M_4 branching ratio that is almost 1:1 for the beginning of the series, but increases a lot going to the heavier rare earths. The spin-orbit coupling in the $4f$-levels favors $4f_{7/2}$ holes, which are only reachable from the $3d_{5/2}$ level, with respect to $4f_{5/2}$. This is the most clear for Yb, where it was shown above that only $3d_{5/2}$ (M_5) absorption is possible.

Moreon the x-rayssspectraa ofrare earths

2.4.3. 1s XAS of 3d trnition metls: the pre-edge

As discussed above, the dipole and quadrupole transitions are in most studies assumed to overlap in energy, or actually they are assumed to be transitions to the same states that therefore must be degenerate. In contrast, for TiO_2 it has been assumed that there is a 2.5 eV energy shift between the dipole and quadrupole transitions, as discussed above. In this section, we will use charge transfer multiplet (CTM) theory in an attempt to unify both models. CTM theory will be outlined in detail in the chapter on soft X-ray absorption. In CTM theory, the ground state of a 3d-metal is described as $3d^N4p^0$, where N indicates the number of 3d electrons. This configuration is mixed with $3d^{N+1}\underline{L}4p^0$, where a virtual excitation from the ligand band (L) to the 3d-band is included. If the relative energy of $3d^{N+1}\underline{L}4p^0$ is set to zero, the energy of the $3d^{N+1}\underline{L}4p^0$ configuration is defined as the charge transfer energy . The number of 4p electrons has been set to zero, but this could be changed to any finite number . There are two extreme cases for the pre-edge calculations:

(1) a system with inversion symmetry, for example octahedral, where the dipole transitions and quadrupole transitions reach final states that belong to different parity and hence do not mix.
(2) A system without inversion symmetry, for example tetrahedral, where the dipole and quadrupole transitions can reach the same final states.

Starting with situation (1), the transitions are:
- $3d^N4p^0+3d^{N+1}\underline{L}4p^0$ (dipole) $1s^13d^N4p^1+1s^13d^{N+1}\underline{L}4p^1$
- $3d^N4p^0+3d^{N+1}\underline{L}4p^0$ (quad.) $1s^13d^{N+1}4p^0+1s^13d^{N+2}\underline{L}4p^0$

The crucial interaction in the final state is the core hole potential on the 3d-electrons. This interaction pulls down the states with additional 3d electrons with a value that is defined as the core hole potential Q. Looking at the dipole respectively quadrupole transitions, a completely different screening behavior is seen. The quadrupole transitions is self-screening as the 1s core electron fills directly a localized 3d state. This situation is much alike the situation of the soft X-ray L edges and the energy ordering of the final states is essentially the same as the ground state, i.e. $1s^13d^{N+2}\underline{L}4p^0$ has an energy of with respect to $1s^13d^{N+1}4p^0$. In practice this implies that transitions to $1s^13d^{N+2}\underline{L}4p^0$ will not be visible in the spectral shape. The situation is completely different for dipole transitions that behave much alike 2p-XPS and the two final state configurations reverse their energy position. The complete energy situation is sketched in figure 9.

In a system without inversion symmetry the dipole final states (dark) and the quadrupole final states (light) do not mix and will be visible independently. This is the case for TiO_2, where a shift is seen between the dipole and quadrupole peaks. The final states at higher energy will in general be (much) weaker than the states at lower energy and they will in general be not visible, also because of the presence of additional edge transitions. In systems without inversion symmetry, the 4p and 3d states mix and form bonding and anti-bonding combinations, both in the initial state and in the final state. This will further complicate the picture, but it will result in the same energy position of the final state configurations with the same number of 3d electrons. This explains why in most cases the energy position of the dipole and quadrupole final states can be assumed to be equal. It is extremely difficult to shed light on this complex situation from an experiment due to the large lifetime broadening. However one can expect new insights from selective XANES and RIXS experiments that will be discussed in section 5.

3. Crystal Field Theory

Crystal Field Theory is a well-known model used to explain the electronic properties of transition metal systems. It has been developed in the fifties and sixties against the background of explaining optical spectra and EPR data. The starting point of the crystal field model is to approximate the transition metal as an isolated atom surrounded by a distribution of charges that should mimic the system, molecule or solid, around the transition metal. At first sight, this seems to be a very simplistic model and one might doubt its usefulness to explain experimental data. However it turned out that such a simple model was extremely successful to explain a large range of experiments, like optical spectra, EPR spectra, magnetic moments, etc.

Maybe the most important reason of the success of the crystal field model is that the explained properties are strongly determined by symmetry considerations. With its simplicity in concept, the crystal field model could make full use of the results of group theory. Group theory also made possible a close link to atomic multiplet theory. Group theoretically speaking, the only thing crystal field theory does is translate, or branch, the results obtained in atomic symmetry to cubic symmetry and further to any other lower point groups. The mathematical concepts for these branching are well developed.

3.1. A short outline of Group Theory

Group theory has been discussed in the lectures on uv-vis spectroscopy. In case of x-ray absorption, some aspects of group theory are particularly important. They are shortly introduced below.

3.1.1. Total Symmetry and Multiplication Tables

The crystal field multiplet calculations for x-ray absorption are performed in total symmetry J, i.e. with the inclusion of the spin-orbit coupling. As discussed in chapter 2, this is necessary because the core hole spin-orbit coupling is large and does not allow using LS-coupling schemes for the final state of the x-ray absorption process. In spherical symmetry the value of J is given as all values that range from |L-S| to L+S, in steps of 1. If one changes spherical symmetry into cubic symmetry, the orbital momentum L is affected as will be discussed in detail later in this chapter. The spin quantum numbers are in principle not affected, but if one includes the core hole spin-orbit coupling one has to modify the symmetry of the spin quantum number also to cubic symmetry, in order to be able to multiply the L and S symmetry states that are both described with the representations given in table 1and 2.

O	A_1	A_2	T_1	T_2	E
A_1	A_1	A_2	T_1	T_2	E
A_2	A_2	A_1	T_2	T_1	E
T_1	T_1	T_2	$T_1 + T_2$ $+E + A_1$	$T_1 + T_2$ $+E + A_2$	T_1+T_2
T_2	T_2	T_1	$T_1 + T_2$ $+E + A_2$	$T_1 + T_2$ $+E + A_1$	T_1+T_2
E	E	E	T_1+T_2	T_1+T_2	A_1+A_2+E

Table 13: *The multiplication table of O symmetry.*

The multiplication rules that apply in O_h and D_{4h} symmetry can be found directly from their character tables. Table 1 gives the multiplication table of O symmetry. For example, multiplying E symmetry with E symmetry yields A_1 plus A_2 plus E symmetry. This can be checked from the character table as follows: E E gives the characters 4, 1, 4, 0 and 0. The first number gives the dimension. The dimension of 4 implies that the added dimensions of the representations must also be 4. If a T_1 or a T_2 state is one of the representations, one can only add an A_1 or A_2 state. The character tables learn that none of these combinations can yield the characters 4,1,4,0,0. One finds that only the combination A_1 A_2 E yields the needed overall characters. In analogy one can determine the complete multiplication table. Table 2 repeats this procedure for D_4 symmetry.

D4	A_1	A_2	B_1	B_2	E
A_1	A_1	A_2	B_1	B_2	E
A_2	A_2	A_1	B_2	B_1	E
B_1	B_1	B_2	A_1	A_2	E
B_2	B_2	B_1	A_2	A_1	E
E	E	E	E	E	A_1+A_2+ B_1+B_2

Table 14: *The multiplication table of D_4 symmetry.*

We have now enough group theoretical information to understand the consequences of the crystal field effect on the atomic multiplet states.

3.2. The Crystal Field Multiplet Hamiltonian

The crystal field multiplet Hamiltonian consists of the atomic Hamiltonian as outlined in the previous chapter, to which an electrostatic field is added:

$$H_{CF} = H_{ATOM} + H_{FIELD}$$

$$H_{ATOM} = \sum_N \frac{p_i^2}{2m} + \sum_N \frac{-Ze^2}{r_i} + \sum_{pairs} \frac{e^2}{r_{ij}} + \sum_N \zeta(r_i)\, l_i \cdot s_i$$

$$H_{FIELD} = - e\varphi(r)$$

The only term added to the atomic Hamiltonian is an electrostatic field, which consists of the electronic charge e times, a potential that describes the surroundings (r). The potential (r) is written as a series expansion of spherical harmonics Y_{LM}'s:

$$\phi(r) = \sum_{L=0}^{\infty} \sum_{M=-L}^{L} r^L A_{LM} Y_{LM}(\psi,\phi)$$

The crystal field is regarded as a perturbation to the atomic result. This implies that it is necessary to determine the matrix elements of (r) with respect to the atomic 3d orbitals <3d| (r)|3d>. One can separate the matrix elements into a spherical part and a radial part, as was done also for the atomic Hamiltonian. The radial part of the matrix elements yields the strength of the crystal field interaction. The spherical part of the matrix element can be written completely in Y_{LM} symmetry, where the two 3d-electrons are written as Y_{2m}. This gives:

$$\left\langle Y_{2m_2} \middle| Y_{LM} \middle| Y_{2m_1} \right\rangle = (-1)^{m_2} \sqrt{15(2L+1)/4\pi} \begin{pmatrix} 2 & L & 2 \\ -m_2 & M & m_1 \end{pmatrix} \begin{pmatrix} 2 & L & 2 \\ 0 & 0 & 0 \end{pmatrix}$$

The second 3J-symbol is zero unless L is equal to 0, 2 or 4. This limits the crystal field potential for 3d electrons to:

$$\phi(r) = A_{00}Y_{00} + \sum_{M=-2}^{2} r^2 A_{2M} Y_{2M} + \sum_{M=-4}^{4} r^4 A_{4M} Y_{4M}$$

The first term $A_{00}Y_{00}$ is a constant. It will only shift the atomic states and it is not necessary to include this term explicitly if one calculates the spectral shape.

3.3. Cubic crystal fields

A large range of systems posses a transition metal ion surrounded by six or eight neighbors. The six neighbors are positioned on the three Cartesian axes, or in other words on the six faces of a cube surrounding the transition metal. They form a so-called octahedral field. The eight neighbors are positioned on the eight corners of the cube and form a so-called cubic field. Both these systems belong to the O_h point group. The character table of O_h symmetry is given above. O_h symmetry is a subgroup of the atomic SO_3 group.

The calculation of the x-ray absorption spectral shape in atomic symmetry involved the calculation of the matrices of the initial state, the final state and the transition. The initial state is given by the matrix element $<3d^N \mid H_{ATOM} \mid 3d^N>$, which for a particular J-value in the initial state gives $_J$<J|0|J>. The same applies for the final state matrix element

$\langle 2p^5 3d^{N+1} \mid H_{ATOM} \mid 2p^5 3d^{N+1}\rangle$, where $_{J'}\langle J'|0|J'\rangle$ is calculated for the values of J' that fulfill the selection rule, i.e. J'=J-1, J and J+1. The dipole matrix element $\langle 3d^N \mid p \mid 2p^5 3d^{N+1}\rangle$ implies the calculation of all matrices that couple J and J': $_{J,J'}\langle J|1|J'\rangle$. To calculate the x-ray absorption spectrum in a cubic crystal field, these atomic transition matrix elements must be branched to cubic symmetry. This is essentially the only task to fulfill.

SO_3		O_h (Butler)	O_h (Mulliken)
S	0	0	A_1
P	1	1	T_1
D	2	$2 + \hat{1}$	$E+T_2$
F	3	$\hat{0} + 1 + \hat{1}$	$A_2+T_1+T_2$
G	4	$0 + 1 + 2 + \hat{1}$	$A_1+E+T_1+T_2$

Table 15 *Branching rules for the symmetry elements by going from SO_3 symmetry to O_h symmetry.*

Table 3 gives the branching from SO_3 to O_h symmetry. This table can be determined from group theory. This table implies that an S symmetry state in atomic symmetry branches only to an A_1 symmetry state in octahedral symmetry. This is the case, because the symmetry elements of an s-orbital in O_h symmetry are determined by the character table of A_1 symmetry, i.e. whatever symmetry operation one applies an s-orbital remains an s-orbital. This is not the case for the other orbitals. For example, a p-orbital can be described with the characters of the T_1 symmetry state in O_h symmetry, for example the class G_3, a two-fold rotation around x, inverts the p-orbital. A d-orbital or a D symmetry state in SO_3, branches to E plus T_2 symmetry states in octahedral symmetry. This can be related to the character table by adding the characters of E and T_2 symmetry, yielding the overall characters 5, -1, 1, -1 and 1, which describe the properties of d-orbitals in O_h symmetry, i.e. the dimension of a d-orbital is 5 and the class G_4 (a fourfold rotation around x) inverts the d-orbitals. This is a well-known result: A 3d electron is separated into t_{2g} and e_g electrons in octahedral symmetry, where the symmetries include the gerade-notation of the complete O_h character table.

One can make the following observations: The dipole transition operator has p-symmetry and is branched to T_1 symmetry. Having a single symmetry in O_h symmetry, there will be no dipolar angular dependence in x-ray absorption. The quadrupole transition operator has d-symmetry and is split into two operators in O_h symmetry, in other words there will be different quadrupole transitions in different directions. The Hamiltonian is given by the unity representation A_1 of the symmetry under consideration. In O_h symmetry the atomic G-symmetry state branches into the A_1 Hamiltonian.

We can lower the symmetry from octahedral O_h to tetragonal D_{4h} and describe this symmetry lowering again with a branching table. Table 4 gives the branching table from O_h to D_{4h} symmetry.

O_h (Butler)	O_h (Mulliken)	D_{4h} (Butler)	D_{4h} (Mulliken)
0	A_1	0	A_1
$\hat{0}$	A_2	2	B_1
1	T_1	$1 + \hat{0}$	$E + A_2$
$\hat{1}$	T_2	$1 + \hat{2}$	$E + B_2$
2	E	$0 + 2$	$A_1 + B_1$

Table 16 *Branching rules for the symmetry elements by going from O_h symmetry to D_{4h} symmetry.*

An atomic s-orbital is branched to D_{4h} symmetry according to the branching series S A_1 A_1. In other words it is still the unity element, and it will always be the unity element in all symmetries. An atomic p-orbital is branched according to P T_1 $E+A_2$. Adding the characters of E and A_2 yields 3, -1, 1, -1 and -1, implying that a two-fold rotation around the z-axis inverts a p-orbital, etc. Similarly an atomic d-orbital is branched according to D $E+T_2$ $A_1+B_1+E+B_2$. Adding the characters of these four representations yields 5, 1, -1, 1 and 1. The dipole transition operator has p-symmetry and hence is branched to $E+A_2$ symmetry, in other words the dipole operator is described with two operators in two different directions implying an angular dependence in the x-ray absorption intensity. The quadrupole transition operator has d-symmetry and is split into four operators in D_{4h} symmetry, in other words there will be four different quadrupole transitions in different directions/symmetries. The Hamiltonian is given by the unity representation A_1. Similarly as in O_h symmetry, the atomic G-symmetry state branches into the Hamiltonian in D_{4h} symmetry according to the series G A_1 A_1. In addition it can be seen that the E symmetry state of O_h symmetry branches to the A_1symmetry state in D_{4h} symmetry. The E symmetry state in O_h symmetry is found from the D and G atomic states. This implies that also the series G E A_1 and D E A_1 become part of the Hamiltonian in D_{4h} symmetry. The three branching series in D_{4h} symmetry are in Butlers notation given as 4 0 0, 4 2 0 and 2 2 0 and the radial parameters related to these branches are indicated as X_{400}, X_{420}, and X_{220}. The X_{400} term is important already in O_h symmetry. This term is closely related to the cubic crystal field term 10Dq as will be discussed below.

3.3.1. *The definitions of the Crystal Field parameters*

In order to compare the X_{400}, X_{420}, and X_{220} definition of crystal field operators to other definitions like Dq, Ds, Dt, we compare their effects on the set of 3d-functions. The most straightforward way to specify the strength of the crystal field parameters is to calculate the energy separations of the 3d-functions. In O_h symmetry there is only one crystal field parameter X_{40}. This parameter is normalized in a manner that creates unitary transformations in the calculations. The result is that it is equal to 1/18* 30 times 10Dq, or 0.304 times10Dq.

In tetragonal symmetry (D_{4h}) the crystal field is given by three parameters, X_{400}, X_{420} and X_{220}. An equivalent description is to use the parameters Dq, Ds and Dt. Table 5 gives the action of the X_{400}, X_{420} and X_{220} on the 3d-orbitals and relates the respective symmetries to the linear combination of X parameters, the linear combination of the Dq, Ds and Dt parameters and the specific 3d-orbital(s) of that particular symmetry.

	Energy expressed in X-terms	Energy in D-terms	orbitals
b_1	$30^{-½}\cdot X_{400}$ $42^{-½}\cdot X_{420}$ $2\cdot 70^{-½}\cdot X_{220}$	6Dq+2Ds 1Dt	$3d_{x2-y2}$

a_1	$30^{-½}\cdot X_{400} + 42^{-½}\cdot X_{420} + 2\cdot 70^{-½}\cdot X_{220}$	6Dq 2Ds 6Dt	$3d_{z2}$
b_2	$-2/3\cdot 30^{-½}\cdot X_{400} + 4/3\cdot 42^{-½}\cdot X_{420}\quad 2\cdot 70^{-½}\cdot X_{220}$	-4Dq+2Ds 1Dt	$3d_{xy}$
e	$-2/3\cdot 30^{-½}\cdot X_{400}\quad 2/3\cdot 42^{-½}\cdot X_{420} + 70^{-½}\cdot X_{220}$	-4Dq-1Ds+4Dt	$3d_{xz}$, $3d_{yz}$

Table 17 *The energy of the 3d orbitals is expressed in X_{400}, X_{420} and X_{220} in the second column and in Dq, Ds and Dt in the third column.*

From this table we can relate both notations and write X_{400}, etc as a function of Dq, Ds and Dt.

$$X_{400} = 6\cdot 30^{½}\cdot Dq\quad 7/2\cdot 30^{½}\cdot Dt$$
$$X_{420} = \quad 5/2\cdot 42^{½}\cdot Dt$$
$$X_{220} = \quad 70^{½}\cdot Ds.$$

The inverse relationship imply:

$$Dq = 1/6\cdot 30^{-½}\cdot X_{400}\quad 7/30\cdot 42^{-½}\cdot X_{420}$$
$$Ds = -70^{-½}\cdot X_{220}$$
$$Dt = -2/5\cdot 42^{-½}\cdot X_{420}$$

These relations allow the quick transfer from for example the values of Dq, Ds and Dt from optical spectroscopy to the X-values as used in x-ray absorption.

3.4. The energies of the $3d^N$ configurations

The crystal field effect modifies the atomic energy levels by the additional terms in the Hamiltonian. We will use the $3d^8$ configuration as an example to show the effects of the O_h and D_{4h} symmetry. Assuming for the moment that the 3d spin-orbit coupling is zero, in O_h symmetry the five term symbols in spherical symmetry split into eleven term symbols. Their respective energies can be calculated by adding the effect of the cubic crystal field 10Dq to the atomic energies. The diagrams of the respective energies with respect to the cubic crystal field (normalized to the Racah parameter B) are known as the Tanabe-Sugano diagrams.

	Relative Energy	Symmetries in O_h	Symmetries in D_{4h}
^1S	4.6 eV	$^1A_1$	$^1A_1$
^3P	0.2 eV	$^3T_1$	$^3E+^3A_2$
^1D	-0.1 eV	$^1E + ^1T_2$	$^1A_1+^1B_1 + ^1E+^1B_2$
$\mathbf{^3F}$	-1.8 eV	$\mathbf{^3A_2} + ^3T_1 + ^3T_2$	$\mathbf{^3B_1} + ^3E + ^3A_2 + ^3E + ^3B_2$
^1G	0.8 eV	$^1A_1+^1T_1+^1T_2+^1E$	$^1A_1+^1E + ^1A_2+^1E+^1B_2+^1A_1+^1B_1$

Table 18 *The five symmetry states of a 3d^8 configuration in SO$_3$ symmetry and their respective energies for Ni^{II} are given in columns 1 and 2. Column 3 gives the respective symmetries of these states in O$_h$ symmetry and column 4 in D$_{4h}$ symmetry. In both cases the spin-orbit coupling has not yet been included.*

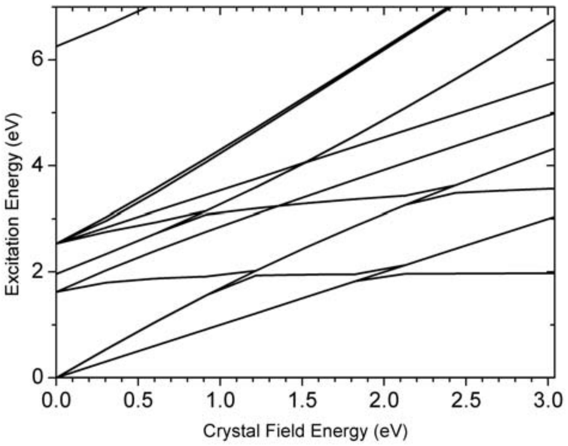

Figure 1: *The Tanabe-Sugano diagram for a 3d^8 configuration in O$_h$ symmetry.*

This figure gives the Tanabe-Sugano diagram for the 3d^8 configuration. The ground state of a 3d^8 configuration in O$_h$ symmetry has $^3A_2$ symmetry. It is set to zero in this figure. If the crystal field energy is 0.0 eV one has effectively the atomic multiplet states. From low energy to high energy, one can observe respectively the ^3F, ^1D, ^3P, ^1G and ^1S states. Including a finite crystal field strength splits these states, for example the ^3F state is split into $^3A_2$ + $^3T_1$ + $^3T_2$. At higher crystal field strengths states start to change their order and they cross. If states actually cross each other or show non-crossing behavior depends on the fact if their symmetries allow them to form a linear combination of states. This also depends on the inclusion of the 3d spin-orbit coupling.

Figure 2 shows the effect of the reduction of the Slater-Condon parameters. The figure is the same as figure 1 up to a crystal field of 1.5 eV. Then for this crystal field value the Slater-Condon parameters have been reduced from their atomic value, indicated with 80% of their Hartree-Fock value to 0%. The spectrum for 0% has all its Slater-Condon parameters reduced to zero, In other words the 2p3d coupling has been turned of and one essentially observes the energies of a 3d^8 configuration, i.e. of a two 3d-holes. This single particle limit has three configurations, respectively the two holes in e_ge_g, e_gt_{2g} and $t_{2g}t_{2g}$ states. The energy difference between e_ge_g and e_gt_{2g} is exactly the crystal field value of 1.5 eV. This figure shows nicely the transition from the single particle picture to the multiplet picture for the 3d^8 ground state.

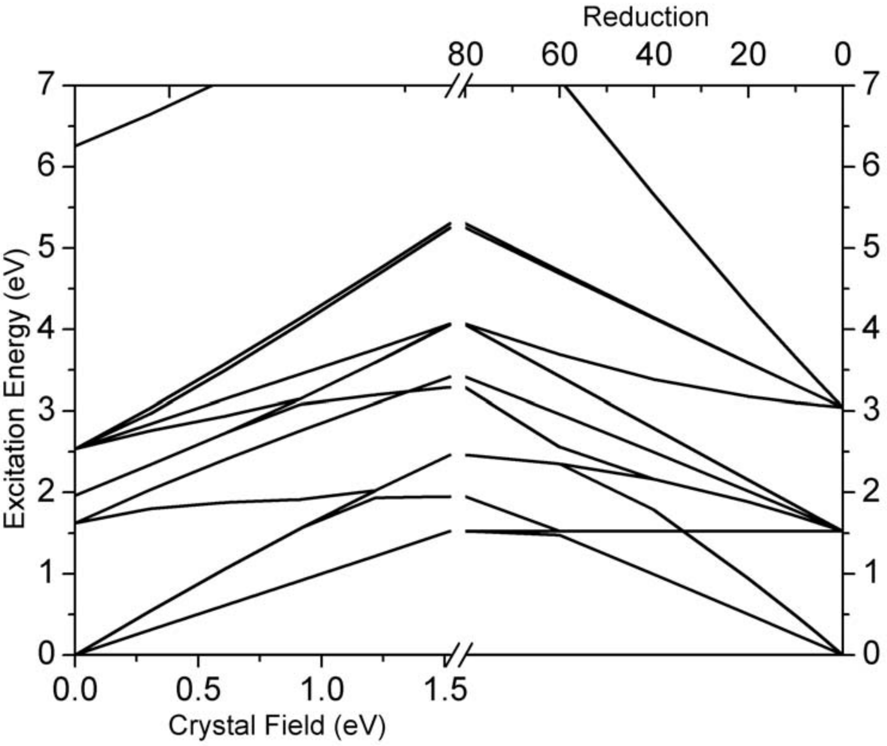

Figure 2 *The Tanabe-Sugano diagram for a 3d^8 configuration in O$_h$ symmetry, including the effect of reduced Slater-Condon parameters.*

The ground state of a 3d^8 configuration in O$_h$ symmetry always remains $^3A_2$. The reason is clear if one compares these configurations to the single particle description of a 3d^8 configuration. In a single particle description a 3d^8 configuration is split by the cubic crystal field into the t$_{2g}$ and the e$_g$ configuration, following the branching rules. Having found these configurations, one adds the eight 3d electrons one-by-one to these configurations. The t$_{2g}$ configuration has the lowest energy and can contain six 3d electrons. The remaining two electrons are placed in the e$_g$ configuration, where both have a parallel alignment according to Hunds rule. The result is that the overall configuration is t$_{2g}$^{6}e$_g$(up)^2. This configuration identifies with the $^3A_2$ configuration.

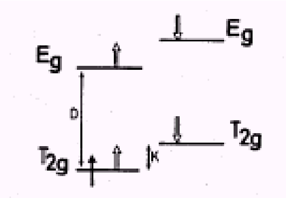

Figure 3 *The splitting of a single 3d-electron under influence of the cubic crystal field D and the Stoner exchange interaction J. A second electron is indicated with an empty arrow to indicate the energy effects.*

Figure 3 shows the splitting of a 3d configuration into an e_g and a t_{2g} configuration. Both configurations are further split by the Stoner exchange splitting J. The Stoner exchange splitting J is given as a linear combination of the Slater-Condon parameters as $J=(F_2+F_4)/14$. The Stoner exchange splitting is an approximation to the effects of the Slater-Condon parameters and in fact a second parameter C, the orbital polarization, can be used in combination with J. The orbital polarization C is given as $C=(9F_2-5F_4)/98$. Often this orbital polarization is omitted from single particle descriptions. In that case the multiplet configuration $^3A_2$ is not exactly equal to the single particle configuration $t_{2g}{}^6e_g(\text{up})^2$. We assume for the moment that the effect of the orbital polarization will not modify the ground states. Then one can show that the ground states of $3d^N$ configurations are those as given in table 7.

Conf.	Ground State in SO_3	HS Ground State in O_h	LS Ground State in O_h
$3d^0$	$^1S_0$	$^1A_1$	-
$3d^1$	$^2D_{3/2}$	$^2T_2$	-
$3d^2$	$^3F_2$	$^3T_1$	-
$3d^3$	$^4F_{3/2}$	$^4A_2$	-
$3d^4$	$^5D_0$	^5E	$^3T_1$
$3d^5$	$^6S_{5/2}$	$^6A_1$	$^2T_2$
$3d^6$	$^5D_2$	$^5T_2$	$^1A_1$
$3d^7$	$^4F_{9/2}$	$^4T_1$	^2E
$3d^8$	$^3F_4$	$^3A_2$	-
$3d^9$	$^2D_{5/2}$	^2E	-

Table 19 *The configurations $3d^0$ to $3d^9$ are given in O_h symmetry for all possible high-spin (HS) and low-spin (LS) states. The third column gives the HS term symbols and the last column the LS term symbols. The fourth and fifth columns give the respective occupations of the t_{2g} and e_g orbitals.*

Table 7 shows that for the configurations $3d^4$, $3d^5$, $3d^6$ and $3d^7$ there are two possible ground state configurations in O_h symmetry. A high-spin ground state that originates from the Hunds rule ground state plus a low-spin ground state for which first all t_{2g} levels are filled. One can directly relate the symmetry of a configuration to the partly filled sub-shell in the single particle model. A single particle configuration with one t_{2g} electron has T_2 symmetry, two t_{2g} electrons imply T_1 symmetry and one e_g electron implies E symmetry. If the t_{2g} electrons are filled and the e_g electrons (of the same spin) are empty the symmetry is A_2. Finally, if both the t_{2g} and e_g states (of the same spin) are filled the symmetry is A_1. The nature of the ground state is important, as we will show below that E symmetry states are susceptible to Jahn-Teller distortions and T_1 and T_2 symmetry states are susceptible to the effects of the 3d spin-orbit coupling.

The transition from high-spin top low-spin ground states is determined by the cubic crystal field 10Dq and the exchange splitting J. The exchange splitting is present for every two parallel electrons. Table 7 gives the high-spin and low-spin occupations of the t_{2g} and e_g spin-up and spin-down orbitals t_{2g+}, e_{g+}, t_{2g-} and e_{g-}. The $3d^4$ and $3d^7$ configuration differ by one t_{2g} versus e_g electron hence one time the crystal field splitting D. The $3d^5$ and $3d^6$ configurations differ by 2D. The exchange interaction J is slightly different for e_ge_g, e_gt_{2g} and $t_{2g}t_{2g}$ interactions and column 5 contains the overall exchange interactions. The last column can be used to estimate the transition point. For this column the exchange splittings were assumed to be equal, yielding the simple rules that for $3d^4$ and $3d^5$ configurations high-spin states are found if the crystal field splitting is less than 3J. In case of $3d^6$ and $3d^7$ configurations the crystal field value should be less than 2J for a high-spin configuration. Because J can be estimated as 0.8 eV, the transition points are approximately 2.4 eV for $3d^4$ and $3d^5$, respectively 1.6 eV for $3d^6$ and $3d^7$. In other words $3d^6$ and $3d^7$ materials have a tendency to be low-spin compounds. This is particularly true for $3d^6$ compounds because of the additional stabilizing nature of the $3d^6$ $^1A_1$ low spin ground state.

Conf.	High-Spin	Low-Spin	10Dq (D)	Exchange (J)	J/D
$3d^4$	$t_{2g+}^3\ e_{g+}^1$	$t_{2g+}^3\ t_{2g-}^1$	1D	$3J_{te}$	3
$3d^5$	$t_{2g+}^3\ e_{g+}^2$	$t_{2g+}^3\ t_{2g-}^2$	2D	$6J_{te}+J_{ee}-J_{tt}$	~3
$3d^6$	$t_{2g+}^3\ e_{g+}^2\ t_{2g-}^1$	$t_{2g+}^3\ t_{2g-}^3$	2D	$6J_{te}+J_{ee}-3J_{tt}$	~2
$3d^7$	$t_{2g+}^3\ e_{g+}^2\ t_{2g-}^2$	$t_{2g+}^3\ t_{2g-}^3\ e_{g+}^1$	1D	$3J_{te}+J_{ee}-2J_{tt}$	2

Table 20 *The high-spin and low-spin distribution of the 3d electrons for the configurations* $3d^4$ *to* $3d^7$*. The fourth column gives the difference in crystal field energy, the fifth column the difference in exchange energy. For the last column, we have assumed that* J_{te}~J_{ee}~J_{tt}=J*.*

3.4.1. The effect of the 3d spin-orbit coupling

As discussed above the inclusion of 3d spin-orbit coupling will bring one to the multiplication of the spin and orbital moments to a total moment. In this process one loses the familiar nomenclature for the ground states of the $3d^N$ configurations. For example the ground state of Ni^{II} in octahedral symmetry is in total symmetry referred to as T_2 and not as $^3A_2$. In total symmetry also the spin moments are branched to the same symmetry group as the orbital moments, yielding for a $^3A_2$ ground state an overall ground state of $T_1\ \ A_2=T_2$. It turns out that in many cases it is better to omit the 3d spin-orbit coupling because it is 'quenched', for example by solid state effects. This has been found to be the case for CrO_2. A different situation is found for CoO, where the explicit inclusion of the 3d spin-orbit coupling is essential for a good description of the 2p x-ray absorption spectral shape. In other words 2p x-ray absorption is able to determine the different role of the 3d spin-orbit coupling in respectively CrO_2 (quenched) and CoO (not quenched).

Table 9 gives the spin-projection to O_h symmetry. The ground states with an odd number of 3d electrons do have a ground state spin moment that is half-integer. These half-integer configurations have not been included in the discussion of the character tables discussed above and can be found elsewhere. Table 9 shows that the degeneracy of the overall symmetry states is often not exactly equal to the spin number as given in the third column. For example the $^3T_1$ ground state is split into four configurations, not three as one would expect. If the 3d spin-orbit coupling is small (and if no other state is close in energy), two of these four states are quasi-degenerate and one finds essentially three states. This is in general the case for all situations. Note that the $^6A_1$ ground state of $3d^5$ is split into two configurations. These configurations are degenerate as far as the 3d spin-orbit coupling is concerned. However because of differences in the mixing of excited term symbols a small energy difference can be found. This is the origin of the small but non-zero zero field splitting in the EPR analysis of $3d^5$ compounds.

Conf.	Ground State in SO3	High-Spin Ground State in Oh	Spin in Oh	Deg.	Overall Symmetry in Oh
$3d^0$	$^1S_0$	$^1A_1$	A_1	1	A_1
$3d^1$	$^2D_{3/2}$	$^2T_2$	U_1	2	$U_2 + G$
$3d^2$	$^3F_2$	$^3T_1$	T_1	4	$E+T_1+T_2+A_1$
$3d^3$	$^4F_{3/2}$	^{4}A2	G	1	G
$3d^4$	$^5D_0$	^5E $3T_1$	$E + T_2$ T_1	5 4	$A_1+A_2+E+T_1+T_2$ $E+T_1+T_2+A_1$
$3d^5$	$^6S_{5/2}$	$^6A_1$ $2T_2$	$G+U_2$ U_1	2 2	$G+U_2$ $G+U_2$
$3d^6$	$^5D_2$	$^5T_2$ $1A_1$	$E+T_2$ A_1	6 1	$A_1+E+T_1+T_1+T_2+T_2$ A_1
$3d^7$	$^4F_{9/2}$	$^4T_1$ 2E	G U_1	4 1	$U_1+U_2+G + G$ G
$3d^8$	$^3F_4$	$^3A_2$	T_1	1	T_2
$3d^9$	$^2D_{5/2}$	^2E	U_1	1	G

Table 9 *The branching of the spin-symmetry states and its consequence on the states that are found after the inclusion of spin-orbit coupling. The fourth column gives the spin-projection and the fifth column its degeneracy. The last column lists all the symmetry states after inclusion of spin-orbit coupling.*

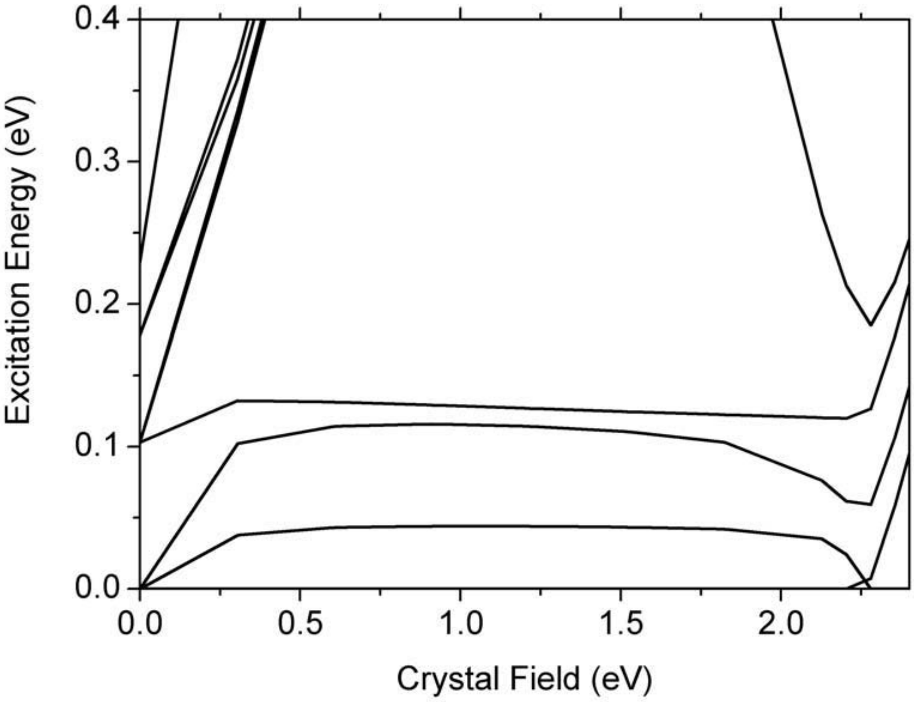

Figure 1. *The Tanabe-Sugano diagram for a* $3d^7$ *configuration in* O_h *symmetry.*

Figure 4 shows the Tanabe-Sugano diagram for a $3d^7$ configuration in O_h symmetry. Only the excitation energies from 0.0 to 0.4 eV are shown to highlight the high-spin low-spin transition at 2.25 eV and also the important effect of the 3d spin-orbit coupling. It can be observed that the atomic multiplet spectrum of Co^{II} has a large number of states at low energy. All these states are part of the $^4F_{9/2}$ configuration that is split by the 3d spin-orbit coupling. After applying a cubic crystal field, most of these multiplet states are shifted to higher energies and only four states remain at low energy. These are the four states of $^4T_1$ as indicated in the table. These four states all remain within 0.1 eV from the U_1 ground state. That this description is actually correct has been shown in detail for the 2p x-ray absorption spectrum of CoO, which has a cubic crystal field of 1.2 eV. At 2.25 eV the high-spin low-spin transition is evident. A new state is coming from high energy and a G-symmetry state replaces the U_1 symmetry state at the lowest energy. In fact there is a very interesting complication: due to the 3d spin-orbit coupling the G-symmetry states of the $^4T_1$ and ^2E configurations mix and form linear combinations. Just above the transition point, this linear combination will have a spin-state that is neither high-spin nor low-spin and in fact a mixed spin-state can be found.

3.4.2. The effects on the x-ray absorption calculations

General calculation $3d^N$ $2p^53d^{N+1}$ in SO_3 symmetry		
Initial State	Transition	Final State
$\mathbf{\langle 0 \vert 0 \vert 0 \rangle}$	$\mathbf{\langle 0 \vert 1 \vert 1 \rangle}$	$\langle 0 \vert 0 \vert 0 \rangle$
$\langle 1 \vert 0 \vert 1 \rangle$	$\langle 1 \vert 1 \vert 0 \rangle$ $\langle 1 \vert 1 \vert 1 \rangle$ $\langle 1 \vert 1 \vert 2 \rangle$	$\mathbf{\langle 1 \vert 0 \vert 1 \rangle}$
$\langle 2 \vert 0 \vert 2 \rangle$	$\langle 2 \vert 1 \vert 1 \rangle$ $\langle 2 \vert 1 \vert 3 \rangle$	$\langle 2 \vert 0 \vert 2 \rangle$
$\langle 3 \vert 0 \vert 3 \rangle$	$\langle 3 \vert 1 \vert 2 \rangle$ $\langle 3 \vert 1 \vert 3 \rangle$ $\langle 3 \vert 1 \vert 4 \rangle$	$\langle 3 \vert 0 \vert 3 \rangle$
$\langle 4 \vert 0 \vert 4 \rangle$	$\langle 4 \vert 1 \vert 3 \rangle$ $\langle 4 \vert 1 \vert 4 \rangle$	$\langle 4 \vert 0 \vert 4 \rangle$

Table 10 *The matrix elements in* SO_3 *symmetry needed for the calculation of 2p x-ray absorption. Boldface matrix elements apply to a* $3d^0$ *configuration.*

Table 10 gives all matrix element calculations that have to be carried out for $3d^N$ $2p^53d^{N+1}$ transitions in SO_3 symmetry for the J-values up to 4. These calculations have been discussed in detail in chapter 2.We will use the transitions $3d^0$ $2p^53d^1$ as examples. $3d^0$ contains only J=0 symmetry states. This limits the calculation for the ground state spectrum to only one ground state, one transition and one final state matrix element. We are now going to apply the SO3 Oh and Oh D_{4h} branching rules to these tables.

General calculation $3d^N$ $2p^53d^{N+1}$ in O_h symmetry		
Initial State	Transition	Final State
$\mathbf{\langle A_1 \vert A_1 \vert A_1 \rangle}$	$\mathbf{\langle A_1 \vert T_1 \vert T_1 \rangle}$	$\langle A_1 \vert A_1 \vert A_1 \rangle$
$\langle T_1 \vert A_1 \vert T_1 \rangle$	$\langle T_1 \vert T_1 \vert A_1 \rangle$ $\langle T_1 \vert T_1 \vert T_1 \rangle$ $\langle T_1 \vert T_1 \vert E \rangle$ $\langle T_1 \vert T_1 \vert T_2 \rangle$	$\mathbf{\langle T_1 \vert A_1 \vert T_1 \rangle}$
$\langle E \vert A_1 \vert E \rangle$	$\langle E \vert T_1 \vert T_1 \rangle$ $\langle E \vert T_1 \vert T_2 \rangle$	$\langle E \vert A_1 \vert E \rangle$
$\langle T_2 \vert A_1 \vert T_2 \rangle$	$\langle T_2 \vert T_1 \vert T_1 \rangle$ $\langle T_2 \vert T_1 \vert E \rangle$ $\langle T_2 \vert T_1 \vert T_2 \rangle$ $\langle T_2 \vert T_1 \vert A_2 \rangle$	$\langle T_2 \vert A_1 \vert T_2 \rangle$
$\langle A_2 \vert A_1 \vert A_2 \rangle$	$\langle A_2 \vert T_1 \vert T_2 \rangle$	$\langle A_2 \vert A_1 \vert A_2 \rangle$

Table 11 *The matrix elements in O_h symmetry needed for the calculation of 2p x-ray absorption. Boldface matrix elements apply to a 3d^0 configuration.*

In octahedral symmetry one has to calculate five matrices for the initial and final states and thirteen transition matrices. Note that this is a general result for all even numbers of 3d electrons, as there are only these five symmetries in O_h symmetry. In the 3d^0 case, the ground state branches to A_1 and only three matrices are needed to generate the spectral shape: $<A_1|A_1|A_1>$ for the 3d^0 ground state, $<A_1|T_1|T_1>$ for the dipole transition and $<T_1|A_1|T_1>$ for the 2p^{5}3d^1 final state.

3.4.3. 3d^0 systems in octahedral symmetry

In this section we will focus on the discussion of the crystal field effects on the spectral shape of 3d^0 systems. The 3d^{0}systems are rather special because they are not affected by ground state effects. Table 11 shows that the 3d^0 2p^{5}3d^1 transition can be calculated from a single transition matrix $<A_1|T_1|T_1>$ in O_h symmetry. The ground state A_1 matrix is 1x1 and the final state T_1 matrix is 7x7, making the transition matrix 1x7. In other words the spectrum consists of a maximum of seven peaks. Chapter 3 showed the complete calculation in SO_3 symmetry. The respective degeneracies of the J-values in SO_3 symmetry and the degeneracies of the representations in O_h symmetry are collected in Table 12.

J in SO_3	Deg.	Branchings	in O_h	Deg.
0	1	A_1	A_1	2
1	3	3 T_1	A_2	3
2	4	4 E, 4 T_2	T_1	7
3	3	3 A_2, 3 T_1,3 T_2	T_2	8
4	1	A_1, E, T_1, T_2	E	5
	12			25

Table 12 *The branching of the J-values in SO_3 symmetry to the representations in O_h symmetry, using the degeneracies of the 2p^{5}3d^1 final state in x-ray absorption.*

A 2p^{5}3d^1 configuration has twelve representations in SO_3 symmetry that are branched to 25 representations in a cubic field. The overall degeneracy of the 2p^{5}3d^1 configuration is 6x10=60, implying a possibility of 60 transitions in a system without any symmetry. From these 25 representations, only seven are of interest for the calculation of the x-ray absorption spectral shape, because only these T_1 symmetry states obtain a finite intensity.

	461.8569	**462.3299**	**462.6130**	**463.4423**	**465.0240**	**468.5886**	**470.4051**
1	0.0924	0.0000	0.0000	0.0000	0.6001	0.0000	0.3075
2	0.9009	0.0000	0.0000	0.0000	0.0384	0.0000	0.0607
3	***0.0068***	***0.0000***	***0.0000***	***0.0000***	***0.3615***	***0.0000***	***0.6318***
4	0.0000	0.0000	0.6019	0.0364	0.0000	0.3617	0.0000
5	0.0000	0.0000	0.0459	0.6674	0.0000	0.2867	0.0000
6	0.0000	0.0000	0.3521	0.2963	0.0000	0.3516	0.0000
7	0.0000	1.0000	0.0000	0.0000	0.0000	0.0000	0.0000

	0.0001	**0.0000**	**0.0000**	**0.0000**	**0.2466**	**0.0000**	**0.7533**

Table 13 *The T_1 final states of the $2p^5 3d^1$ configuration with 10Dq=0.0 eV. The top row gives the energies and the bottom row the relative intensities of the seven final states that are build from seven basis-vectors.*

Table 13 shows the seven T_1 symmetry states calculated with a crystal field splitting of 0.0 eV. One finds the three peaks that are related to J=1 final states, build from vector rows one, two and three. The third row is related to the $^1P_1$ state and the intensity of the peak as given in the bottom row is equal to the square of this row, where the total intensity is normalized to 1.0. Rows four, five and six are related to the J=3 states and row seven is related to a J=4 state. It can be seen that with a value of 10Dq of 0.0 eV, the 7x7 matrix blocks out to two 3x3 and one 1x1 matrices because one essentially is calculating a spectrum in SO_3 symmetry.

	460.828	**461.641**	**462.806**	**464.048**	**465.859**	**468.313**	**471.369**
1	0.0662	0.0037	0.1550	0.0124	0.4916	0.0404	0.2308
2	0.5944	0.0253	0.0007	0.2972	0.0280	0.0078	0.0466
3	***0.0046***	***0.0091***	***0.1128***	***0.0046***	***0.1845***	***0.2666***	***0.4178***
4	0.0161	0.4460	0.0340	0.0980	0.0097	0.2923	0.1039
5	0.0020	0.2973	0.2980	0.0791	0.0331	0.2191	0.0714
6	0.0044	0.0404	0.3986	0.0116	0.2417	0.1738	0.1294
7	0.3124	0.1781	0.0009	0.4972	0.0113	0.0000	0.0001
	0.0001	**0.0003**	**0.0435**	**0.0001**	**0.1164**	**0.2430**	**0.5968**

Table 14 *The T_1 final states of the $2p^5 3d^1$ configuration with 10Dq=3.04 eV. The top row gives the energies and the bottom row the relative intensities of the seven final states that are build from seven basis-vectors.*

Table 14 shows the seven T_1 symmetry states calculated with a crystal field splitting of 3.04 eV. One finds the seven peaks that are all build from the seven basis vectors. The third row is again related to $^1P_1$ symmetry and its square yields the intensity as given in the bottom row. Essentially one observes four main peaks, peaks 3, 5, 6 and 7. Peak 6 and

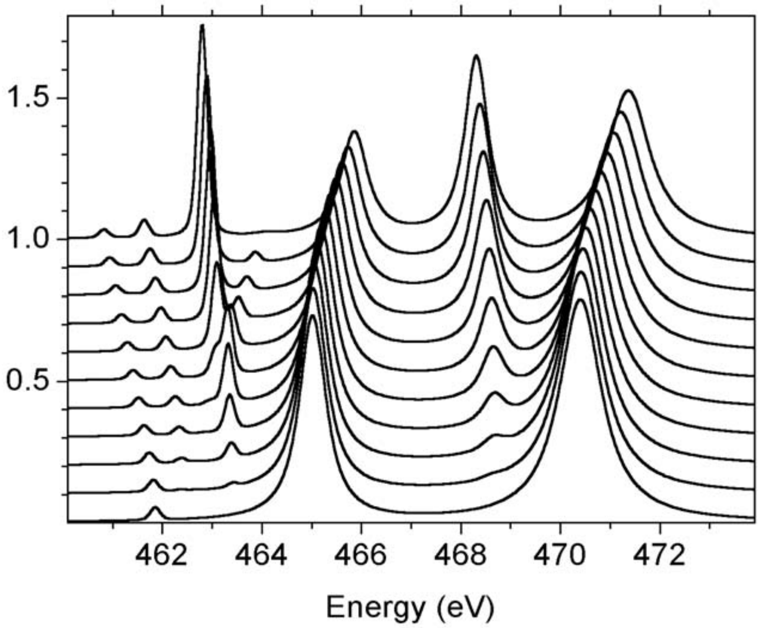

7 are essentially the L_2 edge peaks of respectively t_{2g} and e_g character. They are split by 3.05 eV, essentially the value of 10Dq. Peaks 3 and 5 are the L_3 peaks of t_{2g} and e_g character, also split by 3.05 eV. Peaks 1, 2 and 4 are low-intensity peaks that originate from the 'spin-forbidden transition' in the atomic multiplet calculation.

Figure 5 *The crystal field multiplet calculations for the* $3d^0$ $2p^5 3d^1$ *transition in* Ti^{IV}. *The atomic Slater-Condon parameters and spin-orbit couplings have been used as given in table 2.14. The bottom spectrum is the atomic multiplet spectrum. Each next spectrum has a value of 10Dq that has been increased by 0.3 eV. The top spectrum has a crystal field of 3.0 eV.*

Figure 5 shows the crystal field multiplet calculations for the $3d^0$ $2p^5 3d^1$ transition in Ti^{IV}. The result of each calculation is a set of seven energies with seven intensities. These seven states have been broadened by the lifetime broadening and the experimental resolution. From a detailed comparison to experiment it turns out to be the case that each of the four main lines has to be broadened differently. It is well known that the L_2 part of the spectrum (i.e. the last two peaks) contains an additional Auger decay that accounts for a significant broadening with respect to the L_3 part. This effect has been found to be an additional broadening of 0.5 eV half-width half-maximum (hwhm). An additional difference in broadening is found between the t_{2g} and the e_g states. This broadening has been ascribed to differences in the vibrational effects on the t_{2g} respectively the e_g states. Another cause could be a difference in hybridization effects and in fact charge transfer multiplet calculations indicate that this effect is more important than vibrational effects. Whatever the origin of the broadening, the comparison with experiment shows that if one performs crystal field multiplet calculations, the e_g states must be broadened with an additional 0.4 eV hwhm for the Lorentzian parameter. The experimental resolution has been simulated with a Gaussian broadening of 0.15 eV hwhm.

Figure 6 compares the crystal field multiplet calculation of the $3d^0$ $2p^5 3d^1$ transition in Ti^{IV} with the experimental 2p x-ray absorption spectrum of $FeTiO_3$. The titanium ions are surrounded by six oxygen atoms in a (little) distorted octahedron. The value of 10Dq has been set to 1.8 eV. The calculation is able to reproduce all peaks that are experimentally visible. In particular the two small pre-peaks can be nicely observed. The similar spectrum of $SrTiO_3$ has an even sharper spectral shape, related to the perfect octahedral surrounding of Ti^{IV} by oxygen.

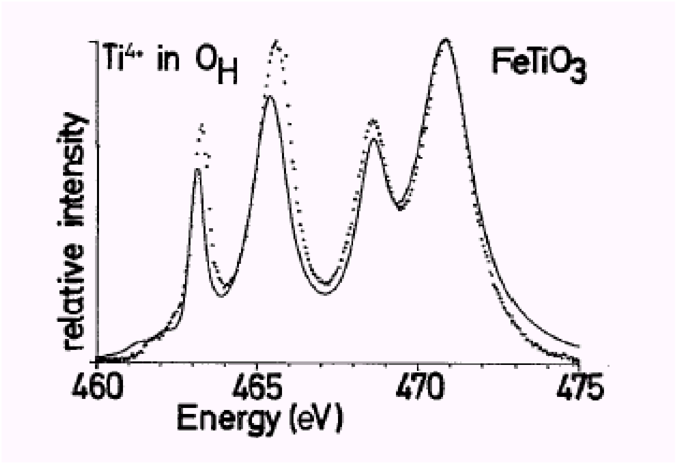

Figure 6 *The 2p x-ray absorption spectrum of* $FeTiO_3$ *compared with a crystal field multiplet calculation for* Ti^{IV} *with a value of 10Dq of 1.8 eV.*

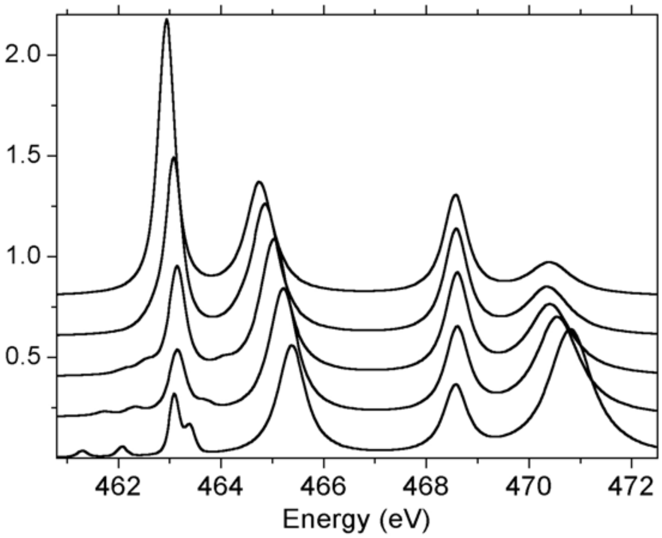

Figure 7 *The crystal field multiplet calculations for the* $3d^0$ $2p^5 3d^1$ *transition in* Ti^{IV}. *The atomic Slater-Condon parameters and spin-orbit couplings have been used as given in table 2.14. The bottom spectrum is the crystal field multiplet spectrum with atomic parameters and corresponds to the fifth spectrum in Figure 5; i.e. 10Dq is 1.5 eV. Each next spectrum has a value of the Slater integrals further reduced by respectively 25%, 50%, 75% and 99%, i.e. the top spectrum is essentially the single particle (crystal field) result.*

Figure 7 shows the effect of the pd Slater-Condon parameters on the spectral shape of the $3d^0$ $2p^5 3d^1$ transition in Ti^{IV}. The bottom calculation is the same as in Figure 5 and used the 80% reduction of the Hartree-Fock values in order to obtain a good estimate of the values in the free atom. In most solids the pd Slater-Condon parameters have essentially the same values as for the free atom, in other words the solid state screening of the pd Slater-Condon parameters is almost zero. The five spectra are calculated by using the same values for the 3d- and 2p-spin-orbit coupling and the same crystal field value of 1.8 eV. The Slater-Condon parameters are rescaled to respectively 80% (bottom), 60%, 40%, 20% and 1% (top). The top spectrum corresponds closely to the single particle picture, where one expects four peaks, respectively the L_3-t_{2g}, the L_3-e_g, the L_2-t_{2g} and the L_2-e_g peak, with respective intensities given by their degeneracies, i.e. 6:4:3:2. This is exactly what is observed in the top spectrum, where it is noted that the intensity ratio is a little obscured by the differences in line width. One can conclude that there is a large difference between the single particle result (top spectrum) and the multiplet result (bottom spectrum). The Slater-Condon parameters have the effect to lower the intensity of the t_{2g} peaks and shift intensity to the e_g peaks. An even larger intensity shift can be observed from the L_3 edge to the L_2 edge and a very clear effect is the creation of additional (pre-)peaks, because additional transitions become allowed.

3.4.4. X-ray absorption spectra of $3d^N$ systems

The description of the x-ray absorption spectra of $3d^N$ systems follows the same procedure as for $3d^0$ systems as described above. The matrix elements must be solved for the initial state Hamiltonian, the transition operator and the final state Hamiltonian.

A difference between $3d^0$ and $3d^N$ ground states is that the latter are affected by dd-interactions and crystal field effects. Whether a system is high-spin or low-spin can be determined directly from the shape of the x-ray absorption spectrum. The calculation of the x-ray absorption spectrum has the following parameters to consider:

a. The atomic Slater-Condon parameters. For trivalent and tetravalent systems these parameters are sometimes reduced. An effective reduction can also (partly) be achieved by the inclusion of charge transfer effects.
b. The inclusion of the cubic crystal field strength 10Dq, optimized to experiment. The value of 10Dq determines the spin-state of the $3d^4$ to $3d^7$ systems.
c. The inclusion of the atomic 3d spin-orbit coupling. Because of an effective quenching of the 3d spin-orbit coupling by lower symmetries and/or translational effects, in some cases the 3d spin-orbit coupling must be set to zero to achieve a good agreement with experiment. This is for example the case for CrO_2. In contrast the case of CoO proves the importance of the inclusion of the 3d spin-orbit coupling as is evident from Figure 8.
d. The inclusion of lower-symmetry parameters, for example Ds and Dt.
e. In many systems it is important to extend the crystal field multiplet program with the inclusion of charge transfer effects as will be discussed in chapter 5.

Figure 8*: The crystal field multiplet calculation of Co^{II} with and without the inclusion of the 3d spin-orbit coupling. The bottom spectrum is without 3d spin-orbit coupling. The 0 K and 300 K spectra have an atomic spin-orbit coupling included, where the close degeneracy of the spin-orbit split states causes temperature effects in the x-ray absorption spectral shape. The experimental CoO spectrum is simulated with the 300 K spectrum.*

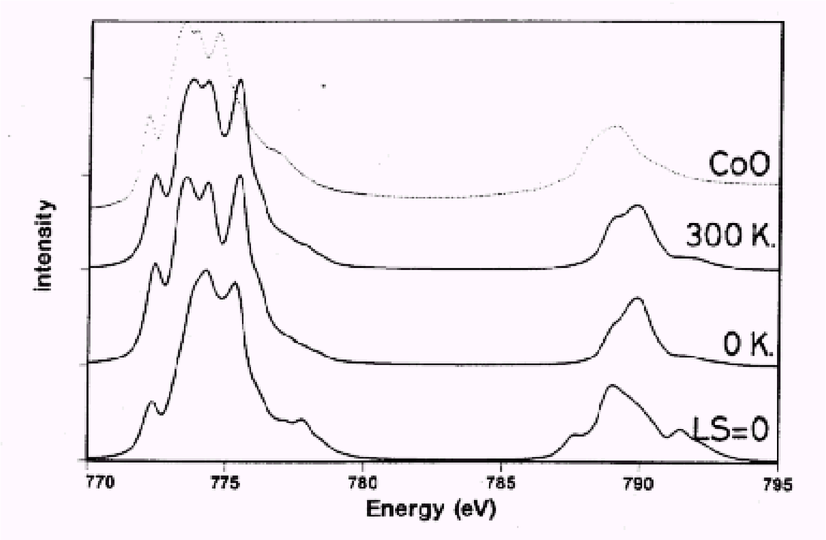

Multiplets in X-ray Spectroscopy

lectures ICTP 2004, by Frank de Groot

4. Charge Transfer Effects

Charge transfer effects are the effects of charge fluctuations in the initial and final states. The atomic multiplet and crystal field multiplet model use a single configuration to describe the ground state and final state. One can combine this configuration with other low-lying configurations similar to the way configuration-interaction works with a combination of Hartree-Fock matrices.

4.1. Initial State Effects

The charge transfer method is based on the Anderson impurity model and related short-range model Hamiltonians that were applied to core level spectroscopies. This line of approach has been developed in the eighties. The Anderson impurity model describes a localized state, the 3d-state, which interacts with delocalized electrons in bands. The Anderson impurity model is usually written in second quantization. In second quantization one starts with the ground state $_0$ and acts on this state with operators that annihilate (a) or create (a) a specific electron. For example a 2p to 3d x-ray absorption transition is written as | $_0a_{2p}$ a_{3d}>. With second quantization one can also indicate the mixing of configurations in the ground state. For example an electron can hop from the 3d-states to a state in the (empty) conduction band, i.e. | $_0a_{3d}$ a_{ck}>, where a_{ck} indicates an electron in the conduction band with reciprocal-space vector k. Comparison to experiment has shown that the coupling to the occupied valence band is more important than the coupling to the empty conduction band. In other words the dominant hopping is from the valence band to the 3d-states. If one annihilates an electron in a state and then re-creates it one effectively is counting the occupation of that state, i.e. $a_{3d}^{\dagger}a_{3d}$ yields n_{3d}. The Anderson impurity Hamiltonian can then be given as:

$$H_{AIM} = \varepsilon_{3d} a_{3d}^{\uparrow} a_{3d} + U_{dd} a_{3d}^{\uparrow} a_{3d} a_{3d}^{\uparrow} a_{3d} + \sum_{k} \varepsilon_{vk} a_{vk}^{\uparrow} a_{vk} + t_{v3d} \sum_{k} (a_{3d}^{\uparrow} a_{vk} + a_{vk}^{\uparrow} a_{3d})$$

These four terms represent respectively the 3d-state, the correlation of the 3d-state, the valence band and the coupling of the 3d-states with the valence band. One can further extend the Anderson Impurity model to include more than a single impurity, i.e. impurity bands. In addition one can include correlation in the valence band, use larger clusters, etc. In case of multiplet calculations of x-ray absorption these approaches lead in most cases to a too large calculation.

Figure 9 sketches the Impurity model with a semi-elliptical band of bandwidth w. Instead of a semi-elliptical band one can use the actual band structure that is found from DFT calculations (bottom). Actually, it has been demonstrated that the use of the real band structure instead of an approximate semi-elliptical or square band structure hardly affects the spectral shape. The multiplet model approximates the band usually as a square of bandwidth w, where n number of points of equal intensity are used for the actual calculation. Often one simplifies the calculation further to n=1, i.e. a single state representing the band. In that case the bandwidth is reduced to zero. In order to simplify the notation we will in the following remove the k-dependence of the valence band and assume a single state describing the band. It must be remembered however that in all cases one can change back this single state to a real band with bandwidth w.

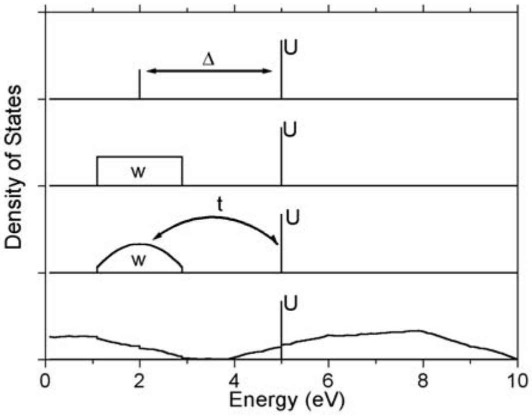

Figure 9: *The interaction of a U-correlated localized state with delocalized bands. From bottom to top are respectively given: a general DOS, a semi-elliptical valence band, a square valence band and a single valence state.*

Removing the k-dependence renders the Hamiltonian into:

$$H_{AIM-1} = \varepsilon_{3d} a_{3d}^{\uparrow} a_{3d} + U_{dd} a_{3d}^{\uparrow} a_{3d} a_{3d}^{\uparrow} a_{3d} + \varepsilon_{k} a_{v}^{\uparrow} a_{v} + t_{v3d} (a_{3d}^{\uparrow} a_{v} + a_{v}^{\uparrow} a_{3d})$$

Bringing the multiplet description into this Hamiltonian implies that the single 3d state is replaced by all states that are part of the crystal field multiplet Hamiltonian of that particular configuration. This implies that the U_{dd}-term is replaced by a summation over four 3d-wavefunctions $3d_{1}$, $3d_{2}$, $3d_{3}$ and $3d_{4}$:

$$H_{AIM} = \varepsilon_{3d} a_{3d}^{\uparrow} a_{3d} + \varepsilon_{k} a_{v}^{\uparrow} a_{v} + t_{v3d} (a_{3d}^{\uparrow} a_{v} + a_{v}^{\uparrow} a_{3d})$$
$$+ \sum_{\Gamma_1,\Gamma_2,\Gamma_3,\Gamma_4} g_{dd} a_{3d1}^{\uparrow} a_{3d2} a_{3d3}^{\uparrow} a_{3d4} + \sum_{\Gamma_1,\Gamma_2} l \cdot s \, a_{3d1}^{\uparrow} a_{3d2} + H_{CF}$$

The term g_{dd} describes all two-electron integrals and includes the Hubbard U as well as the effects of the Slater-Condon parameters F^2 and F^4. In addition there is a new term in the Hamiltonian due to the 3d spin-orbit coupling. H_{CF} describes the effects of the crystal field potential . This situation can be viewed as a multiplet of localized states interacting with the delocalized density of states, as indicated in figure 10. The energy difference to the centre of gravity of the multiplet is indicated with _. The effective energy difference to the lowest state of the multiplet is indicated with . One ingredient is still missing from this description that is if the electron is transferred from the valence band to the 3d-band, the occupation of the 3d-band changes by one. This $3d^{N+1}$ configuration is again affected by multiplet effects, exactly like the original $3d^{N}$ configuration. The $3d^{N+1}$ configuration contains a valence band with a hole. Because the model is used mainly for transition metal compounds, the valence band is in general dominated by ligand character, for example the oxygen 2p valence band in case of transition metal oxides. Therefore the hole is considered to be on the ligand and is indicated with $\underline{L}$, i.e. a ligand hole. The charge transfer effect on the wave function is described as $3d^{N} + 3d^{N+1}\underline{L}$.

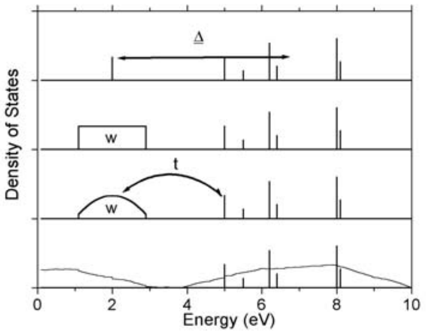

Figure 10: *The interaction of a multiplet of localized states with delocalized bands. From bottom to top are respectively given: a general DOS, a semi-elliptical valence band, a square valence band and a single valence state.*

Because the $3d^{N+1}\underline{L}$ state is also affected by multiplet effects, figure 10 is not correct as the $3d^{N+1}\underline{L}$ state is described with a single $3d^{N+1}$ state in combination with $\underline{L}$, a ligand hole that can have either a single energy or be a band. If one includes the effects of the multiplets on the $3d^{N+1}\underline{L}$ in this figure, for a single state one essentially obtains a configuration-interaction between two sets of multiplet states.

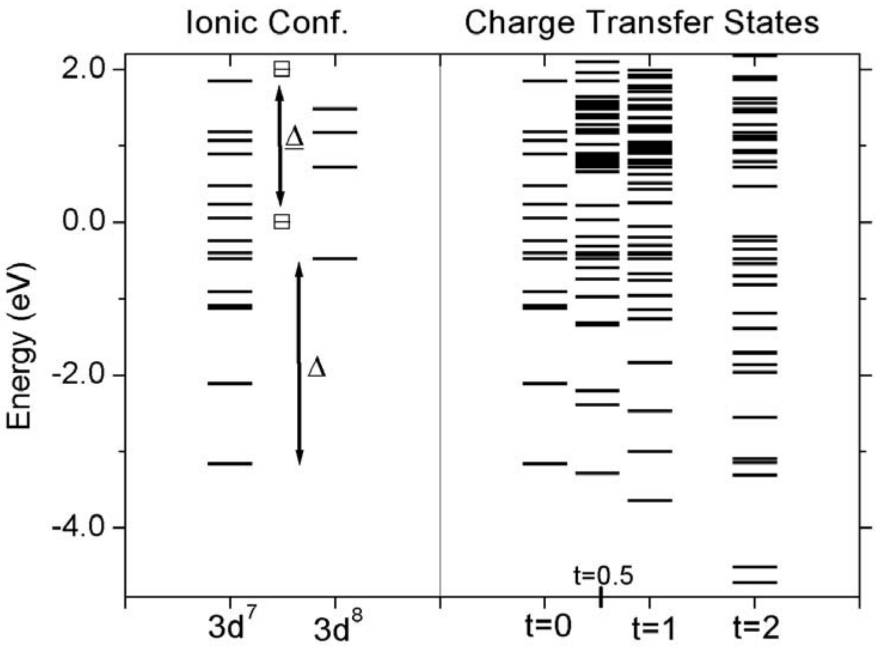

Figure 11: *Left: The crystal field multiplet states of $3d^7$ and $3d^8$ configurations. The multiplet states with energies higher than +2.0 eV are not shown. _ has been set to +2.0 eV. Right: The charge transfer multiplet calculations for the combination of crystal field*

multiplets as indicated on the left and with the hopping ranging from 0.0 eV to 2.0 eV as indicated below the states.

Figure 11 gives the crystal field multiplets for the 3d^7 and 3d$^8\underline{L}$ configurations of Co^{II}. The 3d^7 configurations is centred at 0.0 eV and the lowest energy state is the $^4T_1$ state, where the small splittings due to the 3d spin-orbit coupling have been neglected(de Groot 1994). The lowest state of the 3d$^8\underline{L}$ configuration is the $^3A_2$ state, which is the ground state of for example Ni^{II}. The centre of gravity of the 3d^8 configuration has been set at 2.0 eV, which identifies with a value of _ of 2.0 eV. The effective charge transfer energy is defined as the energy difference between the lowest states of the 3d^7 and the 3d$^8\underline{L}$ configurations as indicated in Figure 11. Because the multiplet splitting is larger for 3d^7 than for 3d$^8\underline{L}$, the effective is larger than _. The effect of charge transfer is to form a ground state that is a combination of 3d^7 and 3d$^8\underline{L}$. The energies of these states have been calculated on the right half of the figure. If the hopping parameter *t* is set equal to zero, both configurations do not mix and the states of the mixed configuration are exactly equal to 3d^7, and at higher energy to 3d$^8\underline{L}$. Turning on the hopping parameter, one observes that the energy of the lowest configuration is further lowered. This state will still be the $^4T_1$ configuration, but with increasing hopping, it will have increasing 3d$^8\underline{L}$ character. One can observe that the second lowest state is split by the hopping and the most bonding combination obtains an energy that comes close to the $^4T_1$ ground state. This excited state is essentially a doublet state and if the energy of this state would cross with the $^4T_1$ state one would observe a charge-transfer induced spin-transition. It has been shown that charge transfer effects can lead to new types of ground states, for example in case of a 3d^6 configuration, crystal field effects lead to a transition of a S=2 high-spin to a S=0 low-spin ground state. Charge transfer effects are also able to lead to an S=1 intermediate spin ground state.

Figure 11 can be expanded to Tanabe-Sugano diagrams for two configurations 3d^N + 3d$^{N+1}\underline{L}$, instead of the usual Tanabe-Sugano diagrams as a function of only one configuration. The energies of such two-configuration Tanabe-Sugano diagrams are affected by the Slater-Condon parameters (often approximated with the B Racah parameter), the cubic crystal field 10Dq, the charge transfer energy _ and the hopping strength t. The hopping can be made symmetry dependent and one can add crystal field parameters related to lower symmetries, yielding to an endless series of Tanabe-Sugano diagrams. What is actually important is to determine the possible types of ground states for a particular ion, say Co^{II}. Scanning through the parameter space of F^2, F^4, 10Dq, Ds, Dt, LS$_{3d}$, t and _ one can determine the nature of the ground state. This ground state can then be checked with 2p x-ray absorption. After the inclusion of exchange and magnetic fields one has also a means to compare the ground state with techniques like x-ray MCD, optical MCD and EPR.

Comparing figure 9 with figure 11 one observes the transition from a single particle picture to a multiplet configurational picture. One can in principle put more band character into this configurational picture and a first step is to make a transition from a single state to a series of 3d$^8\underline{L}$ states, each with its included multiplet but with each a different effective charge transfer energy. One can choose to use a more elaborate cluster model in which the neighbor atoms are actually included in the calculation. These cluster models are not described further here. In all cases where multiplet effects are important, i.e. with at least two holes in correlated states, these cluster models do in general not lead to significantly different conclusions and ground state descriptions.

4.2. Final state effects

The final state Hamiltonian of x-ray absorption includes the core hole plus an extra electron in the valence region. One adds the energy and occupation of the 2p core hole to the Hamiltonian. The core hole potential U_{pd} and its higher order terms g_{pd} give rise to the overlap of a 2p wave function with a 3d wave function and is given as a summation over two 2p and two 3d-wavefunctions $2p_1$, $2p_2$, $3d_1$ and $3d_2$:

$$H_{2p} = \varepsilon_{2p} a^{\uparrow}_{2p} a_{2p} + \sum_{\Gamma_1,\Gamma_2,\Gamma_3,\Gamma_4} g_{pd} a^{\uparrow}_{3d1} a_{2p1} a^{\uparrow}_{2p2} a_{3d2} + \sum_{\Gamma_1,\Gamma_2} l \cdot s\, a^{\uparrow}_{2p1} a_{2p2}$$

The term g_{pd} describes all two-electron integrals and includes U_{pd} as well as the effects of the Slater-Condon parameters F^2, G^1 and G^3. In addition there is a term in the Hamiltonian due to the 2p spin-orbit coupling. There is no crystal field effect on core states.

$$\begin{aligned} H_{AIM} &= \varepsilon_{3d} a^{\uparrow}_{3d} a_{3d} + \varepsilon_k a^{\uparrow}_v a_v + t_{v3d} (a^{\uparrow}_{3d} a_v + a^{\uparrow}_v a_{3d}) \\ &+ \sum_{\Gamma_1,\Gamma_2,\Gamma_3,\Gamma_4} g_{dd} a^{\uparrow}_{3d1} a_{3d2} a^{\uparrow}_{3d3} a_{3d4} + \sum_{\Gamma_1,\Gamma_2} l \cdot s\, a^{\uparrow}_{3d1} a_{3d2} + H_{CF} \\ &+ \varepsilon_{2p} a^{\uparrow}_{2p} a_{2p} + \sum_{\Gamma_1,\Gamma_2,\Gamma_3,\Gamma_4} g_{pd} a^{\uparrow}_{3d1} a_{2p1} a^{\uparrow}_{2p2} a_{3d2} + \sum_{\Gamma_1,\Gamma_2} l \cdot s\, a^{\uparrow}_{2p1} a_{2p2} \end{aligned}$$

This equation is solved in the same manner as the initial state Hamiltonian. Using the two configuration description of Figure 11, one finds for Co^{II} two final states $2p^5 3d^8$ and $2p^5 3d^9\underline{L}$. These states mix in a manner similar to the two configurations in the ground state and as such give rise to a final state Tanabe-Sugano diagram. All final state energies are calculated from the mixing of the two configurations. This calculation is only possible if all final state parameters are known. The following rules are used:

a) The 2p3d Slater-Condon parameters are taken from an atomic calculation. For trivalent ions and higher valences, these atomic values are sometimes reduced.
b) The 2p and 3d spin-orbit coupling are taken from an atomic calculation.
c) The crystal field values are assumed to be the same as in the ground state.
d) The energies of the configurations, i.e. the charge transfer energy, are given by the values of U_{dd} and U_{pd}. Effectively $\_{}_F = \_{}_I + U_{dd} - U_{pd}$. Because in general U_{pd} is approximately 1 to 2 eV larger than U_{dd}, one often assumes $\_{}_F = \_{}_I$ - 1 eV or $\_{}_F = \_{}_I$ - 2 eV.
e) The hopping parameter ***t*** is assumed to be equal in the initial and final states.

Detailed analysis of x-ray absorption and resonant x-ray emission spectra has shown that the crystal field values seem to be smaller by 10 to 20% in the final state. The same observation has been made for the hopping parameters. One can understand these trends from the (slight) compression of the 3d wave function in the final state. From the presence of the 2p core hole one would expect a significant compression of the 3d wave function, but the effect of the 2p core hole is counteracted by the effect of the extra 3d-electron in the final state. Because we have seen that U_{dd} is a bit smaller than U_{pd} this counteracting action is not complete and there will be a small compression of the 3d wave function. In conclusion it can be said that _, ***t*** and 10Dq will all be slightly smaller in the final state. Because the reduction of these parameters has counteracting effects on the spectral shape, in most simulations one varies only _ and keeps ***t*** and 10Dq constant.

4.3. The x-ray absorption spectrum with charge transfer effects

The essence of the charge transfer model is the use of two or more configurations. Ligand field multiplet calculations use one configuration for which it solves the effective atomic Hamiltonian plus the ligand field Hamiltonian, so essentially the following matrices:

$$I_{XAS,1} \propto \left\langle 3d^{N} \mid p \mid 2p^{5}3d^{N+1} \right\rangle^{2}$$

$$H_{INIT,1} = \left\langle 3d^{N} \mid \tfrac{e^2}{r_{12}} + \varsigma_d l_d \cdot s_d + H_{LFM} \mid 3d^{N} \right\rangle$$

$$H_{FINAL,1} = \left\langle 2p^{5}3d^{N+1} \mid \tfrac{e^2}{r_{12}} + \varsigma_p l_p \cdot s_p + \varsigma_d l_d \cdot s_d + H_{LFM} \mid 2p^{5}3d^{N+1} \right\rangle$$

The charge transfer model adds a configuration $3d^{N+1}\underline{L}$ to the $3d^{N}$ ground state. In case of a transition metal oxide, in a $3d^{N+1}\underline{L}$ configuration an electron has been moved from the oxygen 2p-valence band to the metal 3d-band. One can continue with this procedure and add $3d^{N+2}\underline{L}^{2}$ configuration, etc. In many cases two configurations will be enough to explain the spectral shapes, but in particular for high valence states it can be important to include more configurations. As far as x-ray absorption and x-ray emission is concerned, the consequences for the calculations are the replacement of $3d^{N}$ with $3d^{N}+3d^{N+1}\underline{L}$ plus the corresponding changes in the final state. This adds a second initial state, final state and dipole transition:

$$I_{XAS,2} \propto \left\langle 3d^{N+1}\underline{L} \mid p \mid 2p^{5}3d^{N+2}\underline{L} \right\rangle^{2}$$

$$H_{INIT,2} = \left\langle 3d^{N+1}\underline{L} \mid \tfrac{e^2}{r_{12}} + \varsigma_d l_d s_d + H_{LFM} \mid 3d^{N+1}\underline{L} \right\rangle$$

$$H_{FINAL,2} = \left\langle 2p^{5}3d^{N+2}\underline{L} \mid \tfrac{e^2}{r_{12}} + \varsigma_p l_p s_p + \varsigma_d l_d s_d + H_{LFM} \mid 2p^{5}3d^{N+2}\underline{L} \right\rangle$$

The two initial states and two final states are coupled by monopole transitions, i.e. configuration interaction. The mixing parameter ***t*** couples both configurations and   is the energy difference. The Hamiltonian is abbreviated with ***t/*** to describe the monopole interaction*:*

$$H_{MIX\,I1,I2} = \left\langle 3d^{N} \mid t/\Delta \mid 3d^{N+1}\underline{L} \right\rangle$$

$$H_{MIX\,F1,F2} = \left\langle 2p^{5}3d^{N+1} \mid t/\Delta \mid 2p^{5}3d^{N+2}\underline{L} \right\rangle$$

The x-ray absorption spectrum is calculated by solving the equations above. If a $3d^{N+2}\underline{LL'}$ configuration is included its energy is 2_+U_{dd}, where U_{dd} is the correlation energy between two 3d-electrons. The formal definition of U_{dd} is the energy difference one obtains when an electron is transferred from one metal site to another, i.e. a transition $3d^{N} + 3d^{N}$ $3d^{N+1} + 3d^{N-1}$. The number of interactions of two $3d^{N}$ configurations is one more than the number of interactions of $3d^{N+1}$ plus $3d^{N-1}$, implying that this energy difference is equal to the correlation energy between two 3d-electrons.

By analyzing the effects of charge transfer it is found that, for systems with a positive value of , the main effects on the x-ray absorption spectral shape are:

(1) The formation of small satellites.

(2) The contraction of the multiplet structures.

The formation of small satellites or even the absence of visible satellite structures is a special feature of x-ray absorption spectroscopy. Its origin is the fact that x-ray absorption is a neutral spectroscopy and the local charge of the final state is equal to the charge of the initial state. This implies that there is little screening hence little charge transfer satellites. This effect can be explained by using a two-by-two problem as example. We follow the paper of Hu et al.(Hu and others 1998a) to describe the mixing of two configurations that are separated by and mixed by t. This mixing yields a two by two determinant:

$$H = \begin{vmatrix} 0 & t \\ t & \Delta \end{vmatrix}$$

Solving the determinant yields the two states after mixing: The ground state, or bonding combination, $_B$ has a wave function:

$$\Psi_B = \alpha_i \left|3d^N\right\rangle + \beta_i \left|3d^{N+1}\underline{L}\right\rangle$$

The energy of the bonding combination is given as:

$$E_B = \frac{\Delta}{2} - \frac{1}{2}\sqrt{\Delta^2 + 4t}$$

The parameters $_i$ and $_i$ can be defined in and t:

$$\alpha_i = \sqrt{1/1 + \left(\tfrac{X-\Delta}{2T}\right)^2}, \quad X = \sqrt{\Delta^2 + 4T^2}$$

$$\beta_i = \sqrt{1 - \alpha_i^{\,2}}$$

The anti-bonding combination is given as:

$$\Psi_B = \beta_i \left|3d^N\right\rangle - \alpha_i \left|3d^{N+1}\underline{L}\right\rangle$$

The energy of the anti-bonding combination is given as:

$$E_B = \frac{\Delta}{2} + \frac{1}{2}\sqrt{\Delta^2 + 4t}$$

We have found that in the final state the value of $_F$~ -1 eV. This implies that the final state determinant is approximately equal to the initial state determinant:

$$H = \begin{vmatrix} 0 & t_F \\ t_F & \Delta_F \end{vmatrix}$$

This yields for $_f$ and $_f$ that they are approximately equal to $_i$ and $_{i.}$ The results of the initial and final state equations can be used to calculate the x-ray absorption cross section. One can make a transition from $3d^N$ to $2p^5 3d^{N+1}$ and from $3d^{N+1}\underline{L}$ to $2p^5 3d^{N+2}\underline{L}$. This implies that the intensity of the main peak is equal to ($_i$ $_f$+ $_i$ $_f$)^2 while the satellite intensity is equal to ($_i$ $_f$ $_i$ $_f$)^2. The contraction of the multiplet structure due to charge transfer can also be understood using the two by two matrices. Assume two multiplet states split by an energy . They both mix with a charge transfer state that is positioned above the lowest energy multiplet state I. Consequently the charge transfer energy of the second multiplet state II is - . Assuming that the hopping terms are the same for these two states, the energy gain of the bonding combination is:

$$E_B(I) = \frac{\Delta}{2} - \frac{1}{2}\sqrt{\Delta^2 + 4t}$$

$$E_B(II) = \frac{\Delta - \delta}{2} - \frac{1}{2}\sqrt{(\Delta - \delta)^2 + 4t}$$

The higher lying multiplet states have a smaller effective and consequently a larger energy gain. As such their energy comes closer to the lowest energy state and the multiplet appears compressed.

The two by two problem in the initial and final state explains the two main effects of charge transfer: a compression of the multiplet structure and the existence of only small satellites. These two phenomena are visible in the figure of Ni^{II}. In case that the charge transfer is negative, the satellite structures are slightly larger because then the final state charge transfer is increased with respect to the initial state and the balance of the initial and final state 's and 's is less good.

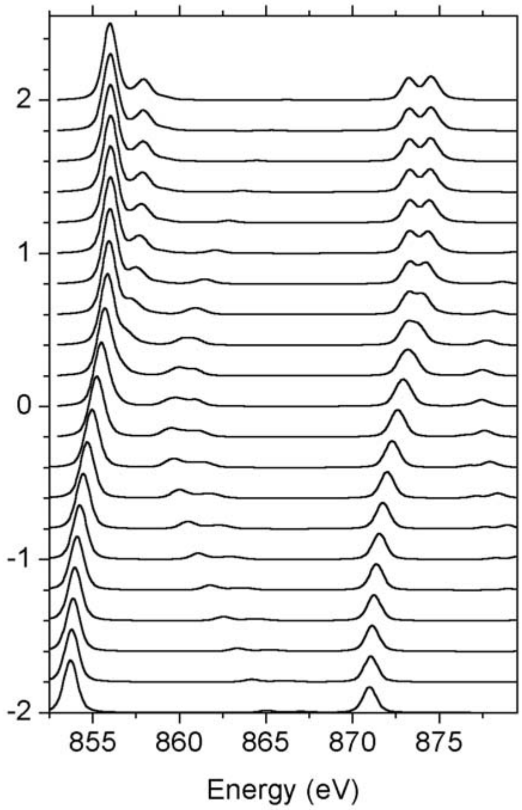

Figure 12: *Series of charge transfer multiplet calculations for the Ni^{II} ground state $3d^8$+$3d^9\underline{L}$. The top spectrum has a charge transfer energy of +10 eV. The bottom spectrum has a charge transfer energy of -10 eV and relates to an almost pure $3d^9$ ground state.*

Figure 12 shows the effect of the charge transfer energy on divalent nickel. We have used the same hopping t for the initial and final state and reduced the charge transfer energy by one eV. In the top spectrum, =10 and the spectrum is essentially the ligand field multiplet spectrum of a Ni^{II} ion in its 3d^8 configuration. The bottom spectrum uses =-10 and now the ground state is almost a pure 3d$^9\underline{L}$ configuration. Looking for the trends in Figure 14, one finds the increased contraction of the multiplet structure by going to lower values of . Going from Ni to Cu the atomic parameters change very little, except the 2p spin-orbit coupling and the 2p binding energy. Therefore the spectra of 3d^N systems of different elements are all very similar and the bottom spectrum is also similar to Cu^{II} systems. Therefore one can also use the spectra with negative -values for Cu^{III} compounds, such as $La_2Li_{1/2}Cu_{1/2}O_4$ and Cs_2KCuF_6. Figure 13 shows the comparison of the 2p x-ray absorption spectrum of these two compounds with charge transfer multiplet calculations. It can be checked in figure 15 that these calculations look similar to the calculations for Ni^{II} systems with negative values of . For such systems with negative values, it is important to carry out charge transfer multiplet calculations, as no good comparison with crystal field multiplet spectra can be made.

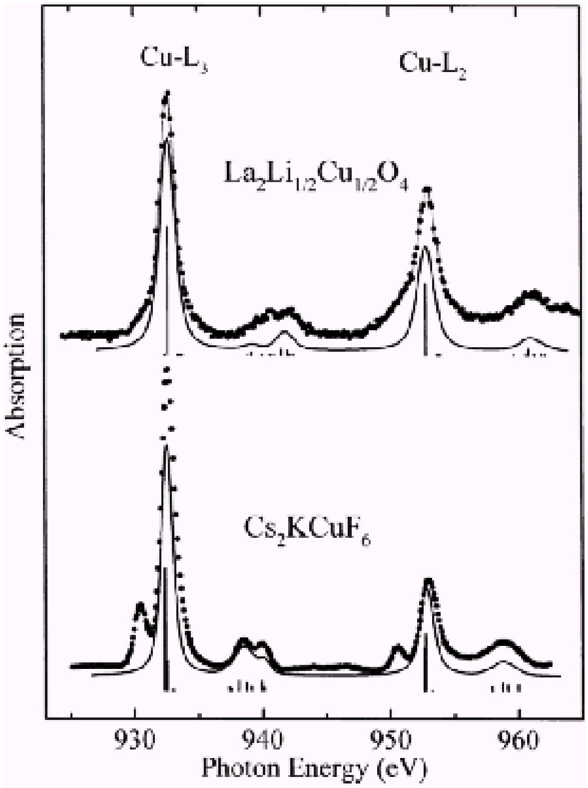

Figure 13: *Results of theoretical simulations of the copper 2p x-ray absorption spectra of* Cs_2KCuF_6 *(bottom) and* $La_2Li_{1/2}Cu_{1/2}O_4$ *(top), in comparison with the experimental spectra.*

X-ray absorption

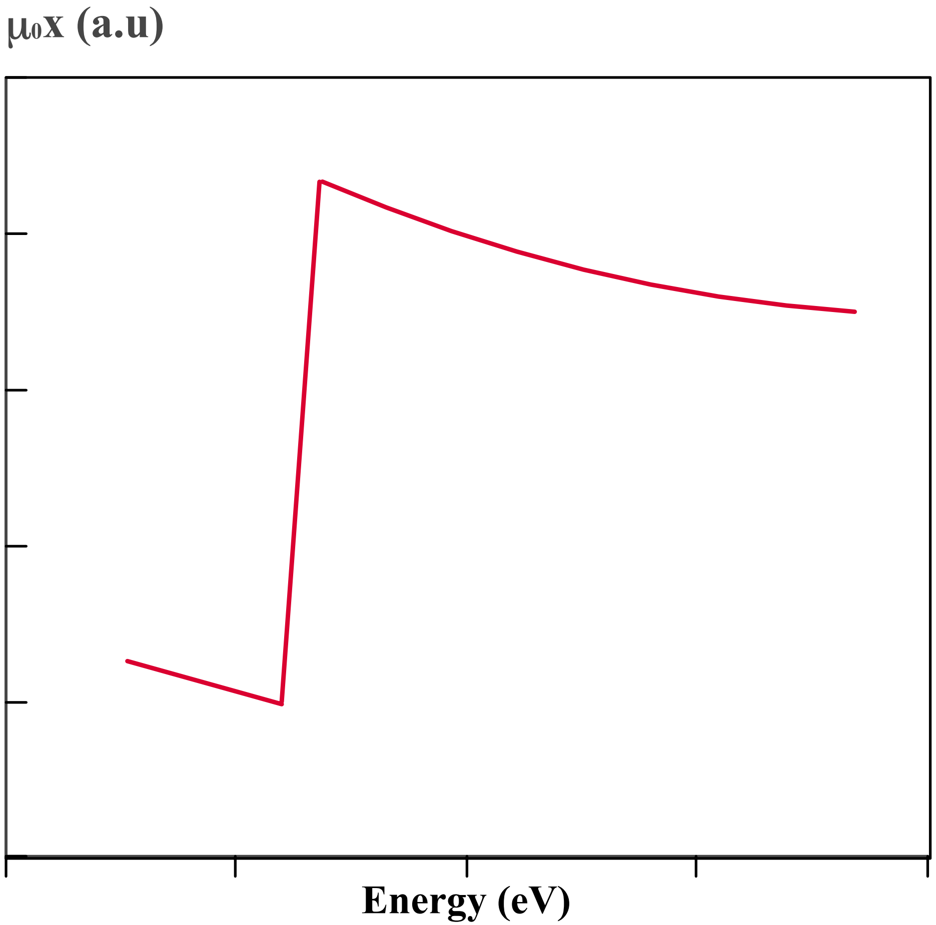

- Absorption edge: each element has its edge at a different energy
- Compare to XPS

X-ray absorption

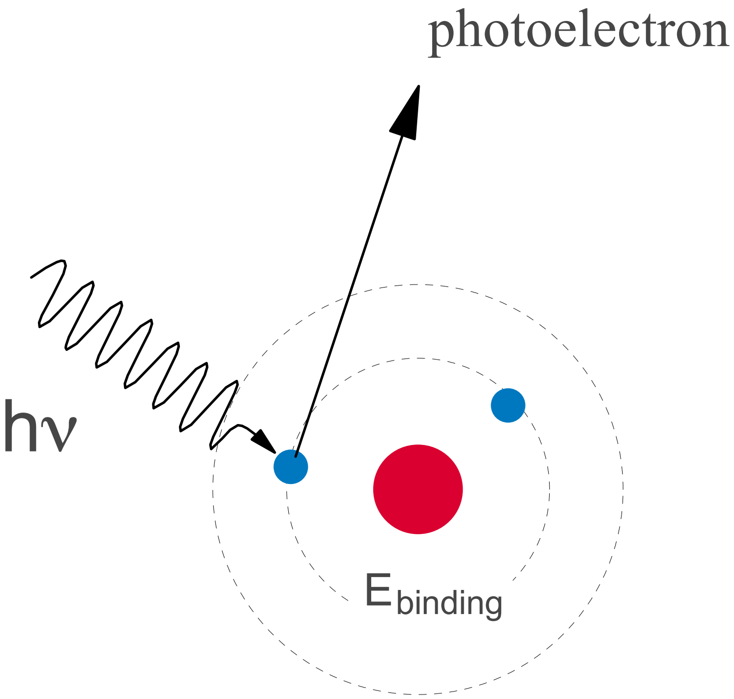

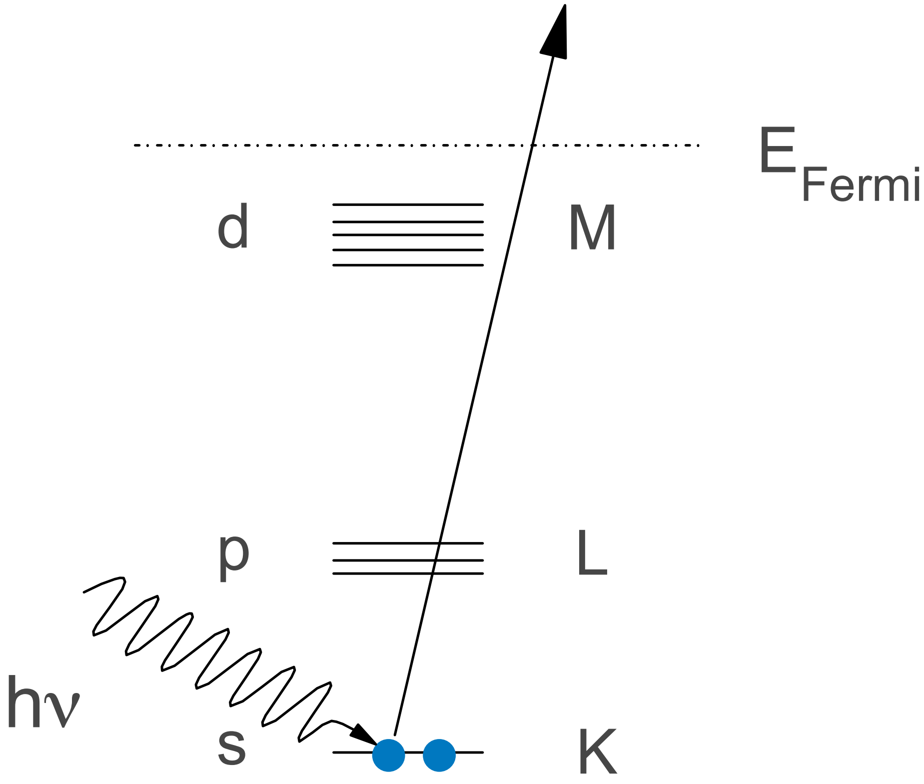

X-ray absorption

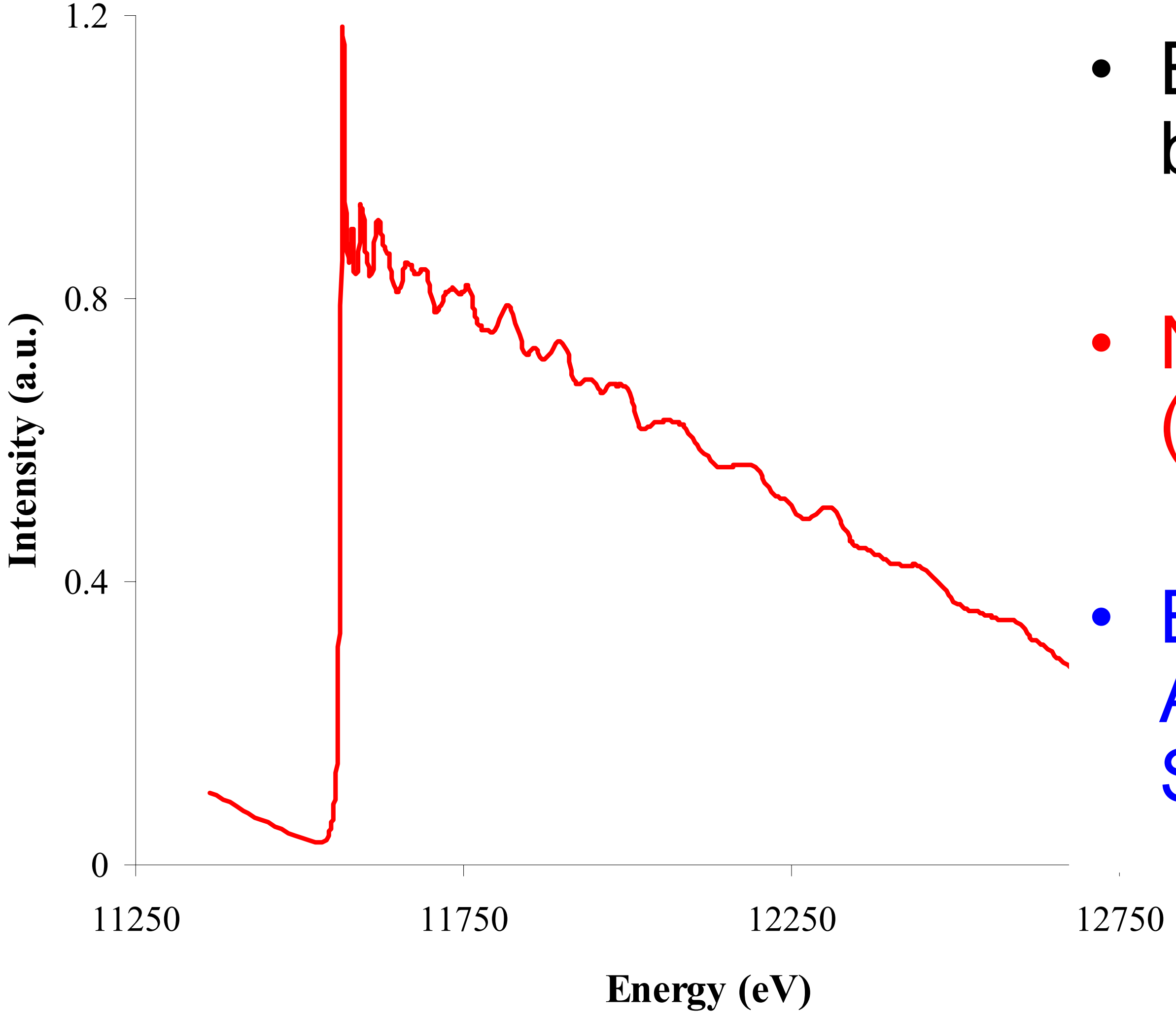

- Edge at Pt 2p binding energy
- Near Edge Structure (XANES)
- Extended X-ray Absorption Fine Structure (EXAFS)

X-ray absorption

Excitation of core electrons to empty states.

Spectrum given by the **Fermi Golden Rule**

(name Golden Rule given by Fermi; rule itself given by Dirac)

$$\boxed{I_{XAS} \sim \Sigma_f \left|\left\langle \Phi_f \middle| \hat{e}\cdot r \middle| \Phi_i \right\rangle\right|^2 \delta_{E_f - E_i - \hbar\omega}}$$

X-ray absorption (single particle interpretation)

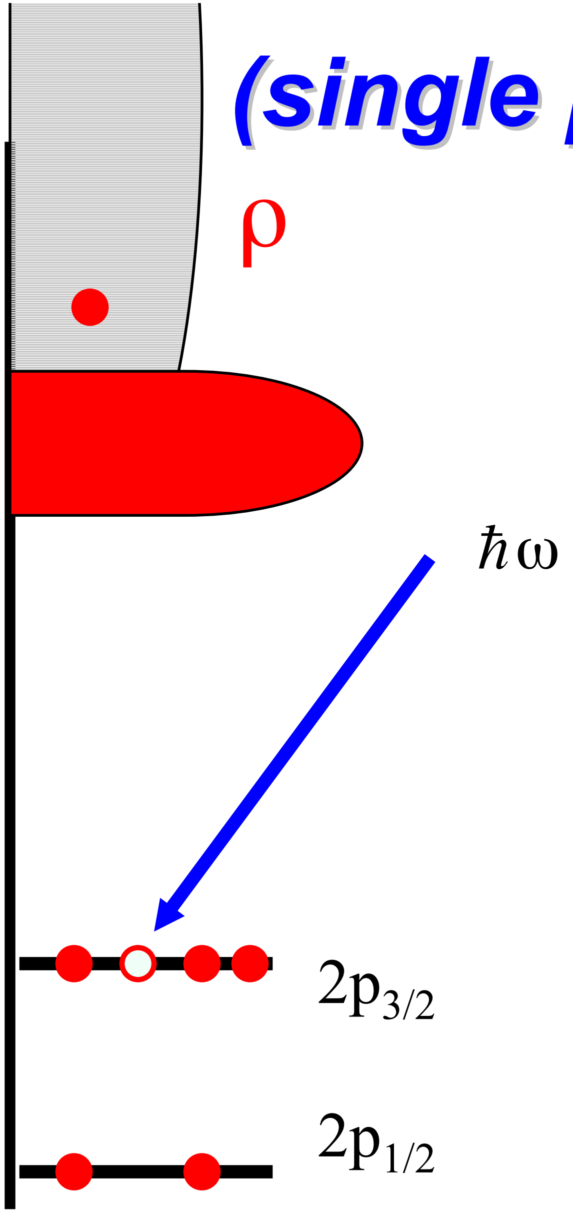

- XAFS Spectral shape gives the Density of empty States (ρ)

- Dipole Selection Rule: From 2p to empty s and d character (Δl=±1)

$$\boxed{I_{XAS} \sim \left|\left\langle \varepsilon \middle| \hat{e}\cdot r \middle| c \right\rangle\right|^2 \cdot \rho}$$

X-ray absorption

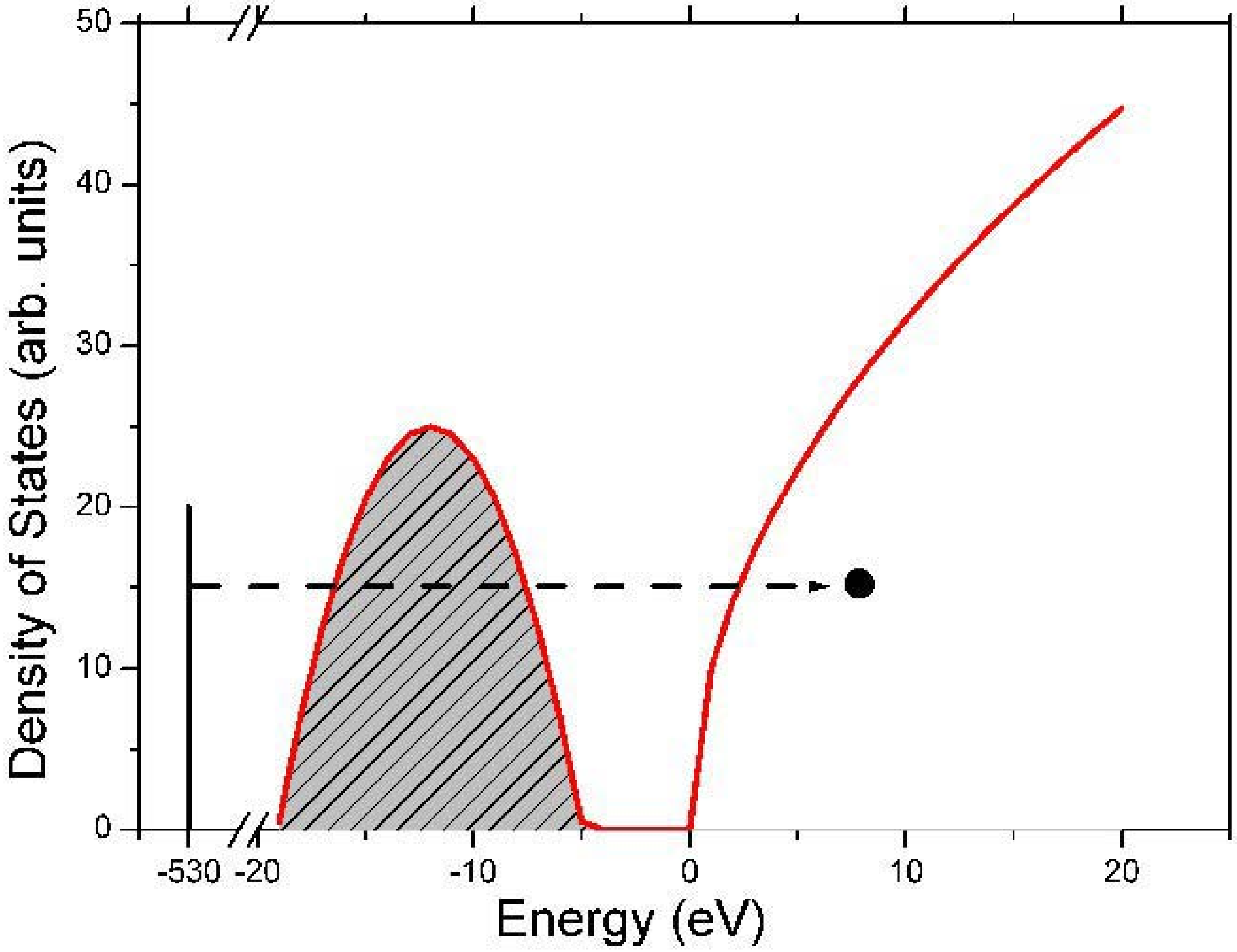

Electronic Structure

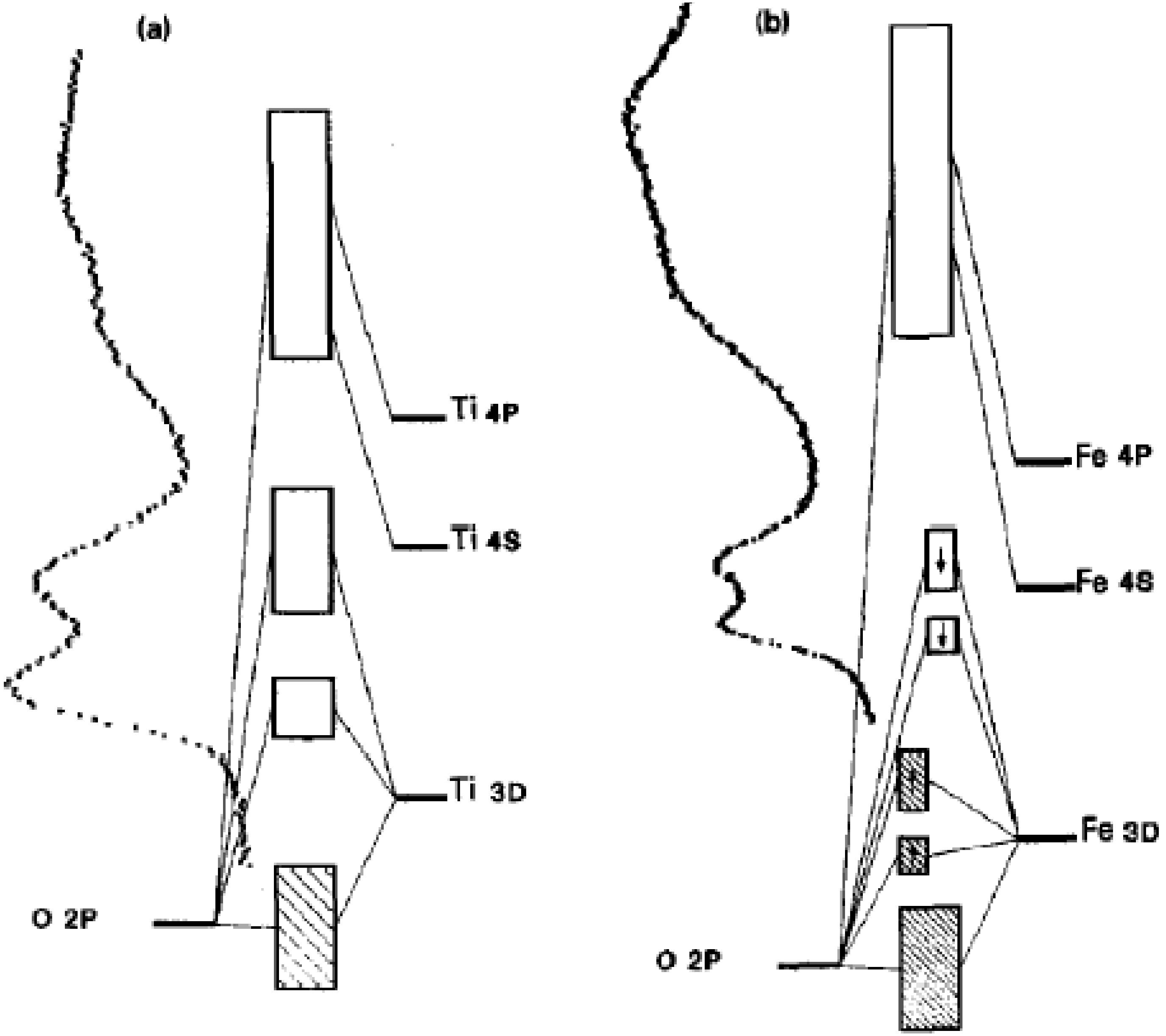

Electronic Structures Database:

http://cst-www.nrl.navy.mil/es-access.html

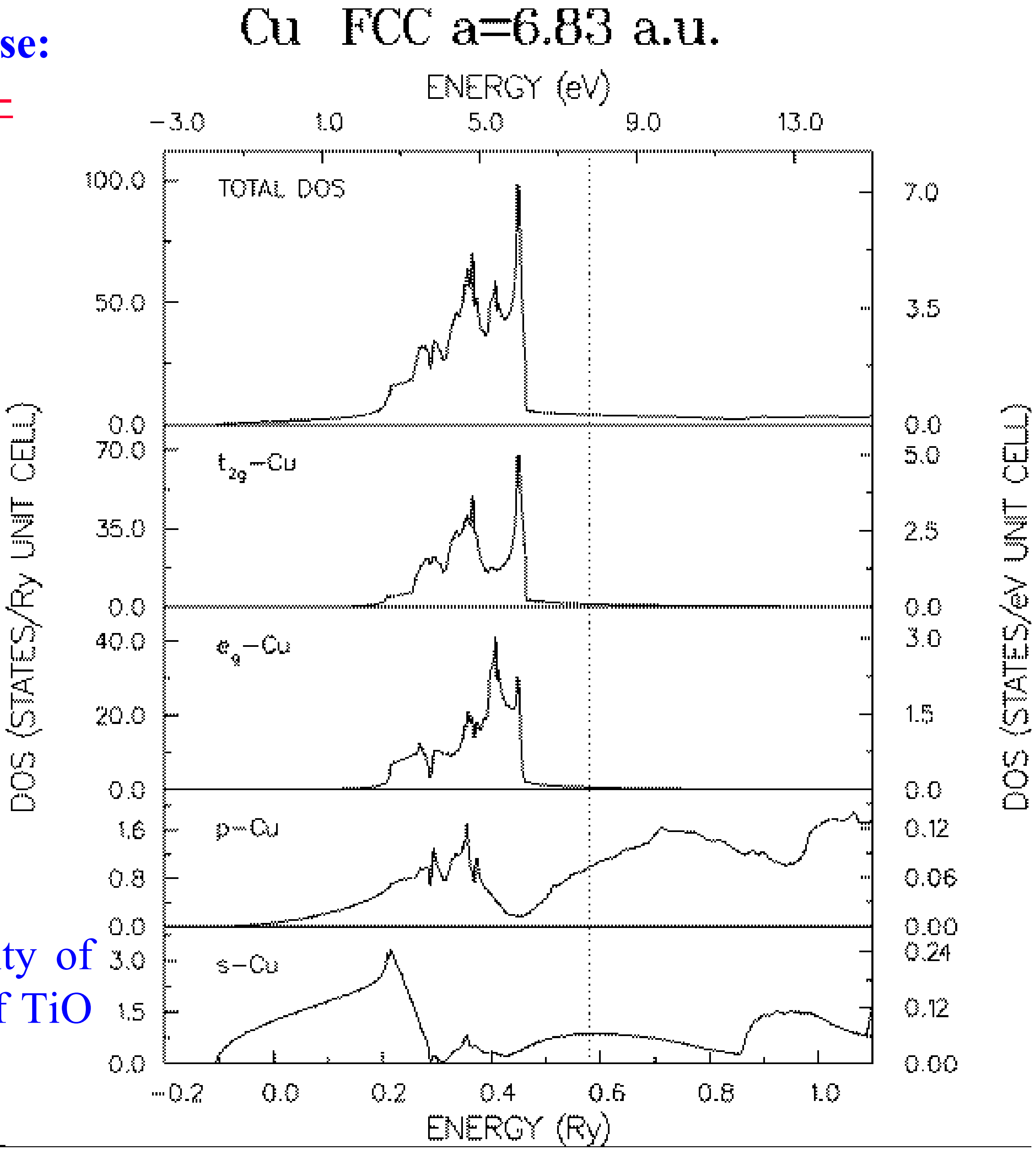

Exercise: Search for the density of states and the band structure of TiO (in the NaCl structure).

Cu FCC a=6.83 a.u.

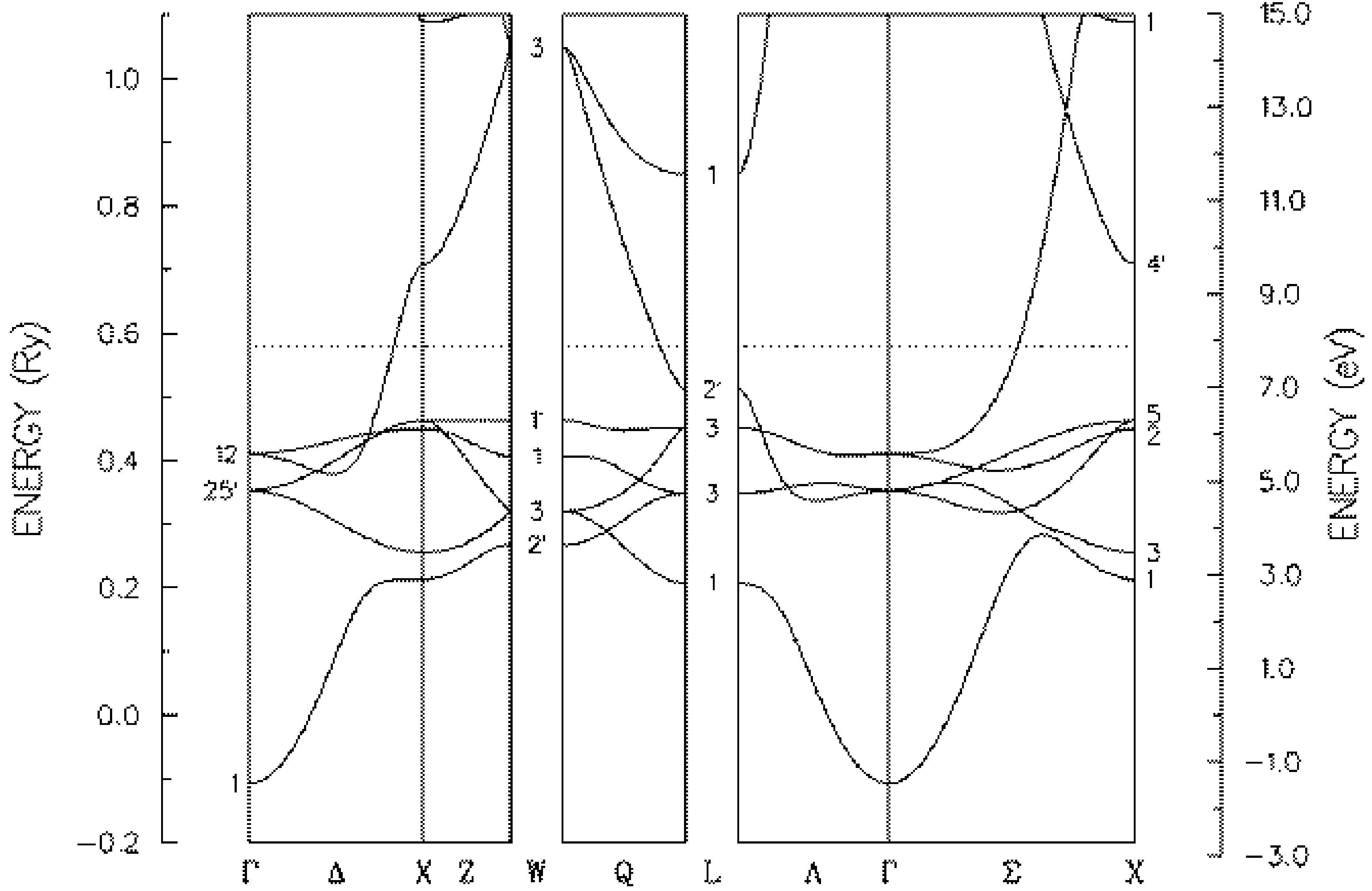

DOS of TiO_2

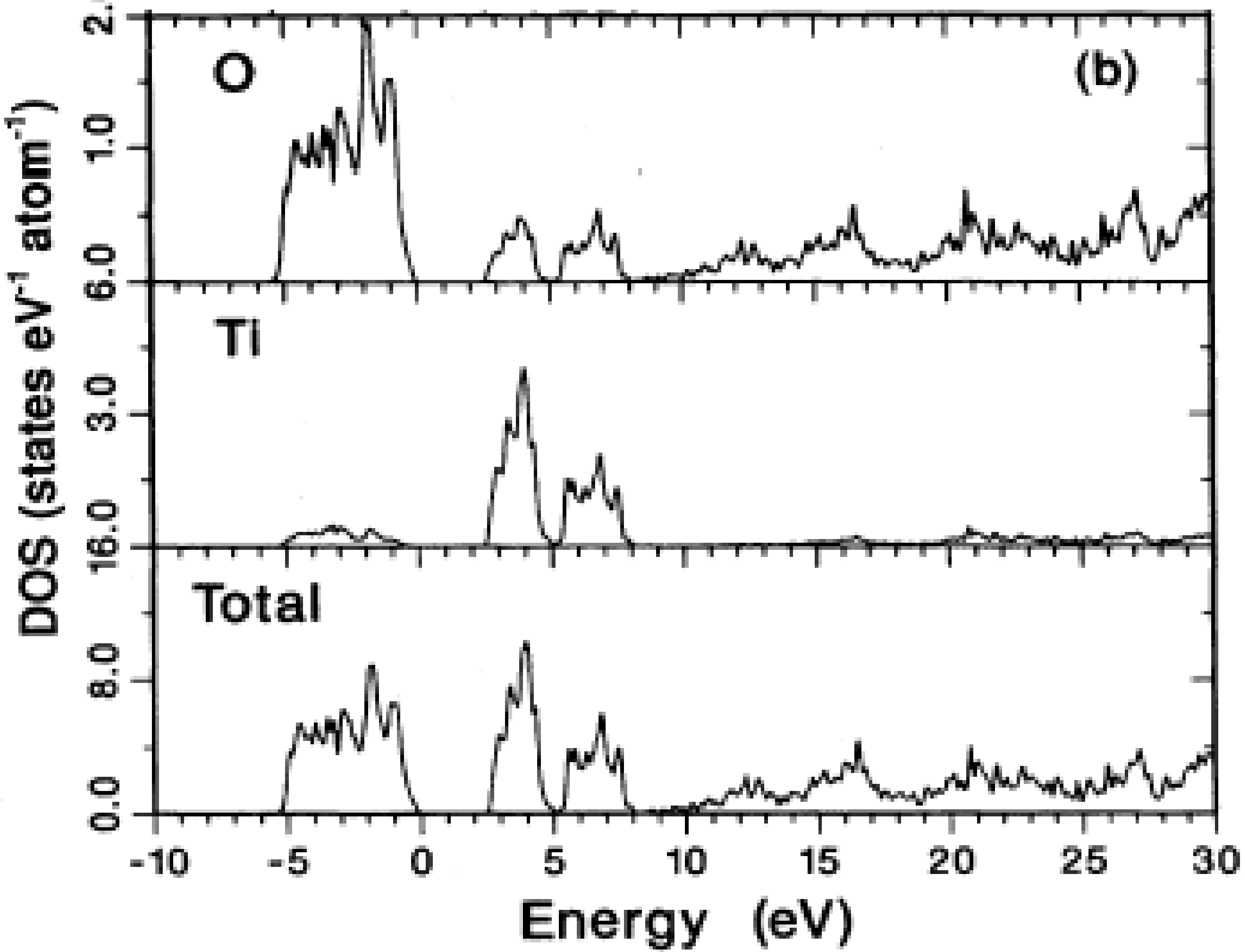
O
(b)
Ti
Total
DOS (states eV^{-1} atom^{-1})
2.0
1.0
6.0
3.0
16.0
8.0
0.0
-10
-5
0
5
10
15
20
25
30
Energy (eV)

Oxygen K edge of TiO_2

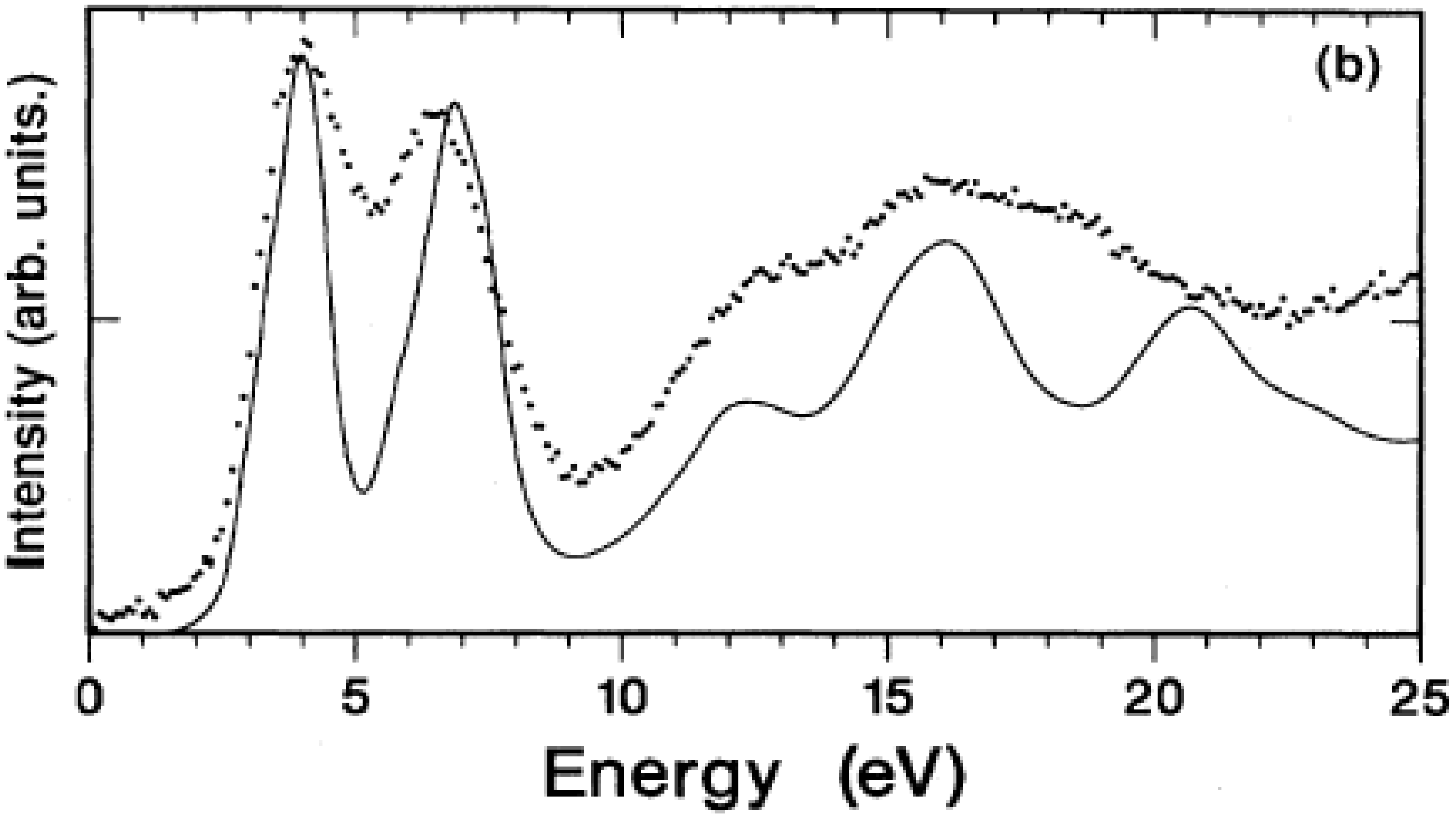

X-ray absorption

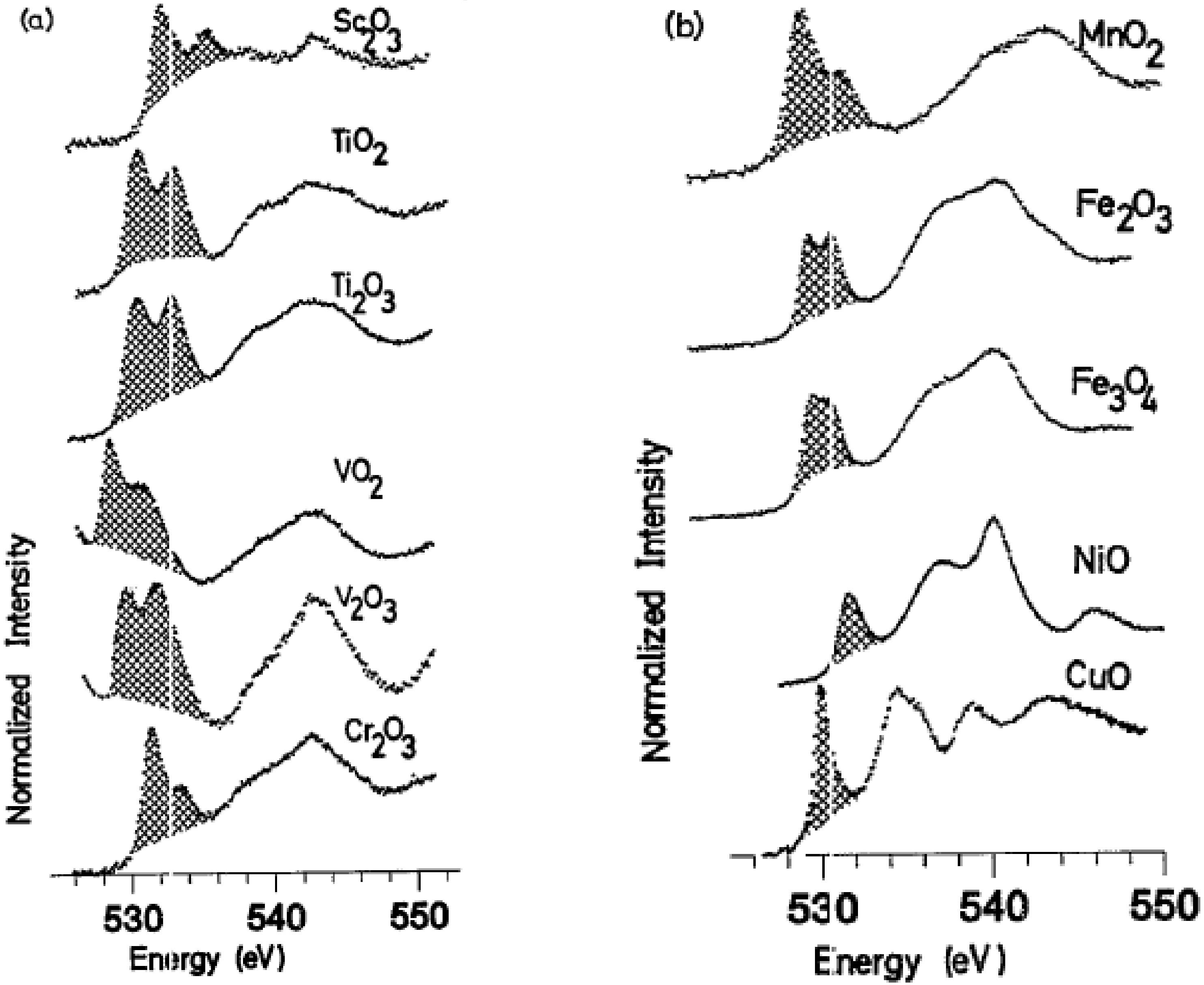

Core Hole Effect in XAS

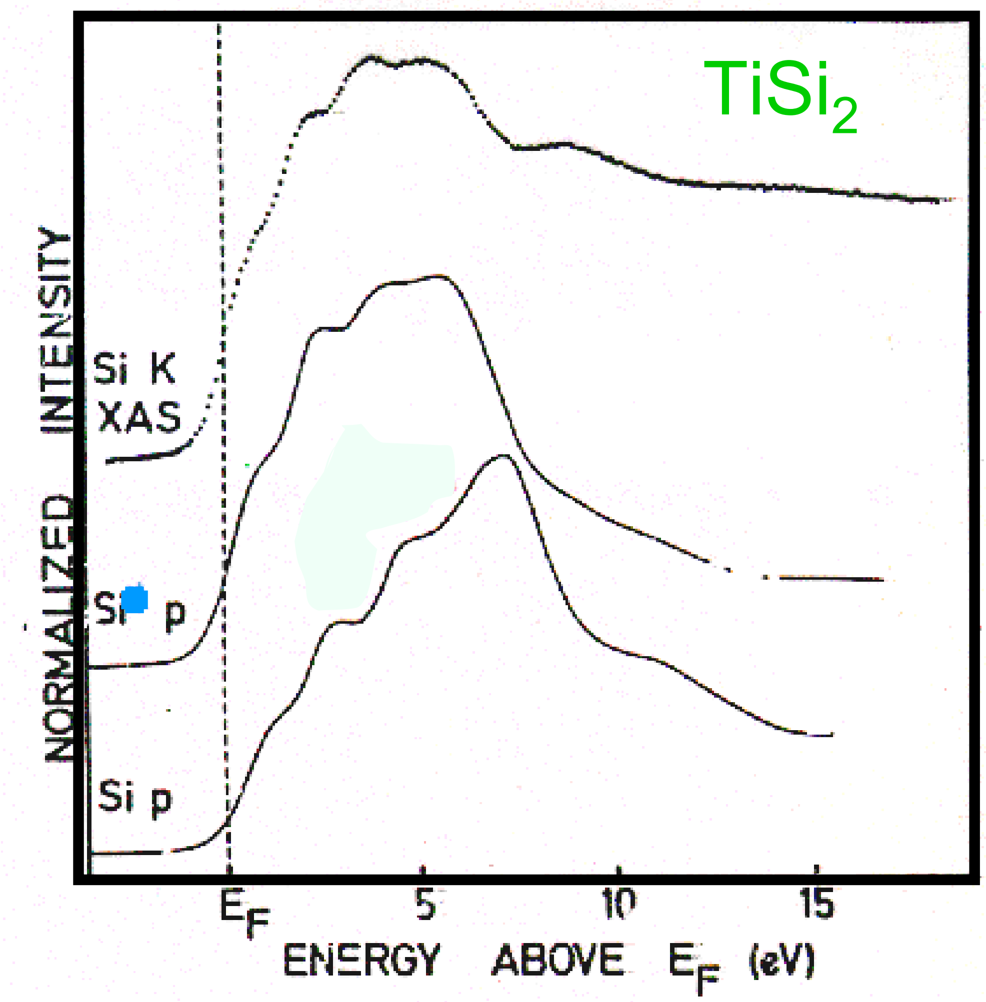

- **Final State Rule:** Spectral shape of XAS looks like final state DOS
- **Initial State Rule:** Intensity of XAS is given by the initial state

Phys. Rev. B. 41, 11899 (1991)

Titanium L edge of $SrTiO_3$

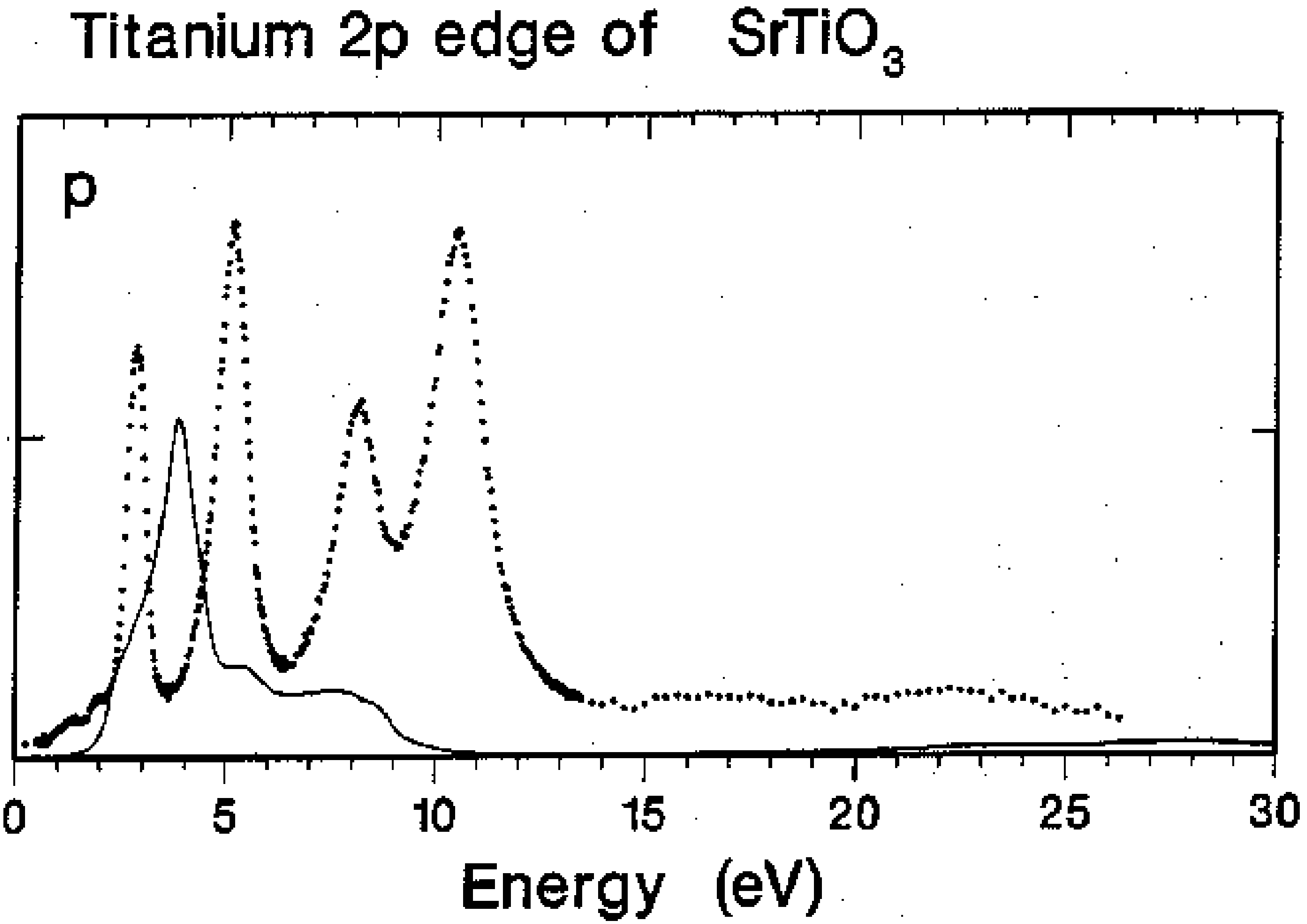

Oxygen K edge of TiO_2

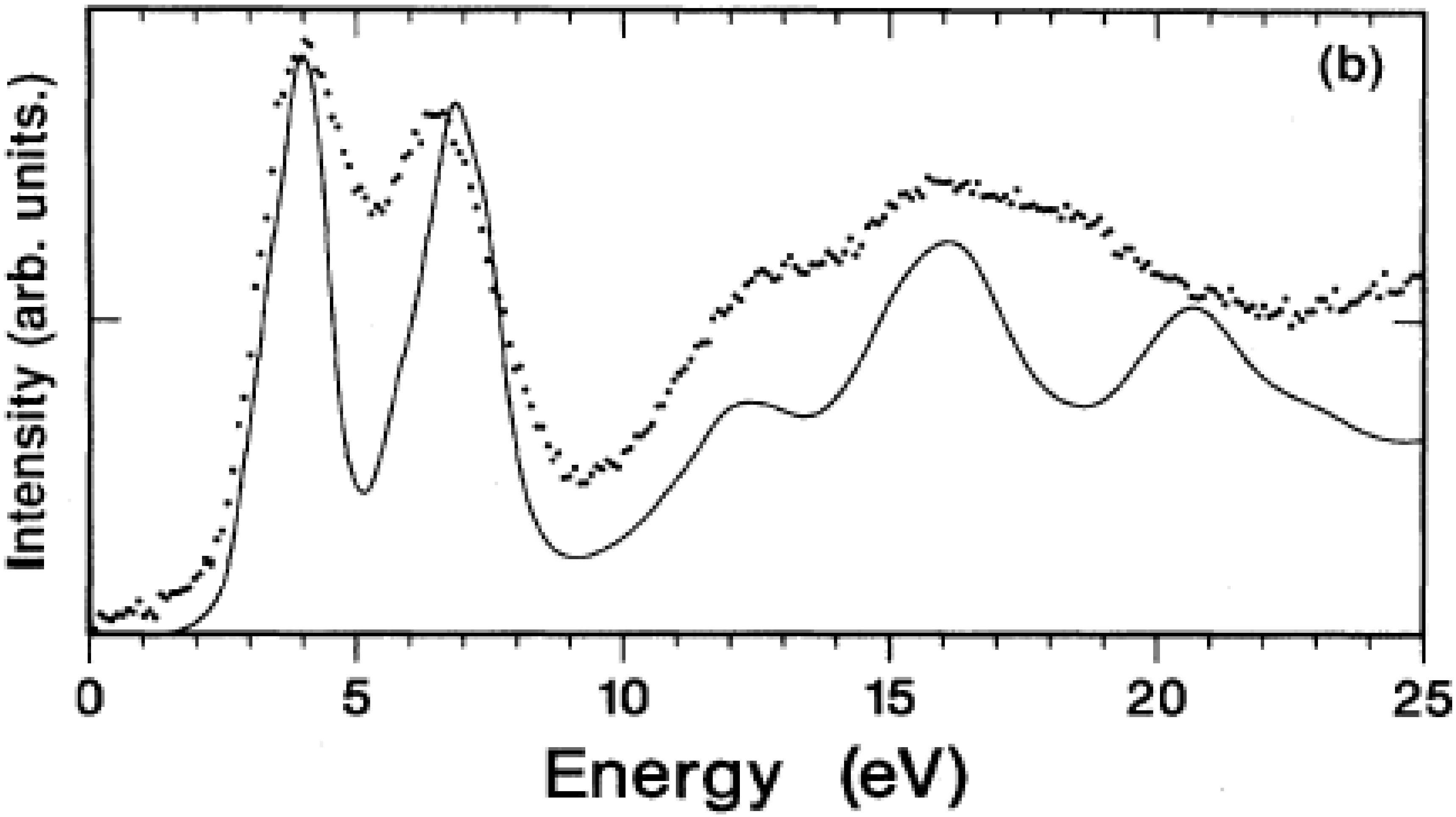

Atomic Multiplet Theory

$$H = \sum_{N} \xcancel{\frac{p_i^2}{2m}} + \sum_{N} \xcancel{\frac{-Ze^2}{r_i}} + \sum_{pairs} \frac{e^2}{r_{ij}} + \sum_{N} \zeta(r_i)\, l_i \cdot s_i$$

$$H_{ee}^{'} = H_{ee} - \left\langle H_{ee} \right\rangle = \sum_{pairs} \frac{e^2}{r_{ij}} - \left\langle \sum_{pairs} \frac{e^2}{r_{ij}} \right\rangle$$

Atomic Multiplet Theory

$$H_{ATOM} = \sum_{pairs} \frac{e^2}{r_{ij}} + \sum_{N} \zeta(r_i)\, l_i \cdot s_i$$

$$\left\langle {}^{2S+1}L_J \,\middle|\, \frac{e^2}{r_{12}} \middle| {}^{2S+1}L_J \right\rangle = \sum_{k} f_k F^k + \sum_{k} g_k G^k$$

Multiplet Effects

1s	2s	2p	3s	3p
0.07	**5**	**8**	**13**	**17**
0	**0**	**17**	**0**	**2**

Core Valence Overlap

Core Spin-orbit coupling

Multiplet Effects

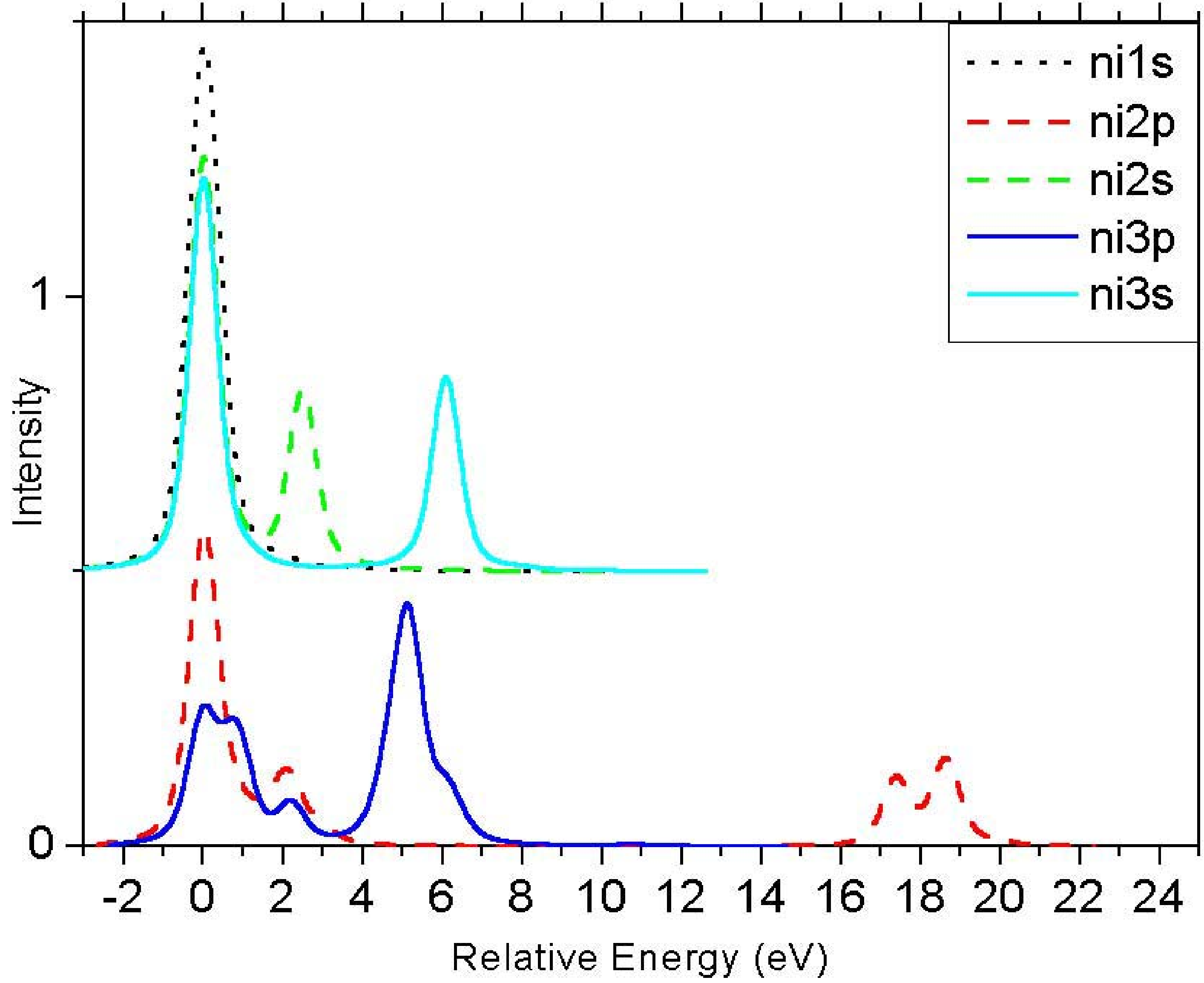

Term Symbols

- **Term Symbol $^{2S+1}L_J$**

- $(2S+1)(2L+1)$
- L=0,1,2,3,4 > S, P, D, F, G
- $|L-S| \leq J \leq L+S$
- Deg. Each J-state: $2J+1$

- s-electron: $^2S_{1/2}$
- p-electron: $^2P_{1/2}$ and $^2P_{3/2}$
- d-electron: $^2D_{3/2}$ and $^2D_{5/2}$

Term Symbols

$2p^2$-configuration

$\vert m_{lb}, m_{sb}>$	$\vert m_{la}, m_{sa}>$	$\vert M_L, M_S>$	**#**	$\vert m_{la}, m_{sa}>$	$\vert m_{lb}, m_{sb}>$	$\vert M_L, M_S>$	**#**
|1, –>	|1, +>	|2, 0>	**1**	|1, –>	|-1, –>	|0, -1>	**1**
|0, +>	|1, +>	|1, 1>	**1**	|0, +>	|0, –>	|0, 0>	**3**
|0, –>	|1, +>	|1, 0>	**1**	|0, +>	|-1, +>	|-1, 1>	**1**
|-1, +>	|1, +>	|0, 1>	**1**	|0, +>	|-1, –>	|-1, 0>	**1**
|-1, –>	|1, +>	|0, 0>	**1**	|0, –>	|-1, +>	|-1, 0>	**2**
|0, +>	|1, –>	|1, 0>	**2**	|0, –>	|-1, –>	|-1, -1>	**1**
|0, –>	|1, –>	|1, -1>	**1**	|-1, +>	|-1, –>	|-2, 0>	**1**
|-1, +>	|1, –>	|0, 0>	**2**				

Term Symbols

ALL	$M_S=1$	$M_S=0$	$M_S=-1$
$M_L=2$	0	1	0
$M_L=1$	1	2	1
$M_L=0$	1	3	1
$M_L=-1$	1	2	1
$M_L=-2$	0	1	0

^1D	$M_S=1$	$M_S=0$	$M_S=-1$
$M_L=2$	0	**1→0**	0
$M_L=1$	1	**2→1**	1
$M_L=0$	1	**3→2**	1
$M_L=-1$	1	**2→1**	1
$M_L=-2$	0	**1→0**	0

^3P	$M_S=1$	$M_S=0$	$M_S=-1$
$M_L=2$	0	0	0
$M_L=1$	**1→0**	**1→0**	**1→0**
$M_L=0$	**1→0**	**2→1**	**1→0**
$M_L=-1$	**1→0**	**1→0**	**1→0**
$M_L=-2$	0	0	0

^1S	$M_S=1$	$M_S=0$	$M_S=-1$
$M_L=2$	0	0	0
$M_L=1$	0	0	0
$M_L=0$	0	**1→0**	0
$M_L=-1$	0	0	0
$M_L=-2$	0	0	0

$2p^2$-configuration: $^1S_{0,}$ $^1D_2$, $^3P_0$, $^3P_1$, $^3P_2$,

Term Symbols

- **Term Symbol $^{2S+1}L_J$**

- $2p^2$-configuration: $^1S_0$, $^1D_2$, $^3P_0$, $^3P_1$, $^3P_2$,
  $1 + 5 + 1 + 3 + 5 = 15$

- $2p3p$-configuration: $^1S_0$, $^1D_2$, $^3P_0$, $^3P_1$, $^3P_2$,
  $+\ ^3S_1$, $^3D_1$, $^3D_2$, $^3D_3$, $^1P_1$,
  $15 + 3 + 3 + 5 + 7 + 3 = 36$

- $^2P \otimes {}^2P = {}^{1,3}S,P,D$

Term Symbols

$3d^1 4d^1$	$^1\mathbf{S}$	^1P	$^1\mathbf{D}$	^1F	$^1\mathbf{G}$	^3S	$^3\mathbf{P}$	^3D	$^3\mathbf{F}$	^3G	Σ
Deg.	**1**	3	**5**	7	**9**	3	**9**	15	**21**	27	100 **45**
J-values	**0**						**0**				
		1				1	**1**	1			
			2				**2**	2	**2**		
				3				3	**3**	3	
					4				**4**	4	
										5	

- $2p^2$-configuration: $^1S_0$, $^1D_2$, $^3P_0$, $^3P_1$, $^3P_2$,
- $3d^2$-configuration: $^1S_0$, $^1D_2$, $^3P_0$, $^3P_1$, $^3P_2$,

  $^1G_4$, $^3F_2$, $^3F_3$, $^3F_4$

Term Symbols

$3d^n$-configuration:

$$\binom{10}{n} = \frac{10!}{(10-n)!n!}$$

$2p^5 3d^n$-configuration:

$$6 \times \binom{10}{n} = 6 \times \frac{10!}{(10-n)!n!}$$

Matrix Elements

$$H_{ATOM} = \sum_{pairs} \frac{e^2}{r_{ij}} + \sum_{N} \zeta(r_i)\, l_i \cdot s_i$$

$$\left\langle {}^{2S+1}L_J \left| \frac{e^2}{r_{12}} \right| {}^{2S+1}L_J \right\rangle = \sum_k f_k F^k + \sum_k g_k G^k$$

Matrix Elements

f_k values:
k is even
$k_{max} = 2 \cdot l_{min}$
$k = k_{max}, k_{max}-2, \ldots\ldots 0$

g_k values:
only for different shells!
k is even if l_1+l_2 is even
$k_{max} = l_1+l_2$
$k = k_{max}, k_{max}-2, \ldots\ldots (0 \text{ or } 1)$

$3d^1$ no integrals
$3d^2$ $l_{min}=2 > k_{max}=4$
f_0, f_2, f_4, no exch.

$1s^2$ $l_{min}=0 > k_{max}=0$,
f_0, no exchange
3d4f $l_{min}=2 > k_{max}=4$
f_0, f_2, f_4,
$l_1+l_2=5 > k_{max}=5$
g_1, g_3, g_5

Matrix Elements

$$\left\langle {}^{2S+1}L_J \left| \frac{e^2}{r_{12}} \right| {}^{2S+1}L_J \right\rangle = \sum_k f_k F^k + \sum_k g_k G^k$$

1s2s $l_{min}=0 > k_{max}=0,$ f_0 $f_0=1$

$l_1+l_2=0 > k_{max}=0,$ g_0 $g_0=1$

$$\left\langle {}^{1}S \left| \frac{e^2}{r_{12}} \right| {}^{1}S \right\rangle = F^0(1s2s) + G^0(1s2s)$$

$$\left\langle {}^{3}S \left| \frac{e^2}{r_{12}} \right| {}^{3}S \right\rangle = F^0(1s2s) - G^0(1s2s)$$

Matrix Elements

$3d^2$ $l_{min}=2 > k_{max}=4$ f_0, f_2, $f_{4,}$no exchange

$$\left\langle {}^{2S+1}L_J \,\middle|\, \frac{e^2}{r_{12}} \middle|\, {}^{2S+1}L_J \right\rangle = \sum_k f_k F^k + \sum_k g_k G^k$$

Calculate energy levels due to e/r integrals

(45x45 matrix blocked into irred. Representations)

		Relative Energy	Relative Energy
^1S	$F^0 + 2/7\ F^2 + 2/7\ F^4$	$0.46F^2$	4.6 eV
^3P	$F^0 + 3/21\ F^2 - 4/21\ F^4$	$0.02F^2$	0.2 eV
^1D	$F^0 - 3/49\ F^2 + 4/49\ F^4$	$-0.01F^2$	-0.1 eV
^3F	$F^0 - 8/49\ F^2 - 1/49\ F^4$	$-0.18F^2$	-1.8 eV
^1G	$F^0 + 4/49\ F^2 + 1/441\ F^4$	$0.08F^2$	0.8 eV

Matrix Elements

Hunds rules:

- Term symbols with maximum spin S are lowest in energy,
- Among these terms:

  Term symbols with maximum L are lowest in energy
- In the presence of spin-orbit coupling, the lowest term has

  J = |L-S| if the shell is less than half full

  J = L+S if the shell is more than half full

$3d^1$ has $^2D_{3/2}$ ground state
$3d^9$ has $^2D_{5/2}$ ground state

$3d^2$ has $^3F_2$ ground state
$3d^8$ has $^3F_4$ ground state

Term Symbols and XAS

$$I_{XAS} \propto \langle 3d^0 \mid p \mid 2p^5 3d^1 \rangle^2$$

Symmetry properties:

$$I_{XAS} \propto \left\langle \left[{}^1S_0\right] \middle| \left[{}^1P_1\right] \middle| \left[{}^{1,3}PDF\right] \right\rangle^2$$

Term Symbols and XAS

Ti^{IV} ion in TiO_2:
Ground state: $3d^0$
Final state: $2p^5 3d^1$
Dipole transition: p-symmetry

$3d^0$-configuration: ^1S $j=0$
$2p^1 3d^9$-configuration: $^2P \otimes {}^2D = {}^{1,3}PDF$ $j' = 0,1,2,3,4$
p-transition: ^1P $\Delta j = +1,0,-1$

ground state symmetry: ^1S $^1S_0$
transition: $^1S \otimes {}^1P = {}^1P$
two possible final states: ^1P $^1P_1, {}^3P_1, {}^3D_1,$

Term Symbols and XAS

	$^3P_0$	**$^3P_1$**	**$^3D_1$**	**$^1P_1$**	$^3P_2$	$^3D_2$	$^3F_2$	$^1D_2$	$^3D_3$	$^3F_3$	$^1F_3$	$^3F_4$
-3.281	1.0											
-2.954		**-0.94**	**0.30**	**0.08**								
0.213		**-0.19**	**-0.77**	**0.60**								
5.594		**0.24**	**0.55**	**0.79**								
-2.381					0.81	-0.46	0.01	0.34				
-1.597					-0.03	-0.50	0.56	-0.65				
3.451					0.04	-0.30	-0.82	-0.47				
3.643					-0.57	-0.65	-0.06	0.48				
-2.198									-0.21	0.77	0.59	
-1.369									0.81	-0.19	0.54	
3.777									-0.53	-0.60	0.59	
-2.481												1.0

Table 1 ***The relative energies of an atomic multiplet calculation for Ti** ^{IV}**.***

Term Symbols and XAS

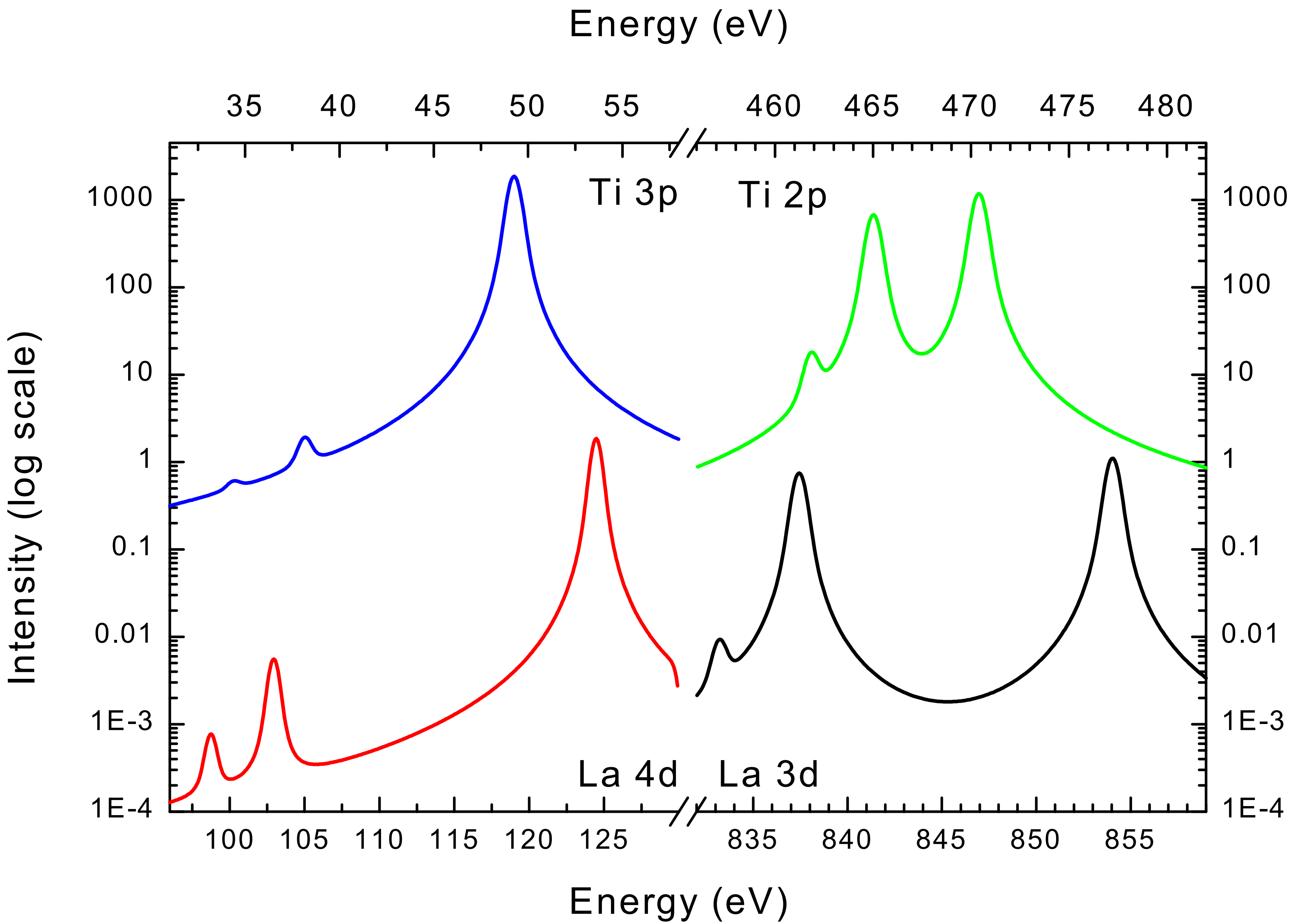

3d0 XAS calculation

$$H_{eff} = H_{ELECTRO} + H_{LS-2p} + H_{LS-3d}$$

$$H_{ELECTRO} = \left\langle 2p^5 3d^1 \,|\, \frac{e^2}{r_{12}} \,|\, 2p^5 3d^1 \right\rangle$$

$$H_{LS-2p} = \left\langle 2p \,|\, \varsigma_p l_p \cdot s_p \,|\, 2p \right\rangle$$

$$H_{LS-3d} = \left\langle 3d \,|\, \varsigma_d l_d \cdot s_d \,|\, 3d \right\rangle$$

$3d^0$ XAS calculation

$H_{electro=0}$ $H_{LS\text{-}2p=0}$ $H_{LS\text{-}3d=0}$

Energy Matrix $\begin{vmatrix} 0 & 0 & 0 \\ 0 & 0 & 0 \\ 0 & 0 & 0 \end{vmatrix}$		*Eigenvectors* $\begin{vmatrix} 1 & 0 & 0 \\ 0 & 1 & 0 \\ 0 & 0 & 1 \end{vmatrix}$
Energy Levels		**Intensities**
0.00	^3P	0.00
0.00	^3D	0.00
0.00	^1P	1.00

$3d^0$ XAS calculation

$H_{electro=ATOM}$ $H_{LS-2p=0}$ $H_{LS-3d=0}$

Energy Matrix $\begin{vmatrix} -1.345 & 0 & 0 \\ 0 & 0.671 & 0 \\ 0 & 0 & 3.591 \end{vmatrix}$		*Eigenvectors* $\begin{vmatrix} 1 & 0 & 0 \\ 0 & 1 & 0 \\ 0 & 0 & 1 \end{vmatrix}$
Energy Levels		**Intensities**
-1.345	^3P	0.00
+0.671	^3D	0.00
+3.591	^1P	1.00

$3d^0$ XAS calculation

$H_{electro=0}$ $H_{LS\text{-}2p=ATOM}$ $H_{LS\text{-}3d=0}$

Energy Matrix

$$\begin{vmatrix} 0.944 & 1.635 & 2.312 \\ 1.635 & -0.944 & 1.335 \\ 2.312 & 1.335 & 0.000 \end{vmatrix}$$

Eigenvectors

$$\begin{vmatrix} 0.5 & -0.5 & -0.707 \\ -0.866 & -0.288 & -0.408 \\ 0.0 & 0.816 & -0.577 \end{vmatrix}$$

Energy Levels		**Intensities**
-1.888	^3P	0.00
-1.888	^3D	0.666
+3.776	^1P	0.333

$3d^0$ XAS calculation

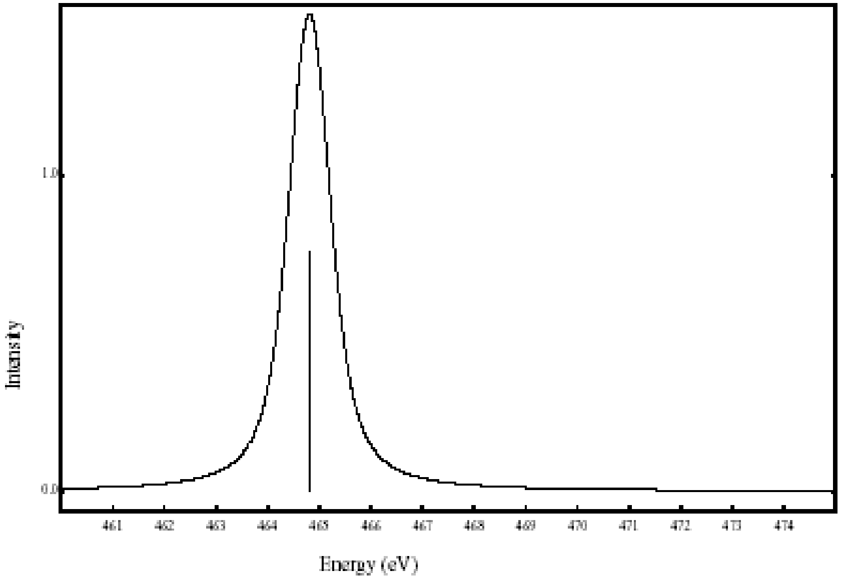

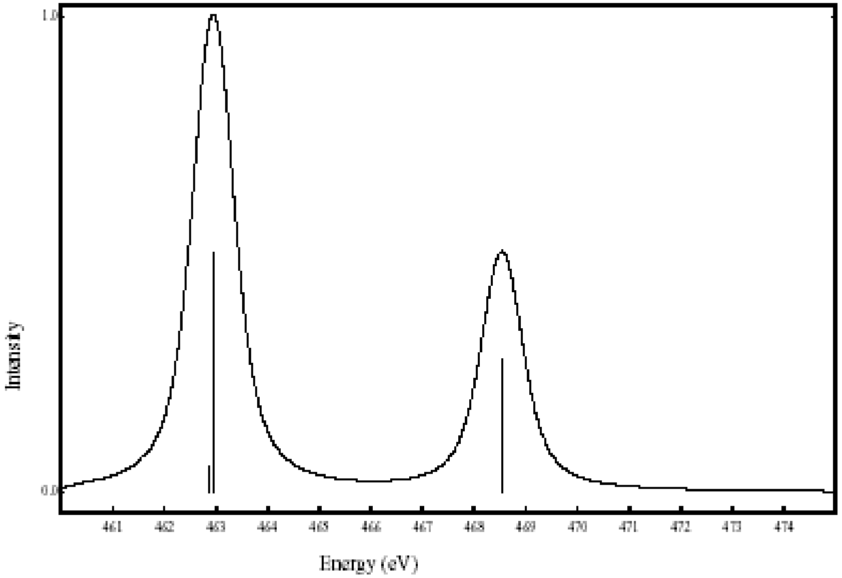

$3d^0$ XAS calculation

$H_{electro=ATOM}$ $H_{LS\text{-}2p=ATOM}$ $H_{LS\text{-}3d=0}$

Energy Matrix

$$\begin{vmatrix} 1.615 & 1.635 & 2.312 \\ 1.635 & -2.289 & 1.335 \\ 2.312 & 1.335 & 3.591 \end{vmatrix}$$

Eigenvectors

$$\begin{vmatrix} 0.297 & -0.776 & 0.557 \\ -0.951 & -0.185 & 0.248 \\ 0.089 & 0.603 & 0.792 \end{vmatrix}$$

Energy Levels		**Intensities**
-2.925	^3P	0.008
+0.207	^3D	0.364
+5.634	^1P	0.628

3d^0 XAS calculation

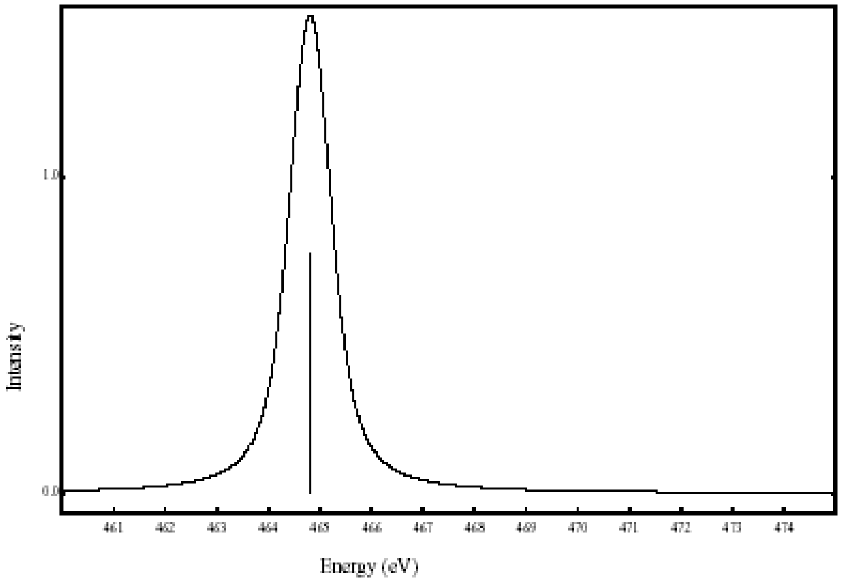

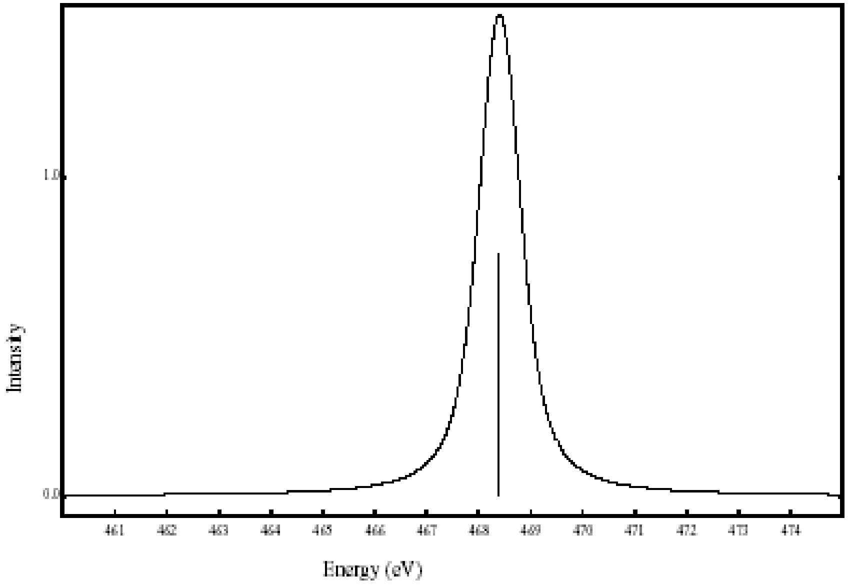

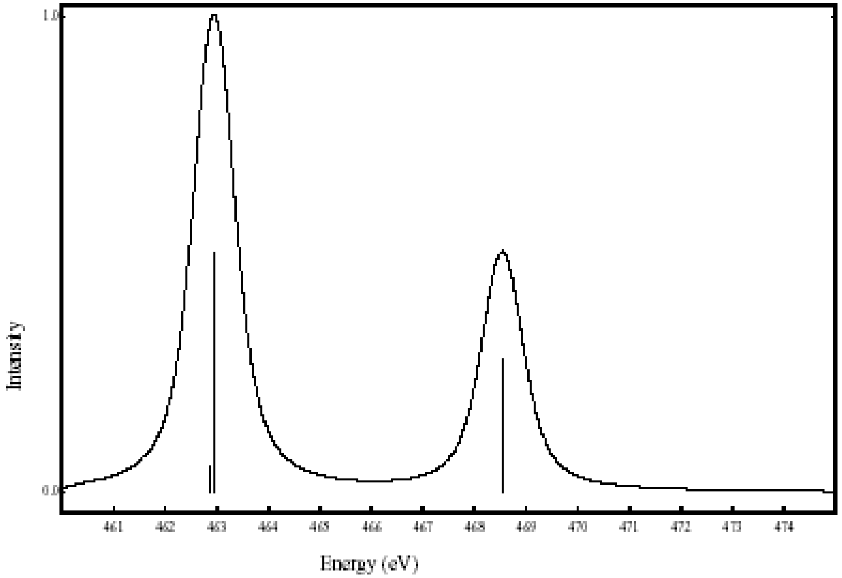

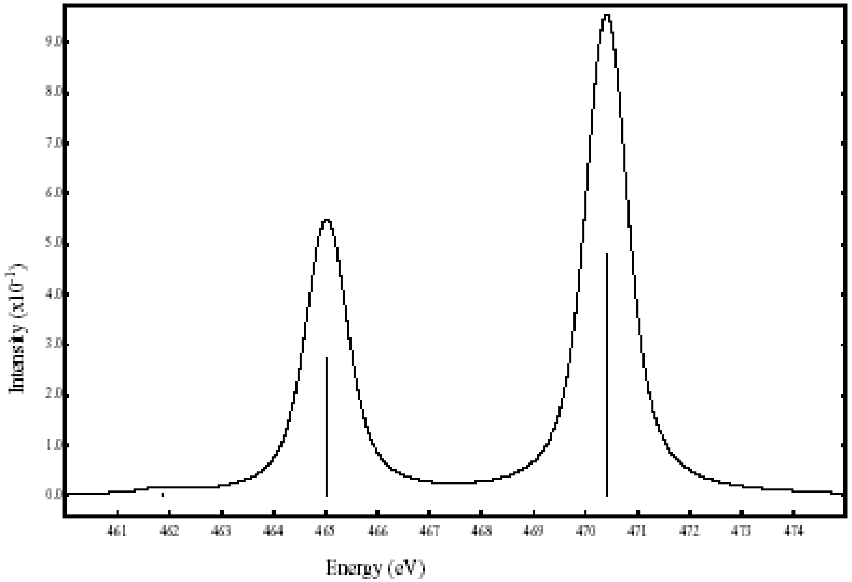

$3d^0$ XAS calculation

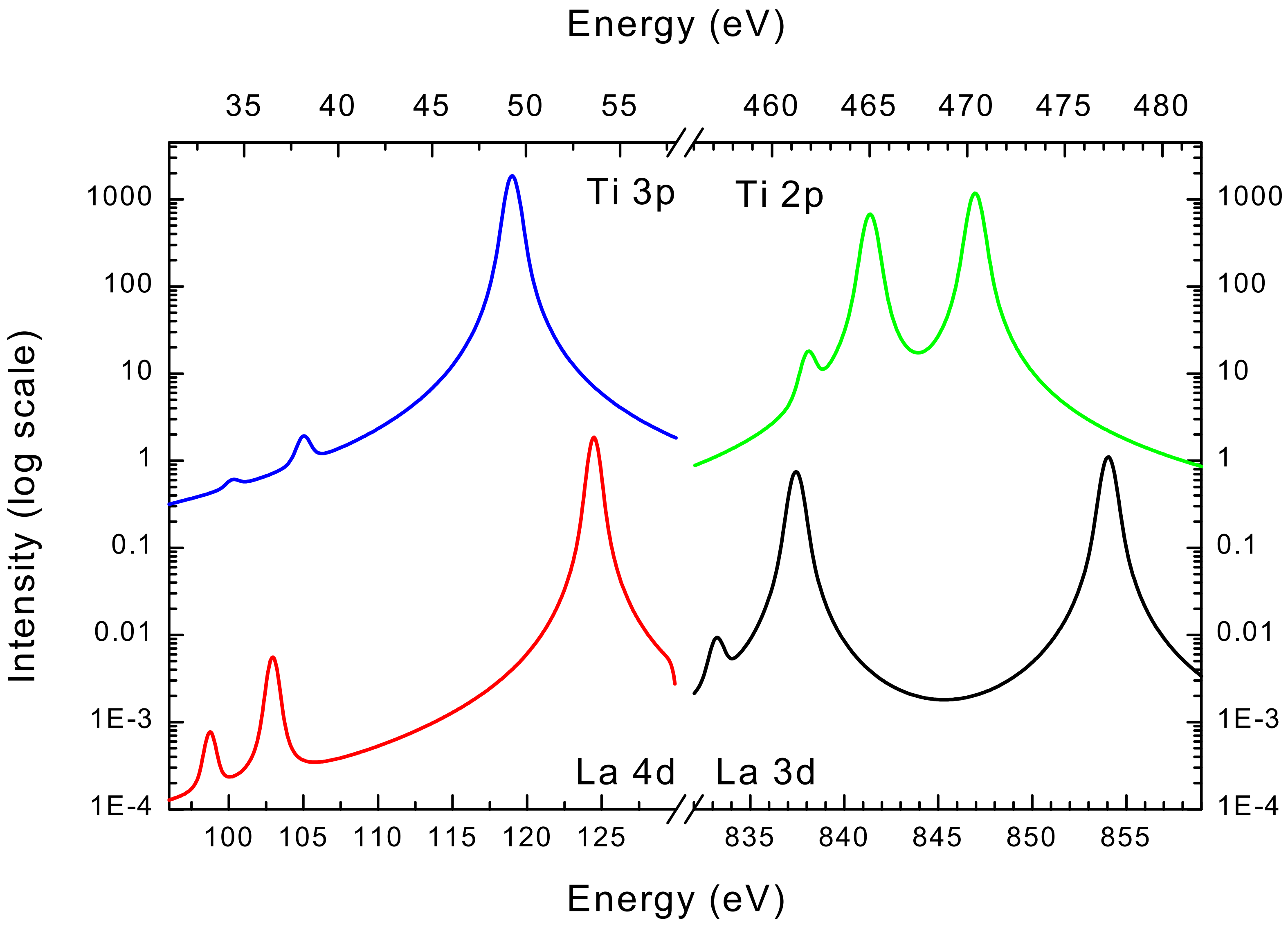

$3d^0$ XAS calculation

Edge	Ti 2p	Ti 3p	La 3d	La 4d
Average Energy (eV)	464.00	37.00	841.00	103.00
Core spin-orbit (eV)	3.78	0.43	6.80	1.12
F^2 Slater-Condon (eV)	5.04	8.91	5.65	10.45
<u>Intensities:</u>				
Pre-peak	0.01	10^{-4}	0.01	10^{-3}
$p_{3/2}$ or $d_{5/2}$	0.72	10^{-3}	0.80	0.01
$p_{1/2}$ or $d_{3/2}$	1.26	1.99	1.19	1.99

$3d^N$ XAS calculation

Transition	Ground	Transitions	Term Symbols
$3d^0 \rightarrow 2p^5 3d^1$	$^1S_0$	3	12
$3d^1 \rightarrow 2p^5 3d^2$	$^2D_{3/2}$	29	45
$3d^2 \rightarrow 2p^5 3d^3$	$^3F_2$	68	110
$3d^3 \rightarrow 2p^5 3d^4$	$^4F_{3/2}$	95	180
$3d^4 \rightarrow 2p^5 3d^5$	$^5D_0$	32	205
$3d^5 \rightarrow 2p^5 3d^6$	$^6S_{5/2}$	110	180
$3d^6 \rightarrow 2p^5 3d^7$	$^5D_2$	68	110
$3d^7 \rightarrow 2p^5 3d^8$	$^4F_{9/2}$	16	45
$3d^8 \rightarrow 2p^5 3d^9$	$^3F_4$	4	12
$3d^9 \rightarrow 2p^5 3d^{10}$	$^2D_{5/2}$	1	2

Term Symbols and XAS

Ti^{IV} ion in TiO_2:
Ground state: $3d^0$
Final state: $2p^5 3d^1$
Dipole transition: p-symmetry

$3d^0$-configuration: ^1S $j=0$
$2p^1 3d^9$-configuration: $^2P \otimes {}^2D = {}^{1,3}PDF$ $j'=0,1,2,3,4$
p-transition: ^1P $\Delta j=+1,0,-1$

ground state symmetry: ^1S $^1S_0$
transition: $^1S \otimes {}^1P = {}^1P$
two possible final states: ^1P $^1P_1, {}^3P_1, {}^3D_1,$

Term Symbols and XAS

Ni^{II} ion in NiO:
Ground state: $3d^8$
Final state: $2p^5 3d^9$
Dipole transition: p-symmetry

$3d^8$-configuration: ^1S, ^1D, ^3P,^1G, ^3F j=4
$2p^5 3d^9$-configuration: $^2P \otimes {}^2D = {}^{1,3}PDF$ j'=0,1,2,3,4
p-transition: ^1P Δj=+1,0,-1

ground state symmetry: ^3F $^3F_4$
transition: $^3F \otimes {}^1P = {}^3DFG$
two possible final states: ^3D, ^3F $^3D_3$,$^3F_3$,$^3F_4$, $^1F_3$

$3d^8$ XAS calculation

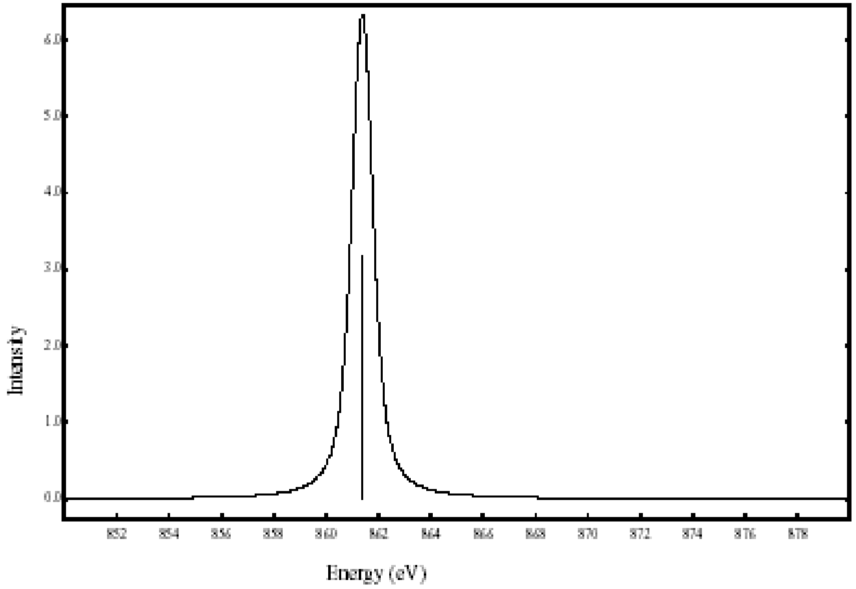

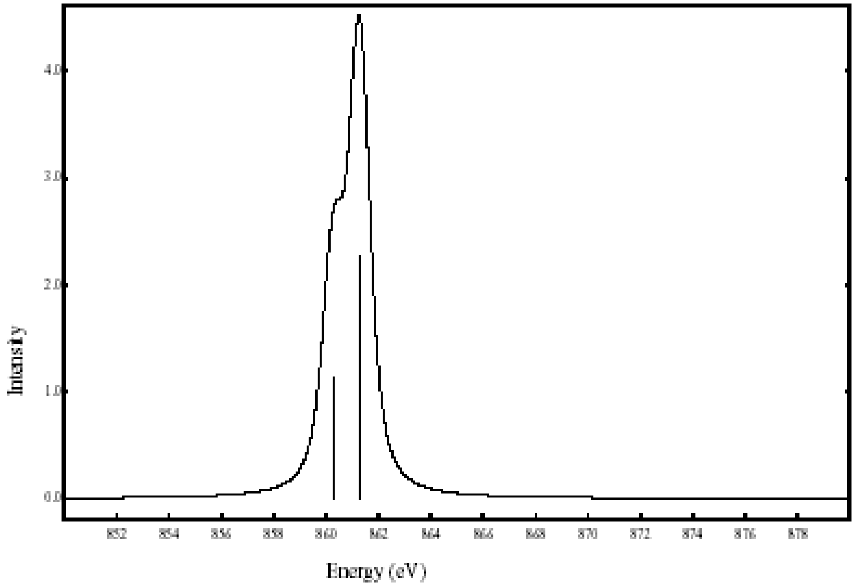

Term Symbols and XAS

Ni^{II} ion in NiO:
Ground state: $3d^8$
Final state: $2p^5 3d^9$
Dipole transition: p-symmetry

$3d^8$-configuration: ${}^1S$, ${}^1D$, ${}^3P$, ${}^1G$, ${}^3F$ j=4
$2p^5 3d^9$-configuration: ${}^2P \otimes {}^2D = {}^{1,3}PDF$ j'=0,1,2,3,4
p-transition: ${}^1P$ $\Delta j=+1,0,-1$

ground state symmetry: ${}^3F$ ${}^3F_4$
transition: ${}^3F \otimes {}^1P = {}^3DFG$
two possible final states: ${}^3D$, ${}^3F$ ${}^3D_3, {}^3F_3, {}^3F_4, {}^1F_3$

$3d^8$ XAS calculation

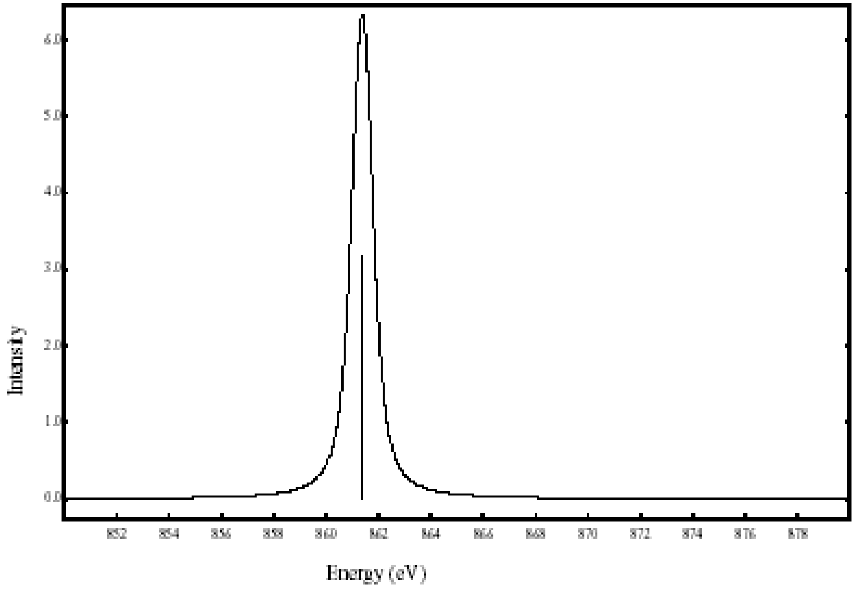

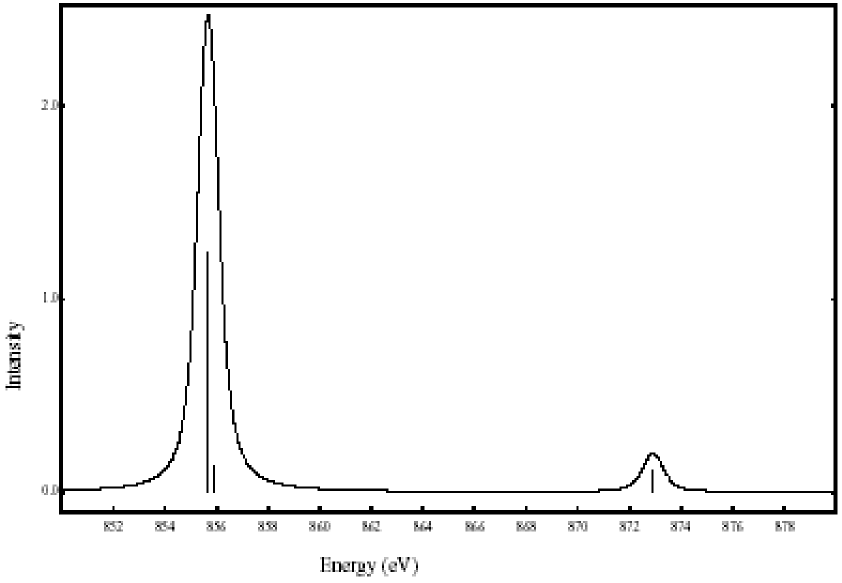

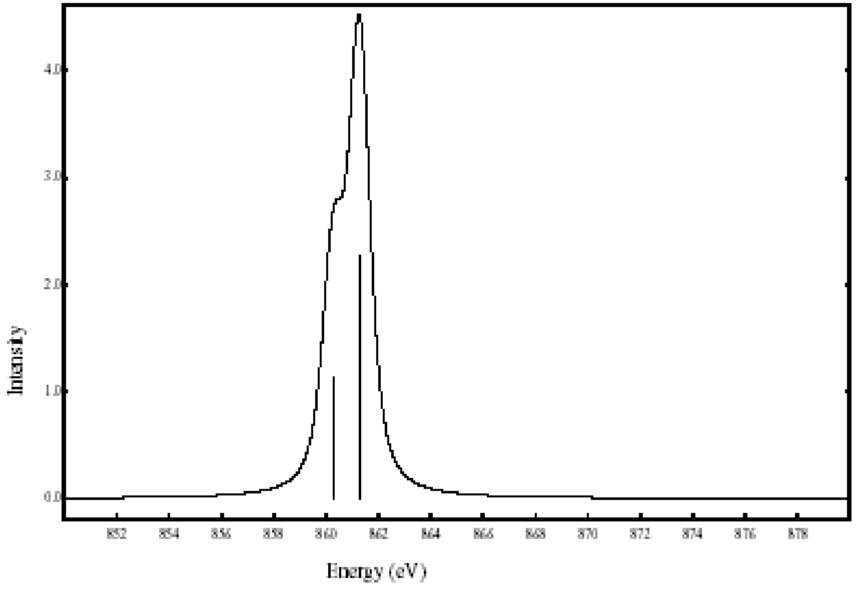

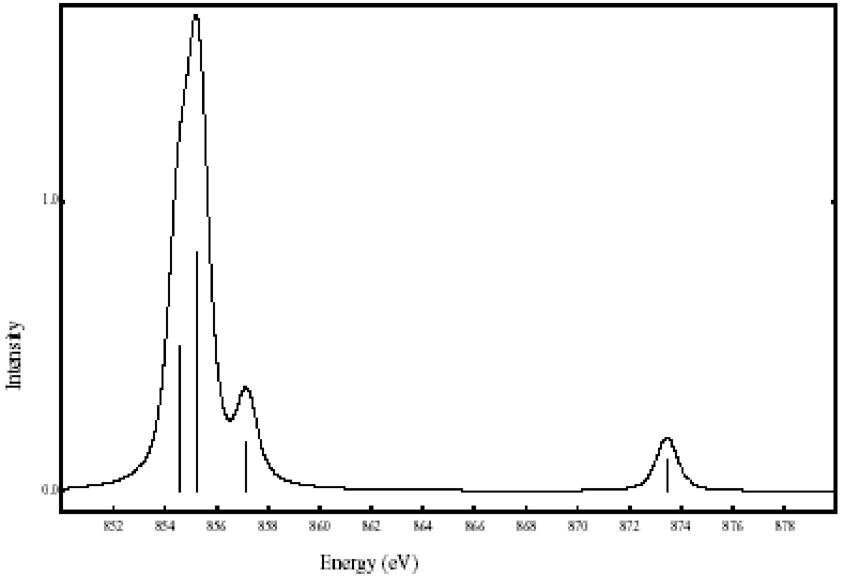

XAS calculations of rare earths

Nd^{III} ion in Nd metal

Ground state: 4f^3

Final state: 3d^{9}4f^4

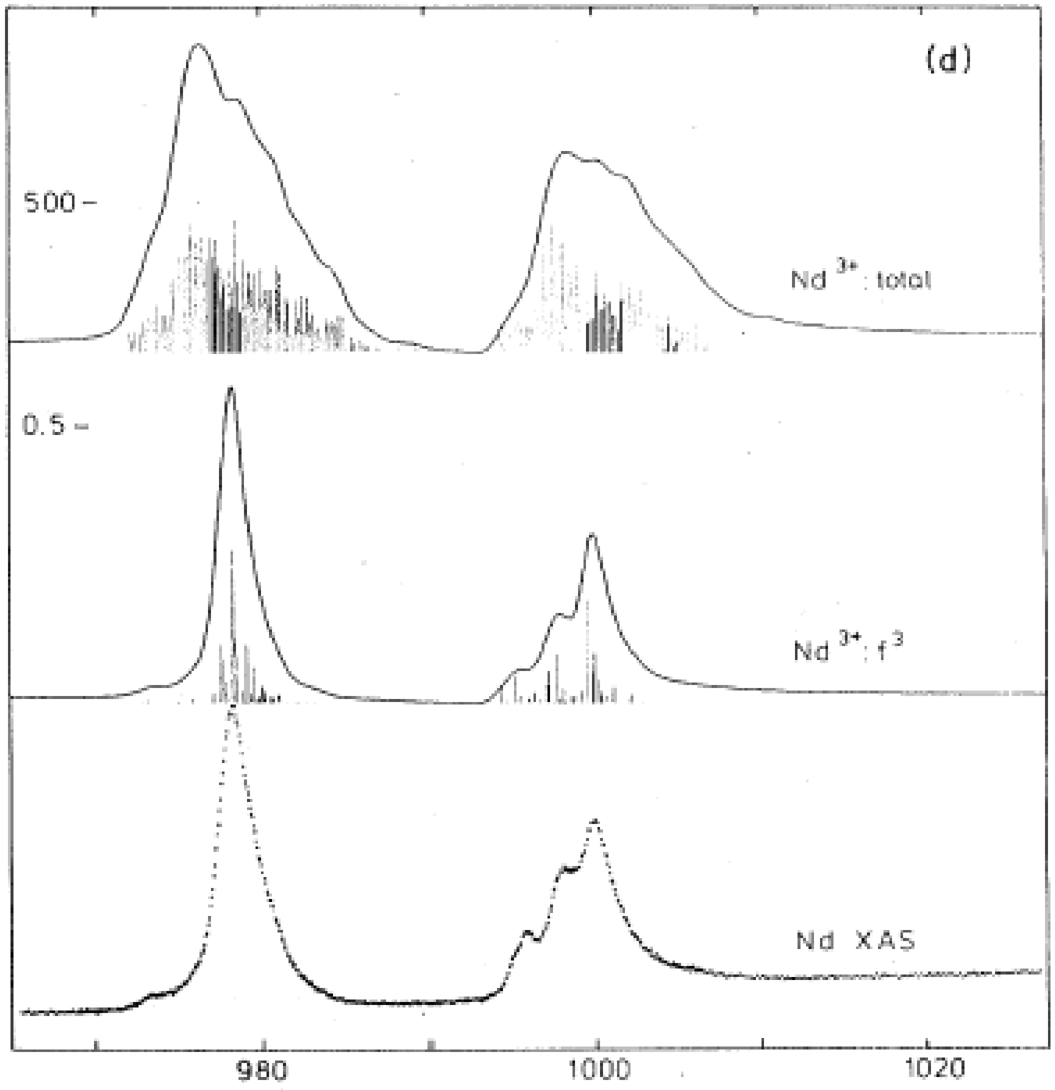

X-ray absorption

Excitation of core electrons to empty states.

Spectrum given by the **Fermi Golden Rule**

(name Golden Rule given by Fermi; rule itself given by Dirac)

$$\boxed{I_{XAS} \sim \Sigma_f \left| \left\langle \Phi_f \middle| \hat{e} \cdot r \middle| \Phi_i \right\rangle \right|^2 \delta_{E_f - E_i - \hbar\omega}}$$

X-ray absorption

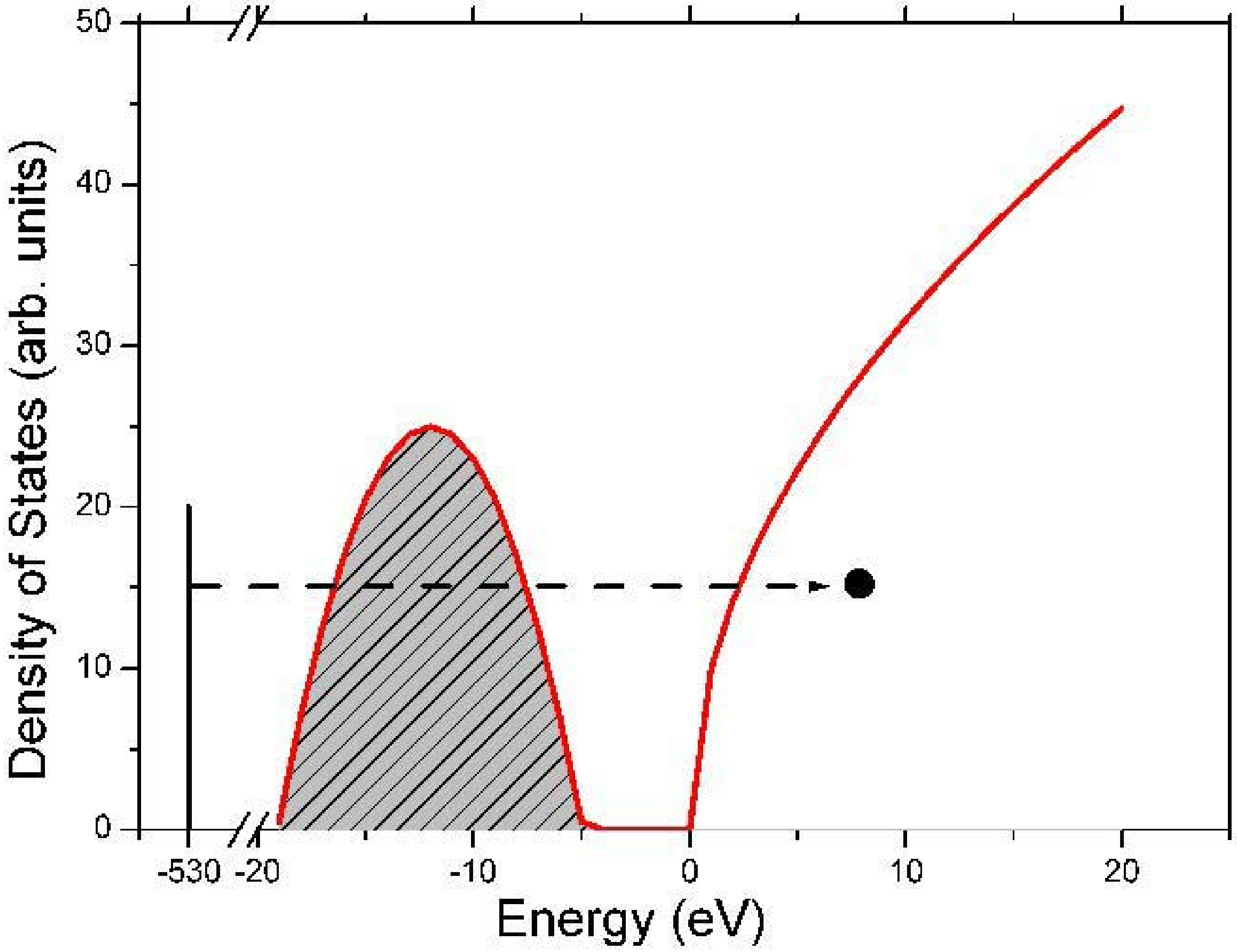

Shapes of d-orbitals

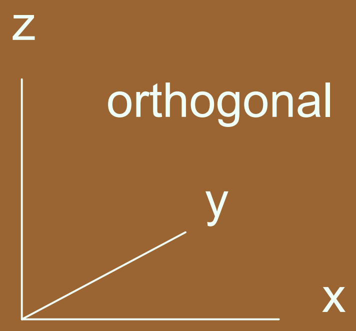

d-orbitals have gerade (g) symmetry

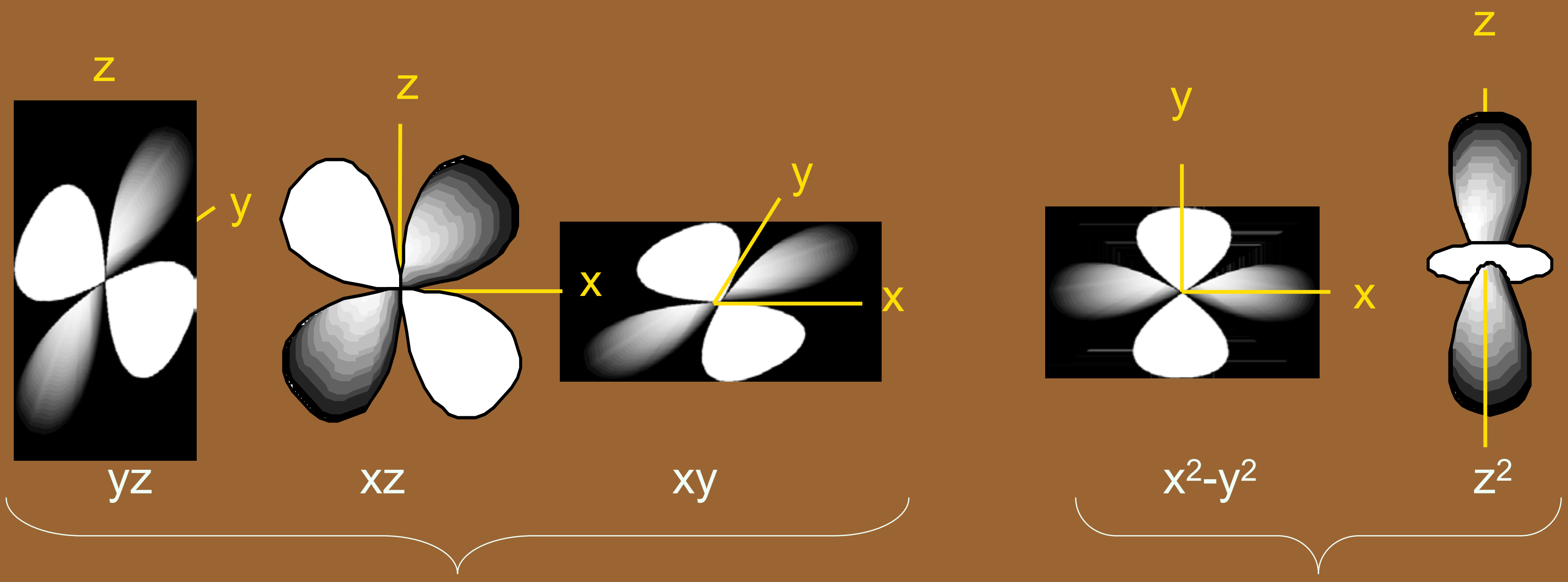

lie between ordinate axes

lie along ordinate axes

In a free ion (no ligands), d-orbitals are degenerate *ie.* they have the same energy

Octahedral crystal field splitting

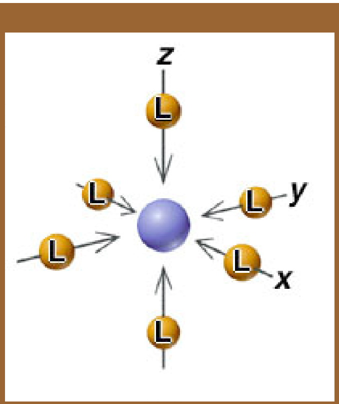

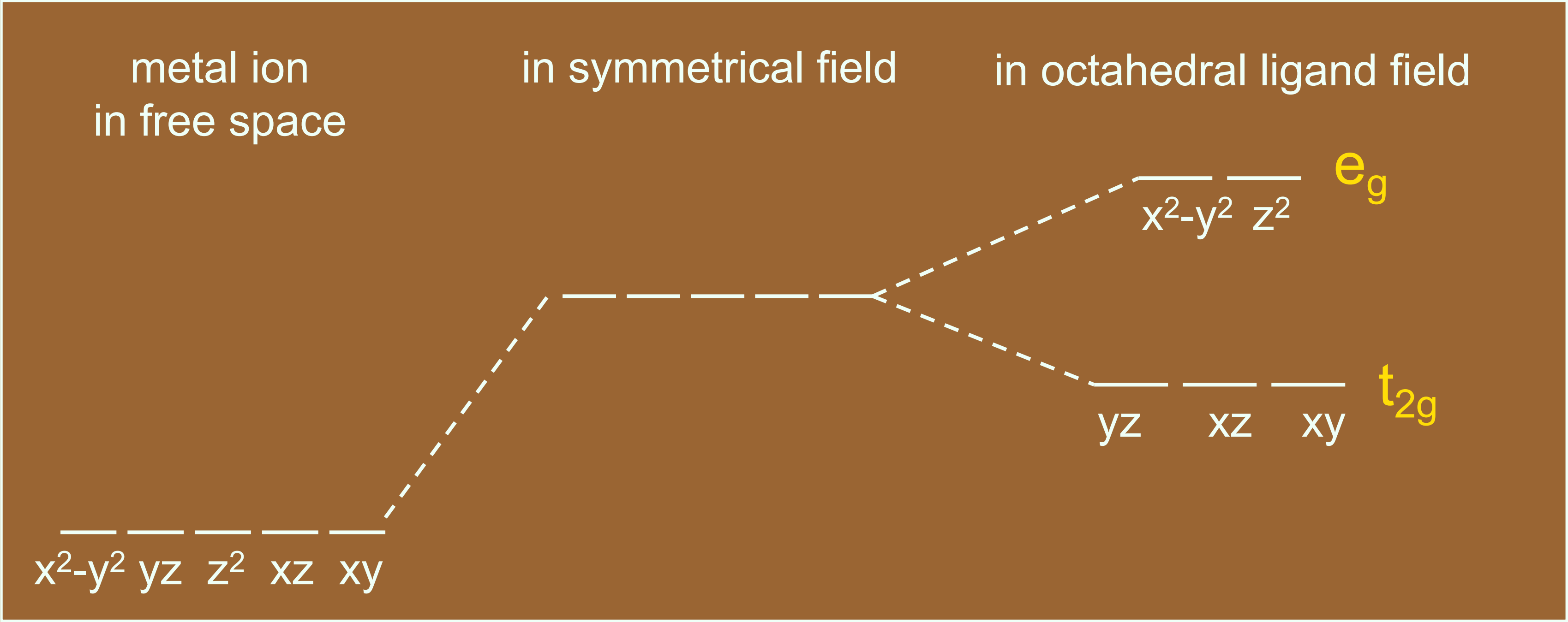

metal ion
in free space

in symmetrical field

in octahedral ligand field

e_g

x^2-y^2 z^2

t_{2g}

yz xz xy

x^2-y^2 yz z^2 xz xy

xy, yz, xz	stabilised relative to symmetrical field	lie between ordinate axes
x^2-y^2, z^2	destabilised relative to symmetrical field	lie along ordinate axes

Effect of ligand field on metal d-orbitals

orbitals forming e_g set

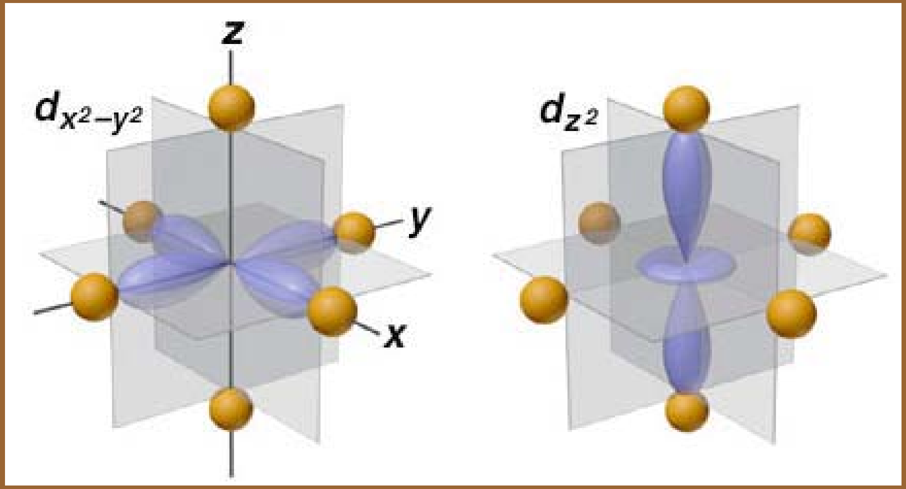

orbitals forming t_{2g} set

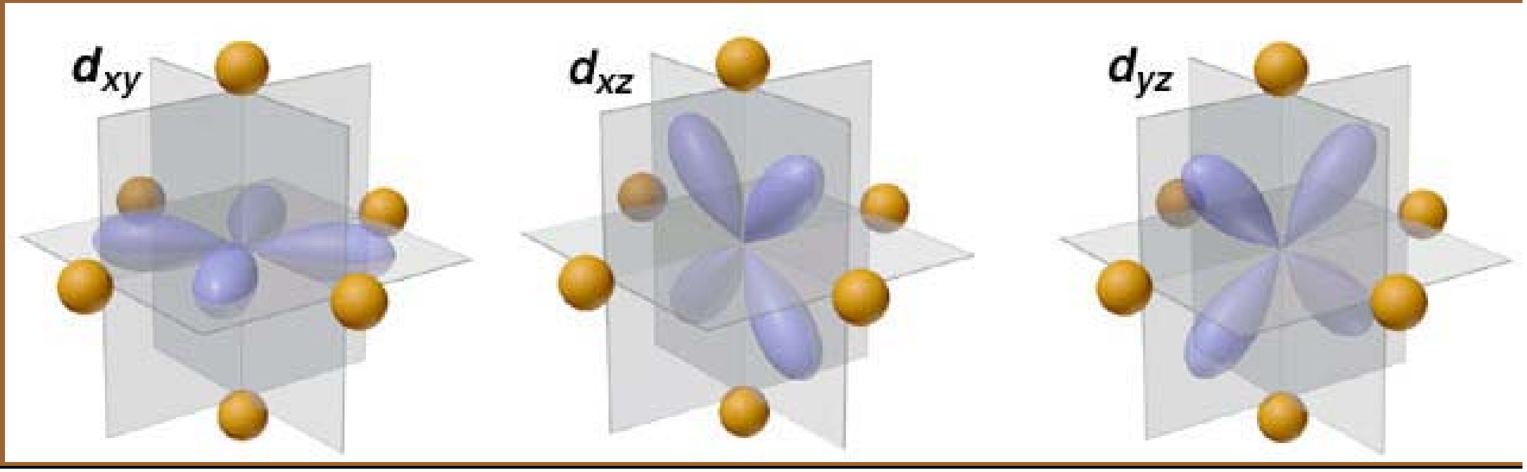

The difference in energy between the e_g and the t_{2g} energy levels is the crystal field splitting parameter, Δ_o□□. This is given the value 10 Dq.

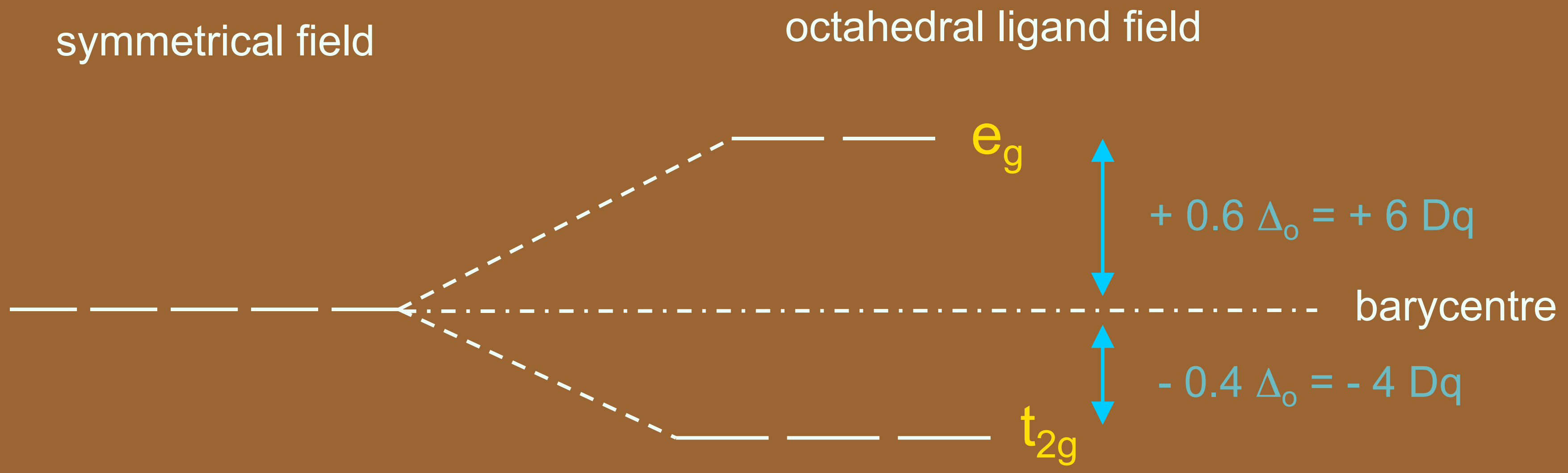

symmetrical field

octahedral ligand field

e_g

$+ 0.6\ \Delta_o = + 6$ Dq

barycentre

$- 0.4\ \Delta_o = - 4$ Dq

t_{2g}

Crystal Field Effects

$$H_{CF} = H_{ATOM} + H_{FIELD}$$

$$H_{FIELD} = -e\phi(r)$$

$$\phi(r) = \sum_{L=0}^{\infty} \sum_{M=-L}^{L} r^{L} A_{LM} Y_{LM}(\psi, \phi)$$

Crystal Field Effects

<3d|φ(r)|3d>.

$$\left\langle Y_{2m_2} \middle| Y_{LM} \middle| Y_{2m_1} \right\rangle = (-1)^{m_2} \sqrt{15(2L+1)/4\pi} \begin{pmatrix} 2 & L & 2 \\ -m_2 & M & m_1 \end{pmatrix} \begin{pmatrix} 2 & L & 2 \\ 0 & 0 & 0 \end{pmatrix}$$

$$\phi(r) = A_{00} Y_{00} + \sum_{M=-2}^{2} r^2 A_{2M} Y_{2M} + \sum_{M=-4}^{4} r^4 A_{4M} Y_{4M}$$

Crystal Field Effects

SO_3		O_h (Butler)	O_h (Mulliken)
S	0	0	A_1
P	1	1	T_1
D	2	2 + ^1	$E+T_2$
F	3	^0+ 1 +^1	$A_2+T_1+T_2$
G	4	0 + 1 + 2 + ^1	$A_1+E+T_1+T_2$

Crystal Field Effects

	Relative Energy	Symmetries in O_h	Symmetries in D_{4h}
^1S	4.6 eV	$^1A_1$	$^1A_1$
^3P	0.2 eV	$^3T_1$	$^3E+^3A_2$
^1D	-0.1 eV	$^1E + ^1T_2$	$^1A_1+^1B_1 + ^1E+^1B_2$
^3F	-1.8 eV	$\mathbf{^3A_2} + ^3T_1 + ^3T_2$	$\mathbf{^3B_1} + ^3E + ^3A_2 + ^3E + ^3B_2$
^1G	0.8 eV	$^1A_1+^1T_1+^1T_2+^1E$	$^1A_1+^1E +$ $^1A_2+^1E+^1B_2+^1A_1+^1B_1$

Crystal Field Effects: Tanabe-Sugano

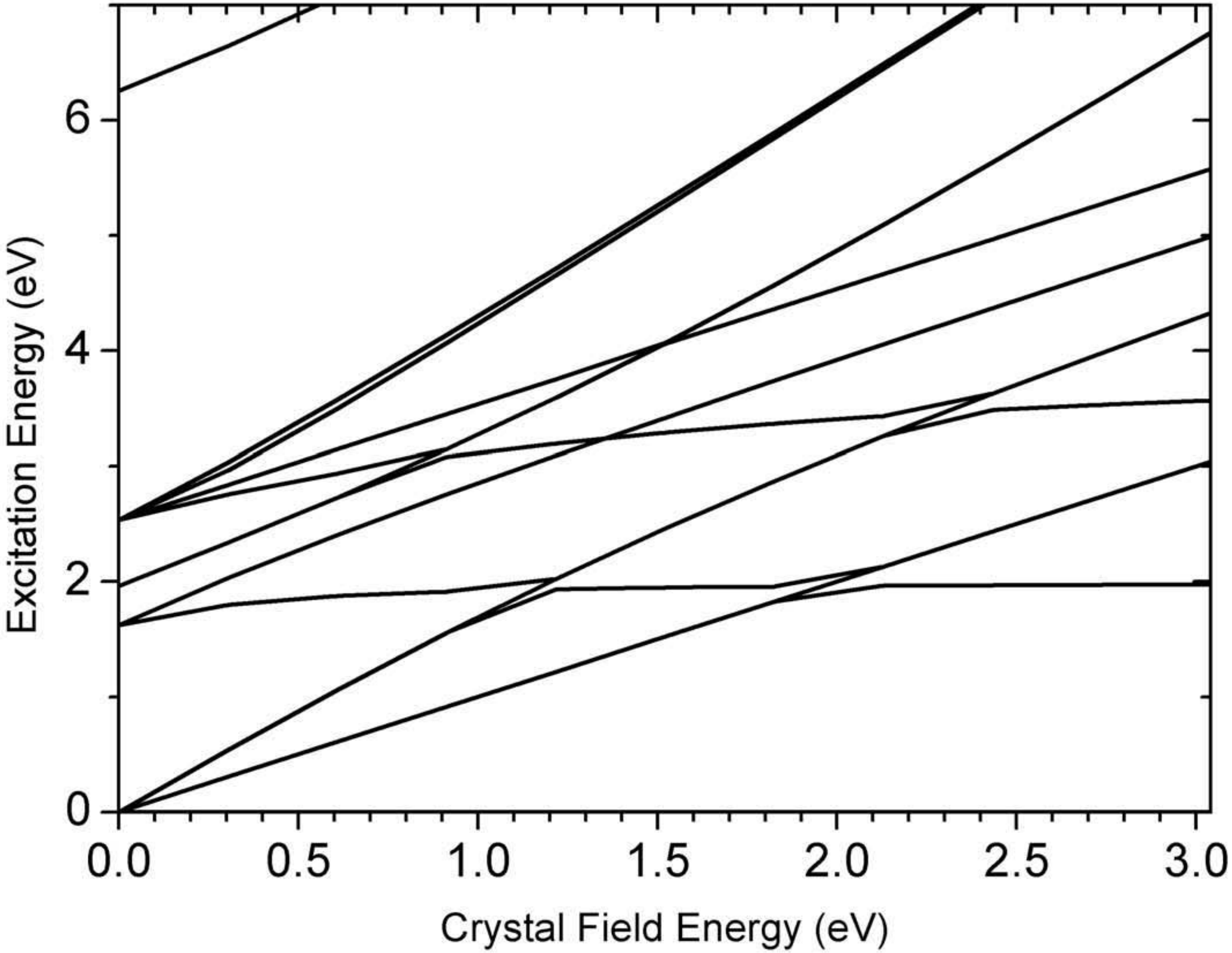

Crystal Field Effects

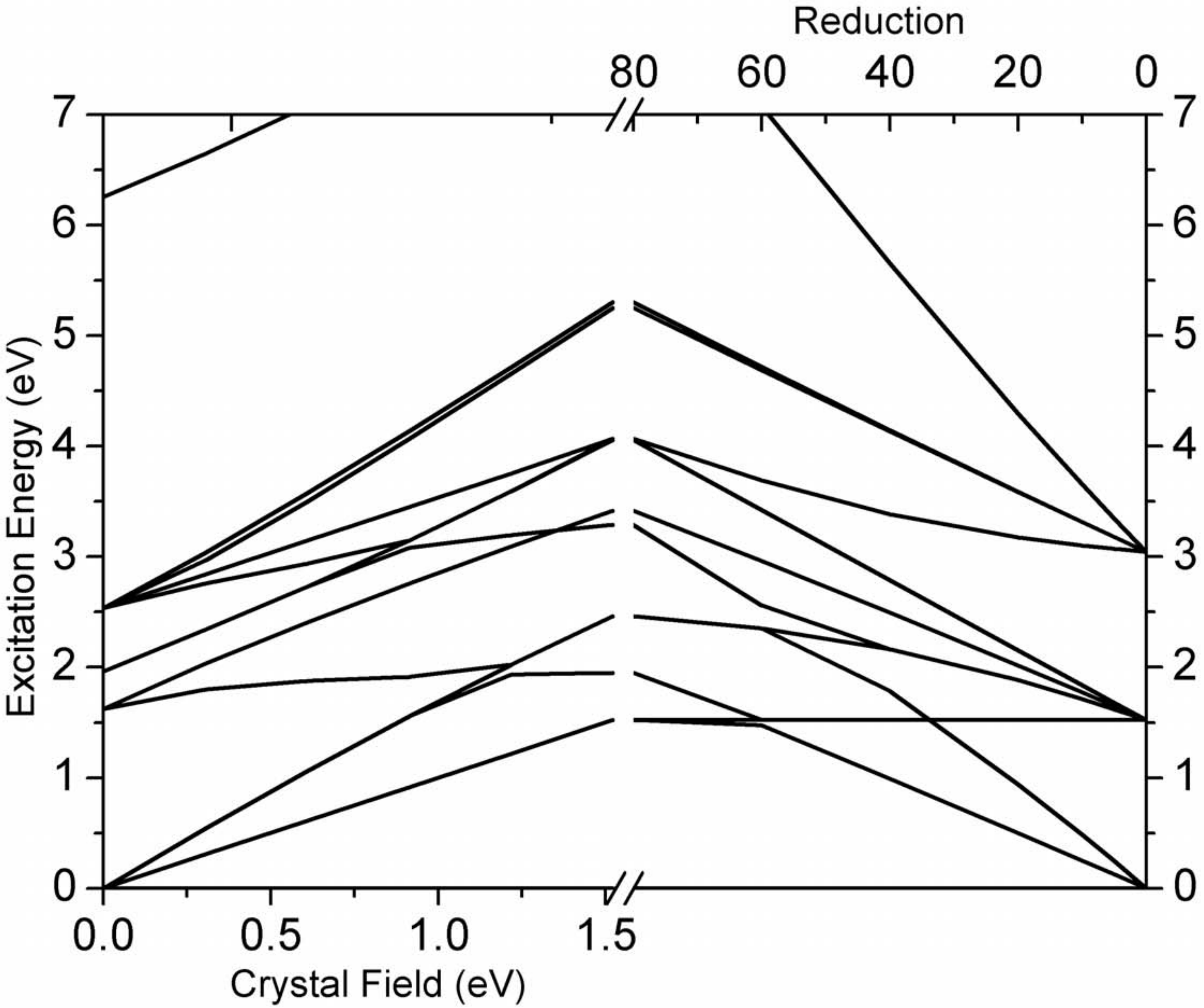

d^4 ions

Two possible arrangements of electrons

High Spin Complex

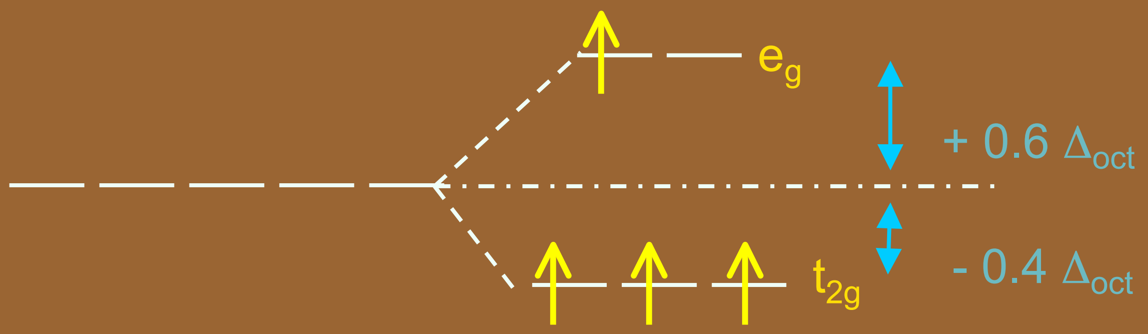

CFSE =

$3 \times -0.4\ \Delta_{oct} + 1 \times 0.6\ \Delta_{oct}$

$= -0.6\ \Delta_{oct}$

Low Spin Complex

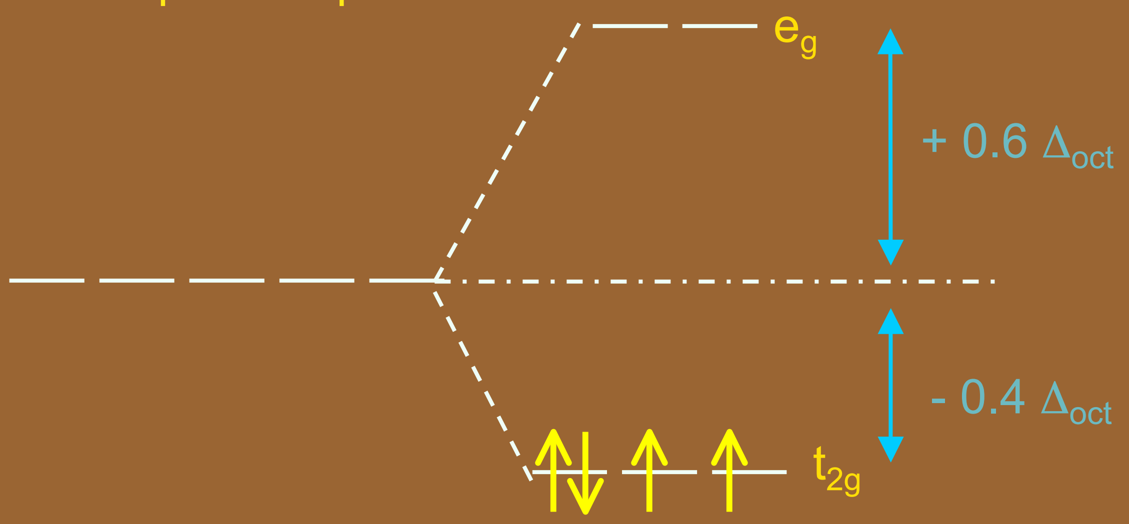

CFSE =

$4 \times -0.4\ \Delta_{oct} + P$

$= -1.6\ \Delta_{oct} + P$

The Pairing Energy P is the energy required to pair two electrons

Crystal Field Effects: High-spin or Low-spin

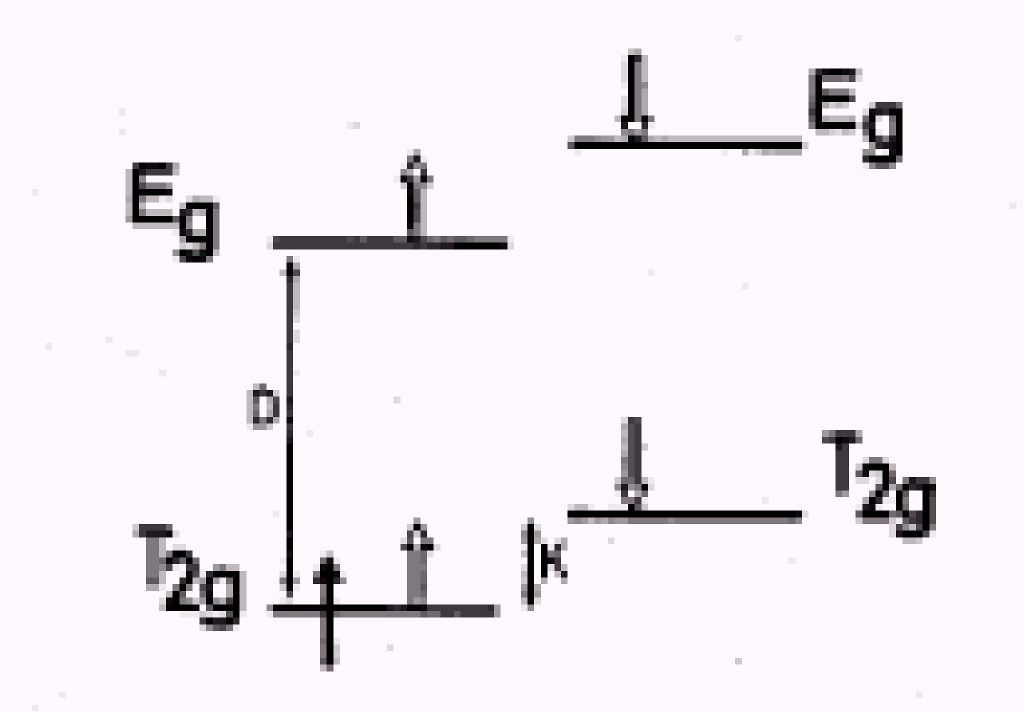

10Dq > 3J
(d^4 and d^5)

10Dq > 2J
(d^6 and d^7)

High-spin or Low-spin

Conf.	Ground State SO_3	HS Ground State in O_h	LS Ground State in O_h
$3d^0$	$^1S_0$	$^1A_1$	-
$3d^1$	$^2D_{3/2}$	$^2T_2$	-
$3d^2$	$^3F_2$	$^3T_1$	-
$3d^3$	$^4F_{3/2}$	$^4A_2$	-
$3d^4$	$^5D_0$	^5E	$^3T_1$
$3d^5$	$^6S_{5/2}$	$^6A_1$	$^2T_2$
$3d^6$	$^5D_2$	$^5T_2$	$^1A_1$
$3d^7$	$^4F_{9/2}$	$^4T_1$	^2E
$3d^8$	$^3F_4$	$^3A_2$	-
$3d^9$	$^2D_{5/2}$	^2E	-

High-spin or Low-spin

Conf.	High-Spin	Low-Spin	10Dq (D)	Exchange (J)	J/D
$3d^4$	$t_{2g+}^3\ e_{g+}^1$	$t_{2g+}^3\ t_{2g-}^1$	1D	$3J_{te}$	3
$3d^5$	$t_{2g+}^3\ e_{g+}^2$	$t_{2g+}^3\ t_{2g-}^2$	2D	$6J_{te}+J_{ee}-J_{tt}$	~3
$3d^6$	$t_{2g+}^3\ e_{g+}^2\ t_{2g-}^1$	$t_{2g+}^3\ t_{2g-}^3$	2D	$6J_{te}+J_{ee}-3J_{tt}$	~2
$3d^7$	$t_{2g+}^3\ e_{g+}^2\ t_{2g-}^2$	$t_{2g+}^3\ t_{2g-}^3\ e_{g+}^1$	1D	$3J_{te}+J_{ee}-2J_{tt}$	2

Crystal Field Effect on XAS

J in SO_3	Deg.	Branchings	Γ in O_h	Deg.
0	1	A_1	A_1	2
1	3	$3\times T_1$	A_2	3
2	4	$4\times E$, $4\times T_2$	T_1	7
3	3	$3\times A_2$, $3\times T_1$, $3\times T_2$	T_2	8
4	1	A_1, E, T_1, T_2	E	5
$\sum$	12			25

Effect of 10Dq on XAS:3d^0

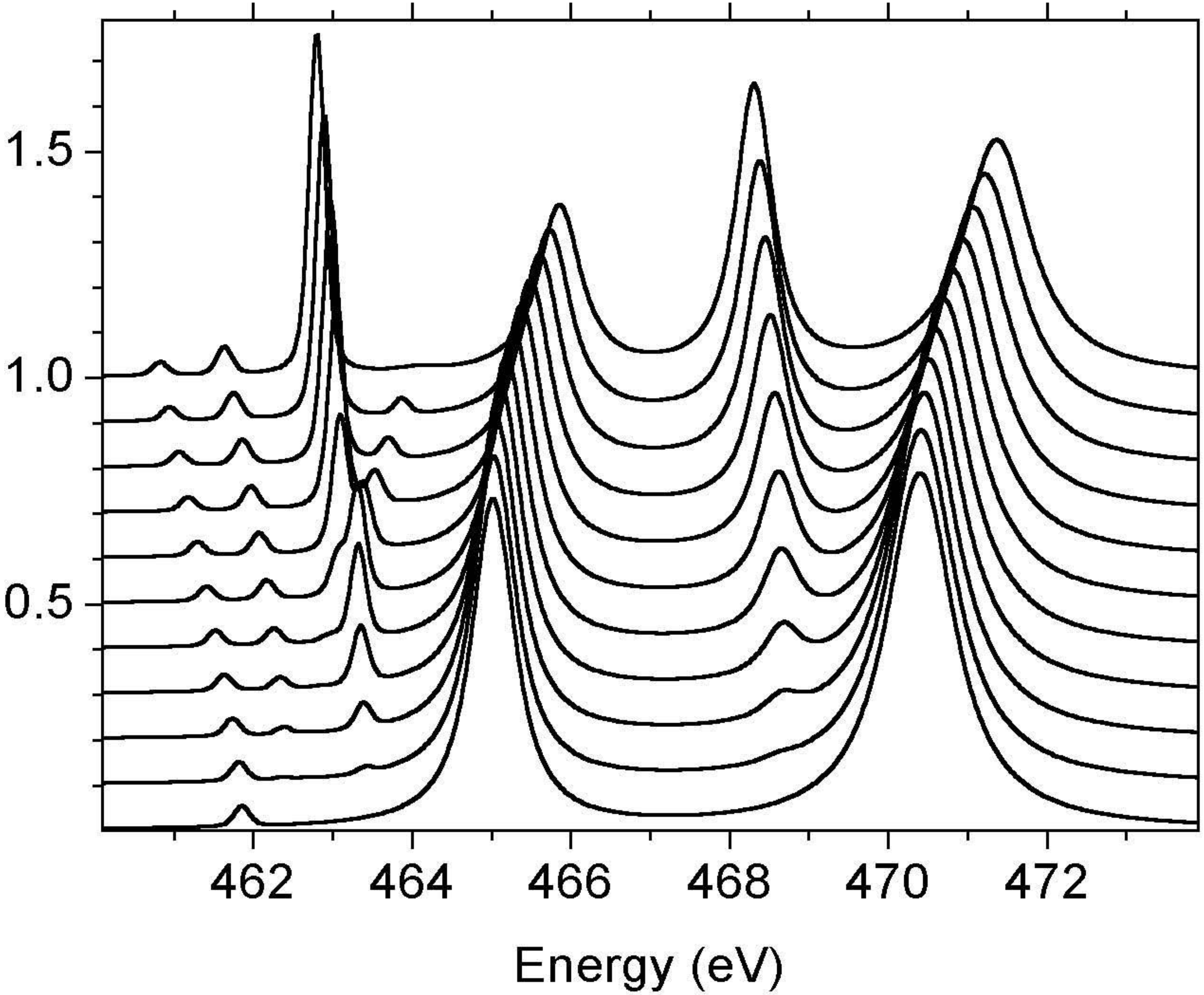

Comparison with Experiment

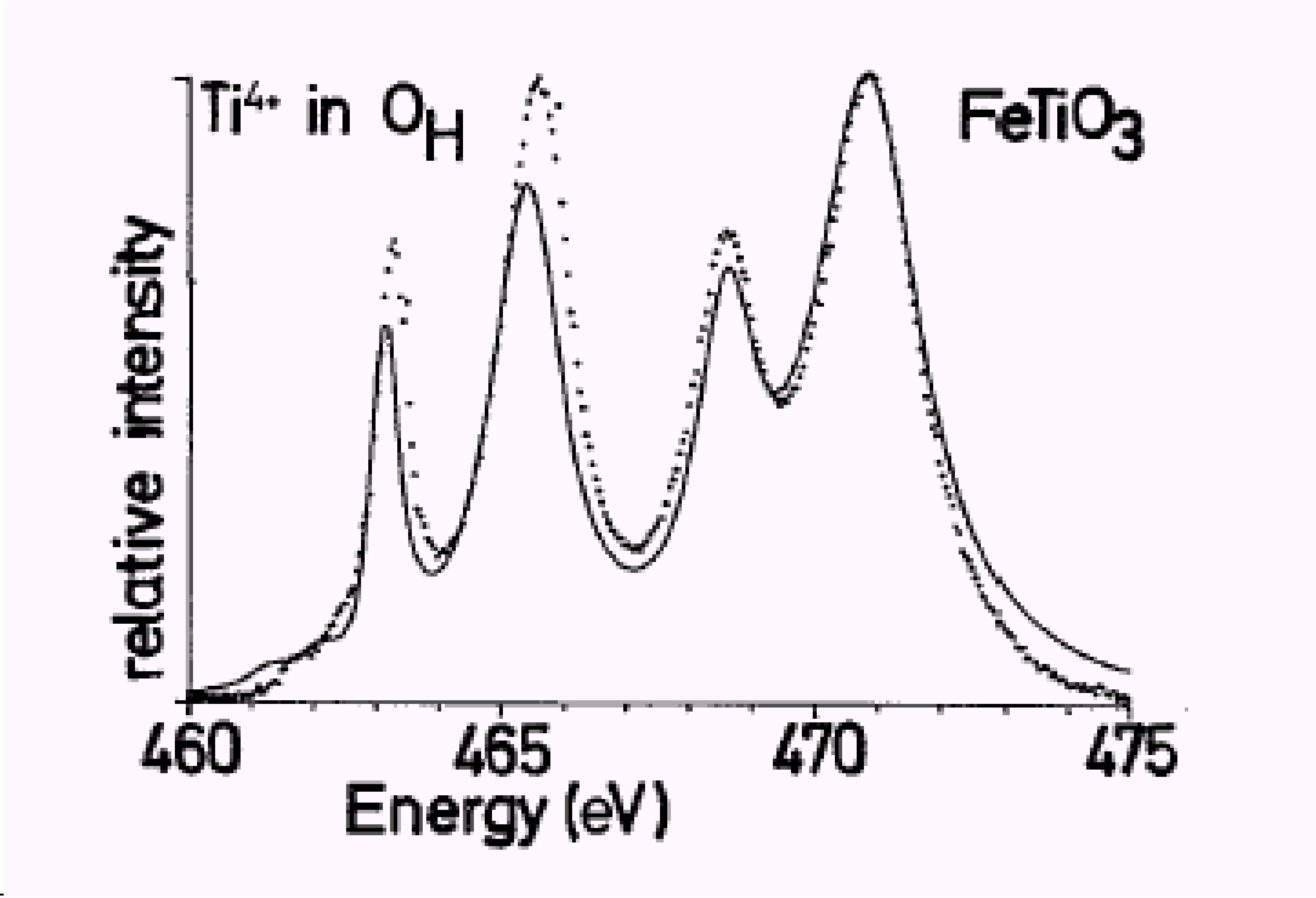

Comparison with Experiment

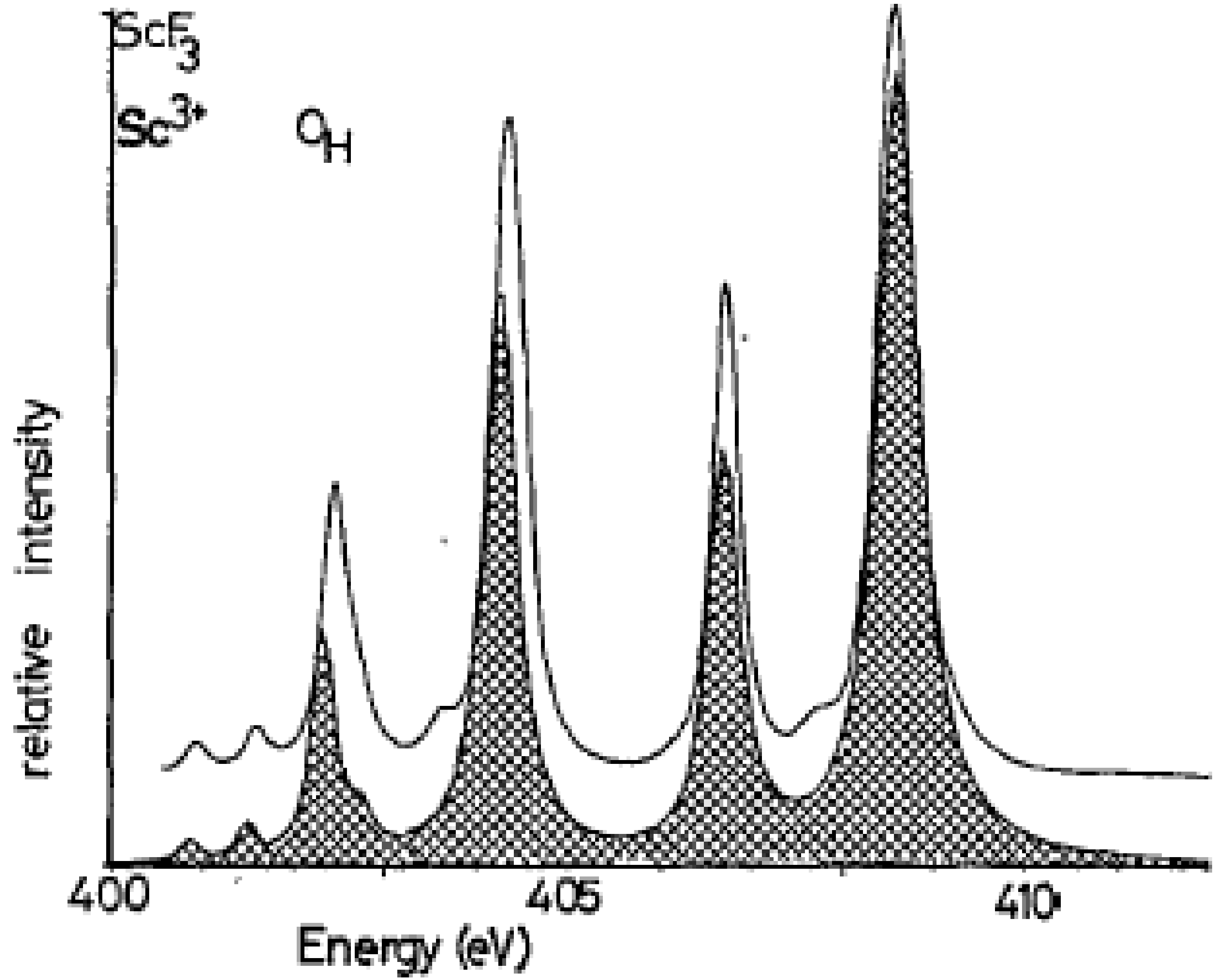

Turning multiplet effects off

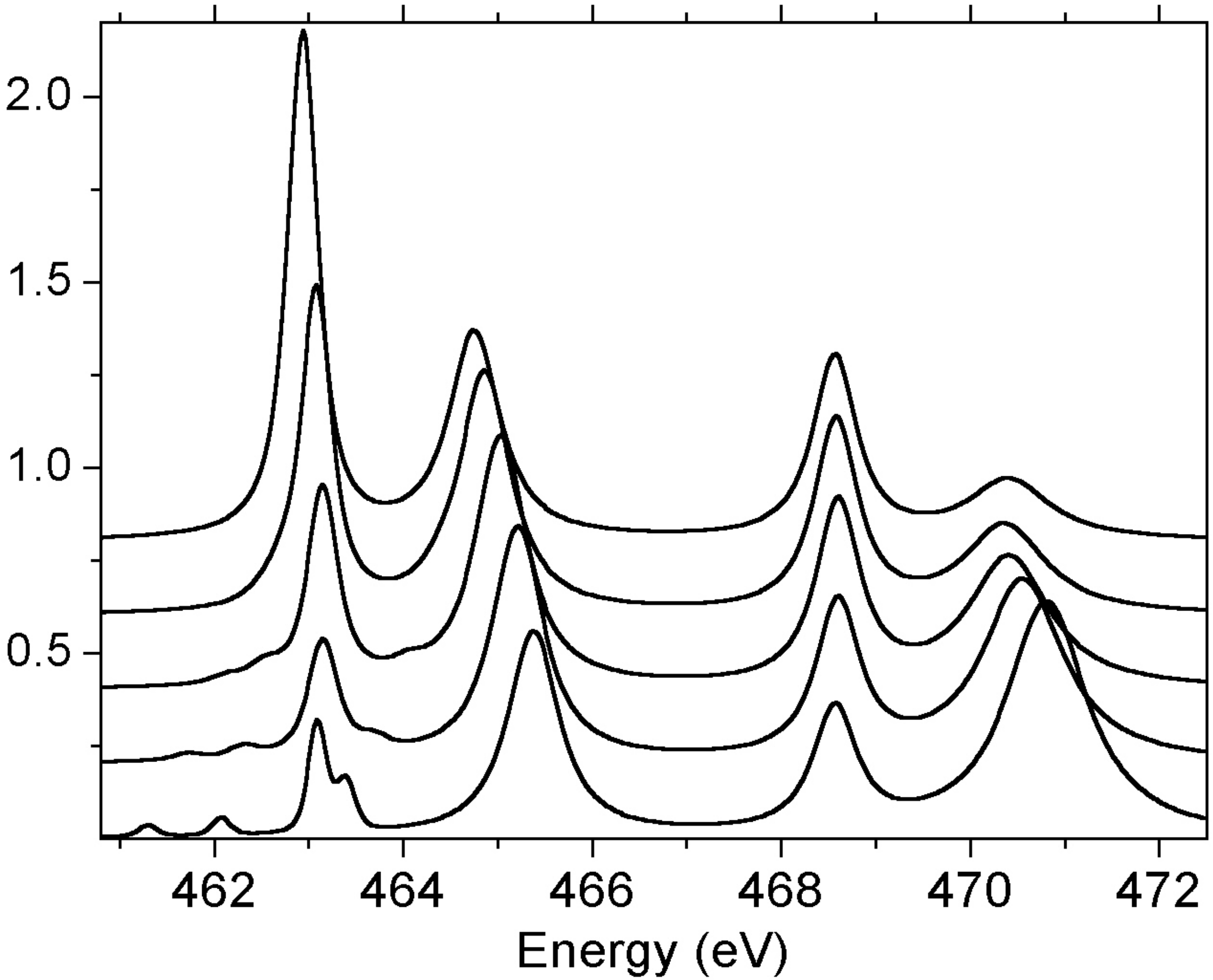

Effect of 10Dq on XAS:3d^N

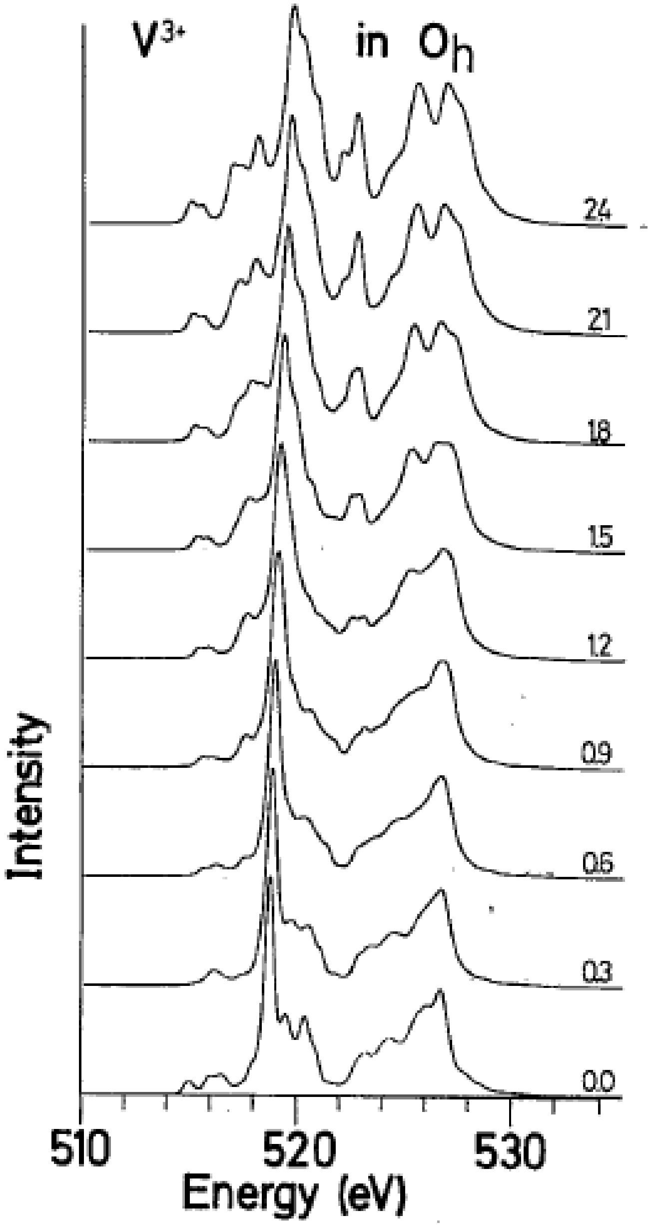

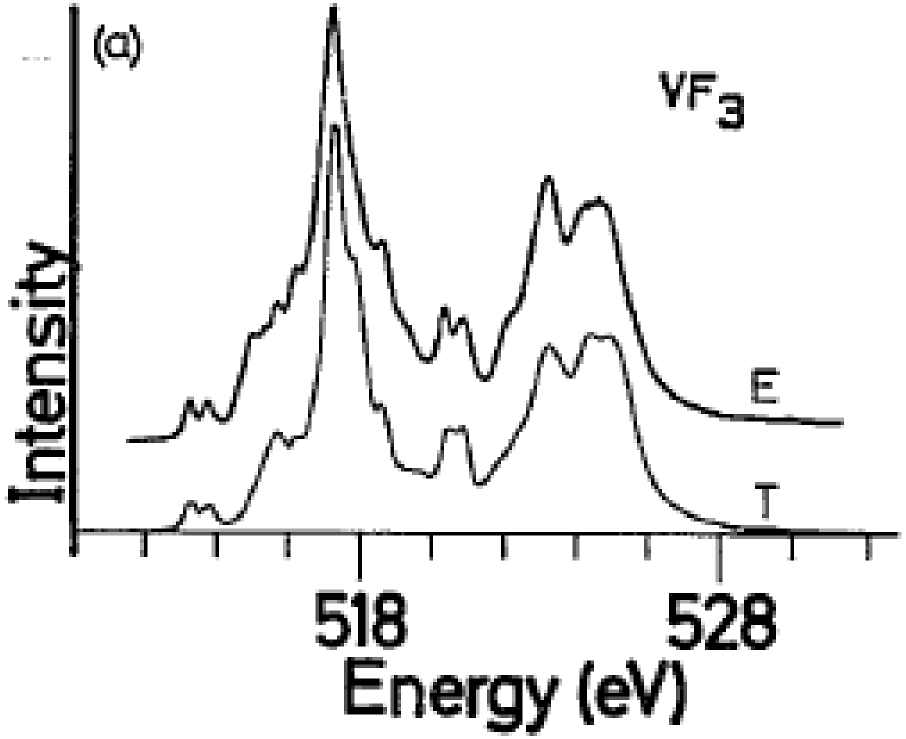

3d spin-orbit coupling

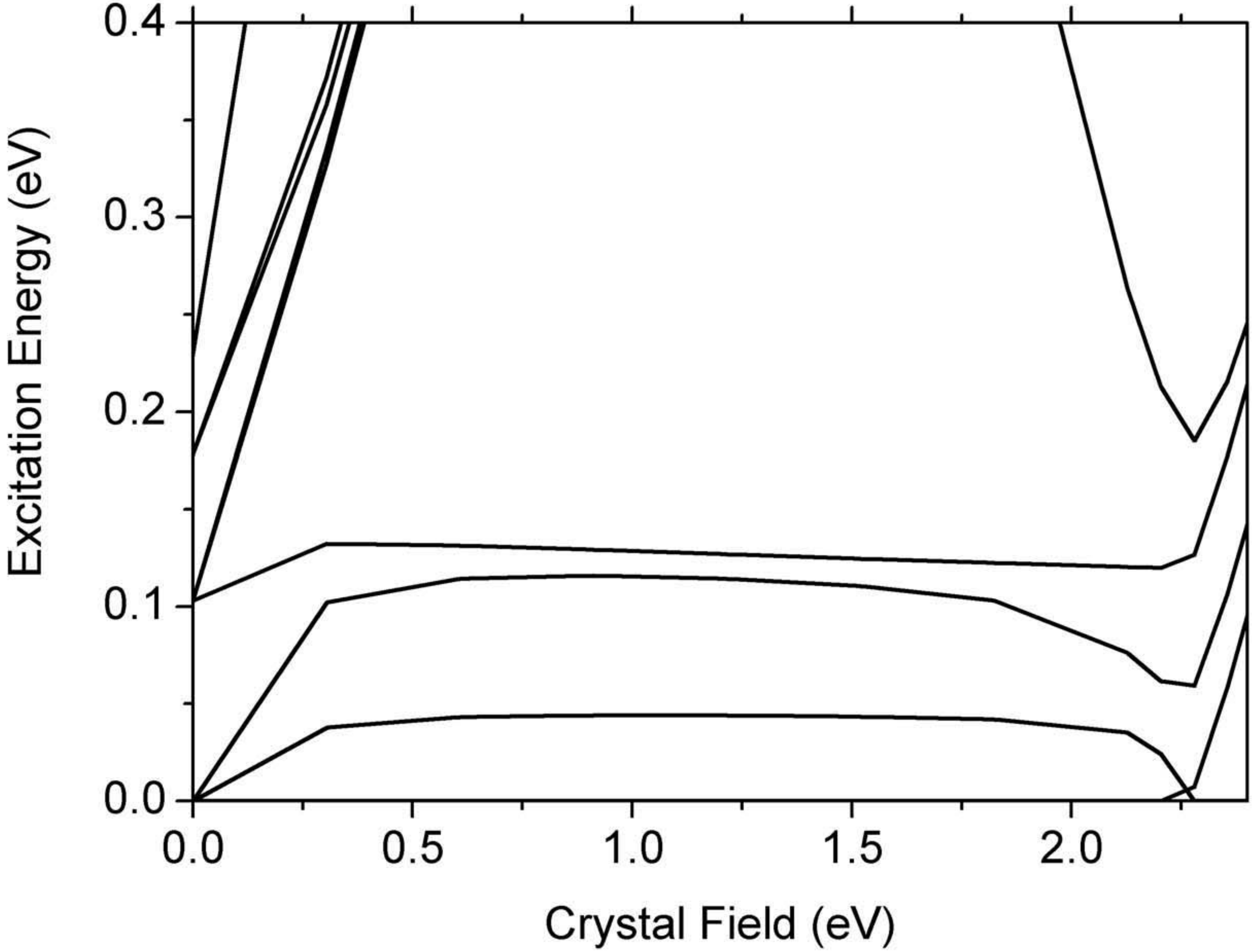

3d spin-orbit coupling

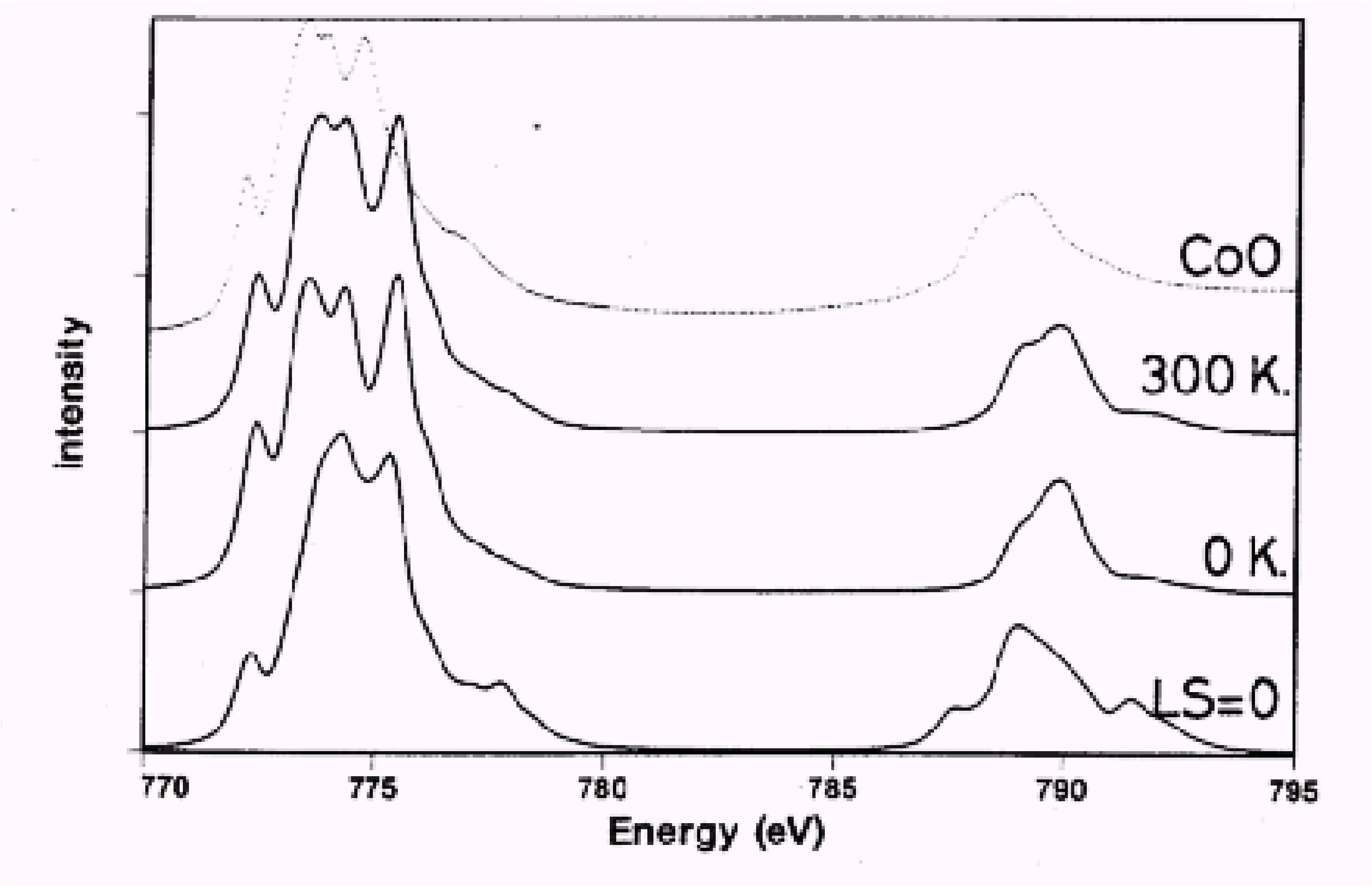

Charge transfer

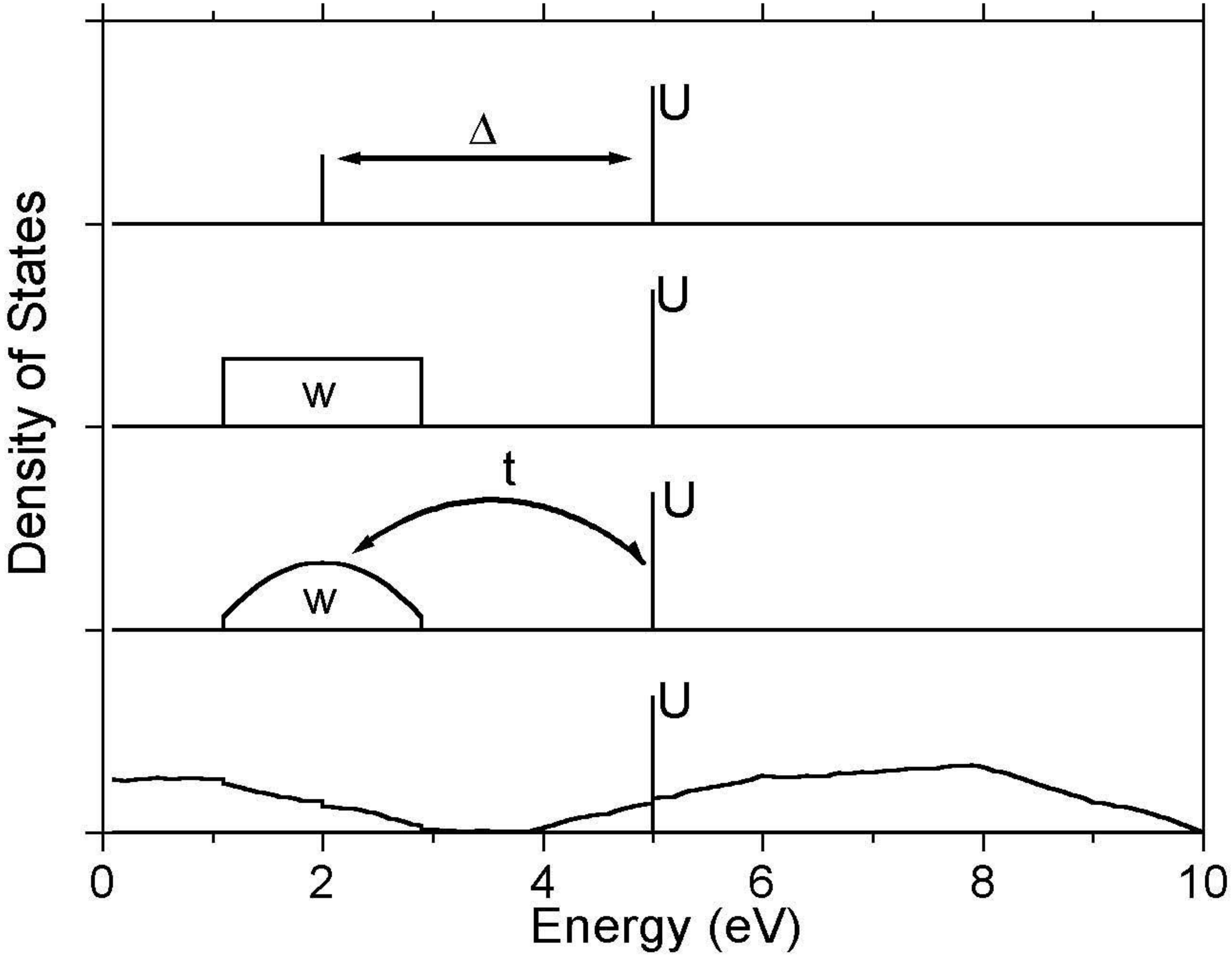

Charge transfer

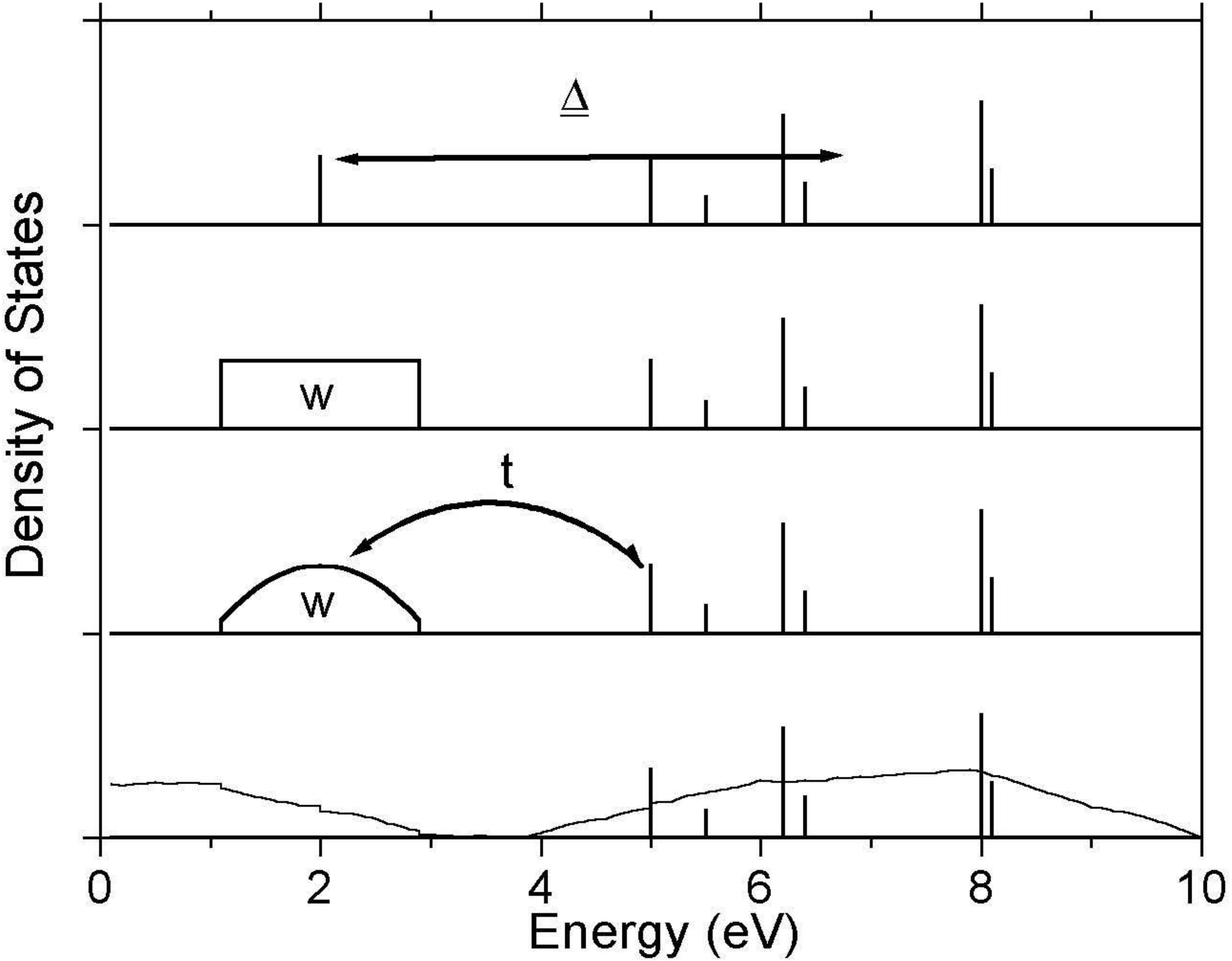

Charge transfer

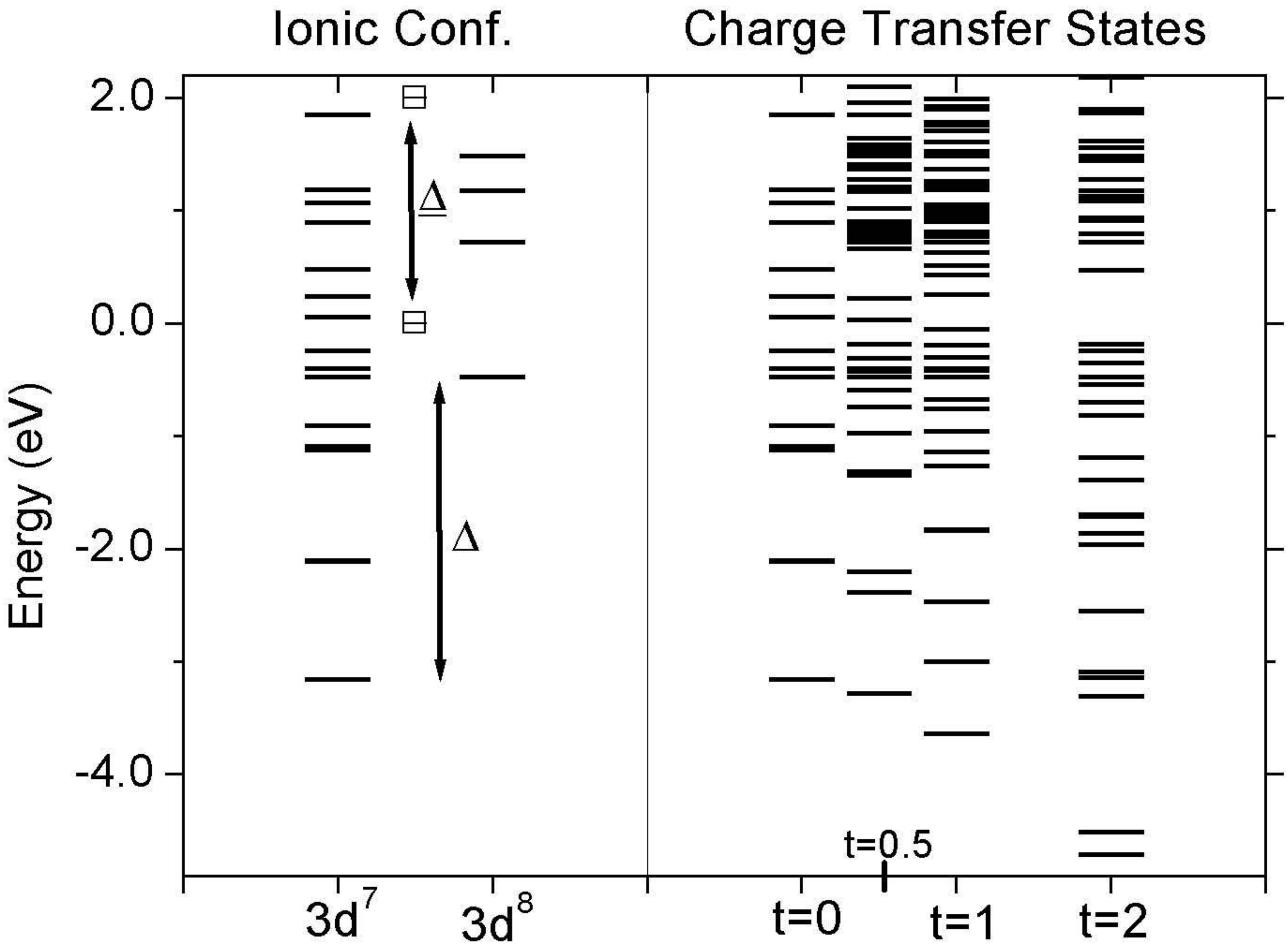

Charge transfer

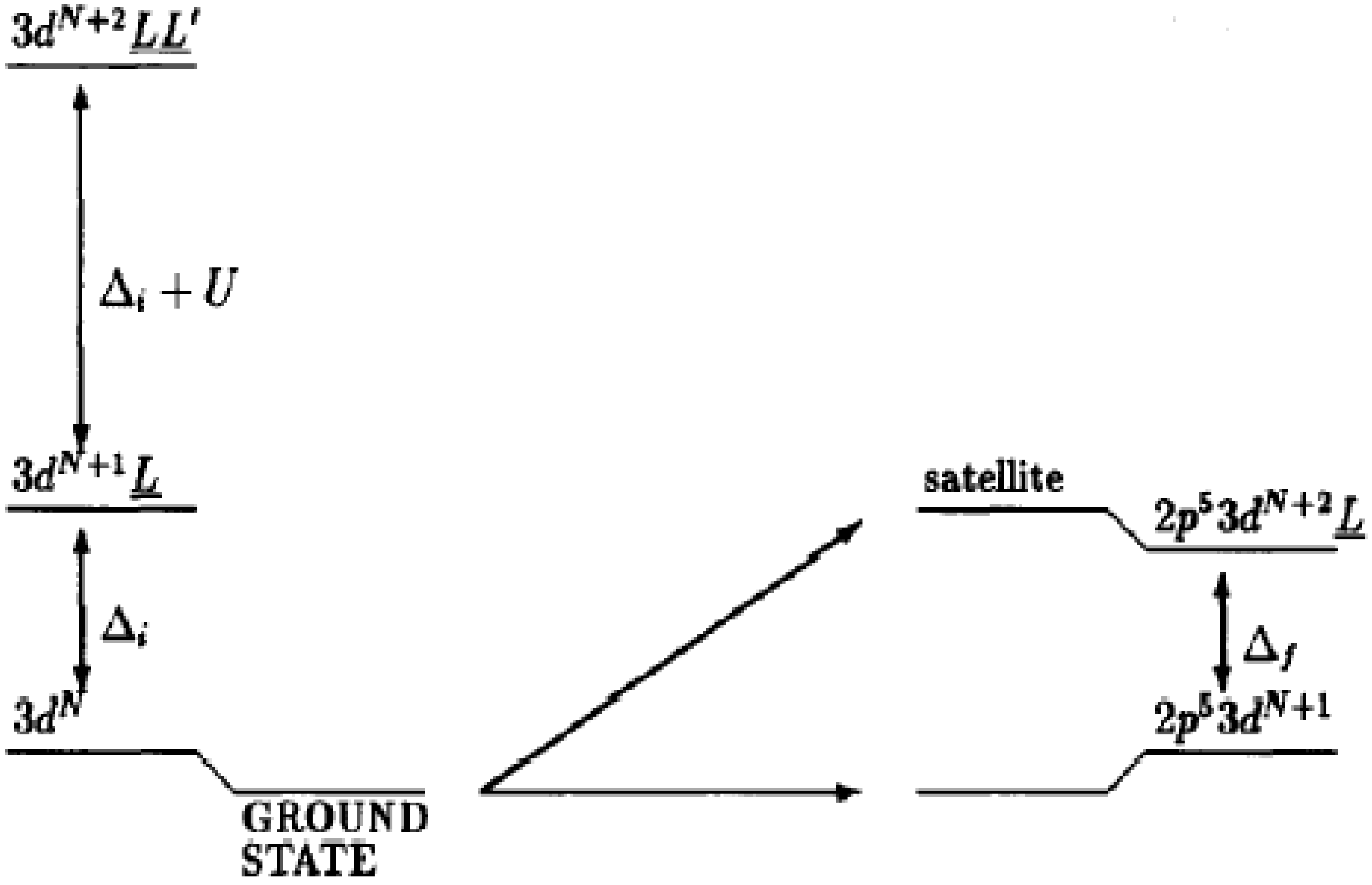

Charge transfer

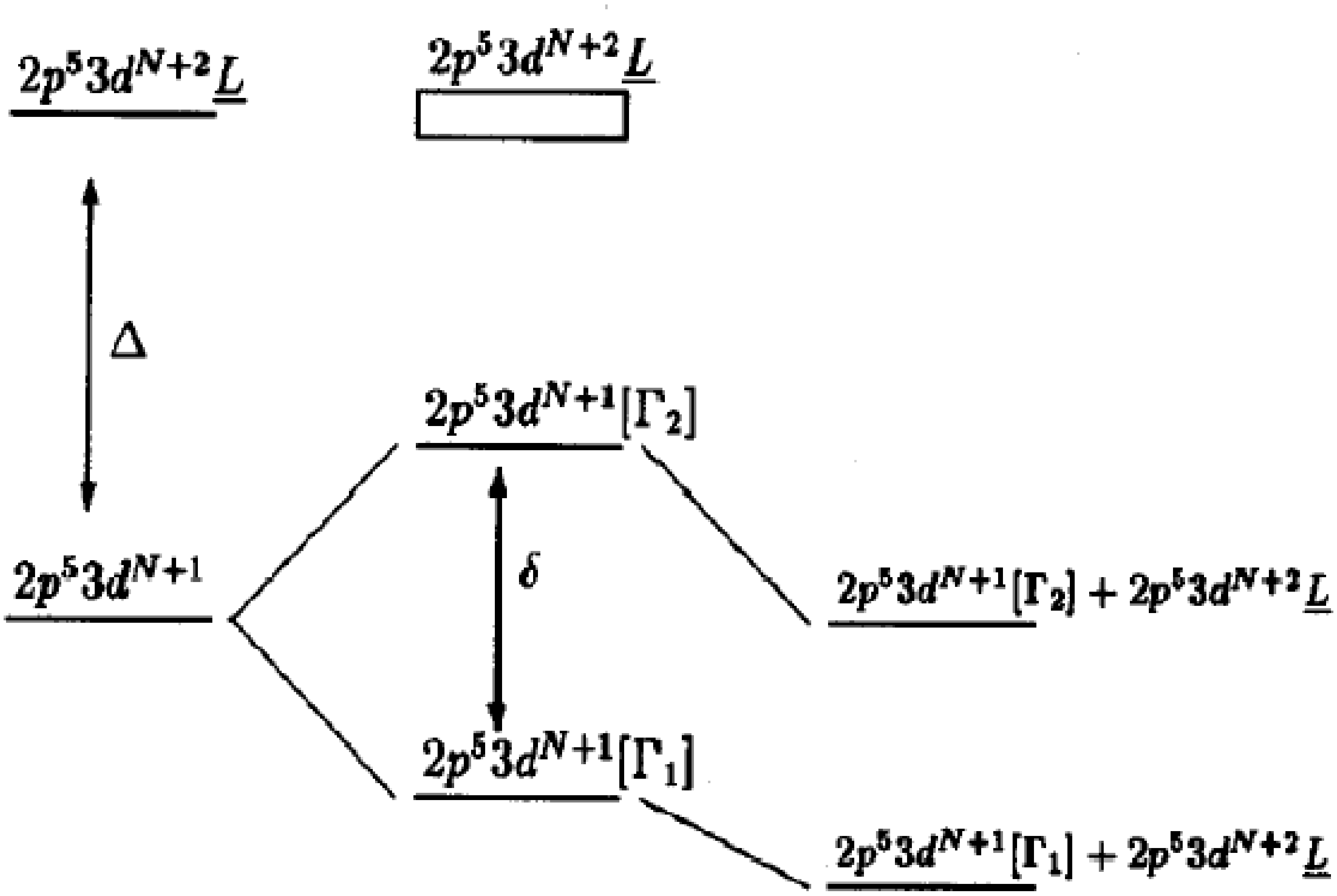

Charge transfer

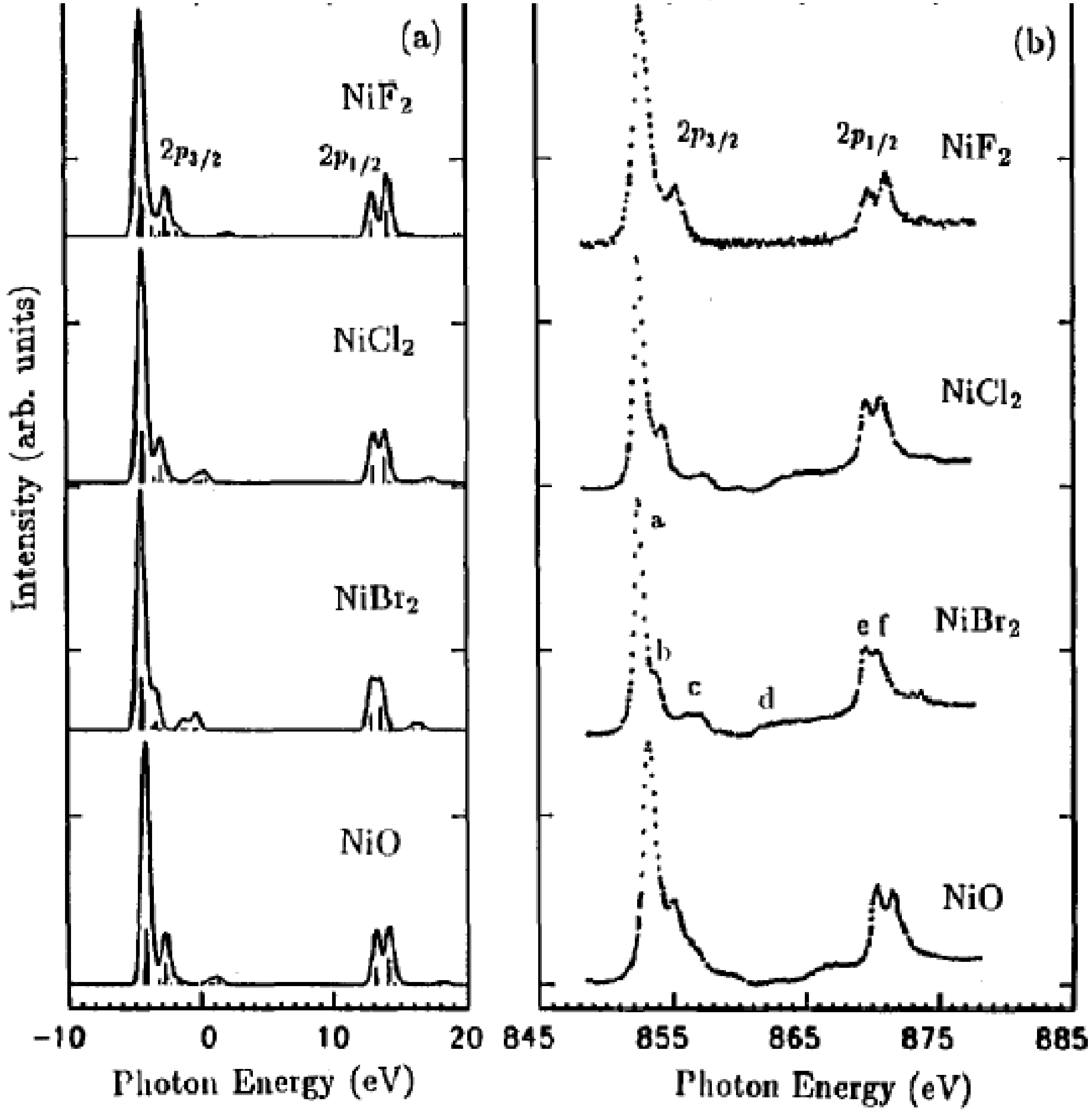

Charge transfer

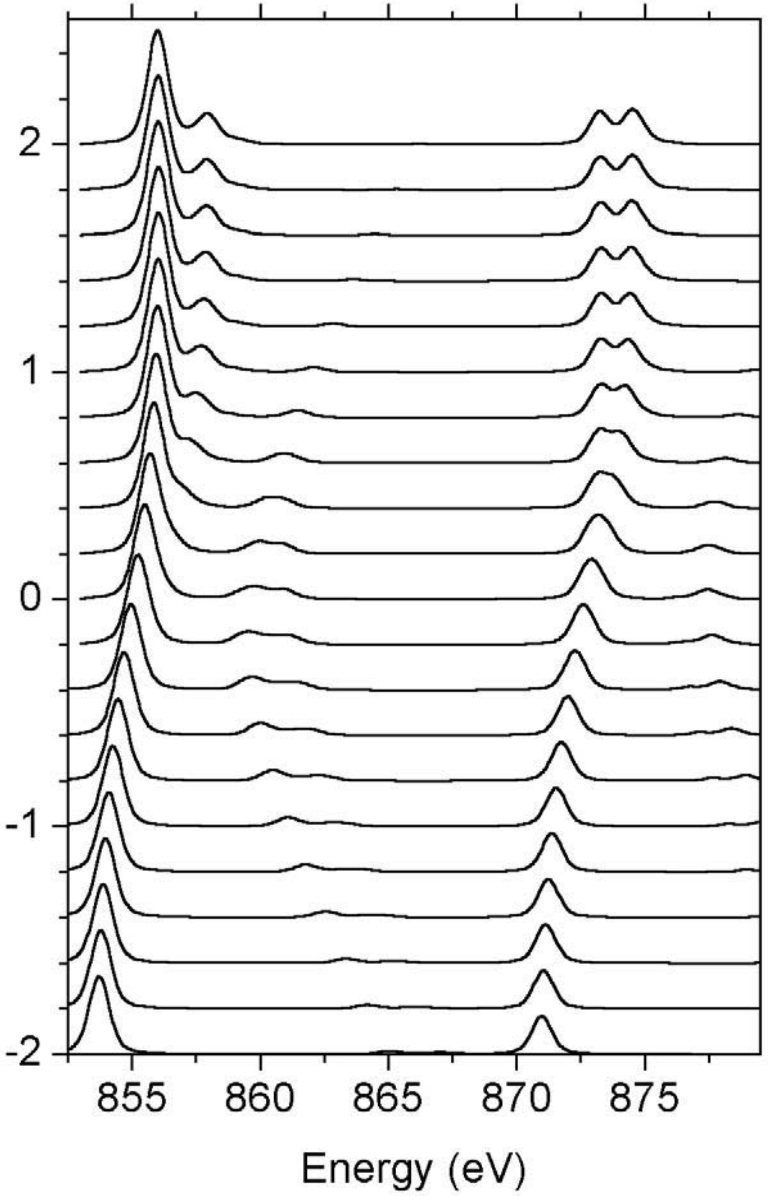

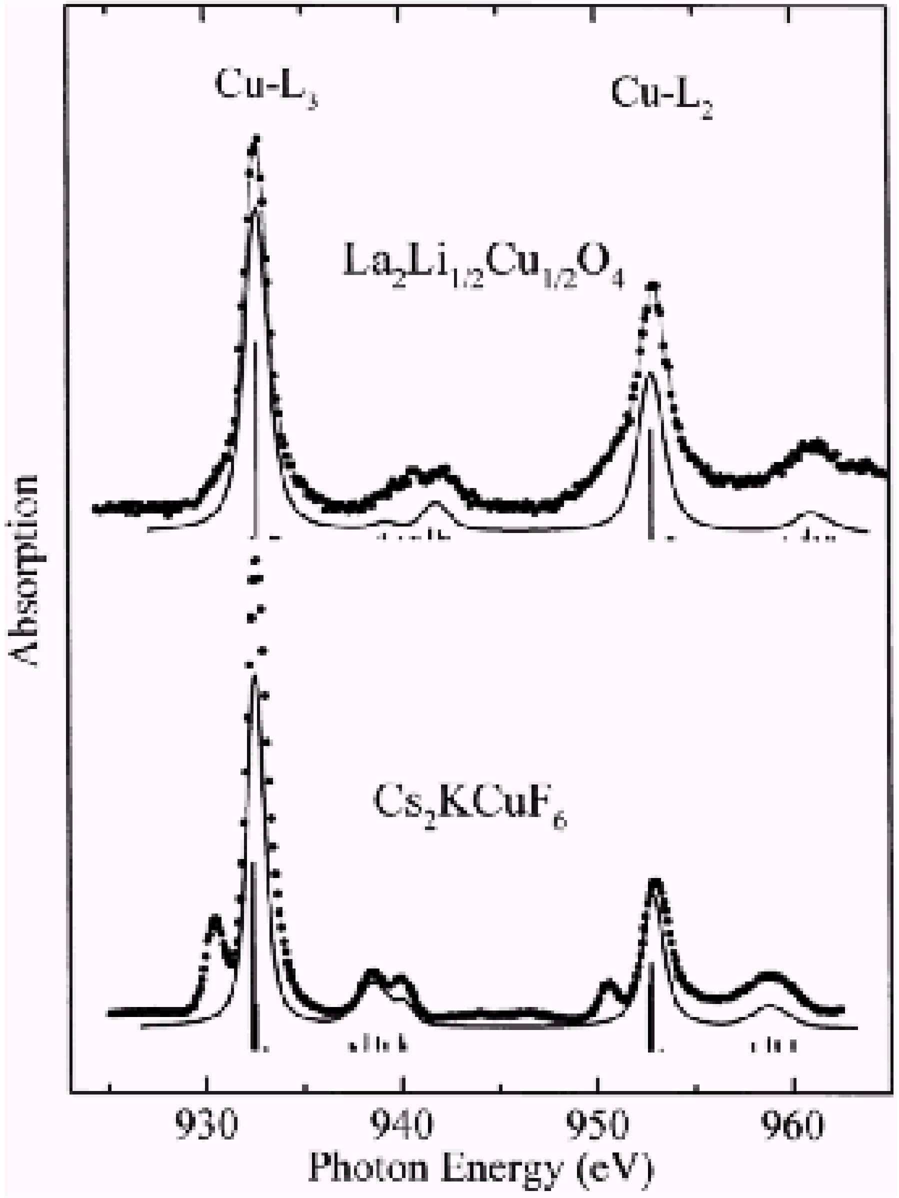

Journal of Electron Spectroscopy and Related Phenomena, 67 (1994) 529–622

Review

X-ray absorption and dichroism of transition metals and their compounds

F.M.F. de Groot[1]

Spectroscopy of Solids and Surfaces, University of Nijmegen, Toernooiveld, 6525 ED Nijmegen, The Netherlands

(First received 28 December 1992; in final form 27 October 1993)

Abstract

This review presents an overview of the X-ray absorption spectra of 3d transition metals and their compounds. The emphasis is on the description of the X-ray absorption process and the various routes to interpret the results within the framework of their electronic structure. This also includes the use of polarization dependent measurements which are particularly used for the study of the magnetic structure. Emphasis will be given to the metal 2p spectra for which the obtainable resolution has been greatly improved over the last 10 years. The interpretation of 2p core spectra, photoemission as well as absorption, is dominated by short range models, such as the Anderson impurity model. It has been shown that 2p X-ray absorption is relatively insensitive to charge transfer effects which simplifies the analysis. The interpretation with a ligand field multiplet model accounts well for the observed spectra and due to its simplicity this model yields accurate and well defined electronic structure parameters. For the 1s X-ray absorption spectra, of the metals as well as of the ligands, it has been shown that they correspond closely to the unoccupied density of states as determined from single particle schemes using either band structure methods or real space multiple scattering. A number of potentially important effects beyond this interpretation will be discussed. Overviews will be given of the published X-ray absorption results for the metal 2p, the metal 1s and the ligand 1s spectra.

Contents

---

[1] Present address: Laboratoire pour l'Utilisation du Rayonnement Electromagnetique, Université Paris-Sud, Bâtiment 209 d, F-91405 Orsay Cedex, France.

SSDI 0368-2048(93)02041-J

1. Introduction

This review is an attempt to give an overview of the field of X-ray absorption, including their magnetic circular dichroism (MCD), of transition metals and their compounds. The main emphasis of this review is the metal 2p spectra. The review concentrates on the analysis using the ligand field multiplet model as well as short range model Hamiltonians. For clarity it is noted that this route of analysis is sometimes envisaged as a particular "school" of spectral analysis which is not universally accepted. Some important other "schools", for example the multiple scattering schemes, are mentioned only very briefly. Most controversies in the analysis are touched upon in the various sections.

The outline of the review is as follows: Section 2 introduces some of the experimental aspects of X-ray absorption experiments. Section 3 gives a short overview of the models used for the description of the electronic structure of transition metals and their compounds. Section 4 describes the interaction of X-rays with matter. It describes core excitations and focuses on the short range model descriptions of core level spectroscopies. Section 5 deals with metal 2p X-ray absorption. The ligand field multiplet model and the charge transfer multiple model are discussed in detail. Section 6 discusses the different routes to interpret MCD spectra. The different models interpreting X-ray absorption, now extended for their sensitivity to circularly polarized X-rays, are compared. Section 7 gives an overview of the existing data of metal 2p spectra, including the linear and circular dichroism studies. Section 8 describes the analysis of metal and ligand 1s X-ray absorption spectra in terms of single particle calculations, including multiple scattering approaches. It also includes a (selected) overview of published data of the 1s edges of the ligands as well as of the metals.

2. Experimental

The normal set-up to measure an X-ray absorption spectrum is in transmission mode as sketched

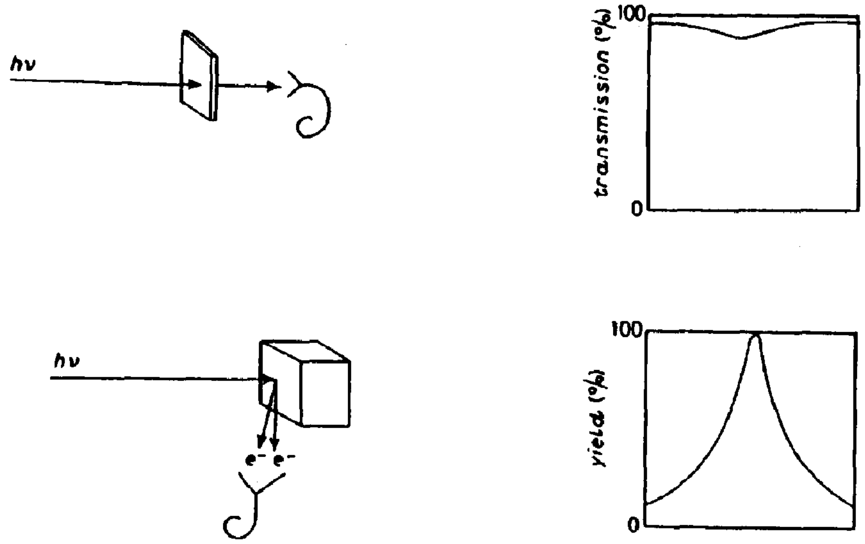

Fig. 1.Transmission mode (top) and yield mode (bottom) X-ray absorption experiments.

in Fig. 1 at the top. The intensity of the X-ray is measured before and after the substrate and the percentage of transmitted X-rays is determined. The X-ray absorption spectrum is generated by repeating the experiment for a series of X-ray energies.

Transmission mode experiments are standard for hard X-rays. For soft X-rays, in order to obtain a detectable signal the substrate has to be thin, typically 0.1 μm. This poses large technological problems for most materials. Soft X-rays also have a large absorption cross section with air; hence the experiments have to be performed in vacuum. An alternative to the transmission mode experiments has been provided by measuring the decay products of the core hole which is created in the absorption process. The decay of the core hole gives rise to an avalanche of electrons, photons and ions escaping from the surface of the substrate. The bottom of Fig. 1 shows a yield mode experiment of the X-ray absorption cross section, with which it is possible to measure samples of arbitrary thickness.

X-ray absorption experiments have been performed since the beginning of this century, but they have been severely restricted because the only available X-ray sources had a restricted set of intense discrete energies with a Bremsstrahlung continuum of relatively low intensity. The advent of synchrotron radiation sources, which provide an intense and continuum spectrum of polarized electromagnetic radiation, created the possibility of immensely improving the X-ray absorption spectra. The intrinsic polarization features of the X-ray beam can be exploited to do dichroism experiments. The following experimental aspects of the X-ray absorption and dichroism experiments will be discussed: synchrotron radiation, X-ray monochromators and detection techniques.

2.1. Synchrotron radiation

Synchrotron radiation is produced when a charged particle, with an energy $E \gg mc^2$, is deflected in a magnetic field. The development of synchrotron radiation is based on the work of Ivanenko and Pomaranchuk [Iva44] and Schwinger [Sci46] in the forties [Koc77, Fug91]. The original synchrotrons were used for high energy physics and the radiation was considered merely as a side product. The experiments which made use of the radiation were performed in a parasitic fashion. However the interesting results which emerged led to the development of

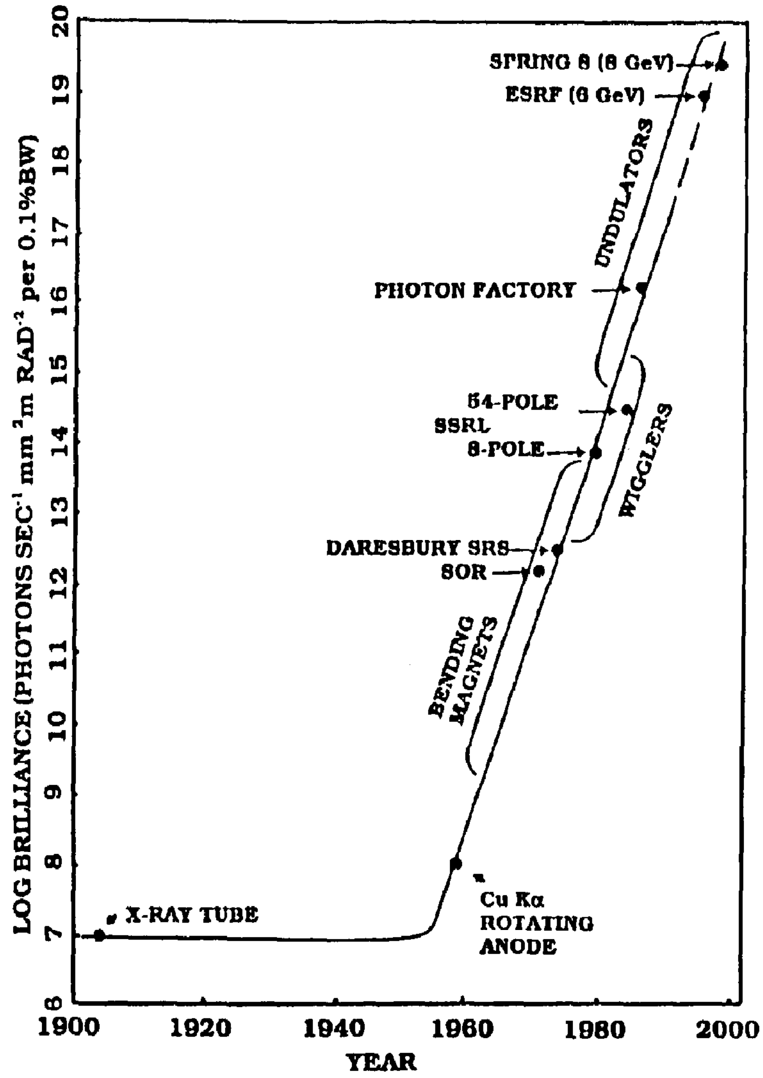

Fig. 2. The historical development of the brilliance of available X-ray sources (from [Fug91]).

dedicated synchrotron radiation sources in the early seventies and the SRS synchrotron in Daresbury can be considered as the first dedicated storage ring for synchrotron radiation. The original emphasis was on the optimization of the life-time, the current and the energy of the beam. In the early eighties the emphasis switched to an optimization of the brilliance and also to the development of insertion devices to increase the intensity of high energy photons [Fug91]. Figure 2 sketches the development of the available X-ray flux during the last century (taken from [Fug91]).

As a typical example of a dedicated VUV-ring the Berliner Elektronen-Speicherring Gesellschaft für SYnchrotronstrahlung (BESSY) [Ber87] will be discussed. BESSY is an electron storage ring with a circumference of about 62 m. From each of the twelve bending magnets synchrotron radiation is directed to a number of experimental stations. The energy of the electrons stored in the ring is 754 MeV. To keep the electrons in orbit they are accelerated at one point in the ring to compensate the energy-loss due to emission of radiation in the bending magnets. The position of the beam within

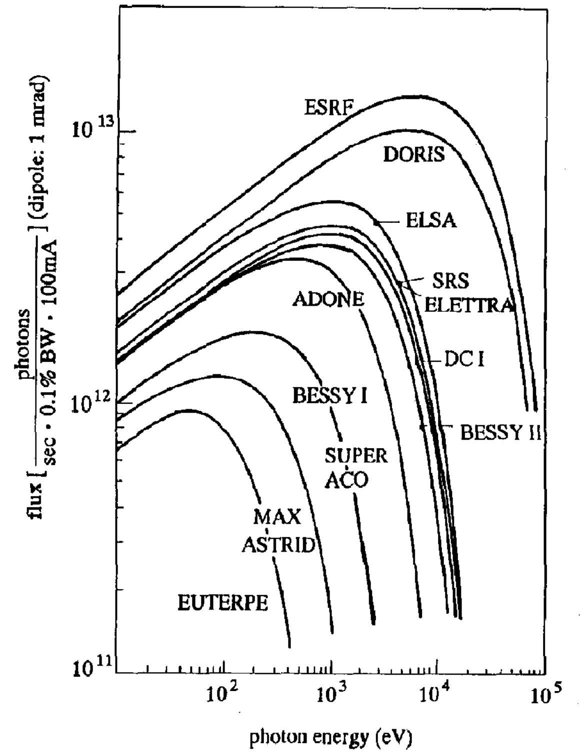

Fig. 3. Intensity distribution of the radiation in the European synchrotron radiation facilities. ESRF, ELETTRA and BESSY II are not as yet operational. DORIS and ELSA are used parasitically (from [Fug91]).

the synchrotron ring is constantly corrected with a series of quadrupolar and sextupolar magnets, but nevertheless the stored current slowly decreases because of scattering with remnant gas, imperfect orbit correction, etc. The typical life-time of an 800 MeV ring such as BESSY, superACO and NSLS-VUV is 2 to 5 h [Fug91].

The deflection of the electrons in the bending magnets creates electromagnetic radiation with an energy distribution as sketched in Fig. 3 [Iva44, Sci46, Ten85]. The critical energy e_c is determined by the energy of the electrons and by the magnetic field in the deflection magnets. For BESSY the critical energy is about 600 eV, which roughly equals the energy with the highest flux as can be checked in Fig. 3. Figure 4 shows the radial distribution of the radiation for three typical X-ray energies relative to the critical energy e_c. The radiation in the plane of the orbiting electrons is linearly polarized. Out-of-plane radiation is partly circularly polarized. By selecting part of this out-of-plane radiation, the circularly polarized X-rays can be used for X-ray magnetic circular dichroism (X-MCD) experiments. The intensity of the out-of-plane radiation decreases quickly, especially for soft X-rays. However the intensity profile can be modified with the use of insertion devices, such as an asymmetric wiggler [Sai92].

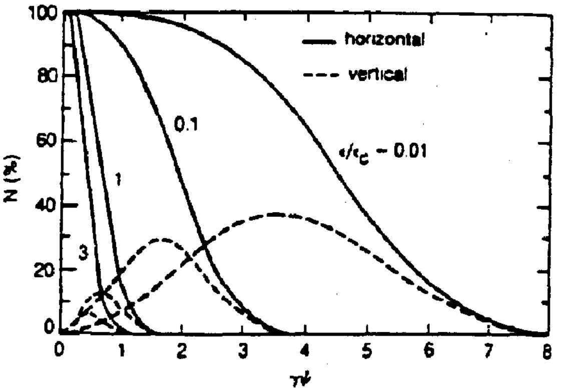

Fig. 4. Radial distribution of intensity. $\gamma\psi$ is the angle (in mrad) with the plane of the electron-orbit.

2.2. X-ray monochromators

X-rays can be monochromatized with crystal monochromators or with gratings. The 1s edges of the 3d transition metals have an energy of 5 to 9 keV and in general Si crystals are used. The 2p edges have an energy in the energy range in between 200 and 1000 eV, that is in between the traditional regions of grating monochromators ($E < 200$ eV) and crystal monochromators ($E > 800$ eV).

2.2.1. Crystal monochromators

For energies above 800 eV the usual way to monochromatize the X-ray is by means of a double crystal monochromator. The X-ray beam impinges on the first crystal and the X-ray energy which satisfies Bragg's equation ($n\lambda = 2d \sin\theta$) is reflected. In principle one crystal is enough to monochromatize the beam; the second crystal improves the resolution slightly but it is used primarily because it allows for a constant direction of the outgoing monochromatized X-ray. The energy range of the double crystal monochromator is defined by the lattice spacing of the crystals used, given that the angle of incidence (θ) is limited to between 10° and 80°. For energies above 2 keV artificial silicon crystals ($2d = 6.271$ Å) are used. The difficult energy range in between 800 and 1500 eV is covered by crystals of natural beryl $Be_3Al_2Si_6O_{18}$ ($2d = 15.95$ Å). For energies lower than 800 eV one has to use crystals with a lattice spacing larger than beryl. The organic crystals with this property are, however, not resistant to the full power of the synchrotron beam. A solution to this problem has been found by using an artificial multilayer as a pre-monochromator [Laa87]; however for energies below 1 keV the grating monochromators are dominant (see Section 2.2.2). The use of beryl has drawbacks because of the limited allowed heatload and particularly the content of aluminium and silicon. Recently YB_{66}, a cubic crystal with $2d = 23.44$ Å, has been tested [Scf92, Won90]. This material has a slightly improved resolution, but its greatest merit is the absence of absorbing elements in between 1 and 2 keV, which makes it a suitable monochromator for silicon and aluminium 2p edges. A complication in the use of crystal monochromators for circular dichroism experiments is the decrease of the degree of polarization in non-grazing geometries.

2.2.2. Grating monochromators

The monochromatizing element is an artificial grating with typically 1000 lines per mm ($2d \approx 5 \times 10^{-7}$ m). The soft X-ray range can be covered by using the grating monochromators in grazing incidence ($\theta \rightarrow 0$). The grazing incidence grating monochromators are divided according to the shape of the grating, which can be toroidal, planar or circular. The toroidal grating monochromators (TGMs) dominate in the energy range up to 200 eV. At present the energy region in between 200 eV and 800 eV is best served with either a planar grating monochromator (PGM) or with a spherical (or cylindrical) grating monochromator (SGM).

A typical SGM is the grasshopper as used at Stanford Synchrotron Radiation Laboratory (SSRL) [Bro78]. This monochromator and also the 10-metre monochromator at Photon Factory [Mae86] use the Rowland circle geometry. The Rowland circle constraints were relaxed in the later designs of Padmore [Pad87, Pad89] and Chen [Che87]. The Dragon monochromator [Che87, Che89, Che90a] at the National Synchrotron Light Source (NSLS) at Brookhaven reached an unprecedented high resolution of $1:10^4$ for the soft X-ray range. The strength of the Dragon monochromator is its relatively simple arrangement of optical components. The entrance slit improves the resolution by making the monochromator less dependent on the source size. The exit slit moves during an energy-scan and the mirrors are situated before the grating. This arrangement facilitates the change of the monochromator position to use out-of-plane (circularly polarized) radiation. A design in which the beam is split in the mirrorbox and radiation from above and below the synchrotron plane is guided to the sample simultaneously (the so-called double headed Dragon) has been proved to be very effective for MCD experiments [Che90b].

The plane grating SX700 monochromators [Pet82, Pet86, Tog86] were designed to monochromatize the synchrotron radiation onto a fixed exit slit, without the necessity of an entrance slit. This can be achieved by a combined movement of the plane grating and the mirrors. The first plane pre-mirror is used to satisfy the focusing condition of the plane grating [Pet82]. The second ellipsoidal mirror refocuses the radiation onto the curved exit slit. The resolution is mainly source limited because there is no entrance slit. The resolution of the SX700/1 is about $1:10^3$ and the SX700/2 monochromator has a resolution of about $1:10^4$ [Dom91]. The SX700/3 monochromator is adapted to the use of out-of-plane circularly polarized light [Wim92].

2.2.3. What do you need for X-ray absorption?

The present resolution of 1 : 10^4, reached by both SGMs and PGMs, is satisfactory, and for solids life-time broadening is of the same order of magnitude (depending on the particular edge and material). For the MCD measurements both the Dragon-like and SX700 monochromators reach similar degrees of polarization. Throughput is in general not a large constraint for X-ray absorption; it is for photoemission.

A large number of SGMs and PGMs usable for (soft) X-ray absorption are available at close to all the synchrotron sources in the world. The new generation of synchrotrons, ESRF, APS, SPRING8 and particularly for the soft X-ray range ALS, ELETTRA, BESSY2 and MAX2, will provide improved brilliance. This can and will further improve the various parameters of the monochromators, particularly the flux, but constraints such as heatload will necessitate further improvements in the design and optical elements.

2.3. Detection techniques

As sketched in Fig. 1, the absorption cross section can be measured by means of electrons which escape from the surface as a result of the decay of the core hole. Instead of electrons, photons or ions can be detected, and the electron, fluorescence and ion-yield methods present an alternative to the transmission mode experiments. In this section the different methods are discussed, specifically with regard to the conditions under which a specific yield measurement represents the X-ray absorption cross section and the related question of the probing depth of the specific yield method.

2.3.1. Auger electron yield

One can measure the intensity of a specific Auger decay channel of the core hole. The energy of the Auger electron is not dependent on the energy of the incoming X-ray and from the universal curve [Sea79] it is found that the mean free path of a 500 eV Auger electron is of the order of 20 Å. Hence the number of Auger electrons emitted is equal to the number of core holes which are created in the first 20 Å from the surface. Because the mean free path of the incoming X-ray is of the order of 1000 Å, the number of core holes created in the first 20 Å is equal to the absorption cross section. Effectively the Auger electron yield method is a measurement of only 20 Å of material; hence the Auger electron yield is rather surface sensitive.

2.3.2. Fluorescence yield

Instead of the Auger decay, the fluorescent decay of the core hole can be used as the basis for the absorption measurement. The amount of fluorescent decay is increased with energy [Cit76], and a comparison of the amount of Auger decay with fluorescent decay shows that for the atomic number $Z \leqslant 20$ Auger decay dominates for all core levels and for $Z \leqslant 50$ Auger decay dominates all edges apart from the K edges for which fluorescent decay starts to dominate [Fug90]. Thus for the 3d metals, the K edges show strong fluorescence and all other edges mainly Auger decay. The photon created in the fluorescent decay has a mean free path of the same order of magnitude as the incoming X-ray, which excludes any surface effect. However, it means that there will be saturation effects if the sample is not dilute. That is, in the limit that there is only one absorption process, all X-ray photons which enter the material contribute to the fluorescence yield signal; hence its intensity will not be equal to the absorption cross section. The relation between the intensity of the fluorescence yield (I_f) and the absorption cross section (σ) is [Jak77]

$$I_f \approx \frac{\sigma_x(E)}{\sigma_x(E) + \sigma_b(E) + \sigma_x(E_f) + \sigma_b(E_f)} \tag{1}$$

For dilute materials, that is if the background absorption (σ_b) dominates the absorption of the specific edge (σ_x), the measured intensity is approximately equivalent to the absorption coefficient ($I_f \approx \sigma_x$). For less dilute materials the spectral shape is modified and the highest peaks will appear compressed with respect to the lower peaks, known as saturation effects. For a given material the background absorption is known and in principle can be corrected for afterwards. However this correction procedure affects the statistics considerably. For concentrated systems, ($\sigma_x > \sigma_b$), the spectral modifications are too large for a sensible analysis. The $M_{4,5}$ edges of rare earths and to a lesser extent also the $L_{2,3}$ edges of transition metals are relatively strong; hence the fluorescence yield signal will be saturated for the pure metals. Compounds with low-Z elements will also show distorted X-ray absorption spectra. The oxygen K edge of metal oxides will show relatively small saturation effects, especially if some high-Z elements are present as is the case for $YBa_2Cu_3O_{7-\delta}$ and related compounds [Tro90]. Equation (1) shows that apart from saturation effects, there can be effects due to so-called self-absorption. If the fluorescent decay of a core hole takes place at an energy (E_f) which is strongly reabsorbed, the spectral shape is modified in a rather complicated manner and the spectrum is difficult to interpret. The large escape depth makes fluorescence yield suited for the measurement of impurities, which are difficult to measure with a surface sensitive technique such as Auger yield. The suitability of fluorescence yield for impurities, for example metal ions in bioinorganic cluster compounds or even complete enzymes, has led to large efforts in the development of fluorescence yield detectors [Cra88, Cra91a].

2.3.3. Ion yield

Another decay product of the core holes is ions. If the absorption process takes place in the bulk and the core hole decays via an Auger process a positively charged ion is formed, but due to further decay and screening processes the original situation will be restored after some time. However, if the absorption process takes place at the surface, the possibility exists that the atom which absorbs the X-ray will be ionized by Auger decay and escape from the surface before relaxation processes can bring it back to the ground state. If the escaping ions are analysed as a function of X-ray energy the signal will again be related to the absorption cross section. Because only atoms from the top layer are measured, ion yield is extremely surface sensitive. The mere possibility of obtaining a measurable signal from ion yield means that the surface is irreversibly distorted, but as there are of the order of 10^{13} surface atoms per mm^2, this does not necessarily mean that a statistically relevant proportion of the surface is modified. The possibility of using ion yield is highly material dependent and it is expected that the highest cross sections will be obtained for ionic solids. The method has been demonstrated for calcium atoms in the surface layer of CaF_2 [Him91].

2.3.4. Total electron yield

The most abundant yield detection technique, which is also the most unclear in its nature, is total electron yield. The difference with Auger electron yield is that the energy of the outgoing electrons is not selected and all escaping electrons are counted. It is clear that the signal is dominated by secondary electrons which are created in the cascade process of the Auger decay electrons [Erb88, Hen79]. The ease of detection and the large signal make total electron yield a much used technique, but questions which remain are the specific processes which take place and specifically the probing depth and the related surface

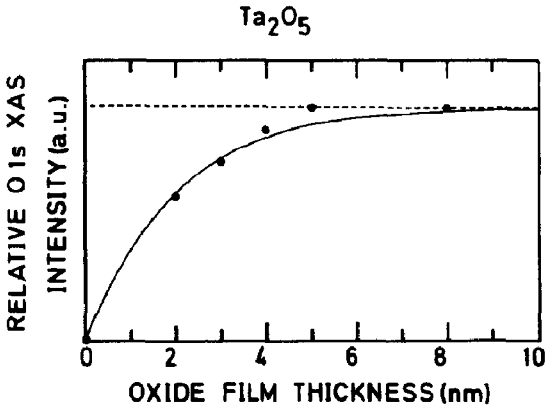

Fig. 5. Relative oxygen K edge X-ray absorption intensity as a function of the thickness of the Ta_2O_5 layer (from [Abb92b]).

Table 1
Probing depths of yield detection of soft X-ray absorption experiments of 3d metal oxides

Detection technique	Probing depth/Å
Ion yield	≈ 2
Auger electron yield	≈ 20
Total electron yield	≈ 40
Fluorescence yield	> 1000

sensitivity are only roughly known. An estimate for the probing depth is to use the Auger probing depth as the lower boundary and something of the order of 200 Å as the upper boundary. As the creation, migration and escape of secondary electrons will be material dependent, the probing depth of total electron yield will be material dependent.

A quantitative study of the mean probing depth of total electron yield for the oxygen *K* edge of thin layers of Ta_2O_5 on tantalum metal has been studied by Abbate et al. [Abb92b]. The tantalum oxide overlayers can be prepared with great accuracy and they are stable with respect to further oxidation if the layers have a thickness of 20 Å or more [San83]. Figure 5 shows the results for a layer thickness between 20 and 80 Å. The figure shows that total electron yield signal is already saturated for layers of the order of 40 Å. More details concerning the processes which determine the probing depth are given in [Abb92a, Erb88, Hen79, Kro90]. In Table 1 the estimates of the probing depths of the different yield methods are collected.

3. Electronic structure models

This section sketches the models which are used to describe the electronic structure of transition metals and their compounds. The two basic electronic structure models are (1) the Hartree–Fock (HF) approximation and (2) the local spin density (LSD) approximation to density functional theory (DFT). While LSD and its extensions/modifications dominate solid state physics, the quantum chemistry domain is dominated by models which use HF as their starting point. In this section HF (3.1) and LSD (3.2) are introduced. The subsequent sections discuss some of the extensions of HF and LSD, such as the generalized gradient approximation (GGA) (3.3), the *GW* approach (3.4), short range model Hamiltonians (3.5), the inclusion of the Coulomb interaction (*U*) in LSD (3.6), the self-interaction correction (SIC) (3.7), orbital polarization (OP) (3.8), the ligand field multiplet (LFM) model (3.9) and recent extensions based on multi-configurational HF descriptions (3.10).

For solids in general LSD overbinds and the band gap is too small, while for HF the band gap is too large. In a sense most of the recent extensions can be viewed as an effort to combine the good points of HF and LSD to arrive at a more accurate description of the ground state.

3.1. The Hartree–Fock (HF) approximation

A well established approximation to determine the electronic structure is the Hartree–Fock (HF) approximation (presented text is based on [Ing91]). It is built on two basic notions. (1) The interaction of the electrons is described by the electrostatic potential, the Hartree potential (V_H)

$$V_H(r) = \sum_j \int dx' \phi_j(x') \phi_j^*(x') \frac{1}{r - r'} \qquad (2)$$

(2) The second ingredient of HF is the antisymmetric structure of the wavefunction which gives rise to the exchange interaction (V_x). V_x acts non-locally on the wavefunction. Apart from the Hartree and exchange potentials HF contains the kinetic term (V_k) and interaction with the nuclei (V_N). In bracket notation the eigenvalue problem is given as

$$E = \sum_i \langle i|V_k + V_N|i\rangle + \langle ij|V_H|ij\rangle + \langle ij|V_x|ji\rangle \qquad (3)$$

A self-consistent HF calculation gives the ground state energy *E*; the ground state wavefunction is given as a Slater determinant: an antisymmetrized determinant of the one-electron orbitals. An important omission in HF is the neglect of correlation. With correlation is meant the notion that as two electrons repel each other, their position and momentum are not independent. In HF correlations are not included, apart from a partial effect for parallel spin from exchange. In general Hartree–Fock overestimates the band gap. For example in the case of $CaCuO_2$ a HF gap of 13.5 eV is to be compared with an experimental band gap of 1.5 eV [Mas92b].

3.2. *The local spin density (LSD) approximation*

Since the establishment of the density functional theorem (DFT), stating that the ground state energy can be expressed as a function of the electron density [Hoh64], and the practical implementation of this theorem in the local (spin) density approximation (LSD) [Koh65], solid state calculations based on this formalism have become important. This is not only to determine the total energy but also to obtain a picture of the electronic structure in terms of the density of states, which in turn is used to analyse spectra.

As in HF the kinetic, nuclear and Hartree potentials are used. The difference is that exchange and correlation effects are described by a combined potential V_{xc}. All potentials are local functions of the electron density n. All complications are collected in the exchange-correlation potential, for which it is assumed that in a solid its value is equal to that of a homogeneous electron gas for a particular n. Thus for the spin-polarized version the potential is given as

$$V_{LSD}[n^+, n^-] = V_k + V_N + V_H + V_{xc} \tag{4}$$

For $V_{xc}[n^+, n^-]$ several alternative formulations are used and for details the reader is referred to review papers on LSD, for example [Jo89b]. The electronic structure and properties of solids are described with a number of alternative realizations of LSD. These methods vary in the use of plane waves (pseudo-potentials and augmented plane waves (APW)) or spherical waves (augmented spherical waves (ASW)); the use of fixed basis sets such as the linear combination of atomic orbitals (LCAO); the use of the electron scattering formulation, such as real space multiple scattering (MS) and Koster–Koringa Rostoker (KKR); linearized versions, such as linearized muffin tin orbitals (LMTO) and linearized APW (LAPW). For each of these methods in general several computer codes exist. Some methods exist in versions for spin-polarized calculations, the inclusion of spin–orbit coupling, fully relativistic codes, full potentials, spin-moment or direction restricted calculations, etc. Some recent reviews include [Jo89b, And87, Zel92].

A usual picture to visualize the electronic structure of a transition metal compound, such as oxides and halides, is to describe the chemical bonding mainly as a bonding between the metal 4sp states and the ligand p states, forming a bonding combination, the valence band and empty antibonding combinations. The 3d states also contribute to the chemical bonding with the valence band which causes them to be antibonding in nature. This bonding, taking place in a (distorted) cubic crystalline surrounding, causes the 3d states to be split into the so-called t_{2g} and e_g manifolds. This situation is visualized for a TiO_6^{8-} cluster in Fig. 6(a). For comparison the oxygen 1s X-ray absorption spectrum is given. In Fig. 6(b) this picture is modified for a partly filled 3d band. The example given is for a FeO_6^{9-} cluster. The 3d band is split by the crystal field splitting and a large exchange splitting.

This qualitative description of the electronic structure of transition metal compounds can be worked out quantitatively within L(S)D: in [Mat72a, Mat72b] a systematic study was made of the band structures of the 3d monoxides. The qualitative picture given above was verified, but in the calculations it was found that the dispersion of the 3d bands is larger than the crystal field splittings, with the result that all monoxides were calculated to be metallic, in conflict with the experimental findings. An important improvement of the L(S)D calculations, already suggested in [Mat72a], came with the inclusion of spin and the correct description of the magnetic structure of the monoxides [And79, Ogu83, Ogu84, Ter84,

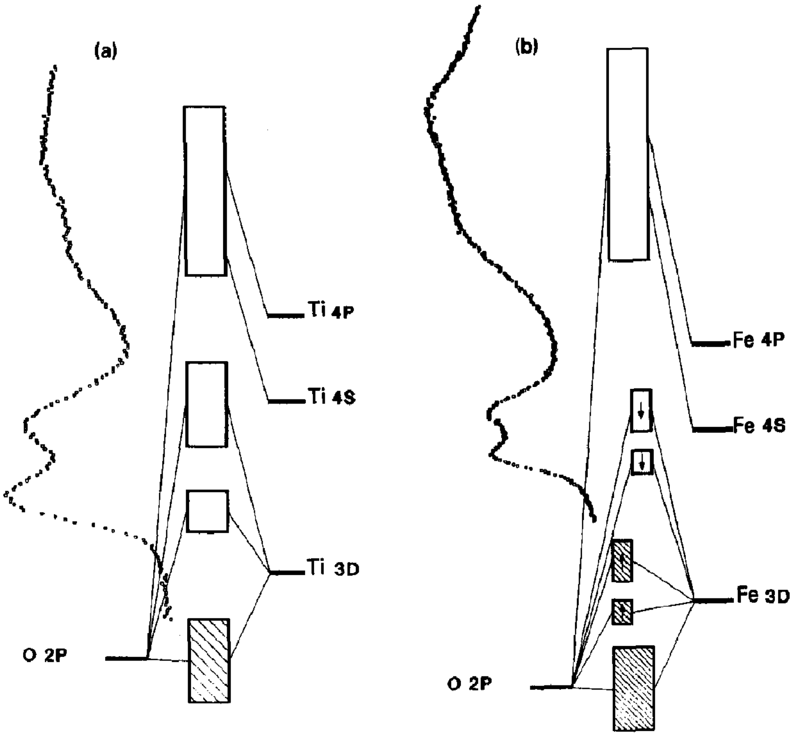

Fig. 6. Schematic band picture of (a) a TiO_6^{8-} cluster and (b) a FeO_6^{9-} cluster. Ti^{4+} has an empty 3d band and Fe^{3+} contains a half filled 3d band.

Yas83]. With the experimentally found antiferromagnetic coupling in the (111) direction it was found from LSD calculations that both MnO and NiO are insulators. In MnO all spin-up states are filled and all spin-down states empty, similar to the situation in Fig. 6(b). Figure 7, reproduced from [Ogu84], shows the result of the LSD calculation for NiO. A band gap of 0.3 eV is found and the occupied states can be roughly divided into an oxygen 2p band at about 6 eV below the Fermi level and a nickel 3d band just below E_F. From the spin-projected nickel 3d states it can be seen that, in first approximation, the spin-down states are rigidly shifted over about 1.2 eV. The $t_{2g}^{\downarrow}$ states are positioned at the same energy as the $e_g^{\uparrow}$ states, or in other words the ligand-field splitting roughly equals the exchange splitting.

3.2.1. The real space multiple scattering formalism

Particularly for hard X-rays, the absorption spectra are calculated with a real space multiple scattering formalism [Vvd92]. It has been shown that if worked out rigorously within its mathematical framework, the real space multiple scattering result is identical to the result obtained from band structure [Jon68, Nat86a, Reh93]. See Section 8 for further discussion.

3.3. The generalized gradient approximation

The generalized gradient approximation (GGA) has been developed to overcome the limitations met in the use of LSD. The goal of GGA is to come closer to the limit of the exact exchange-correlation potential within DFT. In comparison with experiment LSD gives a too strong bonding and hence too small optimized lattice parameters. This result has been linked to the use of a localized potential. In GGA this is replaced with a potential which is not only dependent on the electron density n, but also on its gradient (∇n). The exchange-correlation potential is $V_{xc}[n^+, n^-, \nabla n^+, \nabla n^-]$ [Lan80].

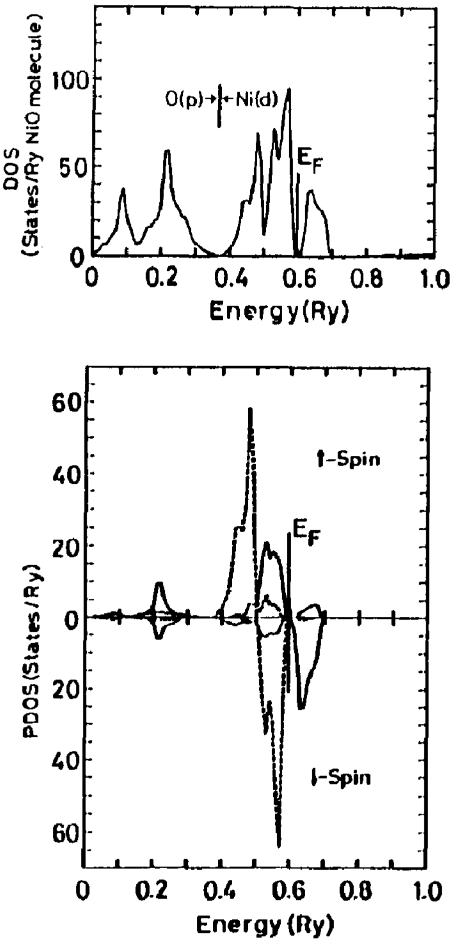

Fig. 7. Total density of states (top) and projected Nid projected density of states (bottom) of an LSDA calculation of NiO (from [Ogu84]).

For transition metals an important result of a GGA calculation is that the ground state of iron is predicted in agreement with experiment. While LSD finds a paramagnetic face-centred cubic (P-FCC) ground state, GGA finds a ferromagnetic body-centred cubic (F-BCC) phase [Bag89]. There are two energy effects of GGA compared to LSD which can be approximated as follows: (1) there is an energy lowering effect linear in the Wigner–Seitz radius which favours the BCC phase; (2) for a fixed radius GGA favours a magnetic moment, which lowers the energy of the ferromagnetic phase. The combination of these effects gives the F-BCC phase at lowest energy [Bag89].

For the precise formulation of the exchange-correlation potential in GGA a number of alternatives exist, normally indicated by the first letters of the authors. Influential formulations are those of Langreth–Mehl–Hu (LMH) [Hu85, Lan83], Perdew–Wang (PW) [Per86a, Per92a, Per92b] and Becke [Bec88]. These GGA potentials are "semi-empirical" in the sense that they make a particular choice for, for example, the real-space-cutoff, which is partly guided by the correspondence to experiment. For details of the potentials the reader is referred to the original literature which is collected in [Per92b].

3.4. GW *calculations*

A well defined model to describe electronic excitations is the so-called *GW* approach [God88, God92, Hed65, Hed69] in which the Green function *G* calculated with a screened Coulomb interaction *W* is used to calculate the excitation energies. In [Ary92] it is noted that one can divide *W* into an exchange part W_x and a correlation part W_c. Then a "GW_x" calculation can be identified with HF. The calculation requires a non-local, energy-dependent so-called self-energy operator. A *GW* calculation gives the density of (quasi-particle) states for the occupied states of the $N-1$ system and the empty states of the $N+1$ system. Hence it gives a direct description of (inverse) photoemission spectra. This is in contrast to LSD calculations, which can be considered as *GW* calculations with a local, energy-independent self-energy operator, thereby yielding an "N-particle density of states". The actual calculation of excitation energies with *GW* is a large task, especially for transition metals, because of the narrow 3d bands, and to my knowledge only for nickel has a *GW* calculation been performed [Ary92]. As far as the valence band is concerned the main effect of *GW* is a compression of the 3d band. The ordering of the bands is not altered from LSD. A *GW* calculation is in progress for NiO [Ary93].

3.5. *The short range ("Anderson impurity") models*

A clear case of disagreement between LSD calculations and experimental results can be found in the XPS/BIS data of NiO. Sawatzky and Allen [Saw84] showed that in NiO XPS/BIS gives a band gap of about 4.3 eV, compared with 0.3 eV from LSD. For clarity I note that formally LSD should not yield the correct band gap, but the large discrepancy with experiment shows that "something is missing" in LSD. The missing factor is the incomplete treatment of the Coulomb interaction U, as indicated in [Fuj84a, Saw84]. The main result of the inclusion of U is that the states closest to E_F are dominated by oxygen 2p character, in contrast to the LSD result which puts the 3d states closest to E_F. This discrepancy will be discussed in more detail below.

A crucial phenomenon for transition metal oxides is the fact that it costs energy to transfer an electron from one metal-ion to another, because of strong two-electron Coulomb integrals $\langle 3d, 3d|1/r|3d, 3d\rangle$, comprising U_{dd}. In LSD calculations this effect is not incorporated correctly and each transition metal contains the same number of (completely delocalized) electrons. In practice to put a number to the occupation one usually assigns all electrons within a particular radius to that atomic site. The fact that U_{dd} is not small means that it costs energy to vary the occupation number of the metal sites and in the extreme limit of infinite U_{dd} each metal site contains an integer number of localized 3d electrons. Models have been built focusing on a correct description of the Coulomb interaction, at the expense of less-complete descriptions of other ingredients [Hub63, Hub64, Hub67]. The model Hamiltonians built from this approach usually consist only of the 3d states and the oxygen 2p states. The Anderson impurity model [Ano61] comprises the energy positions of a localized state ε_d and delocalized states ε_p, the Coulomb interaction U_{dd} and the hopping terms t_{pd} and t_{pp} [Fuj84a, Fuj84b]. The model is often extended by including the Coulomb interaction of the 2p states U_{pp}, U_{pd}, sometimes denoted as the Falicov–Kimball model [Gie91] or in the context of copper oxides as the three-band Hubbard model [Eme87]. The Anderson impurity model and similar short range models are crucial for a sensible description of photoemission, inverse photoemission and core level XPS of transition metal compounds [Saw88].

3.5.1. *Calculation of parameters in model Hamiltonians*

In general the parameters in the Anderson impurity model are optimized to describe the experimental data. An important goal would be to derive the parameters from an ab initio method. The idea is to start with the full Hamiltonian and to project out degrees of freedom which are not included in the model Hamiltonian [Gun90]. The delocalized electrons are projected out and the Coulomb interaction is renormalized to account effectively for this. The Coulomb interaction U and the energy of the localized state $\varepsilon_d - \varepsilon_p$ can be determined from a constrained LSD calculation [Ani91b, Ded84, Hyb89, Mcm88a, Mcm88b, Zaa88]. In a model study Gunnarsson [Gun90] pointed out that the consequences of projecting out delocalized states causes a renormalization of U, first order in V^{-1} (V is the hopping integral of the delocalized states). An additional result is that the hopping of the localized state (t_{pd}) is also affected (in second order). If the localized state is expanded as a function of its occupation, the hopping is affected, in this case strongly [Gun88b]. Also the Coulomb interaction of the localized state with delocalized state renormalized t_{pd} [Gun89b].

3.6. *The inclusion of* U *in LSD calculations*

There have been recent efforts to include U_{dd} in the LSD Hamiltonian [Ani91a, Ani92a]. In these so-called LSD + U calculations the total energy functional is expressed as the L(S)D energy corrected for U and the exchange parameter J. That is, with an LSD calculation the exchange splitting J is determined. It can approximately be assumed to

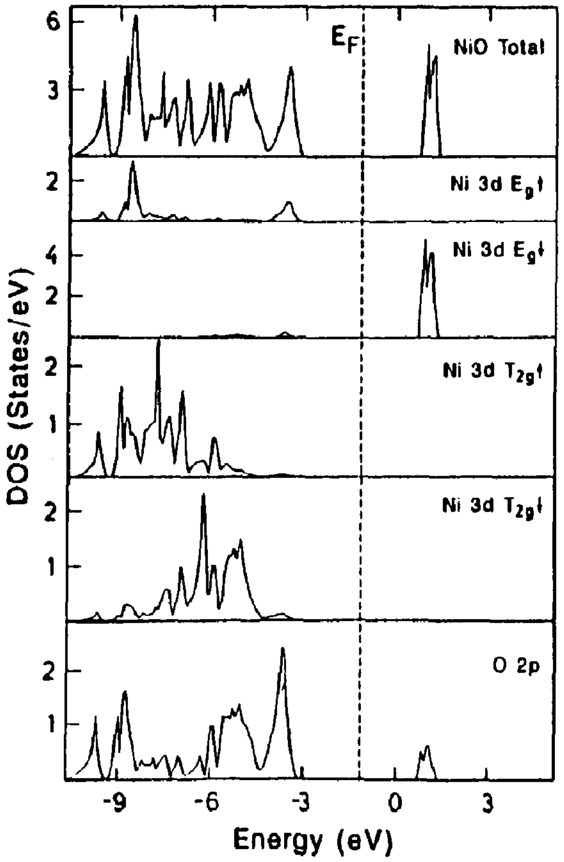

Fig. 8. Total and projected density of states of an LSD + U calculation of NiO (from [Ani91a]).

be k-independent. Also with the constrained LSD method U is determined as discussed above. Then the single particle potential is re-expressed as

$$V_{m\sigma} = V_{\text{LD}} + U\sum_{m'}(n_{m'-\sigma} - n^0) \\ +(U-J)\sum_{m'}(n_{m'\sigma} - n^0) \quad (5)$$

where m and σ refer to orbital and spin momenta respectively. The spin-independent LD potential is corrected for the deviations from the average occupation (n^0). Figure 8, reproduced from [Ani91a], shows the result of an LSD + U calculation using this expression for the potential. The result is a valence band of a width of about 7 eV in which the oxygen and nickel character are strongly mixed. The top of the valence band is indeed dominated by oxygen character in agreement with the earlier Anderson impurity-model predictions [Saw84, Zaa86t].

As yet a number of problems have still to be solved: the choice of the potential to be used is not obvious and one can imagine a number of alternatives. For example one can make U (and n^0) symmetry dependent, etc. [Czy93]. A second uncertainty is the value of U. The method to calculate U first with LSD and then in the second step to include it in an LSD + U calculation offers an ab initio method, although it is not certain whether it presents the "correct value" of U within an LSD + U calculation.

3.7. *The self-interaction correction (SIC)*

An alternative approach to introduce the localization effect due to the two-electron integrals is to introduce a so-called self-interaction correction (SIC). In LSD calculations non-existing self-interactions are included in the electrostatic term and also in the exchange-correlation term. The effects are opposite and tend to cancel, and in fact for the case of an infinitely extended solution they do cancel. For clarity it is noted that the self-interactions are a consequence of LSD and do not occur in the "exact" solution of DFT. In a strongly correlated material the wavefunctions are not infinitely extended and a correction must be added to the Hamiltonian removing the effects of self-interaction, the SIC [Gun74, Ish90, Miy91, Per79, Per80, Sva88a, Sva88b, Sva90a]. In order to have the possibility of finding a localized solution of the LSD + SIC calculations, a symmetry breaking term is introduced. It is tested self-consistently if a localized solution is favoured over delocalization. For example for the 3d monoxides localized solutions are found for MnO to CuO in agreement with experiment [Sva90b, Szo93] and La_2CuO_4 is found to be an antiferromagnetic insulator with a LSD-SIC gap of about 2 eV, close to the experimental value [Sva92, Tem93]. In principle the result of a LSD + SIC calculation is "single particle"-like and one finds the eigen-

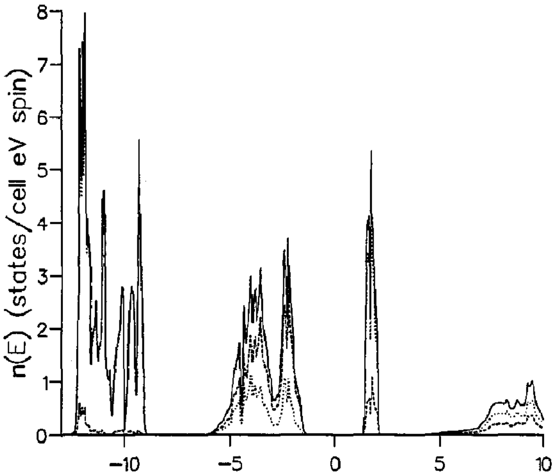

Fig. 9. Projected density of states of an LSD + SIC calculation of NiO. —, Total DOS; ···, Ni-projected DOS; – – –, oxygen projected DOS (from [Szo93]).

values of the ground state. As for normal LSD, one can relate the eigenvalues to excitation energies, though again there is no formal justification.

Figure 9, reproduced from [Szo93], shows the result of an LSD + SIC calculation. The band gap is close to the experimental value. The valence band is separated into two bands, an oxygen 2p-dominated band close to E_F and the nickel 3d band at about 6 eV lower energy. This result is (as far as energy positions are concerned) similar to the experimental XPS spectrum and the model calculations of Fujimori et al. [Fuj84a] and Zaanen et al. [Zaa85a].

3.8. Multiplet effects (orbital polarization)

In LSD one assumes the orbital contribution to the magnetic moment to be negligible and hence the different magnetic m_{lm} states are assumed to have equal average population ($\bar{m}_l$) [Sev93]. To enforce a non-statistical orbital occupation an additional term has been introduced in the LSD Hamiltonian [Eri90a, Eri90b, Nor90].

Recently Severin et al. [Sev93] separated the exchange integral into a spin part and an orbital part. The spin part can be identified with the Stoner-like exchange interaction J, included in LSD. The angular-part of the exchange integral is however (assumed to be) zero in LSD. This angular-part can be identified with the Kanamori C parameter, or the Racah B parameter, both as given in Table 2. For the Slater integrals experimental atomic values, or atomic HF values, are known accurately. For solids it is known that J is screened [Mar88]. Because for C no ab initio solid state information is known, it was assumed that the screening of C is equal to the screening in J [Sev93]. In Slater integral terms this identifies with an equivalent reduction of F^2 and F^4. Then with the inclusion of C, the orbital polarization (OP), the orbital and spin moments are calculated with LSD + OP. The results are in close agreement with experiment [Sev93].

Table 2
The Racah parameters and the Kanamori parameters given as a function of the Slater integrals

Racah	Slater	"Kanamori"	Slater
A	$F^0 - \frac{F^4}{9}$	U	$F^0 - \frac{2}{9}J$
C	$\frac{5F^4}{63}$	J	$\frac{1}{14}(F^2 + F^4)$
B	$\frac{9F^2 - 5F^4}{441}$	C	$\frac{1}{14}(\frac{9}{7}F^2 - \frac{5}{7}F^4)$
A	$F^0 - 0.070F^2$	U	$F^0 - 0.025F^2$
C	$0.050F^2$	J	$0.116F^2$
B	$0.013F^2$	C	$0.060F^2$

It is noted that in this method of Severin et al. the full HF Coulomb and exchange integrals are calculated, but in the LSD + OP calculation the U part of the integrals is omitted. In other words, U is assumed to be zero, as in normal LSD calculations. Svane and Gunnarsson included in their LSD + SIC calculation the effects related to both U and C [Sva90a]. It can be said that, starting from local density, the effects of the Slater integrals formulated as U, J and C (see Table 2) are included as follows: LSD includes J, LSD + OP includes J and C and LDA + U includes J and U. In principle there are no objections to including C in an LSD + U description [Ani91a].

3.9. Ligand field multiplet (LFM) model

The ligand field multiplet (LFM) model describes the ground only in terms of the partly filled 3d band. It is the simplest possible theory to describe the effects of the Coulomb and exchange integrals on the 3d band and hence to describe the symmetry of the ground state in the local symmetry for a transition metal ion in the solid [Grf64]. LFM theory is important for those experiments which are mainly sensitive to symmetry and hence those experiments which involve only the 3d band. This includes dd optical transitions, resonance experiments such as electron paramagnetic resonance (EPR) and as will be discussed in the next sections metal 2p X-ray absorption. Obviously LFM theory does not provide an ab initio calculation of the ground state in solids; it can be viewed as the simplest model Hamiltonian and the way to proceed to an ab initio determination would be to use the mapping of more complete Hamiltonians onto the LFM model. That is, if the Anderson impurity model Hamiltonian is determined ab initio one can go one step further and also delete the delocalized states to arrive at a single 3d band.

3.10. *Multi-configurational approaches*

Most of the preceding sections concentrated on the extension and improvement of LSD. This section discusses briefly some recent approaches which use HF as their basis. The extensions of HF basically deal with two types of shortcomings: (1) the inclusion of weak correlations, and (2) the inclusion of strong correlations where single Slater determinations no longer present good starting points. HF and extensions dominate the electronic structure determinations of molecules, which are discussed first.

Weak correlations can be included by parametrized, statistical, correlation corrections to HF [Cow81]; in other words one includes the electron density correlation functionals [Per86b]. A treatment based on perturbation theory was given by Møller and Plesset in 1934 [Mol34]. An influential method to include weak correlations is the coupled-electron-pair approximation (CEPA) [Ahl84, Mey71].

If strong correlations are important one has to leave the single Slater integral concept by including a specific set of configurations. These calculations can in general be called multi-configurational (MC) HF. Instead of Hartree–Fock one more generally uses the expression self-consistent-field (SCF) which denotes that the HF (like) equations are solved self-consistently using the variational principle [Dol91]. In 1973 Bagus and co-workers performed a MC calculation for the final state in 3s XPS which is dominated by the two configurations $3s^1 3p^6 3d^5$ and $3s^2 3p^4 3d^6$ [Bag73]. These two configurations are very strongly coupled by a 3s3d to 3p3p electron rearrangement process, the same process which causes the super Koster–Kronig Auger decay. There exist a number of generalized criteria to choose the configurations to be included. For example one can do a "first-order" CI (FOCI) [Jan88] by including all single excited states. Dolg et al. performed a MC-SCF calculation for cerocene (cerium sandwiched by two C_8H_8 rings), which constitutes a system with both strong (f states in cerium) and weak (other electrons) correlations [Dol91]. Recently Fulde and Stoll extended the CEPA calculations to a situation with more than one configuration. This then offers a way to include the strong correlations by MC-SCF and to include the weak correlations by CEPA [Ful91].

In going from molecules to solids a problem arises with respect to the embedding of the cluster for which an (MC) HF calculation is performed into "the solids". To account for the long-range Coulomb interactions the solid is often described as point charges around the cluster [Jan88].

4. Core excitations

This section describes the properties of core excitations, that is X-ray photoemission (XPS) and X-ray absorption (XAS). For the analysis of core spectroscopies it is necessary to describe the ground state, the final state and the transition cross section. The ground state electronic structure models have been discussed in the preceding section. In principle the final state can be calculated with these models; however the core hole gives some additional complications. The core hole has three major effects. (1) There is a core electron less, hence the core potential is stronger as if the atomic number is increased by one. (2) Core states with an angular momentum give rise to a core state spin–orbit splitting. (3) Core states with an angular momentum also give rise to strong core valence Coulomb interactions. At present no ab initio method is able to account for these three effects.

For 1s edges effects (2) and (3) do not exist and the core hole potential is the only extra effect to be accounted for in the final state. It is possible to include a core hole potential in real space multiple scattering. Also in a LSD calculation this is possible, at the expense of a larger calculation, by using supercells. It is noted that LSD calculations give a reasonably correct picture of the empty density of states as the Coulomb interactions U do not affect the distribution of empty states in a first order approximation. This is relatively clear to see in the self-interaction framework: as only occupied states have (self) interactions in LSD, only occupied states are directly affected by SIC (see Section 3.7).

For 2p edges the strong core valence Coulomb interactions make impossible any analysis using only the distribution of empty states (as obtained from LSD, MS, etc.). This forces one to use model Hamiltonian descriptions, such as the Anderson impurity model (using atomic Slater integrals for the core valence Coulomb interactions) or even the ligand field multiplet model (using renormalized core valence Coulomb interactions).

4.1. The interaction of X-rays with matter

The interaction of X-rays with matter is described in many textbooks [Bas83]. The Hamiltonian describing this interaction is written as a function of the vector potential of the electromagnetic radiation A and the momentum of the electrons p. It contains terms in A^2 and $A \times p$. For the analysis of X-ray absorption it is sufficient to consider only $A \times p$. In general the dipole approximation can be used [Car90] and the probability for absorption of an X-ray is equal to a squared transition matrix element times a delta function describing the conservation of energy; Fermi's golden rule

$$\sigma = \frac{8\pi e^2 \omega^3 n}{h c^3} |\langle \Phi_f | \mathbf{p}_q | \Phi_i \rangle|^2 \delta_{E_f - E_i + E_{h\nu}} \qquad (6)$$

The momentum operator $\mathbf{p}_q$ (q accounts for the polarization degrees of freedom) can be replaced by the position operator $\mathbf{r}$ as $[\mathbf{r}, \mathscr{H}] = (ih/m)\mathbf{p}$; however this replacement is exact only if the same Hamiltonian is used in the initial and final state. Equation (6) in principle refers to a final state with infinite lifetime. If the finite lifetime is accounted for the δ function is replaced by a Lorentzian.

In theoretical treatments of the X-ray absorption cross section it is customary to reformulate Eq. (6) in terms of a correlation function [Gun83, Zaa86a]. The squared matrix element $|\langle \Phi_f | \mathbf{r} | \Phi_i \rangle|^2$ is rewritten as $\langle \Phi_i | \mathbf{r} | \Phi_f \rangle \times \langle \Phi_f | \mathbf{r} | \Phi_i \rangle$. The radial operator $\mathbf{r}$ is rewritten in second quantization as $T = \sum_v W_v \phi_v^\dagger \phi_c$; ϕ_c annihilates a core electron and $\phi_v^\dagger$ creates a valence electron. The finite lifetime of the excited state Γ is included and the delta function $\delta_{E_f - E_i + E_{h\nu}}$ is reformulated as (one over π times) the imaginary part of the Green function $\mathscr{G}$

$$\mathscr{G} = \frac{1}{\mathscr{H} - E_i + E_{h\nu} - \frac{1}{2} i \Gamma} \qquad (7)$$

After these modifications the total equation takes the shape of a correlation function

$$\sigma \approx -\frac{1}{\pi} \mathscr{I} \langle \phi_i | T^\dagger \mathscr{G} T | \phi_i \rangle \qquad (8)$$

T and $T^\dagger$ project the initial state wavefunction on a series of final states for which the Green function is evaluated. This correlation function formulation is also used in the real space multiple scattering formulation of X-ray absorption (Section 8). The use of correlation functions like this has led one to remark that "everything is a ground state property", because if ϕ_i is known the spectrum can in principle be calculated. This Platonian interpretation can be countered by the Aristotelian remark that one only knows nature, if one knows its movement, in the sense of change. This puts the transition operator T at the centre of attention. ϕ_i is pure "matter" and hence only potential; it is actualized by T (following Aristotle).

4.1.1. Selection rules for X-ray absorption

In the case of an atom the wavefunctions in Eq. (6) can be given J and M (or M_J) quantum numbers. The matrix element $\langle\phi(JM)|\mathbf{r}_q|\phi(J'M')\rangle$ can be separated into a radial and an angular part according to the Wigner–Eckart theorem [Cow81]

$$\langle\phi(JM)|\mathbf{r}_q|\phi(J'M')\rangle = (-1)^{J-M}\begin{pmatrix} J & 1 & J' \\ -M & q & M' \end{pmatrix}\langle\phi(J)\|\mathbf{r}_q\|\phi(J')\rangle \quad (9)$$

The triangular relations of the 3J-symbol determine the selection rules for X-ray absorption. They read as follows: because the X-ray has an angular momentum of $l_{h\nu} = +1$, conservation of angular momentum gives $\Delta l_\mathrm{i} = +1$ or -1; the angular momentum of the excited electron differs by 1 from the original core state. As X-rays do not carry spin, conservation of spin gives $\Delta s_\mathrm{i} = 0$. Given these restrictions the overall momentum quantum number cannot be changed by more than 1; thus $\Delta J = +1$, 0 or -1, with $J + J' \geqslant 1$. The magnetic quantum number M is changed according to the polarization of the X-ray, i.e. $\Delta M = q$.

For linearly polarized X-rays impinging on a sample under normal incidence $q = \pm 1$ and for grazing incidence $q = 0$. This gives a difference in the value of the 3J-symbol, and hence (in potential) a polarization dependence. For circularly polarized X-rays a polarization dependence is found for a magnetic ground state. For an atomic non-magnetic ground state $M = \pm J$ and the 3J-symbol is identical for $q = \pm 1$. The rules for dichroism are discussed in more detail in Section 6.

4.1.2. Extended final states

For extended final states (the Bloch-like wavefunctions in density functional methods) J is not a good quantum number and the only selection rules are $\Delta l_\mathrm{i} = +1$ or -1 and $\Delta s_\mathrm{i} = 0$. In case of an excitation from a 1s core state only p final states can be reached and from a p core state s and d final states can be reached. The absorption cross section (σ) is reformulated as the matrix element squared times the local projected density of states (n_l) [Mul84]

$$\sigma \approx |\langle\Phi^\mathrm{v}_{l-1}|\mathbf{r}_q|\Phi^\mathrm{c}_l\rangle|^2 n^*_{l-1} + |\langle\Phi^\mathrm{v}_{l+1}|\mathbf{r}_q|\Phi^\mathrm{c}_l\rangle|^2 n^*_{l+1} \quad (10)$$

where n^* denotes the final state density of states, which should be used according to the final state rule [Von79, Von82]. Φ^v and Φ^c denote respectively the valence wavefunction and the core wavefunction (see Section 8 for more details).

4.2. XAS versus XPS

In core X-ray photoemission spectroscopy (XPS) the electron is excited to an energy high above the Fermi level and it can be considered as a free electron. The shape of the XPS spectrum is determined by the reaction of the system on the core hole. For example for 2p XPS an important effect is the two-electron integral $\langle 2\mathrm{p}, 3\mathrm{d}|1/r|2\mathrm{p}, 3\mathrm{d}\rangle$, giving rise to a core hole potential U_cd. The core hole spin–orbit coupling is also important and gives rise to the $2\mathrm{p}_{3/2}$ and $2\mathrm{p}_{1/2}$ edges.

In X-ray absorption spectroscopy (XAS) the energy of the X-ray is varied through a core level and an electron is excited to a state just above the Fermi level. If no reaction with the core hole takes place, the shape of the XAS spectrum will reflect the density of empty states (times transition strengths). Because in X-ray absorption the excited electron is not free, the dipole transition poses strong selection rules to the final state. This gives X-ray absorption its site and symmetry selective properties and for example oxygen 1s X-ray absorption will reflect the oxygen p-projected density of states.

However as for XPS the effect of the core hole is important and in fact it localizes the problem and necessitates the use of a short range model. The higher-order terms of the core hole interaction with the 3d band are also important. The two electron integrals $\langle 2p, 3d|1/r|2p, 3d\rangle$ and $\langle 2p, 3d|1/r|3d, 2p\rangle$ contain the higher-order terms F^2, G^1 and G^3. They have large values and give rise to a series of final states with different symmetries and energies: the final state multiplet. In general these effects are denoted as multiplet effects. For photoemission the dipole selection rule is relaxed and all final state symmetries are allowed. There is an important difference between 2p XPS and 2p XAS with regard to the relative importance of charge transfer versus multiplet effects. This can be shown nicely with the use of the short range model.

4.3. Short range models for core spectroscopies

Model Hamiltonians which explicitly include the Coulomb interaction U in the Hamiltonian include, (1) the single band or Hubbard model, (2) the Anderson impurity model comprising both a localized and an itinerant band, (3) the Kimball–Falicov model including also U_{pd}, etc. In Fig. 10 a schematic density of states is given for a 3d transition metal compound. In the short range (Anderson impurity) model as used for core spectroscopies, only the 3d states and the ligand p band are retained. The 3d band is considered localized, with an energy ε_{d} and a Coulomb repulsion energy U_{dd}. The 3d states interact with ligand p states at energy position ε_{p}. The hopping matrices are denoted as t_{pd}. Also the ligand p states interact with each other via t_{pp}. This short range model can be used for a cluster describing the transition metal ion and its nearest neighbour ligand ions. This approach has been applied to core spectroscopy by Fujimori et al. [Fuj84a, Fuj84b]. The ligand states can also be described as bands by including the k-dependence of the p band. Each transition metal atom contains localized 3d states but all other states are in principle described as bands. This approach has been introduced for spectroscopy of cerium compounds by Gunnarsson and Schönhammer [Gun83, Gun85] and has been adapted to transition metal compounds by Zaanen et al. [Zaa86a, Zaa86t].

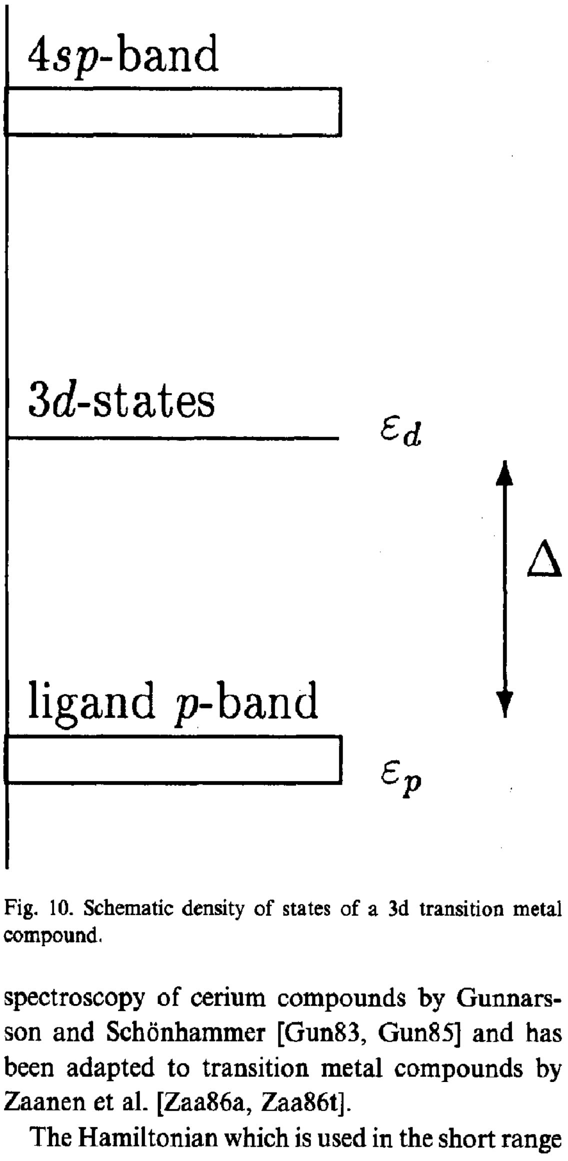

Fig. 10. Schematic density of states of a 3d transition metal compound.

The Hamiltonian which is used in the short range (Anderson impurity) model is

$$\mathscr{H} = \varepsilon_{\mathrm{d}} n_{\mathrm{d}} + \sum_k \varepsilon_{\mathrm{p}k} n_{\mathrm{p}k} + t_{\mathrm{pd}} \sum_k (a_{\mathrm{d}}^{\dagger} a_{\mathrm{p}k} + a_{\mathrm{p}k}^{\dagger}) + U_{\mathrm{dd}} n_{\mathrm{d}} n_{\mathrm{d}} \tag{11}$$

In this equation second quantization is used and $a_{\mathrm{d}}^{\dagger}$ denotes the creation of the localized d state; n_{d} ($\equiv a_{\mathrm{d}}^{\dagger} a_{\mathrm{d}}$) is the occupation-number operator of the localized state. To describe the ground state the ionic ansatz (starting point) is a specific 3d configuration $3d^N$, as given by the formal valency of the ion. If the hopping of this localized state with the ligand p band is considered, this gives rise to $3d^{N+1}\underline{L}$ configurations with an energy $\varepsilon_d - \varepsilon_p$, which is also denoted as Δ, the charge transfer energy.

The electronic configuration of the ground state of the compound is given by a linear combination of $3d^N + 3d^{N+1}\underline{L}$ plus, if necessary, the other more excited states. It is determined by three parameters, U_{dd}, Δ and t_{pd}, plus the shape of the band. The symmetry is in general determined by the formal valency and is not altered by charge transfer effects, provided the ground state is not dominated by a $3d^{N+1}\underline{L}$ configuration. For example Ti^{4+} in TiO_2 has a ground state $3d^0 + 3d^1\underline{L} + 3d^2\underline{LL}'$; its symmetry is ${}^1A_1$ and is not modified by charge transfer.

In the final state of both 2p XPS and 2p XAS a core hole is present which couples strongly to the 3d states via $U_{\underline{c}d}$, which pulls down states with extra 3d electrons. The core hole in principle also couples to other valence states (see Appendix A), but in most cases these couplings are assumed to be effectively included in $U_{\underline{c}d}$ [Saw88]. The final state Hamiltonian becomes

$$\mathcal{H} = \varepsilon_d n_d + \sum_k \varepsilon_{pk} n_{pk} + t_{pd} \sum_k (a_d^\dagger a_{pk} + a_{pk}^\dagger a_d) + U_{dd} n_d n_d + \varepsilon_c n_c \qquad (12)$$

The four parameters, Δ, t_{pd}, U_{dd} and $U_{\underline{c}d}$ determine the shape of the 2p XPS and 2p XAS spectra (neglecting multiplet effects). The energy of the core state (ε_c) determines the energy position of the 2p edge. (Also the core hole spin–orbit coupling is included: see next section.) The situation for a typical charge transfer insulator ($\Delta = 3$, $U_{dd} = 7$ eV) is visualized in Fig. 11 [Deg93c]. The ionic configurations are given and the effects of hybridization are not included. The arrows indicate the transitions in both XPS and XAS. In XPS the ordering of the final states is changed because of the effect of $U_{\underline{c}d}$. The energy difference between the localized state and the band, Δ_f(XPS) is given by $\Delta - U_{\underline{c}d}$, which for charge transfer insulators is negative. In XAS the ordering of states in the final state does not change because the 2p electron is excited directly into a 3d state, which causes the counteracting effects of U_{dd} and $U_{\underline{c}d}$. In general $U_{\underline{c}d}$ is slightly larger than U_{dd}, but

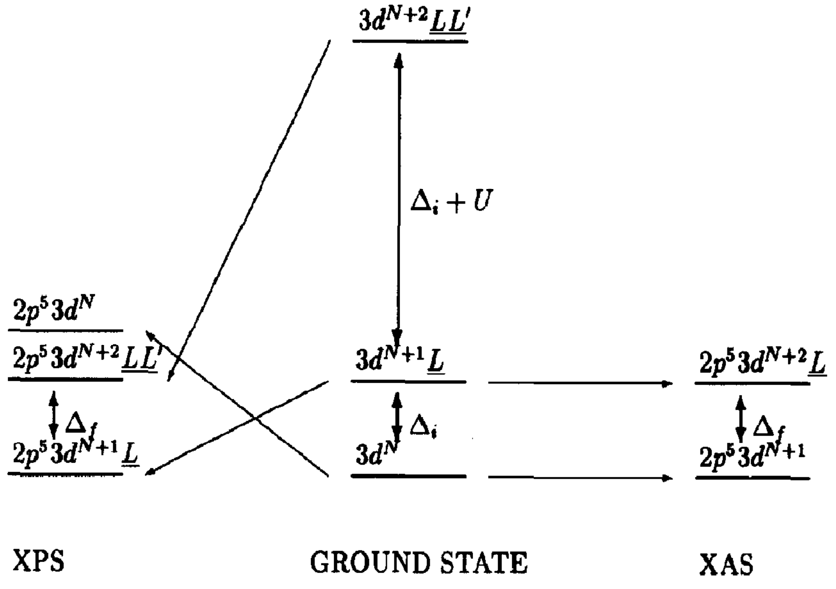

Fig. 11. 2p XPS and 2p XAS in the charge transfer model, neglecting the effects of hybridization. The configurations with lowest energy in the initial and the two final states are set to zero. $\Delta_f = \Delta_i + U_{dd} - U_{\underline{c}d}$. The arrows indicate the transitions in both 2p XPS and 2p XAS.

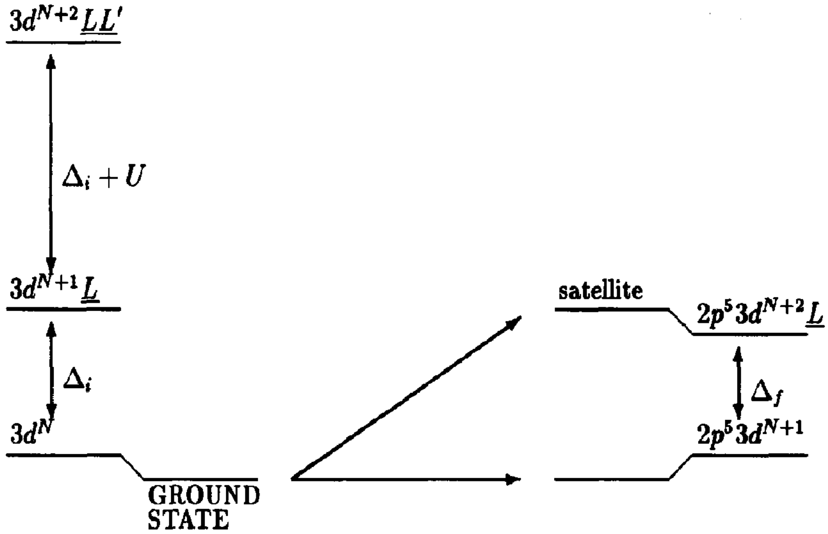

Fig. 12. The effects of hybridization on 2p XAS. If $\Delta_f = \Delta_i$ (and $t_f = t_i$) only the transitions to the lowest mixed configuration in the final state occur (see text).

here they are for simplicity taken as equal. This has the consequence that $\Delta_f(\text{XAS}) = \Delta + U_{dd} - U_{\underline{c}d} \approx \Delta$.

In Fig. 12 the effects of hybridization are included for 2p XAS. The ground state is formed from a combination of $3d^N$ and $3d^{N+1}\underline{L}$. The two configurations in the final state form a bonding and antibonding combination. With the restriction that $U_{\underline{c}d} \approx U_{dd}$ all intensity goes to the bonding combination of the two final state configurations and no satellite is present. The ground state is written as $\Phi_i = \sin\alpha[3d^N] + \cos\alpha[3d^{N+1}\underline{L}]$ and the final states as $\Phi_{f1} = \sin\beta[2p^5 3d^{N+1}] + \cos\beta[2p^5 3d^{N+2}\underline{L}]$ and $\Phi_{f2} = -\cos\beta[2p^5 3d^{N+1}] + \sin\beta[2p^5 3d^{N+2}\underline{L}]$. Then the intensity of the main peak is given as $\cos^2(\beta - \alpha)$ and the satellite equals $\sin^2(\beta - \alpha)$ [Oka92b]. If $U_{\underline{c}d} \approx U$ and $t_f \approx t_i$, then $\alpha \approx \beta$ and the satellite has zero intensity. One set of exceptions to this "rule of no-satellite" can be found at the end of the transition metal series. Systems which are dominated by $3d^9$ will have an altered final state because some of the configurations in the final state are not possible because they would have to contain more than ten 3d electrons. Hence their final state electronic configuration will have to adapt to this situation which can give rise to an increased intensity for the satellites. This will also influence systems with a $3d^9\underline{L}$ ground state such as $NaCuO_2$.

In the case of 2p XPS the situation is rather different. In general there are three low-lying states in the final state and their ordering has been changed with respect to the ground state. Under complete neglect of hybridization only the $2p^5 3d^N$ final state can be reached. If hybridization is turned on the two lower states gain in intensity, partly due to ground state hybridization but mainly due to final state hybridization and additionally due to the interference terms. This has been shown nicely for the nickel halides where all model parameters can be chosen equal with only the charge transfer (Δ) decreasing from fluoride to iodide, giving rise to a large variety in spectral shapes [Zaa86a]. Recently it has been shown that in the case of the 2p XPS spectrum of NiO it is necessary to extend the impurity model to a larger cluster and to allow for non-local screening effects, that is the formation of completely screened core hole ($\underline{c}d^9$ instead of normal $\underline{c}d^9\underline{L}$) while the valence hole moves to a neighbouring nickel to form a $d^8\underline{L}$ state [Vee93a, Vee93b].

From this discussion it can be concluded that the 2p XPS spectrum will contain large charge transfer

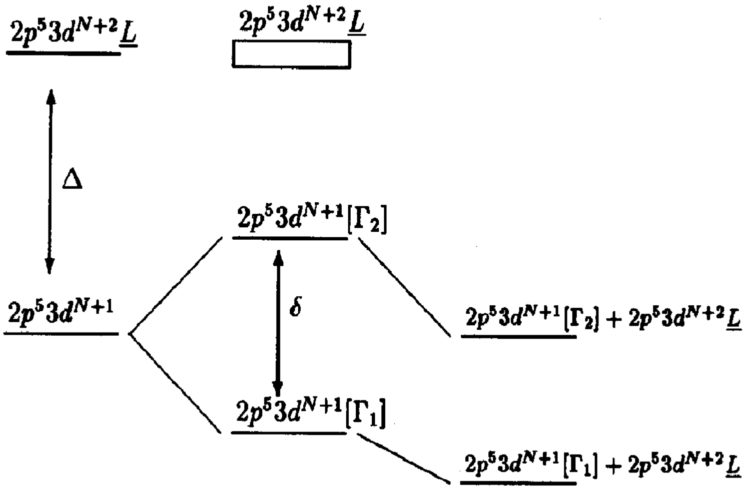

Fig. 13. The interplay of multiplet and charge transfer effects. If, as indicated, $\Delta > \delta/2$, the net result is a compression of the multiplet structure. If $\Delta < \delta/2$ the effects of charge transfer will be more complicated.

satellites, while the 2p XAS spectrum in principle only shows a single peak (with its multiplet splittings). This difference between 2p XPS and 2p XAS can be summarized as follows:

> XPS is sensitive to the charge transfer effects or in other words the *electronic configuration* of the ground state, while XAS is sensitive to the *symmetry* of the ground state with its characteristic multiplet.

4.4. Interplay between charge transfer and multiplet effects

We assume that in a final state of 2p XAS the multiplet lines are spread out over an energy range of several electronvolts (for details of multiplet calculations see Section 5.1). This spread implies that the energy difference of these different states with the $2p^5 3d^{N+2}\underline{L}$ band varies considerably. In Fig. 13 a situation is sketched in which the multiplet splittings ($\delta/2$) are less than the charge transfer energy (Δ). If hybridization is turned on, the energy-gain of the lowest multiplet state (Γ_1) will be less than the energy-gain of the highest multiplet state, because the effective energy difference with the band is much smaller in the latter case. In the case of a multiplet with 100 lines instead of 2 this principle remains valid. The consequence is that the multiplet structure is "compressed" with respect to the atomic multiplet. If the spread of multiplet states is larger than the charge transfer energy, some of the multiplet states will be located within and above the band and the effects of charge transfer will be more complex. To account for these situations the short range model has been extended to include multiplet effects by Jo and Kotani [Jo88a]. This will be discussed in Section 5.3.

5. Metal 2p X-ray absorption

Charge transfer effects are less effective in 2p X-ray absorption and in the first part of this section they will be neglected altogether. What remains is a description of localized 3d states, which can be treated in detail using a multiplet approach. In Section 5.3 the short range model will be extended to include these multiplet effects.

5.1. The ligand field multiplet model

The ligand field multiplet (LFM) model has been proven to be successful in the description of metal 2p X-ray absorption spectra. It was first applied to core spectra by the groups in Tokyo [Asa75, Asa76, Yam77, Sug82, Shi82, Yam82a, Yam82b] and

Winnipeg [Gup74, Gup75]. For an account of the historical development of the model the reader is referred to [Deg91t] and a general history of X-ray absorption can be found in [Stu89].

5.1.1. *Atomic multiplet theory*

Atomic multiplet theory describes the correlated electronic states in partly filled atomic shells. It is the general theory in use for the calculation of core excitation spectra of atoms and as such is described in many textbooks such as those of Condon and Shortley [Con35] and Cowan [Cow81].

The Hamiltonian for atomic multiplets is

$$\mathscr{H} = \mathscr{H}_{3d} + \mathscr{H}_{mu} + \mathscr{H}_{ls} \tag{13}$$

The notation is as used for the short range model (Sections 4 and 5.3). $\mathscr{H}_{3d}$ gives just the average energy of the 3d states, $\mathscr{H}_{mu}$ includes all two-electron integrals which will be described below, and $\mathscr{H}_{ls}$ denotes the 3d spin–orbit coupling. In the final state the core state energy $\mathscr{H}_c$, its two-electron integrals with the 3d states $\mathscr{H}_{c,mu}$, and its spin–orbit splitting $\mathscr{H}_{c,ls}$ must be added. This will be discussed below.

As an introduction some of the simplest atomic multiplets will be discussed. A transition metal atom or ion with a partly filled 3d orbital contains electrons which have ten possible combinations of angular and spin momenta m_l and m_s. Because the spin–orbit coupling is small for 3d electrons, *LS*-coupling gives a good description [Kar70]. For a $3d^1$ configuration the overall quantum numbers *L* and *S* are respectively 2 and $\frac{1}{2}$, hence *J* is either $\frac{3}{2}$ or $\frac{5}{2}$. In general the atomic symmetries are notated with term symbols $^{2S+1}L_J$, which for a single 3d electron are $^2D_{5/2}$ and $^2D_{3/2}$. A $3d^2$ configuration has 45 combinations of *L* and *S*. They are grouped in the irreducible representations $^1G_4$, $^3F_4$, $^3F_3$, $^3F_2$, $^1D_2$, $^3P_2$, $^3P_1$, $^3P_0$ and $^1S_0$. Similarly a $3d^3$ configuration has 120 configurations divided over ^4F, ^4P, ^2H, ^2G, ^2F, ^2D (2 times) and ^2P. To determine the wavefunctions of these three-electron states, a general method has been developed in which first two electrons are coupled to $|d^2\mathbf{LS}\rangle$ and subsequently this two-electron function is coupled with the third electron. From symmetry arguments and recoupling formulae it can be shown that the overall wavefunction $|d^3\mathbf{L'S'}\rangle$ can be formed by a summation over all *LS* combinations of the two-electron wavefunctions multiplied by a specific coefficient [Cow81]

$$|d^3\mathbf{L'S'}\rangle = \sum_{\mathbf{L,S}} |d^2\mathbf{LS}\rangle c_{\mathbf{LS}} \tag{14}$$

For example the ^4F state of $3d^3$ is built from its parent triplet states as

$$|d^3[^4F]\rangle = \tfrac{4}{5}|d^2[^3F]\rangle - \tfrac{1}{5}|d^2[^3P]\rangle \tag{15}$$

Similarly all other $3d^3$ states can be generated. The values with which to multiply the parent states are called coefficients of fractional parentage. The coefficients of fractional parentage are tabulated for all partly filled d and f states by Nielsen and Koster [Nie63].

5.1.1.1. *Slater integrals, Racah parameters and Hund's rules.*

The origin of the energy differences for the different symmetries (term symbols) can be found in the two-electron integrals and the spin–orbit coupling. The usual method of determining the two-electron integrals is by expanding them as a series of Legendre polynomials [Con35, Cow81]. The radial part reduces to the integral

$$R^k(d_1d_2, d_3d_4) = \int_{r_1}\int_{r_2} \frac{r_<^k}{r_>^{k+1}} \times P_1(d_1)P_2(d_2)P_1(d_3)P_2(d_4)dr_1dr_2 \tag{16}$$

It is common practice to divide the radial integrals into Coulomb terms and exchange terms. The Coulomb terms are denoted as $R^k(d_1d_2, d_1d_2) \Rightarrow F^k(d_1, d_2)$ and the exchange terms as $R^k(d_1d_2, d_2d_1) \Rightarrow G^k(d_1, d_2)$, the so-called Slater integrals. The angular part puts strong selection rules on the *k* values in the series expansion, i.e. for two 3d-electrons only F^0, F^2 and F^4 are possible and for a pd interaction F^0, F^2, G^1 and G^3. There is a close relationship between F^2 and F^4 and to about 1% accuracy F^4 equals $0.63F^2$.

Table 3
Relative energy positions of a $3d^2$ configuration; for the values in the third column the representative values $B = 0.1\,\text{eV}$ and $C = 0.4\,\text{eV}$ are used

Symmetry	Relative energy/eV	
$E(^1S)$	$+14B + 7C$	$+4.2$
$E(^1D)$	$-3B + 2C$	$+0.5$
$E(^1G)$	$+4B + 2C$	$+1.2$
$E(^3P)$	$+7B$	$+0.7$
$E(^3F)$	$-7B$	-0.8

A number of alternative closely connected notations are in use. In the subscript F_k notation the F^k Slater integrals are renormalized with a common k-dependent denominator D_k [Con35]. Often the Racah parameters A, B and C are used and Table 2 gives their relation to the Slater integrals. The table also contains the relationship of the Slater integrals to the notation which uses the "Hubbard" U and the "Stoner" exchange J values [Mar88a]. In the bottom half of the table the constant relation between F^2 and F^4 is used.

The effects of the two-electron integrals on the different symmetries of a $3d^2$ configuration are shown in Table 3. The ground state is the ^3F state, which is an example of the rule that for a general $3d^N$ configuration the ground state is that state with highest S, and for these states the state with the highest L, Hund's rule [Hun27] applies. Hund's rule is a direct consequence of the two-electron integrals: S (and L) are maximized because the electron–electron repulsion is minimized if the electrons belong to different m_l-orbitals and also because electrons with parallel spin have an additional exchange interaction which lowers their total energy. Hund's third rule states that if the ^3F state is split because of inclusion of the 3d spin–orbit coupling the ground state is the state with the lowest J, the $^3F_2$ state. In case more than five 3d electrons are present, the highest J value has lowest energy. Notice that the Hund's rules do not explain the ordering of the states (for example ^1D has lower energy than ^1G), but only the symmetry of the ground state.

5.1.1.2. The atomic multiplets of the final state. In the final state of the metal 2p X-ray absorption process a $2p^5 3d^{N+1}$ configuration is formed. The dominating interaction is the core hole spin–orbit coupling, which modifies the couping scheme to jj-coupling for the 2p core state and LS-coupling for the 3d valence state. The overall coupling scheme is a mixture of jj- and LS-coupling. As an example the transition from an empty 3d system ($3d^0$) will be discussed. Its final state has a $2p^5 3d^1$ configuration. Its symmetries are determined by multiplication of a d state with a p state

$$^2P \otimes {}^2D = {}^1P_1 + {}^1D_2 + {}^1F_3 + {}^3P_{0,1,2} + {}^3D_{1,2,3} + {}^3F_{2,3,4} \tag{17}$$

Because of the dominant 2p spin–orbit coupling (ζ_{2p}) the final state is described in an intermediate coupling scheme, which implies that the different symmetries $^3P_{0,1,2}$, etc., will be at quite different energies. If only the 2p spin–orbit coupling, ranging from about 3 eV for scandium to about 10 eV for nickel, is considered the 2p spectra are split into two structures, the L_3 and the L_2 edge, separated by $\frac{3}{2}\zeta_{2p}$. The pd Coulomb and exchange terms F^2_{pd}, G^1_{pd} and G^3_{pd} are of the order of 5 to 10 eV and from Table 3 it can be seen that the dd interactions cause splittings of the order of 5 eV. The combination of the 2p spin–orbit interaction and the dd and pd two-electron integrals results in a complex distribution of states for a general $2p^5 3d^N$ configuration.

5.1.1.3. The calculation of the atomic states. In the calculations presented in this review the atomic Hamiltonian is solved by a Hartree–Fock (HF) method, which is corrected for correlation effects [Cow81]. This method has been developed for atomic spectroscopy and detailed comparison with experiments has revealed that the quantitative agreement is not good. The calculations assume the ground state to be represented by a single $3d^N$ configuration. This introduces errors because the ground state is not single configurational but contains an admixture of a series of configurations. The obvious extension of the calculational scheme is to include excited configurations in a configuration interaction calculation. The situation is, however, not favourable for calculations because there exist an infinite number of small effects.

Theoretical studies indicate that it is possible to approximate the infinite series of excited configurations with a single configuration which has an equivalent dependence on spin- and angular-momenta as the ground state but with an opposite sign [Raj63, Raj64, Wyb65]. This gives a partial justification of the reduction of the HF-values of the Slater integrals to 80% of their original values [Cow81]. It has been found that the disagreement with experiment is largely solved by this semi-empirical correction to the Slater integrals. A recent effort to overcome these problems and to actually perform a multi-configurational calculation has been made by Sarpal and co-workers [Sar91]. Using a multi-configurational Dirac–Fock calculation scheme, the $M_{4,5}$ edges of divalent samarium and thulium atoms were calculated. From comparison with experiment it appears that for the multi-configurational spectrum the agreement is not good, and the renormalized HF results from Thole and coworkers [Tho85c] compare far better with the experimental spectrum.

5.1.1.4. The transition probability. The calculation of the transition probability is the last step to the atomic multiplet spectrum of a 2p X-ray absorption process. As discussed in Section 4.1.1 the transition strength is given as the 3J-symbol times a reduced matrix element

$$\langle 3d^0(JM)|\mathbf{r}_q|2p^5 3d^1(J'M')\rangle = \begin{pmatrix} J & 1 & J' \\ -M & q & M' \end{pmatrix} \langle 3d^0(J)||\mathbf{r}_q||2p^5 3d^1(J')\rangle$$

For the initial state $J = 0$, hence with the dipole selection rules ($\Delta J = \pm 1$, 0 and $J + J' \geqslant 1$) the J-value of the final state must be unity. As shown above, the $2p^5 3d^1$ final state contains three states

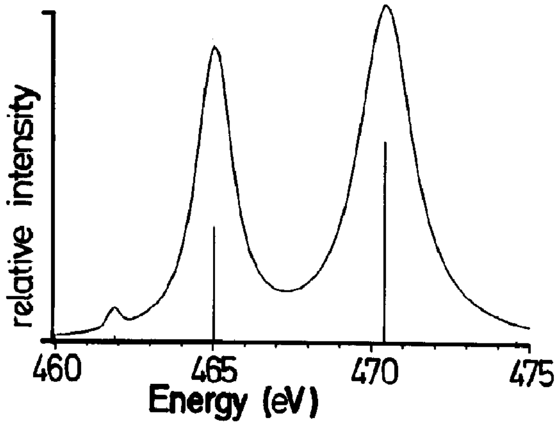

Fig. 14. Atomic multiplet calculation for the $3d^0 \rightarrow 2p^5 3d^1$ transition in tetravalent titanium.

with $J = 1$, $^1P_1$ (L_2 edge) and $^3P_1$ and $^3D_1$ (L_3 edge). Figure 14 shows the $3d^0 \rightarrow 2p^5 3d^1$ transition as calculated for a Ti^{4+} ion. Apart from the L_3 and L_2 peaks split by the 2p spin–orbit coupling, a third low-intensity peak is predicted at lower energy. This three-peaked spectrum is indeed observed, for example for calcium physisorbed on a silicon (111) surface [Him91].

5.1.2. From atoms to solids

If one transfers this atomic method to the solid state, the first question to ask is, is it possible at all to describe a 3d state in a solid quasi-atomic state? The discussion of the short range model in Section 4 has revealed that because of the counteracting effects of U_{dd} and U_{cd} this is indeed the case for X-ray absorption. However there remains the problem of how to accommodate the atomic states in the solid state environment. Particular questions are, (1) how to deal with the different local symmetry, and (2) how to incorporate the different more itinerant electronic features of the solid state, such as the electron density of the s and p states. The inclusion of the local symmetry has been the subject of many studies under the heading of ligand field theory [Grf64]. This has been used particularly to describe the optical absorption spectra of transition metal ions. For core spectroscopies, ligand field theory was developed in the seventies [Asa75, Gup74, Gup75, Yam77]. In this

Table 4
Effect of a cubic ligand field on a 3d electron

Representation	Orbital name	Atomic states	Cartesian notation
E_g	d_{z^2}	$\|20\rangle$	$\frac{1}{2}(3z^2 - r^2)$
	$d_{x^2-y^2}$	$\frac{1}{\sqrt{2}}\|2\bar{2}\rangle + \frac{1}{\sqrt{2}}\|22\rangle$	$\frac{\sqrt{3}}{2}(x^2 - y^2)$
T_{2g}	d_{xy}	$\frac{1}{\sqrt{2}}\|2\bar{2}\rangle - \frac{1}{\sqrt{2}}\|22\rangle$	$\sqrt{3}(xy)$
	d_{yz}	$\frac{1}{\sqrt{2}}\|2\bar{1}\rangle + \frac{1}{\sqrt{2}}\|21\rangle$	$\sqrt{3}(yz)$
	d_{zx}	$\frac{1}{\sqrt{2}}\|2\bar{1}\rangle - \frac{1}{\sqrt{2}}\|21\rangle$	$\sqrt{3}(zx)$

review the more general approach as developed by Thole and co-workers will be discussed in detail [Tho88a].

The itinerant effects of the solid have been described under the heading nephelauxatic effect [Jor62, Jor71] with the analogy to expanding clouds, and hence smaller on-site overlap. In Section 5.3 the effects of itinerant states on multiplets will be described using the short range model approaches. In the next section the emphasis will be on the symmetry effects.

5.1.3. *Symmetry effects in solids*

The dominant symmetry effect in solids is the cubic ligand field. The strength of this operator is usually denoted as the ligand field splitting (10Dq). Atomic multiplet theory can be extended to describe the 3d metal ions by incorporating the ligand field splitting.

In an octahedral environment the field of the neighbouring atoms of the central atom has cubic (O_h) symmetry which divides the fivefold degenerate 3d orbitals into two distinct representations of T_{2g} and E_g symmetry. The twofold degenerate E_g state contains orbitals which point towards the centre of the cube faces, that is directly towards the position of the ligands. Consequently E_g states interact more strongly, electrostatically as well as covalently, with the ligands. The three t_{2g} orbitals point towards the corners of the cube and therefore their interaction with the octahedral ligands is smaller. Table 4 describes the five ligand field states in terms of their atomic constituting functions.

Table 5
The $SO_3 \rightarrow O_h$ branching rules in the Schönflies notation

Spherical	Cubic
S	A_1
P	T_1
D	$E + T_2$
F	$A_2 + T_1 + T_2$
G	$A_1 + T_1 + T_2 + E$
H	$T_1 + T_1 + T_2 + E$
I	$A_1 + A_2 + T_1 + T_1 + T_2 + E$

In the ligand field multiplet model the atomic symmetries are projected to cubic symmetry. Table 5 reproduces the branching rules for projection from atomic to cubic symmetry [But81].

5.1.3.1. *Effects on the energy positions.*

The effects of the cubic ligand field on the energies of the atomic states have been described in the textbooks of Ballhausen [Bal62], Griffith [Grf64] and Sugano et al. [Sug70]. From Table 5 it can be checked that the degeneracy of the atomic states is partially lifted and the D, F, and higher states are split into a series of representations in cubic symmetry. The diagrams representing the effect of a cubic ligand field are denoted as Tanabe–Sugano diagrams. Figure 15, reproduced from [Sug70], sketches the energy positions as functions of the magnitude of the cubic ligand field (10Dq), relative to the Racah parameter B.

In the $2p^5 3d^N$ final state the effects of the cubic ligand field are equivalent to that in the initial state.

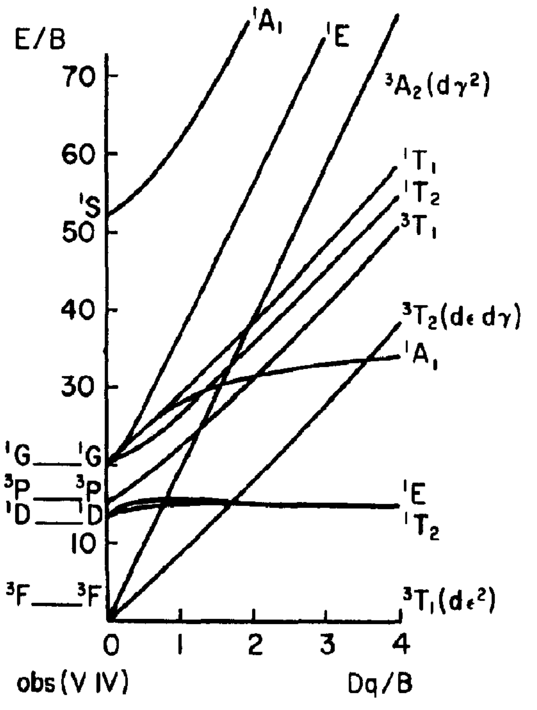

Fig. 15. Tanabe–Sugano diagram for a $3d^2$ ground state in cubic symmetry (from [Sug70]).

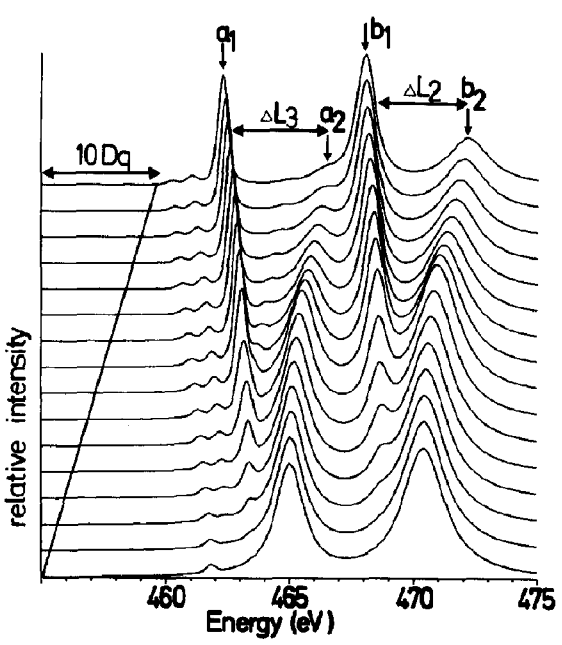

Fig. 16. Ti^{4+} X-ray absorption spectrum, calculated for an increasing cubic crystal field. The value of 10Dq is increased from 0.0 to 4.5 eV.

A difference is that the number of multiplet states is considerably larger: for a $3d^N$ initial state the maximum number of states is 256, while it is 6 times larger (=1536) for a $2p^5 3d^5$ final state. The number of irreducible representations is smaller because of degeneracies.

5.1.3.2. Effects on the transition probabilities. The transition probability for the $3d^0$ systems in cubic symmetry is

$$\langle 3d^0[^1A_1] \| r_q[T_1] \| 2p^5 3d^1[A_1 \otimes T_1 = T_1] \rangle \tag{18}$$

All final states of T_1 symmetry are allowed and have a finite transition probability from the $^1A_1$ initial state. From Table 5 it can be seen that this includes the states of $J = 1$ atomic symmetry, but additionally the states with $J = 3$ and $J = 4$. The degeneracy of these states is respectively 3 and 1, as can be deduced from the $2p^5 3d^1$ states in *jj* coupling [Deg90a]. The total number of allowed final states in cubic symmetry is $3 + 3 + 1 = 7$. Figure 16 shows the effects of an increasing cubic ligand field on the multiplet spectrum of the $3d^0 \rightarrow 2p^5 3d^1$ transition. In this figure it can be seen that for small values of the ligand field (the step size is 0.3 eV) the spectrum is hardly modified. For small values of 10Dq the four states which were forbidden in atomic symmetry have not gained enough intensity to be detectable in the spectrum.

Figure 17 shows the energy splittings between the peaks a_1 and a_2. This splitting is compared with the size of the cubic ligand field splitting and it can be seen that the peak splitting in the spectrum is not directly related to the value of 10Dq. From this figure it becomes clear why, for small values of 10Dq, no detectable amount of intensity is transferred. The energy difference between the two states a_1 and a_2 is about 2 eV in the atomic case when a_2 is allowed and a_1 forbidden. A ligand field splitting of 0.3 or 0.6 eV will hardly affect states which are separated by 2 eV, as is evidenced by the slow increase of the splittings around $10Dq = 0$.

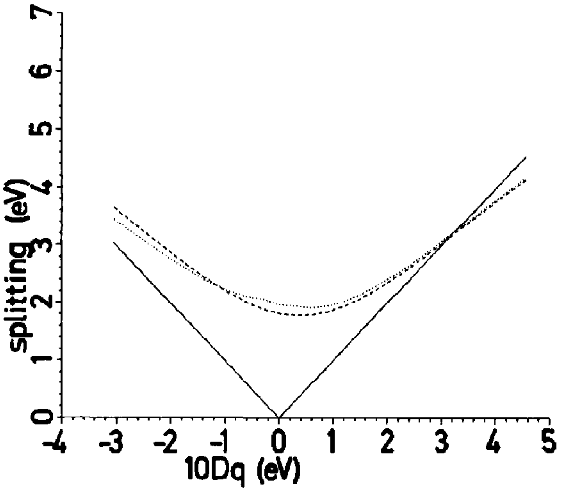

Fig. 17. The dashed line indicates the splitting between the peaks a_1 and a_2 of Fig. 16. The dotted line is for peaks b_1 and b_2.

5.1.3.3. Comparison with experiment. The ligand field multiplet results as calculated with the procedure outlined above can be compared directly with experiment. Figures 18–20 compare the ligand field multiplet calculation of Ca^{2+}, Sc^{3+} and Ti^{4+} ions with the respective 2p X-ray absorption spectra. Atomic Slater integrals were used. For details concerning the broadenings the reader is referred to [Deg90a]. All peaks in the experimental spectrum are reproduced, which is a confirmation that the ligand field multiplets indeed dominate the spectral shape. Note that even the $SrTiO_3$ spectrum is reproduced rather well with atomic values of the Slater integrals. This raises the question how it is possible that titanium can be described as tetravalent, while for example band structure results show that the charge transfer from titanium to oxygen is small and certainly not four electrons [Deg93a]. Part of the answer is that what matters is the symmetry of the ground state and because the 3d band is empty this is $^1A_1$ for titanium in $SrTiO_3$.

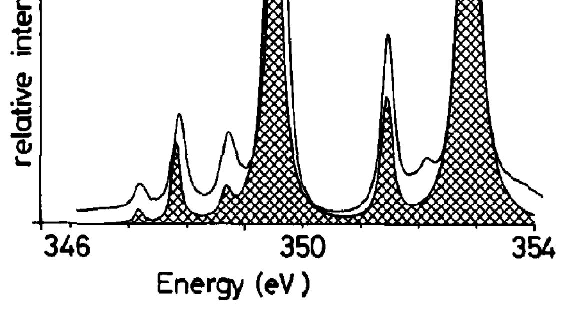

Fig. 18. Calcium 2p X-ray absorption spectrum of CaF_2 (solid line) compared with a ligand field multiplet calculation (hatched area). The value of 10Dq is −0.9 eV.

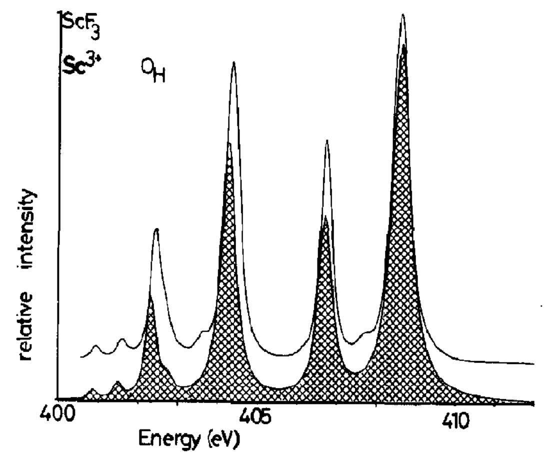

Fig. 19. Scandium 2p X-ray absorption spectrum of ScF_3 (solid line) compared with a ligand field multiplet calculation (hatched area). The value of 10Dq is 1.7 eV.

5.1.3.4. Multiplets of partly filled states. Table 6 gives the (Hund's rule) ground state symmetries of the atomic multiplets and their projection to cubic symmetry. If four electrons have to be accommodated in the 3d orbitals in an octahedral surrounding, two effects are important, the exchange coupling of an e_g electron with a t_{2g} electron (J_{te}) and the cubic ligand field splitting D. (The exchange coupling is connected to the Slater integrals as given in Table 2.) If $3J_{te} > D$, a high-spin $(t_{2g}^+)^3(e_g^+)^1$ configuration with ^5E symmetry is formed from the Hund's rule ^5D ground state. However if $3J_{te} < D$, a low-spin $(t_{2g}^+)^3(t_{2g}^-)^1$ configuration with $^3T_1$ symmetry is formed.

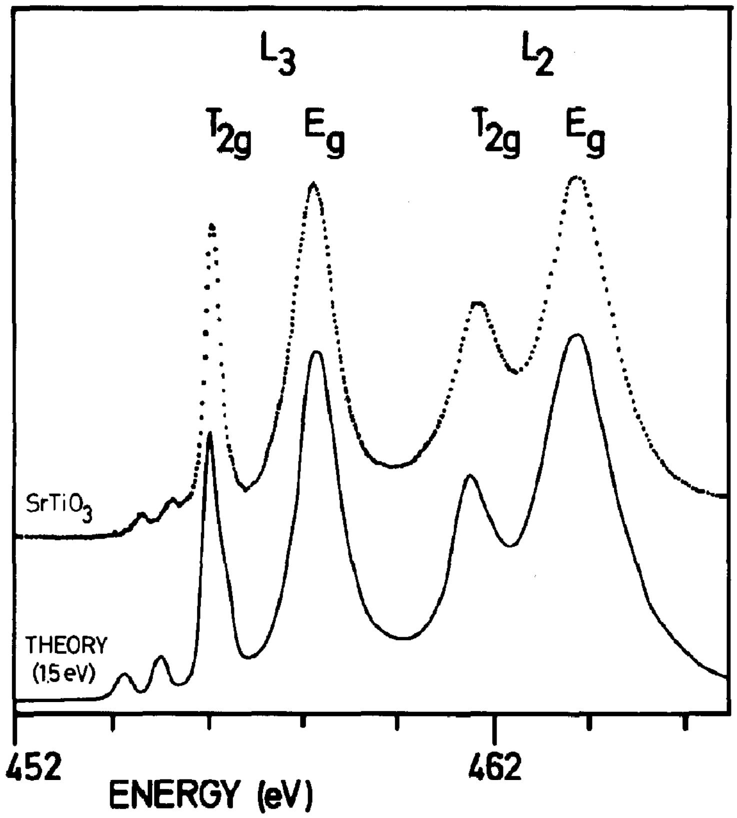

Fig. 20. Titanium 2p X-ray absorption spectrum of $SrTiO_3$ compared with a ligand field multiplet calculation. The value of 10Dq is 1.5 eV.

The criteria for high-spin or low-spin ground state are collected in Table 7. The exchange splittings J are different for different combinations of e_g or t_{2g} electrons, though these differences are small. Approximately $J_{ee} - 0.1 = J_{te} = J_{tt}$ +0.1 eV [Bal62]. The exchange splitting J_{te} is about 0.8 eV for 3d electrons. From this value one can estimate the point where the ligand field is large enough to change from high-spin to low-spin. The estimates are given in the last column of Table 2.

5.1.3.5. Ligand field multiplet calculations for $3d^N$. The calculation of the ligand field multiplet is in principle equivalent to that of the $3d^0$ configuration, with the additional possibility of low-spin ground states. As an example the $3d^5[A_1] \rightarrow 2p^5 3d^6[T_1]$ ligand field multiplet is given in Fig. 21.

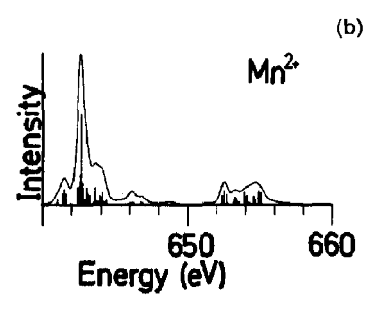

Fig. 21. Mn^{2+} $3d^5$ to $2p^5 3d^6$ transition for (a) 10Dq = 0.0 and (b) 0.9 eV. The line spectrum and the broadened spectrum are given.

Table 6
Symmetries and configurations of all possible $3d^N$ states[a]

State	Atomic symmetry	Cubic symmetry	Configuration	Susceptible for
$3d^1$	^{2}D	$^2T_2$	$(t_{2g}^+)^1$	3d spin–orbit
$3d^2$	^{3}F	$^3T_1$	$(t_{2g}^+)^2$	3d spin–orbit
$3d^3$	^{4}F	$^4A_2$	$(t_{2g}^+)^3$	–
$3d^4_{HS}$	^{5}D	^5E	$(t_{2g}^+)^3(e_g^+)^1$	Jahn–Teller
$3d^4_{LS}$		$^3T_1$	$(t_{2g}^+)^3(t_{2g}^-)^1$	3d spin–orbit
$3d^5_{HS}$	^{6}S	$^6A_1$	$(t_{2g}^+)^3(e_g^+)^2$	–
$3d^5_{LS}$		$^2T_2$	$(t_{2g}^+)^3(t_{2g}^-)^2$	3d spin–orbit
$3d^6_{HS}$	^{5}D	$^5T_2$	$(t_{2g}^+)^3(e_g^+)^2(t_{2g}^-)^1$	3d spin–orbit
$3d^6_{LS}$		$^1A_1$	$(t_{2g}^+)^3(t_{2g}^-)^3$	–
$3d^7_{HS}$	^{4}F	$^4T_1$	$(t_{2g}^+)^3(e_g^+)^2(t_{2g}^-)^2$	3d spin–orbit
$3d^7_{LS}$		^2E	$(t_{2g}^+)^3(t_{2g}^-)^3(e_g^+)^1$	Jahn–Teller
$3d^8$	^{3}F	$^3A_2$	$(t_{2g}^+)^3(e_g^+)^2(t_{2g}^-)^3$	–
$3d^9$	^{2}D	^2E	$(t_{2g}^+)^3(e_g^+)^2(t_{2g}^-)^3(e_g^-)^1$	Jahn–Teller

[a] If the ligand field exceeds the exchange splitting a low-spin state is formed. A T-symmetry ground state is susceptible to 3d spin–orbit coupling and an E-symmetry state is affected by a Jahn–Teller splitting (see next section).

To obtain the 2p X-ray absorption spectra the calculated line spectrum is broadened with a Lorentzian broadening to simulate life-time effects and a Gaussian broadening to simulate the resolution function of the experiment. Figure 22, reproduced from [Deg91t], shows the comparison for MnO. Good agreement is obtained with the atomic values of the Slater integrals and a ligand field splitting of 0.8 eV.

The transition from a high-spin to a low-spin ground state is directly visible in the spectral shape, because a different final state multiplet is reached. This is illustrated for Co^{3+} in Fig. 23. A series of calculations for all common ions has been published in [Deg90b]. In these calculations the 3d spin–orbit coupling has been set to zero. A series of calculations in which the 3d spin–orbit coupling has been included has been published in [Laa92c]. The criterion whether or not 3d spin–orbit coupling is important will be discussed in the next section.

Table 7
Interactions determining the high-spin or low-spin ground state of $3d^4$ to $3d^7$ configurations in octahedral symmetry

State	Criterion	Simplified criterion	Transition point/eV
$3d^4$	$3J_{te}$	$3J$	2.4
$3d^5$	$3J_{te} + \frac{1}{2}J_{ee} - \frac{1}{2}J_{tt}$	$3J$	2.5
$3d^6$	$3J_{te} + \frac{1}{2}J_{ee} - \frac{3}{2}J_{tt}$	$2J$	1.8
$3d^7$	$3J_{te} + J_{ee} - 2J_{tt}$	$2J$	1.9

5.1.4. 3d Spin–orbit coupling

In this section the treatment of the 3d spin–orbit coupling in the ligand field multiplet program is

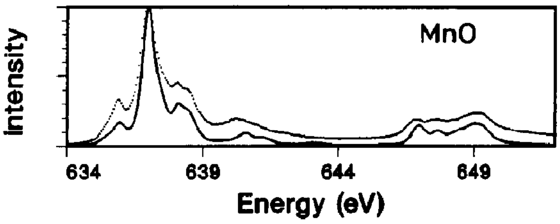

Fig. 22. Manganese 2p X-ray absorption spectrum of MnO (dotted) compared with a ligand field multiplet calculation (solid line). The value of 10Dq is 0.8 eV.

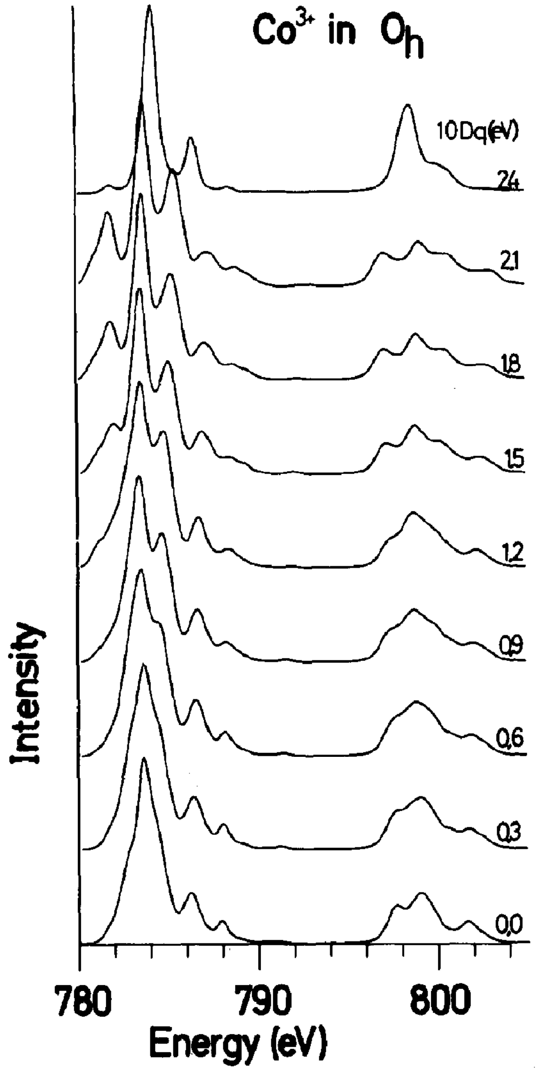

Fig. 23. Co^{3+} $3d^7$ to $2p^5 3d^8$ transition. 10Dq is increased from 0.0 to 2.4 eV. A high-spin to low-spin transition occurs between 2.1 and 2.4 eV.

discussed and arguments are given concerning the effects of the spin–orbit coupling.

For the projection of the spin symmetries from spherical to cubic symmetry the same branching rules as for the angular momentum apply. Compounds with an even number of 3d electrons have an integer spin and the branching rules as given in Table 5 can be used. For compounds with an odd number of 3d electrons the spin will be 1/2, 3/2 or 5/2. The atomic $S = 1/2$ state projects to E_1 symmetry in a cubic ligand field. The notation as used by Sugano, Tanabe and Kitamura is followed [Sug70]. Similarly $S = 3/2$ projects to G symmetry and $S = 5/2$ is split into states of E_2 symmetry and of G symmetry

If the 3d spin–orbit coupling is taken into consideration, the overall symmetry of the spin plus the angular momentum must be determined. In spherical symmetry this is accomplished by multiplying L with S to all possible J values. Similarly in cubic symmetry the irreducible representations of the spin must be multiplied with those of the angular momentum. Table 8 gives the results for the low-spin and high-spin configurations of all $3d^N$ states. It can be seen that in cubic symmetry the multiplicity of the spin $(2S+1)$ does not directly relate to the total number of states. For example the $^5T_2$ state is split into six (and not in five) different states. The ligand field multiplet program uses in all cases the branchings for both spin and angular momentum and thus the overall symmetries of the states. If the 3d spin–orbit coupling is neglected all states with the same angular symmetry are degenerate because the spin in itself does not influence the energy of the state.

3d Spin–orbit coupling does not affect states of A_1 or A_2 symmetry, but it has a large effect on partly filled t_{2g} states, that is the ground states of the $3d^1$, $3d^2$, $3d^4_{LS}$, $3d^5_{LS}$, $3d^6_{HS}$ and $3d^7_{HS}$ symmetries, as indicated in Table 6. The effects on states of E symmetry are small. The difference in effect on T_2 states and E states respectively is related to the way in which a t_{2g} and an e_g wavefunction respectively are built from the atomic wavefunctions. As has been shown in Table 4 an e_g wavefunction is generated from $m_l = 0$ and 2 (or −2) functions. A spin–orbit coupling effect can only affect states which differ by unity in their m_l value. This means that the 3d spin–orbit coupling (ζ_{3d}) is quenched in the case of e_g states. In the case of t_{2g} states this quenching does not occur and if only the t_{2g} states are taken into account they can be approximated with an effective $L = 1$, hence a $^2T_2$ state is split in two, with the eigenvalues $-\frac{1}{2}\zeta$ and ζ and intensity ratio 1 : 2, analogous to the

Table 8
Effects of spin–orbit coupling on $3d^N$ ground state

State	Symmetry	Spin projection	Overall symmetry	Degeneracy
$3d^1$	$^2T_2$	E_1	E_2+G	2
$3d^2$	$^3T_1$	T_1	$E+T_1+T_2+A_1$	4
$3d^3$	$^4A_2$	G	G	1
$3d^4_{HS}$	^5E	$E+T_2$	$A_1+A_2+E+T_1+T_2$	5
$3d^4_{LS}$	$^3T_1$	T_1	$E+T_1+T_2+A_1$	4
$3d^5_{HS}$	$^6A_1$	$G+E_2$	$G+E_2$	(2)
$3d^5_{LS}$	$^2T_2$	E_1	E_2+G	2
$3d^6_{HS}$	$^5T_2$	$E+T_2$	$A_1+E+2T_1+2T_2$	6
$3d^6_{LS}$	$^1A_1$	A_1	A_1	1
$3d^7_{HS}$	$^4T_1$	G	E_1+E_2+2G	4
$3d^7_{LS}$	^2E	E_1	G	1
$3d^8$	$^3A_2$	T_1	T_2	1
$3d^9$	^2E	E_1	G	1

$2p_{3/2}$ and $2p_{1/2}$ splitting for 2p spin–orbit coupling [Sug70].

To describe the full action of 3d spin–orbit coupling the non-diagonal matrix elements, coupling t_{2g} and e_g states have to be included. It can be shown that this affects the e_g states by $(3/2)(\zeta^2/\mathscr{D})$, as compared to the t_{2g} states which were affected by $(3/2)\zeta$. For a typical 3d transition metal compound $\zeta_{3d} \approx 70$ meV and the cubic ligand field splitting $\mathscr{D} \approx 1.0$ eV. This gives splittings of about 100 meV (≈ 1200 K) for T symmetry ground states and of about 8 meV (≈ 100 K) for E symmetry ground states. This implies that for room temperature experiments 3d spin–orbit coupling should be included for T symmetry ground states, but can be neglected for E symmetry ground states. Hence as a first approximation to the experimental spectra one can use the results of [Laa92c] for T symmetry ground states and the results of [Deg90b] for E symmetry ground states. For A symmetry ground states the results are identical. In practice it will in most cases be necessary to make more precise comparisons as for example for T symmetry ground states there will be configurations at energies of about 300 K, which implies that a Boltzmann distribution over the states must be included. (E-symmetry ground states are susceptible to Jahn–Teller distortions, see next section.)

Because the spin–orbit coupling strength increases with the atomic number, the best case to investigate the effect of 3d spin–orbit coupling is the $3d^7_{HS}$ configuration, as is for example found in CoF_2 and CoO. From Table 8 it is found that if 3d spin–orbit coupling is included, the $^4T_1$ ground state of the $3d^7_{HS}$ configuration splits in four states of E_1, E_2 and two times G symmetry. The multiplet calculation with the atomic value of the 3d spin–orbit coupling (83 meV) and a cubic ligand field strength of 0.9 eV gives the four states at energies of respectively 0 (E_2), 44 meV (G), 115 meV (G^*) and 128 meV (E_1). Figure 24 gives the ligand field multiplets of the $3d^7_{HS}[\Gamma_i] \rightarrow 2p^5 3d^8$ transition for the four different symmetries. Given this spread in the initial states, the room temperature (25 meV) spectrum is dominated by the lowest state of E_2 symmetry, with a 17% contribution of the first excited state of G symmetry.

Figure 25 gives the theoretical spectra of the ground state E_2 spectrum (b), the 300 K spectrum (c) and the spectrum under neglect of 3d spin–orbit coupling (a). It is clear that the inclusion of the 3d spin–orbit coupling enhances the agreement

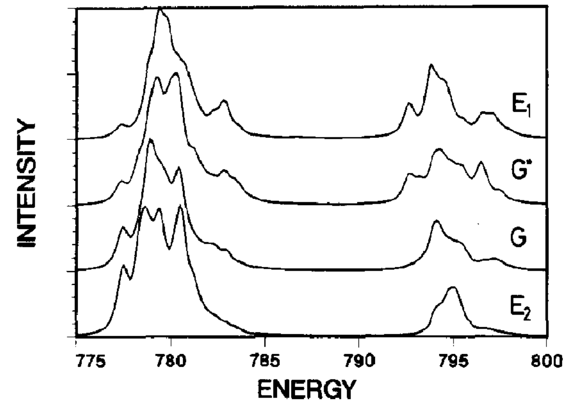

Fig. 24. Theoretical X-ray absorption spectra for the $3d^7_{HS}[\Gamma_i] \rightarrow 2p^5 3d^8$ transition for the four different 3d spin–orbit split symmetries of the $^4T_1$ ground state. The respective symmetries are from bottom to top: E_2, G, G^* and E_1.

considerably. The good agreement between theory and experiment makes it possible to determine the energies of the low-lying excited states from an analysis of the experimental spectrum, preferably measured for a series of temperatures. Hence it can be concluded that temperature dependent X-ray absorption experiments can reveal the magnitude of the 3d spin–orbit coupling, which might be different from the atomic value [Deg91t, Tan92a].

5.1.4.1. The effects of 3d spin–orbit coupling on the high-spin–low-spin transition. In the discussion of the high-spin versus low-spin states it has been assumed that the spin state of a system is that state with the lowest energy, implying that at the crossing point (in the Tanabe–Sugano diagram) the ground state is changed suddenly from high-spin to low-spin. However it turns out that if 3d spin–orbit coupling is included, this will couple high-spin states with low-spin states. This implies that the transition between high-spin and low-spin can be gradual with close to the transition point an admixture of both high-spin and low-spin symmetries. This situation will be discussed for $3d^4$. From Table 6 it can be seen that the high-spin state has ^5E symmetry and is susceptible to Jahn–Teller distortions, while the low-spin state has $^3T_1$ symmetry and is susceptible to 3d spin–orbit coupling. To simplify the problem the ligand field multiplet calculations are performed in octahedral symmetry

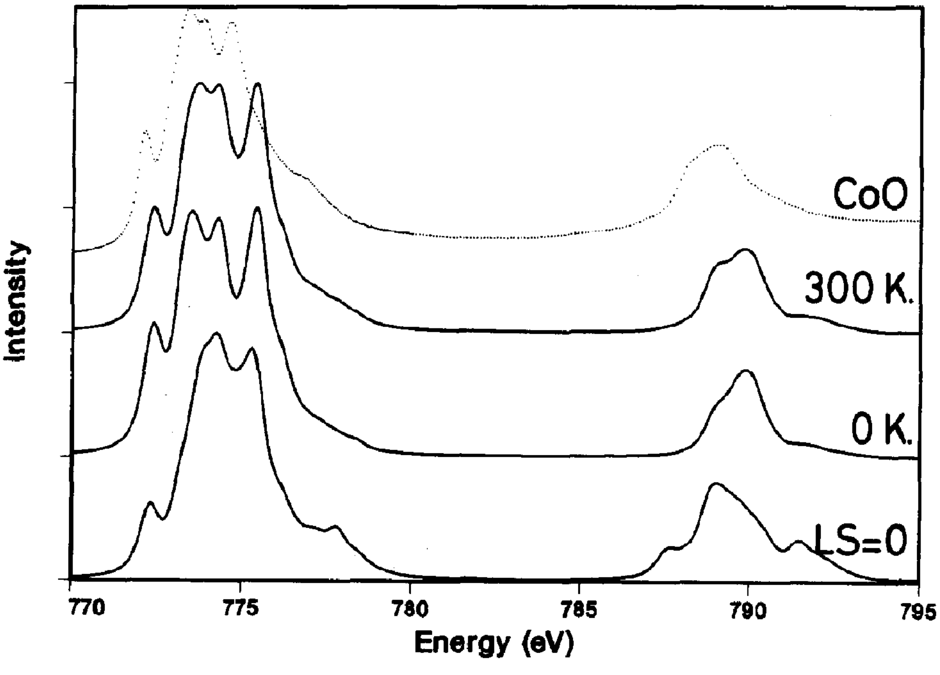

Fig. 25. Comparison of the theoretical spectra of (from bottom to top) (curve a) the spectrum under neglect of 3d spin–orbit coupling, (curve b) the ground state, and (curve c) the spectrum at 300 K, with the experimental spectrum of CoO.

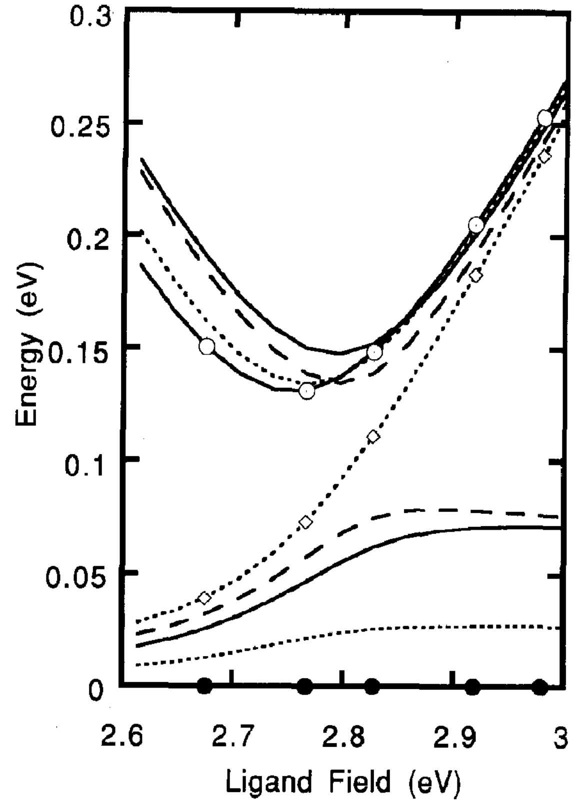

Fig. 26. Distribution of states in the 3d^4 initial state showing the effects of 3d spin–orbit coupling at the high-spin to low-spin transition. On the left hand side the symmetries are from bottom to top: (high spin) A_1, T_1, E, T_2, A_2; (low spin) A_1, T_1, T_2, E.

and effects of the Jahn–Teller distortion have been neglected. The Slater integrals have been reduced to 75% for dd interactions and to 88% for pd interactions and the atomic 3d spin–orbit coupling has been used.

Figure 26 shows the energy levels for ligand field strength between 2.6 and 3.0 eV. The high-spin ^5E configuration splits after inclusion of the 3d spin–orbit coupling into five states of respectively A_1, A_2, T_1, T_2 and E symmetry. Likewise the $^3T_1$ configuration splits into four states of A_1, T_1, T_2 and E symmetry. For a ligand field of 2.6 eV ^5E symmetry is at lowest energy, while for 3.0 eV the system has a low-spin $^3T_1$ ground state. It can be observed directly that a T symmetry state is affected more by the 3d spin–orbit coupling as discussed above. At room temperature (0.025 eV) the high-spin ground state (10Dq < 2.6 eV) will be approximately given as a statistical distribution of the five states. If the cubic ligand field is increased to about 2.8 eV the lowest five states do still relate to the high-spin configuration, but the splittings between the states are enlarged due to considerable admixture of $^3T_1$ character. Note that the state of A_2 symmetry is only contained in the high-spin symmetry state and is not subject to admixture. Hence it can be used as an indication of the position of the high-spin configuration without interaction with the low-spin configuration.

Some 3d^4 systems include $LaMnO_3$, and $LiMnO_2$, which are considered to be high-spin (^5E) insulators, [Bog57, Bog75, Goo63, Goo71], $SrFeO_3$, a low-spin or intermediate spin conductor [Gle85, Mcc65], and $CaFeO_3$, a high-spin compound probably subject to partial charge disproportionation below $T = 290$ K [Gle85]. Though $LiMnO_2$ probably has a high-spin ground state, it can be expected to be not too far from the transition point, in which case it can be affected by 3d spin–orbit coupling. Figure 27 gives the spectral shapes found from the ligand field multiplet calculations for, from bottom to top, the low-spin $^3T_1$ configuration, the high-spin ^5E configuration and the mixed spin state. The experimental spectrum of $LiMnO_2$ is shown with dots.

With regard to a further optimization of the spectral shape there are several factors to be considered. The Slater integrals have been set roughly to reduced values and the symmetry distortion related to the Jahn–Teller effect has been neglected. The Jahn–Teller distortion can have effects on the spectral shape in the range of about 1 eV and might account for the spectral mismatch. Also if the Jahn–Teller distortion is accounted for, the 3d spin–orbit coupling effects still have to be taken into account close to the high-spin to low-spin transition point (in reduced symmetry) [Deg91t].

5.1.5. Effects of non-cubic symmetries

Another type of low-energy splitting of the ligand field multiplet is caused by distortions from cubic symmetry. Large initial state effects of

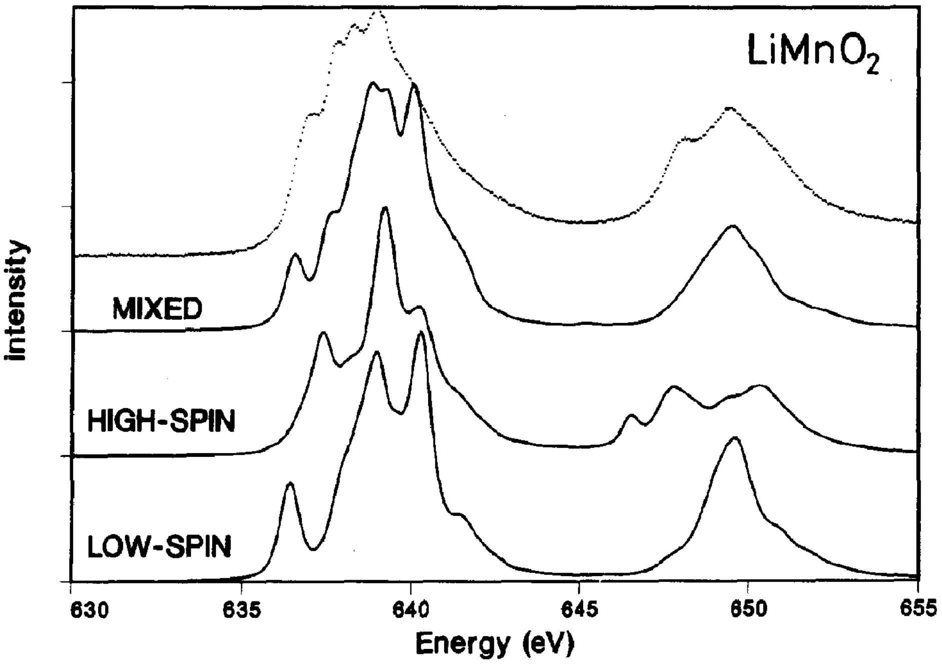

Fig. 27. Crystal field multiplet calculation for the 2d X-ray absorption spectrum of the low-spin, high-spin and mixed (or intermediate) spin ground state for trivalent ($3d^4$) manganese atoms. The top spectrum is the 2p X-ray absorption spectrum of $LiMnO_2$.

lower symmetries are found if the cubic $3d^N$ ground state contains a partly filled e_g band. Elongation of the z axis lifts the degeneracy of the e_g orbitals; the Jahn–Teller effect. Degenerate e_g states are found in systems with $3d^4_{HS}$, $3d^7_{LS}$ and $3d^9$. The effects on the $3d^4_{HS}$ state occur for divalent chromium and trivalent manganese. The tetragonal distortion of the $3d^9$ configuration is well known, for example in the CuO-based high T_c superconductors.

Final state effects of lower symmetries can be important for all $3d^N$ configurations if the site geometry is strongly distorted from cubic. Final state effects of lower symmetries are best observable for $3d^0$ compounds due to their simple spectral shape in which all multiplet transitions are resolved as individual peaks. In rutile (TiO_2) the site symmetry of titanium is D_{2h} and the effective configuration is $3d^0$. Effects of the symmetry reduction can be expected for the $2p^5e_g^1$-like states and indeed the rutile spectrum clearly shows a splitting of the e_g peak which is reproduced in a calculation for D_{4h} symmetry [Deg90a].

Similar final state effects of lower symmetries are expected for systems with a partly filled 3d band. However it can be expected that ligand field effects, including distortions from cubic symmetry, are more important for early 3d compounds. The important parameters are the radial extent of the wavefunctions of the 3d electrons r_ϕ and the inter-atomic distances R. It is known that the ratio r_ϕ/R decreases in the 3d metal series [Fug88, Mar85t], and especially in systems with one or more occupied e_g orbital, relatively large inter-atomic distances are found [Wis72]. Crystal field effects scale with r_ϕ/R; hence effects of lower symmetries (and also the cubic ligand field strengths) are largest for the early 3d metals.

5.1.5.1. Projection rules for lower symmetries. The ligand field multiplet program can handle any point group symmetry. As an example, the branching rules of a D_{2h} point group are given in Fig. 28. The projection from spherical symmetry to D_{2h} symmetry is accomplished in three steps. First the symmetry is reduced to cubic, in the second step

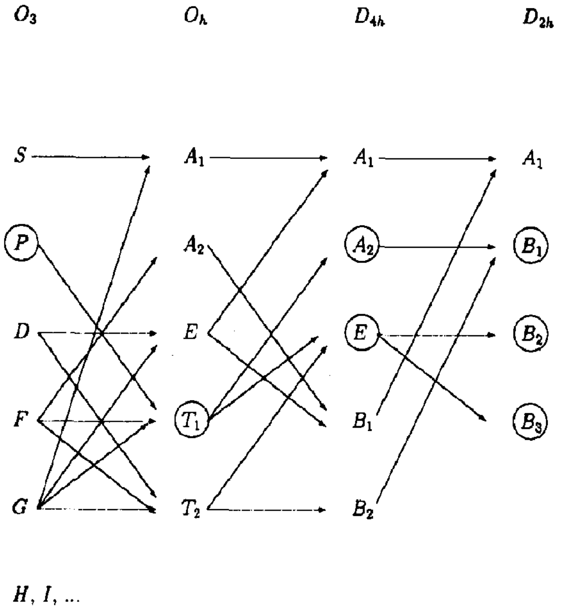

Fig. 28. Schematic branchings from O_3 symmetry (atomic) to D_{2h} symmetry, via O_h and D_{4h}. Encircled are all representations which can be reached from atomic P symmetry.

the cubic (O_h) to tetragonal (D_{4h}) symmetry reduction is included and the third step goes to D_{2h} symmetry. The necessary extra ligand field terms in the Hamiltonian can be deduced directly from this figure: the Hamiltonian has A_1 symmetry, thus all branchings to A_1 symmetry take part in the Hamiltonian. For cubic symmetry, apart from the S state, the G state projects to the A_1 state. This $G \rightarrow A_1$ branching describes the inclusion of a cubic ligand field term in the Hamiltonian. Similarly for tetragonal symmetry the cubic E state projects to the A_1 state. In turn the cubic E state has two parent states in spherical symmetry, hence there are two additional paths $D \rightarrow E \rightarrow A_1$ and $G \rightarrow E \rightarrow A_1$. In other words there are two additional ligand field parameters in the Hamiltonian of D_{4h} symmetry. The total number of ligand field parameters of a specific point group can be found directly from the total number of different paths leading to the A_1 symmetry state. It should be noticed that the "route" to reach the D_{2h} point group is not uniquely defined, and instead of the route via O_h (as given in Fig. 28) an alternative route via $D_{\infty h}$ can be chosen. The choice of the route determines the meaning of the ligand field parameters and because of the central place of the cubic ligand field strength, in general the route via O_h symmetry is used. The different branchings for all point groups and also all possible choices for the routes to reach a specific point group are given in [But81].

Systems with lower symmetries are expected to show large linear dichroism effects as will be discussed in Section 6.3. This can be deduced directly from Fig. 28 as the dipole operator is split in D_{4h} and lower symmetries.

5.2. *When are multiplets important?*

If multiplets are important an absorption edge is preferably described with an atomic approach as described above. In that case the short range models will be the most appropriate starting point because also the Hubbard U, directly related to the F^0_{dd} Slater integral, will be important. In contrast if multiplet effects are small, the band structure (or multiple scattering) approach is most appropriate because of its ab initio description of hybridization.

There is a simple rule for the importance of multiplets:

> Multiplets are important in the case of a direct transition to a partly filled d or f band.

Thus the p edges of transition metals and their compounds are affected by multiplet effects, whereas the s edges are not affected. For rare earths and actinides it means that their d edges are affected, in contrast to their s and, in first approximation, p edges. This rule can be deduced from the values of the atomic Slater integrals. Table 9 gives the values for the edges of iron, ruthenium and osmium. For comparison the values for the 3d edge of terbium are given. These values are expected to be only marginally screened in solid transition metals and their compounds. Depending on the obtainable resolution, mainly determined by the core hole life-time, the multiplet effects are observable. From Table 9 it is clear that

Table 9
Slater integrals as calculated with the HF for the d^5 transition metal ions Fe^{3+}, Ru^{3+} and Os^{3+}

Ion	Edge	Excitation energy/eV	Core hole spin–orbit/eV	F^2_{pd}/eV	G^1_{pd}/eV	G^3_{pd}/eV
Fe^{3+}(3d)	3p	[60]	(< 1)	13.1	16.2	9.9
	2p	[700]	(13)	7.5	5.5	3.2
	1s	[7150]	–	–	0.3	–
Ru^{3+}(4d)	4p	[50]	(3)	9.6	12.1	7.4
	3p	[470]	(22)	4.6	1.0	1.0
	2p	[2900]	(130)	2.1	1.8	1.0
Os^{3+}(5d)	5p	[52]		11.4	18.1	11.6
	4p	[510]		9.8	2.4	2.4
	3p	[2860]	(345)	5.4	1.1	1.2
	2p	[11630]	(1514)	3.1	2.7	1.6
Tb^{3+}(4f)[a]	3d	[1258]	(13)	8.04 3.77 (F^4)	5.79	3.40 3.35 (G^5)

[a] For comparison the 3d4f values of Tb^{3+} are given.

the iron 2p and 3p edges in particular will be dominated by multiplet effects.

5.2.1. Core hole spin–orbit coupling and branching ratios

As discussed in detail by Thole and van der Laan [Laa88a, Laa88b, Laa90a, Laa90d, Tho88b, Tho88c], the interplay between core hole spin–orbit coupling and core hole Slater integrals can give rise to non-statistical branching ratios.

In a single electron picture the overall intensity of the L_3 and the L_2 edges has a ratio of 2 : 1, as their J values are respectively 3/2 and 1/2 and the overall intensity is given by $(2J + 1)$ [Cow81]. This statistical value is found if the magnitude of pd Slater integrals is much smaller than the 2p spin–orbit coupling. From Table 9 it is evident that this is the case for all deep core levels. However for the 2p edge of iron the 2p spin–orbit coupling and the pd Slater integrals are of the same order of magnitude. This implies that the statistical branching ratio will be affected. In Fig. 29 the branching ratios are given for the divalent 3d transition metal ions in a cubic ligand field ($\mathscr{D}$) of 1 eV (the values are taken from [Laa88a]). Although the value of the branching ratio is mainly determined by the 2p spin–orbit coupling and the pd Slater integrals, the cause for a particular value is the symmetry of the ground state.

The ground state symmetry is determined by the dd Slater integrals (Hund's rules), the ligand field strength ($\mathscr{D}$) and the 3d spin–orbit coupling (ζ_d), as discussed above. An important factor for the branching ratio is the spin state, caused by the

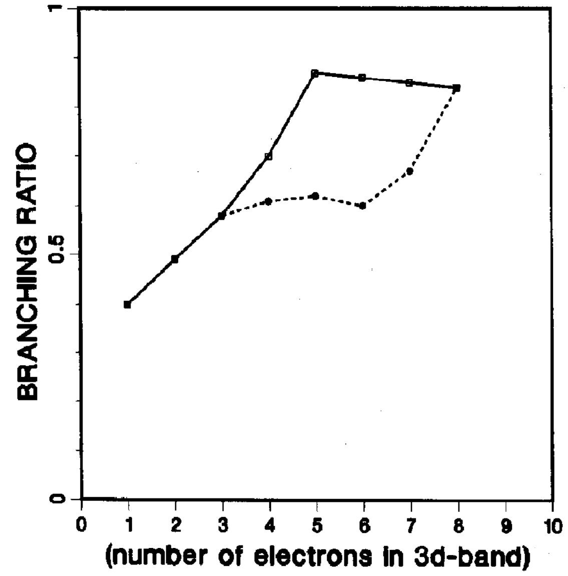

Fig. 29. Branching ratio of the divalent 3d transition metal ions as predicted from a ligand field multiplet model. High spin, squares and solid line; low spin, circles and dashed line.

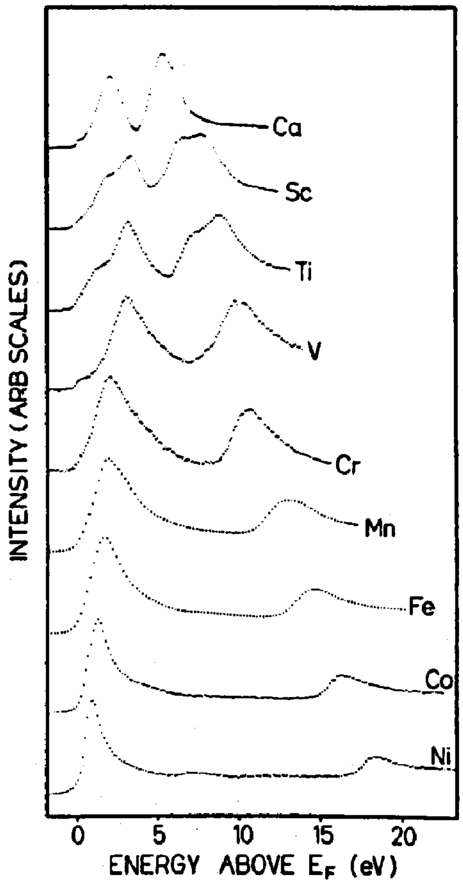

Fig. 30. The 2p X-ray absorption spectra of the 3d transition metals (from [Fin85]).

interplay of dd Slater integrals ("exchange") and ligand field strength. Within a particular high-spin or low-spin state the precise values of the ligand field strength and the 3d spin–orbit coupling have only a small effect on the branching ratio. This influence can be approximated as $\zeta_d/\mathscr{D} \approx 0.05/1.0$ [Laa90d, Tho88b]. This implies that for solids the potential influence of 3d spin–orbit coupling on the branching ratio is limited due to a finite ligand field strength. In the case of atoms (ions) 3d spin–orbit coupling can have large effects, such as for divalent nickel ions where 3d spin–orbit coupling causes a transition to be forbidden for right circularly polarized light [Laa91].

Also the branching ratios of the 2p spectra of the 3d transition metals are non-statistical as can be checked in Fig. 30. In the case of metals the ground state symmetry is basically described by band structure methods, where the Slater integrals (Hund's rules) enter under the heading of "orbital polarization". All metals can be assumed to contain a ground state symmetry analogous to a high-spin symmetry in 3d metal complexes and it is expected that in first approximation the branching ratios follow the trend given in Fig. 29.

These interplay effects between core hole spin–orbit coupling and core-valence Slater integrals are different for shallow core levels such as the iron 3p edge, which has a very small core hole spin–orbit coupling and is completely dominated by the Slater integrals. Deep core levels, such as ruthenium $L_{2,3}$ edges, will have a statistical branching ratio as they are separated by a large energy and no intensity can be transferred by the core hole Slater integral. However they still do affect the spectral shape of the individual edges (by interplay with the ligand field splitting), which causes small differences between the L_3 and L_2 edges [Deg●●].

5.3. The short range model extended for multiplets

The short range (Anderson impurity) model has been extended to include multiplets by the groups of Kotani and Jo [Ima89a, Ima89b, Ima90, Jo88a, Jo88b, Jo88c, Jo89a, Kot89]. Its first application was to cerium compounds, but attention has since partly been shifted to transition metal compounds. The extra ingredient of its application to transition metal compounds is the inclusion of the cubic ligand field as has been discussed above. The inclusion of multiplets implies that for the localized configuration not a single state is included, but a series of states with different energy (ε_d) and symmetry (Γ) belonging to the ligand field multiplet. For the Hamiltonian of the short range model used this implies

$$\varepsilon_d n_d \Rightarrow \sum_{\Gamma} \varepsilon_{d\Gamma} n_{d\Gamma}$$

In general a single metal with 4 or 6 ligand atoms is described and the band-like states are also written out in the symmetries of the localized 3d states. In practice this is accomplished within the ligand field multiplet model, by exciting a 2p electron to a "delocalized" *n*d state, representing the ligand band. In this manner the symmetries of the band-like states are more or less automatically formulated in the symmetry of the localized 3d states. The energy of these delocalized states ($\varepsilon_{pk\Gamma}$), relative to the localized states, is then set according to the charge transfer parameter

$$\sum_k \varepsilon_{pk} n_{pk} \Rightarrow \sum_{k,\Gamma} \varepsilon_{pk\Gamma} n_{pk\Gamma}$$

The interaction-terms t_{pd} have to be given for all symmetries (Γ)

$$t_{pd} \sum_k (a_d^{\dagger} a_{pk} + a_{pk}^{\dagger} a_d) \Rightarrow \sum_{\Gamma} t_{pd\Gamma} \times \sum_k (a_{d\Gamma}^{\dagger} a_{pk\Gamma} + a_{pk\Gamma}^{\dagger} a_{d\Gamma})$$

The U-term is modified to include all higher-order effects and the 3d spin–orbit coupling. Here I will follow the notation used by the groups of Kotani and Jo [Oka92a]

$$U_{dd} n_d n_d \sum_{(4)} g_{dd} a_{d\Gamma_1}^{\dagger} a_{d\Gamma_2} a_{d\Gamma_3}^{\dagger} a_{d\Gamma_4} + \zeta_d \sum_{(2)} \mathbf{ls} a_{d\Gamma_1}^{\dagger} a_{d\Gamma_2}$$

The summation of g_{dd} is over four different symmetries (Γ_i) and the summation of the spin–orbit coupling is over two symmetries. In the final state the multiplet effects caused by the core states are also included

$$\varepsilon_c n_c \Rightarrow \sum_{\Gamma} \varepsilon_{c\Gamma} n_{c\Gamma} + \sum_{(4)} g_{cd} a_{d\Gamma_1}^{\dagger} a_{d\Gamma_2} a_{c\Gamma_3}^{\dagger} a_{c\Gamma_4} + \zeta_c \sum_{(2)} \mathbf{ls} a_{c\Gamma_1}^{\dagger} a_{c\Gamma_2}$$

The term g_{dd} includes the dd Slater integrals F_{dd}^0, F_{dd}^2 and F_{dd}^4 and g_{cd} includes F_{cd}^2, G_{cd}^1 and G_{cd}^3. The total Hamiltonian in the final state then consists of

$$\mathcal{H} = \mathcal{H}_{band} + \mathcal{H}_{3d} + \mathcal{H}_{mu} + \mathcal{H}_{ls} + \mathcal{H}_{mix}(+\mathcal{H}_c + \mathcal{H}_{c.mu} + \mathcal{H}_{c.ls}) \qquad (19)$$

Table 10
The parameters of the short range model as used for the analysis of 2p XPS of the nickel halides, with ^{M} and without inclusion of multiplets

Compound	Charge transfer		Core potential		Coulomb repulsion		Hopping	
	Δ	Δ^M	U_{cd}	U_{cd}^M	U_{dd}	U_{dd}^M	t_{pd}	t_{pd}^M
NiF_2	6.5	4.3	7.0	7.5	5.0	7.3	2.0	2.0
$NiCl_2$	3.6	1.3	7.0	7.5	5.0	7.3	2.0	1.3
$NiBr_2$	2.6	0.3	7.0	7.5	5.0	7.3	2.0	1.4
NiO	7.0	2.0	7.0	7.5	5.0	7.3	2.3	2.0

For the ground state this is a two-state model: a ligand band ($\mathcal{H}_{band}$) and a localized 3d state including its spin–orbit coupling ($\mathcal{H}_{3d} + \mathcal{H}_{mu} + \mathcal{H}_{ls}$). In the final state a core state is added ($\mathcal{H}_c + \mathcal{H}_{c.ls}$) and also its interaction with the 3d state is included ($\mathcal{H}_{c.mu}$). This Hamiltonian has to be solved for the initial state and final state and all transition matrix elements must be calculated, similarly as discussed before.

5.3.1. 2p XPS of the nickel halides

An important confirmation of the usefulness of the short range (Anderson impurity) model for the description of core spectroscopies is the description of the 2p XPS spectra of the nickel halides [Zaa86a]. No multiplet effects have been included and the description of the short range model as outlined in Section 4.3 is followed. The parameters as used are collected in Table 10. An equivalent analysis has been given in [Par88]. The ground state of all nickel halides is formed by a linear combination of $3d^8$ and $3d^9\underline{L}$ character. The $3d^{10}\underline{L}\underline{L}'$-states are positioned at high energy ($U_{dd} + 2\Delta$). U_{dd} is basically determined by the cation which is Ni^{2+} in all cases. The same holds for U_{cd}. The hopping is determined from comparison to experiment. The t_{pd} given is the value for the e_g orbitals: $t_{pd} = \langle e_g|\mathcal{H}|\underline{L}(e_g)\rangle$. The value for the t_{2g} orbitals is smaller by a factor of two [Mat72a]. The effective hopping, denoted as V_{eff} in [Kot92], is $\sqrt{n_h} t_{pd}$ (with the number of holes (n_h) equal to 2). The value of Δ decreases from NiF_2 to NiI_2 and basically determines the

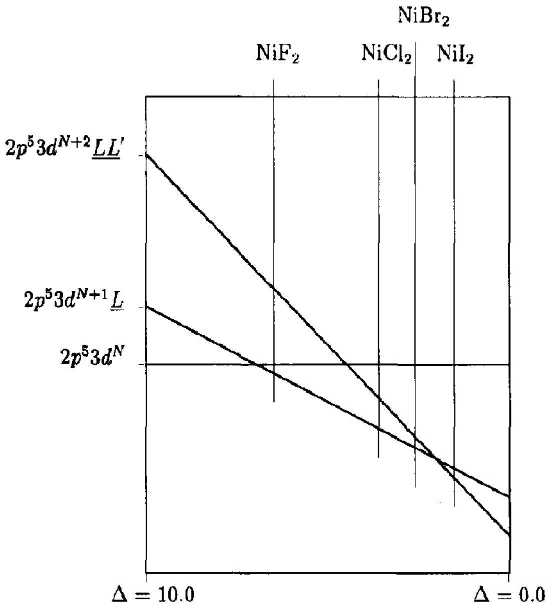

Fig. 31. The final state electronic configurations in 2p XPS of the nickel halides

ionicity of the system: NiF$_2$ is most ionic and contains only 14% of $3d^9\underline{L}$ character. In the final state of 2p XPS the configurations with extra 3d electrons are pulled down and Fig. 31 shows the final state configurations using the short range model without multiplets. The final state of NiF$_2$ contains close to degenerate d^8 and d^9 configurations, and the other three halides have close to degenerate d^9 and d^{10} configurations. This will give two peaks in NiF$_2$ in first approximation related to transitions from the 3d^8 ground state to the bonding and antibonding combinations in the final state. The other halides will have three peaks because the 3d^{10} configurations enter the description.

Okada and Kotani [Kot92, Oka89, Oka90, Oka91a, Oka92a, Oka92b] performed calculations for the nickel halides in which they included the multiplet effects explicitly, as described above. The results of their method, denoted by them as the charge transfer-multiplet (CT-M) method, are given in Fig. 32. Though all features were already described without multiplets, the agreement with experiment has clearly been improved.

The values of U_{dd} and to a lesser extent also U_{cd} increased if multiplets were included. In [Oka92b] calculations have been done with and without multiplets and the values found for NiF$_2$ are larger if the multiplets are included; however the values without multiplets are also larger than the values used in [Zaa86a]. Important values for the final state are the ionic energy positions of the three configurations as sketched in Fig. 31. The positions of d^9 and d^{10} are respectively −0.5 and 2 in [Zaa86a], −2 and 3 in [Oka92b] (without multiplets) and −3.2 and 1 in [Oka92b] (with multiplets). Thus the ordering of the states is not modified, but there is some uncertainty in the relative energy

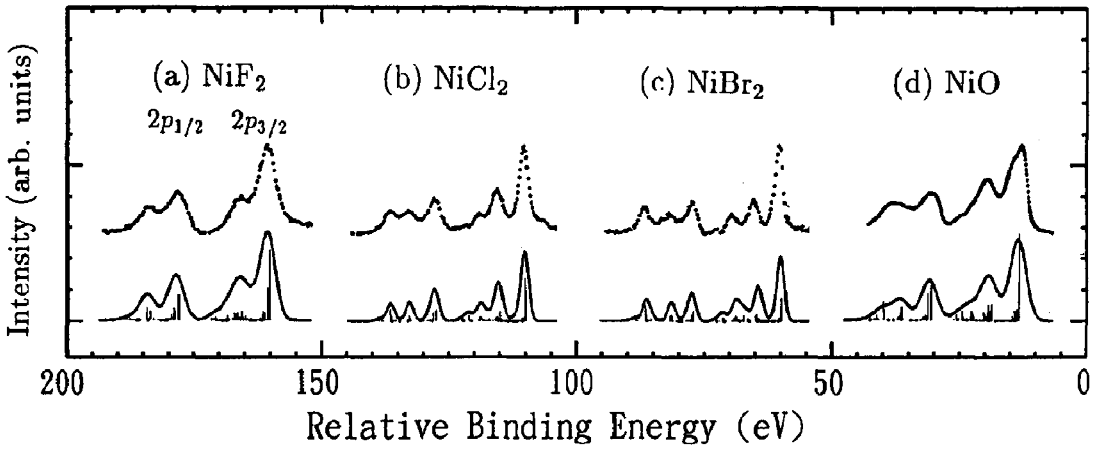

Fig. 32. The 2p XPS spectra of nickel compounds (a, NiF$_2$; b, NiCl$_2$; c, NiBr$_2$; d, NiO) (dots) compared with short range model calculations, including multiplets (bottom, solid line) (from [Oka92b]).

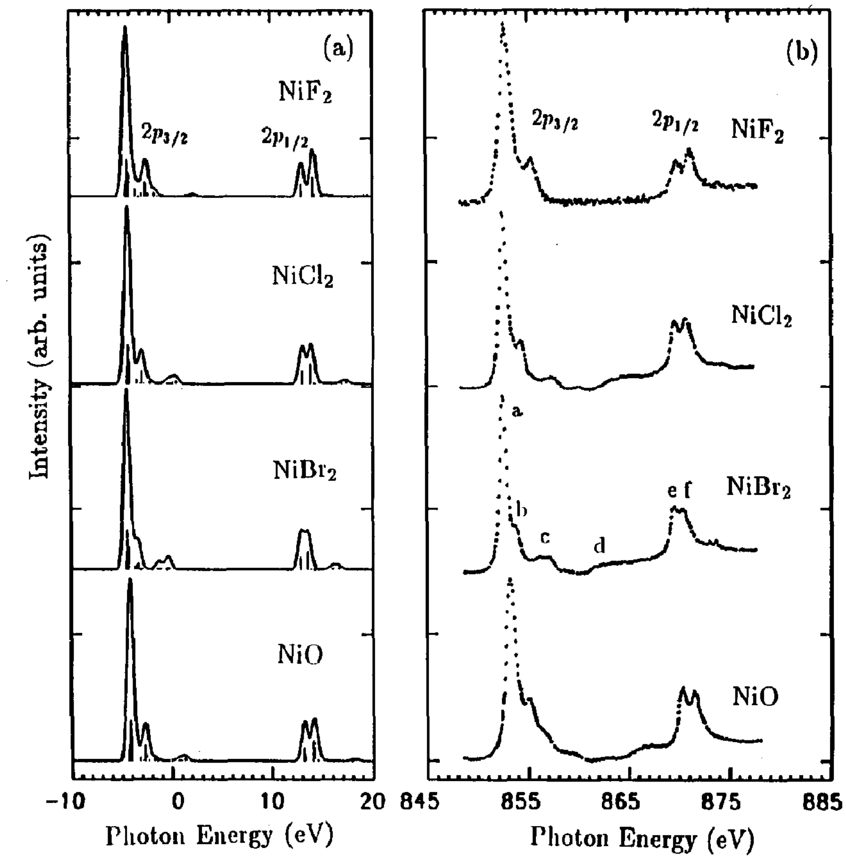

Fig. 33. The 2p XAS spectra of nickel compounds (left) (from [Laa86a]), compared with short range model calculations including multiplets (right) (from [Kot92]).

positions. Okada and Kotani argue that they need larger U values to account also for the spectral shape of the $2p_{1/2}$ spectrum, while in [Par88, Zaa86a] only the $2p_{3/2}$ has been analysed. Also it can be concluded that a smaller value of Δ must be chosen if multiplets are included.

A problem which is not touched in most papers is the additional interactions in the final state. It is assumed that the core hole only will give rise to local interactions, which can be gathered in one parameter U_{cd} [Saw88]. Also the values of the hopping and to a lesser extent U_{dd} need not be identical in the final state [Gun88a, Zaa86a]. This problem is discussed in Appendix A.

Recently the occurrence of non-local contributions to the screening has been shown to be important for 2p XPS of NiO (and in general charge transfer insulators) [Vee93a].

5.3.2. 2p XAS of the nickel halides

The important advantage of the short range model including multiplets, the CT-M model, is that it can also be applied to 2p XAS, which is dominated by multiplets and where in most cases charge transfer effects give rise to relatively small modifications. The 2p XAS spectra of the nickel halides have been measured by van der Laan et al. [Laa86a]. In their analysis they used both the ligand field multiplet model (for NiF_2) and the short range (Anderson impurity) model. Figure 33 shows the CT-M results of [Kot92], with the parameters as given in Table 10. In [Laa86a] a ligand field strength of 1.5 eV was used, while in [Kot92] a ligand field strength of 0.5 eV was used. Additionally the hopping was reduced from 2.0 eV to 1.5 eV in [Laa86a], to account for the difference in the final state. The analysis of [Kot92] gives the best agreement with all spectral shapes. This confirms the fact that although 2p XAS is dominated by ligand field multiplets, the effects of charge transfer remain visible.

If one uses the ligand field multiplets without charge transfer the value of the cubic ligand field is considerably larger because one has effectively to include the difference in hopping between the t_{2g} and e_g states. The fact that $t_{pd\sigma} \approx 2t_{pd\pi}$ causes the largest contribution to the ligand field splitting in the short range model. This effect is not accounted for in the ligand field multiplet analysis and it must be incorporated in the value of 10Dq.

5.3.2.1. Reducing the Slater integrals. As was demonstrated in Section 4.3 in 2p XAS the final state value of Δ is equivalent to the ground state value, which largely excludes charge transfer effects. The main effect of charge transfer is a reduction of the multiplet splitting. This reduction can be applied directly to a ligand field multiplet by reducing the values of the Slater integrals.

Lynch and Cowan used this approach to simulate the $M_{4,5}$ edges of Ce^{3+} and Pr^{3+} [Lyn87]. The hybridization of ligand character $|L\rangle$ into the original atomic $|4f\rangle$ wavefunction was accounted for by reducing the ff Slater integrals by 20% and the df Slater integrals by 10%. Because the core states are not modified in a solid the reduction is about twice as large for valence–valence interaction than for core–valence interactions. The results of Lynch and Cowan [Lyn87] showed a complex reordering of states as a result of the Slater integral reduction.

To test the validity of Slater integral reduction and to compare it with the impurity model, the nickel dihalide spectra have been simulated [Deg91t]. The divalent nickel compounds are simulated as $3d^8 \rightarrow 2p^5 3d^9$ transitions. This presents a special case as the $2p^5 3d^9$ final state contains only a single 3d hole and does not contain any dd correlations. This simplifies the multiplet calculation and, apart from the spin–orbit coupling which is not essential for this problem, only two sets of Slater integrals remain: F^2_{dd} and F^4_{dd} for the initial state and F^2_{pd}, G^1_{pd} and G^3_{pd} for the final state. Furthermore the X-ray absorption spectral shape is not sensitive to the values of the ground state dd integrals as the $^3A_2$ ground state is the sole state of this symmetry and consequently does not mix with any excited state. The only set of parameters which determines the spectral shape is the final state pd Slater integrals. To test the Slater integral reduction they have been reduced stepwise from their atomic values and Fig. 34 shows the corresponding spectral changes. For a cubic ligand field a value of 0.9 eV is used, in agreement with the values determined from optical spectroscopy. (For NiO it is necessary to increase 10Dq to 1.5 eV.)

Reduction of the pd Slater integrals reduces the splitting between the main peak and its high-energy shoulder, a similar effect to that observed in going from NiF_2 to NiI_2. Also the modifications in the L_2 edge are reproduced nicely. From this agreement it can be considered that in the case of the nickel dihalides the Slater integral reduction gives a good account of the main spectral modifications upon increasing hybridization. A difference with the CT-M calculations is that the satellite structure is not reproduced by reducing the Slater integrals. It is important to note that the amount of Slater integral reduction gives an alternative measure of the amount of hybridization. For the halides it is found that whereas the fluoride corresponds to the atomic values, for chloride, bromide and iodide the Slater integrals have to be approximately reduced to respectively 75%, 65% and 25% of their atomic value. This trend is a nice example of the so-called nephelauxatic series obtained from the analysis of optical spectra [Jor62, Jor71].

5.3.3. General results of the short range model for 2p XAS

From the discussion of the nickel halides it is clear that the short range model including multiplets describes all observed features in the 2p X-ray absorption spectra. The trends in the spectral shape in going from fluoride to iodide are reproduced and the satellites are found at about the correct places

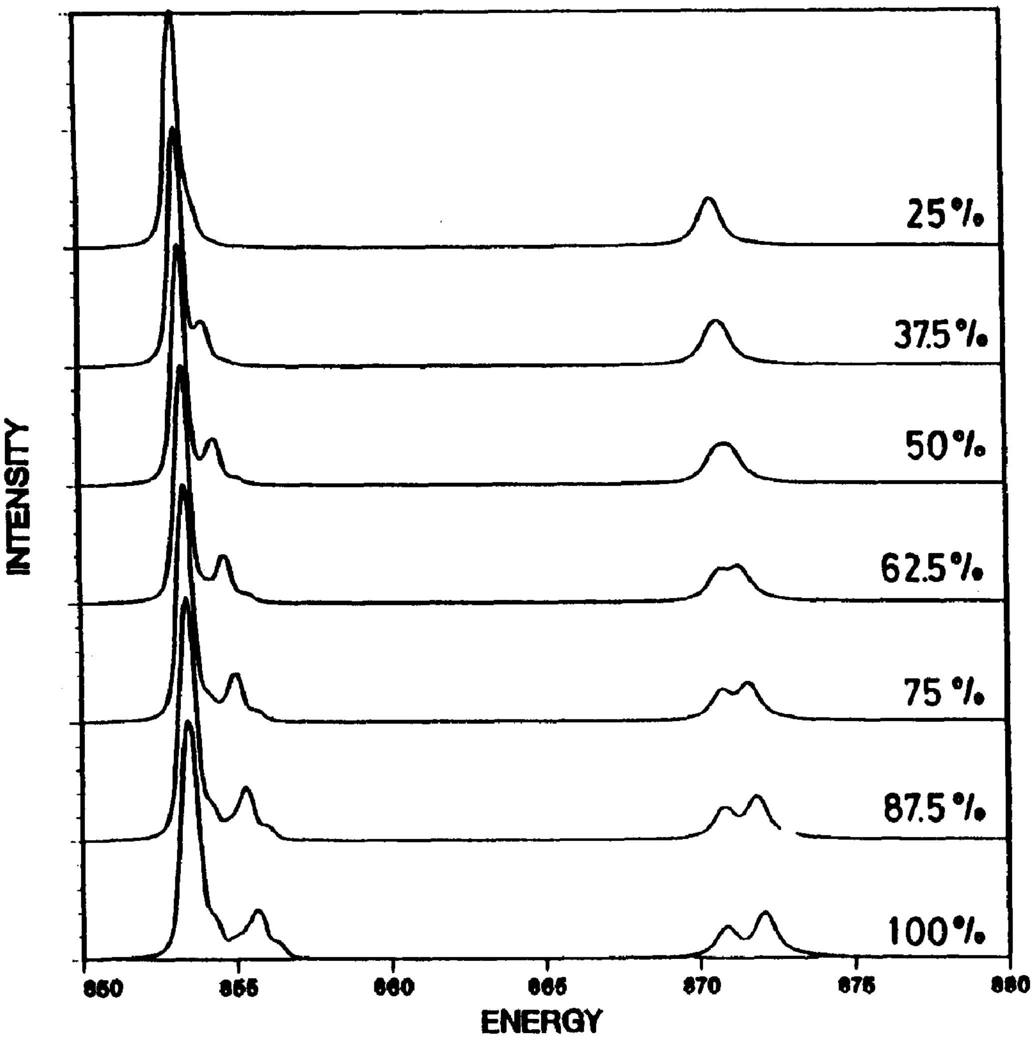

Fig. 34. $3d^8 \rightarrow 2p^53d^9$ ligand field multiplet calculations for divalent nickel. The Slater integrals have been reduced as indicated on the right (100% relates to the atomic values).

with correct intensities. As discussed the satellite structures are small because U_{dd} is about equal to U_{cd}.

A study of the 2p X-ray absorption spectrum (and 2p XAS) of CoO also shows good agreement [Oka92b]. Again there is some spread of the parameters used by different groups [Deg93a]. In particular the values for U_{dd} and U_{cd} as used in [Oka92b] are larger than the other studies. The effect of the short range model is a reduction of the multiplet peaks, which as discussed can also be simulated by Slater integral reduction [Deg93a].

Recently the short range model, including multiplets, has also been applied to early transition metal compounds, and in particular to tetravalent titanium oxides [Oka93]. The early transition metal oxides belong to a different class of materials (see next section) and the parameters of the short range model are different compared to the late transition metal compounds.

From Table 11 it can be seen that for TiO_2, U_{cd} and particularly U_{dd} are smaller, while Δ and t_{pd} are larger. Because the 3d band is empty the effective interaction V_{eff} is $\sqrt{(11/2)}t_{pd}$ compared with

Table 11
The parameters of the short range model as used by Okada and Kotani for the analysis of 2p XAS of various oxides

Compound	Charge transfer, Δ	Core potential, $U_{\underline{c}d}$	Coulomb repulsion, U_{dd}	Hopping	
				$t_{pd\sigma}$	V_{eff}
NiO	2.0	7.5	7.3	2.0	2.7
CoO	2.5	7.0	7.0	2.0	3.0
TiO_2	3.0	6.0	4.0	3.0	7.0

$\sqrt{2}t_{pd}$ for NiO. In general $V_{eff} = \sqrt{n_h}t_{pd\sigma}$, but because six of the ten holes for TiO_2 are of π origin, they must be accounted for with $t_{pd\pi}$, taken as half of $t_{pd\sigma}$. This modifies the calculation of V_{eff} to $\sqrt{(n_\sigma + (1/4)n_\pi)}$. Because of the large hybridization it is better to speak about a bonding and an antibonding combination of $3d^0 + 3d^1\underline{L}$, and similarly for the final state of $2p^5 3d^1 + 2p^5 3d^2 \underline{L}$. As discussed, because of the cancellation effect of $U_{\underline{c}d}$ and U_{dd}, the satellites are weak as most intensity goes to the bonding combination.

In Fig. 35 the result of the short range model calculation is compared with a 2p X-ray absorption spectrum of $SrTiO_3$. The short range model reproduces the spectrum including the satellites correctly. For the main structures there are some changes: the first peak is sharpened compared to the ligand field multiplet model, while the other three main peaks are broadened because of the interaction with the band. In [Oka93] this finding is used to explain the experimentally found broadening. Other sources of broadening are symmetry reduction, which is important in for example $FeTiO_3$ and particularly TiO_2 [Deg90a] and the core hole life-time effects which are different for the different states and to first approximation are expected to increase for states at higher energy, and to be particularly large for the L_2 edge. Also some spectra, such as that for ScF_3 given in Fig. 19, do show an asymmetric first peak in experiment. Additionally it is noted that the ligand field multiplet spectrum of $SrTiO_3$ has a sharp leading peak (as can be checked in Fig. 20). The result given in Fig. 35 is not the optimized result as far as the ligand field multiplet model is concerned.

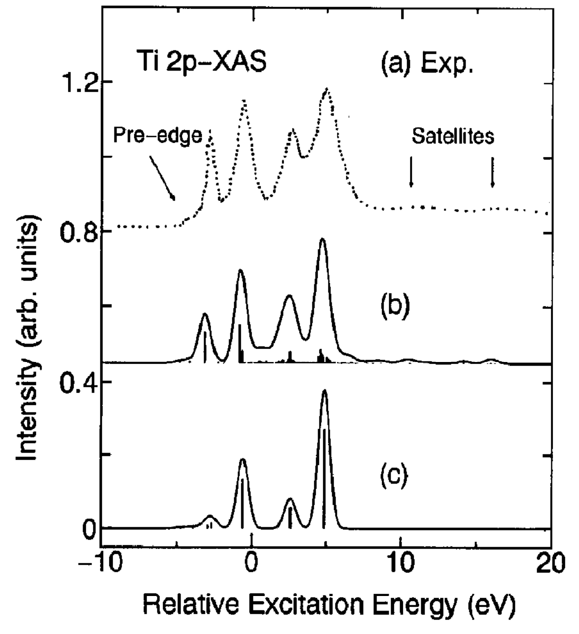

Fig. 35. Titanium 2p X-ray absorption spectrum of $SrTiO_3$ (top, a) compared with a CT-M calculation (middle, b) and a ligand field multiplet calculation (bottom, c) (from [Oka93]).

Thus although the CT-M model is necessary to explain the satellites, for the main peaks the ligand field multiplet calculations can compete with the CT-M results as far as accuracy is concerned, particularly if the Slater integrals are allowed to be reduced (though this is not necessary for systems with empty 3d bands). The main structures, including an accurate account of the intensity ratios, are obtained directly from the ligand field multiplet calculations, as has been discussed in Section 5.1. The CT-M results, though in principle better justified, give only a small improvement and have an important drawback in the basic uncertainties in the parameters used. Particularly if one focuses on the symmetry properties of a system, such as Jahn–Teller distortions, high-spin to low-spin transitions, etc. it will be easier to study them with ligand field multiplets alone, because of computational limitations and also because of the relatively transparent meaning of all parameters used.

The use of the CT-M model implies for the satellites that they are of charge transfer nature, in contrast to the former assignment in terms of polaronic satellites [Boe84, Laa90b, Laa90c]. In fact the use of the charge transfer mechanism is questioned in these studies and the inclusion of an additional excitation mechanism is introduced to explain the relatively large satellites which were hard to explain. A definitive answer to the question of the relative importance of the different possible excitation processes is as yet not found.

5.3.4. *Trends in the short range (Anderson impurity) model parameters*

In this section some of the trends of the parameters in the short range model are discussed. As this is a whole subject of its own only some basic remarks will be made. A first estimate to the configuration averaged (see below) values of $\bar{U}_{dd}$ and $\bar{\Delta}$ can be made from the atomic estimates of the Slater integrals [Zaa86t]: $\bar{U}_{dd} \equiv E(3d^{N+1}) + E(3d^{N-1}) - 2E(3d^N) \approx P_{N+1}F^0(3d^{N+1}) + P_{N-1}F^0(3d^{N-1}) - 2P_NF^0(3d^N) \approx F^0(3d^N)$. In this formulation ligand field effects and the Slater integrals F^2 and F^4 have been omitted for the moment. The calculation is basically a counting of electron-pairs (P_N). The number of electron-pairs of the $N+1$ plus $N-1$ states exceeds the two pairs of the N states by 1 (for all possible N). Hence its value is basically determined by F^0 and the values of $\bar{U}_{dd}$ determined in such a manner gradually increase from about 15 eV for titanium to 18 eV for nickel, because the value of F^0 is gradually increasing with atomic number (Z) throughout the 3d series, mainly as a result of contraction of the 3d states.

For the charge transfer $\bar{\Delta}$ a decreasing trend is found and its value is a gradually decreasing function of Z ($\Delta = E(3d^{N+1}\underline{L}) - E(3d^N) \approx \text{constant} - F^0(3d^N)$). Its value is about 31 eV for titanium and 28 eV for nickel. The parameters determined as such must be corrected for polarization effects in the solid. This effect is accounted for by a constant correction factor for both $\bar{U}_{dd}$ and $\bar{\Delta}$. This brings the values of $\bar{U}_{dd}$ to range from 3 eV for titanium increasing to 6 eV for copper and $\bar{\Delta}$ to range from 7 eV decreasing to 4 eV. For clarity it is noted that this general subtraction procedure is not exactly correct and the values found are not to be taken as quantitatively accurate.

5.3.4.1. Charge transfer versus Mott–Hubbard insulators. It has been shown by Zaanen et al. [Zaa85a] that the two parameters U_{dd} and Δ basically determine the nature of the band gap in transition metal compounds. The lowest states to be filled are always the empty 3d states. If $U_{dd} > \Delta$ the highest states to be excited are ligand p states, and if $U_{dd} < \Delta$ the highest states are the 3d states. This divides the transition metal compounds into two basic categories: charge transer systems versus Mott–Hubbard systems. See for example [Abb93b, Fuj93] for recent discussions on this matter. From the basic trends in $\bar{U}_{dd}$ and $\bar{\Delta}$ it can immediately be concluded that the early transition metal compounds will have a large tendency to be Mott–Hubbard systems and the late transition metal compounds are likely to behave as charge transfer systems.

5.3.4.2. Corrections due to multiplet and ligand field effects. The values for $\bar{U}_{dd}$ and $\bar{\Delta}$ have been determined with the average energies of the respective $3d^N$ configurations. However the determining energies are not these average values, but instead the lowest states in the respective multiplets. As has been discussed at length in Section 5.1 the energies in the ligand field multiplets of transition metal compounds are basically determined by the dd Slater integrals and the cubic ligand field splitting. These corrections can be worked out for the

Table 12
Corrections on $\bar{U}_{dd}$ and $\bar{\Delta}$ from the multiplet (B and C) and crystal field ($\mathscr{D}$) effects[a]

Configuration	Corrections on $\bar{U}_{dd}$		Corrections on $\bar{\Delta}$
$3d^1[^2T_2]$ and $3d^6[^5T_2]$	$-5B$	$(+2/5)\mathscr{D}$	$-5B\,(-2/5)\mathscr{D}$
$3d^2[^3T_1]$ and $3d^7[^4T_1]$	$-5B$	0	$-10B\,(-2/5)\mathscr{D}$
$3d^3[^4A_2]$ and $3d^8[^3A_2]$	$+4B$	$(+5/5)\mathscr{D}$	$-6B\,(+3/5)\mathscr{D}$
$3d^4[^5E]$ and $3d^9[^2E]$	$-8B$	0	$-14B\,(+3/5)\mathscr{D}$
$3d^5[^6A_1]$	$+14B+7C$	$(-5/5)\mathscr{D}$	$+7C\,(-2/5)\mathscr{D}$

[a] For the configurations $3d^6$ and $3d^9$ an extra correction of $+7C$ should be included for Δ. (The corrections for $3d^2$ and $3d^7$ states due to configuration interaction have been neglected.)

respective $3d^N$ configurations [Deg91t, Grf64, Zaa86t] and from this the corrections on $\bar{U}_{dd}$ and $\bar{\Delta}$ can be determined as indicated in Table 12.

Figure 36 gives the rough estimate for U_{dd} and Δ of divalent transition metal compounds based on the linear trend in their mean values and the corrections from ligand field and multiplet effects as indicated in Table 12. The parameters used were $B = 0.1$, $C = 0.4$ and $\mathscr{D} = 1.0$ eV. It should be noted that these determinations of U_{dd} and Δ are only rough indications, merely to account for the trends, and do not have to be taken as absolute. More accurate empirical as well as theoretically determined values are given by, for example, the groups of Sawatzky [Vel90t, Vel91a, Zaa86t], Fujimori [Boc92a, Fuj93], Kotani [Kot92, Oka92b] and Oh [Par88]. As discussed there is a considerable variation in the parameters determined by different groups (with different models).

From Fig. 36 it can be seen that the main effect of the multiplet and ligand field effects is the increase in the values of U_{dd}, and to a minor extent also of Δ, for the $3d^3$, $3d^5$ and $3d^8$ configurations. This effect is superimposed on the respective increasing or decreasing trends. For all late transition metal oxides $U_{dd} > \Delta$, that is they all belong to the class of charge transfer systems. Also they are all insulating as Δ is still relatively large compared with $t_{pd} \approx 2.0$ eV. Mn^{2+} has both very large U_{dd} and Δ

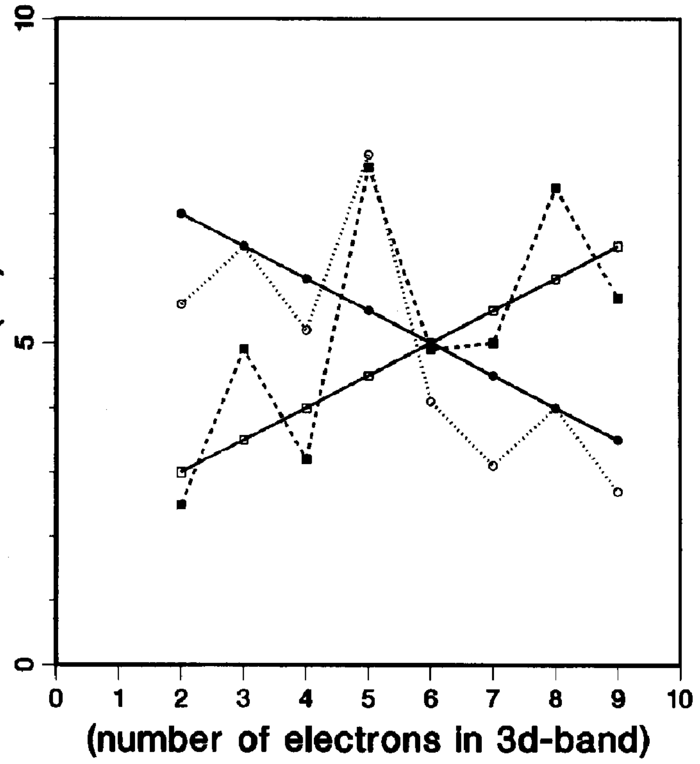

Fig. 36. Estimates for $\bar{U}_{dd}$ (□, solid line), U_{dd} (■, dashed line), $\bar{\Delta}$(●, solid line) and Δ (○, dotted line).

because of the exchange splitting of the five unpaired spins. Because both 3d^3 and 3d^5 are stable configurations, Cr^{2+} is liable to be unstable with respect to charge disproportionation. The band gaps of the early transition metal systems are determined by U_{dd} and they are also predicted to be closer to the metal–insulator transition point. In fact TiO and VO are both metallic.

5.3.4.3. Effects of different ligands. The effect of the ligands has been discussed for the case of the nickel halides and it has been found that the ligand largely determines the value of Δ and in first approximation does not affect U_{dd}. For empirical studies of these trends the reader is referred to the recent papers of Bocquet and co-workers [Boc92a, Boc92b] and Fujimori and co-workers [Fuj93]. $\bar{\Delta}$ is found to increase as, $F > O \approx Cl > Br \approx S > I \approx Se > Te$. Assuming a rigid shift of $\bar{\Delta}$ this effect will bring the late divalent transition metal sulphides and iodides closer to the metallic region and, for example, CoS and NiS are indeed metallic [Wis72]. Because of the large value of Δ of the 3d^5 configurations, the divalent manganese compounds are insulating.

5.3.4.4. Effects of different valencies. For the general case of a formally trivalent transition metal ion we shall for simplicity assume that the change in Δ is a constant and as an example a value of 2.5 eV is subtracted. Also U_{dd} will be slightly affected and it is increased by 0.5 eV. An increasing valency will also increase the hopping (t_{pd}) and affect the ligand field splitting, which is approximately doubled from 1.0 eV to 2.0 eV [Sug70]. This relatively large increase of the ligand field splitting is mainly caused by the covalent contribution which is related to t_{pd}^2/Δ.

Figure 37 gives the rough estimates for U_{dd} and Δ of trivalent transition metal compounds based on the linear trend and the corrections from ligand field and multiplet effects as indicated in Table 12.

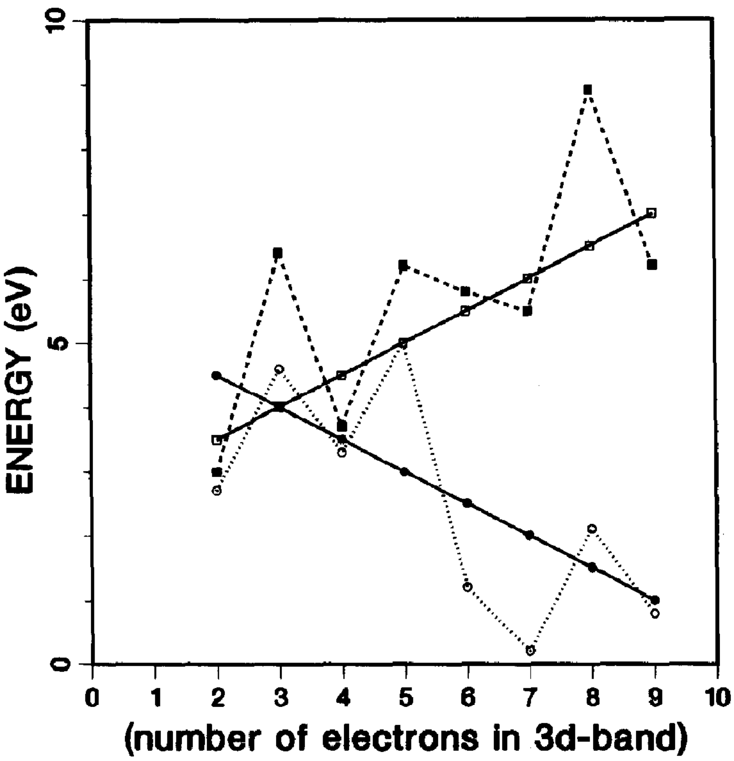

Fig. 37. Estimates for $\bar{U}_{dd}$ (□, solid line), U_{dd} (■, dashed line), $\bar{\Delta}$ (●, solid line) and Δ (○, dotted line) for a trivalent transition metal oxide.

The parameters used were $B = 0.1$, $C = 0.4$ and $\mathscr{D} = 2.0\,\mathrm{eV}$. The figure as drawn is probably most appropriate for the early trivalent transition metal ions. Trivalent iron oxides with a $3d^5$ configuration have large values of both U_{dd} and Δ and will form charge transfer insulators [Boc92a, Fuj93]. For a discussion of the tetravalent systems the reader is referred to [Boc92a, Fuj93, Deg91t].

5.3.4.5. Effects of the crystal structure. The links between crystal structure and electronic and magnetic structure are the subject of much research and can be found in the papers of, for example, Wilson [Wis72, Wis88], Goodenough [Gle85, Goo71] and Torrance et al. [Tor92], and references therein. As far as the short range Hamiltonians are concerned, the crystal structure will for all affect the hopping term t_{pd}. As discussed, a transition metal ion in a perfect octahedral surrounding of oxygen or a halide will obey the relation $t_{pd\sigma} \approx 2t_{pd\pi}$. Distortions from the octahedral symmetry would need the inclusion of more symmetry specific hopping terms, such as for example in [Laa92a] for D_{3d} symmetry. If one does not allow for more hopping terms, distortions are likely to mix the σ and π bonding of the ligands [Deg93a].

5.3.5. The relation with other parameter sets

Apart from the parameters of the short range model, there are other parameter sets which have been used to describe the transition metal compounds and complexes. For example much work has been done on the 2-parameter ligand field multiplet model, in which optical spectra have been described with two basic parameters: the ligand field splitting $\mathscr{D}$ and the Slater integral reduction B_{eff}. The variations in ligand field splitting have been described with the so-called spectrochemical series. The ligand field strength decreases $C > N > O > F > S > Cl > Br > I$ [Sug70]. The variations in the Slater integrals are denoted as the nephelauxatic series: their values decrease as $F > O > N > Cl > Br > I > S > Se > Te$ [Jor71]. The word "nephelauxatic" refers to an expanding cloud, and it can be seen that the series relates directly to the polarizability of the ligand. (Closely related to the nephelauxatic effect is the covalency factor N, which is used in papers on electron paramagnetic resonance (EPR); the Racah parameters are scaled down with N^4 and the spin–orbit coupling with N^2 [Cur74, Kua92].)

For fluorine the atomic value of the Slater integrals can be used and the values decrease towards tellurium. The nephelauxatic series runs in parallel with the variations in the charge transfer energy Δ. As discussed in Section 4 this relates to the fact that a decreasing Δ effectively increases the mixing of $3d^{N+1}\underline{L}$ in the ground state, which within a short range model description reduces the multiplet splitting. Within the short range model this reduction of Slater integrals can be estimated and Table 13 contains the reduction parameters as obtained

Table 13
The parameters of the short range model[a]

Compound	Charge transfer, Δ	Hopping, $t_{pd\sigma}$	Ligand field splitting, $\mathscr{D}$	Reduction, R/%
NiF_2	6.5	2.0	0.42 (0.79) 0.90	92 (99)
$NiCl_2$	3.6	2.0	0.63 (0.85) 0.95	82 (75)
$NiBr_2$	2.6	2.0	0.75 (0.95) 0.91	75 (65)
NiI_2	1.5	2.0	0.89 (0.99) 0.91	66 (25)
NiF_2	4.3	2.0	0.56 (0.92) 0.90	85 (99)
$NiCl_2$	1.3	1.7	0.74 (0.93) 0.95	65 (75)
$NiBr_2$	0.3	1.4	0.63 (0.83) 0.91	54 (65)

[a] Top series as used by Zaanen and co-workers; bottom series with modified parameters as used by Okada et al. An ionic contribution has been added for the ligand field values in brackets and in the third column the optical values are given. The reduction factors (R) are compared with the optimized values from the Slater integral reduction method (in brackets).

from the parameters of [Laa86a, Zaa86a]. The reduction factor can be determined from

$$R = \frac{1}{2} + \frac{\sqrt{(\Delta_{\Gamma_1}^2 + 4t_{\mathrm{pd}}^2)} - \sqrt{(\Delta_{\Gamma_2}^2 + 4t_{\mathrm{pd}}^2)}}{2\delta E} \qquad (20)$$

where Δ_{Γ_i} is the final state energy difference of a particular multiplet state Γ_i with the band. δE is the energy difference between the two multiplet states, which is equal to $\Delta_{\Gamma_1} - \Delta_{\Gamma_2}$. If the hopping t_{pd} is zero then $R = 1$. With increasing hopping (and constant charge transfer) R slowly decreases. From comparison with the values obtained from the Slater integral reduction method one finds that these values lie in between the values obtained from the two sets of parameters as used by Zaanen [Zaa86t] and Okada et al. [Oka92a].

The anion spectrochemical series has a more complex relation to the short range model. If Δ is decreased by constant t_{pd}, the ligand field splitting will increase due to the increased mixing of ligand p with metal d states. However the opposite trend is laid down in the spectrochemical series. This apparent discrepancy is related to the fact that the ligand field splitting is partly ionic in origin and the ionic contribution is related to the anion–cation distance, which for the halides is smallest for a fluoride (see for example [Deg90a]). The covalent contribution to the ligand field can be estimated from the short range model parameters as

$$\mathcal{D}_{\mathrm{cov}} = \sqrt{(\Delta^2 + 4t_{\mathrm{pd}\sigma}^2)} - \sqrt{(\Delta^2 + 4t_{\mathrm{pd}\pi}^2)} \qquad (21)$$

The values of the ligand field in Table 13 are determined from the energy difference between t_{2g} states and e_g states assuming the rule $t_{\mathrm{pd}\sigma} = 2t_{\mathrm{pd}\pi}$. It is noted that if an ionic contribution to the ligand field splitting ($\mathcal{D}_{\mathrm{ion}}$) is included this will increase the energy splitting for the σ interaction by $\Delta_\sigma = \Delta + \frac{1}{2}\mathcal{D}_{\mathrm{ion}}$ and decrease Δ_π by the same amount. Effectively this will slightly decrease the covalent contribution to the ligand field splitting. By adding ionic contributions to 0.4 eV for fluoride (nickel–fluorine distance is 2.54 Å) and 0.25 eV for chloride (3.14 Å) and bromide (3.27 Å), the total ligand field splittings take the values given in brackets. Notice that the parameter set as used by Okada et al. [Oka92a] gives $NiCl_2$ a larger ligand field splitting than $NiBr_2$, in accord with experiment.

For the metal ions the spectrochemical series is $Mn^{4+} > Co^{3+} > V^{3+} > Cr^{3+} > Fe^{3+} > V^{2+} > Fe^{2+} > Co^{2+} > Ni^{2+} > Mn^{2+}$. The nephelauxatic series reads, $Mn^{2+} > V^{2+} > Ni^{2+} > Co^{2+} > Cr^{3+} > Fe^{3+} > Co^{3+} > Cu^{3+} > Mn^{4+}$. From the valency point of view the series are clear: Mn^{4+} has the largest ligand field splitting and the smallest Slater integrals, which is in accord with the large covalency of the tetravalent materials. Within the short range model, tetravalent materials will have a relatively small Δ compared with t_{pd} [Boc92a]. Within a certain valency the variations are in general small. The $3d^5$ systems have a large Δ and U_{dd}, so they are expected to be most "ionic", implying the smallest ligand field splitting and the largest Slater integrals. This is indeed reflected in the position of Mn^{2+} and Fe^{3+} in both series. For the crystal field a further expected trend is that the late transition metal ions are most localized and have the smallest ligand fields. An exception to this rule is Co^{3+} which turns over to a low-spin configuration thereby largely increasing its crystal field strength.

It is noted that the parameters in the short range model are further expected to have close relationships with, for example, the dielectric constants ($\approx$ Slater integral reduction) and the redox potentials ($\approx$ trends in U_{dd} and Δ). Also there are other models which try to explain the trends in the transition metals, of which the model of Wooley is an interesting alternative [Woo87]. This model uses U_{dd} and t_{pd} as in the short range (Anderson impurity) model (but omitting Δ) and is extended with the electron–lattice coupling effects (v) which can be of a large energy scale in localized systems [Woo87]. These electron–lattice coupling effects are missing in the present short range model approaches to core spectroscopy and a future extension in this direction will be important. A number of studies of short range (Anderson impurity) model calculations with coupling to vibrations have been performed in the context of superconductivity. The coupling to the lattice can give rise to small polarons which form pairs, leading to the co-existence of narrow boson-pairs with wide fermion bands [Rob87].

6. X-ray magnetic circular dichroism (X-MCD)

In this section the question of the calculation of the X-ray magnetic circular dichroism (X-MCD) signal is addressed. Recently this field has gained much interest because of the promise of the determination of the ground state values of the spin and orbital moments using sum rules.

6.1. The atomic single electron model

An atomic, single electron, model has been worked out by Erskine and Stern [Ers75]. It describes the transitions of the 2p core state to the 3d valence state. p → s transitions are neglected and in the model core hole effects are neglected. The valence d states are explicitly written as an expansion of the spin and angular degrees of freedom, using spherical harmonics. The relative intensities of the reduced transition probabilities σ for the various possible combinations of polarization and magnetization are then worked out. They are collected in Table 14, under the additional assumption that the radial part of the matrix element is equal for $J = 3/2$ and $J = 1/2$ core states. For a mathematically rigorous determination of these values I refer to the paper of Brouder and Hikam [Bru91]; here I would like to concentrate only on the resulting numbers.

Table 14
Atomic, single electron model of p → d transitions; values given are the relative transition probabilities

Edge	Polarization	Magn. +	Magn. −	No magn.
L_2	+	3	1	4
	−	1	3	4
L_3	+	3	5	8
	−	5	3	8

From Table 14 all intensities and their ratios can be deduced. The overall $L_3 : L_2$ intensity ratio using linear (or non) polarized X-rays is 8 : 4, as given directly by the J value of the core state. This ratio is also found in the case of circularly polarized X-rays and a non-magnetic system. The X-MCD signal is defined as the normalized difference in absorption between right and left polarized X-rays

$$I_{\mathrm{MCD}} \equiv \frac{\sigma^+ - \sigma^-}{\sigma^+ + \sigma^-} \tag{22}$$

With this definition it is found that for the L_2 edge the X-MCD signal is −1/2 and for the L_3 edge it is +1/4, hence the $L_3 : L_2$ X-MCD intensity ratio is −1 : 1. The intensity ratios for right polarized X-rays can also be obtained directly from the table. They are 3 : 3 in the case of a parallel magnetic field and 1 : 5 for an antiparallel magnetic field. This atomic, single electron, model is often used as a starting point to analyse X-MCD spectra [Bau91, Bru91, Ers75, Kap91, Tob92]. In the following I will try to discuss how to proceed to other models. Here one can follow two routes:

(1) To include band structure effects, including the "Stoner" exchange splitting (I_s^*) and 3d spin–orbit coupling (ζ_d), with relativistic LSD calculations.

(2) To include the multiplet effects of the core hole in the final state.

6.1.1. X-MCD in the multiplet model

I will start with an outline of the second route, that is to include multiplets, in other words the core–valence Slater integrals as well as the valence–valence Slater integrals. In that case the 3J-symbol description, as explained in Section 4, is appropriate. For atoms the matrix element is given by the square of the 3J-symbol

$$\begin{pmatrix} J & 1 & J' \\ -M & q & M' \end{pmatrix}^2 \tag{23}$$

An atom in a magnetic field will have a ground state with $M = -J$. The spectral

Table 15
Branching ratios for different polarizations versus magnetizations; results are given for a series of ions within the atomic multiplet (AM) model[a]

System	Symmetry	Linear	Magn. −	Magn. +
AS-model	All	0.67	0.87	0.50
V^{4+}	$^{2}D_{3/2}$	0.46	0.63	0.41
Fe^{3+}	$^{5}T_2$	0.78	0.85	0.61
($\zeta_d = 0$)	$^{5}T_2$	0.72	0.86	0.59
	$^{1}A_1$	0.63	0.63	0.63
($\zeta_d = 0$)	$^{1}A_1$	0.60	0.60	0.60

[a] In the case of the Fe^{3+} ion a small (high-spin) and large (low-spin) ligand field has been added; the values are taken from Table IV in Ref. [Laa91]. The atomic, single electron (AS) model yields the same values for all ions.

shape for left respectively right polarized X-rays will be given by the squared 3J-symbol for respectively $q = \pm 1$ times the final state multiplet [Car91, Tho85a, Tho85b]. An important difference with the atomic, single electron, model is that the branching ratio will be affected by the symmetry of the ground state, which in turn is determined by the dd Slater integrals (Hund's rules). As discussed in Section 5.2.1, because of the interplay between core hole spin–orbit coupling and core hole Slater integrals the branching ratio will not be statistical.

In Table 15 the branching ratios are given for some transition metal ions, as calculated with the multiplet model. They are compared with the values from the atomic, single electron, model. The branching ratios are very sensitive to the ground state symmetry, which has been discussed in detail in Section 5.1 [Laa88a]. The branching ratio is always larger for a high-spin state; compare for example the $^{1}A_1$ and $^{5}T_2$ states of trivalent iron. As discussed in Section 5.2.1 the changes in the branching ratio due to the 3d spin–orbit coupling, that is the difference between $\zeta_d = 0$ and its atomic value, are not large (compared to the difference between high-spin and low-spin). Additional effects can occur due to further ligand field symmetry reduction, such as Jahn–Teller distortions.

6.1.2. X-MCD in short range models

As for the discussion of the spectral shape, for the X-MCD spectra the multiplet model can be extended to include charge transfer effects. The short range (Anderson impurity) model has been used to explain the X-MCD in the 2p X-ray absorption spectrum of nickel.

The ground state of nickel is expected to be rather well described with relativistic LSD calculations. This makes the use of short range models less justified compared with, for example, a charge transfer insulator such as NiO. However to account for a correct description of the localized final state of 2p X-ray absorption, including the action of the core-valence Slater integrals, it is necessary also to describe the ground state in a manner that can be used in a short range model analysis. There have been three papers on the description of the 2p MCD in nickel with short range models. In Table 16 the parameters used are collected.

The first calculation was performed by Jo and Sawatzky [Jo91]. They described the ground state of nickel as $17\%|d^8v^2\rangle + 65\%|d^9v\rangle + 18\%|d^{10}\rangle$, using the parameters as collected in the second column. v denotes delocalized electrons positioned in unoccupied states close to the Fermi level. Good

Table 16
Model parameters, ground state ionic energies and occupation numbers of three short range model calculations of nickel

Parameter	X-MCD [Jo91, Jo92]	X-MCD + XPS [Laa92a]	X-MCD + XPS [Tan92b, Tan92c]
Δ/eV	−1.0	+0.75	−0.5
U_{dd}/eV	5.0	1.5	3.5
U_{cd}/eV	6.0	2.5	4.5
t_{vd}/eV	0.65	⟨1.0⟩	0.7
Energies/eV			
d^8	4.0	2.25	3.0
d^9	0.0	0.0	0.0
d^{10}	1.0	−0.75	0.5
Ground state/%			
d^8	17	18	17
d^9	65	49	59
d^{10}	18	33	24

agreement with the 2p MCD spectrum of nickel was obtained. In the subsequent study of Tanaka et al. [Tan92b], the analysis was extended to also include 2p and 3p XPS spectra, which allow for a more critical test on some of the model parameters. It turned out that in order to describe the satellite structure in XPS accurately, it is necessary to decrease U_{dd}, U_{cd} and Δ as indicated in the last column. This modifies the energy positions of the different configurations. Because of the decrease of Δ and U_{dd} the energy difference between the lowest energy d^9 configuration and the d^{10} and d^8 configurations decreases. This mostly affects the occupation of the d^{10} configuration which is increased from 18% to 24%.

An alternative calculation by van der Laan and Thole [Laa92a] differs in some aspects. First the calculations of [Jo91] use only one interaction strength t_{pv}, while in [Laa92a] the states are projected to D_{3d} symmetry and different couplings are used for the different symmetries: $a \leftarrow t$, $e \leftarrow t$ and $e \leftarrow e$ ($D_{3d} \leftarrow O_h$). D_{3d} symmetry is chosen because the holes are expected to be formed near the L-points of the Brillouin zone. The ground state is notated as $|d^8\rangle + |d^9\underline{v}\rangle + |d^{10}\underline{v}^2\rangle$, instead of $|d^8v^2\rangle + |d^9v\rangle + |d^{10}\rangle$. That is, holes are used for the reservoir-states instead of electrons. The consequence is that the Δ as given in [Laa92a] (−0.75), must be reversed to +0.75 in order to bring it into comparison with the other calculations. A last point of difference is in the approach to U_{cd} which is assumed to be spectroscopy dependent and values of 2.5 eV and 4.5 eV are used respectively for XAS and XPS. In contrast with the other calculations, as well as with all calculations of Okada and Kotani discussed in Section 4.3, U_{cd} is not varied. For a further discussion of this point the reader is referred to Appendix A. For comparison it is noted that for the determination of the valence band photoemission spectrum of nickel a value of $U_{dd} = 4.3$ eV has been used by Falicov and Victora [Fal84, Vic85], using an exact solution of the Hubbard model in combination with the LSD calculation of Wang and Callaway [Wan77].

The different calculations can best be compared for their ionic energy positions as given in Table 16. It turns out that the ordering of states is different and while the d^{10} configuration is lowest for [Laa92a], the d^9 configuration is lowest for the other calculations. This has a direct consequence for the ground state occupation numbers, with the d^{10} configuration contributing more in [Laa92a]: 33% versus 24%. As far as the description of the spectra is concerned both calculations of [Laa92a] and [Tan92b] give good agreement with the observed spectral shapes in the XAS, X-MCD and XPS spectra. It is concluded that the short range model can give an accurate description of the spectral shapes and X-MCD of nickel, but to accomplish this task there is apparently still a reasonably large range of parameter combinations.

6.1.3. *X-MCD in relativistic LSD calculations*

A different route to explain the X-MCD spectra is to perform relativistic LSD calculations. This route is certainly most appropriate if multiplet effects can be neglected such as for the K edge of transition metals and (to a large extent) the $L_{2,3}$ edge of rare earths. However relativistic LSD calculations (and all other models neglecting the core hole effects) are not appropriate to describe the $L_{2,3}$ edge of nickel and the other 3d transition metals.

In Fig. 38 a schematic view is given of the various models with the important parameters which are included in various stages. In the band structure approach, the spin-polarized density of states is calculated using relativistic LSD calculations. To date relativistic LSD programs have been developed for KKR [Ack84], MS [Str89], LMTO [Ebe88a, Ebe88b] and ASW [Kru88]. The X-ray absorption spectrum and the X-MCD signal are determined from Fermi's golden rule (Eq. (4)) or with the Green function formulation (Eq. (6)). The relativistic LSD approximation includes the "magnetic" exchange effects and the 3d spin–orbit coupling exactly but neglects all core hole (exchange) effects in the final state. In Fig. 38 the

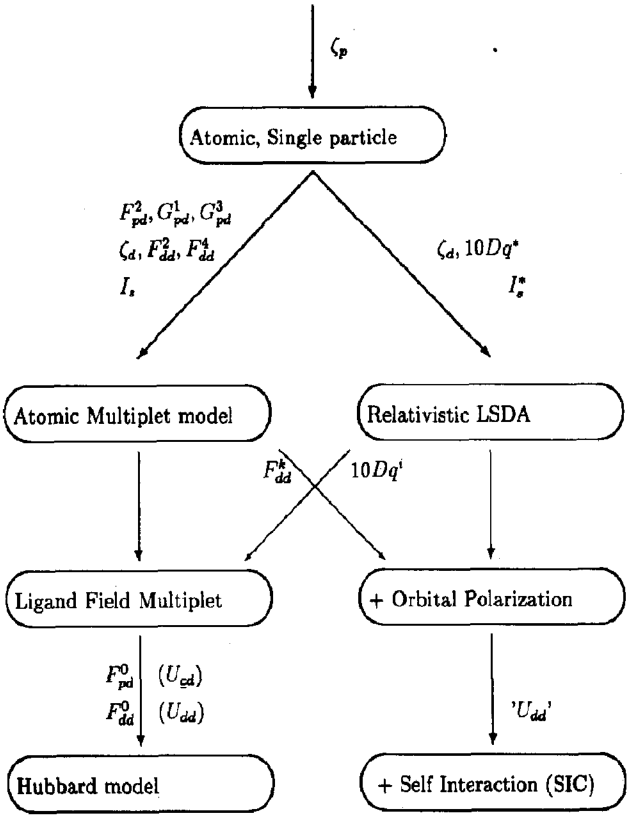

Fig. 38. Schematic picture of the models used for the analysis of MCD spectra.

3d spin–orbit coupling is denoted as ζ_d. The (magnetic) exchange coupling is denoted as I_s^*, that is within the calculational scheme the exchange is not a constant, but from the calculation an effective exchange coupling can be obtained. The same is true for the cubic crystal field splitting (10Dq*).

As has been shown by Schütz and co-workers [Fis90a, Sch87, Sch88, Sch89], an important experimental parameter is the normalized difference in absorption between right and left polarized X-rays as given in Eq. (22). If multiplets are not important it can be shown that its value is related as

$$I_{\mathrm{MCD}} \equiv \frac{\sigma^+ - \sigma^-}{\sigma^+ + \sigma^-} \cong P_e \frac{n^+ - n^-}{n^+ + n^-} \tag{24}$$

where n is the spin-polarized projected density of states. P_e is a constant related to the Fano effect and its value is determined in the atomic single electron model: P_e is −0.5 for the L_3 edge and 0.25 for L_2. For K edges the value is only about 0.01 due to the absence of core hole spin–orbit coupling [Sch92]. Equation (24) implies that from the X-MCD signal the degree in spin-polarization of the ground state is obtained directly, or in other words as X-ray absorption is a local probe the local magnetic moment. This has been shown for 5d impurities in iron [Sch92, Wie91] and for a series of platinum alloys and Pt–Co multilayers [Ebe91, Rue91, Sch90] (but see next section on sum rules).

It appears that the magnetic moments as determined from X-MCD experiments and Eq. (24) do show close agreement with relativistic LSD calculations for the K edge of iron, the $L_{2,3}$ edges of 5d metals and the L_1 and $L_{2,3}$ edges of gadolinium

[Ebe88a, Ebe88b, Ebe89a, Ebe89b, Ebe90, Ebe91]. In these calculations the spin-up and spin-down projected density of states (of 3d systems) are determined by two important parameters, the 3d spin–orbit coupling and the effective exchange splitting between up and down.

Smith and co-workers [Che91, Smi92] explained the $L_{2,3}$ X-MCD spectrum of nickel from a relativistic LSD model. To obtain the correct branching ratios they had to renormalize the 3d spin–orbit coupling and the effective (Stoner) exchange splitting. This is in contrast to the approach by using the short range model including multiplets, where the largest contribution to the non-statistical branching ratios is the final state effects, that is, the core–valence Slater integrals. Because the core–valence Slater integral effects are important for the pure metals, as can be most directly seen from Fig. 38, a model which does not include them cannot be expected to be correct for the description of the spectral shape. Therefore the renormalization of the 3d spin–orbit coupling and the effective exchange coupling "hides" the final state core hole exchange effects in the ground-state description, which is not a preferable choice. Hence, an accurate description of the ground state is only possible with correct inclusion of final state effects.

6.2. Sum rules

Recently it has been shown by Thole, Carra and co-workers [Car92, Car93, Tho92] that the normalized integrated X-MCD signal can be related to the ground state expectation values of the orbital angular momentum $\langle L_z\rangle$ and the spin momentum $\langle S_z\rangle$. Using the discrete energy range of the $2p \rightarrow 3d$ transitions the optical sum rule as derived by Smith [Smi76] can be used to a good approximation for the $L_{2,3}$ edges of the 3d systems and the $M_{4,5}$ edges of the rare earths [Tho92]. We concentrate here on the $L_{2,3}$ edges which involve a p to d transition. In that case for the orbital moment divided by the number of holes of 3d character (n_h) one finds

$$\frac{\langle L_z\rangle}{n_h} = 2\frac{\int_{\text{edge}}(\sigma^+ - \sigma^-)}{\int_{\text{edge}}(\sigma^+ + \sigma^- + \sigma^0)} \tag{25}$$

$$\frac{\langle S_z\rangle}{n_h} = +\frac{3}{2}\frac{\int_{L_3\text{edge}}(\sigma^+ - \sigma^-) - 2\int_{L_2\text{edge}}(\sigma^+ - \sigma^-)}{\int_{\text{edge}}(\sigma^+ + \sigma^- + \sigma^0)} \tag{26}$$

In the original papers [Tho92, Car93] the prefactors $l(l+1)+2-c(c+1)/l(l+1)$ (c denotes the angular momentum of the core state, l that of the valence state) and $l(l+1)-2-c(c+1)/3c$ were given. For a p ($c=1$) to d ($l=2$) transition they are respectively equal to 1 and 2/3. In using these sum rules the following assumptions have been made: (A0) The radial matrix element is assumed to be energy independent and is hence equal for the L_3 and L_2 edges. This approximation is assumed to hold to within 10%. Also relativistic corrections are not included. (A1) The intensity of the L_3 edge is assumed to be twice the intensity of the L_2 edge. This implies separable edges which, as indicated in [Car93], is correct to about 5% at the end of the transition metal series, but worse in the beginning due to the small core hole spin–orbit coupling. (A2) In the present discussion I omitted for simplicity the magnetic dipole operator ($\langle T_z\rangle$). If one includes a finite $\langle T_z\rangle$, $\langle S_z\rangle/n_h$ must be replaced by $\langle S_z\rangle + (7/2)\langle T_z\rangle/n_h$ [Car93].

These optical sum rules bear a close relationship to the semi-empirical rules as derived by Schütz and co-workers [Sch93, Wie91]

$$\frac{\langle L_z\rangle}{n_h} = \frac{1}{3}\left[\int_{L_3\text{edge}}\frac{4(\sigma^+ - \sigma^-)}{(\sigma^+ + \sigma^-)} + \int_{L_2\text{edge}}\frac{2(\sigma^+ - \sigma^-)}{(\sigma^+ + \sigma^-)}\right] \tag{27}$$

$$\frac{\langle S_z\rangle}{n_h} = \frac{4}{3}\left[\int_{L_3\text{edge}}\frac{(\sigma^+ - \sigma^-)}{(\sigma^+ + \sigma^-)} - \int_{L_2\text{edge}}\frac{(\sigma^+ - \sigma^-)}{(\sigma^+ + \sigma^-)}\right] \tag{28}$$

As these rules were derived from a band structure point of view some additional approximations have been introduced. (A3) Instead of an integral of the dichroic signal and the total cross section, the dichroic signal is divided point by point (chosen because this is experimentally more appropriate). Mathematically this implies that the integration and division are exchanged, hence it is assumed that

$$\frac{\int x}{\int y} = \int \frac{x}{y} \tag{29}$$

This assumption is only exactly correct if the dichroic signal follows the total spectrum, that is if $y = c(\text{constant})x$. It can be expected that this assumption is appropriate if the spectrum consists of a single L_3 and L_2 peak without too much fine structure as often is the case for 3d metals. (A4) The use of $(\sigma^+ + \sigma^-)$ in the denominator implicitly assumes that $\sigma^0 = (\sigma^+ + \sigma^-)/2$, which is correct within band structure, but not necessarily so within multiplet theory.

We now rewrite the formulations (27) and (28) assuming that the approximations (A3) and (A4) hold exactly. In the first step we rewrite the denominator to $(\sigma^+ + \sigma^- + \sigma^0)$. The intensity of $(\sigma^+ + \sigma^-)_{L_3}$ is equal to $(2/3)(\sigma^+ + \sigma^-)$, following approximation (A1). Also, following (A4), $(\sigma^+ + \sigma^-)$ is equal to $(2/3)(\sigma^+ + \sigma^- + \sigma^0)$.

With these modifications Eqs. (27) and (28) are changed to

$$\frac{\langle L_z\rangle}{n_\mathrm{h}} = \frac{1}{3}\left[\int_{L_3\mathrm{edge}} \frac{4(\sigma^+ - \sigma^-)}{\frac{2}{3}\frac{2}{3}(\sigma^+ + \sigma^- + \sigma^0)} + \int_{L_2\mathrm{edge}} \frac{2(\sigma^+ - \sigma^-)}{\frac{1}{3}\frac{2}{3}(\sigma^+ + \sigma^- + \sigma^0)}\right] \tag{30}$$

$$\frac{\langle S_z\rangle}{n_\mathrm{h}} = \frac{4}{3}\left[\int_{L_3\mathrm{edge}} \frac{(\sigma^+ - \sigma^-)}{\frac{2}{3}\frac{2}{3}(\sigma^+ + \sigma^- + \sigma^0)} - \int_{L_2\mathrm{edge}} \frac{(\sigma^+ - \sigma^-)}{\frac{1}{3}\frac{2}{3}(\sigma^+ + \sigma^- + \sigma^0)}\right] \tag{31}$$

Then using the (mathematically incorrect) identity (A3) one finds

$$\frac{\langle L_z\rangle}{n_\mathrm{h}} = 3\frac{\int_\mathrm{edge}(\sigma^+ - \sigma^-)}{\int_\mathrm{edge}(\sigma^+ + \sigma^- + \sigma^0)} \tag{32}$$

$$\frac{\langle S_z\rangle}{n_\mathrm{h}} = 3\frac{\int_{L_3\mathrm{edge}}(\sigma^+ - \sigma^-) - 2\int_{L_2\mathrm{edge}}(\sigma^+ - \sigma^-)}{\int_\mathrm{edge}(\sigma^+ + \sigma^- + \sigma^0)} \tag{33}$$

That is, one finds the correct optical sum rules as derived in [Tho92, Car93], but with a different prefactor. For $\langle L_z\rangle$ one finds 3 instead of 2; for $\langle S_z\rangle$ one finds 3 instead of 3/2. In other words in the semi-empirical rules as in [Sch93, Wie91] the factors used were too large (assuming the optical sum rules to be correct).

On the basis of a single particle transition, Stöhr and Wu [Sto93] also derived relations between the observed X-MCD signals and the orbital and spin-moments. Their rule for $\langle L_z\rangle$ is qualitatively equivalent to the optical sum rule, although their prefactor is different. For $\langle S_z\rangle$ they find a qualitatively different relationship, specifically related to their model description [Sto93].

6.2.1. *The use of the sum rules*

The sum rules present a powerful method to determine both the local spin and orbital moment. However in the practical use of the rules there are some problems which will be shortly discussed. The sum rules can be formulated as

$$\langle\ \rangle = c n_\mathrm{h} f(\sigma^+, \sigma^-) \tag{34}$$

The constant c is known, but both the number of holes n_h and the experimentally determined function $f(\sigma^+, \sigma^-)$ present some complications.

To find the value for n_h one uses LSD band structure methods and determines site and angular momentum projections of the distribution of states. This gives the number of occupied states of metal 3d character n_d, and with $n_\mathrm{h} = 10 - n_\mathrm{d}$

the number of holes. There are two complicating factors. First the LSD methods used (LAPW, LMTO and ASW) do contain interstitial regions and/or empty spheres. It is not obvious what to do with the charge density in these regions. Secondly the radius of the sphere around the metal site is chosen to perform a correct calculation, but this sphere does not have much meaning in the sense that the metal atom ends there. That is, the determination of the amount of d character depends on the sphere size which is not obviously "correct" for this purpose. In fact because the experiment probes states starting from the 2p core state this makes the problem even more complicated, because one should use a radius (or radial function) related to the core wavefunction. The consequence is that the number of d character found is at the moment largely method-dependent and not uniformly defined. For this reason it is safer to give the expectation values per hole ($\langle L_z \rangle / n_h$).

To determine the experimental function $f(\sigma^+, \sigma^-)$ there are also some complications. One problem is related to the determination of the normalization by the total absorption cross section ($\sigma^+ + \sigma^- + \sigma^0$). In an experimental 2p spectrum one finds not only the localized transitions to 3d states, but also the "step-like" absorption edge to delocalized states. Additionally the background is often not horizontal due to experimental conditions and sometimes other absorption edges. This gives a difficult task to first sort out the "correct" absorption spectrum and then to separate it into the localized part and the edge jump. This procedure leaves some space for particular treatments and hence systematic errors. For example it is not obvious how an edge jump should be included and also it is likely that the edge jumps are compound (crystal structure) dependent.

An additional experimental complication is the incomplete circular polarization. If the rate of polarization is known one can generate the 100% polarized spectra, however with loss of statistics. Some monochromators have energy-dependent polarization rates which further complicates this procedure. If one uses left and right polarization (instead of changing the magnetic field) one should take care of small energy shifts and small differences in the degree of polarization. Also the magnetization is in general not 100% and, depending on the detection technique (Section 2), sample preparation and cleaning procedures, the part of the sample under investigation is not always single phase and/or clean. In many cases a clean, single phase sample poses strong technological demands which are not always met. One should always be careful to have quantitative knowledge on the rate of polarization, magnetization and sample purity, if using the sum rules.

As shown by Carra et al. [Car93] the problems related to n_h as well as most experimental complications disappear, or at least strongly diminish, for the determination of the value for $\langle L_z \rangle / \langle S_z \rangle$. This ratio can be found by combining Eqs. (25) and (26)

$$\frac{\langle L_z \rangle}{\langle S_z \rangle} = \frac{4}{3} \frac{\int_{\mathrm{edge}} (\sigma^+ - \sigma^-)}{\int_{L_3 \mathrm{edge}} (\sigma^+ - \sigma^-) - 2 \int_{L_2 \mathrm{edge}} (\sigma^+ - \sigma^-)} \tag{35}$$

It can be seen that, apart from n_h, the normalization disappears from the formula. The remaining values for this ratio can be determined directly from experiment. Some of the experimental problems which remain are incomplete separation of L_3 and L_2, and some of the uncertainties caused by the rate of polarization and magnetization. The values for iron, cobalt and iron determined by this rule from X-MCD experiments do show close agreement with the available neutron data [Car93].

Wu et al. [Wuy92] have used the sum rule to analyse their data of cobalt and a Co/Pd multilayer. Using $n_h = 2$ they have found values for $\langle L_z \rangle$ of respectively 0.17 and 0.24, in good agreement with theoretical predictions from Daalderop et al. [Daa91]. It is noted that the choice for n_h to be equal to two is not well defined, as discussed above.

6.3. *Linear dichroism*

Linear dichroism, or polarization dependence, is the difference in absorption between transitions of X-rays with $q = \pm 1$ compared to X-rays with $q = 0$.

6.3.1. *Experimental*

Because synchrotron radiation is linearly polarized, the difference between normal incidence and grazing incidence probes the linear dichroism of the axis perpendicular to the surface, that is for example effects from the surface itself, or from perpendicular magnetization. Grazing incidence spectra are susceptible to "saturation effects", that is the electron yield intensity is not exactly proportional to the absorption coefficient. This happens because the penetration depth of the X-rays can become comparable to the escape depth of the electrons as has been analysed in detail for LaF_3 [Laa88c] and for thin layers of NiO [Ald93]. To avoid the complications due to these saturation effects it is preferable to avoid grazing incidence spectra. The angle at which saturation does not yet play a role depends strongly on the absolute absorption cross section, that is on the material and edge measured. If one wants to measure the linear dichroism spectrum for compounds with an electrostatic and/or magnetic axis, it is preferable to position the axis in the plane of the surface and to measure in normal incidence. In doing so one can measure the linear dichroism by turning the axis under consideration from horizontal to vertical, thereby avoiding any artefacts due to these saturation effects. Additionally the (eventual) linear dichroism effect due to the surface is not altered in this set-up.

6.3.2. *Selection rules*

The condition for the occurrence of linear dichroism is a macroscopic asymmetry in the electronic and/or magnetic structure. The symmetry criterion which determines a possible polarization dependence is given by the space group of the crystal and not by the point group of the atom. Consider for example a crystal which has a cubic space group and the absorbing atom a tetragonal point group. In this case the shape of the metal 2p spectrum is determined by the point group; however no linear dichroism is found because the potentially dichroic effect of the two atoms, oriented horizontally and vertically, cancels exactly [Bru90a].

The dipole transition can be denoted as P-like ($\Delta J = +1$, -1 or 0) in the atom. From Fig. 28 it can be checked that in octahedral symmetry no polarization dependence can occur, in contrast to tetragonal symmetry. The linear dichroism of all space groups can be deduced directly from the symmetry projection rules [But81]. For a D_{2h} space group there are three different directions, and in principle there will be linear dichroism effects with respect to all axes [Bru90a]. From Fig. 28 it is clear that the linear dichroism of quadrupole transitions (which have atomic D symmetry) is different, and already in octahedral symmetry linear dichroism effects occur. This can be used to distinguish quadrupole and dipole transitions [Bru90a, Hah82].

Linear dichroism can be caused by both electronic and magnetic effects, in contrast to circular dichroism which can only be caused by magnetic effects. Ligand fields can never cause a difference between the $\Delta M = -1$ and $\Delta M = +1$ transitions, which is a direct consequence of Kramer's theorem [Kra30] which states that the lowest state in a static electric field is always at least twofold degenerate. The only way to break the degeneracy of the Kramer's doublet is by means of a time asymmetric field, in other words a magnetic field.

6.3.3. *Linear dichroism of layer compounds*

Layer compounds contain at least one axis which is distinguishable from the others; hence the X-ray absorption spectra are polarization dependent with respect to this axis. For example $BaCoF_4$ crystallizes in a $C_{2v}^{12}(A_{2_1am})$ space group. Along the [001] direction (a axis) a macroscopic electric polarization has been found, which can be reversed by reordering the CoF_4 sheets. At room temperature

$BaCoF_4$ is ferroelectric and paramagnetic. Below $T_N = 68\,K$ it is antiferromagnetic [Kev70].

The cobalt 2p X-ray absorption spectra of $BaCoF_4$ show a large linear dichroism for $E \perp a$ and for $E \parallel a$ [Che90a]. It has been shown that the linear dichroism effects of $BaCoF_4$ can be simulated with ligand field multiplet calculations for a $3d^7_{HS} \rightarrow 2p^5 3d^8$ transition [Deg91t]. Atomic Slater integrals have been used and the atomic 3d spin–orbit coupling has been included. The calculations reproduce the observed temperature dependence of the dichroism. The temperature dependence shows a sudden step at 68 K, related to the additional linear dichroism effects of the magnetic exchange coupling [Sin••].

6.3.4. *Linear dichroism of surfaces and adsorbates*

A surface presents a clear breaking of the (x, y, z) symmetry, and will present a rather large linear dichroism between polarizations in the surface plane and perpendicular to it. A linear polarized X-ray impinging perpendicularly upon a surface excites core electrons to bonds lying in the surface plane. A grazing incident X-ray excites exclusively bonds perpendicular to the surface plane, which can be used to determine the surface electronic structure.

A problem with electron yield is that due to its mean probing depth of the order of 50 Å the surface signal is overwhelmed by the signal from the bulk. To separate the surface signal it is fruitful to use ion yield which, with its probing depth of only 1 or 2 layers, is a true surface probe. The combination of ion-yield and electron-yield detection has been applied to the CaF_2–Si(111) system [Him91].

Surface dichroism effects are particularly useful for adsorbates. A nice example is given for the adsorption of boron on a silicon (111) surface, for which the sharp boron π-peak, related to the silicon–boron bond, is visible solely with p-polarized X-rays [Mcl90]. Given that the adsorbates are present on the surface only, the X-ray absorption spectrum can be measured with any method [Ped89, Som92]. Because electron yield measurements are easier in their use, adsorbates are usually measured with (partial) electron yield. Besides an interest in the structure of the X-ray absorption edges, the surface extended X-ray absorption fine structure (SEXAFS) is important for the determination of, for example, the surface bond lengths [XAS91]. The common procedure of analysis for the "near edge structure" is by means of multiple scattering calculations. Emphasis is given to the complicated problem of correct determination of the surface structure [Ped90].

6.3.5. *Linear dichroism of magnetic materials*

Magnetic effects generate circular dichroism, but they also have a large effect on the linear dichroism as was first shown by van der Laan et al. [Laa86b]. The magnetic field determines an axial direction in the crystal and with respect to this axis linear dichroism occurs. Within atomic multiplet theory this can be calculated directly by evaluation of the properties of the 3J-symbol. Under the assumption that only the $M_J = -J$ magnetic level of the ground state is filled, a strong correlation between the polarization vector q and the various final states with different J values is found. This correlation is given in Table 17.

Atomic multiplet theory can be used directly for the rare earths and because the J values for the rare earths are found to be in between 5/2 and 8, $\Delta J = \pm 1$ transitions are almost exclusively correlated with $q = \Delta M_J = \pm 1$ transitions.

The polarization averaged spectrum is formed from a combination of all transitions from the $4f^N$ ground state of specific J to all $3d^9 4f^{N+1}$

Table 17
Correlation between ΔJ and ΔM_J

ΔJ	$(\Delta M_J = -q)$		
	-1	0	$+1$
-1	1	0	0
0	$\frac{1}{J+1}$	$\frac{J}{J+1}$	0
$+1$	$\frac{1}{(2J+3)(J+1)}$	$\frac{2J+1}{(2J+3)(J+1)}$	$\frac{(2J+1)(J+1)}{(2J+3)(J+1)}$

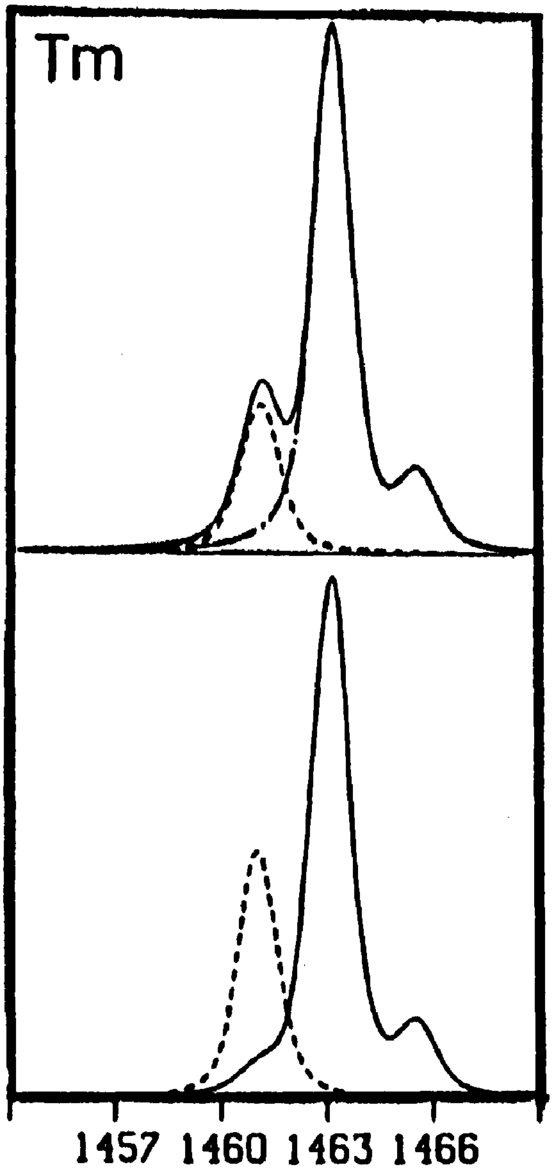

Fig. 39. Atomic multiplet calculation of M_5 edge of thulium. Top spectrum: – – –, $\Delta J = 0$ and –· – ·–, $\Delta J = -1$, ——, total spectrum. Bottom spectrum: the resulting spectra for $E \perp M$ (– – –), and $E \parallel M$ (——).

final states of $J+1$, J and $J-1$, and it turns out that the oscillator strength to the final states of the different J values is grouped in different regions of the spectrum [Goe88]. Figure 39 shows the atomic multiplet spectrum for Tm^{3+}.

The M_5 edge has three possible transitions, the first one with $\Delta J = 0$ (dashed line) and the two others with $\Delta J = -1$ (chain-dotted line). Owing to the J_q correlation, the transitions to $\Delta J = -1$ are solely visible in the $q = \pm 1$ spectrum, and the $\Delta J = 0$ transition is largely restricted to $q = 0$ polarized X-rays. The small low-energy shoulder in the $q = \pm 1$ spectrum is an effect of the incomplete correlation. The linear and circular dichroism of the $M_{4,5}$ spectra of all rare earths, including the effects of finite temperature, have been given in [Goe88, Goe89t]. Experimental evidence of linear dichroism, caused by magnetic and electrostatic effects, is given in [Goe89t, Kap92t, Sac91a, Sac91b, Sac92a, Sac92b, Vog93]. For the 3d systems, a nice example of linear dichroism as a result of magnetic ordering has been given for the Morin spin–flip transition in Fe_2O_3 by Kuiper and coworkers [Kui93].

7. Overview of the published metal 2p spectra

In this section an overview is given of the published 2p X-ray absorption spectra. From papers which contain results on a series of minerals, complexes, etc., only some of the compounds will be included. The emphasis is on the papers which focus on the elaboration of the various theoretical models. For the 2p spectra this will be mainly the LFM model and its extension within the short range models, the CT-M model. However the one-particle models, be it LSD band structure or MS, are also developed further and applied to 2p spectra, although it has been argued in Section 5 that one of the crucial ingredients for the shape of the 2p spectra, the pd Slater integrals, is missing in these models.

The 2p spectra can be seen in analogy with a microscope as magnifying the symmetry of the ground state. The ground state symmetry can be studied with optical spectroscopy including X-MCD as well as resonance techniques (EPR, etc.), causing transitions within the $3d^N$ configuration, coupling to vibrations, etc. These studies give much detail and the question about the eventual additional information from X-ray excitations is understandable. However as discussed in

Table 18
Calcium 2p X-ray absorption spectra

Compound	Ref.	Remarks
Ca	[Fin85, Zaa85b]	Hubbard model on band structure
	[Him91]	Atomic multiplet
Ca on Si(111)	[Him91]	Atomic multiplet
$CaCO_3$	[Wad86]	–
CaF_2	[Deg90a, Him91]	LFM: 10Dq = −0.75 eV
	[Bor92]	MS: 10Dq = −1.36 eV
	[Ela93]	Autoionization
$CaCl_2$	[Ela93]	Autoionization
CaO	[Him91]	LFM: 10Dq = +1.2 eV
	[Sol91]	MS
$CaSi_2$	[Him91]	LFM
$Bi_2Sr_2CaCu_2O_8$	[Bor92]	MS

the preceding section, 2p X-ray absorption spectra show characteristic multiplets which can be related back to a particular ground state symmetry. This comes with the enormous advantage over optical spectroscopy of the element selectivity of X-ray absorption, with the opportunity to study in detail the ground state symmetry of low-concentration metal sites in a background of other metallic, inorganic or biological material. Hence, some of the important applications of 2p X-ray absorption can be found in the earth sciences, metal centres in organic complexes and biological systems and materials science. Other applications make use of the (circular) polarization of X-rays obtained at synchrotron radiation sources for the study of magnetic materials.

In the following sections the spectra of the 3d elements are collected and some of the papers focusing on a particular application are highlighted.

7.1. Calcium 2p X-ray absorption spectra

Metallic calcium has been studied in detail by Zaanen et al. [Zaa85b]. They analysed the spectrum as a combination of atomic multiplet effects and band structure. The spectrum, reproduced in Fig. 30, does show little structure and in fact it can be fully reproduced by a Gaussian broadening of the atomic multiplet, i.e. all information on the details of the band structure is lost.

2p X-ray absorption studies are only infrequently applied to surfaces due to the basic problem of a probing depth of 50 Å which always gives a dominant bulk contribution (for normal incidence spectra). The study of Himpsel et al. [Him91] uses ion yield to focus on the real surface layer of a CaF_2 crystal. The analysis with the LFM model shows that the surface introduces additional transitions due to a lowering of the symmetry. In a study by Borg and coworkers [Bor92], the L_2 edge of divalent calcium is considered as not affected by multiplet effects. They attribute the additional feature in between the two main peaks of the L_2 edge to effects of the solid state and show that it can be reproduced by a larger cluster for the multiple scattering calculations. In the LFM calculations this extra feature has been related to a reduced symmetry, as emphasized in the surface spectrum. If the structure is indeed present for the real bulk spectrum, solid state effects must be the cause. However in the spectrum taken of a CaF_2 sample covered with BaF_2, this feature is not present. It is present in other spectra only because of the surface sensitivity of electron yield. From Table 18 it can be seen that the result for the final state ligand field parameter is −0.75 eV with LFM and −1.36 with MS 1.36 eV is also the distance between the peaks in the experimental spectrum. A problem for the determination of the ligand field splitting in the final state of 2p XAS is its definition. In LFM the definition is the magnitude

Table 19
Scandium 2p X-ray absorption spectra

Compound	Ref.	Remarks
Sc	[Fin85, Zaa85b]	Hubbard model on band structure
	[Bar83]	Non-statistical branching ratio
ScF_3	[Deg90a, Set90]	LFM; 10Dq = 1.7 eV
Sc_2O_3	[Deg90a, Wad86]	LFM; 10Dq = 1.8 eV
	[Ela93]	Autoionization

of the extra operator in the Hamiltonian with respect to the atomic multiplet. It has been shown in detail [Deg90a] that this does not correspond to a measured splitting in the experiment, though there is a constant (and known) relationship. The experimental splitting is a complex feature built from various ingredients and can be considered as an "effective ligand field splitting".

7.2. *Scandium 2p X-ray absorption spectra*

Only a few scandium 2p edges have been published. On comparing the spectra of ScF_3 and Sc_2O_3 with the theoretical ligand field multiplet spectra, both show good agreement (see Table 19). An important difference is the much sharper spectrum of ScF_3, which is a typical feature of fluorides [Deg90a]. Within the Anderson impurity description this is caused by the large value of Δ which gives fluorides a ground state which is strongly dominated by $3d^N$ (in this case $3d^0$) character, or in other words fluorides are close to the ionic limit. The admixture of more $3d^1\underline{L}$ character, for example, in the case of oxides implicates a larger broadening due to a large number of possible final states, as has been discussed in [Oka93].

7.3. *Titanium 2p X-ray absorption spectra*

For titanium compounds (Table 20) a number of problems are discussed frequently. First there is the evidence of a clear satellite structure in the titanium 2p spectra of tetravalent titanium oxides [Laa90b]. These satellites, and their analogues for 2p XPS, are discussed under the same charge transfer origin as the late transition metal oxides by Okada and Kotani [Oka93]. However it is claimed in papers of de Boer et al. [Boe84] and van der Laan [Laa90b] that the origin of the satellites cannot be of charge transfer nature. They formulate an alternative, polaronic, excitation process ($3d^N \rightleftharpoons 3d^N4d\underline{L}$), that is a transition from the valence band to the conduction band accompanying the X-ray absorption process. To date no clear-cut answer can be given to decide between these two (and eventual other) excitation processes.

Table 20
Titanium 2p X-ray absorption spectra

Compound	Ref.	Remarks
$CaTiSiO_5$	[Deg92]	Series of minerals
$LaTiO_3$	[Abb91b]	LFM
$La_{1-x}Sr_xTiO_3$	[Abb91b, Fuj92a, Fuj92b]	LFM, mixed valence
Ti	[Fin85,Zaa85b]	Hubbard model on bands
	[Bar83, Gru83]	LDA band structure
	[Lea80, Lea82]	EELS, MO picture
	[Pea86, Pco88]	Branching ratio
TiO_2	[Lea82, Wad86]	EELS
	[Deg90a, Deg92]	LFM, rutile + anatase
	[Laa90b]	"Polaronic" satellites
	[Oka93]	Charge transfer satellites
	[Bry89, Bry92]	MS, rutile + anatase
TiF_3	[Set90]	LFM gives no good agreement
$FeTiO_3$	[Deg92]	Series of minerals
$SrTiO_3$	[Deg92]	LFM: 10DQ = 1.5 eV

A series of $La_{1-x}Sr_xTiO_3$ oxides have been measured [Abb91b, Deg90a]. In this series the formal valency of titanium is changed from tetravalent to trivalent, which can be equated with respectively "$3d^0$" and "$3d^1$" like configurations. The oxide systems are rather covalent so the actual electronic configuration has a considerable amount of $3d^{N+1}\underline{L}$ character; however as discussed the symmetry remains largely determined by the $3d^N$ nature. The $La_{1-x}Sr_xTiO_3$ series can then be used as a reference series for unknown mixed valent systems. A series of natural minerals has been published in [Deg92]. For all minerals measured, including a number of silicates, no trivalent titanium could be detected.

Table 21
Vanadium 2p X-ray absorption spectra

Compound	Ref.	Remarks
Cu_3VS_4	[Cre92]	Series of minerals
FeV_2O_4	[Cre92]	Series of minerals
V	[Fin85, Zaa85b]	Impurity model on band structure
VF_3	[Deg90b, Set90]	LFM
	[Tan92a]	LFM, temperature effects
V_2O_3	[Spa84, Abb93a]	LFM
VO_2	[Abb91a]	Phase transition
V_2O_5	[Deg91t, Abb93a]	LFM
$Zn_{1-x}Li_xV_2O_4$	[Deg91t]	LFM, mixed valence

7.4. *Vanadium 2p X-ray absorption spectra*

An important aspect of vanadium oxides is the occurrence of a series of phase transitions as a function of temperature in, for example, VO_2, V_2O_3 and $LiVO_2$ [Goo71], and also as a function of concentration in, for example, $Zn_{1-x}Li_xV_2O_4$ [Goo71]. For VO_2 it has been shown that this phase transition is reflected in the oxygen 1s X-ray absorption spectrum [Abb91a]. However the vanadium 2p X-ray absorption spectra show in general no clear sign of the phase transition (see Table 21). This can be related to the fact that the metal 2p X-ray absorption spectra are largely dominated by the local symmetry and are only slightly affected by the modifications in their surroundings (in the sense of ligand field effects), while most phase transitions for vanadium oxides occur due to some kind of vanadium–vanadium interactions and/or coupling to vibrations, which are only of relatively minor influence on the symmetry state of the vanadium ions. These effects can be expected to be of far more influence on oxygen 1s spectra which are directly related to the empty density of states. (In contrast if the spin state is affected in the phase transition, such as the high-spin to low-spin transition in $LaCoO_3$, this is directly and clearly observable in the metal 2p edges [Abb93b].)

7.5. *Chromium 2p X-ray absorption spectra*

Table 22
Chromium 2p X-ray absorption spectra

Compound	Ref.	Remarks
Cr	[Lea80, Fin85]	Branching ratio
CrF_2	[Set90]	Jahn–Teller distorted
CrF_3	[Nak85]	
Cr_2O_3	[Lea82, Krv90]	
CrO_2	[Knu93]	X-MCD
K_2CrO_4	[Deg••]	LFM, reduced Slater integrals
$CrAu_4$	[Pea86]	
$La_{1-x}Sr_xCrO_3$	[Pot••]	LFM, mixed valence

Chromium compounds are on the borderline between the early, rather delocalized, transition metal compounds and the late transition metal compounds, dominated by localized features. CrO is a notorious compound because of its non-existence and the stable divalent chromium compounds are characteristic because of their strong Jahn–Teller distortions. Trivalent chromium has a stable $3d^3$ configuration such as in Cr_2O_3. Their 2p X-ray absorption spectra (Table 22) do correspond closely to the LFM calculations for a $3d^3[^4A_2]$ ground state. CrO_2 is ferromagnetic and recently its X-MCD spectrum has been measured [Knu93]. Because of its strong covalent character, it is rather surprising that this X-MCD spectrum can be simulated accurately with ligand field multiplet theory without the need to include charge transfer effects [Knu93].

The chromium 2p spectra of the Cr^{6+} oxides are characteristic for a $3d^0$ configuration. In order to obtain quantitative agreement with the observed spectral shape the ligand field multiplet calculations must be performed with the Slater integrals decreased to about 25% of their atomic value [Deg••], a sign of the strong covalent character.

7.6. *Manganese 2p X-ray absorption spectra*

Most compounds contain manganese in its formal valencies 2, 3 and 4. Mn^{2+} contains five 3d electrons which in most compounds constitute a high-spin $^6A_1$ ground state. Divalent manganese compounds have large values of U_{dd} and Δ (see Section 5.3.4) and because of their A_1 nature their

Table 23
Manganese 2p X-ray absorption spectra

Compound	Ref.	Remarks
Mn	[Fin85]	EELS
$Mn_2(CO)_{10}$	[Hit90]	Series of complexes
MnF_2	[Nak85, Set90]	Crystal field effects
	[Deg90b]	LFM
$MnFe_2O_4$	[Cre92]	Series of minerals
MnO	[Deg91t]	LFM
	[Pat90, Spa84]	EELS
Mn_3O_4	[Krv90, Pat90]	EELS
Mn_2O_3	[Pat90, Spa84]	EELS
MnO_2	[Pat90, Spa84]	EELS
$MnPS_3$	[Ohn85]	
MnS	[Cra91b]	LFM, ligand field splittings
$KMnO_4$	[Spa84]	Mn^{7+}
$K_4Mn(CN)_6$	[Cra91b]	Low-spin Mn^{2+}
$LaMnO_3$	[Abb92a]	LFM
$La_{1-x}Sr_xMnO_3$	[Abb92a, Deg91t]	Mixed valence
$LiMnO_2$	[Deg91t]	LFM
$LiMn_2O_4$	[Deg91t]	LFM
Li_2MnO_3	[Deg91t]	LFM
$SrMnO_3$	[Deg91t]	LFM
ZnMnS	[Wei90]	Atomic multiplets

spectral shape is not sensitive to 3d spin–orbit coupling and symmetry distortions. These circumstances enable the 2p X-ray absorption spectra of divalent manganese compounds (see Table 23) to be described accurately by the LFM calculations [Cra91b]. One of the results of this comparison has been that the ligand field value determined as such is smaller (by 25%) than its optical analogue. The cyanide $K_4Mn(CN)_6$ contains divalent manganese in its low-spin configuration [Cra91b].

Mn^{3+} has a high-spin ground state of ^5E symmetry (in octahedral symmetry) susceptible to Jahn–Teller distortions. In addition this d^4 state is less stable than its d^5 and d^3 neighbours. Mn^{4+} has a stable $^4A_2$ ground state. In a study of the spectral variations with valency a series of lithium–manganese oxides have been measured. Figure 40 shows their spectral shape. The spectra show many-peaked fine structure and shift to higher energy with valency. The mixed valence series $La_{1-x}Sr_xMnO_3$ shows similar spectra to $LiMnO_2$ and Li_2MnO_3 [Abb92a].

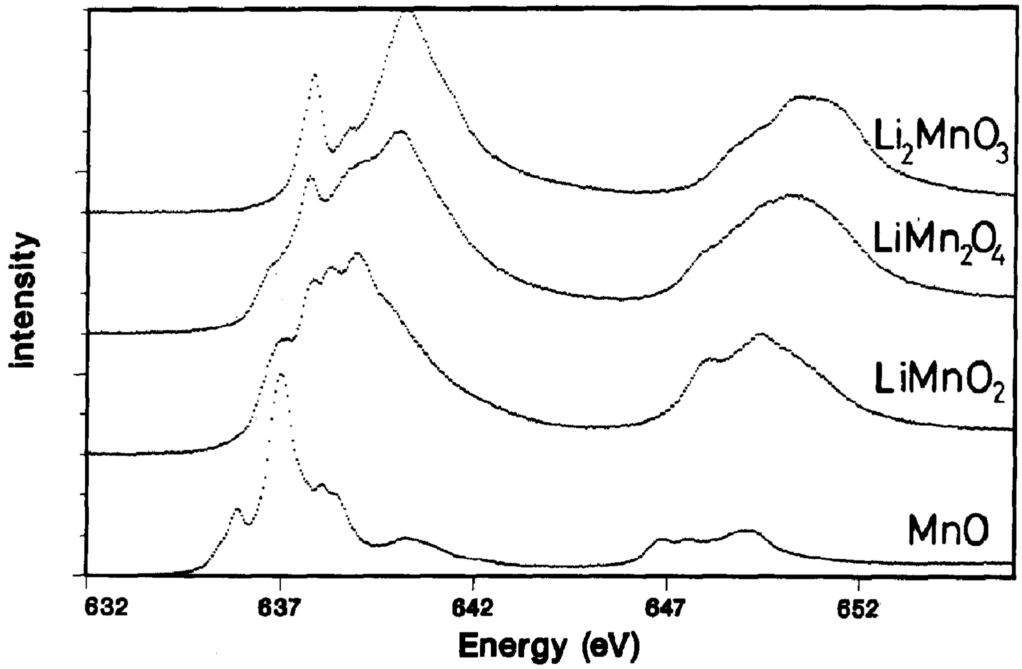

Fig. 40. The manganese 2p X-ray absorption spectra of a series of lithium manganese oxides: MnO + 1% Li (bottom), $LiMnO_2$, $LiMn_2O_4$ and Li_2MnO_3 (top).

7.7. Iron 2p X-ray absorption spectra

Iron has two basic valencies: divalent iron has a $3d^6$ configuration in either a high-spin ($^5T_2$) or a low-spin ($^1A_1$) state and trivalent iron is similar to divalent manganese and has in general a high-spin symmetry ($^6A_1$). Cyanides and some other complexes are low-spin ($^2T_1$).

The high-spin and low-spin states of divalent iron are close to degenerate in many divalent compounds and complexes. In a number of cases a transition occurs as a function of temperature and/or pressure. A nice example is $Fe(phen)_3(NCS)_2$, which undergoes a sharp high-spin to low-spin transition at 170 K (see Table 24). The iron 2p X-ray absorption spectra taken below and above this temperature are a direct confirmation of the respective spin states [Cat93].

The trivalent iron in Fe_2O_3 undergoes a magnetic phase transition at 250 K. In this so-called Morin spin–flip transition the high-spin state is not changed, but the direction of the magnetization is changed by 90°. As discussed, a magnetic field gives rise to both linear and circular dichroism, with the additional complication that the linear dichroism can also be caused by an asymmetric electrostatic field. The spectra for Fe_2O_3 below and above the Morin spin–flip transition temperature do show complete reversal of the linear dichroism signal, or in other words of the direction of the magnetic orientation in the crystal [Kui93].

Table 24
Iron 2p X-ray absorption spectra

Compound	Ref.	Remarks
Fe	[Gru83, Fin85]	Branching ratio
	[Set91]	X-MCD
$Fe(Cp)_2$	[Hit89b, Hit90]	(Cp = cyclopentadiene)
FeF_2	[Nak85, Set90]	Sharp features
$Fe(NEt_4)(Br_4)$	[Cat91]	Series of complexes
$Fe(Phen)_2(NCS)_2$	[Cat93, Che93]	Spin transition
FeO	[Col91, Lea82]	EELS
Fe_2O_3	[Col91, Krv90]	EELS, α and γ forms
	[Cat91, Wad86]	
	[Kui93]	LFM, Linear dichroism
Fe_3O_4	[Col91]	
FePC	[Koc85,Tho88a]	First use of LFM
Fe_3Pt	[May91, May92]	
$FePS_3$	[Ohn85]	
Amphibole	[Cre92]	Series of minerals
Chromite	[Taf82]	EELS, site specific detection
$CoFe_2O_4$	[Set91]	MCD
Fayalite	[Kri90]	Series of minerals
$Gd_3Fe_5O_{12}$	[Rud92, Set91]	MCD, temperature dependence
$La_{1-x}Sr_xFeO_3$	[Abb93b]	LFM, mixed valence
Leucite	[Kri90]	Series of minerals

Another range of problems is connected with the question of mixed valence, that is with systems containing both Fe^{2+} and Fe^{3+} in equivalent, or in non-equivalent sites. In such situations iron 2p X-ray absorption is a direct probe of the occurrence of the actual valencies and sites [Cre92]. However with regard to the nature of doping related effects on the electronic configuration 2p X-ray absorption is not a favourable spectroscopy, and instead more detailed information can be gained from, for example, oxygen 1s X-ray absorption [Abb92a, Deg91t] or photoemission experiments [Boc92a].

Like manganese, iron is an important element for metal centres in biological systems, such as, for example, rubredoxin. The iron 2p X-ray absorption spectra of rubredoxin of *Pyrococcus furiosus* have been studied in its oxidized and reduced form and the spectra can be related to respectively the Fe^{3+} and Fe^{2+} therein [Geo92].

7.8. Cobalt 2p X-ray absorption spectra

In the ligand field multiplet analysis of CoF_2 and CoO it became evident that the effects of 3d spin–orbit coupling are important [Deg90b, Deg93b, Tan92a]. This has been discussed in Section 5.1.4. For CoO a study including both charge transfer and multiplets has been performed by Okada and Kotani [Oka92b] (see Section 5.3.3). A detailed temperature dependent study of the linear dichroism of $BaCoF_4$ has been performed by Sinkovic and coworkers [Sin••]. In this study the peak-asymmetry related to the linear dichroism is shown to give a jump at the Néel temperature

Table 25
Cobalt 2p X-ray absorption spectra

Compound	Ref.	Remarks
Co	[Fin85]	Branching ratio
	[Set91]	X-MCD
Co on Si(111)	[Dec89]	Adsorption
Co/Pt multilayer	[Wuy92]	MCD, orbital polarization
$Co(Cp)_2$	[Hit90]	(Cp = cyclopentadiene)
CoF_2	[Deg90b, Set90]	LFM, 3d spin–orbit
	[Tan92a]	LFM, 3d spin–orbit and temp. dep.
$CoFe_2O_4$	[Set91]	X-MCD
	[Ima92]	X-MCD with LFM
CoO	[Krv90, Szy90]	EELS
	[Deg93b]	LFM, 3d spin–orbit
Co_3O_4	[Szy90]	
$BaCoF_4$	[Che90a, Set90]	Linear dichroism
$LaCoO_3$	[Abb93b]	High-spin to low-spin transition
$LiCoO_2$	[Deg93b]	LFM

which marks the onset of the additional linear dichroism effects of the antiferromagnetic ordering. At low temperatures $LaCoO_3$ has a low-spin ($^1A_1$) ground state. It is known that with temperature a gradual occupation of the high-spin ($^5T_2$) ground state takes place, which is nicely reflected in the cobalt 2p X-ray absorption spectra taken at different temperatures [Abb93b] (see Table 25).

7.9. Nickel 2p X-ray absorption spectra

The analysis of the nickel 2p X-ray absorption (and photoemission) spectra listed in Table 26 has

Table 26
Nickel 2p X-ray absorption spectra

Compound	Ref.	Remarks
Ni	[Fin85, Sha87]	Branching ratio
	[Lea80, Lea82]	EELS
	[Che91]	X-MCD
Ni on Cu(100)	[Tje91]	MCD, temperature and thickness dep.
NiAl	[Pea79, Sha87]	
$Ni_{1-x}P_x$	[Cho85]	
Ni_2Si	[Dep86]	
NiSb	[Sha87]	
La_2NiO_4	[Kui91]	
$NiBr_2$	[Laa86a]	Impurity model, CT-M
$NiCl_2$	[Bon66]	
	[Laa86a, Oka91]	Impurity model, CT-M
NiF_2	[Nak85]	
	[Laa86a]	Impurity model
NiI_2	[Laa86a]	Impurity model
NiO	[Laa86a]	Impurity model
	[Dav86a, Krv90]	
$Ni_{1-x}Li_xO$	[Kui90t]	Effects of doping
$LiNiO_2$	[Vel91b]	"LFM of $3d^8\underline{L}$"
$Cs[NiCr(CN)_6]\cdot 2H_2O$	[Sai93]	X-MCD

been discussed in detail in Sections 5.3.1 and 5.3.2. The X-MCD of the 2p X-ray absorption spectrum of nickel has been the stereotype for X-MCD spectra and analysis [Che91, Jo91, Laa92a, Smi92] and has been discussed in Section 6.

7.10. *Copper 2p X-ray absorption spectra*

The divalent copper oxides have attracted enormous interest because of the superconductivity found in doped, layered copper oxides. A divalent copper ion contains nine 3d electrons and its symmetry is ^2D. In octahedral symmetry the only non-occupied 3d state has ^2E symmetry, which is a Jahn–Teller sensitive state. The degeneracy of the d_{z^2} and $d_{x^2-y^2}$ orbitals will be broken and in the tetragonal, or ultimately square planar, surroundings the empty state will have $d_{x^2-y^2}$ symmetry. In actual systems the symmetry of the ground state can contain admixtures of other symmetries.

The copper L_3 (and L_2) edges of the copper oxides have been much studied (see Table 27). For papers published between 1987 and 1989 the reader is referred to [Als90]. The final state has the configuration $2p^53d^{10}$, that is the single hole has become occupied. Because in the final state the 3d band is full, the Slater integrals, which dominated the other 3d systems, become ineffective and do not play any role for the spectral shape. The spectrum will consist of a single transition to a $2p^53d^{10}$ "exciton" and at higher energy there will be structures related to unoccupied states of d and s character. The absence of Slater integrals implies that one-particle models should be correct to describe the spectral shape (taking into account the core hole potential, etc., as discussed in Section 8). For this purpose multiple scattering has been used [Bia92, Pom91]. It is found that in the undoped systems the "d^{10}" peak has constant energy [Pom91], while for doped systems the peak shows a small energy-dependence with polarization [Abb90, Bia88].

8. Metal and ligand 1s X-ray absorption

In this section the interpretation of both ligand and metal 1s X-ray absorption spectra is discussed.

Table 27
Copper 2p X-ray absorption spectra

Compound	Ref.	Remarks
$CuFeS_2$	[Gri89b]	Effects of valency
Cu_2O	[Hul84, Gri89b]	
	[Tje92a]	Resonant photoemission
Cu_2S	[Gri89b]	Series of compounds
Cu_3VS_4	[Cre92]	Series of minerals
Cu	[Fin85]	
	[Lea80, Lea82]	EELS
CuO	[Lea82, Krv90]	EELS
	[Lop92, Tje92a]	Resonant photoemission
$Bi_2Sr_2CaCu_2O_8$	[Tje92a]	Resonant photoemission
	[Bia92]	MS, polarized
$Bi_2Sr_2CaCu_2O_{8+\delta}$	[Bia88]	Polarized, shift of "d^{10}"
$Bi_{1.7}Pb_{0.3}Sr_2CaCu_2O_8$	[Abb90]	Polarized, shift of "d^{10}"
La_2CuO_4	[Gri89b]	
	[Pom91]	MS, polarized
$La_{2-x}Sr_xCuO_4$	[Als90]	Bibliography 1987–1989
	[Che92a]	Linear dichroism
$YBa_2Cu_3O_{7-x}$	[Als90]	Bibliography 1987–1989
$NaCuO_2$	[Kai89]	Cu^{3+}
Na_3CuF_6	[Cat90]	Cu^{3+}

In Sections 3 and 4 it has been explained that 1s X-ray absorption spectra can be rather accurately described with single particle methods within density functional theory. Both band structure methods and multiple scattering calculations can be used. From the work of von Barth and Grossmann [Von79, Von82] it is clear that one should include the core hole in the calculation, that is one should calculate the distribution of empty states in the final state of the absorption process; the final state rule [Alm83].

From the discussion in Section 3 it evolved that the two-electron Coulomb interactions in the 3d band might cause problems. For the distribution of empty states U is not important directly, but the "orbital polarization" (Section 3.8) might give rise to a modification of the spectral shape at the edge. They are discussed in Section 8.3.2.

According to the final state rule, the 1s X-ray absorption cross section is given as the squared transition matrix from the core state (Φ^c) to the empty valence states (Φ_p^v) times the p-projected final state density of states (n_p^*). The explicit relation has been given, for example, in the work of Müller and co-workers [Mul78, Mul82, Mul84].

$$\sigma = \frac{\omega}{6|\langle\Phi_p^v\rangle|^2}|\langle\Phi_p^v|\mathbf{r}_q|\Phi^c\rangle|^2 n_p^* \tag{36}$$

Because it is rather involved to calculate the final state density of states, often the ground state density of states is compared directly with the X-ray absorption spectrum. Final state calculations are discussed in Section 8.3.6. Also the matrix elements are not always calculated and instead the site (α) and symmetry (p) projected density of states (n_p^α) is used. This site and symmetry projection implicitly assumes the matrix element to be unity within the sphere allocated to a particular site, being zero elsewhere.

8.1. Band structure techniques

As discussed in Section 3.2 various methods exist to calculate the single particle density of states. A short overview focusing on the unoccupied states is given in [Zel92]. Frequently used techniques for X-ray absorption are the linearized augmented plane wave (LAPW) method, for example in [Mul78, Mul82, Mul84]; the linearized muffin-tin orbital (LMTO) method [And75, And84, And85], the augmented spherical wave (ASW) method [Wil79] and the localized (augmented) spherical wave (LSW) method [Leu90].

8.2. Multiple scattering formulation

An alternative route to the calculation of the X-ray absorption cross section is presented by the multiple scattering calculations. In multiple scattering theory the Schrödinger equation is reformulated in scattering theory. This approach is particularly appropriate for the calculation of the empty states which can be calculated for arbitrary large energies. Multiple scattering calculations are usually performed with the Green function approach, that is the Lippmann–Schwinger equation is used as the starting point. The Green function $\mathcal{G}_0 = (e^{ik|r-r'|})/(4\pi|r-r'|)$ describes the propagation of the electron in the solid, which is scattered by the atoms surrounding the absorbing atom. The X-ray absorption cross section is then written as a correlation function (compare with Eq. (8)) [Duh82, Vvd92]

$$\sigma \approx \mathcal{S}\sum_{L,L'}\langle\phi_i|\mathbf{r}_q|\tilde{\phi}_L^0(r)\rangle\tau_{LL'}^{00}\langle\tilde{\phi}_{L'}^0(r)|\mathbf{r}_q|\phi_i\rangle \tag{37}$$

where L stands for both l and m. $\tilde{\phi}_L^0(r)$ is essentially an atomic quantity and it is related to the wavefunction within the muffin-tin potential as discussed in [Gyo73, Vvd92]. $\tau_{LL'}^{00}$ describes the reaction of the surroundings containing all scattering paths. It can be rewritten to describe the effective reflectivity of the surrounding medium, transforming an outgoing wave from the excited atom to an incoming wave toward the excited atom [Vvd92]. For detailed accounts of the multiple scattering method the reader is referred to [Bru91, Nat86b, Reh93, Vvd92] and references therein.

There are a number of advantages of the multiple scattering formulation. Because it can be performed as a cluster calculation, the calculations can relatively easily be done not only for the bulk but also for surfaces, interfaces, etc. In general any ordered and disordered system can be calculated. To accomplish this in a band structure calculation, in general the unit cell must be extended to account for the possible disorder effects, such as slab-calculations for surfaces, etc. This also implies that the core hole potential on the absorbing atom can be added directly in multiple scattering, while for a band structure calculation it necessitates super-cells (see below). Another advantage of multiple scattering is that it can be performed in steps of growing cluster sizes and it is an appealing picture to observe the (theoretical) spectral changes from the effects of increasing the number of back-scatterers and scattering paths around the absorbing atom. Also particular scattering paths can be selected, etc. A disadvantage of (most) multiple scattering calculations is that the potential used is not determined self-consistently.

It has been shown that the multiple scattering formalism and the band structure formalism indeed give equivalent results if worked out rigorously in their mathematical basis [Nat86a, Bru91, Reh93]. For comparison to experiment both the LSD and the multiple scattering results will be treated on the same footing, using the "density of states" picture as guidance.

8.3. Ligand 1s X-ray absorption

Ligand 1s X-ray absorptions have excitation energies which for the often studied light elements, carbon, nitrogen, oxygen and fluorine, are positioned between 300 and 700 eV, that is in the soft X-ray range. The interpretation of 1s spectra in the soft X-ray range is dominated by band structure approaches, in contrast to the hard X-ray region where multiple scattering is most often used. One of the reasons for this is the energy scale of the spectra. For soft X-rays most studies are oriented towards electronic structure determinations of correlated systems and in general only the first 20 to 30 eV of the edge are measured, with the focus on the states at the edge. This 20 eV energy range is relatively easily accessible with band structure methods, which offer the advantage of self-consistently determined potentials. In the hard X-ray range emphasis is on EXAFS analysis and the near-edge region is measured over its full range and analysed with multiple scattering over about 50 to 100 eV in many cases. Such an energy range is not trivially obtained with band structure methods; see Section 8.3.2.

8.3.1. Oxides with empty 3d bands

I will first focus on transition metal compounds with an empty 3d band. As an example the 1s X-ray absorption spectra of titanium oxides are discussed. Figure 41 compares the oxygen p-projected density of states with the oxygen 1s X-ray absorption spectrum of $SrTiO_3$ and TiO_2 (rutile) [Deg93a]. The spectra have been aligned at the position of the first peak. For rutile the spectral shape is reproduced and if the broadening is optimized a close to perfect fit of the experiment can be obtained [Deg93a]. It thus can be concluded that the density of states as obtained from a ground state calculation gives an accurate description of the oxygen 1s X-ray absorption spectral shape. This implies that, (1) the core hole potential does not have a large influence on the spectral shape, and (2) the transition matrix elements do not have to be considered explicitly. Thus in the case of TiO_2, the oxygen 1s X-ray absorption spectral shape gives a direct picture of the oxygen p-projected density of states. Overall, for $SrTiO_3$ similar features are also seen, though some difference between theory and experiment is observed. The sharp t_{2g} peak is followed by a small e_g peak in experiment, which is blurred by the next structure in the calculations. This difference is caused by the core hole potential [Deg93a].

The conclusion is that overall for transition metal oxides with an empty 3d band the oxygen p-projected density of states of a LSD calculation gives a good simulation of the spectral shape. As far as reproducing the oxygen 1s spectral shape

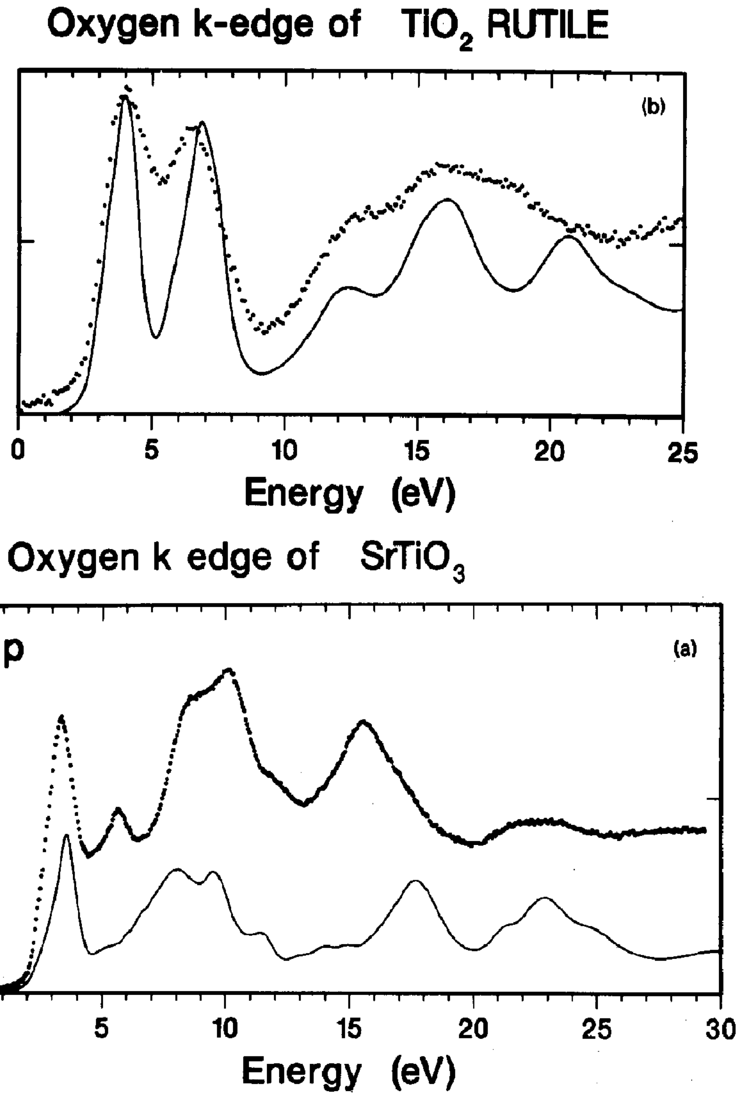

Fig. 41. Ground state oxygen p-projected density of states compared with oxygen 1s X-ray absorption spectra for (a) $SrTiO_3$ and (b) TiO_2.

is concerned, the effectiveness of the core hole potential largely depends on details in the crystal structure.

8.3.2. Oxides with partly filled 3d bands

For oxides with a partly filled 3d band some limitations of normal LSD calculations are met. This has been discussed in Section 3, where a number of recent extensions to LSD were briefly discussed. To account for the observed band gaps it seems to be unavoidable to include the Hubbard "U" in one way or another, such as is attempted in LSD + U calculations [Ani91a, Czy93] and also by LSD + SIC calculations [Sva92, Szo93]. For oxygen 1s X-ray absorption spectra, probing the unoccupied oxygen p states, it is important to remark that the unoccupied density of states is largely unaffected by self-interaction effects. The self-interactions directly affect only the occupied states and their effect on the empty states is indirect, via the reordering of the occupied states. The unoccupied density of states of the LSD + SIC (and also the LSD + U) calculations performed so far [Ani91a, Czy93, Szo93] do show large similarities to their analogues as determined from normal LSD calculations [Ogu84]. This result leads to the conclusion that for comparison to oxygen 1s X-ray absorption spectra it is a rather good approximation to use the oxygen p-projected density of states of a LSD calculation.

In the literature comparisons between LSD results and oxygen 1s X-ray absorption spectra have been made for CuO [Gri89a] and $LiCoO_2$ (Czy92]. In both cases a close overall agreement has been found. Also for VO_2 and $LiVO_2$ [Pen••] and for MnO_2 and CrO_2 [Deg••] good agreement is found. The LSD calculations for MnO and CoO as performed by Terakura et al. [Ter84] show the empty spin-down t_{2g} and e_g bands split by the cubic crystal field, in close agreement with the oxygen 1s X-ray absorption results [Deg89, Deg91t].

Thus it can be concluded that the observations made so far do not pinpoint clear differences between LSD calculations and oxygen 1s X-ray absorption and fair agreement can be obtained.

8.3.2.1. Multiplet effects on oxygen 1s spectra. It has been argued that oxygen 1s spectra will be susceptible to multiplet effects, as far as the 3d part of the spectrum is concerned [Vel90t, Vel91a]. For transition metal oxides with a partly filled 3d band the two-electron Coulomb integrals are important for the electronic structure (see Section 3.8). Cluster calculations with the short range model including multiplet effects, originally developed for inverse photoemission spectroscopy (IPS), have been used to simulate the oxygen 1s X-ray absorption spectra of CoO and NiO [Vel91a]. The absorption process is simulated as the transition $3d^{N+1}\underline{L} \rightarrow 3d^{N+1}$ with the normal configurations for the initial and final states. Agreement has been found for both IPS and XAS, though there are problems with regard to the intensity ratio of the t_{2g} to e_g peak which is not correctly reproduced for X-ray absorption. Also there are questions with regard to the usability of the model because in the model the number of electrons is changed by 1, which is correct for IPS but not for X-ray absorption which is a charge neutral process and the extra valence electron is counterbalanced by the core hole, resulting in a charge neutral process. The "neglect of the core hole" leaves a number of uncertainties, for example, with regard to the parameters to be used in the final state. Because of these uncertainties it is not yet possible to give a detailed answer to the question of the importance of two-electron integrals in oxygen 1s X-ray absorption.

8.3.3. Oxygen 1s spectra of the "CuO" superconductors

The oxygen 1s X-ray absorption spectra of the high T_c superconductors, based on copper-oxide layers, have been much studied in the last six years, both experimentally and theoretically. The non-doped systems, for example La_2CuO_4, consist of a single peak at threshold followed by a structure related to the delocalized states. This single peak can be identified with a "$d^9 \rightarrow d^{10}$" transition, or more precisely a transition of $d^{10}\underline{L}$ character mixed into the d^9 ground state to d^{10}. This peak can be identified with the "upper Hubbard band" [Esk91a, Hyb92], but one can also formulate the transition in a single particle manner as the transitions to the empty states of the copper 3d band [Ben93]. As the Coulomb interaction U has no large effect on the description of the empty states no real distinction can be made between these two descriptions of the X-ray absorption spectrum.

Upon doping a new electronic state occurs related to Cu^{3+}. It has been shown convincingly that the ground state of Cu^{3+} is dominated by $d^9\underline{L}$ character, with little contribution of d^8; see [Esk92t] for an introduction and detailed explanations. In experiment a new peak evolves as a function of the doping, while the second peak drops in intensity. In the single particle (MS) description this is identified with the increased intensity of the 3d band due to the increased number of holes. (The lower energy is caused by the higher effective valence.) The total

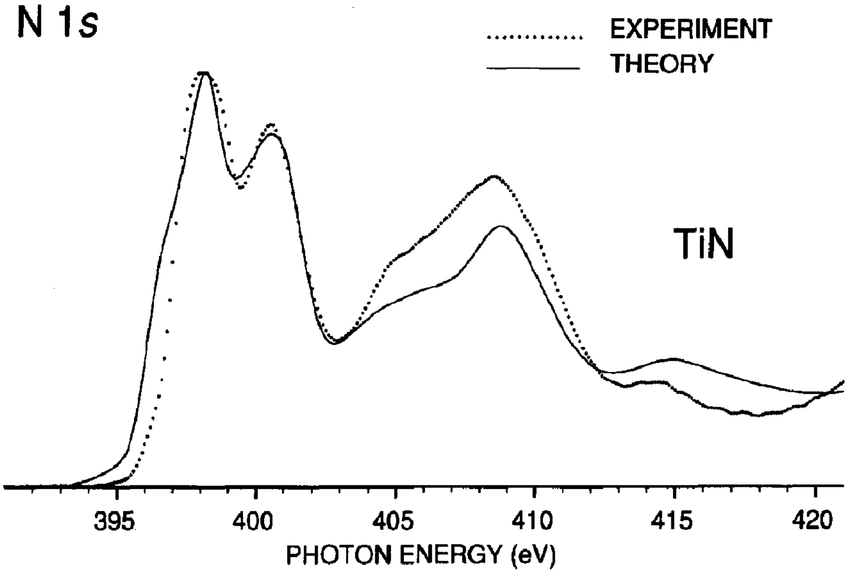

Fig. 42. Ground state nitrogen p-projected density of states (solid line) compared with nitrogen 1s X-ray absorption spectra for TiN (dots) (from [Sor93]).

spectrum is then formed by the addition of doped and undoped cases [Ben93]. In the correlated model Hamiltonian the two situations of Cu^{2+} (undoped) and Cu^{3+} (doped) are coupled and intensity is transferred to the peak at lowest energy, basically because of spectral weight interference effects [Esk91b]. (It is noted that the spectral weight transfer is zero in the ionic limit [Esk91b].) Though not all experimental data can clearly identify spectral weight transfer, it is clear in, for example, $La_{2-x}Sr_{x}$-$_{x}CuO_4$ [Che92a] and Li-doped NiO [Kui89].

8.3.4. 1s Edges of nitrides, silicides and sulphides

For other, in general more covalent, ligands such as nitrides, silicides and sulphides a similar interpretation as for oxides is expected to hold. Thus their ligand 1s X-ray absorption spectra are expected to show close comparison to the projected density of states from LSD band structure calculation, which has been used for nitrides and silicides. For sulphides a comparison will be made with a multiple scattering calculation. For nitrides a detailed comparison between an LSD calculation and a nitrogen 1s spectrum has been published for TiN [Sor93], reproduced in Fig. 42. The calculation has been performed with the LSW method using an extended basis set in order to accurately reproduce the unoccupied states.

The sulphur and silicon 1s edges at about 1500 and 2300 eV have been traditionally more related to the hard X-ray absorption spectra interpreted with real space multiple scattering techniques.

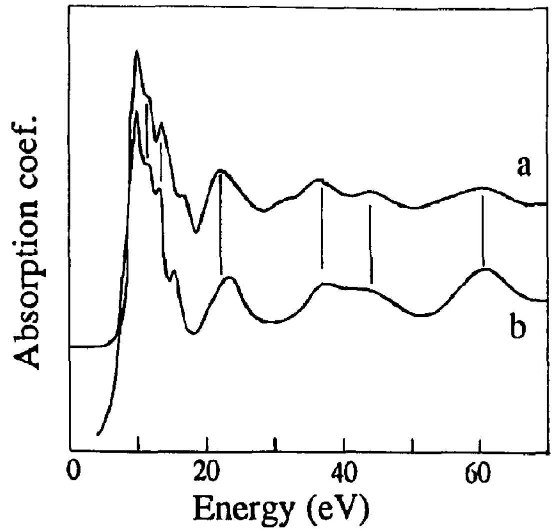

Fig. 43. Real space multiple scattering calculations (b), compared with the sulphur 1s edge of ZnS (a) (from [Sai89]).

For ZnS a multiple scattering calculation has been performed by Sainctavit et al. [Sai89], reproduced in Fig. 43. They used the "screened and relaxed" atomic potentials (implying the inclusion of the core hole potential) and found that best agreement with experiment is obtained with the use of the Dirac–Hara exchange potential. A disadvantage over LSD band structure calculations is that no self-consistent potential is used in these multiple scattering calculations, which leads to a basic problem that even if the calculated spectral shape converges for a particular cluster size, the uncertainty in the potential remains. An important advantage of multiple scattering is that if it is performed in steps of growing cluster sizes, an appealing picture is obtained of the relative importance of the various shells. The same is true if only a particular kind of scattering path is included and the effects on the spectral shape are monitored. For ZnS the spectral shapes are given for 1, 3 and 5 shells in [Sai90], where it is found that a five shell calculation is capable of reproducing the experimental spectral shape rather accurately.

The silicon 1s spectra of a series of transition metal silicides have been studied by Weijs et al. [Wey91]. They compared the observed spectral shapes with a series of ground state LSD calculations using the LSW method. As an example the comparison for the monosilicides is given in Fig. 44. Reasonable agreement could be obtained, though it is clear that in the experimental spectra weight appears contracted to lower energy. This phenomenon is likely to be related to the effect of the core hole potential, not included in the calculations as given in Fig. 44 (see below).

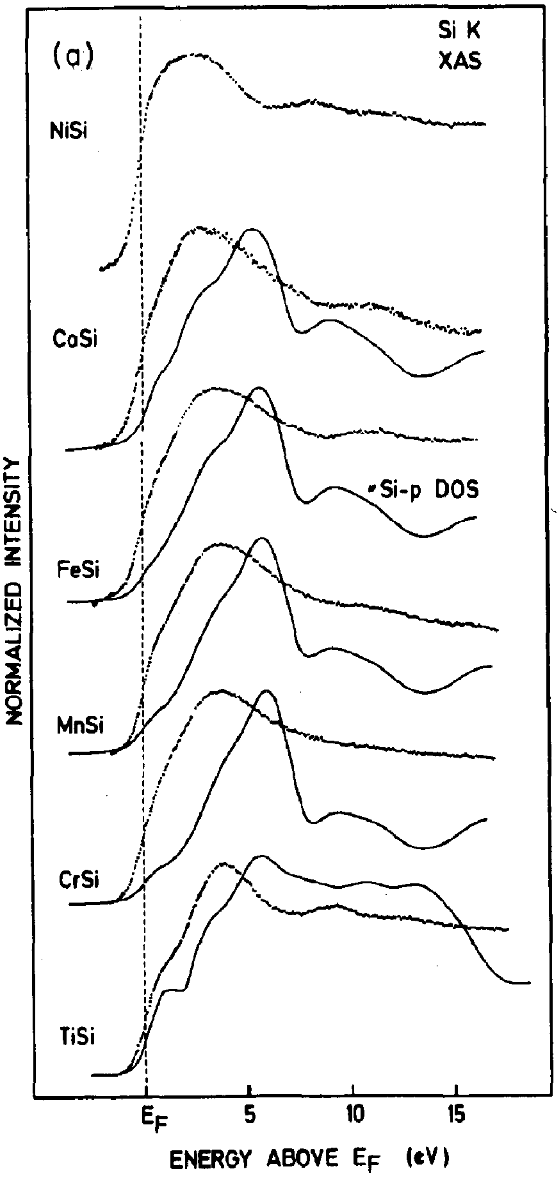

Fig. 44. Ground state silicon p-projected density of states compared with silicon 1s X-ray absorption spectra for a series of transition metal monosilicides (from [Wey91]).

8.3.5. Inclusion of the core hole potential

The core hole potential has been included in the LSD calculations by the removal of a core electron of one of the atoms. To reduce non-physical interactions between two sites with a core hole, the size of the unit cell must increase. For this so-called supercell, a new self-consistent calculation of $n_{\underline{c}N+1}$ instead of n_N must be performed. This approach has been applied successfully to the silver 2p edges of Ag_2O [Czy89, Czy90], the silicon 1s edge of TiSi and $TiSi_2$ [Czy90, Wey91] and the oxygen 1s edge of $LiCoO_2$ [Czy92].

The inclusion of the core hole potential has clear effects on the density of states of $TiSi_2$. If the unoccupied silicon p-projected density of states is compared with experiment a quantitatively correct

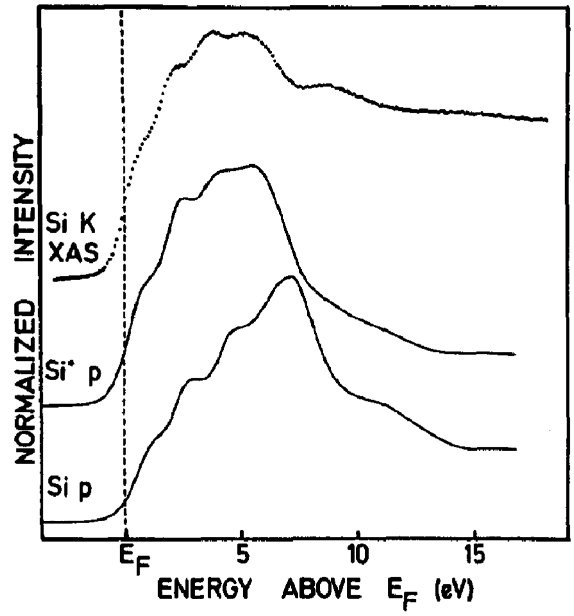

Fig. 45. Silicon p-projected density of states for the ground state (Sip) and final state (Si*p) compared with silicon 1s X-ray absorption spectrum of $TiSi_2$ (from [Wey91]).

"contraction" of the states is found as can be seen in Fig. 45. In some cases this core hole effect can also be simulated with a Clogston–Wolff model calculation using the ground state density of states as an input [Van90, Van90t, Wey91].

A second example of a calculation for which a super cell calculation of the final state is performed is the case of $LiCoO_2$. In $LiCoO_2$ cobalt has the low-spin $3d^6$ configuration ($^1A_1$ symmetry) and consequently the t_{2g} band is full, while all e_g states are empty. The oxygen 1s X-ray absorption spectrum probes the e_g band and at higher energies the other empty bands. Figure 46 compares the X-ray absorption spectrum with the density of states, with and without inclusion of the core hole. A general agreement is found and the overestimation of the intensity of the e_g band is clearly removed after inclusion of the core hole. The core hole effect as calculated for the $LiCoO_2$ spectrum confirms that an oxygen 1s core hole will pull down states to the bottom of

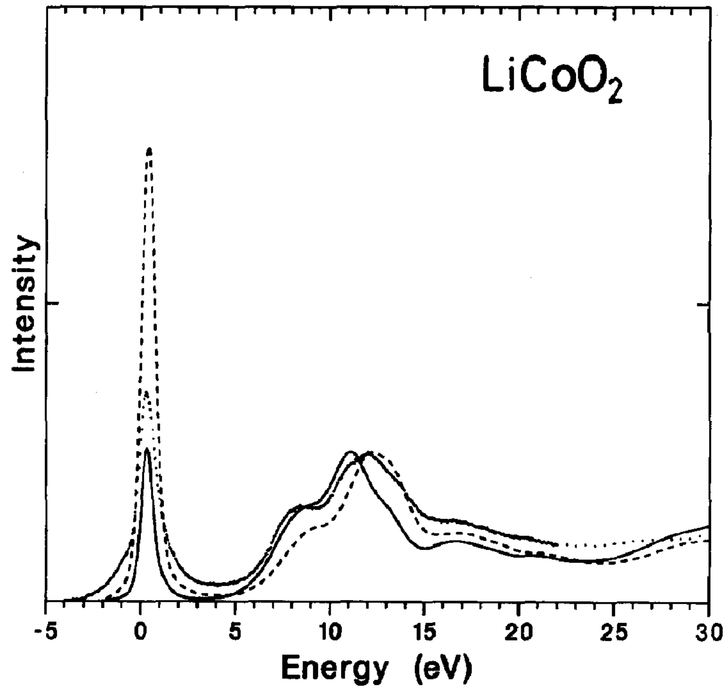

Fig. 46. The oxygen 1s X-ray absorption spectrum of $LiCoO_2$ (dots) compared with the broadened oxygen p-projected density of states. The dashed line refers to the ground state density of states. The solid line refers to the density of states after inclusion of the oxygen 1s core hole $\mathscr{P}_{\underline{c}N+1}$ (from [Czy92]).

the bands. This implies for 3d metal oxides that the dispersional broadening is counteracted. The bands at higher energy are less influenced because they are more extended. The main effect is a redistribution of spectral weight which in general results in an increase of intensity at the bottom of each band.

8.4. Metal 1s X-ray absorption spectra

The metal 1s edges can be interpreted with LSD calculations. As the core hole is created on the metal site, charge transfer (in this context denoted as "multichannel effects") might be expected to have a larger influence, as will be discussed below. The higher energy of the X-rays also makes quadrupole transitions more important, and they have to be considered.

8.4.1. Multiple scattering versus band structure

The metal 1s edges have energies ranging from about 4 to 9 keV. They are often used for EXAFS and their related near edge spectra, denoted as XANES in this context, are traditionally interpreted with multiple scattering methods. A reason for the use of multiple scattering (instead of band structure DOS) is that the XANES spectra are normally measured over an energy range of about 50 eV, which is not easily calculated with band structure methods based on basis functions (such as LAPW, LMTO, ASW and LSW). Real space multiple scattering, and its reciprocal space analogue (the so-called KKR method) do not enter into these basis set problems which makes them more suited for larger energy scales. However with the recent efforts to extend the basis sets to larger energy regions, dedicated to the unoccupied states, the band structure methods are applied also to metal 1s edges, at least for the first 30 eV above the edge [Czy93].

Multiple scattering calculations have been performed, for example, for a series of 3d metal oxides by Norman et al. [Nor85], for TiO$_2$ in the rutile and anatase forms by Brydson and co-workers [Bry87, Bry89, Bry92] and also by Ruiz-Lopez and Munoz-Paez [Rui91] and for a

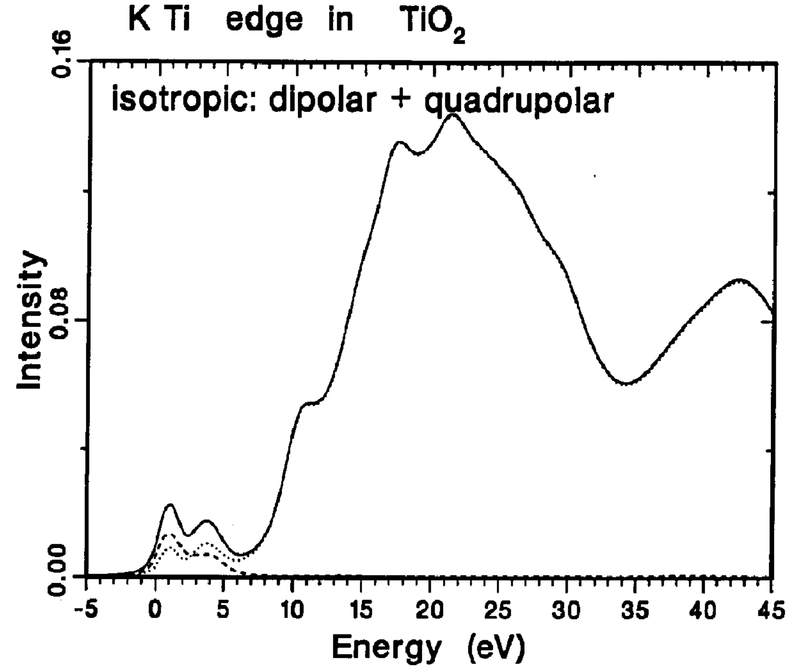

Fig. 47. Simulated titanium 1s edge of TiO$_2$ from a LSW band structure calculation by Czyżyk et al. [Czy••]). Indicated are the dipole transition (dots), the quadrupole transition (dashed line) and the total DOS (solid line).

Table 28
Ligand 1s X-ray absorption spectra for titanium compounds

Compound	Ref.	Element	Remarks
TiC	[Pfl82]	C	EELS
TiN	[Pfl82]	N	EELS
	[Sor93]	N	DOS from LSD
TiO	[Nak87]	O	MS
TiO_2	[Bro86a, Gru83]	O	Molecular orbitals
	[Deg89, Deg93a]	O	DOS from LSD
Ti_2O_3	[Bro86a]	O	
TiS_2	[Fis73, Ohn83]	S	
Ti_2S_3	[Bon86]	S	
TiSi	[Czy90, Wey91]	Si	DOS from LSD
$TiSi_2$	[Czy90, Wey91]	Si	LSD (core hole)
$La_{1-x}Sr_xTiO_3$	[Abb91b]	O	Mixed valence
$SrTiO_3$	[Deg93a]	O	DOS from LSD

high-spin to low-spin transition in an iron(II) complex by Cartier et al. [Cat93]. For TiO_2, band structure approaches have been used by Poumellec and co-workers [Pou91] and Czyżyk [Czy93]. As mentioned above the basic problem is the limited basis set which makes the calculation unreliable above a certain energy. The calculation of [Czy93] has the largest basis set and is expected to be reliable up to about 25 to 30 eV above the edge. The oxygen p-projected density of states of the ground state calculation is reproduced in Fig. 47. This result is in close agreement with experiment up to about 25 eV.

It is concluded that both band structure and multiple scattering methods are able to reproduce the near edge spectrum. Multiple scattering contains problems with regard to the choice of the potential, while band structure methods have a self-consistent potential but suffer from problems related to the limitations of the basis set and hence limitations of the energy range.

Table 29
Ligand 1s X-ray absorption spectra for vanadium compounds

Compound	Ref.	Element	Remarks
V_2O_3	[Abb93a, Deg91t]	O	
VO_2	[Abb91a]	O	Phase transition
V_2O_5	[Abb93a, Deg91t]	O	
VN	[Pfl82]	N	EELS
V_2S_3	[Bon86]	S	
VSi_2	[Van90, Wey91]	Si	DOS from LSD
$Zn_{1-x}Li_xV_2O_4$	[Deg91t]	O	Mixed valence

Table 30
Ligand 1s X-ray absorption spectra for chromium compounds

Compound	Ref.	Element	Remarks
Cr_2O_3	[Gru83]	O	Molecular orbitals
CrSi	[Wey91]	Si	DOS from LSD
$CrSi_2$	[Van90, Wey91]	Si	DOS from LSD

8.4.2. *The "pre-edge" region*

The "pre-edge" region of the transition metal 1s edges has led to a number of debates regarding the quadrupole and/or dipole nature and possible excitonic effects. The "pre-edge" region is related to transitions to the 3d bands. Both direct 1s → 3d quadrupole transitions and dipole transitions to p character hybridized with the 3d band are possible. For the quadrupole transitions the matrix elements are only about 1% of the dipole transition, but the amount of the 3d character in the 3d band is far larger than the p character. This can make, depending on the particular system, the contributions of quadrupole and dipole transitions equivalent in intensity. A direct manner to check the nature of the transitions is to measure the polarization dependence which is different for quadrupole and dipole (as discussed in Section 5.1). This has been checked by Hahn et al. for $CuCl_4^{2-}$ [Hah82] and by Brouder et al. for (the first peak of) TiO_2 [Bru90b]. In both cases a clear and dominant quadrupole contribution could be proven. Recently Yamazaki et al. showed that for the X-MCD spectrum of the "pre-edge" in holmium–iron–garnet

Table 31
Ligand 1s X-ray absorption spectra for manganese compounds

Compound	Ref.	Element	Remarks
$Mn_2(CO)_{10}$	[Hit89a]	C	Organometallic molecules
MnF_2	[Nak88]	F	
MnO	[Nak87]	O	
MnO_2	[Deg89]	O	
MnSi	[Wey91]	Si	
$La_{1-x}Sr_xMnO_3$	[Abb92a]	O	Mixed valence
$LiMnO_2$	[Deg91t]	O	

Table 32
Ligand 1s X-ray absorption spectra for iron compounds

Compound	Ref.	Element	Remarks
$CuFeS_2$	[Sai91]	S	MS
Fe_4B	[Bla89]	B	
FeF_2	[Nak88]	F	
FeMo-protein	[Hem91]	S	Oxidation–reduction
FeO	[Bro86a, Gru83]	O	
	[Col91, Nak87]	O	
α-Fe_2O_3	[Col91, Bro86a]	O	
γ-Fe_2O_3	[Col91]	O	
Fe_3O_4	[Col91]	O	
Fe_2SiO_4	[Bro86a]	O	
$La_{1-x}Sr_xFeO_3$	[Abb93b]	O	Mixed valence

the quadrupole contribution is less than 0.1% [Yaz93].

The case of TiO_2 in its rutile crystal structure has been strongly debated. There are three pre-peaks and the traditional interpretation has been to subscribe the second and third peaks to, respectively, the t_{2g}-like and e_g-like states and the first peak to some kind of exciton. Uozumi et al. [Uoz92] described the "pre-edge" region as a superposition of a quadrupole transition to 3d states and a dipole transition to p states. Both are split by the crystal field and the two doublets are shifted with respect to each other due to the stronger interaction with the 1s core hole with the states of 3d nature. Both the crystal field splitting and the difference in core hole coupling are (assumed to be) about 2.5 eV. The result is three peaks, the first of pure quadrupole nature, the second a mixture and the third a pure dipole peak. This interpretation explains the quadrupole polarization dependence of the first peak. The second peak has a smaller but still considerable quadrupole polarization dependence in the theoretical simulation [Uoz92], but it is almost completely absent in experiment [Bru90b]. Czyżyk also performed a simulation of the "pre-edge" peaks using the projected density of states of a final state band structure calculation [Czy93]. This calculation yields an excitonic peak which is completely dominated by 3d character followed by the t_{2g} and e_g peaks which contain a mixture of d and p character. Including the matrix elements one obtains a first peak which is dominated by quadrupole transitions, though with a dipole contribution of about 25%. The second peak is dominated by dipole transitions, with less than 10% quadrupole and the third peak (and the rest of the spectrum) is almost pure dipole in nature. This result explains better the quadrupole polarization dependence of the first peak and its absence in the second peak. The three-peaked structure has also been reproduced by a ground state LSD calculation [Rui91], which is not compatible with the analysis as given above.

Table 33
Ligand 1s X-ray absorption spectra for cobalt compounds

Compound	Ref.	Element	Remarks
CoF_2	[Nak88]	F	
CoO	[Szy90]	O	
Co_3O_4	[Szy90]	O	
$Co_{1-x}Li_xO$	[Deg93b, Vel91a]	O	
CoSi	[Wey91]	Si	LSD (core hole)
$CoSi_2$	[Van90, Wey91]	Si	
$LaCoO_3$	[Abb93b]	O	Phase transition
$LiCoO_2$	[Czy92]	O	LSD
$ZnCo_2O_4$	[Szy90]		

The intensity of the "pre-edge" region is much larger for compounds in which the metal site has tetrahedral symmetry than for (distorted) octahedral systems [Bia85, Lyt88]. In tetrahedral symmetry the local mixing of p and d nature is symmetry allowed, while for a system with inversion symmetry such as octahedral symmetry it is

Table 34
Ligand 1s X-ray absorption spectra for nickel compounds

Compound	Ref.	Element	Remarks
$LiNiO_2$	[Vel92]	O	Multiplet effects
$Ni(Cp)_2$	[Hit89a]	C	(Cp = cyclopentadiene)
NiF_2	[Nak88]	F	
NiO	[Gru83, Nak87]	O	
	[Dav86b, Vel92]	O	
Ni_2SiO_4	[Bro86a]	O	
NiSi	[Wey91]	Si	DOS from LSD
$NiSi_2$	[Van90, Wey91]	Si	DOS from LSD

"forbidden". This rule is relaxed in the solid and if the density of states is calculated with band structure methods one finds small admixture of p states into the 3d band, as shown for cubic $SrTiO_3$ [Deg91t]. However this admixture is far smaller than for tetrahedral systems which explains the small "pre-edge".

If an octahedral metal site is distorted then, depending on the particular distortion taking place, in general more p character will be mixed into the 3d band. The result is that a distortion of the octahedron will show up as an increased intensity of the "pre-edge" peak(s). That this is indeed the case has been shown by Waychunas for a series of minerals [Way87]; a roughly linear relationship between the bond angle variance (a measure of the distortion) and the "pre-edge" intensity relative to the "step" was demonstrated.

8.4.3. "Multichannel" effects

In their description of the copper 1s edge spectrum of $CuCl_2$ Bair and Goddard [Bai80] introduce the possibility of a "shake-down" satellite structure. Within the framework of the short-range (Anderson impurity) models used for the interpretation of 2p XPS and 2p XAS this process can be related to a charge transfer satellite. Copper is divalent and its ground state is written as $3d^9 + 3d^{10}\underline{L}$. Because of the 1s core hole in the final state the ordering of the ionic configurations is reversed in the final state similar to the case of 2p XPS. This results in two final states ($1s^1 3d^9$ and $1s^1 3d^{10}\underline{L}$). The 1s X-ray absorption spectrum is then assumed to be a multiplication of this double peak structure with the "projected unoccupied states". That is if the two peaks are separated by 7 eV and have an intensity ratio of 1 : 2 then the 1s XAS spectrum is a superposition of the (projected empty) DOS and this DOS shifted over 7 eV with half the intensity. If one of the two peaks completely dominates (or if the energy difference is small) these "multichannel" effects will not appear. This "multichannel" interpretation is used to interpret the characteristic double structure in the copper 1s spectra of the divalent copper oxides such as La_2CuO_4 [Tol92, Tol93]. This double structure is absent in the structurally related Pr_2NiO_4.

8.4.4. The $1/R^2$ rule

Under certain conditions the peak positions of the XANES spectrum can be correlated with the nearest neighbour distances. This phenomenon is known as the $1/R^2$ rule which states that the $\Delta E/R^2$ is constant. This relation between $1/R^2$ and the energy position has often been encountered, for example by Müller et al. [Mul82]. Natoli

Table 35
Ligand 1s X-ray absorption spectra for copper compounds

Compound	Ref.	Element	Remarks
CuF_2	[Nak88]	F	
$CuFeS_2$	[Sai91]	S	MS
$CuGaS_2$	[Sai91]	S	MS
CuO	[Gru83, Nak87]	O	LSD
	[Gri89a]	O	LSD
$CuAl_2O_4$	[Szy90]	O	
$La_{2-x}Sr_xCuO_4$	[Che92a]	O	Linear dichroism
$Ba_2Cu_3O_{7-x}$	[Kui88]	O	

Table 36
Titanium 1s X-ray absorption spectra

Compound	Ref.	Remarks
Ti	[Gru83]	
Ti in B	[Won89]	3d Metals in boron
TiC	[Baz83]	
$TiCl_4$	[Kue90]	
TiFe	[Baz83]	
TiO	[Nor85]	MS
TiO_2	[Baz80, Gru83]	Molecular orbitals
	[Mot90]	Mineral
	[Dur90]	Temperature dependence
	[Bru90b]	Temp. + pol. dependence
	[Pou90]	Polarization dependence
	[Rui91]	MS; 3 prepeaks in ground state
	[Uoz92]	Charge transfer model; quadrupole transition
	[Czy93]	LSD plus core hole; quadrupole transition
Ti_2O_3	[Way87]	Trivalent
$Ti^{4+}[O_4)$	[Bia85]	Tetrahedral site
$BaTiO_3$	[Baz80, Baz83]	
Ba_2TiO_4	[Mot90]	Tetrahedral site
Kaersutite	[Way87]	Series of minerals
$LaTiO_3$	[Kna82]	
$LiTi_2O_4$	[Dur90]	
$SrTiO_3$	[Baz80]	
	[Fis90b]	High pressure

[Nat83] justified the use of this rule for non-atomic resonances, that is resonances with a small variation in phase shifts (related to the lattice parameter). ΔE refers to the energy difference between the peak position and the point of "zero kinetic energy" which has the problem that it is not well defined within an experimental spectrum.

This $1/R^2$ rule has been used successfully by Bianconi [Bia83b], Sette et al. [Set84] and Stöhr et al. [Sto84] for the determination of the bond length of (adsorbed) small molecules. The rule can be used as a measure to directly relate the peak positions to the distances around the absorbing atom. It is used as such for example for NiO and Cu by Lytle et al. [Lyt88]. Because copper in its divalent oxides contains large Jahn–Teller distortions there exist two different nearest neighbour oxygen–copper distances which for X-ray

Table 37
Vanadium 1s X-ray absorption spectra

Compound	Ref.	Remarks
V in B	[Won89]	3d Metals in boron
VO	[Kut84, Won84]	
	[Lyt88]	
VO_x	[Kut84]	Effects of vacancies
V_2O_3	[Won84]	Series of vanadium compounds
V_4O_7	[Won84]	
VO_2	[Bia82a, Won84]	
V_2O_5	[Bia82a, Won84]	
	[Sti89]	Polarization dependence
VN	[Won84]	
VSi_2	[Won84]	
$V^{5+}(H_2O)$	[Bia85]	Tetrahedral site
V (porphyrin)	[Rui86]	

Table 38
Chromium 1s X-ray absorption spectra

Compound	Ref.	Remarks
Cr	[Gru83, Kit86]	
Cr_2O_3	[Gru83]	
K_2CrO_4	[Bia91]	Multielectron excitations
	[Kut80]	
$LaCrO_3$	[Kna82]	

Table 39
Manganese 1s X-ray absorption spectra

Compound	Ref.	Remarks
Mn	[Bel80]	
Mn (atom)	[Arp91]	Atomic manganese
Mn in CaF_2	[Bak92]	
Mn $(acac)_3$	[Cat86a]	Coordination complexes
MnF_2	[Bak92]	
MnF_3	[Bak92]	
Mn_2CrO_4	[Cal86]	
MnO	[Bel80, Nor85]	
	[Kna82, Lyt88]	
	[Ham93]	Spin-polarized; reduced life-time
Mn_2O_3	[Bel80]	
MnO_2	[Bel80]	
$MnHPO_4$	[Bel80]	
Mn-photosystem	[Kus91]	Pre-edge structure
$KMnO_4$	[Bel80]	
	[Bia91]	Multielectron excitations
$KMnF_3$	[Kit90, Shu76]	
$LaMnO_3$	[Kna82]	
TTF $(MnCl_4)_{0.28}$	[Bri92]	(TTF is tetrathiafulvalene)

absorption spectra can be disentangled by the use of polarization dependent measurements. This has been shown nicely by Tolentino and co-workers [Tol92, Tol93] for a series of copper oxides. They included a measurement of Nd_2CuO_4 and because the axial oxygens are "at infinite distance" in this compound the point of "zero energy" has been chosen at the position of the first peak in the Nd_2CuO_4 spectrum [Tol92] and it is found that $\Delta E/R^2$ is indeed constant.

In a recent paper of Kizler [Kiz92a] the $1/R^2$ rule is re-examined with a detailed comparison to multiple scattering calculations and it is claimed that the rule is "disproved for bulk materials"; that is, it is shown that the rule cannot be used for shells other than the first (and second) nearest neighbours. Thus an extensive use as for example in [Lyt88] is disproved, but not its use for the nearest neighbours as for example in [Tol92]. This warning concerning the (limited) use of the rule has also been given in Natoli's paper [Nat83].

8.5. Overview of the ligand 1s spectra

Table 40
Iron 1s X-ray absorption spectra of iron compounds

Compound	Ref.	Remarks
Fe	[Buf87, Gru83]	
	[Kit86]	MS
$FeAl_2O_4$	[Jac91, Kna82]	
	[Bro86b]	
Fe_2B	[Kiz89]	
Fe_4B	[Kiz88, Kiz91]	
$FeCr_2O_4$	[Cal86, Pei83]	
$Fe(Cp)_2$	[Iwa86]	(Cp is cyclopentadiene)
Fe/Gd	[Ito93]	X-MCD (multilayers)
$Fe_5Ho_3O_{12}$	[Yaz93]	X-MCD
FeO	[Chu86, Gru83]	
	[Gar87, Nor85]	MS
	[Lyt88, Mot91]	
$Fe_{0.5}Mg_{0.5}O$	[Kna82]	
$Fe_{0.05}Mg_{0.95}O$	[Way90]	
α-Fe_2O_3	[Chu86, Gru83]	
Fe_3O_4	[Chu86, Gar87]	
$Fe_{1-x}Ni_x$	[Sak93]	X-MCD
FePC	[Fra86]	(PC is phthalocyanine)
$Fe_4(RE)$	[Kob93]	X-MCD (where RE is Sm, Gd, Tb, Dy)
FeS_2	[Pei83]	
Fe_3Si	[Bud89]	(Doped with V, Mn and Co)
Fe_2SiO_4	[Cal86]	(Olivine)
$FeW_{1-x}Nb_xO_4$	[Gar87]	
Fe_2SiO_4	[Jac91]	High temperature
$Fe(phen)_2(NCS)_2$	[Cat86b]	Complexes
Fe(porphyrin)	[Ver86]	
	[Pen91]	Pol. dependent pre-edges
Fe (haemoglobin)	[Bia83a]	
Gillespite	[Way90]	Polarization dependence
$KFeF_3$	[Kit90, Shu76]	
$K_3Fe(CN)_6$	[Bia82b]	(also $K_4Fe(CN)_6$)
$K_4[Fe_2(CN)_{10}]$	[Edw89]	
$LaFeO_3$	[Buf87, Kna82]	
$LiFeO_2$	[Way83]	
$Na_2FeSi_3O_8$	[Bro86b]	Fe in silicates
$Ni_xFeCr_{2-x}O_4$	[Len86]	
Orthopyroxene	[Mot91]	
$SrFeO_3$	[Buf87]	
Staurolite	[Pei83]	Pre-edge

A partial overview is given of a choice of published ligand 1s spectra of 3d transition metal compounds (Tables 28–35). The emphasis is given to oxides and the list is far from complete particularly for chlorides and sulphides. Also more application-oriented studies on catalysis, earth sciences and organic complexes are only partially included. The ligand spectra are

Table 41
Cobalt 1s X-ray absorption spectra

Compound	Ref.	Remarks
Co	[Buf87, Len88]	
$CoAl_2O_4$	[Kna82]	
Co_2CrO_4	[Cal86]	
CoO	[Len88, Nor85] [Kna82]	
Co_3O_4	[Len88]	
$CoRh_2O_4$	[Len88]	
$CuCoO_2$	[Len88]	
$LaCoO_3$	[Buf87, Kna82]	
	[Kag91]	Temperature dependence
$La_{0.5}Sr_{0.5}CoO_3$	[Kag91]	Temperature dependence
$La_2Li_{0.5}Co_{0.5}O_6$	[Buf87]	
$KCoF_3$	[Kit90, Shu76]	
$Co(imad)_2$	[Des83]	
$TTF(CoCl_4)_{0.28}$	[Bri92]	(TTF = tetrathiafulvalene)

tabulated per metal ion, starting with titanium and ending with copper. Most studies on the high T_c superconducting copper oxides have not been included.

8.6. Overview of the metal 1s spectra

A partial overview is given on the metal 1s X-ray absorption spectra (Tables 36–43). In this context hard X-rays are often denoted as X-ray absorption near edge structure (XANES), to distinguish them from the EXAFS analysis. Emphasis is given to recent papers on simple, mostly inorganic, compounds and papers which concentrate on theory.

Table 42
Nickel 1s X-ray absorption spectra

Compound	Ref.	Remarks
Ni	[Gru83]	
Ni_4B	[Kiz88]	
$NiCr_2O_4$	[Len86, Cal86]	
NiF_2	[Len86]	
$NiFe_{2-x}Cr_xO_4$	[Len86]	
$Ni(N_4)$	[Sco89]	Ni^{II} metalloenzymes
NiO	[Gru83, Nor85] [Kna82, Len86]	
Ni(PC)	[Loo89]	MS, (phthalocyanines)
Ni(urease)	[Has83]	
$KNiF_3$	[Shu76, Kit90]	
La_2NiO_4	[Tan93]	Hole doping

Table 43
Copper 1s X-ray absorption spectra

Compound	Ref.	Remarks
Cu	[Gru83]	
Cu (atom)	[Arp91]	Atomic copper
Cu in B	[Won89]	3d Metals in boron
CuO	[Gru83]	Molecular orbitals
	[Kau87]	
Cu_2O	[Nor85]	MS
CuCl	[Haz90]	
$CuCl_4^{2-}$	[Hah82]	Quadrupole transition
CuI	[Haz90]	
$CuTiO_3$	[Lyt88]	$1/R^2$ rule
Cu(II) CN-SOD	[Str91]	(SOD is superoxide dismutase)
$La_{2-x}Sr_xCuO_4$	[Als90]	Bibliography 1987–1989
	[Tan93]	
$La_2CuO_{4-\delta}$	[Oya89]	Polarization dependence
	[Tol92]	Polarization dependence
$YBa_2Cu_3O_7$	[Lyt88]	$1/R^2$ rule
	[Als90]	Bibliography 1987–1989

A recent review concentrating on the structural aspects of XANES spectra is given by Kizler [Kiz92b]. A review focusing on linear polarization dependence is given by Brouder [Bru90a]. Most studies on the high T_c superconducting copper oxides have not been included.

9. Concluding remarks and outlook

9.1. The metal 2p X-ray absorption spectra

The metal 2p X-ray absorption spectra are described with short range Hamiltonians such as the Anderson impurity model, including multiplets. Because in the final state the Coulomb repulsions U_{dd} and U_{cd} largely cancel, the ligand field multiplet model is appropriate for ionic compounds. The ligand field multiplet model has the advantage of its simplicity and the absence of adjustable parameters apart from an effective cubic ligand field strength.

9.2. The ligand 1s X-ray absorption spectra

The 1s X-ray absorption spectra do show large similarities with single particle calculations of the empty states. For these calculations use can be made of band structure methods such as LAPW, LMTO, ASW and LSW or of multiple scattering methods. If the empty density of states is calculated with a self-consistent potential and large enough basis sets, accurate agreement with the X-ray absorption spectra is found. The agreement is improved if the core hole potential is included, while it turns out that matrix elements can, to good approximation, be taken as energy independent. Small effects of multiplets are expected in the part of the spectrum related to the 3d band, but the quantitative results available are not conclusive.

9.3. The valency and symmetry of the metal ions

2p X-ray absorption is an excellent means for the determination of the valency and the symmetry (spin-state) of 3d transition metal ions in compounds and complexes. Due to the "fingerprint" provided by the characteristic final state multiplet structure the valency and spin state can be determined directly and conclusively. More detailed studies, including linear and circular dichroism, can provide additional information on the 3d spin–orbit coupling, lower symmetries, the magnetic ordering and the orbital polarization.

9.4. The electronic configuration

With regard to the details of the electronic configuration 2p X-ray absorption is not the ideal tool, mainly because of the insensitivity of some of the parameters of the model Hamiltonians to the simulations of the spectral shape. In this respect 2p XPS and valence band photoemission are better tools in order to determine the parameter values in the various short range models presently in use.

9.5. The short range model Hamiltonians

Much is still unclear for short range model Hamiltonians as used for core spectroscopies. There are variations and uncertainties in the Hamiltonian itself, the values of the parameters, final state effects and multiplet effects.

Important Hamiltonians presently in use include the Hubbard model (one band with Coulomb repulsion), the Anderson impurity model (two bands, one with repulsion), the Kimball–Falicov model (adding interband repulsion) and the three-band Hubbard model (adding repulsion also in the second band). Additionally these models can be made to interact with the lattice.

The values of the parameters used in these models are normally determined empirically from the simulation of various experiments, or alternatively they are determined from ab initio electronic structure models. In any case the values are model dependent and in that sense "effective" and there is a particular uncertainty with respect to their values.

With respect to the simulation of core spectroscopies there is the problem of the values of the parameters in the final state. A core excitation is expected to modify the electronic structure and as a consequence the effective parameters used for the ground state can (and will) be modified. The way in which this happens can largely be predicted, but many questions still remain.

Multiplet effects play a role in the ground state of 3d systems, but this role is enormously magnified if a 2p core hole is created, due to its strong couplings with the partly filled 3d band. These multiplet effects, or in other words the higher-order terms of the Coulomb repulsions and exchange interactions, play an important role in 2p XPS and particularly in 2p XAS.

9.6. The use of X-ray absorption for the study of materials

Due to the experimental progress in synchrotron radiation, the resolution of soft X-ray monochromators and detection techniques, (soft) X-ray absorption has become an important new tool for the study of materials in basically all fields which study 3d systems. X-ray absorption is element selective and sensitive to "impurities", which includes the role of metal centres in biological systems, catalysis, mineralogy, the search for new magnetic and electronic materials (including superconductors), etc. The analysis with the ligand field multiplet model provides a wealth of information on metal centres (see above), which can "compete", or better assist, the information from for example optical (laser) spectroscopies and resonance experiments.

Acknowledgements

This review is dedicated to the memory of Professor John C. Fuggle. For discussions and advice on particular points I should like to thank Ferdi Aryasetiawan, Christian Brouder, Chien-Te Chen, Steve Cramer, Marek Czyżyk, Henk Eskes, Alain Fontaine, Olle Gunnarsson, Volker Heine, John Inglesfield, Ove Jepsen, Pieter Kuiper, Sasha Liechtenstein, John Michiels, Maurizio Sacchi, Gisela Schütz, Hao Tjeng, Jan van Elp and Jan Vogel. Special thanks to Miguel Abbate, George Sawatzky and Theo Thole. This work was partially supported by the European Community Human Capital and Mobility program.

I thank M. Abbate, V. Anisimov, M. Czyżyk, J. Goedkoop, J. Fink, A. Kotani, K. Okada, Ph. Sainctavit, L. Soriano, S. Sugano, Z. Szotek, K. Terakura, G. van der Laan, P.J. Weiss and also the Journal of Electron Spectroscopy, the Journal of Physics Condensed Matter, the Journal of the Physical Society of Japan, Physica B, Physical Review B, Physics and Chemistry of Minerals, and Surface and Interface Analysis for permission to reproduce their figures.

References

[Abb90] M. Abbate, M. Sacchi, J.J. Wnuk, W.M. Schreurs, Y.S. Wang, R. Lof and J.C. Fuggle, Phys. Rev. B, 42 (1990) 7914.

[Abb91a] M. Abbate, F.M.F. de Groot, J.C. Fuggle, Y.J. Ma, C.T. Chen, F. Sette, A. Fujimori, Y. Ueda and K. Kosuge, Phys. Rev. B, 43 (1991) 7263.

[Abb91b] M. Abbate, F.M.F. de Groot, J.C. Fuggle, A. Fujimori, Y. Tokura, Y. Fujishima, O. Strebel, M. Domke, G. Kaindl, J. van Elp, B.T. Thole, G.A. Sawatzky, M. Sacchi and N. Tsuda, Phys. Rev. B, 44 (1991) 5419.

[Abb92a] M. Abbate, F.M.F. de Groot, J.C. Fuggle, A. Fujimori, O. Strebel, F. Lopez, M. Domke, G. Kaindl, B.T. Thole, G.A. Sawatzky, M. Takano, Y. Takeda, H. Eisaki and S. Uchida, Phys. Rev. B, 46 (1992) 4511.

[Abb92b] M. Abbate, J.B. Goedkoop, F.M.F. de Groot, M. Grioni, J.C. Fuggle, S. Hoffman, H. Petersen and M. Sacchi, Surf. Interface Anal., 18 (1992) 65.

[Abb93a] M. Abbate, H. Pen, M.T. Czyżyk, F.M.F. de Groot, J.C. Fuggle, Y.J. Ma, C.T. Chen, F. Sette, A. Fujimori, Y. Ueda and K. Kosuge, J. Electron Spectrosc. Relat. Phenom., 62 (1993) 185.

[Abb93b] M. Abbate, J.C. Fuggle, A. Fujimori, L.H. Tjeng, C.T. Chen, R. Potze, G.A. Sawatzky, H. Eisaki and S. Uchida, Phys. Rev. B, 47 (1993) 16124.

[Ack84] B. Ackermann, R. Feder and E. Tamura, J. Phys. F, 14 (1984) L173.

[Ahl84] R. Ahlrichs and P. Scharf, Adv. Chem. Phys., 67 (1987) 501.

[Ald93] D. Alders, unpublished results.

[Alm83] C.O. Almbladh and L. Hedin, Beyond the one-electron model: many-body effects in atoms, molecules and solids, in E.E. Koch (Ed.), Handbook on Synchrotron Radiation, Vol. 1A, North Holland, Amsterdam, 1983, p. 607.

[Als90] F. Al-Shamma and J.C. Fuggle, Physica C, 169 (1990) 325.

[And75] O.K. Andersen, Phys. Rev. B, 12 (1975) 3060.

[And79] O.K. Andersen, H.L. Skriver, H. Nohl and B. Johansson, Pure Appl. Chem., 52 (1979) 93.

[And84] O.K. Andersen and O. Jepsen, Phys. Rev. Lett., 53 (1984) 2571.

[And85] O.K. Andersen, O. Jepsen and D. Glötzel, in F. Bassani, F. Fumi and M. Tosi (Eds.), Highlights of Condensed Matter Theory, North Holland, Amsterdam, 1985, pp. 59 ff.

[And87] O.K. Andersen, O. Jepsen and M. Sob, Linearized band structure methods, in M. Yussouf (Ed.), Electronic Band Structure and its Applications, Springer Lecture Notes, 1987.

[Ani91a] V.I. Anisimov, J. Zaanen and O.K. Andersen, Phys. Rev. B, 44 (1991) 943.

[Ani91b] V.I. Anisimov and O. Gunnarsson, Phys. Rev. B, 43 (1991) 7570.

[Ani92a] V.I. Anisimov, M.A. Korotin, J. Zaanen and O.K. Andersen, Phys. Rev. Lett., 68 (1992) 345.

[Ano61] P.W. Anderson, Phys. Rev., 124 (1961) 41.

[Arp91] U. Arp, G. Materlik, M. Meyer, M. Richter and B. Sonntag, in S.S. Hasnain (Ed.), X-ray Absorption Fine Structure, Ellis Horwood, Chichester, 1991, p. 44.

[Ary92] F. Aryasetiawan, Phys. Rev. B, 46 (1992) 13051.

[Ary93] F. Aryasetiawan, unpublished results.

[Asa75] S. Asada, C. Satako and S. Sugano, J. Phys. Soc. Jpn., 37 (1975) 855.

[Asa76] S. Asada and S. Sugano, J. Phys. Soc., Jpn., 41 (1976) 1291.

[Bag73] P.S. Bagus, A.J. Freeman and F. Sasaki, Phys. Rev. Lett., 30 (1973) 851.

[Bag89] P. Bagno, O. Jepsen and O. Gunnarsson, Phys. Rev. B, 40 (1989) 1997.

[Bai80] R.A. Bair and W.A. Goddard III, Phys. Rev. B, 22 (1980) 2767.

[Bak92] J.H. Barkyoumb and A.N. Mansour, Phys. Rev. B, 46 (1992) 8768.

[Bal62] C.J. Ballhausen, Introduction to Ligand Field Theory, McGraw-Hill, New York, 1962

[Bar83] J. Barth, F. Gerken and C. Kunz, Phys. Rev. B, 28 (1983) 3608.

[Bas83] F. Bassani and M. Altarelli, Interaction of radiation with condensed matter, in E.E. Koch (Ed.), Handbook on Synchrotron Radiation, Vol. 1A, North Holland, Amsterdam, 1983, p. 463.

[Bau91] F. Baudelet, E. Dartyge, A. Fontaine, C. Brouder, G. Krill, J.P. Kappler and M. Piecuch, Phys. Rev. B, 43 (1991) 5857.

[Baz80] A. Balzarotti, F. Comin, L. Incoccia, M. Piacentini, S. Mobilio and A. Savoia, Solid State Commun., 35 (1980) 145.

[Baz83] A. Balzarotti, in A. Bianconi, L. Incoccia and S. Stipcich (Eds.), EXAFS and Near Edge Structure, Springer-Verlag, Berlin 1983, p. 135.

[Bec88] A.D. Becke, Phys. Rev. A, 38 (1988) 3098.

[Bel80] M. Belli, A. Scafati, A. Bianconi, S. Mobilio, L. Palladino, A. Reale and E. Burattini, Solid State Commun., 35 (1980) 355.

[Ben93] M. Benfatto, Z.Y. Wu and C.R. Natoli, Jpn. J. Appl. Phys., 32 (1993) 590.

[Ber87] S. Bernstorff et al., Phys. Scr., 36 (1987) 15.

[Bia82a] A. Bianconi, Phys. Rev. B, 26 (1982) 2741.

[Bia82b] A. Bianconi, M. Dell' Ariccia, P.J. Durham and J.B. Pendry, Phys. Rev. B, 26 (1982) 6502.

[Bia83a] A. Bianconi, in A. Bianconi, L. Incoccia and S. Stipcich (Eds.), EXAFS and Near Edge Structure, Springer-Verlag, Berlin, 1983, p. 118.

[Bia83b] A. Bianconi, M. Dell'Ariccia, A. Gargano and C.R. Natoli, in A. Bianconi, L. Incoccia and S. Stipcich (Eds.), EXAFS and Near Edge Structure, Springer-Verlag, Berlin, 1983, p. 57.

[Bia85] A. Bianconi, E. Fritsch, G. Calas and J. Petiau, Phys. Rev. B, 32 (1985) 4292.

[Bia88] A. Bianconi, M. De Santis, A.M. Flank, A. Fontaine, P. Lagarde, A. Marcelli, H. Katayama-Yoshida and A. Kotani, Phys. Rev. B, 38 (1988) 7196.

[Bia91] A. Bianconi, J. Garcia, M. Benfatto, A. Marcelli, C.R. Natoli and M.F. Ruiz-Lopez, Phys. Rev. B, 43 (1991) 6885.

[Bia92] A. Bianconi, C. Li, S. Della Longa and M. Pompa, Phys. Rev. B, 45 (1992) 4989.

[Bla89] W. Blau, R. Dudde and H. Petersen, Solid State Commun., 69 (1989) 147.

[Boc92a] A.E. Bocquet, A. Fujimorui, T. Mizokawa, T. Saitoh, H. Namatame, S. Suga, N. Kimizuka, Y. Takeda and M. Takano, Phys. Rev. B, 45 (1992) 1561.

[Boc92b] A.E. Bocquet, T. Mizokawa, T. Saitoh, H. Namatame and A. Fujimori, Phys. Rev. B, 46 (1992) 3771.

[Boe84] D.K.G. de Boer, C. Haas and G.A. Sawatzky, Phys. Rev. B, 29 (1984) 4401.

[Bog57] P.F. Bongers, Ph.D. Thesis, University of Leiden, 1957.

[Bog75] P.F. Bongers, in C.J.M. Rooymans and A. Rabenau (Eds.), Crystal Structure and Chemical Bonding in Inorganic Chemistry, Elsevier, Amsterdam, 1975, Chap. 4.

[Bon66] C. Bonnele, Ann. Phys., 1 (1966) 439.

[Bon86] D. Bonnin, J. Phys. (Paris) C, 8 (1986) 623.

[Bor92] A. Borg, P.L. King, P. Pianetta, I. Lindau, D.B. Mitzi, A. Kapitulnik, A.V. Soldatov, S. Della Longa and A. Bianconi, Phys. Rev. B, 46 (1992) 8487.

[Bri92] V. Briois, R.M. Lequan, M. Lequan, C. Cartier, G. van der Laan, A. Michalowicz and M. Verdaguer, Chem. Mater., 4 (1992) 484.

[Bro78] F.C. Brown, R.Z. Bachrach and N. Lien, Nucl. Instrum. Methods, 152 (1978) 73.

[Bro86a] G.E. Brown Jr., G.A. Waychunas, J. Stohr and F. Sette, J. Phys. (Paris) C, 8 (1986) 685.

[Bro86b] G.E. Brown Jr., G.A. Waychunas, C.W. Ponader, W.E. Jackson and D.A. Mckeown, J. Phys. (Paris) C, 8 (1986) 661.

[Bru90a] C. Brouder, J. Phys. C, 2 (1990) 701.

[Bru90b] C. Brouder, J.P. Kappler and E. Beaurepaire, in A. Balerna, E. Bernieri and S. Mobilio (Eds.), Proc. 2nd European Conference on Progress in X-ray Synchrotron Radiation Research, Rome, November 1989, SIF, Bologna, 1990, p. 19.

[Bru91] C. Brouder and M. Hikam, Phys. Rev. B, 43 (1991) 3809.

[Bry87] R. Brydson, B.G. Williams, W. Engel, H. Sauer, E. Zeitler and J.M. Thomas, Solid State Commun., 64 (1987) 609.

[Bry89] R. Brydson, H. Sauer, W. Engel, J.M. Thomas, E. Zeitler, N. Kosugi and H. Kuroda, J. Phys. Condensed Matter, 1 (1989) 797.

[Bry92] R. Brydson, H. Sauer, W. Engel and F. Hofer, J. Phys. Condensed Matter, 4 (1992) 3429.

[Bud89] J.I. Budnick, Z. Tan and D.M. Pease, Physica B, 158 (1989) 31.

[Buf87] B. Buffat and M.H. Tuilier, Solid State Commun., 64 (1987) 401.

[But81] P.H. Butler, Point Group Symmetry Applications: Methods and Tables, Plenum Press, New York, 1981.

[Cal86] G. Calas, J. Petiau and A. Manceau, Phys. (Paris) C, 8 (1986) 813.

[Car90] P. Carra and M. Altarelli, Phys. Rev. Lett., 64 (1990) 1286.

[Car91] P. Carra, B.N. Harmon, B.T. Thole, M. Altarelli and G.A. Sawatzky, Phys. Rev. Lett., 66 (1991) 2495.

[Car92] P. Carra, Synchrotron Radiat. News, 5 (1992) 6:21.

[Car93] P. Carra, B.T. Thole, M. Altarelli and X. Wang, Phys. Rev. Lett., 70 (1993) 694.

[Cat86a] C. Cartier, M. Verdaguer, S. Menage, J.J. Girerd, J.P. Tuchagues and B. Mabad, J. Phys. (Paris) C, 8 (1986) 623.

[Cat86b] C. Cartier, P. Thuery, M. Verdaguer, J. Zarembowitch and A. Michailowicz, J. Phys. (Paris) C, 8 (1986) 563.

[Cat90] C. Cartier, M. Verdaguer, A.M. Flank, P. Lagarde, F. Baudelet, J. Darriet, A. Tressaud and A. Lelirzin, in A. Balerna, E. Bernieri and S. Mobilio (Eds.), Proc. 2nd European Conference on Progress in X-ray Synchrotron Radiation Research, Rome, November 1989, SIF, Bologna, 1990, p. 907.

[Cat91] C. Cartier and A.M. Flank, in S.S. Hasnain (Ed.), X-ray Absorption Fine Structure, Ellis Horwood, Chichester, 1991, p. 659.

[Cat92] C. Cartier, P. Rudolf, A.M. Flank and C.T. Chen, J. Phys. Chem., 96 (1992) 6196.

[Cat93] C. Cartier dit Moulin, A.M. Flank, P. Rudolf and C.T. Chen, Jpn. J. Appl. Phys., 32 (1993) 308.

[Che87] C.T. Chen, Nucl. Instrum. Methods, 256 (1987) 595.

[Che89] C.T. Chen and F. Sette, Rev. Sci. Instrum., 60 (1989) 1616.

[Che90a] C.T. Chen and F. Sette, Phys. Scr. T, 31 (1990) 119.

[Che90b] C.T. Chen, F. Sette and N.V. Smith, Appl. Opt., 29 (1990) 4235.

[Che91] C.T. Chen, N.V. Smith and F. Sette, Phys. Rev. B, 43 (1991) 6785.

[Che92a] C.T. Chen, L.H. Tjeng, J. Kwo, H.L. Kao, P. Rudolf, F. Sette and R.M. Fleming, Phys. Rev. Lett., 68 (1992) 2543.

[Che92b] C.T. Chen, Rev. Sci. Instrum., 63 (1992) 1223.

[Che93] C.T. Chen, Jpn. J. Appl. Phys., 32 (1993) 155.

[Cho85] M. Choi, D.M. Pease, W.A. Hines, G.H. Hayes, J.I. Budnick, S.M. Heald, R. Hasegawa and H.E. Schone, Phys. Rev. B, 32 (1985) 7670.

[Chu86] S.H. Chou, J. Guo and D.E. Ellis, Phys. Rev. B, 34 (1986) 12.

[Cit76] P.H. Citrin, P. Eisenberger and B.M. Kincaid, Phys. Rev. Lett., 36 (1976) 1346.

[Col91] C. Colliex, T. Manoubi and C. Ortiz, Phys. Rev. B, 44 (1991) 11402.

[Con35] E.U. Condon and G.H. Shortley, The Theory of Atomic Spectra, University Press, Cambridge, UK, 1935.

[Cow81] R.D. Cowan, The Theory of Atomic Structure and Spectra, University of California Press, Berkeley, 1981, p. 307.

[Cra88] S.P. Cramer, O. Tench and G.N. George, Nucl. Instrum. Methods A, 266 (1988) 586.

[Cra91a] S.P. Cramer, H. Kraner, S.J. George, L. Rogers, S. Rescia, V. Radeka, M. Yocum, J. Coloresi, O. Tench and O.C. Mullins, in S.S. Hasnain (Ed.), X-ray Absorption Fine Structure, Ellis Horwood, Chichester, 1991, p. 640.

[Cra91b] S.P. Cramer, F.M.F. de Groot, Y. Ma, C.T. Chen, F. Sette, C.A. Kipke, D.M. Eichhorn, M.K. Chan, W.H. Armstrong, E. Libby, G. Christou, S. Brooker, V. McKee, O.C. Mullins and J.C. Fuggle, J. Am. Chem. Soc., 113 (1991) 7937.

[Cre92] G. Cressey, C.M.B. Henderson and G. van der Laan, Phys. Chem. Miner., 20 (1993) 111.

[Cur74] D. Curie, C. Barthon and B. Canny, J. Chem. Phys., 61 (1974) 3048.

[Czy89] M.T. Czyżyk, R.A. de Groot, G. Dalba, P. Fornasini, A. Kisiel, F. Rocca and E. Burattini, Phys. Rev. B, 39 (1989) 9831.

[Czy90] M.T. Czyżyk and R.A. de Groot, in A. Balerna, E. Bernieri and S. Mobilio (Eds.), Proc. 2nd European Conference on Progress in X-ray Synchrotron Radiation Research, Rome, November 1989, SIF, Bologna, 1990, p. 47.

[Czy92] M.T. Czyżyk, R. Potze and G.A. Sawatzky, Phys. Rev. B, 46 (1992) 3729.

[Czy93] M.T. Czyżyk, unpublished results.

[Daa91] G.H.O. Daalderop, P.J. Kelly and M.F.H. Schuurmans, Phys. Rev. B, 44 (1991) 12054.

[Dav86a] I. Davoli, A. Marcelli, A. Bianconi, M. Tomellini and M. Fanfoni, Phys. Rev. B, 33 (1986) 2979.

[Dav86b] I. Davoli, M. Tomellini and M. Fanfoni, J. Phys. (Paris) C, 8 (1986) 517.

[Dec89] M. de Crescenzi, J. Derrien, E. Chainet and K. Orumchian, Phys. Rev. B, 39 (1989) 5520.

[Ded84] P.H. Dederichs, S. Blügel, R. Zeller and H. Akai, Phys. Rev. B, 53 (1984) 2512.

[Deg89] F.M.F. de Groot, M. Grioni, J.C. Fuggle, J. Ghijsen and G.A. Sawatzky, Phys. Rev. B, 40 (1989) 5715.

[Deg90a] F.M.F. de Groot, J.C. Fuggle, B.T. Thole and G.A. Sawatzky, Phys. Rev. B, 41 (1990) 928.

[Deg90b] F.M.F. de Groot, J.C. Fuggle, B.T. Thole and G.A. Sawatzky, Phys. Rev. B, 42 (1990) 5459.

[Deg91t] F.M.F. de Groot, Ph.D. Thesis, University of Nijmegen, 1991.

[Deg92] F.M.F. de Groot, M.O. Figueiredo, M.J. Basto, M. Abbate, H. Petersen and J.C. Fuggle, Phys. Chem. Miner., 19 (1992) 140.

[Deg93a] F.M.F. de Groot, J. Faber, J.J.M. Michiels, M.T. Czyżyk, M. Abbate and J.C. Fuggle, Phys. Rev. B, 48 (1993) 2074.

[Deg93b] F.M.F. de Groot, M. Abbate, J. van Elp, G.A. Sawatzky, Y.J. Ma, C.T. Chen and F. Sette, J. Phys. Condensed Matter, 5 (1993) 2277.

[Deg93c] F.M.F. de Groot, J. Electron Spectrosc. Relat. Phenom., 62 (1993) 111.

[Deg●●] F.M.F. de Groot, unpublished results.

[Dep86] U. del Pennino, C. Mariani, S. Valeri, G. Ottavianni, M.G. Betti, S. Nannarone and M. de Crescenzi, Phys. Rev. B, 34 (1986) 2875.

[Des83] A. Desideri and C. Rotilio, in A. Bianconi, L.

Incoccia and S. Stipcich (Eds.), EXAFS and Near Edge Structure, Springer-Verlag, Berlin, 1983, p. 342.

[Dol91] M. Dolg, P. Fulde, W. Küchle, C.S. Neumann and H. Stoll, J. Chem. Phys., 94 (1991) 3011.

[Dom91] M. Domke, C. Xue, A. Puschmann, T. Mandel, E. Hudson, D.A. Shirley, G. Kaindl, C.H. Greene, H.R. Sadeghpour and H. Petersen, Phys. Rev. Lett., 66 (1991) 1306.

[Duh82] P.J. Durham, J.B. Pendry and C.H. Hodges, Comp. Phys. Commun., 25 (1982) 193.

[Dur90] O. Durmeyer, J.P. Kappler, E. Beaurepaire, J.M. Heintz and M. Drillon, J. Phys. Condensed Matter, 2 (1990) 6127.

[Ebe88a] H. Ebert, P. Strange and B.L. Gyorffy, J. Appl. Phys., 63 (1988) 3055.

[Ebe88b] H. Ebert, P. Strange and B.L. Gyorffy, Z. Phys. B, 73 (1988) 77.

[Ebe89a] H. Ebert and R. Zeller, Physica B, 161 (1989) 191.

[Ebe89b] H. Ebert, B. Drittler, R. Zeller and G. Schütz, Solid State Commun., 69 (1989) 485.

[Ebe90] H. Ebert and R. Zeller, Phys. Rev. B, 42 (1990) 2744.

[Ebe91] H. Ebert, R. Wienke, G. Schütz and W.M. Temmerman, Physica B, 172 (1991) 71.

[Edw89] B. Edwards, C.D. Garner and G. Stedman, Physica B, 158 (1989) 223.

[Ela93] M. Elango, A. Ausmees, A. Kikas, E. Nommiste, A. Saar, J.F. van Acker, J.N. Andersen, R. Nyholm and I. Martinson, Phys. Rev. B, 47 (1993) 11736.

[Eme87] V.J. Emery, Phys. Rev. Lett., 58 (1987) 2794.

[Erb88] A. Erbil, G.S. Cargill III, R. Frahm and R.F. Boehme, Phys. Rev. B, 37 (1988) 2450.

[Eri90a] O. Eriksson, L. Nordström, A. Pohl, L. Severin, A.M. Boring and B. Johansson, Phys. Rev B, 41 (1990) 11807.

[Eri90b] O. Eriksson, B. Johansson, R.C. Albers, A.M. Boring and M.S.S. Brooks, Phys. Rev. B, 42 (1990) 2707.

[Ers75] J.L. Erskine and E.A. Stern, Phys. Rev. B, 12 (1975) 5016.

[Esk91a] H. Eskes and G.A. Sawatzky, Phys. Rev. B, 43 (1991) 119.

[Esk91b] H. Eskes, M.B.J. Meinders and G.A. Sawatzky, Phys. Rev. Lett., 67 (1991) 1035.

[Esk92t] H. Eskes, Some Unusual Aspects of Correlated Systems, Ph.D. Thesis, University of Groningen, 1992.

[Fal84] L.M. Falicov and R.H. Victora, Phys. Rev. B, 30 (1984) 1695.

[Fin85] J. Fink, Th. Müller-Heinzerling, B. Scheerer, W. Speier, F.U. Hillebrecht, J.C. Fuggle, J. Zaanen and G.A. Sawatzky, Phys. Rev. B, 32 (1985) 4899.

[Fis73] D.W. Fisher, Phys. Rev. B, 8 (1973) 3576.

[Fis90a] P. Fisher, G. Schütz and G. Wiesinger, Solid State Commun., 76 (1990) 777.

[Fis90b] M. Fisher, B. Bonello, J.P. Itie, A.P. Polian, E. Dartyge, A. Fontaine and H. Tolentino, Phys. Rev. B, 42 (1990) 8494.

[Fra86] K.H. Frank, E.E. Koch and H.W. Biester, in J. Phys. (Paris) C, 8 (1986) 653.

[Fug88] J.C. Fuggle, G.A. Sawatzky and J.W. Allen (Eds.), Narrow Band Phenomena, Plenum Press, New York, 1988, p. 3.

[Fug90] J.C. Fuggle, Core Level Spectroscopies and Synchrotron Radiation, in R. Rosei (Ed.), Proc. Int. School of Physics, North Holland, Amsterdam, 1990, p. 127.

[Fug91] I.H. Munro, C.A. Boardman and J.C. Fuggle, World Compendium of Synchrotron Radiation Facilities, European Synchrotron Radiation Society, 1991.

[Fuj84a] A. Fujimori, F. Minami and S. Sugano, Phys. Rev. B, 29 (1984) 5225.

[Fuj84b] A. Fujimori and F. Minami, Phys. Rev. B, 30 (1984) 957.

[Fuj92a] A. Fujimori, I. Hase, H. Namatame, Y. Fujishima, Y. Tokura, M. Nakamura, A. Misu, M. Abbate, F.M.F. de Groot, M.T. Czyżyk, J.C. Fuggle, O. Strebel, F. Lopez, M. Domke and G. Kaindl, Phys. Rev. B, 46 (1992) 9841.

[Fuj92b] A. Fujimori, I. Hase, Y. Tokura, M. Abbate, F.M.F. de Groot, J.C. Fuggle, H. Eisaki and S. Uchida, Physica B, 186–188 (1993) 981.

[Fuj93] A. Fujimori, A.E. Bocquet, T. Saitoh and T. Mizokawa, J. Electron Spectrosc. Relat. Phenom., 62 (1993) 141.

[Ful91] P. Fulde and H. Stoll, J. Chem. Phys., 97 (1992) 4185.

[Gar87] K.B. Garg, H.S. Chauhan, U. Chandra, K.S. Jerath and F. Grandjean, Solid State Commun., 62 (1987) 575.

[Geo92] S. George, J. van Elp, J. Chen, Y. Ma, C.T. Chen, J.B. Park, M.W.W. Adams, B.G. Searle, F.M.F. de Groot, J.C. Fuggle and S.P. Cramer, J. Am. Chem. Soc., 114 (1992) 4426.

[Gie91] A. Giesekus and L.M. Falicov, Phys. Rev. B, 44 (1991) 10449.

[Gle85] C. Gleitzer and J.B. Goodenough, Struct. Bonding (Berlin), 61 (1985) 1.

[God88] R.W. Godby, M. Schlüter and L.J. Sham, Phys. Rev. B, 37 (1988) 10159.

[God92] R.W. Godby, in J.C. Fuggle and J.E. Inglesfield (Eds.), Unoccupied Electronic States, Springer, Berlin, 1992, p. 51.

[Goe88] J.B. Goedkoop, B.T. Thole, G. van der Laan, G.A. Sawatzky, F.M.F. de Groot and J.C. Fuggle, Phys. Rev. B, 37 (1988) 2086.

[Goe89t] J.B. Goedkoop, X-ray Dichroism of Rare Earth Materials, Ph.D. Thesis, University of Nijmegen, 1989.

[Goo63] J.B. Goodenough, Magnetism and the Chemical Bond, Wiley Interscience, New York, 1963.

[Goo71] J.B. Goodenough, in H. Reiss (Ed.), Progress in Solid State Chemistry, Pergamon Press, Oxford, 1971.

[Grf64] J.S. Griffith, The Theory of Transition Metal Ions, University Press, Cambridge, UK, 1964, Chapt. 9.

[Gri89a] M. Grioni, M.T. Czyżyk, F.M.F. de Groot, J.C. Fuggle and B.E. Watts, Phys. Rev. B, 39 (1989) 4886.

[Gri89b] M. Grioni, J.B. Goedkoop, R. Schoorl, F.M.F. de Groot, J.C. Fuggle, F. Schäfers, E.E. Koch, G. Rossi, J.M. Esteva and R.C. Karnatak, Phys. Rev. B, 39 (1989) 1541.

[Gru83] L.A. Grunes, Phys. Rev. B, 27 (1983) 2111.

[Gun74] O. Gunnarsson, B.I. Lundqvist and J.W. Wilkins, Phys. Rev. B, 10 (1974) 1319.

[Gun83] O. Gunnarsson and K. Schönhammer, Phys. Rev. B, 28 (1983) 4315.

[Gun85] O. Gunnarsson and K. Schönhammer, Phys. Rev. B, 31 (1985) 4815.

[Gun88a] O. Gunnarsson, O.K. Andersen, O. Jepsen and J. Zaanen, in J. Kanamori and A. Kotani (Eds.), Core-Level Spectroscopy in Condensed Systems, Springer-Verlag, Berlin, 1988, p. 82.

[Gun88b] O. Gunnarsson and O. Jepsen, Phys. Rev. B, 38 (1988) 3568.

[Gun89a] O. Gunnarsson, O.K. Andersen, O. Jepsen and J. Zaanen, Phys. Rev. B, 39 (1989) 1708.

[Gun89b] O. Gunnarsson and K. Schönhammer, Phys. Rev. B, 40 (1989) 4160.

[Gun90] O. Gunnarsson, Phys. Rev. B, 41 (1990) 514.

[Gup74] R.P. Gupta and S.K. Sen, Phys. Rev. B, 10 (1974) 71.

[Gup75] R.P. Gupta and S.K. Sen, Phys. Rev. B, 12 (1975) 15.

[Gyo73] B.L. Gyorffy and M.J. Stott, in D.J. Fabian and L.M. Watson (Eds.), Band Structure Spectroscopy in Metals and Alloys, Academic Press, London, 1973, p. 385.

[Hah82] J.E. Hahn, R.A. Scott, K.O. Hodgson, D. Doniach, S.R. Desjardins and E.I. Solomon, Chem. Phys. Lett., 88 (1982) 595.

[Ham93] K. Hämäläinen, C.C. Kao, J.B. Hastings, D.P. Siddons, L.E. Berman, V. Stojanoff and S.P. Cramer, Phys. Rev. B, 46 (1992) 14274.

[Has83] S.S. Hasnain and B. Piggott, in A. Bianconi, L. Incoccia and S. Stipcich (Eds.), EXAFS and Near Edge Structure, Springer-Verlag, Berlin, 1983, p. 358.

[Haz90] S. Hamza, M.A. Khan, S. Lewonczuk, J. Ringeissen, J. Petiau and P. Sainctavit, in A. Balerna, E. Bernieri and S. Mobilio (Eds.), Proc. 2nd European Conference on Progress in X-ray Synchrotron Radiation Research, Rome, November 1989, SIF, Bologna, 1990, p. 809.

[Hed65] L. Hedin, Phys. Rev. A, 139 (1965) 796.

[Hed69] L. Hedin and B.I. Lundqvist, Solid State Phys., 23 (1969) 1.

[Hem91] B. Heddman, P. Frank, K.O. Hodgson, B.J. Feldman, S.F. Gheller, F.A. Schutz and W.E. Newton, in S.S. Hasnain (Ed.), X-ray Absorption Fine Structure, Vol. VI, Ellis Horwood, Chichester, 1991, p. 168.

[Hen79] B.L. Henke, J. Liesegang and S.D. Smith, Phys. Rev. B, 19 (1979) 3004.

[Him91] F.J. Himpsel, U.O. Karlsson, A.B. McLean, L.J. Terminello, F.M.F. de Groot, M. Abbate, J.C. Fuggle, J.A. Yarmoff, B.T. Thole and G.A. Sawatzky, Phys. Rev. B, 43 (1991) 6899.

[Hit89a] A.P. Hitchcock and E. Rühl, Physica B, 158 (1989) 403.

[Hit89b] A.P. Hitchcock, S. Bodeur and M. Tronc, Physica B, 158 (1989) 257.

[Hit90] A.P. Hitchcock, A.T. Wen and E. Rühl, Chem. Phys., 147 (1990) 51.

[Hoh64] P.C. Hohenberg and W. Kohn, Phys. Rev., 136 (1964) 864.

[Hu85] C.D. Hu and D.C. Langreth, Phys. Scr., 32 (1985) 391.

[Hub63] J. Hubbard, Proc. R. Soc. London, Ser. A, 276 (1963) 238.

[Hub64] J. Hubbard, Proc. R. Soc. London, Ser. A, 277 (1964) 237.

[Hub67] J. Hubbard, Proc. R. Soc. London, Ser. A, 281 (1967) 401.

[Hul84] S.L. Hulbert, B.A. Bunker, F.C. Brown and P. Pianetta, Phys. Rev. B, 30 (1984) 2120.

[Hun27] F. Hund, Linienspektren und Periodisches System der Elemente, Julius Springer, Berlin, 1927, pp. 124 ff.

[Hyb89] M.S. Hybertsen, M. Schlüter and N.E. Christensen, Phys. Rev. B, 39 (1989) 9028.

[Hyb92] M.S. Hybertsen, E.B. Stechel, W.M.C. Foulkes and M. Schlüter, Phys. Rev. B, 45 (1992) 32.

[Ima89a] S. Imada and T. Jo, J. Phys. Soc. Jpn., 58 (1989) 402.

[Ima89b] S. Imada and T. Jo, J. Phys. Soc. Jpn., 58 (1989) 2665.

[Ima90] S. Imada and T. Jo, Phys. Scr., 41 (1990) 115.

[Ima92] S. Imada and T. Jo, J. Magn. Magn. Mater., 104 (1992) 2001.

[Ing91] J.E. Inglesfield, Principles of Band Structure, Workshop, Vlieland, April 1991, unpublished.

[Ish90] Y. Ishii and K. Terakura, Phys. Rev. B, 42 (1990) 10924.

[Ito93] F. Itoh, M. Nakamura, H. Sakurai, H. Kiriake, M. Nawate, S. Honda and H. Kawata, Jpn. J. Appl. Phys., 32 (1993) 326.

[Iva44] D. Ivanenko and J. Pomeranchuk, Phys. Rev., 65 (1944) 343.

[Iwa86] K. Iwai, M. Iwai, K. Suto, S. Nakashima, I. Motoyama, H. Sano, I. Ikemoto, N. Kosugi and H. Kuroda, Bull. Chem. Soc. Jpn., 59 (1986) 2675.

[Jac91] W.E. Jackson, G.E. Brown Jr., G.A. Waychunas, J. Mustre de Leon, S.D. Conradson and J.M. Combes, in S.S. Hasnain (Ed.), X-ray Absorption Fine Structure, Vol. VI, Ellis Horwood, Chichester, 1991, p. 298.

[Jak77] J. Jaklevic, J.A. Kirby, M.P. Klein, A.S. Robertson, G.S. Brown and P. Eisenberger, Solid State Commun., 23 (1977) 679.

[Jan88] G.J.M. Jansen and W.C. Nieuwport, Phys. Rev. B, 38 (1988) 3449.

[Jo88a] T. Jo and A. Kotani, Theory of high energy spectroscopy in CeO_2, in J. Kanamori and A. Kotani (Eds.), Core Level Spectroscopy, Springer-Verlag, Berlin, 1988, p. 34.

[Jo88b] T. Jo and A. Kotani, J. Phys. Soc. Jpn., 57 (1988) 2288.

[Jo88c] T. Jo and A. Kotani, Phys. Rev. B, 38 (1988) 830.

[Jo89a] T. Jo, J. Phys. Soc. Jpn., 58 (1989) 1452.

[Jo89b] R.O. Jones and O. Gunnarsson, Rev. Mod. Phys., 61 (1989) 689.

[Jo91] T. Jo and G.A. Sawatzky, Phys. Rev. B, 43 (1991) 8771.

[Jo92] T. Jo, A. Yoshida and G.A. Sawatzky, J. Magn. Magn. Mater., 104 (1992) 2087.

[Jon68] K.H. Johnson, Phys. Lett. A, 27 (1968) 138.

[Jor62] C.K. Jorgensen, Absorption Spectra and Chemical Bonding in Complexes, Pergamon Press, Oxford, 1962.

[Jor71] C.K. Jorgensen, Modern Aspects of Ligand Field Theory, North Holland, Amsterdam, 1971.

[Kag91] H. Kageyama and N. Kamijo, in S.S. Hasnain (Ed.), X-ray Absorption Fine Structure, Vol. VI, Ellis Horwood, Chichester, 1991, p. 442.

[Kai89] G. Kaindl, O. Strebel, A. Kolodziejczyk, W. Schäfer, R. Kiemel, S. Lösch, S. Kemmler-Sack, R. Hoppe, H.P. Müller and D. Kissel, Physica B, 158 (1989) 446.

[Kap91] R.J.H. Kappert, H.R. Borsje and J.C. Fuggle, J. Magn. Magn. Mater., 100 (1991) 363.

[Kap92t] R.J.H. Kappert, Spectroscopic Studies of Local Magnetic Properties in Metals, Ph.D. Thesis, University of Nijmegen, 1992.

[Kar70] K.M. Karplus and R.N. Porter, Atoms and Molecules, Benjamin, Marlo Park, 1970.

[Kau87] L.S. Kau, D.J. Spira-Solomon, J.E. Penner-Hahn, K.O. Hodgson and E.I. Solomon, J. Am. Chem. Soc., 109 (1987) 6433.

[Kev70] E.T. Keve, S.C. Abrahams and J.L. Bernstein, J. Chem. Phys., 53 (1970) 3279.

[Kit86] M. Kitamura, S. Muramatsu and C. Sugiura, Phys. Rev. B, 33 (1986) 5294.

[Kit90] M. Kitamura and S. Muramatsu, Phys. Rev. B, 41 (1990) 1158.

[Kiz88] P. Kizler, P. Lamparter and S. Steeb, Z. Naturforsch., Teil A, 44 (1988) 189.

[Kiz89] P. Kizler, P. Lamparter and S. Steeb, Physica B, 158 (1989) 392.

[Kiz91] P. Kizler, Phys. Rev. Lett., 67 (1991) 3555.

[Kiz92a] P. Kizler, Phys. Rev. B, 46 (1992) 10540.

[Kiz92b] P. Kizler, Phys. Lett. A, 172 (1993) 66.

[Kna82] G.S. Knapp, B.W. Veal, H.K. Pan and T. Klippert, Solid State Commun., 44 (1982) 1343.

[Knu93] M. Knülle, S. Stähler, G. Schütz, P. Fisher, F.M.F. de Groot, P. Blaha and K. Schwartz, submitted to Phys. Rev. B.

[Kob93] K. Kobayashi, H. Maruyama, H. Maeda and H. Yamazaki, Jpn. J. Appl. Phys., 32 (1993) 311.

[Koc77] E.E. Koch, B. Kunz and B. Sonntag, Phys. Rep., 29 (1977) 153.

[Koc85] E.E. Koch, Y. Yugnet and F.J. Himpsel, Chem. Phys. Lett., 116 (1985) 7.

[Koh65] W. Kohn and L.J. Sham, Phys. Rev., 140 (1965) 1133.

[Kot89] A. Kotani, H. Ogasawara, K. Okada, B.T. Thole and G.A. Sawatzky, Phys. Rev. B, 40 (1989) 65.

[Kot92] A. Kotani and K. Okada, Core-level spectroscopy in transition metal compounds, in Recent Advances in Magnetism of Transition Metal Compounds, World Scientific, Singapore, 1992.

[Kra30] K. Kramers, Akad van Wetenschappen, Amsterdam, 33 (1930) 959.

[Kri90] K.M. Krishnan, Ultramicroscopy, 32 (1990) 309.

[Kro90] A. Krol, C.J. Sher and Y.H. Kao, Phys. Rev. B, 42 (1990) 3829.

[Kru88] B.C.H. Krutzen and F. Springelkamp, J. Phys. Condensed Matter, 1 (1989) 8369.

[Krv90] O.L. Krivanek and J.H. Paterson, Ultramicroscopy, 32 (1990) 313.

[Kua92] X.Y. Kuang, Z. Wu and I. Morgenstern-Badarau, Phys. Rev. B, 45 (1992) 8104.

[Kue90] U. Kuetgens and J. Hormes, in A. Balerna, E. Bernieri and S. Mobilio (Eds.), Proc. 2nd European Conference on Progress in X-ray Synchrotron Radiation Research, Rome, November 1989, SIF, Bologna, 1990, p. 59.

[Kui88] P. Kuiper, G. Kruizinga, J. Ghijsen, M. Grioni, P.J.W. Weijs, F.M.F. de Groot, G.A. Sawatzky, H. Verweij, L.F. Feiner and H. Petersen, Phys. Rev. B, 37 (1988) 6483.

[Kui89] P. Kuiper, G. Kruizinga, J. Ghijsen and G.A. Sawatzky, Phys. Rev. Lett., 62 (1989) 221.

[Kui90t] P. Kuiper, Ph.D. Thesis, University of Groningen, 1990.

[Kui91] P. Kuiper, J. van Elp, G.A. Sawatzky, A. Fujimori, S. Hosoya and D.M. de Leeuw, Phys. Rev. B, 44 (1991) 4570.

[Kui93] P. Kuiper, B.G. Searle, P. Rudolf, L.H. Tjeng and C.T. Chen, Phys. Rev. Lett., 70 (1993) 1549.

[Kus91] M. Kusunoki, T. Ono, Y. Inoue, M. Suzuki, A. Uehara, T. Matsushita and H. Oyanagi, in S.S. Hasnain (Ed.), X-ray Absorption Fine Structure, Vol. VI, Ellis Horwood, Chichester, 1991, p. 174.

[Kut80] F.W. Kutzler, C.R. Natoli, D.K. Misemer, S. Doniach and K.O. Hodgson, J. Chem. Phys., 73 (1980) 3274.

[Kut84] F.W. Kutzler and D.E. Ellis, Phys. Rev. B, 29 (1984) 6890.

[Laa86a] G. van der Laan, J. Zaanen, G.A. Sawatzky, R. Karnatak and J.-M. Esteva, Phys. Rev. B, 33 (1986) 4253.

[Laa86b] G. van der Laan, B.T. Thole, G.A. Sawatzky, J.B. Goedkoop, J.C. Fuggle, J.-M. Esteva, R.C. Karnatak, J.P. Remeika and H.A. Dabkowska, Phys. Rev. B, 34 (1986) 6529.

[Laa87] G. van der Laan, J.B. Goedkoop and A.A. MacDowell, J. Phys. E, 20 (1987) 1496.

[Laa88a] G. van der Laan and B.T. Thole, Phys. Rev. Lett., 60 (1988) 1977.

[Laa88b] G. van der Laan and B.T. Thole, Phys. Rev. B, 37 (1988) 6587.

[Laa88c] G. van der Laan and B.T. Thole, J. Electron Spectrosc. Relat. Phenom., 46 (1988) 123.

[Laa90a] G. van der Laan and B.T. Thole, Phys. Rev. B, 42 (1990) 6670.

[Laa90b] G. van der Laan, S.C. Mythen and H.A. Padmore, Europhys. Lett., 11 (1990) 67.

[Laa90c] G. van der Laan, Phys. Rev. B, 41 (1990) 12366.

[Laa90d] G. van der Laan, in A. Balerna, E. Bernieri and S. Mobilio (Eds.), Proc. 2nd European Conference on Progress in X-ray Synchrotron Radiation Research, Rome, November 1989, SIF, Bologna, 1990, p. 243.

[Laa91] G. van der Laan and B.T. Thole, Phys. Rev. B, 43 (1991) 13401.

[Laa92a] G. van der Laan and B.T. Thole, J. Phys. Condensed Matter, 4 (1992) 4181.

[Laa92c] G. van der Laan and Kirkmann, J. Phys. Condensed Matter, 4 (1992) 4189.

[Lan80] D.C. Langreth and J.P. Perdew, Phys. Rev. B, 21 (1980) 5469.

[Lan83] D.C. Langreth and M.J. Mehl, Phys. Rev. B, 28 (1983) 1809.

[Lea80] R.D. Leapman and L.A. Grunes, Phys. Rev. Lett., 45 (1980) 397.

[Lea82] R.D. Leapman, L.A. Grunes and P.L. Fejes, Phys. Rev. B, 26 (1982) 614.

[Len86] M. Lenglet, R. Guillamet, A.D. D'Huyser, J. Dürr and C.K. Jorgensen, J. Phys. (Paris) C, 8 (1986) 764.

[Len88] M. Lenglet, A.D. D'Huyser and J. Dürr, Ann. Chim. Fr., 13 (1988) 505.

[Leu90] H. van Leuken, A. Lodder, M.T. Czyżyk, F. Springelkamp and R.A. de Groot, Phys. Rev. B, 41 (1990) 5613.

[Loo89] M. Loos, P. Friant, J.M. Barbe and R. Guillard, Physica B, 158 (1989) 231.

[Lop92] M.F. Lopez, A. Höhr, C. Laubschat, M. Domke and G. Kaindl, Europhys. Lett., 20 (1992) 357.

[Lyn87] D.W. Lynch and R.D. Cowan, Phys. Rev. B, 36 (1987) 9228.

[Lyt88] F.W. Lytle, R.B. Greegor and A.J. Panson, Phys. Rev. B, 37 (1988) 1550.

[Mae86] H. Maezawa, S. Nakai, S. Mitani, H. Noda, T. Namioka and T. Sasaki, Nucl. Instrum. Methods, 246 (1986) 310.

[Mar85t] D. van der Marel, Ph.D. Thesis, University of Groningen, 1985.

[Mar88] D. van der Marel and G.A. Sawatzky, Phys. Rev. B, 37 (1988) 10674.

[Mas92b] S. Massida, M. Posternak and A. Baldereshi, Phys. Rev. B, 46 (1992) 11705.

[Mat72a] L.F. Mattheiss, Phys. Rev. B, 5 (1972) 290.

[Mat72b] L.F. Mattheiss, Phys. Rev. B, 5 (1972) 306.

[May91] H. Maruyama, T. Iwazumi, H. Kawata, A. Koizumi, M. Fujita, H. Sakurai, F. Itoh, K. Namikawa, H. Yamazaki and M. Ando, J. Phys. Soc. Jpn., 60 (1991) 1456.

[May92] H. Maruyama, A. Koizumi, H. Yamazaki, T. Iwazumi and H. Kawata, J. Magn. Magn. Mater., 104 (1992) 2055.

[Mcc65] J.B. McChesney, R.C. Sherwood and J.F. Potter, J. Chem. Phys., 43 (1965) 1907.

[Mcl90] A.B. McLean, L.J. Terminello and F.J. Himpsel, Phys. Rev. B, 41 (1990) 7694.

[Mcm88a] A.K. McMahan, R.M. Martin and S. Satpathy, Phys. Rev. B, 38 (1988) 6650.

[Mcm88b] A.K. McMahan and R.M. Martin, in J.C. Fuggle, G.A. Sawatzky and J.W. Allen (Eds.), Narrow Band Phenomena, Plenum Press, New York, 1988, p. 133.

[Mey71] W. Meyer, Int. J. Quantum Chem., S5 (1971) 341.

[Miy91] T. Miyazaki, Y. Ishii and K. Terakura, Prog. Theor. Phys., Suppl., 106 (1991) 173.

[Mol34] C. Møller and M.S. Plesset, Phys. Rev., 46 (1934) 618.

[Mot90] A. Mottana, E. Paris, G. Della Ventura and J.L. Robert, Rend. Fis. Acc. Lincei, 1 (1990) 387.

[Mot91] A. Mottana, E. Paris, I. Davoli and L.M. Anovitz, Rend. Fis. Acc. Lincei, 2 (1991) 379.

[Mul78] J.E. Müller, O. Jepsen, O.K. Andersen and J.W. Wilkins, Phys. Rev. Lett., 40 (1978) 720.

[Mul82] J.E. Müller, O. Jepsen and J.W. Wilkins, Solid State Commun., 42 (1982) 365.

[Mul84] J.E. Müller and J.W. Wilkins, Phys. Rev. B, 29 (1984) 4331.

[Nak85] S.I. Nakai, K. Ogata, M. Ohashi, C. Sugiura, T. Mitsuishi and H. Maezawa, J. Phys. Soc. Jpn., 54 (1985) 4034.

[Nak87] S.I. Nakai, T. Mishuishi, H. Sugawara, H. Maezawa, T. Matsukawa, S. Mitani, K. Yamasaki and T. Fujikawa, Phys. Rev. B, 36 (1987) 9241.

[Nak88] S.I. Nakai, A. Kawata, M. Ohashi, M. Kitamura, C. Sugiura, T. Mitsuishi and H. Maezawa, Phys. Rev. B, 37 (1988) 10895.

[Nat83] R. Natoli, in A. Bianconi, L. Incoccia and S. Stipcich (Eds.), EXAFS and Near Edge Structure, Springer-Verlag, Berlin, 1983, p. 43.

[Nat86a] C.R. Natoli and M. Benfatto, J. Phys. (Paris) C, 8 (1986) 11.

[Nat86b] C.R. Natoli, M. Benfatto and S. Doniach, Phys. Rev. B, 34 (1986) 4682.

[Nie63] C.W. Nielson and G.F. Koster, Spectroscopic Coefficients for the p^N, d^N and f^N Configurations, M.I.T. Press, Cambridge, Massachusetts, 1963.

[Nor85] D. Norman, K.B. Garg and P.J. Durham, Solid State Commun., 56 (1985) 895.

[Nor90] M.R. Norman, Phys. Rev. Lett., 64 (1990) 1162; 64 (1990) 2466 (E).

[Ogu83] T. Oguchi, T.K. Terakura and A.R. Williams, Phys. Rev. B, 28 (1983) 6443.

[Ogu84] T. Oguchi, K. Terakura and A.R. Williams, J. Appl. Phys., 55 (1984) 2318.

[Ohn83] Y. Ohno, K. Hirama, S. Nakai, C. Sugiura and S. Okada, Phys. Rev. B, 27 (1983) 3811.

[Ohn85] Y. Ohno and S.I. Nakai, J. Phys. Soc. Jpn., 54 (1985) 3591.

[Oka89] K. Okada and A. Kotani, J. Phys. Soc. Jpn., 58 (1989) 2578.

[Oka90] K. Okada and A. Kotani, J. Electron Spectrosc. Relat. Phenom., 53 (1990) 313.

[Oka91a] K. Okada and A. Kotani, J. Phys. Soc. Jpn., 60 (1991) 772.

[Oka92a] K. Okada, A. Kotani and B.T. Thole, J. Electron Spectrosc. Relat. Phenom., 58 (1992) 325.

[Oka92b] K. Okada and A. Kotani, J. Phys. Soc. Jpn., 61 (1992) 449.

[Oka93] K. Okada and A. Kotani, J. Electron Spectrosc. Relat. Phenom., 62 (1993) 131.

[Oya89] H. Oyanagi, K. Oka, H. Unoki, Y. Nishihara and K. Murata, Physica B, 158 (1989) 436.

[Pad87] H. Padmore, in Proceedings of the International Conference on Soft X-ray Optics and Technology, SPIE J., 733 (1987) 253.

[Pad89] H. Padmore, Rev. Sci. Instrum., 60 (1989) 1608.

[Par88] J. Park, S. Ryu, M.S. Han and S.J. Oh, Phys. Rev. B, 37 (1988) 10867.

[Pat90] J.H. Paterson and O.L. Krivanek, Ultramicroscopy, 32 (1990) 319.

[Ped89] M. Pedio, J.C. Fuggle, J. Somers, E. Umbach, J. Haase, Th. Lindner, U. Höfer, M. Grioni, F.M.F. de Groot, B. Hilert, L. Becker and A. Robinson, Phys. Rev. B, 40 (1989) 7924.

[Ped90] M. Pedio, L. Becker, B. Hillert, S.D. Addato and J. Haase, Phys. Rev. B, 41 (1990) 7462.

[Pea79] D.M. Pease and L.V. Azaroff, J. Appl. Phys., 50 (1979) 6605.

[Pea86] D.M. Pease, S.D. Bader, M.B. Brodsky, J.I. Budnick, T.I. Morrison and N.J. Zaluzec, Phys. Lett. A, 114 (1986) 491.

[Pei83] J. Petiau and C. Calas, in A. Bianconi, L. Incoccia and S. Stipcich, EXAFS and Near Edge Structure, Springer-Verlag, Berlin, 1983, p. 144.

[Pen91] J.E. Penner-Hahn, S. Wang and G.S. Waldo, in S.S. Hasnain (Ed.), X-ray Absorption Fine Structure, Ellis Horwood, Chichester, 1991, p. 146.

[Pen●●] H. Pen, unpublished results.

[Peo88] D.H. Pearson, B Fultz and C.C. Ahn, Appl. Phys. Lett., 53 (1988) 1405.

[Per79] J.P. Perdew, Chem. Phys. Lett., 64 (1979) 127.

[Per80] J.P. Perdew and A. Zunger, Phys. Rev. B, 23 (1980) 5048.

[Per86a] J.P. Perdew and Y. Wang, Phys. Rev. B, 33 (1986) 8800.

[Per86b] J.P. Perdew, Phys. Rev. B, 33 (1986) 8822.

[Per92a] J.P. Perdew and Y. Wang, Phys. Rev. B, 45 (1992) 13298.

[Per92b] J.P. Perdew, J.A. Chevary, S.H. Vosko, K.A. Jackson, M.R. Pederson, D.J. Singh and C. Fiolhais, Phys. Rev. B, 46 (1992) 6671.

[Pet82] H. Petersen, Opt. Commun., 40 (1982) 402.

[Pet86] H. Petersen, Nucl. Instrum. Methods A, 246 (1986) 260.

[Pfl82] J. Pflüger, J. Fink, G. Crecelius, K.P. Bohnen and H. Winter, Solid State Commun., 44 (1982) 489.

[Pom91] M. Pompa, C. Li, A. Bianconi, A. Congiu Catellano, S. Della Longa, A.M. Flank, P. Lagarde and D. Udron, Physica C, 184 (1991) 51.

[Pot●●] R. Potze, unpublished results.

[Pou90] B. Poumellec, R. Cortes, G. Tourillon and J. Berthon, in A. Balerna, E. Bernieri and S. Mobilio (Eds.), Proc. 2nd European Conference on Progress in X-ray Synchrotron Radiation Research, Rome, November 1989, SIF, Bologna, 1990, p. 23.

[Pou91] B. Poumellec, P.J. Durham and G.Y. Guo, J. Phys. Condensed Matter, 3 (1991) 8195.

[Raj63] K. Rajnak and B.G. Wybourne, Phys. Rev., 132 (1963) 280.

[Raj64] K. Rajnak and B.G. Wybourne, Phys. Rev., 134 (1964) 596.

[Reh93] J.J. Rehr, Jpn. J. Appl. Phys., 32 (1993) 8.

[Rob87] S. Robaszkiewicz, R. Micnas and J. Ranninger, Phys. Rev. B, 36 (1987) 180.

[Rud92] P. Rudolf, F. Sette, L.H. Tjeng, G. Meigs and C.T. Chen, J. Magn. Magn. Mater., 109 (1992) 109.

[Rue91] S. Rüegg, G. Schütz, P. Fisher, R. Wienke, W.P. Zeper and H. Ebert, J. Appl. Phys., 69 (1991) 5655.

[Rui86] M.F. Ruiz-Lopez, D. Rinaldi, C. Esselin, J. Goulon, J.L. Poncet and R. Guillard, J. Phys. (Paris) C, 8 (1986) 637.

[Rui91] M.F. Ruiz-Lopez and A. Munoz-Paez, J. Phys. Condensed Matter, 3 (1991) 8981.

[Sac91a] M. Sacchi, O. Sakho and G. Rossi, Phys. Rev. B, 43 (1991) 1276.

[Sac91b] M. Sacchi, R.J.H. Kappert, J.C. Fuggle and E.E. Marinero, Appl. Phys. Lett., 59 (1991) 872.

[Sac92a] M. Sacchi, F. Sirotti, G. Rossi, R.J.H. Kappert, J. Vogel and J.C. Fuggle, J. Electron Spectrosc. Relat. Phenom., 58 (1992) 240.

[Sac92b] M. Sacchi, F. Sirotti and G. Rossi, Solid State Commun., 81 (1992) 977.

[Sai89] P. Sainctavit, J. Petiau, M. Benfatto and C.R. Natoli, Physica B, 158 (1989) 347.

[Sai90] P. Sainctavit, J. Petiau, M. Benfatto and C.R. Natoli, in A. Balerna, E. Bernieri and S. Mobilio (Eds.), Proc. 2nd European Conference on Progress in X-ray Synchrotron Radiation Research, Rome, November 1989, SIF, Bologna, 1990, p. 31.

[Sai91] P. Sainctavit and J. Petiau, in S.S. Hasnain (Ed.), X-ray Absorption Fine Structure, Ellis Horwood, Chichester, 1991, p. 35.

[Sai92] P. Sainctavit, D. Lefebvre, C. Cartier, C. Laffon, G. Krill, C. Brouder, J.P. Kappler, J.P. Schille and J. Goulon, J. Appl. Phys., 72 (1992) 1985.

[Sai93] P. Sainctavit, D. Lefebvre, M.A. Arrio, C. Cartier dit Moulin, J.P. Kappler, J.P. Schille, G. Krill, C. Brouder and M. Verdaguer, Jpn. J. Appl. Phys., 32 (1993) 295.

[Sak93] H. Sakurai, F. Itoh, H. Maruyama, A. Koizumi, K. Kobayashi, H. Yamazaki, Y. Tanji and H. Kawata, J. Phys. Soc. Jpn., 62 (1993) 459.

[San83] J.M. Sanz and S. Hoffman, Surf. Interface Anal., 5 (1983) 210.

[Sar91] B.K. Sarpal, C. Blancard, J.P. Connerade, J.M. Esteva, J. Hormes, R.C. Karnatak and U. Kuetgens, J. Phys. B, 24 (1991) 1593.

[Saw84] G.A. Sawatzky and J.W. Allen, Phys. Rev. Lett., 53 (1984) 2339.

[Saw88] G.A. Sawatzky, in J. Kanamori and A. Kotani (Eds.), Core-Level Spectroscopy in Condensed Systems, Springer Series in Solid State Science, Berlin, 1988, p. 99.

[Scf92] F. Schäfers, B.R. Müller, J. Wong, T. Tanaka, Y. Kamimura, M. Krumrey and P. Müller, BESSY Jahresbericht, 1991.

[Sch87] G. Schütz, W. Wagner, W. Wilhelm, P. Kienle, R. Zeller, R. Frahm and G. Materlik, Phys. Rev. Lett., 58 (1987) 737.

[Sch88] G. Schütz, M. Knülle, R. Wienke, W. Wilhelm, P. Kienle and R. Frahm, Z. Phys. B, 73 (1988) 67.

[Sch89] G. Schütz, R. Wienke, W. Wilhelm, W. Wagner, P. Kienle and R. Frahm, Z. Phys. B, 75 (1989) 495.

[Sch90] G. Schütz, R. Wienke, W. Wilhelm, W.P. Zeper, H. Ebert and K. Spörl, J. Appl. Phys., 67 (1990) 4456.

[Sch92] G. Schütz and P. Fisher, Z. Phys. A, 341 (1992) 227.

[Sch93] G. Schütz, P. Fisher, S. Stähler, M. Knülle and K. Attenkofer, Jpn. J. Appl. Phys., 32 (1993) 869.

[Sci46] J. Schwinger, Phys. Rev., 70 (1946) 798.

[Sco89] R.A. Scott, Physica B, 158 (1989) 84.

[Sea79] M.P. Seah and W.A. Dench, Surf. Interface Anal., 1 (1979) 2.

[Set84] F. Sette, Stöhr and A.P. Hitchcock, Chem. Phys. Lett., 110 (1984) 517.

[Set90] F. Sette and C.T. Chen, in A. Balerna, E. Bernieri and S. Mobilio (Eds.), Proc. 2nd European Conference on Progress in X-ray Synchrotron Radiation Research, Rome, November 1989, SIF, Bologna, 1990, p. 363.

[Set91] F. Sette, C.T. Chen, Y. Ma, S. Modesti and N.V. Smith, in S.S. Hasnain (Ed.), X-ray Absorption Fine Structure, Vol. VI, Ellis Horwood, Chichester, 1991, p. 96.

[Sev93] L. Severin, M.S.S. Brooks and B. Johansson, Int. J. Mod. Phys. B, 7 (1993) 255.

[Sha87] T.K. Sham, Solid State Commun., 64 (1987) 1103.

[Shi82] S. Shin, S. Suga, M. Taniguchi, H. Kanzaki, S. Shibuya and T. Yamaguchi, J. Phys. Soc. Jpn., 51 (1982) 906.

[Shu76] R.G. Shulman, Y. Yafet, P. Eisenberger and W.E. Blumberg, Proc. Natl. Acad. Sci. USA, 73 (1976) 1384.

[Sin●●] B. Sinkovic, unpublished results.

[Smi76] D.Y. Smith, Phys. Rev. B, 13 (1976) 5303.

[Smi92] N.V. Smith, C.T. Chen, F. Sette and L.F. Mattheiss, Phys. Rev. B, 46 (1992) 1023.

[Sol91] A.V. Soldatov, T.S. Ivanchenko, S. Della Longa and A. Bianconi, Phys. Status Solidi B, 168 (1991) K43.

[Som92] J. Somers, X-ray absorption spectroscopy of small molecules, in J.C. Fuggle and J. Inglesfield (Eds.), Unoccupied Electronic States, Springer, Berlin, 1992, p. 177.

[Sor93] L. Soriano, M. Abbate, H. Pen, M.T. Czyżyk and J.C. Fuggle, J. Electron Spectrosc. Relat. Phenom., 62 (1993) 197.

[Spa84] T.G. Sparrow, B.G. Williams, C.N.R. Rao and J.M. Thomas, Chem. Phys. Lett., 108 (1984) 547.

[Sti89] S. Stizza, G. Mancini, M. Benfatto, C.R. Natoli, J. Garcia and A. Bianconi, Phys. Rev. B, 40 (1989) 12229.

[Sto84] J. Stöhr, F. Sette and A.L. Johnson, Phys. Rev. Lett., 53 (1984) 1684.

[Sto93] J. Stöhr and Y. Wu, New directions in research with third generation soft X-ray synchrotron radiation sources, NATO-ASI Ser., Kluwer, Deventer, 1993.

[Str89] P. Strange, H. Ebert, J.B. Staunton and B.L. Gyorffy, J. Phys. Condensed Matter, 1 (1989) 2959.

[Str91] R.W. Strange, L.W. Murphy, P. Durham and S.S. Hasnain, in S.S. Hasnain (Ed.), X-ray Absorption Fine Structure, Vol. VI, Ellis Horwood, Chichester, 1991, p. 32.

[Stu89] R. Stumm von Bordwehr, Ann. Phys. Fr., 14 (1989) 377.

[Sug70] S. Sugano, Y. Tanabe and H. Kitamura, Multiplets of Transition Metal Ions, Academic Press, New York, 1970.

[Sug82] S. Suga, S. Shin, M. Taniguchi, K. Inoue, M. Seki, I. Nakada, S. Shibuya and T. Yamaguchi, Phys. Rev. B, 25 (1982) 5487.

[Sva88a] A. Svane and O. Gunnarsson, Phys. Rev. B, 37 (1988) 9919.

[Sva88b] A. Svane and O. Gunnarsson, Europhys. Lett., 7 (1988) 171.

[Sva90a] A. Svane and O. Gunnarsson, Phys. Rev. Lett., 65 (1990) 1148.

[Sva90b] A. Svane and O. Gunnarsson, Solid State Commun., 76 (1990) 851.

[Sva92] A. Svane, Phys. Rev. Lett., 68 (1992) 1900.

[Szo93] Z. Szotek, W.M. Temmermann and H. Winter, Phys. Rev. B, 47 (1993) 4029.

[Szy90] R. Szymanski and E. Payen, in A. Balerna, E. Bernieri and S. Mobilio (Eds.), Proc. 2nd European Conference on Progress in X-ray Synchrotron Radiation Research, Rome, November 1989, SIF, Bologna, 1990, p. 805.

[Taf82] J. Taftø and O.L. Krivanek, Phys. Rev. Lett., 48 (1982) 560.

[Tan92a] A. Tanaka and T. Jo, J. Phys. Soc. Jpn., 61 (1992) 2040.

[Tan92b] A. Tanaka, T. Jo and G.A. Sawatzky, J. Phys. Soc. Jpn., 61 (1992) 2636.

[Tan92c] A. Tanaka and T. Jo, J. Phys. Soc. Jpn., 61 (1992) 2669.

[Tan93] Z. Tan, S.M. Heald, S.W. Cheong, A.S. Cooper and A.R. Moodenbaugh, Phys. Rev. B, 47 (1993) 12365.

[Tem93] W.M. Temmermann, Z. Szotek and H. Winter, Phys. Rev. B, 47 (1993) 11533.

[Ten85] I.M. Ternov, V.V. Mikhailov and V.R. Khalilov, Synchrotron Radiation and its Applications, Harwood Academic, 1985.

[Ter84] K. Terakura, T. Oguchi, A.R. Williams and J. Kübler, Phys. Rev. B, 30 (1984) 4734.

[Tho85a] B.T. Thole, G. van der Laan and G.A. Sawatzky, Phys. Rev. Lett., 55 (1985) 2086.

[Tho85b] B.T. Thole, G. van der Laan, J.C. Fuggle, G.A. Sawatzky, R.C. Karnatak and J.-M. Esteva, Phys. Rev. B, 32 (1985) 5107.

[Tho85c] B.T. Thole, R.D. Cowan, G.A. Sawatzky, J. Fink and J.C. Fuggle, Phys. Rev. B, 31 (1985) 6856.

[Tho88a] B.T. Thole, G. van der Laan and P.H. Butler, Chem. Phys. Lett., 149 (1988) 295.

[Tho88b] B.T. Thole and G. van der Laan, Phys. Rev. B, 38 (1988) 3158.

[Tho88c] B.T. Thole and G. van der Laan, Phys. Rev. A, 38 (1988) 1943.

[Tho92] B.T. Thole, P. Carra, F. Sette and G. van der Laan, Phys. Rev. Lett., 68 (1992) 1943.

[Tje91] L.H. Tjeng, Y.U. Idzerda, P. Rudolf, F. Sette and C.T. Chen, J. Appl. Phys., 70 (1991) 5939.

[Tje92a] L.H. Tjeng, C.T. Chen and S.W. Cheong, Phys. Rev. B, 45 (1992) 8205.

[Tob92] J.G. Tobin, G.D. Waddill and D.P. Pappas, Phys. Rev. Lett., 68 (1992) 3642.

[Tog86] R. Torge, F. Riemer, E. Heynacher and W. Opitz, Zeiss Inform., 29 (1986) 55.

[Tol92] H. Tolentino, M. Medarde, A. Fontaine, E. Dartyge, D. Guay and G. Tourillon, Phys. Rev. B, 45 (1992) 8091.

[Tol93] H. Tolentino, M. Medarde, A. Fontaine, F. Baudelet and E. Dartyge, J. Electron Spectrosc. Relat. Phenom., 62 (1993) 167.

[Tor92] J.B. Torrance, P. Lacorre, A.I. Nazzal, E.J. Ansaldo and Ch. Niedermayer, Phys. Rev. B, 45 (1992) 8209.

[Tro90] L. Tröger, D. Arvanitis, H. Rabus, L. Wenzel and K. Baberschke, Phys. Rev. B, 41 (1990) 7297.

[Uoz92] T. Uozumi, K. Okada, A. Kotani, O. Durmeyer, J.P. Kappler, E. Beaurepaire and J.C. Parlebas, Europhys. Lett., 18 (1992) 85.

[Van90] J.F. van Acker, P.J.W. Weijs, W. Speier, J.C. Fuggle and R. Zeller, in A. Balerna, E. Bernieri and S. Mobilio (Eds.), Proc. 2nd European Conference on Progress in X-ray Synchrotron Radiation Research, Rome, November 1989, SIF, Bologna, 1990, p. 55.

[Van90t] J.F. van Acker, Magnetism and Covalence: The Electronic Structure of Localized Perturbations, Ph.D. Thesis, University of Nijmegen, 1990.

[Vee93a] M. van Veenendaal and G.A. Sawatzky, Phys. Rev. Lett., 70 (1993) 2459.

[Vee93b] M. van Veenendaal, H. Eskes and G.A. Sawatzky, Phys. Rev. B, 47 (1993) 11463.

[Vel90t] J. van Elp, Ph.D. Thesis, University of Groningen, 1990.

[Vel91a] J. van Elp, J.L. Wieland, P. Kuiper, G.A. Sawatzky, F.M.F. de Groot and T.S. Turner, Phys. Rev. B, 44 (1991) 6090.

[Vel91b] J. van Elp, B.G. Searle, G.A. Sawatzky and M. Sacchi, Solid State Commun., 80 (1991) 67.

[Vel92] J. van Elp, H. Eskes, P. Kuiper and G.A. Sawatzky, Phys. Rev. B, 45 (1992) 1612.

[Ver86] M. Verdaguer, C. Cartier, M. Momenteau, E. Dartyge, A. Fontaine, G. Tourillon and A. Michalowicz, J. Phys. (Paris) C, 8 (1986) 649.

[Vic85] R.H. Victora and L.M. Falicov, Phys. Rev. Lett., 55 (1985) 1140.

[Vog93] J. Vogel, M. Sacchi, F. Sirotti and G. Rossi, Appl. Surf. Sci., 65/66 (1993) 170.

[Von79] U. von Barth and G. Grossmann, Solid State Commun., 32 (1979) 645.

[Von82] U. von Barth and G. Grossmann, Phys. Rev. B, 25 (1982) 5150.

[Vvd92] D.D. Vvedensky, in J.C. Fuggle and J.E. Inglesfield (Eds.), Unoccupied Electronic States, Springer, Berlin, 1992, p. 139.

[Wad86] W.G. Waddington, P. Rez, J.P. Grant and C.J. Humphreys, Phys. Rev. B, 34 (1986) 1467.

[Wan77] C.S. Wang and J. Callaway, Phys. Rev. B, 15 (1977) 298.

[Way83] G.A. Waychunas, M.J. Apted and G.E. Brown, Jr., Phys. Chem. Miner., 10 (1983) 1.

[Way87] G.A. Waychunas, Am. Mineral., 72 (1987) 89.

[Way90] G.A. Waychunas and G.E. Brown, Jr., Phys. Chem. Miner., 17 (1990) 420.

[Wei90] R. Weidemann, B. Burmester, H.E. Gumlich, C. Jung, T. Kleemann, T. Kreitler, A. Krost, H.U. Middlemann, U. Becker, M. Kupsch and S. Bernstorff, J. Cryst. Growth, 101 (1990) 916.

[Wey91] P.J.W. Weijs, M.T. Czyżyk, J.F. van Acker, W. Speier, J.B. Goedkoop, H. van Leuken, H.J.M. Hendrix, R.A. de Groot, G. van der Laan, K.H.J. Buschow, G. Wiech and J.C. Fuggle, Phys. Rev. B, 41 (1990) 11899.

[Wie91] R. Wienke, G. Schütz and H. Ebert, J. Appl. Phys., 69 (1991) 6147.

[Wil79] A.R. Williams, J. Kübler and C.D. Gelatt, Jr., Phys. Rev. B, 19 (1979) 6094.

[Wim92] M. Willmann, H. Petersen, F. Schäfers, M. Mast, B.R. Müller and W. Gudat, BESSY Jahresbericht, 1991.

[Wis72] J.A. Wilson, Adv. Phys., 19 (1972) 1.

[Wis88] J.A. Wilson, in J.C. Fuggle, G.A. Sawatzky and J.W. Allen (Eds.), Narrow Band Phenomena, Plenum Press, New York, 1988, p. 209.

[Won84] J. Wong, F.W. Lytle, R.P. Messmer and D.H. Maylotte, Phys. Rev. B, 30 (1984) 5596.

[Won89] J. Wong and G.A. Slack, Physica B, 158 (1989) 627.
[Won90] J. Wong, G. Shimkaveg, W. Goldstein, M. Eckart, T. Tanaka, Z. Rek and H. Tompkins, Nucl. Instrum. Methods A, 291 (1990) 243.
[Woo87] R.G. Woolley, Int. Rev. Phys. Chem., 6 (1987) 93.
[Wuy92] Y. Wu, J. Stöhr, B.D. Hermsmeier, M.G. Samant and D. Weller, Phys. Rev. Lett., 69 (1992) 2307.
[Wyb65] B.G. Wybourne, Phys. Rev., 137 (1965) 364; Spectroscopic Properties of Rare Earths, Interscience, New York, 1965, Chapt. 2, 17.
[XAS91] S.S. Hasnain (Ed.), X-ray Absorption Fine Structure, Vol. VI, Ellis Horwood, Chichester, 1991, Chapt. IV, pp. 191–282 and references cited therein.
[Yam77] T. Yamaguchi and S. Sugano, J. Phys. Soc. Jpn., 42 (1977) 1949.
[Yam82a] T. Yamaguchi, S. Shibuya and S. Sugano, J. Phys. C, 15 (1982) 2625.
[Yam82b] T. Yamaguchi, S. Shibuya, S. Suga and S. Shin, J. Phys. C, 15 (1982) 2641.
[Yas83] J. Yamashita and S. Asano, J. Phys. Soc. Jpn., 52 (1983) 3506.
[Yaz93] H. Yamazaki, H. Miroshi, K. Kobayashi and K. Shimomi, Jpn. J. Appl. Phys., 32 (1993) 317.
[Zaa85a] J. Zaanen, G.A. Sawatzky and J.W. Állen, Phys. Rev. Lett., 55 (1985) 418.
[Zaa85b] J. Zaanen, G.A. Sawatzky, J. Fink, W. Speier and J.C. Fuggle, Phys. Rev. B, 32 (1985) 4905.
[Zaa86a] J. Zaanen, C. Westra and G.A. Sawatzky, Phys. Rev. B, 33 (1986) 8060.
[Zaa86t] J. Zaanen, The Electronic Structure of Transition Metal Compounds in the Impurity Model, Ph.D. Thesis, University of Groningen, 1986.
[Zaa88] J. Zaanen, O. Jepsen, O. Gunnarsson, A.T. Paxton, O.K. Andersen and A. Svane, Physica C, 153–155 (1988) 1636.
[Zaa90] J. Zaanen and G.A. Sawatzky, J. Solid State Chem., 88 (1990) 8.
[Zel92] R. Zeller, in J.C. Fuggle and J.E. Inglesfield (Eds.), Unoccupied Electronic States, Springer-Verlag, Berlin, 1992, p. 25.

Appendix A: Final state effects on Hubbard model parameters

An important question for the description of core level spectroscopies using short range model Hamiltonians is possible final state effects on the model parameters used. In many papers this question is not touched upon and it is tacitly assumed that one can use identical parameters in the final state as used in the initial state. The final state is described by adding the effect on the core hole potential (U_{cd}) acting on the localized states. It is however not obvious that the Coulomb repulsion U_{dd}, the (symmetry dependent) hopping terms t_{pd} and the cubic crystal field splitting (10Dq) are equal in the final state.

In most papers using the Anderson impurity model, or related short range models, it is assumed that the hopping should increase in the final state of 2p XPS due to the presence of the core hole, which gives an extra term in the matrix element [Zaa86t, Zaa90]. Gunnarsson et al. [Gun88a, Gun89a] analysed the final state hopping in detail. They pointed out two counteracting effects: (1) the extra term in the matrix element, and (2) the fact that the localized wavefunctions (ϕ_d) tend to localize further because of the core hole. For the case of Mn of CdTe the finding is that if a core hole is included, the hopping is reduced by about 20%. In other words the localization effect is found to be more important than the extra hopping term.

Apart from differences between initial state and final state there can also be differences between different experiments, such as 2p XPS, 2p XAS and 1s XAS, particularly because the screening processes will be different. For example in [Laa92a] U_{cd} is chosen to be different in 2p XPS and 2p XAS. Moreover if the hopping in the final state is different from the ground state this will affect the spectral shape. Another consequence is that if a (single) value for the hopping is determined empirically from core level spectroscopy, this value will correspond to the final state value (or to some kind of effective mean value of ground state and final state).

Also the Coulomb repulsion U_{dd} is not necessarily identical in the final state. In atomic multiplet calculations the two electron integrals $\langle 3d, 3d|1/r|3d, 3d\rangle$ are calculated ab initio. It turns out in the final state of 2p XAS that these integrals are increased by about 5 to 10% (see for example the table for the Slater integrals in Ref. [Deg90a]), hence the atomic (unscreened) value of U_{dd} will also be 5 to 10% larger. For this reason also the final state value of U_{dd} can be expected to be slightly larger than the value in the ground state.

A detailed study has been performed for the creation of an oxygen 1s core hole in the copper oxides [Hyb92]. Apart from the large effect of the core hole potential on the oxygen 2p states (U_{cp}), also the effect on the neighbouring 3d states (U^{κ}_{cd}) was considered. (κ denotes inter-electronic Coulomb repulsions.) It was shown that there is an effect on the Coulomb repulsion of the neighbouring sites. U_{dd} decreases from 4.1 to 3.7 eV. This finding can be generalized to the following statement:

A core hole created on site increases U_{dd}, but created at a neighbouring site it decreases U_{dd}.

Another finding of this study is that the hopping t_{pd} is significantly decreased from 0.43 eV to 0.20 eV, which is (qualitatively) a similar result to the Mn in CdTe system discussed above.

Another problem is that for the simulation of metal 1s X-ray absorption the parameters which give the best description of the spectral shape are modified in the final state, which is motivated from the final state effects of the excited electron in an np state. Within the model description with only metal 3d and ligand 2p the effective parameters in the final state are likely to be re-adjusted [Tol92].

Thus it can be concluded that the model parameters in the final states of different experiments are in general only roughly known and systematic final state effects, apart from the inclusion of U_{cd}, are in general not used. In my opinion this is an important problem because the eventual final state effects on model parameters are important for the accurate determination of the ground state values, that is for our understanding of the ground state electronic structure. In other words

> An accurate description of the ground state is only possible with correct inclusion of final state effects.

Appendix B: Abbreviations, etc.

The often used abbreviations and symbols are given. In many sections symbols are used (and defined) within the context given. They are not repeated here.

Group theory symmetry notations (A_1, E, etc.) can be found in [Sug70]. Some alternative notations are in use (0, 1, etc.) or (Γ_1, etc.); see Butler [But81] for details.

Angular momentum notations (L, S, J, M_J, ...) and term symbols ($^4T_1$) can be found in, for example, [Sug70, Grf64].

Electronic structure models

ASW	Augmented spherical wave method
CEPA	Coupled electron pair approximation
CT-M	Charge transfer-multiplet model
DOS	Density of states
DFT	Density functional theory
FOCI	First order configuration-interaction
GGA	Generalized gradient approximation
GW	*G* (Green function) *W* (screened Coulomb interaction) method
HF	Hartree–Fock approximation
KKR	Koster Koringa Rostoker
LAPW	Linearized augmented plane wave
LFM	Ligand field multiplet
LMTO	Linearized muffin-tin orbital
LSD	Local spin density approximation
MC	Multi-configurational
MS	Multiple scattering
OP	Orbital polarization
SCF	Self-consistent field
SIC	Self-interaction correction

Experimental techniques

BIS	Bremsstrahlung Isochromat Spectroscopie = (inverse (X-ray) photoemission)
EELS	Electron energy loss spectroscopy
EPR	Electron paramagnetic resonance
EXAFS	Extended X-ray absorption fine structure
IPS	Inverse photoemission spectroscopy
K edge	X-ray excitation of 1s state
L_I edge	X-ray excitation of 2s state

$L_{2,3}$ edge	X-ray excitation of 2p state (split by core state spin–orbit coupling)
TEY	Total electron yield
XANES	X-ray absorption near edge structure
XAS	X-ray absorption spectroscopy
XPS	X-ray photoelectron spectroscopy

Symbols

B	Racah parameter ("orbit") (see Table 2)
C	Racah parameter ("spin") (see Table 2)
C	Kanamori parameter ("orbit") (see Table 2)
10Dq*	Cubic ligand field splitting (the asterisk denotes an average value)
$(\mathscr{D})$	Cubic ligand field splitting
F^2	Slater integral
G^1	Slater (exchange) integral
I_s^*	(mean) Stoner exchange coupling
J	Exchange splitting (see Table 2) (Kanamori parameter ("spin"))
$\langle L_z \rangle$	Orbital moment
n	Density of states
n^+	...spin-up
n^-	...spin-down
P_e	Fano constant
Φ and ϕ	Wavefunction (subscript denotes orbital quantum number, superscript denotes core (c) or valence (v))
q	polarization of the X-ray (−1, 0, +1)
σ	X-ray absorption cross section
σ^+	...right circularly polarized
σ^-	...left circularly polarized
σ^0	...z polarized
$\langle S_z \rangle$	Spin moment
ζ	Spin–orbit coupling

Anderson impurity model

$a^\dagger$	Creation operator (second quantization)
Δ	Charge transfer energy ($\varepsilon_d - \varepsilon_{pk}$)
ε_d	Energy position of d state
ε_{pk}	Energy position of p band
n	Occupation number ($a^\dagger a$)
t_{pd}	Hopping terms
U	Coulomb interaction energy
V_{eff}	Effective interaction strength

High-Resolution X-ray Emission and X-ray Absorption Spectroscopy

Frank de Groot

Department of Inorganic Chemistry and Catalysis, Utrecht University, Sorbonnelaan 16, 3584 CA Utrecht, Netherlands

Received July 31, 2000

Contents

I. Introduction

In this review, high-resolution X-ray emission and X-ray absorption spectroscopy will be discussed. The focus is on the 3d transition-metal systems. To understand high-resolution X-ray emission and resonant X-ray emission, it is first necessary to spend some time discussing the X-ray absorption process. Section II discusses 1s X-ray absorption, i.e., the K edges, and section III deals with 2p X-ray absorption, the L edges. X-ray emission is discussed in, respectively, section IV on 1s2p and 2s3p X-ray emission and section V on 2p3s and 2p3d X-ray emission. Section VI focuses on magnetic dichroism effects, and in section VII selective X-ray absorption experiments are discussed.

To limit the scope of this review paper, many related topics (for example, EELS, XPS, and resonant photoemission, phonon-oriented inelastic X-ray scattering, and X-ray microscopy) will not be discussed. In addition, many aspects of X-ray absorption, such as reflection experiments, diffraction absorption fine structure, and related experiments, will remain untouched. EXAFS will be discussed very briefly, and its X-ray emission analogue EXEFS[69,71] will not be discussed.

A. X-ray Absorption

X-ray absorption is a synchrotron-based characterization technique that can be divided into near-edge spectroscopy (XANES) and extended X-ray absorption fine structure (EXAFS). In recent years a number of books, book chapters, and review papers have been published on X-ray absorption analysis. NEXAFS spectroscopy by Stöhr deals in detail with the analysis of soft X-ray 1s XANES spectra.[101] A recent review on soft X-ray XANES has been written by Chen.[24] Hard X-ray XANES and EXAFS has been discussed in the book by Koningsberger and Prins.[72] Rehr and Albers recently wrote a review on the theory of hard X-ray XANES and EXAFS.[92] In the *Encyclopaedia of Analytical Chemistry*, a recent chapter on X-ray absorption has been written by Kawai.[70]

10.1021/cr9900681 CCC: $36.00 PAGE EST: 29.5

Frank M. F. de Groot grew up in Nuenen, The Netherlands, received his Ph.D. degree from the University of Nijmegen (with J. C. Fuggle), and was a postdoctoral fellow at the LURE Synchrotron in Orsay, France. He was a Royal Netherlands Academy of Arts (KNAW) fellow at the University of Groningen. He then moved to Utrecht University, where he is now Lecturer in the Department of Inorganic Chemistry and Catalysis. His research is in the fields of inorganic chemistry and solid-state chemistry and physics with emphasis on the basic understanding and application of core-level spectroscopies to study the electronic and magnetic structure of condensed matter, in particular the bulk and surfaces of transition-metal oxides, magnetic nanoparticles, heterogeneous catalysts, and bioinorganic materials.

In the X-ray absorption process, a core electron is excited to an empty state and, as such, X-ray absorption probes the unoccupied part of the electronic structure of the system.[52] In the EXAFS region, the excited electron has significant kinetic energy and EXAFS analysis yields for many systems an accurate determination of the local geometry. The XANES structure can also be simulated with the multiple scattering formalism. Alternatively, one can use electronic structure models such as density-functional theory to calculate the unoccupied density of states (DOS).[101] An important aspect of the usefulness of X-ray absorption is that one obtains element-specific information. This also implies that if two or more types of atoms of a particular element are present, the X-ray absorption spectral shape is a linear combination of all individual sites. This aspect limits the usefulness of XANES and EXAFS in systems with atoms in a variety of sites. This problem can be partly solved with the use of selective XAFS as will be discussed in section VII.

The X-ray absorption spectral shape is described with the Fermi Golden rule

$$I_{\mathrm{XAS}} \sim |\langle \Phi_{\mathrm{f}}|\hat{e}\cdot r|\Phi_i\rangle|^2\, \delta_{E_{\mathrm{f}}-E_{\mathrm{i}}-\hbar\omega} \tag{1a}$$

The intensity I_{XAS} is proportional to a dipole matrix element ($\hat{e}\cdot r$) coupling the initial state (Φ_{i}) and the final state (Φ_{f}). The delta function (δ) takes care of the conservation of energy. In the final state, a core electron has been excited. It can be described as the initial state with a continuum electron (ϵ) added and a core electron removed, i.e., $\Phi_{\mathrm{f}} = \underline{c}\epsilon\ \Phi_{\mathrm{i}}$.

$$I_{\mathrm{XAS}} \sim |\langle \Phi_{\mathrm{i}}\underline{c}\epsilon|\hat{e}\cdot r|\Phi_i\rangle|^2\, \delta_{E_{\mathrm{f}}-E_{\mathrm{i}}-\hbar\omega} \tag{1b}$$

An important approximation is to assume that the matrix element can be rewritten into a single-electron matrix element by removing all electrons that are inactive in the transition itself; in other words, the initial state minus the core hole is removed from eq 1b. All electron rearrangements that take place when a core hole is excited to a continuum electron are neglected, the series of delta functions identifies with the density of states (ρ), and the X-ray absorption spectral shape becomes[82]

$$I_{\mathrm{XAS}} \sim |\langle \epsilon|\hat{e}\cdot r|c\rangle|^2\cdot\rho \tag{1c}$$

The dipole matrix element dictates that the density of states has an orbital moment that differs by 1 from the core state ($\Delta L = \pm 1$), while the spin is conserved ($\Delta S = 0$). In the case of X-rays, the quadrupole transitions are some hundred times weaker then the dipole transitions and can be neglected in most cases. They will be discussed for the preedge region in section II.B. Because in the final state a core hole is present, the density of states should be calculated with a core hole present. In many cases, this approximation gives an adequate simulation of the XAS spectral shape.

II. 1s Edge X-ray Absorption

1s X-ray absorption spectra can be accurately described with single-particle methods within density functional theory. This is in many case true both for metal and ligand K-edge and band structure methods or multiple scattering calculations can be used. Following the final state rule,[117] one calculates the distribution of empty states in the final state of the absorption process. Because band structure calculations are carried out in reciprocal space, it is involved to calculate the final state density of states. It would imply the use of (large) supercells to include the core hole. Therefore, the ground-state density of states is often compared directly with the X-ray absorption spectrum. Various methods exist to calculate the single-particle density of states, for example, LMTO, LSW, LAPW, and KKR.[126]

A formally closely related though conceptually different method is the calculation of the X-ray absorption cross section by a real-space multiple scattering calculation. Multiple scattering is particularly appropriate for the calculation of the empty states that can be easily calculated for arbitrary large energies. Multiple scattering calculations are usually performed with the Green function approach, with the X-ray absorption cross section written as a correlation function. The Green function describes the propagation of the electron in the solid, which is scattered by the atoms surrounding the absorbing atom. Detailed accounts of the multiple scattering are given in refs 78, 84, 93, and 118.

Because multiple scattering is performed as a real-space cluster calculation, the calculations can relatively easily be carried out for any system, ordered crystals but also for surfaces, interfaces, enzymes, etc. In addition, the core hole potential on the absorbing atom can be added directly in multiple scattering. Another advantage of multiple scattering is that it can be performed in steps of growing cluster sizes, and it is an appealing picture to observe the changes in the theoretical spectra from the effects of increasing the number of backscatterers or from varying the included scattering paths around the absorbing atom. It has been shown that the multiple scattering formalism and the band structure formalism indeed give equivalent results if worked out rigorously in their mathematical basis. For comparison to experiment, both band structure calculations and multiple scattering results will be treated on the same footing using the density of states picture for guidance.

A. Metal 1s X-ray Absorption Spectra

The 1s edges of the 3d transition metals have energies ranging from about 4 to 9 keV. They are often used for EXAFS analysis, and also their XANES spectra are often used in many applied research investigations. An overview of 1s XANES spectra of 3d transition-metal systems is given in ref 29. Metal 1s XANES spectra are traditionally interpreted with multiple scattering methods. Self-consistent full potential multiple scattering calculations have recently been carried out for TiO_2 by Cabaret and co-workers.[20] They show that with polarization-dependent calculations the complete spectral shape of TiO_2 is nicely reproduced. In particular, the preedge region is also described correctly. It can be concluded that the 1s edges of 3d transition metals do correspond to the metal p-projected density of states.

In most applications, the systems studied are not well-known. The metal 1s edges do show fine structure and edge shifts that can be used without the explicit calculation of the density of states. Figures 1 and 2 show a number of Fe 1s XANES spectra from Westre and co-workers.[124] The Fe^{II} and Fe^{III} halide spectra given at the top do show significant variations within a certain valence. Analysis of unknown iron complexes can be carried out by comparison to spectra of known systems. The Fe^{III} edges are shifted to higher energy with respect to the Fe^{II} edges. The shift to higher energies with higher valence is a general phenomenon that can be used to determine the valence of 3d transition metals in unknown systems.

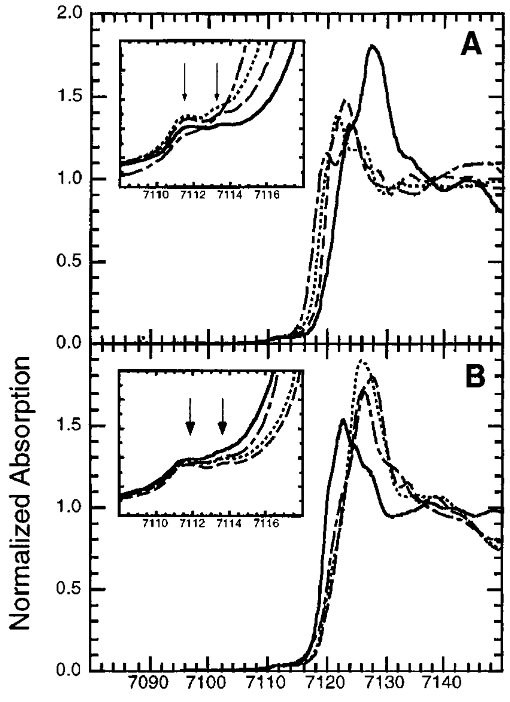

Figure 1. Fe K-edge XAS spectra of octahedral high-spin Fe^{II} complexes. At the top are given (A) FeF_2 (—), $FeCl_2$ (- - -), $FeBr_2$ (·· ·), and FeI_2 (- · -) and (B) rinneite (—), $[Fe(H_2O)_6][SiF_6]$ (- - -), $[Fe(H_2O)_6](NH_4)_2(SO_4)_2$ (·· ·), and $[Fe(imidazole)_6]Cl_2$ (- · -). The insets show expanded views of the 1s3d preedge region. (Reprinted with permission from ref 124. Copyright 1997 American Chemical Society.)

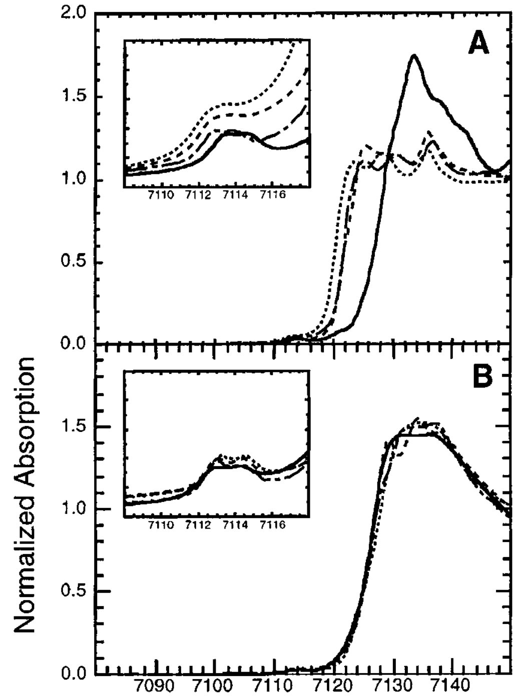

Figure 2. Fe K-edge XAS spectra of octahedral high-spin Fe^{III} complexes. Fe K-edge spectra of (A) FeF_3 (—), $FeCl_3$ (- - -), $FeBr_3$ (·· ·), and $[FeCl_6][Co(NH_3)_6]$ (- · -) and (B) $Fe(acac)_3$ (—), $(NH_4)_3Fe(malonate)_3$ (- - -), $[Fe(H_2O)_6](NH_4)(SO_4)_2\cdot 6H_2O$ (·· ·), and $Fe(urea)_6(ClO_4)_3$ (- · -). The insets show expanded views of the 1s3d preedge region. (Reprinted with permission from ref 124. Copyright 1997 American Chemical Society.)

1. Metal 1s Edge Shifts

A nice example of the use of the metal 1s edge shifts was recently given by Bae and co-workers.[4] They did experiments on iron porphyrins adsorbed on carbon in acid electrolytes and follow the iron K edge as a function of the potential. Figure 3 shows the iron K-edge spectra and Figure 4 plots the shifts in the edge energy. The intact iron porphyrin shows an edge jump of 2.0 eV, indicating a sudden valence change.[4]

B. The Preedge Region

The preedge region of the transition-metal 1s edges has led to a number of debates regarding the quadrupole and/or dipole nature and possible excitonic effects. The preedge region is related to transitions to the 3d bands. Both direct 1s3d quadrupole transitions and dipole transitions to 4p character hybridized with the 3d band are possible. For the quadrupole transitions, the matrix elements are only about 1% of the dipole transition, but on the other hand,

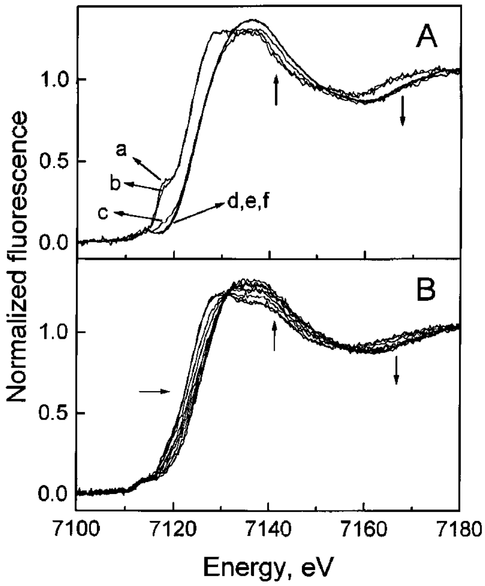

Figure 3. Series of in situ Fe K-edge XANES for intact iron porphyrin at different potentials (A) and heat-treated FeTMPPCl/BP (B). (Reprinted with permission from ref 4. Copyright 1998 American Chemical Society.)

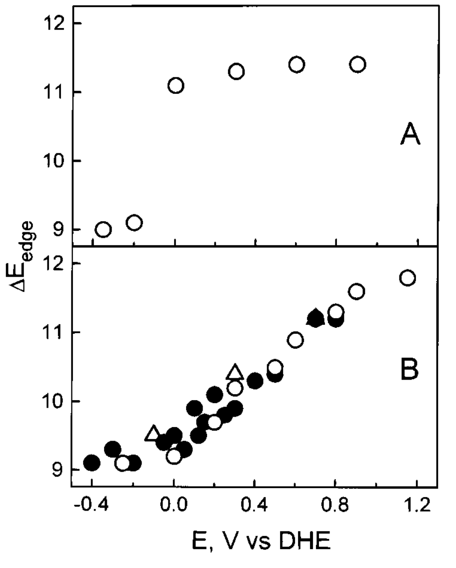

Figure 4. Plots of the edge energy versus the potential extracted from data of the type shown in Figure 3. (Reprinted with permission from ref 4. Copyright 1998 American Chemical Society.)

the amount of 3d character is by far larger than the p character. This can make, depending on the particular system, the contributions of quadrupole and dipole transitions equivalent in intensity. A direct manner to check the nature of the transitions is to measure the polarization dependence, which is different for quadrupole and dipole transitions. The multiple scattering results of TiO_2 reproduce the three prepeaks that are caused by two effects: (1) the crystal-field splitting between the t_{2g} and e_g orbitals and (2) the core hole effect on the quadrupole peaks.[10,13,14,21]

The preedge region of iron compounds has systematically been investigated by Westre and co-workers.[124] Some spectra are given in Figures 1 and 2. The preedges are analyzed in terms of quadrupole transitions, and analysis showed that the spectra should be interpreted in terms of multiplet theory, including the crystal field and the atomic interactions in LS coupling. This is an approximation to the multiplet calculations as carried out in ligand-field multiplet theory, as will be explained in section III. Figure 5 shows the effect if, in addition to the crystal field and LS coupling, the 3d spin−orbit coupling is included also. The Fe^{III} spectra are calculated from the quadrupole transitions of $3d^5$ to $1s^13d^6$. The Fe^{II} spectra use $3d^6$ as the ground state. It can be concluded that the calculations of Westre contain the essence of the spectral shapes and that the effects of 3d spin−orbit coupling are small in the preedge region. In addition, it can be shown that charge transfer (explained in section III.C.) hardly affects the spectral shape. In contrast, the effects of the spin−orbit coupling and charge transfer are very large for the 2p edges, as will be discussed below. That the preedge region in Fe_2O_3 is almost completely of quadrupole nature can be shown from 1s2p resonant X-ray emission experiments that will be discussed in section IV.D

The intensity of the preedge region is much larger for compounds in which the metal site has tetrahedral symmetry than for (distorted) octahedral systems. In tetrahedral systems, the local mixing of p and d nature is symmetry allowed, while for a system with inversion symmetry such as octahedral symmetry, it is 'forbidden'. This rule is relaxed in the solid, and if the density of states is calculated, one finds a small admixture of p states into the 3d band also for cubic systems such as $SrTiO_3$.[62] This admixture is less than for tetrahedral systems, which explains the small preedge. If an octahedral metal site is distorted then, depending on the particular distortion, more p character will be mixed into the 3d band. The result is that a distortion of the octahedron will show up as an increased intensity of the 'preedge' peak(s). That this is indeed the case has been shown by Waychunas and co-workers for a series of minerals.[122] They show a roughly linear relationship between the bond angle variance (a measure of the distortion) and the preedge intensity relative to the step. In a recent paper of Arrio and co-workers,[3] the preedges are calculated with multiplet theory in low symmetry, allowing for the explicit inclusion of the coupling of the dipole and quadrupole transitions. A number of iron mineral preedge spectra are divided into their dipole and quadrupole nature.

C. Ligand 1s X-ray Absorption

Oxygen, carbon, and nitrogen 1s X-ray absorption spectra have excitation energies between 300 and 700 eV, which is in the soft X-ray range. The interpretation of 1s spectra in the soft X-ray range has been dominated by band structure approaches because the details of the potential are crucial and until recently multiple scattering calculations did not reach good agreement. Figure 6a shows the density of states of rutile TiO_2.[35] The total density of states has been separated into its oxygen and titanium contributions. The zero of energy is the top of the oxygen 2p valence band, which can be seen to have a significant titanium contribution. The two sharp peaks between

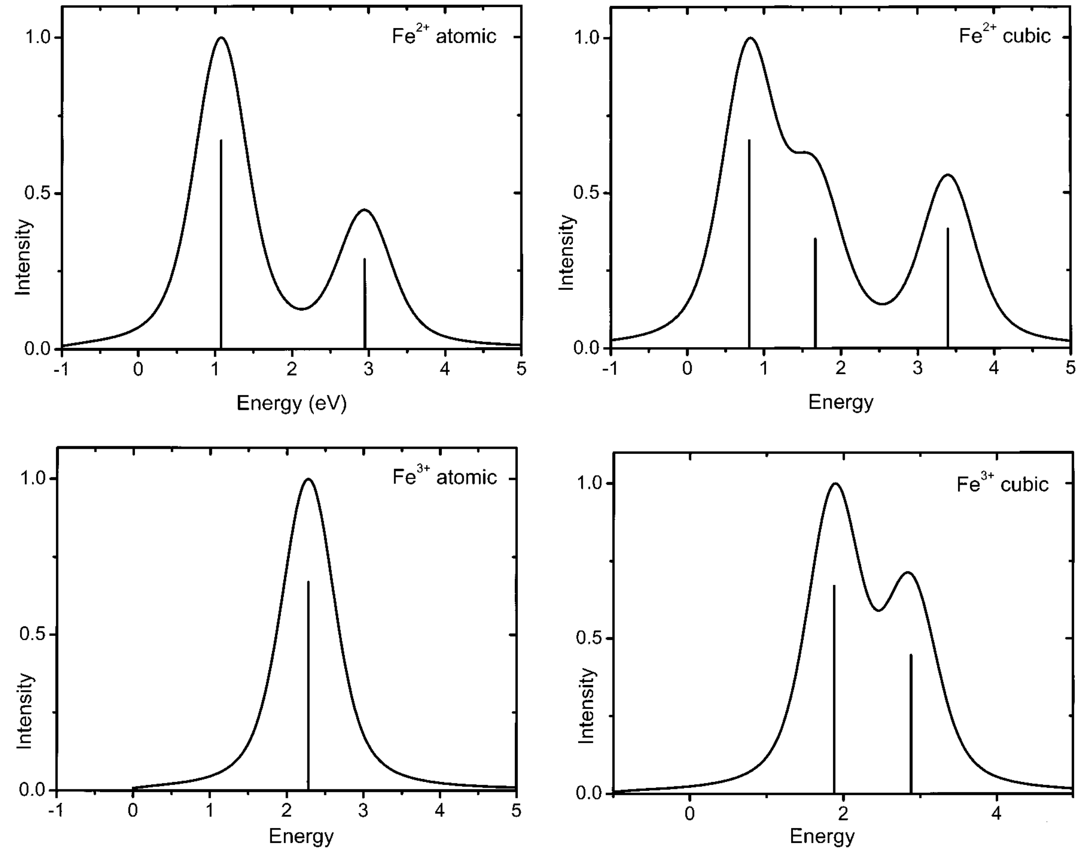

Figure 5. Atomic and ligand-field multiplet calculations for the quadrupole transitions $3d^5 \rightarrow 1s^13d^6$ for Fe^{III} (bottom) and $3d^6 \rightarrow 1s^13d^7$ for Fe^{II} (top). The left spectra are the atomic multiplets; the right spectra have an additional cubic crystal field of 1.0 eV.

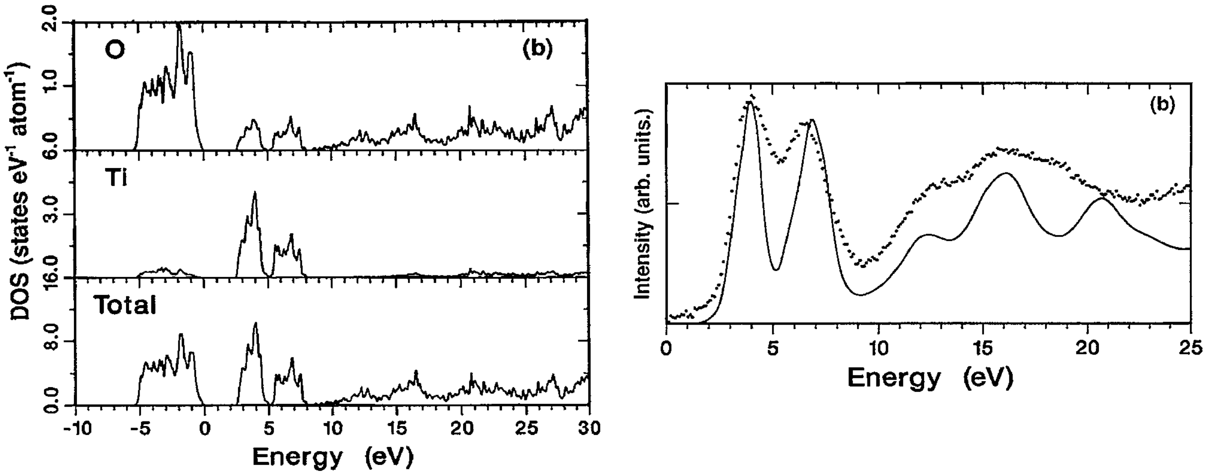

Figure 6. Right: comparison of the oxygen K-edge X-ray absorption spectra (·· ·) with the oxygen p-projected density of states (—) for rutile TiO_2; left: unbroadened density of states of rutile TiO_2. (Reprinted with permission from ref 35. Copyright 1993 American Physical Society.)

3 and 8 eV are the titanium 3d peaks. They relate to, respectively, the t_{2g} and e_g orbitals that are split by the cubic crystal field. Both have a significant oxygen contribution, indicating the covalent nature of TiO_2. The structures at 10 eV and higher are the titanium 4s and 4p bands plus all higher lying continuum states. These delocalized states have a similar density of states for oxygen and titanium. Figure 6b compares the oxygen p-projected density of states with the 1s X-ray absorption spectra of rutile TiO_2. The spectral shape is reproduced, and if the broadening is further optimized, a close to perfect fit of the experiment can be obtained. It can be concluded that in TiO_2 the density of states as obtained from a ground-state calculation gives an accurate description of the oxygen 1s X-ray absorption spectral shape. This implies that the core hole potential does not have a large influence on the spectral shape.

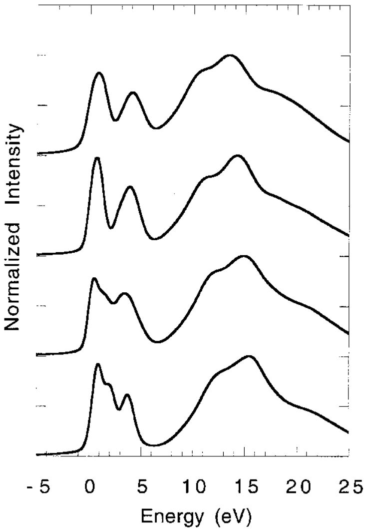

Figure 7. Series of oxygen p-projected density of states calculations of (from top to bottom)TiO_2, VO_2, CrO_2, and MnO_2 in their (magnetic) ground states.

Figure 7 shows the oxygen p-projected density of states of, from top to bottom, TiO_2, VO_2, CrO_2, and MnO_2. The calculations have been carried out with the LMTO code without core hole and with the oxides in their magnetic ground-state configuration.[28] The TiO_2 density of states is the same as given in Figure 6 with some additional broadening. In the series from TiO_2 to MnO_2, each time one electron is added to the 3d band that is empty for TiO_2. Each added 3d electron fills a t_{2g}-up state. VO_2 has a $t_{2g}{}^1$ configuration, CrO_2 a $t_{2g}{}^2$ configuration, and MnO_2 a $t_{2g}{}^3$ configuration. The interatomic couplings of these t_{2g} electrons gives rise to a phase transition for VO_2, a half-metallic ferromagnetic system for CrO_2, and a magnetic ground state for MnO_2. The region between 0 and 5 eV is related to the empty 3d states. A $3d^0$ ground state leaves all 10 3d electrons empty. They are split by the cubic crystal field that is about 2.5 eV for all these dioxides. The $t_{2g}{}^1$ configuration in VO_2 implies that one of the six t_{2g} holes is filled, and compared with TiO_2 only a sharper first peak is visible. In CrO_2 with its $t_{2g}{}^2$ configuration, the two filled 3d electrons have a significant exchange interaction with each other, implying an energy difference between spin-up and spin-down states of about 1.5 eV. This is seen in the spectral shape as a split of the first peak. MnO_2 has a $t_{2g}{}^3$ configuration with an increased splitting between spin-up and spin-down. In this case the three visible structures are related to, respectively, t_{2g}(down), e_g(up), and e_g(down). It can be seen that the spectral shape between 10 and 20 eV is equivalent for all oxides. This region of the spectrum is related to the 4sp and continuum density of states and reflects the equivalent crystal structures, i.e., all dioxides have a rutile crystal structure.

Comparison with experiment[39] shows excellent agreement for all these oxides, and it can be concluded that the oxygen 1s X-ray absorption spectra are described well with the oxygen p-projected density of states. Some papers argue that oxygen 1s spectra are susceptible to multiplet effects,[116] as far as the 3d part of the spectrum is concerned. The good agreement of the density of states with experiments shows, however, that multiplet effects are hardly (or not at all) visible in the spectrum.

For other ligands such as carbides, nitrides, and sulfides, a similar interpretation as that for oxides is expected to hold. Their ligand 1s X-ray absorption spectra are expected to show close comparison to the projected density of states, as confirmed by calculations.[24,30,99]

III. 2p Edge X-ray Absorption

In the case of 2p X-ray absorption (L edges), the single-particle approximation breaks down and the XANES structures are affected by the core hole wave function. The core hole and free electron of eq 1b are rewritten to a 2p core hole ($\underline{2p}$) and a 3d electron. All valence electrons except the 3d electrons are omitted, and this yields eq 2b, which is the starting point for all calculations.

$$I_{XAS} \sim |\langle \Phi_i \underline{2p} 3d | \hat{e}\cdot r | \Phi_i \rangle|^2 \delta_{E_f - E_i - \hbar\omega} \qquad (2a)$$

$$I_{XAS} \sim |\langle \underline{2p} 3d^{N+1} | \hat{e}\cdot r | 3d^N \rangle|^2 \delta_{E_f - E_i - \hbar\omega} \qquad (2b)$$

This so-called multiplet effect will be discussed in some detail because it is an important effect for all 2p X-ray absorption, the 1s preedges, as well as all X-ray emission experiments.

The Multiplet Effect. The breakdown of the single-particle model is important in all systems with electrons in narrow bands, for example, the 3d metals and the rare-earth metals. In these systems the p and d core wave functions strongly overlap with the 3d and 4f, respectively, valence wave functions. This strong local interaction has to be considered in order to obtain an accurate description of the XANES spectral shape. A successful analysis method has been developed based on a ligand-field multiplet model.[29] It offers large sensitivity to the valence and the symmetry of the element studied.

A. Atomic Multiplet Theory

The basic starting point for a large part of the analysis of core-level spectra is atomic multiplet theory.[25,123] Faced with the situation of a solid with its combination of extended valence states and a localized core hole, the problem is to find the best way to treat the X-ray absorption process. A localized approach makes it possible to treat the core hole in detail, while an itinerant approach is in most cases the best approach to the ground state of the solid. In the following some aspects of atomic multiplet theory that are important for the analysis of X-ray absorption and X-ray emission spectra will be briefly introduced.

It has been shown over the last 30 years that a completely localized approach, based on atomic multiplet theory, can be very fruitful to core-level spectroscopy. In this section atomic multiplet theory will be developed. Some basic quantum-mechanic results of atomic theory will be partly repeated, but the focus will be on the specific problems of a core hole in a solid.

1. The Atomic Hamiltonian

The atomic Hamiltonian is given by the Schrödinger equation for an N-electron atom. The Schrödinger equation consists of the kinetic energy of the N electrons ($\sum_N p_i^2/2m$), the electrostatic interaction of the N electrons with the nucleus of charge $+Z$ ($\sum_N -Ze^2/r_i$), the electron−electron repulsion ($H_{ee} = \sum_{pairs} e^2/r_{ij}$), and the spin−orbit coupling of each electron ($H_{ls} = \sum_N \zeta(r_i) l_i \cdot s_i$). The overall Hamiltonian reads

$$H = \sum_N \frac{p_i^2}{2m} + \sum_N \frac{-Ze^2}{r_i} + \sum_{pairs} \frac{e^2}{r_{ij}} + \sum_N \zeta(r_i)\, l_i \cdot s_i \quad (3a)$$

The kinetic energy and the interaction with the nucleus are the same for all electrons in a certain atomic configuration, for example, $3d^5$ in the case of Mn^{II}. They define the average energy of a certain state (H_{av}). This leaves the electron−electron repulsion and the spin−orbit coupling as the important interactions. The basic difficulty when solving the Schrödinger equation is that H_{ee} is too large to be treated as a perturbation. This problem has been solved with the *central field approximation*, in which the spherical average of the electron−electron interaction is separated from the nonspherical part. The spherical average $\langle H_{ee} \rangle$ is added to H_{av} to form the average energy of a configuration. In the modified electron−electron Hamiltonian H'_{ee}, the spherical average has been subtracted.

$$H'_{ee} = H_{ee} - \langle H_{ee} \rangle = \sum_{pairs} \frac{e^2}{r_{ij}} - \left\langle \sum_{pairs} \frac{e^2}{r_{ij}} \right\rangle \quad (3b)$$

This leaves the two interactions H'_{ee} and H_{ls} to determine the energies of the various electronic symmetry configurations within the atomic configuration.

2. Term Symbols

Electronic symmetry configurations are indicated with their orbital moment L, spin moment S, and total moment J. Together, these three quantum numbers indicate a certain state and determine its specific energy. If spin−orbit coupling is neglected, all configurations with the same L and S moments have the same energy. A specific configuration is indicated with a so-called term symbol $^{2S+1}L_J$. A term symbol gives all three quantum numbers and as such determines the symmetry and energy of a certain configuration. A single 1s electron has an orbital moment $L = 0$, a spin moment $S = 1/2$, and a total moment $J = 1/2$. This is written with a term symbol as $^2S_{1/2}$. A 2p electron has two possible symmetries depending on the spin−orbit coupling, $^2P_{1/2}$ and $^2P_{3/2}$. These two configurations are related to, respectively, the L_2 and the L_3 edge in 2p X-ray absorption. In the case of a transition-metal ion, the important initial state configurations are $3d^N$. In the final state with a 3s or a 3p core hole, the important configurations are $3s^1 3d^N$ and $3p^5 3d^N$. The main quantum number does not influence the coupling schemes, so exactly the same term symbols can be found for 4d and 5d systems and for 2s and 2p core holes.

A $3d^1$ configuration is 10-fold degenerate and has the term symbols $^2D_{5/2}$ and $^2D_{3/2}$ with, respectively, six and four electrons. The degeneracy of a term symbol $^{2S+1}L_J$ is given as $2J + 1$. The overall degeneracy of a term symbol ^{2S+1}L is $(2S + 1)(2L + 1)$. The LS term symbols of a $3d^1 4d^1$ configuration can be found by multiplying $^2D \otimes {}^2D$. The multiplication of L and S is independent, and one finds that the total orbital moment L is equal to 0, 1, 2, 3, or 4. S is equal to 0 or 1. This gives the term symbols as indicated in Table 1. The total degeneracy of the $3d^1 4d^1$ configuration is 100, which can be checked by adding the degeneracies of the 10 term symbols. After inclusion of spin−orbit coupling, a total of 18 $^{2S+1}L_J$ term symbols is found.

Table 1: Ten Term Symbols of a $3d^1 4d^1$ Configuration Are Given. The Second Row Gives Their Degeneracies Adding up to 100. The Bottom Row Gives for Each LS Term Symbol the Possible *J* Values

$3d^1 4d^1$	^1S	^1P	^1D	^1F	^1G	^3S	^3P	^3D	^3F	^3G	Σ
degen.	1	3	5	7	9	3	9	15	21	27	100
J values	0	1	2	3	4	1	0 1 2	1 2 3	2 3 4	3 4 5	

A $3d^2$ configuration does not have a degeneracy of 100. The Pauli exclusion principle forbids two 3d electrons to have the same quantum numbers, which has the consequence that the second electron has not 10 but only 9 possible states. In addition, the sequence of the quantum states for the two electrons make no difference, which divides the number of different two-electron states by two. This give $10 \times 9/2 = 45$ possible states. One can write out all 45 combinations of a $3d^2$ configuration and sort them by their M_L and M_S quantum numbers. Analysis of the combinations of the allowed M_L and M_S quantum numbers yields the term symbols ^1G, ^3F, ^1D, ^3P, and ^1S. This is a subset of the term symbols of a $3d^1 4d^1$ configuration. The term symbols can be divided into their J quantum numbers as $^3F_2$, $^3F_3$, $^3F_4$, $^3P_0$, $^3P_1$, $^3P_2$, $^1G_4$, $^1D_2$, and $^1S_0$. In the case of a $3d^3$ configuration, a similar approach gives that the possible spin states are doublet and quartet. The quartet states have all spins parallel, and the Pauli principle implies that there are two quartet term symbols, respectively, ^4F and ^4P. The doublet states have two electrons parallel, and for these two electrons, the Pauli principle yields the combinations identical to the triplet states of the $3d^2$ configuration. To these two parallel electrons a third electron is added antiparallel, where this third electron can have any value of its orbital quantum number m_l. Writing out all combinations and separating them into the total orbital moments M_l gives the doublet term symbols ^2H, ^2G, ^2F, ^2D, another ^2D, and ^2P. By adding the degeneracies, it can be checked that a $3d^3$ configuration has 120 different states, i.e., $10 \times 9/2 \times 8/3$. The general formula to determine the degeneracy of a $3d^N$ configuration is

$$\begin{pmatrix} 10 \\ n \end{pmatrix} = \frac{10!}{(10-n)!n!} \qquad (4)$$

A new result with respect to the s and p electrons is that one finds for a $3d^3$ configuration two states with an identical term symbol. To distinguish both term symbols, the so-called *seniority number* is introduced. The seniority number is the number N of the $3d^N$ configuration for which a term symbol occurs first. For example, the ^2D term symbol occurs for a $3d^1$ configuration; hence, it has seniority number 1. The term symbol could be rewritten as ${}^{2}_{1}D$. The second ^2D term symbol of $3d^3$ takes its seniority number from the next lowest number N and is written as ${}^{2}_{3}D$. The discussion of the seniority number brings us to another observation, which is that the term symbols of a configuration $3d^N$ do also exist in a configuration $3d^{N+2}$. Thus, the term symbols of $3d^4$ contain all term symbols of $3d^2$, which contains the ^1S term symbol of $3d^0$. Similarly, the term symbols of $3d^5$ contain all term symbols of $3d^3$, which contains the ^2D term symbol of $3d^1$. In addition, there is a symmetry equivalence of holes and electrons; hence, $3d^3$ and $3d^7$ have exactly the same term symbols.

An important X-ray absorption process is the 2p → 3d excitation process. The 2p X-ray absorption edge is often studied for the 3d transition-metal series, and it provides a wealth of information. Crucial for its understanding are the configurations of the $2p^53d^N$ final states. The term symbols of the $2p^53d^N$ states are found by multiplying the configurations of $3d^N$ with a ^2P term symbol. The total degeneracy of a $2p^53d^N$ state is given in eq 5. For example, a $2p^53d^5$ configuration has 1512 possible states. Analysis shows that these 1512 states are divided into 205 term symbols, implying, in principle, 205 possible final states. Whether all these final states have finite intensity depends on the selection rules.

$$6 \times \begin{pmatrix} 10 \\ n \end{pmatrix} = 6 \times \frac{10!}{(10-n)!n!} \qquad (5)$$

3. The Matrix Elements

Above found the number and symmetry of the states of a certain $3d^N$ configuration were found. The next task is to calculate the matrix elements of these states with the Hamiltonian H_{ATOM}. As discussed in the previous section, H_{ATOM} consists of the effective electron−electron interaction H'_{ee} and the spin−orbit coupling H_{ls}

$$H_{\mathrm{ATOM}} = \sum_{\mathrm{pairs}} \frac{e^2}{r_{ij}} + \sum_{N} \zeta(r_i) l_i \cdot s_i \qquad (6)$$

The electron−electron interaction commutes with L^2, S^2, L_z, and S_z, which implies that all off-diagonal elements are zero. A simple example is a 1s2s configuration consisting of ^1S and ^3S term symbols. The respective energies can be shown to be

$$\left\langle {}^1S \left| \frac{e^2}{r_{12}} \right| {}^1S \right\rangle = F^0\,(1s2s) + G^0\,(1s2s) \qquad (7)$$

$$\left\langle {}^3S \left| \frac{e^2}{r_{12}} \right| {}^3S \right\rangle = F^0\,(1s2s) - G^0\,(1s2s) \qquad (8)$$

F^0 and G^0 are the Slater−Condon parameters for, respectively, the direct Coulomb repulsion and the Coulomb exchange interaction. The main result can be stated as “the singlet and the triplet state are split by the exchange interaction”. This energy difference is $2G^0$ (1s2s). An analogous result is found for a 1s2p state for which the singlet and triplet states are split by $2/3G^0$ (1s2p). The 2/3 prefactor is determined by the degeneracy of the 2p state. The general formulation of the matrix elements of two-electron wave functions can be written as

$$\left\langle {}^{2S+1}L_J \left| \frac{e^2}{r_{12}} \right| {}^{2S+1}L_J \right\rangle = \sum_k f_k F^k + \sum_k g_k G^k \qquad (9)$$

To obtain this result, the radial parts F^k and G^k have been separated using the Wigner-Eckardt theorem and Hamiltonian $1/r_{12}$ has been expanded in a series.[123] The angular parts f_k and g_k can be calculated using angular momentum coupling, and the result is written in terms of $3j$ and $6j$ symbols

$$f_k = (2l_1+1)(2l_2+1)\cdot(-1)^L \begin{pmatrix} l_1 & k & l_1 \\ 0 & 0 & 0 \end{pmatrix} \begin{pmatrix} l_2 & k & l_2 \\ 0 & 0 & 0 \end{pmatrix} \begin{pmatrix} l_1 & l_2 & L \\ l_2 & l_1 & k \end{pmatrix} \qquad (10)$$

$$g_k = (2l_1+1)(2l_2+1)\cdot(-1)^S \begin{pmatrix} l_1 & k & l_2 \\ 0 & 0 & 0 \end{pmatrix} \begin{pmatrix} l_1 & k & l_2 \\ 0 & 0 & 0 \end{pmatrix} \begin{pmatrix} l_1 & l_2 & L \\ l_2 & l_1 & k \end{pmatrix} \qquad (11)$$

For equivalent electrons, g_k is not present and f_k can be simplified by setting $l = l_1 = l_2$. The values of k can be determined from the so-called *triangle conditions* of the $3j$ symbols. The triangle conditions imply that for $3j$ symbols with all zeros for m_j (given in the bottom row), the sum of the j values (given in the top row) must be even and that the maximum j value is equal to the sum of the two others. Using the two $3j$ symbols of eqs 10 and 11, this implies for f_k that k must always be even. $k = 0$ is always present, and the maximum value for k equals two times the lowest value of l. For g_k it implies that k is even if $l_1 + l_2$ is even and k is odd if $l_1 + l_2$ is odd. The maximum value of k equals $l_1 + l_2$. Table 2 gives the possible k values for some important configurations.

Table 2: Possible Values of k for the Angular Coefficients f_k and g_k

conf.	f_k	g_k	conf.	f_k	g_k	conf.	f_k	g_k
$1s^2$	0		1s2s	0	0	1s2p	0	1
$2p^2$	0 2		2p3p	0 2	0 2	2p3d	0 2	1 3
$3d^2$	0 2 4		3d4d	0 2 4	0 2 4	3d4f	0 2 4	1 3 5

The energies of the representations of the $3d^2$ configuration are calculated. First, it can be shown that f_0 is equal to the number of permutations (n(n

− 1)/2) of n electrons, i.e., f_0 is equal to 1.0 for two-electron configurations. The electrons come from the same shell; hence, there are no exchange interactions. One is left with the calculation of f_2 and f_4 for the five term symbols ^{1}S, ^{3}P, ^{1}D, ^{3}F, and ^{1}G. $l_1 = l_2 = 2$, which implies that the prefactor $(2l_1 + 1)(2l_2 + 1)$ is equal to 25. The 3j symbols are only dependent on k and are equal to $\sqrt{2/35}$. For all five states this gives a prefactor of 25 × 2/35 = 10/7, i.e., f_k is equal to

$$f_k = \frac{10}{7}\cdot\begin{Bmatrix} 2 & 2 & L \\ 2 & 2 & k \end{Bmatrix}\cdot(-1)^L \qquad (12)$$

The Slater−Condon parameters F^2 and F^4 have approximately a constant ratio: $F^4 = 0.62F^2$. The last column in Table 3 gives the approximate energies of the five term symbols. In case of the 3d transition-metal ions, F^2 is approximately equal to 10 eV. For the five term symbols this gives the energies as ^{3}F at −1.8 eV, ^{1}D at −0.1 eV, ^{3}P at +0.2 eV, ^{1}G at +0.8 eV, and ^{1}S at +4.6 eV. The ^{3}F term symbol has lowest energy and is the ground state of a 3d^2 system. This is in agreement with Hund's rules, which will be discussed in the next section. The three states ^{1}D, ^{3}P, and ^{1}G are close in energy, 1.7−2.5 eV above the ground state. The ^{1}S state has a high energy of 6.3 eV above the ground state, the reason being that two electrons in the same orbit strongly repel each other.

Table 3: Energies of the Five Term Symbols of a 3d^2 Configuration. The Energy in the Last Column Is Calculated Using the Approximation that the Radial Integrals F^2 and F^4 Have a Constant Ratio of 0.62

	f_2		f_4		energy
^{1}S	$\frac{10}{7}\begin{Bmatrix}2&2&0\\2&2&2\end{Bmatrix}$	2/7	$\frac{10}{7}\begin{Bmatrix}2&2&0\\2&2&4\end{Bmatrix}$	2/7	$0.46F^2$
3P	$-\frac{10}{7}\begin{Bmatrix}2&2&1\\2&2&2\end{Bmatrix}$	3/21	$-\frac{10}{7}\begin{Bmatrix}2&2&1\\2&2&4\end{Bmatrix}$	−4/21	$0.02F^2$
1D	$\frac{10}{7}\begin{Bmatrix}2&2&2\\2&2&2\end{Bmatrix}$	−3/49	$\frac{10}{7}\begin{Bmatrix}2&2&2\\2&2&4\end{Bmatrix}$	4/49	$-0.01F^2$
3F	$-\frac{10}{7}\begin{Bmatrix}2&2&3\\2&2&2\end{Bmatrix}$	−8/49	$-\frac{10}{7}\begin{Bmatrix}2&2&3\\2&2&4\end{Bmatrix}$	−1/49	$-0.18F^2$
1G	$\frac{10}{7}\begin{Bmatrix}2&2&4\\2&2&2\end{Bmatrix}$	4/49	$\frac{10}{7}\begin{Bmatrix}2&2&4\\2&2&4\end{Bmatrix}$	1/441	$0.08F^2$

Table 4 gives three related notations that are used to indicate the radial integrals: the Slater−Condon parameters F^k, the normalized Slater−Condon parameters F_k, and the Racah parameters A, B, and C. The bottom half of Table 4 uses the relationship between F^2 and F^4 and further uses a typical F^2 value of 10 eV and a F^0 value of 8 eV. For three and more electrons, the situation is more complex. It is not straightforward to write down an antisymmetrized three-electron wave function. It can be shown that the three-electron wave function can be build from two-electron wave functions with the use of the so-called *coefficients of fractional parentage*. The coefficients of fractional parentage are indicated with $C^{LS}_{L_1S_1}$. The three-electron wave function with quantum numbers LS is generated from a series of two-electron wave functions with quantum numbers L_1S_1.

Table 4: Relations between the Slater−Condon Parameters and Racah Parameters. The Top Half Gives the Relationships between the Three Parameter Sets. The Bottom Half Uses F^0 = 8.0 eV, F^2 = 10.0 eV, and F^4 = 6.2 eV

Slater−Condon	normalized	Racah
F^0	$F_0 = F^0$	$A = F_0 - 49F_4$
F^2	$F_2 = F^2/49$	$B = F_2 - 5F_4$
F^4	$F_4 = F^4/441$	$C = 35F_4$
$F^0 = 8.0$	$F_0 = 8.0$	$A = 7.3$
$F^2 = 10.0$	$F_2 = 0.41$	$B = 0.13$
$F^4 = 6.2$	$F_4 = 0.014$	$C = 0.49$

4. Atomic Multiplet Ground States of 3d^N Systems

The ground-state symmetries of the transition-metal compounds that are characterized with a partly filled 3d band will be discussed. The term symbols with the lowest energy are found after calculating the matrix elements. The term symbols found to be at the lowest energy are indicated in Table 5. The finding of the ^{3}F state as the ground state of a 3d^2 configuration is an example of the so-called Hund's rules. On the basis of experimental information, Hund did formulate three rules to determine the ground state of a 3d^N configuration. The Hund rules are as follows: (1) term symbol with maximum spin S, (2) term symbol with maximum orbital moment L, and (3) term symbol with maximum total moment J, if the shell is more than half full.

Table 5: 2p X-ray Absorption Transitions from the Atomic Ground State to All Allowed Final-State Symmetries, after Applying the Dipole Selection Rule: $\Delta J = -1, 0,$ or $+1$

transition	no. of term symbols: ground state	symmetry: ground state	no. of term symbols: final state	no. of allowed transitions
$3d^0 \rightarrow 2p^53d^1$	1	$^1S_0$	12	3
$3d^1 \rightarrow 2p^53d^2$	2	$^2D_{3/2}$	45	29
$3d^2 \rightarrow 2p^53d^3$	9	$^3F_2$	110	68
$3d^3 \rightarrow 2p^53d^4$	19	$^4F_{3/2}$	180	95
$3d^4 \rightarrow 2p^53d^5$	34	$^5D_0$	205	32
$3d^5 \rightarrow 2p^53d^6$	37	$^6S_{5/2}$	180	110
$3d^6 \rightarrow 2p^53d^7$	34	$^5D_2$	110	68
$3d^7 \rightarrow 2p^53d^8$	19	$^4F_{9/2}$	45	16
$3d^8 \rightarrow 2p^53d^9$	9	$^3F_4$	12	4
$3d^9 \rightarrow 2p^53d^{10}$	2	$^2D_{5/2}$	2	1

A configuration has the lowest energy if the electrons are as far apart as possible. Hund's first rule of 'maximum spin' can be understood from the Pauli principle: Electrons with parallel spins must be in different orbitals, which overall implies larger separations, hence lower energies. This is, for example, evident for a 3d^5 configuration, where the ^{6}S state has its five electrons divided over the five spin-up orbitals, which minimizes their repulsion. In case of 3d^2, Hund's first rule implies that either the ^{3}P or ^{3}F term symbol must have the lowest energy. From the previous section, one finds that the ^{3}F term symbol is lower than the ^{3}P term symbol, the reason being that the ^{3}F wave function tends to minimize electron repulsion. The effects of spin−orbit coupling are well-known in the case of core states. Consider, for example, the 2p XAS or XPS spectrum of nickel. The $^2P_{3/2}$ peak is positioned at approximately 850 eV and the $^2P_{1/2}$ at about 880 eV, where the state with the lowest binding energy is related to the lowest energy of the configuration. The case of the 2p core state is an example of d Hund's third rule: the configuration is $2p^5$, which is more than half-full, implying that the highest J value has the lowest energy. The third rule implies that the ground state of a $3d^8$ configuration is $^3F_4$, while it is $^3F_2$ in the case of a $3d^2$ configuration.

5. X-ray Absorption Spectra Described with Atomic Multiplets

I will start with the description of closed-shell systems. The 2p X-ray absorption process excites a 2p core electron into the empty 3d shell, and the transition can be described as $2p^63d^0 \rightarrow 2p^53d^1$. The ground state has $^1S_0$ symmetry, and it is found that the term symbols of the final state are $^1P_1$, $^1D_2$, $^1F_3$, $^3P_{012}$, $^3D_{123}$, and $^3F_{234}$. The energies of the final states are affected by the 2p3d Slater−Condon parameters, the 2p spin−orbit coupling, and the 3d spin−orbit coupling. The X-ray absorption transition matrix elements to be calculated are

$$I_{\mathrm{XAS}} \propto \langle 3d^0|p|2p^53d^1\rangle^2 \tag{13a}$$

The symmetry aspects are

$$I_{\mathrm{XAS}} \propto \langle [^1S_0]|[^1P_1][|^{1,3}PDF]\rangle^2 \tag{13b}$$

The symmetry of the dipole transition is given as $^1P_1$, according to the dipole selection rules, which state that $\Delta J = +1, 0, -1$. Within LS coupling, also $\Delta S = 0$ and $\Delta L = 1$. The dipole selection rule reduces the number of final states that can be reach from the ground state. The J value in the ground state is zero. In this case, the dipole selection rule proclaims that the J value in the final state must be 1; thus, only the three term symbols $^1P_1$, $^3P_1$, and $^3D_1$ can obtain finite intensity. The problem of calculating the 2p absorption spectrum is reduced to solving the 3×3 energy matrix of the final states with $J = 1$. As discussed above, the atomic energy matrix consists of terms related to the two-electron Slater integrals and the 2p and 3d spin−orbit couplings.

A series of X-ray absorption spectra of tetravalent titanium 2p and 3p edges and the trivalent lanthanum 3d and 4d edges is compared. The ground states of Ti^{IV} and La^{III} are, respectively, $3d^0$ and $4f^0$, and they share a ^1S ground state. The transitions at the four edges are, respectively

$$Ti^{IV}\ L_{2,3}\ \text{edge:}\ 3d^0 \rightarrow 2p^53d^1$$

$$Ti^{IV}\ M_{2,3}\ \text{edge:}\ 3d^0 \rightarrow 3p^53d^1$$

$$La^{III}\ M_{4,5}\ \text{edge:}\ 4f^0 \rightarrow 3d^94f^1$$

$$La^{III}\ N_{4,5}\ \text{edge:}\ 4f^0 \rightarrow 4d^94f^1$$

These four calculations are equivalent, and all spectra consist of three peaks with $J = 1$ as described above in the case of the 2p edge of Ti^{IV}. The things that change are the values of the atomic Slater−Condon parameters and core hole spin−orbit couplings. They are given in Table 6 for the four situations. The G^1 and G^3 Slater−Condon parameters have an approximately constant ratio with respect to the F^2 value. The important factor for the spectral shape is the ratio of the core spin−orbit coupling and the F^2 value. Finite values of both the core spin−orbit and the Slater−Condon parameters cause the presence of the prepeak. It can be seen in Table 6 that the 3p and 4d spectra have small core spin−orbit couplings, implying small $p_{3/2}$ ($d_{5/2}$) edges and extremely small prepeak intensities. The deeper 2p and 3d core levels have larger core spin−orbit splitting with the result of a $p_{3/2}$ ($d_{5/2}$) edge of almost the same intensity as the $p_{1/2}$ ($d_{3/2}$) edge and a larger prepeak. Note that none of these systems comes close to the single-particle result of a 2:1 ratio of the p edges or the 3:2 ratio of the d edges. Figure 8 shows the X-ray absorption spectral shapes. They are given on a logarithmic scale to make the preedges visible.

Table 6: Relative Intensities, Energy, Core Hole Spin−Orbit Coupling, and F_2 Slater−Condon Parameters Are Compared for Four Different $^1S_0$ Systems

edge	Ti 2p	Ti 3p	La 3d	La 4d
average energy (eV)	464	37	840	103
core spin−orbit (eV)	3.78	0.43	6.80	1.12
F^2 Slater−Condon (eV)	5.04	8.91	5.65	10.45
relative intensities				
prepeak	10^{-2}	10^{-4}	10^{-2}	10^{-3}
$p_{3/2}$ or $d_{5/2}$	0.72	10^{-3}	0.80	10^{-2}
$p_{1/2}$ or $d_{3/2}$	1.26	1.99	1.19	1.99

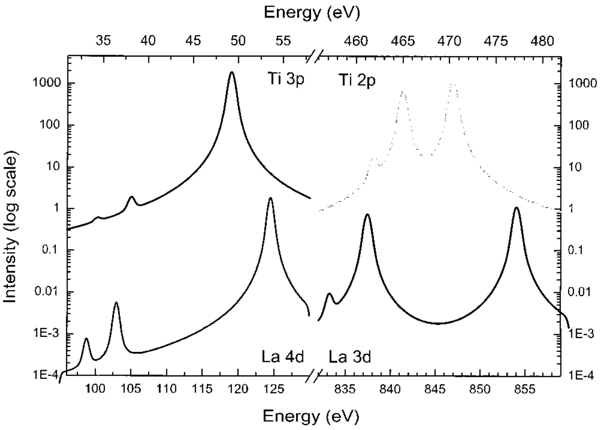

Figure 8. Atomic multiplet calculations for the $3d^0$ and $4f^0$ ions Ti^{IV} and La^{III}. Given are the transitions $3d^0 \rightarrow 2p^53d^1$, $3d^0 \rightarrow 3p^53d^1$, $4f^0 \rightarrow 3d^94f^1$, and $4f^0 \rightarrow 4d^94f^1$. All spectra are given on a logarithmic scale to make the prepeaks clearly visible.

In Table 5 the term symbols of all $3d^N$ systems are given. Together with the dipole selection rules, this sets immediately strong limits to the number of final states which can be reached, similar to the case of a $3d^0$ ground state. Consider, for example, the $3d^3 \rightarrow 2p^53d^4$ transition: The $3d^3$ ground state has $J = 3/2$ and there are, respectively, 21, 35, and 39 states of $2p^53d^4$ with $J' = 1/2$, $J' = 3/2$, and $J' = 5/2$. This implies a total of 95 allowed peaks out of the 180 final-state term symbols. From Table 5 some special cases can be discriminated: a $3d^9$ system makes a transition to a $2p^53d^{10}$ configuration, which has only two term symbols, out of which only the term symbol with $J' = 3/2$ is allowed. In other words, the L_2 edge has zero intensity. $3d^0$ and $3d^8$ systems have only three and four peaks, respectively, because of the limited amount of states for the $2p^53d^1$ and $2p^53d^9$ configurations.

Atomic multiplet theory is able to accurately describe the 3d and 4d X-ray absorption spectra of the rare earth metals.[55] In the case of the 3d metal ions, atomic multiplet theory cannot simulate the X-ray absorption spectra accurately because the effects of the neighbors on the 3d states are too large. It turns out that it is necessary to include both the symmetry effects and the configuration-interaction effects of the neighbors explicitly. Ligand-field multiplet theory takes care of all symmetry effects, while charge-transfer multiplet theory allows the use of more than one configuration.

B. Ligand-Field Multiplet Theory

If one transfers this atomic method to the solid state, two questions that arise are (1) how to deal with the different local symmetry and (2) how to incorporate the different more itinerant electronic features of the solid state, such as the electron density of the s and p states. The inclusion of the local symmetry has been the subject of many studies under the heading of ligand-field theory.[12] This has been used particularly to describe the optical absorption spectra of transition-metal ions. For core spectroscopies, ligand-field theory has been developed by Thole and co-workers.[110] The effects of itinerant states on multiplets will be described using the charge-transfer multiplet approach as described in the next section.

The dominant symmetry effect in solids is the cubic ligand field. The strength of this operator is usually denoted as the ligand-field splitting (10Dq). Atomic multiplet theory can be extended to describe the 3d metal ions by incorporation of the ligand-field splitting. In an octahedral environment, the field of the neighboring atoms on the of the central atom has cubic (O_h) symmetry which divides the 5-fold-degenerate 3d orbitals into two distinct representations of T_{2g} and E_g symmetry. The 2-fold-degenerate E_g state contains orbitals that point toward the center of the cube faces, which is directly toward the position of the ligands. Consequently, E_g states interact stronger, electrostatically as well as covalently, with the ligands. The three t_{2g} orbitals point toward the corners of the cube, and therefore, their interaction with the octahedral ligands is smaller.

The effect of the cubic ligand field on the energies of the atomic states has been described in the textbooks of Ballhausen,[51] Griffith,[12] and Sugano, Tanabe, and Kitamura.[105] It is found that the degeneracy of the atomic states is partially lifted and the D, F, and higher states are split into a series of representations in cubic symmetry. In the $2p^53d^N$ final state, the effects of the cubic ligand field are equivalent to that in the initial state. A difference is that the number of multiplet states is considerably larger: For a $3d^5$ initial state, the maximum number of states is 256, while it is six times larger (1512) for a $2p^53d^5$ final state.

The transition probability for the $3d^0$ systems in cubic symmetry is

$$W \propto \langle 3d^0[A_1]|p[T_1]|2p^53d^1[T_1]\rangle^2 \qquad (14)$$

All final states of T_1 symmetry are allowed and have a finite transition probability from the A_1 initial state. This includes the states of $J = 1$ atomic symmetry and additionally the atomic states with $J = 3$ and $J = 4$. The degeneracy of these states is, respectively, 3 and 1. The total number of allowed final states in cubic symmetry is $3 + 3 + 1 = 7$. Figure 9 shows the effects of an increasing cubic ligand field on the multiplet spectrum of the $3d^0 \rightarrow 2p^53d^1$ transition. In this figure it can be seen that for small values of the ligand field (the step size is 0.3 eV) the spectrum is hardly modified. For small values of 10Dq, the four states which were forbidden in atomic symmetry have not gained enough intensity to be detectable in the spectrum. The peak splitting in the spectrum is related to the value of 10Dq, but it is not a direct measure of it. This implies that one cannot measure the crystal-field splitting directly in a 2p X-ray absorption spectra.

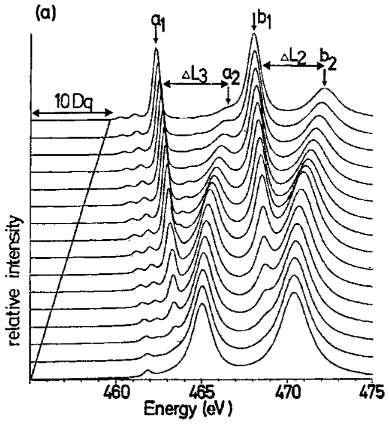

Figure 9. Ligand-field multiplet calculations of the transition $3d^0 \rightarrow 2p^53d^1$ for the Ti^{IV} system. The bottom spectrum has a cubic crystal field of 0.0 eV; the top spectrum has a cubic crystal-field value 10Dq of 4.5 eV. (Reprinted from ref 38. Copyright 1990 American Physical Society.)

The ligand-field multiplet results as calculated with the procedure outlined above can be directly compared with experiment. Figure 10 compares the ligand-field multiplet calculation of CaF_2 with the 2p X-ray absorption spectrum of CaF_2. Atomic Slater integrals were used. For details, see refs 37 and 38. All peaks in the experimental spectrum are reproduced, which is a confirmation that the ligand-field multiplets indeed dominate the spectral shape. When resonant X-ray emission will be discussed, CaF_2 will be used as an example of what happens if one excites to these multiplet peaks.

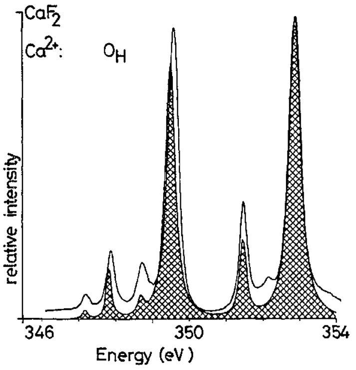

Figure 10. Calcium 2p X-ray absorption spectrum of CaF_2 compared with a ligand-field multiplet calculation. The value of 10Dq is −0.9 eV. (Reprinted with permission from ref 38. Copyright 1990 American Physical Society.)

Table 7: Projection of the 2p X-ray Absorption Transitions from Atomic Symmetry (SO_3) to Octahedral Symmetry (O_h). Degeneracies of the Configurations Are Given. The Last Column Gives the Degeneracies without Any Symmetry (C_1)

transition	degeneracies in spherical symmetry	degeneracies in octahedral symmetry	degeneracies without symmetry
$3d^0 \to 2p^53d^1$	1 → 12	1 → 25	1 → 60
$3d^1 \to 2p^53d^2$	2 → 45	3 → 90	10 → 270
$3d^2 \to 2p^53d^3$	9 → 110	20 → 300	45 → 720
$3d^3 \to 2p^53d^4$	19 → 180	39 → 420	120 → 1260
$3d^4 \to 2p^53d^5$	34 → 205	91 → 630	210 → 1512
$3d^5 \to 2p^53d^6$	37 → 180	86 → 420	252 → 1260
$3d^6 \to 2p^53d^7$	34 → 110	91 → 300	210 → 720
$3d^7 \to 2p^53d^8$	19 → 45	39 → 90	120 → 270
$3d^8 \to 2p^53d^9$	9 → 12	20 → 25	45 → 60
$3d^9 \to 2p^53d^{10}$	2 → 2	3 → 2	10 → 6

Table 7 gives the ground-state symmetries of the atomic multiplets and their projection to cubic symmetry. If four electrons have to be accommodated in the 3d orbitals in an octahedral surrounding, two effects are important: The exchange coupling of two 3d electrons (J) and the cubic ligand-field splitting (D). The exchange coupling is connected to the Slater integrals: $J = (F^2 + F^4)/14$, where the difference between the exchange couplings of e_g and t_{2g} electrons is neglected.[30] If $3J > D$, a high-spin configuration with ^5E symmetry is formed from the Hund's rule ^5D ground state. If $3J < D$, a low-spin configuration with $^3T_1$ symmetry is formed. It can be checked that the same criterion applies to a $3d^5$ configuration, while for $3d^6$ and $3d^7$ configurations, one should compare $2J$ with D. The exchange coupling J is about 0.8 eV for 3d electrons, implying a high-spin low-spin transition point of approximately 2.4 eV for $3d^4$ and $3d^5$ and 1.8 eV for $3d^6$ and $3d^7$.

The calculation of the ligand-field multiplet spectrum is equivalent to that of the $3d^0$ configuration, with the additional possibility of low-spin ground states. To obtain the 2p X-ray absorption spectra, the calculated line spectrum is broadened with a Lorentzian broadening to simulate lifetime effects and a Gaussian broadening to simulate the resolution function of the experiment. Figure 11 shows the comparison for MnO. Excellent agreement is obtained with the atomic values of the Slater integrals and a ligand-field splitting of 0.8 eV. Or, to be more specific, the Slater integrals have been calculated by Hartree−Fock, and these Hartree−Fock values have been reduced to 80% of their calculated value. This procedure reproduces the experimental Slater integrals of atomic spectra. In the case of covalent systems, further reduction of the Slater integrals (according to the nephelauxatic effect) is often used. If one uses the charge-transfer multiplet model, charge transfer should take care of the effective reduction of Slater integrals. For more details, the reader is referred to refs 27 and 29 and references therein.

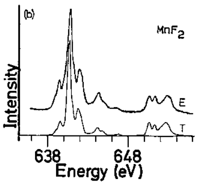

Figure 11. Manganese 2p X-ray absorption spectrum of MnF_2 compared with ligand-field multiplet calculations. (Reprinted with permission from ref 37. Copyright 1990 American Physical Society.)

The transition from a high-spin to a low-spin ground state is directly visible in the spectral shape, because a different final-state multiplet is reached. This is shown theoretically and experimentally for a series of Mn^{II} compounds by Cramer and co-workers.[26] An important advantage of soft X-ray edges is their high resolution, which can be less than 0.1 eV due to the long lifetime of the core states. The high resolution makes the spectra sensitive to details of the electronic structure, such as the valence, symmetry, spin state, and crystal-field value.[26,29] It is important to realize that multiplet effects are a general phenomenon in all cases where a 2s, 2p, or 3p core hole is present in a 3d metal.

C. Charge-Transfer Multiplet Theory

The essence of the charge-transfer model is the use of two or more configurations. Ligand-field multiplet calculations use one configuration for which it solves the effective atomic Hamiltonian plus the ligand-field Hamiltonian, so essentially the following matrixes

$$I_{\mathrm{XAS},1} \propto \langle 3\mathrm{d}^N|\mathrm{p}|2\mathrm{p}^5 3\mathrm{d}^{N+1}\rangle^2 \tag{15a}$$

$$H_{\mathrm{INT},1} = \left\langle 3\mathrm{d}^N\left|\frac{e^2}{r_{12}} + \varsigma_d l_d \cdot s_d + H_{\mathrm{LFM}}\right|3\mathrm{d}^N\right\rangle \tag{15b}$$

$$H_{\mathrm{FINAL},1} = \left\langle 2\mathrm{p}^5 3\mathrm{d}^{N+1}\left|\frac{e^2}{r_{12}} + \varsigma_p l_p \cdot s_p + \varsigma_d l_d \cdot s_d + H_{\mathrm{LFM}}\right|2\mathrm{p}^5 3\mathrm{d}^{N+1}\right\rangle \tag{15c}$$

The charge-transfer model adds a configuration $3d^{N+1}\underline{L}$ to the $3d^N$ ground state. In the case of a transition-metal oxide, in a $3d^{N+1}\underline{L}$ configuration an electron has been moved from the oxygen 2p valence band to the metal 3d band. The energy difference between the $3d^N$ and $3d^{N+1}\underline{L}$ configurations is the so-called charge-transfer energy (Δ). One can continue with this procedure and add a $3d^{N+2}\underline{L}^2$ configuration, etc. In many cases two configurations will be enough to explain the spectral shapes, but in particular for high valence states, it can be important to include more configurations.[45,80] The 3d states are described in a correlated fashion, while all other electrons are described in a band-like fashion.[125] This is essentially the Anderson impurity model. The actual calculations can be carried out for a cluster or a quasiatomic model.

As far as X-ray absorption and X-ray emission are concerned, the consequences for the calculations are the replacement of $3d^N$ with $3d^N + 3d^{N+1}\underline{L}$ plus the corresponding changes in the final state. This adds a second initial state, final state, and dipole transition

$$I_{\mathrm{XAS},2} \propto \langle 3d^{N+1}\underline{L}|p|2p^5 3d^{N+2}\underline{L}\rangle^2 \tag{15d}$$

$$H_{\mathrm{INIT},2} = \left\langle 3d^{N+1}\underline{L}\left|\frac{e^2}{r_{12}} + \varsigma_d l_d{\cdot}s_d + H_{\mathrm{LFM}}\right|3d^{N+1}\underline{L}\right\rangle \tag{15e}$$

$$H_{\mathrm{FINAL},2} = \left\langle 2p^5 3d^{N+2}\underline{L}\left|\frac{e^2}{r_{12}} + \varsigma_p l_p{\cdot}s_p + \varsigma_d l_d{\cdot}s_d + H_{\mathrm{LFM}}\right|2p^5 3d^{N+2}\underline{L}\right\rangle \tag{15f}$$

The two initial states and two final states are coupled by monopole transitions, i.e., configuration interaction. The mixing parameter t couples both configurations, and as Δ is the energy difference, the Hamiltonian is indicated with t/Δ

$$H_{\mathrm{MIX}\ I1,I12} = \langle 3d^N|t/\Delta|3d^{N+1}\underline{L}\rangle \tag{15g}$$

$$H_{\mathrm{MIX}\ F1,F2} = \langle 2p^5 3d^{N+1}|t/\Delta|2p^5 3d^{N+2}\underline{L}\rangle \tag{15h}$$

The spectrum is calculated by solving the eqs 15a–h. If a $3d^{N+2}\underline{LL}'$ configuration is included, its energy is $2\Delta + U$, where U is the correlation energy between two 3d electrons.[125] The formal definition of U is the energy difference one obtains when an electron is transferred from one metal site to another, i.e., a transition $3d^N + 3d^N \rightarrow 3d^{N+1} + 3d^{N-1}$. The number of interactions of two $3d^N$ configurations is one more than the number of interactions of $3d^{N+1}$ plus $3d^{N-1}$, implying that this energy difference is equal to the correlation energy between two 3d electrons.

In the final state of the X-ray absorption process, the configurations are $2p^5 3d^{N+1}$ and $2p^5 3d^{N+2}\underline{L}$. A 2p electron is annihilated, and a 3d electron is created. Because the 3d electrons are relatively localized, this is an almost self-screened process. The consequence is that the relative ordering of the configurations does hardly change. To be precise: the energy difference between $2p^5 3d^{N+1}$ and $2p^5 3d^{N+2}\underline{L}$ is given as $\Delta + U - Q$, where U is the 3d3d correlation energy and Q the core hole potential, which identifies with the 2p3d correlation energy. From the systematic analysis of core-level photoemission spectra, it has been found that Q is slightly larger than U. Typical values are Q equal to 9 eV with U equal to 7 or 8 eV. This is the reason that only small charge-transfer satellites are visible in X-ray absorption, in contrast to the large satellites in photoemission.[29]

By analyzing the effects of charge transfer, it is found that (for systems with a positive value of Δ) the main effects on the X-ray absorption spectral shape are (1) the contraction of the multiplet structures and (2) the formation of small satellites. Figure 12 shows the effect of the charge-transfer energy on divalent nickel. In the top spectrum, $\Delta = 10$ and the spectrum is essentially the ligand-field multiplet spectrum of a Ni$^{\mathrm{II}}$ ion in its $3d^8$ configuration. The bottom spectrum uses $\Delta = -10$, and now the ground state is almost a pure $3d^9\underline{L}$ configuration. Looking for the trends in Figure 12, one nicely finds the increased contraction of the multiplet structure by going to lower values of Δ. This is exactly what is observed in the series NiF_2 to $NiCl_2$ and $NiBr_2$.[87–89,115] Going from Ni to Cu, the atomic parameters change very little, except the 2p spin–orbit coupling and the 2p binding energy. Therefore, the spectra of $3d^N$ systems of different elements are all very similar and the bottom spectrum is also similar to Cu$^{\mathrm{II}}$ systems. Therefore, one can also use the spectra with negative Δ values for Cu$^{\mathrm{III}}$ compounds, such as $La_2Li_{1/2}Cu_{1/2}O_4$ and Cs_2KCuF_6. Figure 13 shows the comparison of the 2p X-ray absorption spectrum of these two compounds with charge-transfer multiplet calculations.[63,64] It can be checked in Figure 12 that these calculations look similar to the calculations for Ni$^{\mathrm{II}}$ systems with negative values of Δ. For such systems with negative Δ values, it is important to carry out charge-transfer multiplet calculations as no good comparison with ligand-field multiplet spectra can be made.

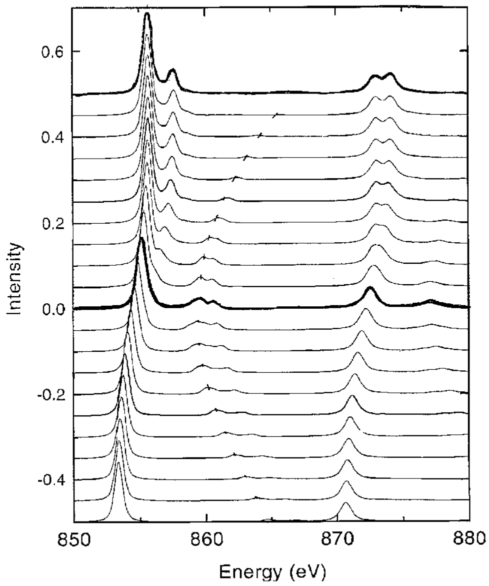

Figure 12. Series of charge-transfer multiplet calculations for the ground state $3d^8 + 3d^9L$. The top spectrum has a charge-transfer energy Δ of +10 eV and relates to an almost pure $3d^8$ state; the bottom spectrum has a value of Δ of −10 eV and relates to an almost pure $3d^9L$ state.

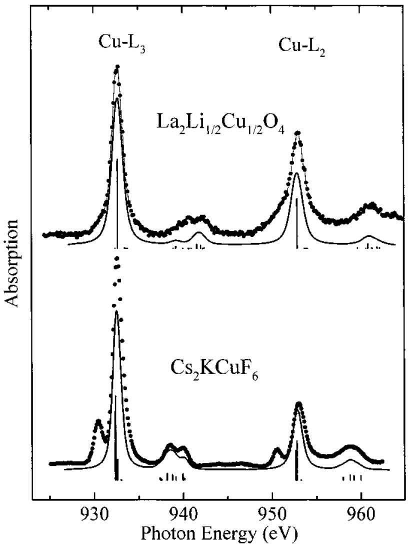

Figure 13. Results of theoretical simulations of the Cu 2p X-ray absorption spectra of Cs_2KCuF_6 (bottom) and $La_2Li_{1/2}Cu_{1/2}O_4$ (top), in comparison with the experimental spectra. (Reprinted with permission from ref 63. Copyright 1998 Elsevier Science.)

IV. 1s X-ray Emission

Now the X-ray emission spectra will be discussed. The theory for X-ray emission spectra and resonant X-ray emission spectra has been described in, for example, the works of Åberg[1,2,113] and Kotani.[81,106] In this paper the models derived in these works will be used, starting with a simpler model.

A. 1s3p X-ray Emission in the Ligand-Field Multiplet Model

First the 1s3p X-ray emission spectral shape will be discussed, also known as Kβ fluorescence. With divalent manganese as an example, a scheme to interpret the experimental spectral shapes using the multiplet models as described for X-ray absorption will be developed step by step. The ground state of Mn^{II} has its five spin-up electrons filled. The five spin-down states are empty. It is first assumed that the core hole creation, for example, by an above-resonance X-ray excitation, does not modify the valence electron situation. The intermediate state has a $1s^13d^5$ configuration and after the 1s3p decay the final state is $3p^53d^5$

$$3d^5 \rightarrow 1s^13d^5 + \epsilon 1s^13d^5 \Rightarrow 3p^53d^5$$

The spectral shape consists of two structures separated by the 3p3d exchange interaction. This assignment is essentially the original model as used by Tsutsumi and co-workers.[111,112] Starting from this model, the effects of the 3p and 3d spin−orbit coupling, the symmetry effects of the cubic crystal field, will step by step be included. In section V.A the model is extended to describe covalence effects as included with charge transfer and include the combined effects of off-resonance excitation and decay. Resonance effects will be discussed in section V.C.

Assuming a Mn^{II} ion, the atomic ground-state symmetry is ^6S. In the $1s^13d^5$ configuration, the total symmetry can be found by multiplying the 1s electron with the ^6S symmetry of the 3d electrons. This gives either a ^5S state for antiparallel alignment of the 1s and 3d electrons or ^7S for parallel alignment. The dipole selection rules imply that transitions are possible from ^5S to ^5P and from ^7S to ^7P, with the energy difference between ^5P and ^7P given by the 3p3d exchange interaction. Things are a bit more complex in reality because more then one ^5P configuration can be made from a $3p^53d^5$ configuration. Writing out all symmetry combinations one finds three ^5P states and one ^7P state. Figure 14a shows the atomic multiplet spectrum for which the 3d and 3p spin−orbit couplings have been set to zero. The overall intensities of the states are 7:5 for the ^7P versus the ^5P states. The main peak is the ^7P state. The shoulder and the satellite are the ^5P states, and the small peak at about −6482 eV is the third ^5P state. The satellite can be related to the antiparallel aligned 3p and 3d electrons, while the shoulder and low-intensity state relate to orderings of the 3d electrons different from the ground state. In fact, the three ^5P states are linear combinations of the three *LS*-like atomic states that are mixed by the strong 3p3d as well as 3d3d multiplet effects.

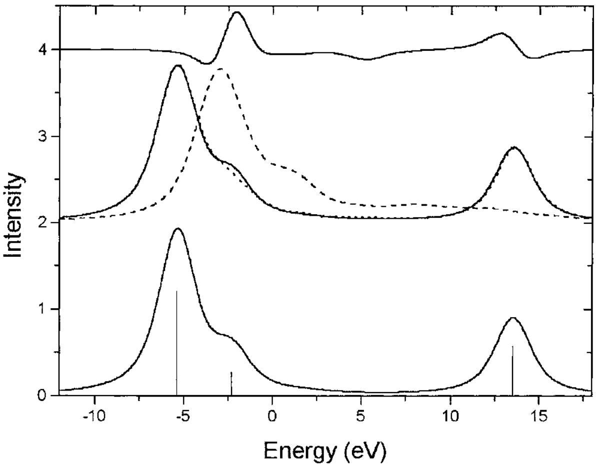

Figure 14. Theoretical 1s3p X-ray emission spectral shapes calculated with the ligand-field multiplet model. Bottom: (a) The ligand-field, 3d and 3p spin−orbit couplings have all been set to zero. Middle: The spin−orbit couplings are set to their atomic values. (solid, b) A cubic crystal field of 2.0 has been added. (dotted, c) A cubic crystal field of 4.0 eV has been added. (dashed, d) Top: Difference between b and c (×10).

Figure 14b shows the effects of the atomic 3p and 3d spin−orbit coupling. Essentially the ^7P and ^5P states are split into their three substates $^7P_4$, $^7P_3$, and $^7P_2$. The intensities of the peaks are related to the J quantum numbers as $2J + 1$, and it can be seen that the lowest energy peak is the $^7P_4$ state. The situation for the ^5P states is similar, and the satellite is split into $^5P_3$, $^5P_2$, and $^5P_1$, with the $^5P_1$ state at the lowest energy. A similar situation is visible for the shoulder at −6487 eV. Comparing part a and b of Figure 14, it can be seen that the effects of the spin−orbit coupling on the broadened spectral shapes are minimal.

Figure 14c shows the effects of the addition of a cubic crystal field of 2.0 eV. This is already a relatively large crystal field, and all oxides and halide systems have smaller crystal fields. It can be seen that compared to Figure 14b, most peaks shift a little bit. In particular, the ^5P states are modified while the ^7P states do still look very much like the atomic result. After broadening the sticks with the experimental and lifetime broadening, little changes are visible. This implies that 1s3p X-ray emission spectra are insensitive to the crystal-field effects, much less sensitive than, for example, 2p X-ray absorption. The positive aspect of this is that one can assume that the 1s3p X-ray emission spectra are virtually the same for all high-spin divalent manganese atoms. This finding is important for the use of the 1s3p X-ray emission channel for selective X-ray absorption measurements as will be discussed in section VII. It is noted that all other crystal-field effects in systems such as oxides will have no effect at all on the spectral shape (within the ligand-field multiplet model) as long as the spin state stays the same. Things are different for low-spin Mn^{II} compounds. Figure 14d shows the effect of a cubic crystal field of 4.0 eV. A completely different spectrum is found. The reason is that the ground-state symmetry has changed from $^6A_1$ to $^2T_2$. Thus, only one unpaired 3d electron remains, leading to a very small 3p3d exchange splitting and essentially no satellite. It is clear that 1s3p X-ray emission will immediately tell if a system is in its high-spin or low-spin state.

Similar to 2p X-ray absorption, 1s3p X-ray emission is sensitive to the valence of the metal. Mn^{II} has a $3d^5$ ground state and Mn^{III} a $3d^4$ ground state.[90] This obviously leads to a different spectral shape in the experiments. Figure 15 shows an example of the variations in the manganese 1s3p X-ray emission spectral shapes. Each spectrum can be simulated with a multiplet calculation leading to the determination of the valence. It can be seen that there is a clear shift between the spectra.

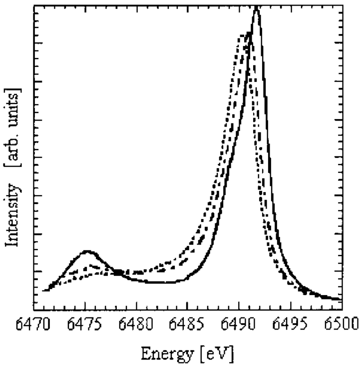

Figure 15. 1s3p X-ray emission spectra of a Mn^{II} (—), Mn^{III} (- - -) and Mn^{IV} (· · ·) compound. The compounds are, respectively, $Mn(Oac)_2$, $Mn(Oac)_3$, and $Mn[HB\text{-}(3,5\text{-}Me_2pz)_3]_2$. (Reprinted with permission from ref 90. Copyright 1994 American Chemical Society.)

These chemical shifts have been studied in detail by Bergmann and co-workers, who established that it was more accurate to use the center of gravity of the 1s3p X-ray emission spectral shape as an energy indicator.[7,94] The nature of the Mn oxidation states involved in the oxygen-evolving complex in photosystem II has been studied with this method. The measurements have been made on the dark-adapted S_1 state and on the hydroquinone-reduced state. The results are compatible with models involving conversion of $Mn^{III}{}_2Mn^{IV}{}_2$ to $Mn^{II}{}_2Mn^{IV}{}_2$ clusters.[7]

B. 1s3p X-ray Emission in the Charge-Transfer Multiplet Model

In the previous sections the approximation that one can calculate the 1s3p X-ray emission spectral shape from a model using the following two transitions was used, where the excitation step is not used explicitly in the results

$$3d^5 \rightarrow 1s^1 3d^5 + \epsilon 1s^1 3d^5 \Rightarrow 3p^5 3d^5$$

In Mn^{II}, this model gives a good account of the spectral shape. If one looks at other systems though, an agreement that is not as good is found. The main reason for this is that in the 1s excitation step major screening or charge-transfer effects occur. Essentially one is removing a core electron, implying a core charge that has increased by one. This pulls down the valence 3d electrons by the core hole potential. Because the 3d electrons are pulled down in a larger energy than the 4s and 4p electrons, the intermediate-state configurations will be different from the ground-state configurations. Essentially one has to subtract the core hole potential Q from the ground-state energy positions as used in the charge-transfer model. Below the transitions are given for two configurations

$$3d^5 + 3d^6\underline{L} \rightarrow 1s^1 3d^5\epsilon + 1s^1 3d^6\underline{L}\epsilon$$

$$1s^1 3d^5 + 1s^1 3d^6\underline{L}(\text{lowest}) \Rightarrow 3p^5 3d^5 + 3p^5 3d^6\underline{L}$$

The lowest two intermediate states are selected, and the 1s3p X-ray emission spectrum is calculated for these states, which implies that one assumed the intermediate states to relax to their lowest configuration(s). Two states are used, because the lowest state is split by the 1s3d exchange interaction. This 'relaxed' model has been used in the calculations of the 1s3p X-ray emission spectra of divalent nickel compounds.[36] Using an intermediate-state configuration, $1s^1 3d^8 + 1s^1 3d^9\underline{L} + 1s^1 3d^{10}\underline{LL'}$. The charge-transfer values for $NiBr_2$ and NiF_2 are, respectively, 4.3 and 0.3 eV, and with a core hole potential of 7.5 eV and a correlation energy U of 7.3 eV, this gives that the lowest energy is the $1s^1 3d^9\underline{L}$ configuration. For NiF_2, the $1s^1 3d^8$ configuration has an energy of 3.2 eV and the $1s^1 3d^{10}\underline{LL'}$ configuration of 4. 1 eV. In the case of $NiBr_2$, these values are, respectively, 7.2 eV and 0. 1 eV.[36]

The 'relaxed' charge-transfer model used is not necessarily the correct model. Another approach is to assume that the intermediate states do not relax at all. In this section this approximation will be followed. The model is the same as in the previous section

$$3d^5 + 3d^6\underline{L} \rightarrow 1s^13d^5\epsilon + 1s^13d^6\underline{L}\epsilon$$

$$1s^13d^5 + 1s^13d^6\underline{L}(\text{XPS spectrum}) \Rightarrow 3p^53d^5 + 3p^53d^6\underline{L}$$

One calculates the 1s XPS spectral shape, and then for all these intermediate states the 1s3p X-ray emission spectral shape is calculated. One then adds the 1s3p spectra with the intensities from the 1s XPS calculation. In principle, one should use the Kramers−Heisenberg formula to account for interference effects, but in the case of 1s core levels, interference effects are absent. In section V the Kramers−Heisenberg formula for 2p3s and 2p3d resonant X-ray emission spectral shapes will be explicity used.

1. K Capture 1s3p X-ray Emission

The effects of the excitation process can be studied by using two different excitation processes. Recently Glatzel and co-workers compared the usual above resonance X-ray excitation with K-capture excitation for MnO.[6] The X-ray excitation process follows the scheme as outlined above. The 1s electron leaves the atom as a continuum electron, and the spectrum is calculated by adding the 1s3p spectra of the 1s XPS spectrum states. In the K-capture process, the 1s electron annihilates a proton and is captured in the core.[6] The calculation is the same as that for X-ray excitation as given above. The difference is the ordering of the configurations. As indicated in Figure 16, the energy difference between $1s^13d^5$ and $1s^13d^6\underline{L}$ is equal to Δ − Q. Because the core hole potential is larger than the charge-transfer energy, this is a negative number and the lowest energy configuration is $1s^13d^6\underline{L}$. In the case of K capture, the 1s electron that has 'left' is part of the nucleus and the total charge of the nucleus plus the 1s core level is not modified. This implies that the outer valence electrons hardly notice any effect on the positions of the various configurations and the energy difference between $1s^13d^5$ and $1s^13d^6\underline{L}$ is equal to that in the ground state, being Δ. The K-capture spectrum is sharper, and the satellite structure is found at a lower energy, which is a consequence of additional states in the X-ray excited spectrum. The simulated spectra correspond nicely with the experimental results.[6]

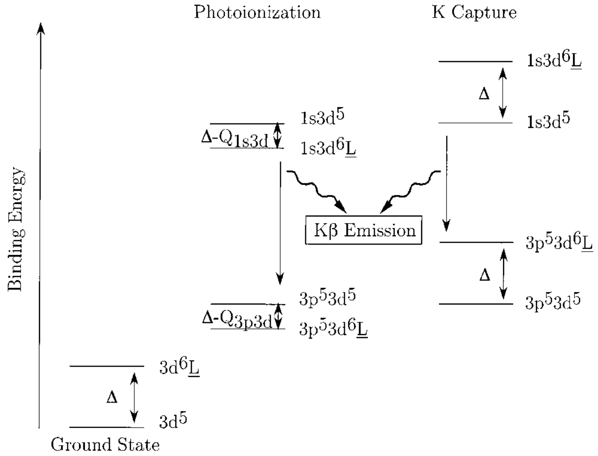

Figure 16. Scheme of the configurations in the initial, intermediate, and final states of, respectively, X-ray excited and K-capture X-ray emission calculations.

2. Temperature- and Pressure-Dependent 1s3p X-ray Emission

1s3p X-ray emission spectra involve hard X-rays for both excitation and decay. Because only hard X-rays are involved in the experiment, one has a large flexibility in the experimental setup as well as sample environment. This makes it relatively straightforward to carry out the 1s3p X-ray emission experiment in situ, for example, at high-temperature, high-pressure, etc.[33]

Tyson and co-workers[91,114] measured a series of manganese perovskites using 1s3p X-ray emission to determine the valences of Mn in these systems. In particular, they measured the temperature dependence of the 1s3p X-ray emission spectral shape. The low-temperature spectrum of $La_{.5}Ca_{.5}MnO_3$ has more weight close to the center of gravity compared with the room temperature spectrum. From Figure 15 (and more clearly Figure 32b), it can be concluded that spectral weight closer to the center of gravity indicates a smaller 3p3d exchange splitting, implying less unpaired 3d electrons. The reason for the decrease in unpaired 3d electrons can be either a valence change or a spin transition. In the case of $La_5Ca_5MnO_3$, the decrease of unpaired 3d-electrons is attributed to a valence increase.[91] Rueff and coworkers[97,98] used the 1s3p X-ray emission spectral shape for the analysis of pressure-dependent spectra of Fe and FeS. The structural and magnetic transition between the magnetic (bcc) and the nonmagnetic (hcp) iron phases has been observed from the shift of intensity toward the center of gravity.

C. 1s2p X-ray Emission

The situation of the 1s2p or Kα X-ray emission spectra is analogous to the 1s3p X-ray emission spectra. This situation is alike the comparison between 2p X-ray absorption and 3p X-ray absorption. The calculation in the various models discussed above is exactly the same, the only difference being the different parameters of the 2p instead of the 3p core electrons. The 2p spin−orbit coupling is much larger than the 3p spin−orbit coupling, typical values being, respectively, 10 and 1 eV. This implies that the spin−orbit-split states are clearly visible in the experimental spectral shapes. In contrast, the 2p3d exchange interaction is much smaller than the 3p3d exchange. This implies that the satellites visible in the 1s3p X-ray emission spectra will only be shoulders in the case of 1s2p X-ray emission.

Figure 17 shows the theoretical 1s2p X-ray emission spectra of Fe^{II}, and Figure 18 shows the corresponding 1s3p X-ray emission spectra. The calculations are performed with the ligand-field multiplet approach as discussed in section IV.A. The spectra have been divided into spin-up and spin-down, and this aspect will be discussed in the next section. The

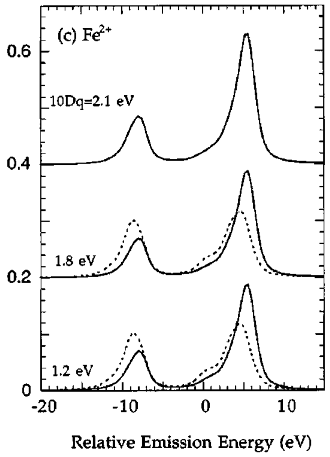

Figure 17. Theoretical spin-polarized 1s2p X-ray-emission spectra Fe^{II} using the ligand-field multiplet calculation. Plotted are spin-down (—) and spin-up spectra (· · ·). (Reprinted with permission from ref 121. Copyright 1997 American Physical Society.)

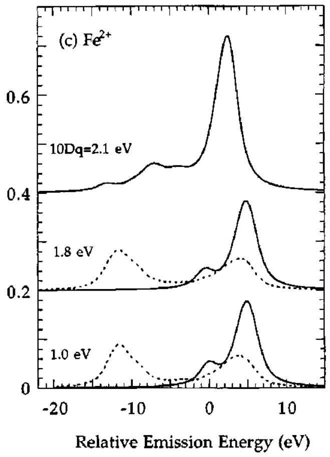

Figure 18. Theoretical spin-polarized 1s3p X-ray-emission spectra of Fe^{II} using the ligand-field multiplet calculation. Plotted are spin-down (—) and spin-up spectra (· · ·). (Reprinted with permission from ref 121. Copyright 1997 American Physical Society.)

1s3p X-ray emission spectrum is split into a main peak at +5 eV, where 0 eV is the average 1s3p excitation energy. A satellite is visible at about −12 eV, the energy difference being the 3p3d exchange splitting. The 1s2p X-ray emission spectrum also has its main peak at +5 eV and a satellite at about −9 eV. This general spectral shape thus looks similar to the 1s3p case, but the origin of the splitting is different, 2p-spin−orbit, respectively, and 3p3d exchange. This assignment is confirmed if one looks at the top spectra that relate to low-spin Fe^{II} systems. Low-spin Fe^{II} has no unpaired 3d electrons (i.e., a $^1A_1$ ground state); hence, no exchange splitting and the satellite is absent. Only some low-energy shoulders are visible due to other (multiplet) effects. In the case of the 1s2p X-ray emission spectrum, not much has changed for the low-spin situation. The 2p spin−orbit coupling is the same, and the satellite maintains a similar structure and intensity.

The 1s2p X-ray emission spectrum is a few times more intense than the 1s3p X-ray emission spectrum, and one might expect more studies using the 1s2p channel. However, the chemical sensitivity of the 3p3d exchange interaction makes the 1s3p X-ray emission spectrum more useful for determining the spin state and valence.[7,94]

D. 1s2p Resonant X-ray Emission

In this section I focus on the effects that occur if one excites at resonance. I will go deeper into this issue when the soft X-ray 2p resonances, where interference effects are more important, are discussed. This section deals with resonance effects at the K edges. It will be shown that the study of 1s2p resonant X-ray emission sheds light on the nature of the intermediate states, in other words the final states of the X-ray absorption process.

Figure 19 shows the 1s2p resonant X-ray emission spectra of Fe_2O_3 excited at resonance. Spectra a, b, and c have been measured at the positions of the K edge as indicated in Figure 20. The spectrum is normalized so that the measured absorption coefficients for photon energies immediately below and well above the absorption edge are the same as the theoretical values. Several weak preedge peaks are clearly observed. The first two preedge peaks, located

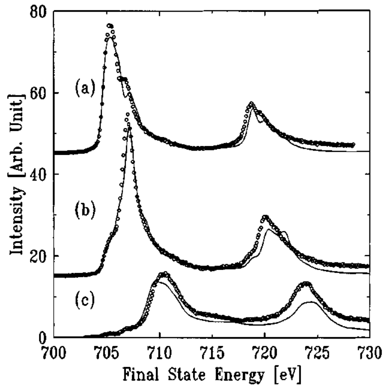

Figure 19. Calculated spectra (—) as a function of the energy difference of the incident and scattered photon together with the measured spectra (○). (Reprinted with permission from ref 23. Copyright 1998 American Physical Society.)

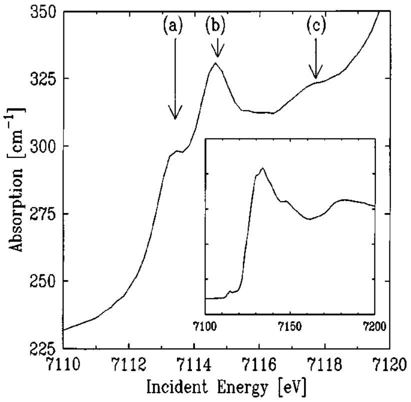

Figure 20. Fe K-absorption edge of Fe_2O_3. The preedge region is shown in more detail, and the whole edge is shown in the inset. (Reprinted with permission from ref 23. Copyright 1998 American Physical Society.)

at 7113.4 and 7114.8 eV, are assigned to the quadrupole transitions from the Fe 1s orbital to the crystal-field split t_{2g} and e_g orbitals. These spectra have been measured by Caliebe and co-workers [23] at NSLS beamline X21 with an overall resolution of 0.45 eV. With this high experimental resolution, 1s2p X-ray emission spectra are measured well.

Recently, Dräger and co-workers performed similar experiments on single crystals of MnO. The manganese 1s preedge structure is different for measurements with a (100) and (110) orientation of the rock salt crystal structure. The (100) spectrum gives transitions to the empty e_g states and the (110) spectrum to the empty t_{2g} states. The resonant 1s3p X-ray emission spectra have been used to disentangle the spin-polarization of the X-ray absorption spectrum.[46]

The 1s2p resonant X-ray emission spectra can be calculated with the charge-transfer multiplet model as described for X-ray absorption above. Charge-transfer multiplet calculations have been carried out for the $3d^5$ ground state, the $1s^13d^6$ intermediate states (ϕ_x), and the $2p^13d^6$ final states, including the quadrupole excitation (Q) and the dipole decay (D)

$$\frac{d^2\sigma}{d\Omega d\omega} \sim \left| \sum_{\phi_x} \frac{\langle 2p^5 3d^6 | D | 1s^1 3d^6 \rangle \langle 1s^1 3d^6 | Q | 3d^5 \rangle}{E_{1s^1 3d^6} - E_{3d^5} - \hbar\omega - i\Gamma_{1s}} \right|^2 \quad (16)$$

Three configurations $3d^5$, $3d^6\underline{L}$, and $3d^7\underline{LL}'$ have been used for the ground state, and the corresponding three configurations have been used for the intermediate and final states. The result of the calculations is indicated in Figure 19 as the solid lines. For these calculations, the dipole transitions to $1s^13d^54p^1$ states have been included also but they do not significantly affect the calculated spectral shapes.[23]

Why is this resonant experiment so interesting? One could say that the only result of the experiment is a 1s2p resonant X-ray emission spectrum that could also be measured directly with 2p X-ray absorption. There are at least two interesting consequences of this experiment. First, it adds additional proof as to the quadrupole nature of the prepeaks in the K edge of Fe_2O_3. Second, it makes it possible to measure a spectrum similar to 2p X-ray absorption by making use of hard X-rays. This makes it possible to measure these spectra under essentially any condition and as such gives a good possibility for in situ measurements in, for example, electrochemistry or catalysis research.

E. 1s Valence Band X-ray Emission

Valence-to-core transitions are obvious candidates for chemically sensitive X-ray emission spectra, since the character of the valence orbitals changes the most between different chemical species. Figure 21 sketches the various fluorescence transitions to a 1s core hole in MnO. The binding energy of the manganese 1s core hole is approximately 6540 eV. Dipole transitions are possible from the manganese 2p, 3p, and 4p levels. This gives, respectively, 1s2p (Kα), 1s3p ($K\beta_{1,3}$), and 1s valence band ($K\beta_{2,5}$) X-ray emission.[83] The manganese 4p states are hybridized with the oxygen 2s and 2p states. This induces X-ray emission peaks at energies related to the oxygen 2s and 2p states. The peak related to the 2s state is sometimes referred to as crossover X-ray emission. The peaks related to the oxygen 2p bands are the valence band X-ray emission spectra. Apart from dipole X-ray emission, there can be quadrupole X-ray emission directly from the 3d states.

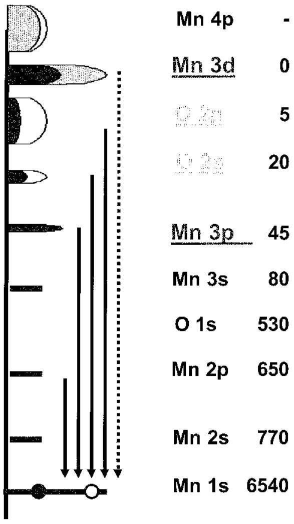

Figure 21. X-ray emission decay to a 1s core hole in MnO. Indicated are, respectively, 1s2p (Kα), 1s3p ($K\beta_{1,3}$), and 1s-valence band ($K\beta_{2,5}$) X-ray emission.

Figure 22 shows a comparison of a Kβ, crossover, and valence band X-ray emission spectra of MnO.[8] As indicated in the figure, there is a Kβ peak related to manganese 3p core holes, the crossover peak related to oxygen 2s core holes, and the valence band realted to oxygen 2p holes. Figure 23 shows a series of valence band X-ray emission spectra for manganese oxides. The bottom two spectra are manganese metal and MnF_2. The energy of the valence band peak in the oxides shifts approximately 1 eV per increment in oxidation state. This is indicated in the inset.[8]

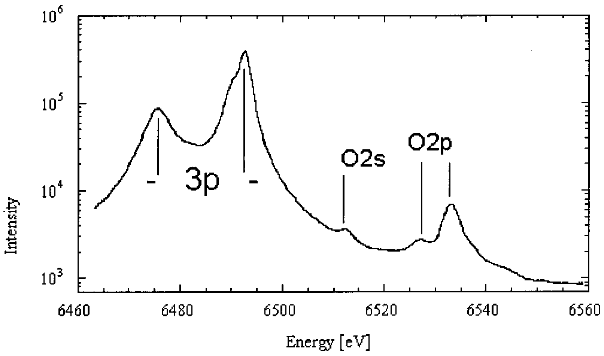

Figure 22. 1s3p, crossover, and valence band X-ray emission spectrum of MnO. The intensity is given on a logarithmic scale.

The intensities of the crossover peaks change significantly in the various oxides indicated in Figure 24. The integrated intensity of the crossover peak can be normalized by the main Kβ region, correcting for the number of oxygen atoms per Mn. Assuming that the integrated intensity per Mn of the main Kβ region

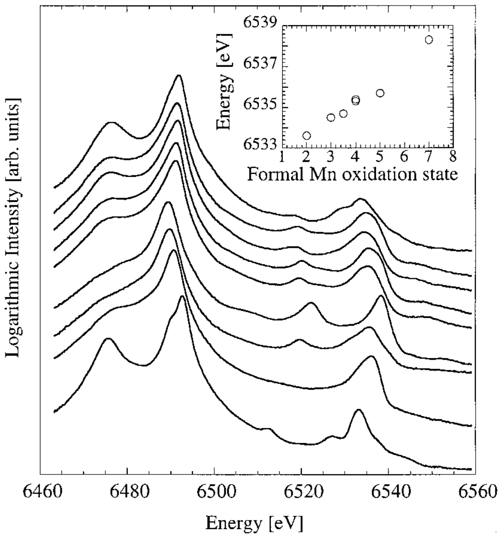

Figure 23. Logarithmic intensity plot of Kb spectra for a variety of Mn complexes: (top to bottom) MnO, $LiMn_2O_4$, $ZnMn_2O_4$, Li_2MnO_3, MnO_2, $KMnO_4$, A Mn(IV) complex, Mn metal, and MnF_2. (inset) $K\beta_{2,5}$ main peak energies as a function of Mn formal oxidation state. (Reprinted with permission from ref 8. Copyright 1999 Elsevier Science.)

is chemically invariant, this procedure yields the relative crossover transition probability per Mn−O pair. The inset of Figure 24 shows that the bond length varies exponentially with distance, and it can be concluded that the intensity of the crossover peak can be used as a tool to determine Mn−O distances to within 0.1 Å.[8]

V. 2p X-ray Emission

The 2p core levels of the 3d transition metals are positioned in the soft X-ray range between 400 and 1000 eV. As discussed in section III, the 2p X-ray absorption spectra are dominated by multiplet effects and do show a complex multipeaked spectral shape. This makes 2p X-ray emission ideally suitable for resonance studies. Therefore, this begins with a discussion of the resonant 2p X-ray emission spectral shapes. Both 2p3s and 2p3d resonant X-ray emission will be discussed.

If the core hole is created with an energy close to the 2p absorption edge, the X-ray absorption and X-ray emission processes do occur coherently and the overall 2p3d process (of a $3d^5$ ground state) is described with the Kramers−Heisenberg formula

$$I(\omega,\omega') \sim \left|\sum_{2p^53d^6} \frac{\langle 3d^5|\hat{e}'\cdot r|2p^53d^6\rangle\langle 2p^53d^6|\hat{e}\cdot r|3d^5\rangle}{E_{2p^53d^6} - E_{3d^5} - \hbar\omega - i\Gamma_{2p}}\right|^2 \qquad (17)$$

This formula forms the basis of all resonant X-ray processes. The intensity (I) is given as a function of the excitation (ω) and the emission (ω') energies. The initial state ($3d^5$) is excited to an intermediate state ($2p^53d^6$) with the dipole operator ($\hat{e}\cdot r$), and the second dipole operator ($\hat{e}'\cdot r$) describes the decay to the final state ($3d^5$). The denominator contains the binding energy of the intermediate state and its lifetime broadening. A resonance occurs if the excitation energy is equal to the binding energy of the intermediate state. Looking at the MnO 2p X-ray absorption spectrum of Figure 11, each multiplet line can give rise to a different resonant 2p3d X-ray emission spectral shape.

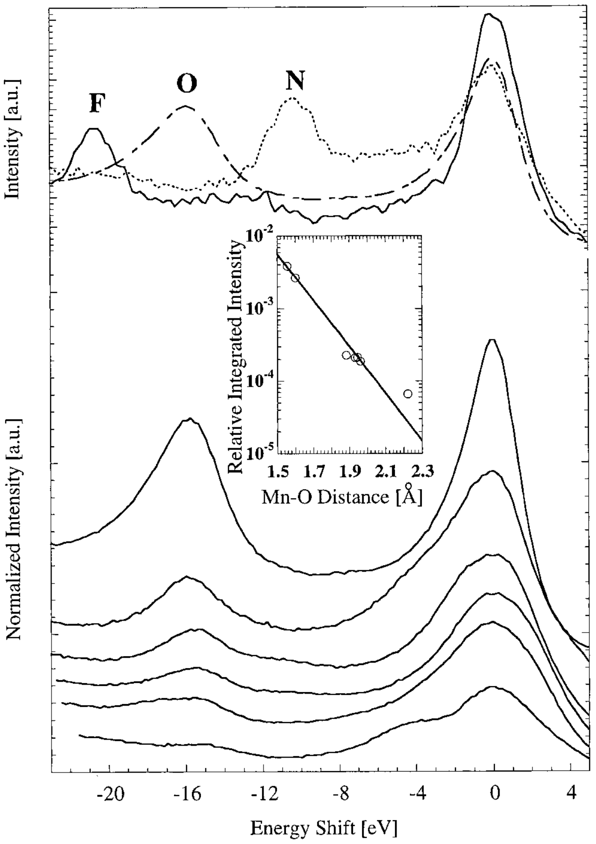

Figure 24. (top) $K\beta''$ and $K\beta_{2,5}$ regions for samples with Mn−F, Mn−O, and Mn−N ligation. (bottom) $K\beta''$ and $K\beta_{2,5}$ regions of manganese oxides with different Mn oxidation states. (top to bottom) $KMn^{VII}O_4$, $[Et_4N][Mn^{V}(O)(\eta^4\text{-}L)]$, $\beta\text{-}Mn^{IV}O_2$, $LiMn^{III}Mn^{IV}O_4$ and $ZnMn^{III}{}_2O_4$, $Mn^{II}O$, $Li_2Mn^{IV}O_3$. (inset) Normalized intensities of $K\beta''$ as a function of Mn−O distance. (Reprinted with permission from ref 8. Copyright 1999 Elsevier Science.)

The general spectral landscape can be viewed as a two-dimensional space with axis ω and ω'. Figure 26 shows a contour plot of the 2p3d resonant X-ray emission spectrum of Ni^{II} using a crystal field of 1.12 eV to simulate NiO. The darkest area has the highest intensity. The horizontal axis shows the X-ray excitation energy. The main peak of the 2p X-ray absorption spectrum of NiO has an energy of 855.7 eV with a shoulder at 857.5 eV.[50] The vertical axis shows the X-ray energy loss, that is the energy of 0.0 eV means that the 2p3d decay energy is equal to the 2p3d excitation energy, in other words this refers to resonant elastic scattering. There is a large peak visible with its peak position at (855.7 eV, 0.0 eV). There is a second peak at an energy loss of 1.1 eV. This peak relates to a ligand-field excitation from the $^3A_2$ ground state to the $^3T_2$ excited state. A third peak is visible at approximately −2.0 eV.

A number of cross sections can be made. This paper focuses on the (resonant) X-ray emission spectral shape excited with a fixed energy. This will be indicated as $I^{\omega}_{XES}(\omega')$. In Figure 25, this relates to vertical cross sections. For example, the resonant X-ray emission spectrum excited at 855.7 eV relates to a vertical line at 855.7 eV. If the excitation energy is (far) above a resonance, this is normal X-ray emission or fluorescence. Close to a resonance, it is called *resonant X-ray emission*. With 2p3d resonant X-ray emission, one studies the elementary excitations by probing the energy difference between the initial and final state. These spectra can be plotted in two ways: (1) as resonant X-ray emission spectra, i.e., $I^{\omega}_{XES}(\omega')$, or (2) as *resonant inelastic X-ray scattering* $I^{\omega}_{XES}(\omega' - \omega)$. These spectra are off course exactly the same, but if one compares spectra excited at different excitation energies, the resonant X-ray emission spectra shift with the excitation energies while the RIXS spectra align all elementary excitations. RIXS can be used to study, for example, the dd excitations in transition metals as will be discussed below.[41]

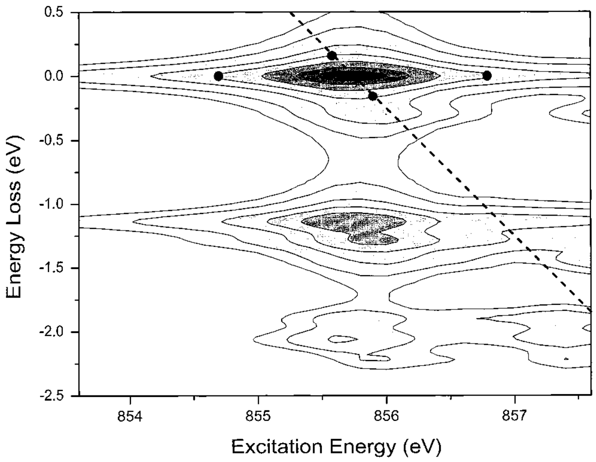

Figure 25. Contour plot of the resonant X-ray emission channels of a Ni^{II} ion with its ligand field set at 1. 12 eV to simulate NiO. The excitation energy is given on the horizontal axis; the final state energy loss is shown on the vertical axis.

Another cross section is to measure the X-ray absorption spectrum at a fixed emission energy: $I^{\omega'}_{XAS}(\omega)$. This relates to the diagonal line in Figure 25. It is this mode that is used in selective XAFS, discussed in section VII. From Figure 25 one can derive the information on the effective lifetime related broadening. The 2p intermediate state lifetime broadening has been made artificially large and the full-width half-maximum is about 2.2 eV, indicated by the distance between the two dots. The lifetime broadening of the 3d final state has been set to fwhm = 0.32 eV. If one measures along the diagonal $I^{\omega'}_{XAS}(\omega)$, the two points where the line crosses the half-maximum point are indicated with dots. Reading of the difference in excitation energy one finds about 0.3 eV. This is a graphical illustration of the 'disappearance' of the intermediate-state lifetime broadening that will be discussed in more detail in section VII. The effective lifetime broadening of selective X-ray absorption (for a single peak) is equal to $1/\sqrt{[(1/\Gamma_{2p}^2) + (1/\Gamma_{3d}^2)]}$,[32] which for the present case gives 0.29 eV. It is interesting to compare this with off-resonance X-ray emission where the effective lifetime broadening equals $\Gamma_{2p} + \Gamma_{3d}$, which is 2.52 eV in the present case.

A. 2p3s Resonant X-ray Emission

Before returning to the 2p3d resonant X-ray emission spectra, the 2p3s resonant X-ray emission spectra will be discussed first as the 2p3s case gives a good opportunity to describe essentially all peaks with a simple model. The calculation of the 2p3s resonant X-ray emission spectra of CaF_2 will be followed. The X-ray absorption spectrum of CaF_2 has been given in Figure 10. In resonant 2p3s X-ray emission, one is exciting at all seven peaks in the absorption spectrum and measures the 2p3s X-ray emission spectral shape, as measured by Rubensson and co-workers.[95,96] The 3s2p inelastic X-ray scattering cross section is dominated by resonant scattering via the $2p^53d^1$ intermediate states. It has been shown that one can reduce the calculation to the transitions of $3d^0$, via $2p^53d^1$, to $3s^13d^1$ states. The effects of charge transfer are small and can be neglected. Both the X-ray absorption and X-ray emission steps essentially conserve the local charge, and it has been shown that in those experimental conditions, ionic systems such as CaF_2 can be described in close detail by the ligand-field approximation. One has to fill in the X-ray absorption and X-ray emission steps in the Kramers–Heisenberg formula

$$I(\omega,\omega') \sim \left|\sum_{2p^53d^1} \frac{\langle 3s^13d^1|\hat{e}'\cdot r|2p^53d^1\rangle\langle 2p^53d^1|\hat{e}\cdot r|3d^0\rangle}{E_{2p^53d^1} - E_{3d^0} - \hbar\omega - i\Gamma_{2p}}\right|^2 \quad (18)$$

This calculation can almost be carried out 'by hand'. Starting from the situation in CaF_2 with all bands completely full, one has the advantage of strong restrictions on the possible symmetry states. Ligand-field multiplet calculations have been performed for the $3d^0$ initial state, the $2p^53d^1$ intermediate states, and the $3s^13d^1$ final states in cubic symmetry. The $3d^0$ initial state consists of only one state with $^1A_1$ symmetry. The only $2p^53d^1$ intermediate states thatcan be reached in X-ray absorption must have T_1 symmetry, and as there will be seven of those states.[38] The $3s^13d^1$ final states are split by only two interactions, the 3s3d exchange and the cubic crystal field. This gives a total of four peaks in the final state. The complete calculation is then the transition of one initial state via seven intermediate states to four final states. The results of these seven absorption matrix elements and 28 (in fact 49 due to degeneracies)[31] emission matrix elements are fed into the Kramers–Heisenberg formula and this gives Figure 26 as its result.

Figure 27 gives the resulting resonant 2p3s X-ray emission spectral shapes. One can observe that in all comparisons of interference-on (solid line) and interference-off (dashed), the integrated intensities of the solid and dashed line are equivalent or in fact identical as the integrated intensity is conserved by

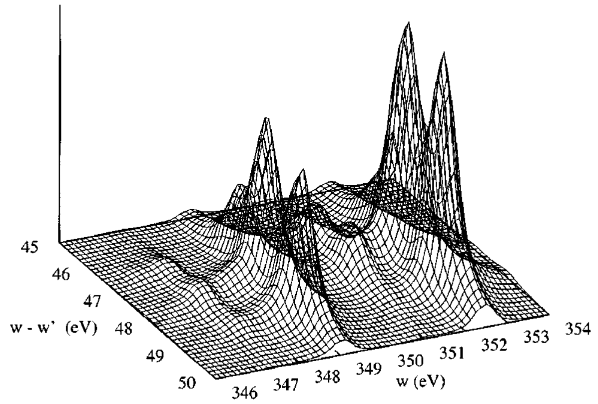

Figure 26. Plot of the two-dimensional resonant landscape of CaF_2. The excitation energy is given on the x axis; the final-state energy is given on the y axis. (Reprinted from ref 31. Copyright 1996 American Physical Society.)

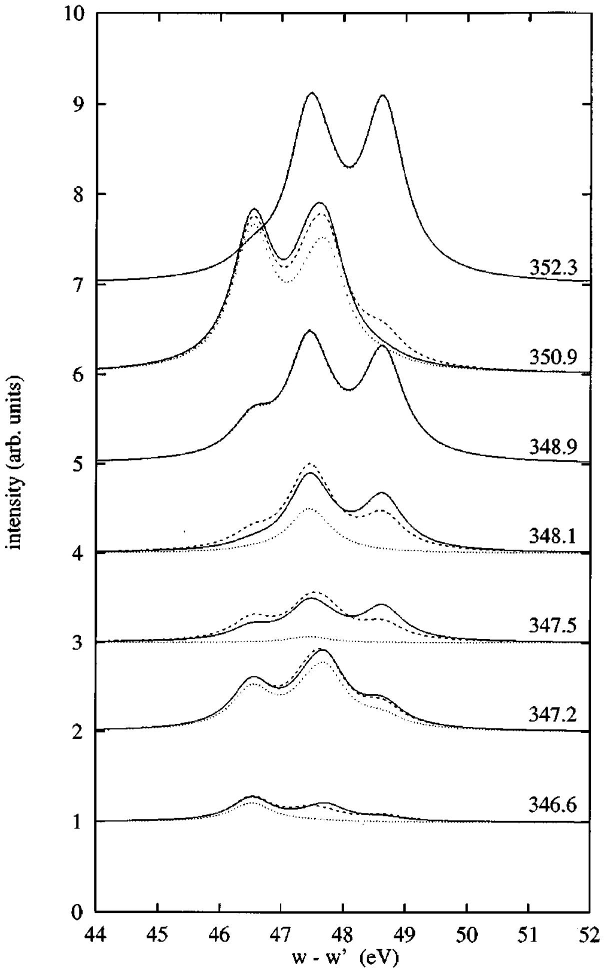

Figure 27. Cross sections through Figure 22 at the excitation energies as indicated on the right. The dotted lines give the decay of only the excited state at precisely the energy indicated. The dashed lines include the Lorentzian tails of the neighboring states, and the solid lines include interference effects. (Reprinted with permission from ref 31. Copyright 1996 American Physical Society.)

a sum rule. Relatively large interference effects can be seen for the spectra excited at 347.5 and 348.1 eV. These two energies relate to weak excitations; hence, the decay spectrum is dominated by the Lorentzian tails of the neighbors. That is, interference effects are largest if two channels have a comparable effective strength at a certain energy. The experimental results are reproduced with these calculations.

A topic not discussed in this paper is the consequences of intermediate-state decay/relaxation, also known as postcollision interactions,[81] as observed in the experimental spectra. These decay channels do give rise to nonresonant X-ray emission. Far above the edge the situation is clear and these nonresonant channels are the normal fluorescence lines at constant energy, but the nonresonant channels close to and even at resonance present a theoretical challenge as they can (and will) be different both from resonant X-ray emission and also from the normal nonresonant channels. To shed light on this situation, one has to understand in great detail what happens exactly in the various relaxation and decay channels, both elastic as inelastic. In solids this is a dramatically complex situation and little is known quantitatively. The situation is a bit better known in atomic spectra, and the interested reader is referred to those papers, for example, the recent review by Gel'mukhanov and Agren.[53]

B. 2p3d Resonant X-ray Emission

The first high-resolution 2p3d resonant X-ray emission experiments have been carried out by the group of Nordgren.[17,18,57,86] Figure 28 shows the resonant 2p3d X-ray emission spectra of MnO. The absorption spectrum of MnO has been discussed in section II. On various positions of the 2p X-ray absorption spectrum, the resonant 2p3d X-ray emission spectrum has been measured as indicated at the top of Figure 28. The spectra have been simulated with an atomic multiplet calculation of the 2p3d matrix elements fed into the Kramers−Heisenberg formula. (In the curves in Figure 28, interference effects have been omitted.) It can be seen that the experimental spectra are essentially reproduced.[16] Including ligand fields, charge transfer, and interference effects improves the comparison.[13]

In Figure 28 one can see the elastic peak related to transitions of the $3d^5$ ground state via any $2p^53d^6$ intermediate state back to itself. In addition, one observes peaks at constant energy loss, for example, at about −4.0 eV. These peaks relate to dd transitions. They essentially map the Tanabe−Sugano diagrams of the electronic configurations of a $3d^5$ ground state. It is important to notice that the relative intensity of these various peaks is not constant over the excitation energies but varies. This is an indication of the relative matrix elements from the $2p^53d^6$ intermediate states back to the $3d^5$ states. In spectra f, g, and h, one also observes a peak shifting to higher energy losses. This is a signal of the off-resonant 2p3d fluorescence that is visible because of the relaxation of the intermediate states.

1. Charge-Transfer Transitions and dd (ff) Transitions

Butorin recently published a series of 2p3d resonant X-ray emission spectra experiments for $FeCO_3$, CoO, NiO, and $LaCoO_3$14. The 2p3d spectra of $FeCO_3$

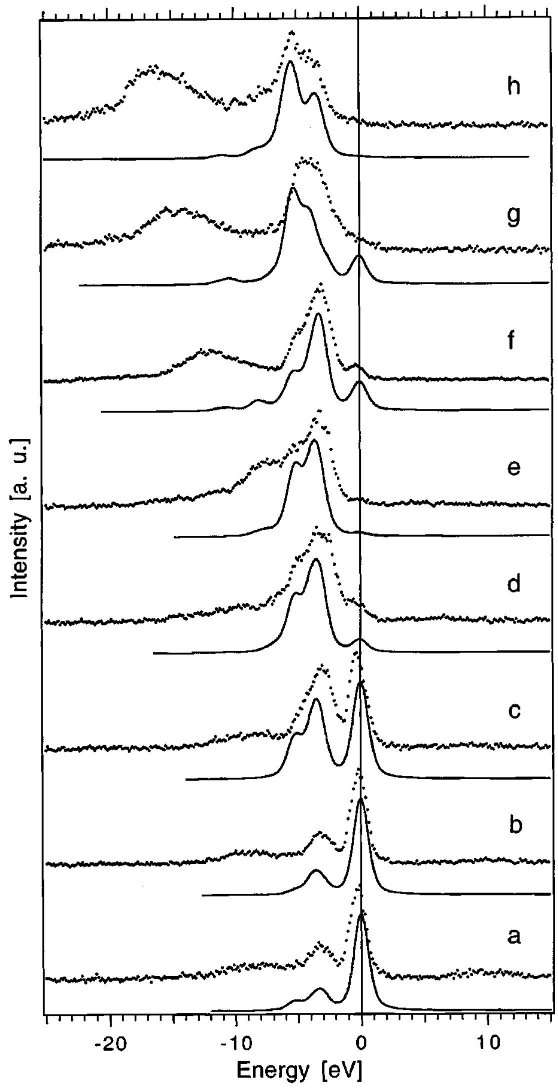

Figure 28. Mn 2p3d resonant X-ray emission spectra of MnO recorded at different excitation energies near the Mn 2p threshold, as indicated in the X-ray absorption spectrum at the top. The experimental spectra (• • •) are plotted as energy loss spectra and are compared to atomic multiplet calculations for the Mn^{II} ion (—). (Reprinted with permission from ref 16. Copyright 1996 American Physical Society.)

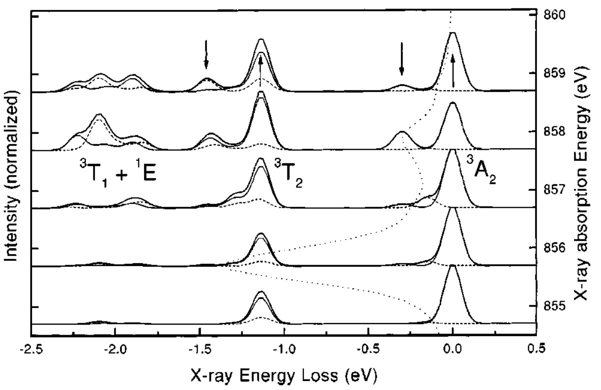

Figure 29. Resonant 2p3d X-ray emission spectra of a Ni^{II} system in octahedral symmetry, using the crystal-field parameter of NiO. Indicated are F_{xx} scattering (—), F_{zx} scattering (- - -), and the total scattering (—). The X-ray absorption spectrum is given with dots. The symmetries of the states are given at the middle spectrum. (Reprinted with permission from ref 41. Copyright 1998 American Physical Society.)

could be nicely explained with ligand-field multiplet calculations, while the other oxides needed the inclusion of charge-transfer effects. The calculations confirm that it is crucial to include the correct angle between incoming and outgoing X-rays, i.e., the correct combinations of X-ray polarization. The NiO and CoO spectra excited at the charge-transfer satellites of the 2p X-ray absorption reveal large satellites in the resonant X-ray emission. These satellites are positioned at a similar X-ray energy as the off-resonance 2p3d X-ray emission, but the charge-transfer multiplet calculations show that they are caused by resonant satellites related to a final state with a ligand hole. The transition can be envisaged as $3d^N \rightarrow 2p^5 3d^{N+1} + 2p^5 3d^{N+2}\underline{L} \rightarrow 3d^{N+1}\underline{L}$, where the initial and final states are simplified to their main configuration, i.e., one observes the charge-transfer excitation. The situation of the 3d4f resonant X-ray emission spectra of the rare-earth metals is very interesting. One can beautifully observe the resonances of the charge-transfer satellites.[15,19,73] In addition, one observes ff transitions from which one can determine the crystal-field values of the 4f electrons.[14]

2. Coster−Kronig Transitions

Hague and co-workers[59] recently showed that in the case of resonant X-ray emission of $TiCl_4$ molecules, it is not enough to include only the direct resonances as described with eq 18. In addition, the three-step transition via a Coster−Kronig decay channel must be added to describe the observed spectral shapes.

$$I(\omega,\omega') \sim$$

$$\left|\sum_{X_1X_2} \frac{\langle 3d^0 + 3d^1\underline{L}|\hat{e}'\cdot r|X_2\rangle\langle X_2|H_{CK}|X_1\rangle\langle X_1|\hat{e}\cdot r|3d^0 + 3d^1L\rangle}{(E_{X_1} - E_{3d_0} - \hbar\omega - i\Gamma_{2p})(E_{X_2} - E_{3d^0} - \hbar\omega - i\Gamma_{2p})}\right|^2 \qquad (19)$$

Equation 19 shows the Kramers−Heisenberg formula for this three-step pathway. The initial and final states are $3d^0 + 3d^1L$. The intermediate states X_1 and X_2 have a configuration $2p^5 3d^1 + 2p^5 3d^2 L$. In ref 59, transitions to the continuum have also been included. It was shown that the experimental spectral shapes could only be described correctly with the inclusion of both the Coster−Kronig channel and the explicit inclusion of continuum states.

3. Spin-Flip Transitions

Above it was shown that resonant 2p3d X-ray emission can give information on dd excitations and charge-transfer excitations. Also, other low-energy excitations can be studied, for example, it has been shown[77] that spin-flip transitions can be observed in resonant 2p3d and 3p3d X-ray emission of nickel and copper oxides.[41]

Figure 29 shows the resonant 2p3d X-ray emission spectra at the 2p X-ray absorption spectrum of NiO. This figure is related to Figure 25 discussed above. The resonant elastic peak of $^3A_2$ symmetry is visible at 0.0 eV, and the dd transitions to the $^3T_2$, $^3T_1$, and ^1E states are visible at energies of 1.1 eV and at about 2.0 eV energy loss. However, some additional peaks are visible at low-energy loss. For example, a peak is visible at about 0.25 eV. This peak can be assigned to a spin-flip transition in which a Ni^{II} ion flips its spin state from +1.0 to −1.0 (or reversed). The consequence of this spin flip is that the antiferromagnetic neighbors now see an apparent ferromagnetic neighbor and the energy involved is the energy loss observed in resonant X-ray emission. The spin-flip peak is highest at an excitation energy of 858 eV that is at the shoulder of the 2p X-ray absorption spectral shape. The reason is that this shoulder relates to a state in which the 2p and 3d electrons are essentially antiparallel aligned, in contrast to the parallel alignment of the main peak. This antiparallel alignment facilitates the spin-flip transitions to occur.

It is good to note that in the literature two completely distinct transitions are called spin flip. There is the spin flip as described above that is related to the transition of a $ms = -1$ state to a $ms = +1$ state. The other usage of the term spin flip is given to transitions in which the spin ‘flips’ from, for example, a sextet state to a quartet state. These types of ‘spin flip’ can be seen in all but the elastic transition in Figure 28. The total spin state has been modified in such a spin-flip transition. In my opinion it is better to refer to such transitions simply as dd transitions.

The measurement of spin-flip transitions is important for the study of the antiferromagnetic coupling in transition-metal oxides. There is, however, an experimental complication which is that the overall resolution of the experiment should preferably be on the order of 0.2 eV. This is at the edge of the present technology and still suffers from low intensities. A first measurement has been performed by Kuiper and co-workers using the 3p3d resonance instead of 2p3d.[77] In the future, more studies of the spin-flip effect are expected to yield important new information on the magnetic couplings in transition-metal oxides and other transition-metal systems.

From the discussion of the 2p3d resonant inelastic X-ray scattering, it is concluded that there are many aspects that must be included for a correct description of the spectral shapes. It depends essentially on the resolution (and system) used and what excitations and pathways must be included. In principle, one can extend the model further by adding other configurations and pathways. Important excitations one can observe are charge-transfer transitions, dd transitions, and spin-flip transitions. Excitations into the continuum and Coster−Kronig three-step pathways could until now only be established in molecular systems. This must be related to a difference in electronic structures between molecular systems and solids.

VI. X-ray Magnetic Circular Dichroism

X-ray magnetic circular dichroism (X-MCD) is an important phenomenon in both X-ray absorption and X-ray emission. The magnetic structure of a system is studied by making use of circular or linear polarized X-rays. In the last 10 years many papers have been published on X-MCD. In this review, some general features of X-MCD are discussed. A recent overview is given by Duda.[47] The focus is on X-ray emission MCD, and in line with the historic development, X-ray absorption MCD is introduced first.

A. MCD in X-ray Absorption

The MCD effect in X-ray absorption is defined as the difference in absorption between left- and right-polarized X-rays. A nonzero MCD effect is observed only in magnetic systems (the natural dichroism effects are neglected). The MCD effect has a maximum if the polarization vector of the X-ray is parallel or antiparallel to the magnetization vector of the system.

The MCD effect in X-ray absorption has been measured for the first time by Schütz and co-workers.[49] They showed that the absorption cross section is different for left- and right-polarized X-rays. The difference between the left- and right-polarized X-rays was shown to be proportional to the spin-polarized density of states. Using the proportionality between X-ray absorption (I_{XAS}) and the density of state (ρ) as the starting point, one obtains

$$I_{MCD} \equiv \frac{I^{L}_{XAS} - I^{R}_{XAS}}{I^{L}_{XAS} + L^{R}_{XAS}} = P_{e}\frac{\rho_{+} - \rho_{-}}{\rho_{+} + \rho_{-}} \tag{20}$$

where I^L denotes left- polarized X-rays and I^R denotes right-polarized X-rays. ρ_+ and ρ_- relate to, respectively, spin-up and spin-down density of states. The proportionality factor P_e is the Fano factor. The original paper used the iron K edge as an example and did find a small effect, in other words, did find a Fano factor of approximately 0.01. It was later shown that this small MCD effect was particular to the use of a 1s core level and was related to the absence of a core hole spin−orbit coupling. For details on many aspects of this effect, the reader is referred to the book *Spin−orbit influenced spectroscopies of magnetic solids*.[48]

If a core level has spin−orbit coupling, the MCD effect in X-ray absorption is much larger. If one neglects the overlap of the core and valence wave functions and uses single-electron transition matrix elements, one can simply explain the size of the MCD effect.[49] For example, p → d transitions have relative magnitudes for parallel and antiparallel alignments at the $2p_{3/2}$ edge of $P_{3/2} = 5$ and $A_{3/2} = 3$, respectively. The related numbers at the $2p_{1/2}$ edge are, respectively, $P_{1/2} = 1$ and $A_{1/2} = 3$. This directly yields the relative intensity of the $2p_{3/2}$ and $2p_{3/2}$ edges of 8:4. The MCD effect is given as $(P - A)/(P + A)$, leading to +1/4 for the L_3 edge and −1/2 for the L_2 edge.

An important development in the use of X-MCD was the development of sum rules by Thole and co-workers.[107] It was shown that the integral of the X-MCD signal could be related to the ground-state expectation value of the orbital moment $\langle L_z \rangle$. A second sum rule was postulated relating the weighted integration of the L_3 edge plus the L_2 edge to an effective spin moment. Many papers deal with the validity, derivation, and experimental complications of the sum rules. The reader is referred to the Theo Thole memorial issue of the *Journal of Electron Spectroscopy*.[34]

Recently, the X-MCD signal at the $L_{2,3}$ edges has been used as a probe signal for microscopy using a photoemission electron microscope (PEEM).[85,100,102] In addition, the MCD signal has been used for nanosecond time-resolved studies by the group of Alain Fontaine.[79]

1. MLD in X-ray Absorption

Magnetic linear dichroism (MLD) is essentially the angular dependence of the absorption cross section. This is an often used technique in X-ray absorption, in particular to study directional variations in the electron density, used, for example, for surfaces and single crystals and to disentangle dipole and quadrupole contributions.[101] In 1985, Thole and co-workers[109] predicted a strong magnetic effect on the polarization dependence, an effect that became studied as X-MLD in the last 15 years.

In contrast to X-MCD that probes the magnetic direction, X-MLD only probes the orientation of the magnetic moment, in other words it probes the squared expectation value of the magnetic moment. This automatically implies that X-MLD can intrinsically not make a distinction between magnetic effects and other effects that cause a directional variation of the absorption cross section. To study a magnetic effect with X-MLD, one always has to make sure that the effect is indeed magnetic in origin, for example, by a measurement of the same system without being magnetically ordered. The same reasoning applies to MLD in X-ray emission.

B. MCD in X-ray Emission

In 1991, Strange and co-workers[104] pointed out that dichroism in X-ray emission spectra can be studied with incident photons that are circularly polarized. It was argued that such an experiment would probe the spin-polarization of the valence band. These experiments are discussed below, where soft X-ray and hard X-ray experiments will be differentiated, i.e., decay to metal 2p and metal 1s core holes, respectively.

If one uses circularly polarized X-rays for the excitation process, naturally this has consequences for the resonant X-ray emission spectra. The basic idea is that the use of circular polarization for the 2p core excitation will create an imbalance between 2p spin-up and spin-down core holes (with respect to the magnetization of the 3d valence electrons). This imbalance implies that detecting the decay of the 3d valence band electrons to the polarized 2p core hole will create an imbalance in the spectral shape that is proportional to the spin polarization of the conduction band. With this starting point in mind, many experiments have been carried out.[9,22,58,68] It turned out that the situation in the soft X-ray range is complex because of both experimental and theoretical complications.

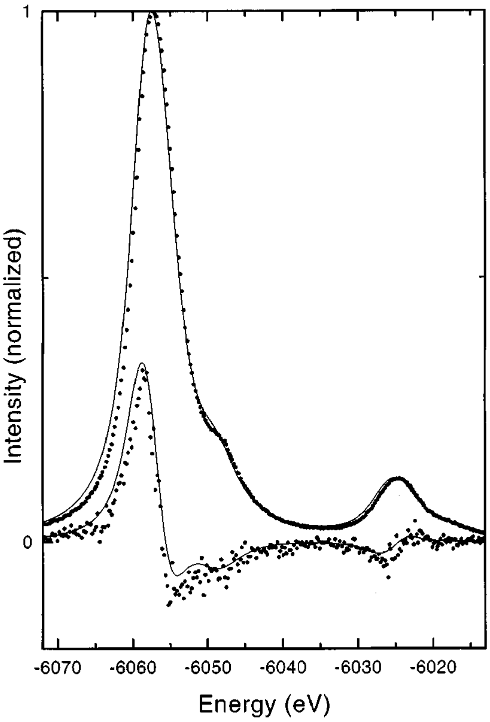

Figure 30. Comparison of the calculated 2p3d X-ray emission spectral shape (—) with the $2p_{3/2}3d$ experimental results (• • •). (Reprinted with permission from ref 42. Copyright 1997 American Physical Society.)

On the level of a single-particle analysis, already the situation is complex. The single-particle analysis assumes that the MCD effect can be described by the p → d matrix elements only. This approach can be found in the works of Erskine and Stern,[49] Stöhr and Wu,[103] Jo and co-workers,[65−67] and Kuiper.[76] In the last reference the argument was used that spin is not a constant of motion in the 2p core hole state. Because of the large core hole spin−orbit coupling, the spin of the core hole will not remain aligned with the spin of the photoelectron. This has direct consequences on the nonresonant and resonant X-ray emission MCD effects.[76]

An important experimental complication is the self-absorption-caused saturation effects. A high concentration of the element that is absorbing the X-rays implies that an emitted X-ray emission signal can be re-adsorbed before leaving the sample to be measured at the detector. Saturation effects affect the X-ray emission spectral shapes, including the MCD effects. In principle, they can be corrected for, but in the case of concentrated systems, this is a nontrivial exercise.[10] Braicovich and co-workers recently showed that by using the 2p3s X-ray emission channel, self-absorption effects can be excluded.[11] This paper used the fact that there is an angular dependence of the fluorescence and of the MCD effect therein.[42,108]

In the hard X-ray range, most of the experimental complications disappear. However, it is known that the K-edge MCD effect is very small.[49] There has been a series of studies on the MCD effect of the rare-earth L edges. Figure 30 shows the MCD effect in the $2p_{3/2}3d$ X-ray emission spectrum of Gd metal.[5,74,75] By taking care of the multiplet interactions and the

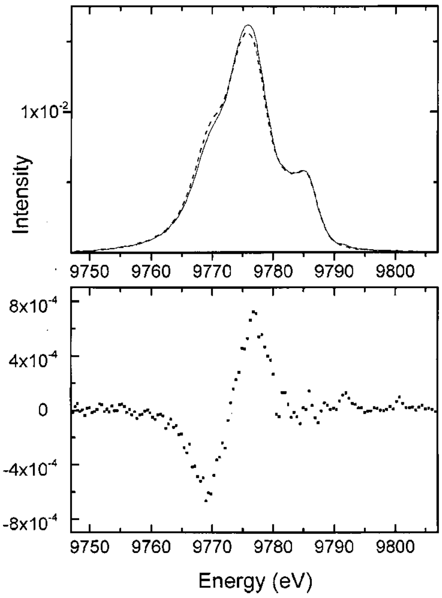

Figure 31. (top) $2p_{1/2}4d$ X-ray emission spectral shape as a function of X-ray emission energy at detection angles of 30° (• • •) and 70° (—). (bottom) Difference spectrum (70°−30°). (Reprinted with permission from ref 40. Copyright 2000 American Physical Society.)

angles between incident X-rays, emitted X-rays, and magnetic field, one can simulate the experimental spectra as shown in Figure 30.

1. MLD in X-ray Emission

In analogy with absorption magnetic linear dichroism (MLD), the X-ray emission MLD effect is the angular dependence of the X-ray emission cross section with respect to the magnetization vector.

Figure 31 shows the magnetic linear dichroism effect in the Yb $2p_{1/2}4d$ X-ray emission spectrum of $Yb_3Fe_5O_{12}$.[40] X-ray emission spectra were recorded at 110° and 150° scattering angles, corresponding to an angle between the magnetic field direction and the emitted X-rays of 70° and 30°, respectively. The bottom spectrum shows the difference between these two detection angles. From this difference spectrum, the MLD spectrum can be derived by extrapolating the spectra to the situation of, respectively, parallel and perpendicular magnetic fields and detection directions. This MLD effect can nicely be reproduced with multiplet calculations.[40]

It is interesting to look at the difference between this MLD experiment and the MCD X-ray emission experiments. In these MCD experiments, the dichroism is part of the excitation step, while in the emission MLD effects discussed above, the linear dichroism is part of the decay step. Note that both the MCD- and emission MLD-integrated intensities are equal to zero.[40]

In the case of emission MLD, this is evident as the total X-ray emission integrated over an edge must be spherically symmetric, because only core levels are involved in the X-ray emission process itself. This implies a zero integrated intensity over the MLD effect in the 2p4d X-ray emission spectrum. In principle, one could envisage a finite emission MLD effect for the $2p_{1/2}$ edge, which is compensated for at the $2p_{3/2}$ edge, similar to the situation in the MCD of soft X-ray absorption. The 2p spin−orbit coupling, however, is so large that the $2p_{1/2}$ and $2p_{3/2}$ states can be assumed to be pure, implying zero integrated intensity for the emission MLD effect. The same is true for the MCD effect, as the electron is excited from a core state to a continuum state some 100 eV above the edge, where no significant MCD effect is expected in the absorption. While the integrated intensity of the MCD and emission MLD effects is zero, their amplitude is proportional to the 4f magnetization, because it is the 4d4f exchange interaction which gives rise to the appearance of the dichroism signal. It therefore shares this sensitivity with the 3d and 4d absorption MCD and absorption MLD spectra of the rare-earth metals. It can be shown that the size of the emission MLD effect appears as a property that is sensitive to the 4f magnetic moments of the rare-earth metals. This technique is therefore complementary to absorption MCD spectroscopies at the rare-earth 3d and 4d edges, which have to be performed in the soft X-ray regime. This technique can obviously be extended to 3d transition-metal systems where the 1s2p and 1s3p X-ray emission channels will have a MLD effect that is, in this case, sensitive to the 3d magnetic moment. Magnetic linear dichroism in X-ray emission is likely to become a useful new technique in the study of magnetic materials, since it circumvents the intrinsic complications of soft X-ray spectroscopies such as a high-vacuum environment and electron detection. Furthermore, the use of hard X-rays implies that the technique is a bulk-sensitive probe and in situ experiments will be possible.

E. Spin-Polarized 1s2p and 1s3p X-ray Emission

Spin-polarized 1s2p X-ray emission does not make use of any spin detector or circular-polarized X-rays, but instead uses an internal spin reference, namely, the intermediate state with its 1s core hole.

It has been eluded already in section III that 1s2p and 1s3p X-ray emission spectra are spin-polarized. In all models discussed to interpret these spectra there will always be a small exchange interaction between the 1s core hole and the 3d electrons. The result is that in the calculations each transition is essentially split into two subpeaks split by the 1s3d exchange. The energies involved are only a few meVs, and as a result there will be no visible effects in the spectral shape. So why is this an interesting and in fact very useful effect?

The reason is that in the final state the configurations are $3p^5 3d^N$ and, as discussed, the 3p3d exchange interaction is very large, creating in a first approximation a main peak that is spin-up and a satellite at some 15 eV distance that is spin-down. Things are not as easy as this simple division, and to calculate the actual division into spin-up and spin-down, it is very useful to make use of the small 1s3d exchange interaction in the calculations. Because the 1s2p and 1s3p X-ray emission channels will conserve their spin state, the two 1s intermediate states will essentially map the spin-up and spin-down states, refer to the paper of Wang and co-workers for details.[121]

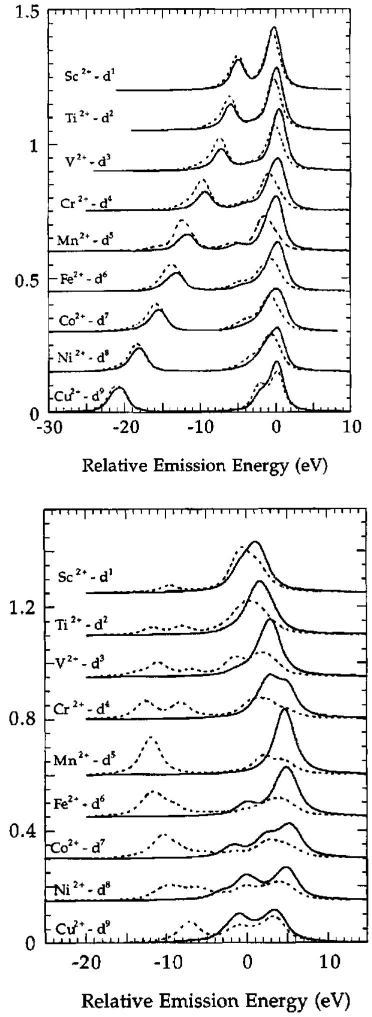

Figure 32. Theoretical spin-polarized 1s2p (top) and 1s3p (bottom) X-ray-emission spectra of the divalent 3d transition-metal ions using the ligand-field multiplet calculation. Plotted are spin-down (—) and spin-up spectra (·· ·). (Reprinted with permission from ref 121. Copyright 1997 American Physical Society.)

Figure 32 shows the separation into spin-up and spin-down using ligand-field multiplet calculations. The situation does not change significantly if one includes charge transfer.[36,121] One can immediately see that the 1s2p X-ray emission spectra only have a minor separation into spin-up and spin-down. Both the main peak and the satellite essentially show a shift between spin-up and spin-down. The situation is completely different in the case of the 1s3p X-ray emission spectra. Here a pure spin-down peak is seen for the satellite, while the main peak is mostly spin-up. This is particularly clear in the middle of the series where the exchange interaction is largest. It is because of this difference between 1s2p and 1s3p spectra that the 1s3p spectra can ideally be used to perform spin-selective X-ray absorption experiments that will be discussed in section VII.

VII. Selective X-ray Absorption

Selective X-ray absorption is an experiment that makes use of a particularly chosen X-ray emission decay channel.[42] One could also use a photoemission/Auger channel, but these experiments will not be discussed in this paper. The onset of selective X-ray absorption can be found in the work of Hämäläinen and co-workers, who showed that selective X-ray absorption effectively removes the lifetime broadening[61] and who later showed the possibility of measuring spin-dependent X-ray absorption.[60]

In section V, it was pictorially shown that the lifetime broadening effectively is removed if one measures selective X-ray absorption at resonance. Here the discussion on lifetime broadening disappearance will be extended. Figure 33 shows schematically the excitation of a 1s core electron at 3000 eV to the edge. One detects the 3p electrons that decay to the 1s hole. The lifetime broadening of the 1s level is chosen to be very large, and the 3p level is chosen to be infinitely sharp. Then by putting the energy difference between excitation and decay exactly to 1000 eV, one detects only those electrons that go from the 3p level to the 1s level, following the 1s to edge excitation. In this process the broadening of the 1s level does not matter, for example, the two processes indicated by the arrows both are possible and are detected at the same energy difference. The exact description of the removal of the lifetime broadening is the Kramers−Heisenberg formula as discussed above. One can rewrite this formula by assuming that there is no interference, which is certainly a correct assumption in the case of 1s core hole intermediate states. This removes the denominator and gives

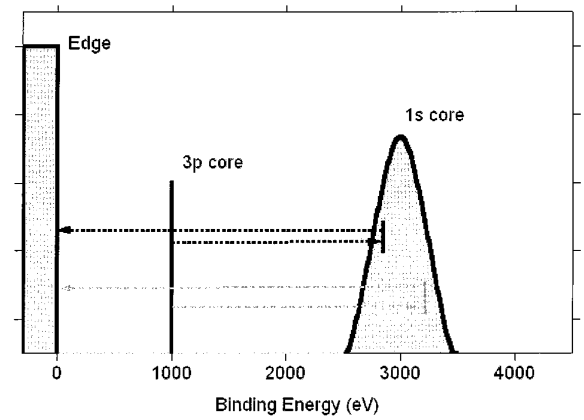

Figure 33. Removal of the lifetime broadening. An electron is excited from the broad 1s core level to the edge and a 3p electron fills the 1s hole. The detector is set at an energy equal to the binding energy of the 3p state. In that case, it does not matter if the top or bottom transitions do take place (see text).

$$I(\omega) \sim \sum_f \sum_x \langle \Phi_f | \hat{e}\cdot r | \Phi_x \rangle^2 \langle \Phi_x | \hat{e}\cdot r | \Phi_i \rangle^2 \qquad (21)$$

The summation of the X-ray emission matrix element yields a constant (I_{XES}) and can be removed from the formula. What remains is analogous to the normal XAFS

$$I(\omega) \sim \sum_x \langle \Phi_x | \hat{e}\cdot r | \Phi_i \rangle^2 \, \delta_{E_f - E_i - (\hbar\omega - \hbar\omega')} \qquad (22)$$

It can be seen that the matrix element concerns the intermediate-state Φ_x, for example, a 1s state, and the delta function (that is rewritten to a Lorentzian broadening) contains the final state and initial state, without the intermediate state. In other words, the lifetime broadening of the intermediate state is completely removed from the equation. In section V it was shown that in the case of 2p core holes, interference effects modify this picture a little bit, but the essential conclusion remains that selective X-ray absorption can measure X-ray absorption spectra with a resolution much better than the core hole lifetime broadening.

It was shown that the combination of X-ray absorption and X-ray emission gives us (a) lifetime broadening removed X-ray absorption and (b) spin-, valence-, and site-selective X-ray absorption.

A. Lifetime Broadening Removed X-ray Absorption

One can make use of one of these possibilities to improve upon the normal 2p X-ray absorption experiments. That is, one can remove the 2p lifetime broadening of ca. 4 eV and replace it by the 3d or 4d lifetime broadening of less than 0.5 eV. This results in enormously sharper $L_{2,3}$ edges. Figure 34 shows the platinum L_3 edge with fluorescence yield X-ray absorption (points) and with $2p_{3/2}3d$-detected X-ray absorption (dashed), both measured simultaneously at beamline ID26 at ESRF. Details on the experiment and the analysis will be published elsewhere. As expected, the L_3 is sharper if the 2p lifetime broadening is removed. This sharpening makes it possible to measure the L_3 edge with very high resolution, provided the monochromator resolution is very good. The high-resolution XANES spectra can be used to study small variations in the lowest empty states.

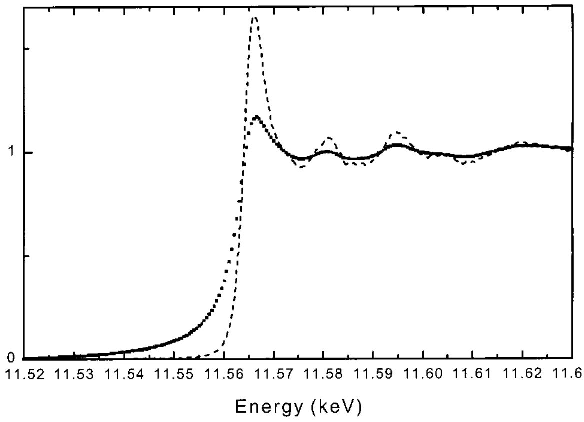

Figure 34. Platinum L_3 edge measured with fluorescence yield XAFS (• • •) and with $2p_{3/2}3d$ detected XAFS (- - -).

B. Valence-, Spin-, and Site-Selective X-ray Absorption

The central point of selective X-ray absorption is to make use of a particular fluorescence channel to measure the X-ray absorption spectrum. For example, by measuring the X-ray absorption spectral shape at the peak positions of the $K\beta_{1,3}$ and the $K\beta'$ peaks, one can obtain the spin-selective X-ray absorption spectral shape.[43,121] This is important for the study of magnetic materials. This applies not only to the XANES region, but just as well to the EXAFS region, which allows for studies on the local geometry that are, for example, separated for their spin.[119,120]

1. Valence-Selective X-ray Absorption

As shown in Figure 15, the 1s3p fluorescence spectral shapes shift to higher energy with increasing valence. One can tune the energy of the fluorescence detector to the peak position of one valence and vary the energy of the incoming X-ray, thereby measuring the X-ray absorption spectrum of that particular valence. This can be repeated for the other valence. Consequently, one obtains separate X-ray absorption spectra for the various valences present, in other words valence-selective X-ray absorption.[56]

Recently, valence-selective X-ray absorption has been applied to $Fe^{III}_4(Fe^{II}(CN)_6)_3$ (Prussian Blue). Prussian Blue can be considered the prototype of mixed-valence compounds. It contains two kinds of iron in different oxidation and spin states. The ferrous ion presents a coordination shell constituted by six carbons at 1.92 Å and is surrounded by six nitrogens at 3.04 Å and six ferric ions at 5.08 Å. The formal oxidation number is II, and the strong crystal field exhibited by the carbon atoms yields a low-spin ground-state configuration. The ferric ion Fe^{III} has a high-spin configuration. The bulk ratio Fe^{III} to Fe^{II} is 4:3. Glatzel and co-workers[54] showed that the 1s3p X-ray emission spectrum of Prussian Blue can be simulated by a 4:3 ratio of the spectra of Fe_2O_3 and $K_4Fe(CN)_6$. Using these two systems as a reference for the Fe^{III} and Fe^{II} spectra, valence-selective X-ray absorption spectra were measured by tuning the crystal analyzer to fluorescence energies that mainly detect contributions from the element in one specific site while the energy of the incident X-ray beam is scanned through the iron K-edge region, including the EXAFS. EXAFS analysis shows good agreement of the Fe^{III} and Fe^{II} sites with X-ray diffraction data.[54]

2. Spin-Selective X-ray Absorption

Figure 32 in section V.E explained the measurement of spin-polarized X-ray emission spectra. Tuning the detector to a photon energy related to either spin-up or spin-down while scanning through an absorption edge, the spin-polarized X-ray absorption spectrum is measured. From Figure 32b, it is evident that Mn^{II} is the ideal case to carry out spin-selective X-ray absorption. It turns out that the critical parameter is the number of unpaired 3d electrons. The strong 3p3d exchange interaction will create large splittings that reach a maximum for high-spin $3d^5$. The spin-selective X-ray absorption spectrum can be measured for all systems that carry a local moment on a transition-metal ion. This includes ferromagnets, antiferromagnets, and paramagnetic systems.

Spin-selective X-ray absorption was measured for the first time by Hämäläinen and co-workers.[60] By detecting the main peak and the satellite of the 1s3p X-ray emission spectrum of the antiferromagnet MnF_2, they could measure separate X-ray absorption spectra for spin-up and spin-down. It is interesting to compare the spin-selective X-ray absorption spectrum with the MCD spectrum of ferromagnets. For ferromagnets, the spin-selective X-ray absorption spectrum identifies with the spin-polarized density of states. As discussed in section IV.A (eq 20), K-edge MCD measures the spin-polarized density of states times the Fano factor. By measuring both the MCD and the spin-selective X-ray absorption spectra of the same system, one is able to determine directly the magnitude of the Fano factor, including its potential energy dependence. Measurements on a ferromagnetic MnP sample did show a large energy dependence of the Fano factor, reaching −4% at the edge and decreasing to a much smaller value above the edge.[43,44]

The measurement of spin-selective X-ray absorption is easiest for $3d^5$ systems. This, however, does not imply that spin-selective X-ray absorption is impossible for systems that have only one or two unpaired electrons. Recently, Wang and co-workers[121] measured the spin-selective X-ray absorption spectrum of the high-spin Ni^{II} system $(PPh_4)_2Ni(SePh)_4$. Using the spin-polarized signal of the 1s2p X-ray emission main peak (cf. Figure 32a), the spin-selective X-ray absorption spectrum was measured.

3. Site-Selective X-ray Absorption

A final possibility is site-selective X-ray absorption. This possibility arises from the oxygen to metal crossover decay channel, i.e., the $K\beta''$ peak in Figure 16. Because the oxygen 2s peak is present only for the metal atoms that are neighbors to the oxygen, one can measure the X-ray absorption spectra of only those metal atoms. It is important to note that the X-ray absorption (including EXAFS) analysis is essentially the same as for normal X-ray absorption and all atoms surrounding the excited atom do contribute to the electron scattering. Only the X-ray excitation and decay process is specific for one type of neighbor, while the electron scattering determining the X-ray absorption spectral shape is not. Site-selective X-ray absorption opens a large range of new series of experiments, but the intrinsic low intensity will make it very hard experiments too.

It can be concluded that selective X-ray absorption provides a new useful tool for the study of systems that contain an element in two distinct situations. This adds an extra advantage to the element selectivity of normal X-ray absorption. Because only hard X-rays are involved, further applications are envisaged in in situ characterization in fields such as electrochemistry, heterogeneous catalysis, high-pressure studies, etc.

VIII. Conclusions and Outlook

In this paper a review of high-resolution X-ray emission and X-ray absorption experiments has been given. The emphasis has been on the fundamental aspects of the interpretation and, in addition, on recent advances in this field. The enormous amount of (high-resolution) X-ray emission literature from nonsynchrotron sources has been largely neglected.

In conclusion, it can be remarked that at present there is a situation in which X-ray absorption spectra are analyzed either with density functional theory for the 1s core levels or multiplet theory for all other edges. X-ray emission always involves a core level that necessitates multiplet analysis of the spectral shape. The field of high-resolution X-ray emission is still in a stage of large experimental progress, and more and higher resolution spectra are expected soon. This will in turn cause the theoretical interpretations to become more refined. Some examples of this development are the detection of spin-flip transitions and the realization that Coster−Kronig channels are important for a good description. A picture of X-ray emission will never be complete without the equivalent understanding of the nonradiative decay channels, i.e., resonant photoemission and Auger.

Because high-resolution X-ray emission is a relatively new technique at synchrotron radiation sources, a large part of the experiments carried out today and in the past can be envisioned as prototype experiments. As such, they often belong to the realm of physics. However, a number of dedicated hard X-ray emission beamlines are projected and/or build at least at the APS, ESRF, and HASYLAB. New soft X-ray emission (resonant inelastic X-ray scattering) beamlines are present at, for example, ALS, MAXLAB, and ELETTRA. These beamlines will make techniques such as RIXS and selective X-ray absorption more accessible to nonexperts, and it is expected that this will largely extend the scope of experiments to be performed. It is hoped that this review serves as a good starting point for the planning of these experiments in fields such as (bio)catalysis, coordination chemistry, electrochemistry, magnetic devices, surface science, etc.

IX. Acknowledgment

For collaborations and discussions, I thank Steve Cramer, Uwe Bergmann, Pieter Glatzel, Chi-chang Kao, Michael Krisch, Pieter Kuiper, Sergei Butorin, Keijo Hämäläinen, Teijo Åberg, Alain Fontaine, Akio Kotani, and George Sawatzky.

X. References

(1) Åberg, T. *At. Phys. High Brilliance Synchrotron Sources, Proc. Workshop* **1994**, 167−82.
(2) Åberg, T. *Phys. Rev.* **1967**, *156* (1), 35−41.
(3) Arrio, M. A.; Rossano, S.; Brouder, C.; Galoisy, L.; Calas, G. *Europhys. Lett.* **2000**, *51* (4), 454.
(4) Bae, I. T.; Tryk, D. A.; Scherson, D. A. *J. Phys. Chem. B* **1998**, *102*, 4114.
(5) Bartolome, F.; Tonnerre, J. M.; Seve, L.; Raoux, D.; Lorenzo, J. E.; Chaboy, J.; Garcia, L. M.; Bartolome, J.; Krisch, M.; Rogalev, A.; Serimaa, R.; Kao, C.-C.; Cibin, G.; Marcelli, A. *J. Appl. Phys.* **1998**, *83* (11, Pt. 2), 7091−7093.
(6) Bergmann, U.; Glatzel, P.; de Groot, F. M. F.; Cramer, S. P. *J. Am. Chem. Soc.* **1999**, *121* (20), 4926−4927.
(7) Bergmann, U.; Grush, M. M.; Horne, C. R.; Demarois, P.; Pennerhahn, J. E.; Yocum, C. F.; Wright, D. W.; Dube, C. E.; Armstrong, W. H.; Christou, G.; Eppley, H. J.; Cramer, S. P. *J. Phys. Chem B* **1998**, *102* (42), 8350−8352.

(8) Bergmann, U.; Horne, C. R.; Collins, T. J.; Workman, J. M.; Cramer, S. P. *Chem. Phys. Lett.* **1999**, *302* (1−2), 119−124.
(9) Borgatti, F.; Braicovich, L.; Brookes, N. B.; Ghiringhelli, G.; Tagliaferri, A. *J. Electron Spectrosc. Relat. Phenom.* **1999**, *101−103*, 467−471.
(10) Braicovich, L.; Dallera, C.; Ghiringhelli, G.; Brookes, N. B.; Goedkoop, J. B. *Phys. Rev. B* **1997**, *55* (22), 14729−14732.
(11) Braicovich, L.; Van Der Laan, G.; Ghiringhelli, G.; Tagliaferri, A.; Van Veenendaal, M. A.; Brookes, N. B.; Chervinskii, M. M.; Dallera, C.; De Michelis, B.; Durr, H. A. *Phys. Rev. Lett.* **1999**, *82* (7), 1566−1569.
(12) Butler, P. H. *Point Group Symmetry Applications: Methods and Tables*; Plenum Press: New York, 1981.
(13) Butorin, S. M. Private Communication, 1999.
(14) Butorin, S. M. *J. Electron Spectrosc.* **2000**, *110*, 213.
(15) Butorin, S. M.; Duda, L. C.; Guo, J. H.; Wassdahl, N.; Nordgren, J.; Nakazawa, M.; Kotani, A. *J. Phys.: Condens. Matter* **1997**, *9* (38), 8155−8160.
(16) Butorin, S. M.; Guo, J.-H.; Magnuson, M.; Kuiper, P.; Nordgren, J. *Phys. Rev. B* **1996**, *54* (7), 4405−4408.
(17) Butorin, S. M.; Guo, J.-H.; Magnuson, M.; Nordgren, J. *Phys. Rev. B* **1997**, *55* (7), 4242−4249.
(18) Butorin, S. M.; Magnuson, M.; Ivanov, K.; Shuh, D. K.; Takahashi, T.; Kunii, S.; Guo, J.-H.; Nordgren, J. *J. Electron Spectrosc. Relat. Phenom.* **1999**, *101−103*, 783−786.
(19) Butorin, S. M.; Mancini, D. C.; Guo, J. H.; Wassdahl, N.; Nordgren, J.; Nakazawa, M.; Tanaka, S.; Uozumi, T.; Kotani, A.; Ma, Y.; Myano, K. E.; Karlin, B. A.; Shuh, D. K. *Phys. Rev. Lett.* **1996**, *77* (3), 574−577.
(20) Cabaret, D.; Sainctavit, P.; Ildefonse, P.; Flank, A. M. *J. Phys. IV* **1997**, *7* (C2, X-Ray Absorption Fine Structure, Vol. 1), 157−158.
(21) Cabaret, D.; Sainctavit, P.; Ildefonse, P.; Flank, A.-M. *Am. Mineral.* **1998**, *83* (3−4), 300−304.
(22) Caliebe, W. A.; Kao, C.-C.; Berman, L. E.; Hastings, J. B.; Krisch, M. H.; Sette, F.; Hämäläinen, K. *J. Appl. Phys.* **1996**, *79* (8, Pt. 2B), 6509−11.
(23) Caliebe, W. A.; Kao, C.-C.; Hastings, J. B.; Taguchi, M.; Kotani, A.; Uozumi, T.; de Groot, F. M. F. *Phys. Rev. B* **1998**, *58*(*20*), 13452−13458.
(24) Chen, J. G. *Surf. Sci. Rep.* **1997**, *30* (1−3), 5−152.
(25) Cowan, R. D. *The Theory of Atomic Structure and Spectra*; University of California Press: Berkeley, 1981.
(26) Cramer, S. P.; de Groot, F. M. F.; Ma, Y. J.; Chen, C. T.; Sette, F.; Kipke, C. A.; Eichhorn, D. M.; Chan, M. K.; Armstrong, W. H.; Libby, E.; Christou, G.; Brooker, S.; McKee, V.; Mullins, O. C.; Fuggle, J. C. *J. Am. Chem. Soc.* **1991**, *113*, 7937.
(27) de Groot, F. M. F. Ph.D. Thesis, 1991.
(28) de Groot, F. M. F. *J. Electron Spectrosc. Relat. Phenom.* **1993**, *62* (1−2), 111−30.
(29) de Groot, F. M. F. *J. Electron Spectrosc. Relat. Phenom* **1994**, *67* (4), 529−622.
(30) de Groot, F. M. F. *Physica B* **1994**, *209*, 15.
(31) de Groot, F. M. F. *Phys. Rev. B* **1996**, *53* (11), 7099−110.
(32) de Groot, F. M. F. *Raman Emiss. X-Ray Scattering, Proc. Workshop* **1996**, 61−70.
(33) de Groot, F. M. F. *Top. Catal.* **2000**, *10* (3−4), 179−186.
(34) de Groot, F. M. F *J. Electron Spectrosc. Relat. Phenom* **1997**, *86* (1−*3*), 5.
(35) de Groot, F. M. F.; Faber, J.; Michiels, J. J. M.; Czyzyk, M. T.; Abbate, M.; Fuggle, J. C. *Phys. Rev. B* **1993**, *48* (4), 2074−80.
(36) de Groot, F. M. F.; Fontaine, A.; Kao, C. C.; Krisch, M. H. *J. Phys. Condens. Matter* **1994**, *6* (34), 6875−6884.
(37) de Groot, F. M. F.; Fuggle, J. C.; Thole, B. T.; Sawatzky, G. A. *Phys. Rev. B* **1990**, *42* (9), 5459−68.
(38) de Groot, F. M. F.; Fuggle, J. C.; Thole, B. T.; Sawatzky, G. A. *Phys. Rev. B* **1990**, *41* (2), 928−37.
(39) de Groot, F. M. F.; Grioni, M.; Fuggle, J. C.; Ghijsen, J.; Sawatzky, G. A.; Petersen, H. *Phys. Rev. B* **1989**, *40* (8), 5715−23.
(40) de Groot, F. M. F.; Krisch, M. H.; Sette, F.; Vogel, J. *Phys. Rev. B* **2000**, *62* (1), 379−384.
(41) de Groot, F. M. F.; Kuiper, P.; Sawatzky, G. A. *Phys. Rev. B* **1998**, *57* (23), 14584−14587.
(42) de Groot, F. M. F.; Nakazawa, M.; Kotani, A.; Krisch, M. H.; Sette, F. *Phys. Rev. B* **1997**, *56* (12), 7285−7292.
(43) de Groot, F. M. F.; Pizzini, S.; Fontaine, A.; Hämäläinen, K.; Kao, C. C.; Hastings, J. B. *Phys. Rev. B* **1995**, *51* (2), 1045−1052.
(44) de Groot, F. M. F.; Pizzini, S.; Fontaine, A.; Hämäläinen, K.; Kao, C. C.; Hastings, J. B. *Physica B* **1995**, *209* (1−4), 763−764.
(45) De Nadai, C.; Demourgues, A.; Grannec, J.; de Groot, F. M. F. *Phys. Rev. B* **2001**, *63*, 125123.
(46) Dräger, G.; Kirchner, Th.; Bocharov, S.; Kao, C. C. *J. Synchrotron Radiat.* **2001**, *8*398.
(47) Duda, L. C. *J. Electron Spectrosc. Relat. Phenom* **2000**, *110* (1−3), 287−304.
(48) Ebert, H.; Schütz, G. E. *Spin−Orbit Influenced Spectroscopies of Magnetic Solids*; Springer-Verlag: Berlin, 1996.
(49) Erskine, J. L.; Stern, E. A. *Phys. Rev. B* **1975**, *12*, 5016.
(50) Finazzi, M.; Brookes, N. B.; de Groot, F. M. F. *Phys. Rev. B* **1999**, *59* (15), 9933−9942.
(51) Fontaine, A. *Interaction of X-rays With Matter: Absorption Spectroscopy;* HERCULES: Grenoble, 1995; Vol. 1
(52) Fuggle, J. C.; Inglesfield. J. E. *Unoccupied Electronic States*; Springer-Verlag: Berlin, 1992.
(53) Gel′mukhanov, F.; Agren, H. *Phys. Rep.* **1999**, *312* (3−6), 87−330.
(54) Glatzel, P.; Jacquamet, L.; Bergmann, U.; de Groot, F. M. F.; Cramer, S. P. *Angew. Chem.,* submitted for publication.
(55) Goedkoop, J. B.; Thole, B. T.; Vanderlaan, G.; Sawatzky, G. A.; de Groot, F. M. F.; Fuggle, J. C. *Phys. Rev. B* **1988**, *37*, 2086.
(56) Grush, M. M.; Christou, G.; Hämäläinen, K.; Cramer, S. P. *J. Am. Chem. Soc.* **1995**, *117* (21), 5895−5896.
(57) Guo, J.-H.; Glans, P.; Skytt, P.; Wassdahl, N.; Nordgren, J.; Luo, Y.; Aagren, H.; Ma, Y.; Warwick, T.; *Phys. Rev. B* **1995**, *52* (15), 10681−4.
(58) Hague, C. F.; Mariot, J.-M.; Guo, G. Y.; Hricovini, K.; Krill, G. *Phys. Rev. B* **1995**, *51* (2), 1370−3.
(59) Hague, C. F.; Tronc, M.; Yanagida, Y.; Kotani, A.; Guo, J. H.; Sathe, C. *Phys. Rev. A* **2001**, *63*, 12511.
(60) Hämäläinen, K.; Kao, C.-C.; Hastings, J. B.; Siddons D. P.; Berman L. E. *Phys. Rev. B* **1992**, *46*, 14274.
(61) Hämäläinen, K.; Siddons, D. P.; Hastings, J. B.; Berman, L. E. *Phys. Rev. Lett.* **1991**, *67*, 2850.
(62) Himpsel, F. J.; Karlsson, U. O.; McLean, A. B.; Terminello, L. J.; de Groot, F. M. F.; Abbate, M.; Fuggle, J. C.; Yarmoff, J. A.; Thole, B. T.; Sawatzky, G. A. *Phys. Rev. B* **1991**, *43*, 6899.
(63) Hu, Z.; Kaindl, G.; Warda, S. A.; Reinen, D.; De Groot, F. M. F.; Muller, B. G. *Chem. Phys.* **1998**, *232* (*1*, *2*), 63−74.
(64) Hu, Z.; Mazumdar, C.; Kaindl, G.; de Groot, F. M. F.; Warda, S. A.; Reinen, D. *Chem. Phys. Lett.* **1998**, *297* (*3*, *4*), 321−328.
(65) Jo, T. *J. Electron Spectrosc. Relat. Phenom* **1997**, *86* (1−3), 73−82.
(66) Jo, T.; Parlebas, J. C. *J. Phys. Soc. Jpn.* **1999**, *68* (4), 1392−1397.
(67) Jo, T.; Tanaka, A. *J. Phys. Soc. Jpn.* **1998**, *67* (4), 1457−1465.
(68) Journel, L.; Sacchi, M.; Gallet, J.-J.; Hague, C. F.; Mariot, J.-M.; Brookes, N. B.; Finazzi, M.; Felsch, W.; Krill, G. *J. Electron Spectrosc. Relat. Phenom.* **1999**, *101−103*, 733−738.
(69) Kawai, J. *Microbeam Analysis 2000, Proceedings*, Williams, D., Shimizu, R., Eds.; Institute of Physics Conference Series: 2000; Vol. 165, p 463.
(70) Kawai, J. In *Encyclopedia of Analytical Chemistry*; Meyers, R. A., Ed.; Wiley: Chichester, 2000; pp 13288−13315.
(71) Kawai, J.; Hayashi, K. *J. Electron Spectrosc. Relat. Phenom.* **1998**, *92* (1−3), 243−245.
(72) *X-ray Absorption*; Koningsberger, D. C., Prins, R., Eds.; Wiley: New York, 1987.
(73) Kotani, A. *J. Phys. IV* **1997**, *7* (C2), 1−8.
(74) Krisch, M. H.; Kao, C. C.; Sette, F.; Caliebe, W. A.; Hämäläinen, K.; Hastings, J. B. *Phys. Rev. Lett.* **1995**, *74* (24), 4931−4.
(75) Krisch, M. H.; Sette, F.; Masciovecchio, C.; Verbeni, R. *J. Electron Spectrosc. Relat. Phenom.* **1997**, *86* (1−3), 159−164.
(76) Kuiper, P. *J. Phys. Soc. Jpn.* **2000**, *69* (3), 874−877.
(77) Kuiper, P.; Guo, J.-H.; Sathe, C.; Duda, L.-C.; Nordgren, J.; Pothuizen, J. J. M.; de Groot, F. M. F.; Sawatzky, G. A. *Phys. Rev. Lett.* **1998**, *80* (23), 5204−5207.
(78) Lyttle, F. W.; Greegor, R. B.; Panson, A. J. *Phys. Rev. B* **1988**, *37*, 1550.
(79) M.Bonfim, M.; Ghiringhelli, G.; Montaigne, F.; Pizzini, S.; Brookes, N. B.; Petro, F.; Vogel, J.; Camarero, J.; Fontaine, A. *Phys. Rev. Lett.* **2001**, *86*, 3646.
(80) Mahadevan, P.; Sarma, D. D. *Phys. Rev. B* **2000**, *61* (11), 7402−7408.
(81) Mori, A.; Kayanuma, Y.; Kotani, A. *Prog. Theor. Phys. Suppl.* **1991**, *106*, 75−93.
(82) Muller J. E.; Jepsen O.; Andersen O. K.; Wilkins J. W. *Phys. Rev. Lett.* **1978**, *40*, 720.
(83) Natoli, C. R. *EXAFS and Near Edge Structure*; Springer: Berlin, 1983.
(84) Natoli, C. R.; Benfatto, M.; Doniach, S. *Phys. Rev. B* **1986**, *34*, 4682.
(85) Nolting, F.; Scholl, A.; Stohr, J.; Seo, J. W.; Fompeyrine, J.; Siegwart, H.; Locquet, J. P.; Anders, S.; Luning, J.; Fullerton, E. E.; Toney, M. F.; Scheinfein, M. R.; Padmore, H. A. *Nature* **2000**, *405* (6788), 767−769.
(86) Nordgren, E. J. *Roentgen Centen.* **1997**, 364−380.
(87) Okada, K.; Kotani, A. *J. Phys. Soc. Jpn.* **1992**, *61* (2), 449−453.
(88) Okada, K.; Kotani, A. *J. Phys. Soc. Jpn.* **1992**, *61* (12), 4619−4637.
(89) Okada, K.; Kotani, A.; Thole, B. T *J. Electron Spectrosc. Relat. Phenom* **1992**, *58* (4), 325−343.
(90) Peng, G.; de Groot, F. M. F.; Hämäläinen, K.; Moore, J. A.; Wang, X.; Grush, M. M.; Hastings, J. B.; Siddons, D. P.; Armstrong,

W. H.; Mullins, O. C.; Cramer, S. P. *J. Am. Chem. Soc.* **1994**, *116* (7), 2914−2920.
(91) Qian, Q.; Tyson, T. A.; Kao, C. C.; Croft, M.; Cheong, S. W.; Greenblatt, M. *Phys. Rev. B* **2000**, *62* (20), 13472−13481.
(92) Rehr, J. J.; Albers, R. C. *Rev. Mod. Phys.* **2000**, *72* (3), 621−654.
(93) Rehr, J. J.; Ankudinov, A.; Zabinsky, S. I. *Catal. Today* **1998**, *39* (4), 263−269.
(94) Robblee, J. H.; Messinger, J.; Fernandez, C.; Cinco, R. M.; Visser, H.; Mcfarlane, K. L.; Bergmann, U.; Glatzel, P.; Cramer, S. P.; Sauer, K.; Klein, M. P. *J. Inorg. Biochem.* **1999**, *74* (1−4), 278−278.
(95) Rubensson, J. E.; Eisebitt, S.; Nicodemus, M.; Boske, T.; Eberhardt, W. *Phys. Rev. B* **1994**, *50* (13), 9035−9045.
(96) Rubensson, J.; Eisebitt, S.; Nicodemus, M.; Boske, T.; Eberhardt, W. *Phys. Rev. B* **1994**, *49* (2), 1507−1510.
(97) Rueff, J. P.; Kao, C. C.; Struzhkin, V. V.; Badro, J.; Shu, J.; Hemley, R. J.; Hao, H. K. *Phys. Rev. Lett.* **1999**, *82* (16), 3284−3287.
(98) Rueff, J. P.; Krisch, M.; Cai, Y. Q.; Kaprolat, A.; Hanfland, M.; Lorenzen, M.; Masciovecchio, C.; Verbeni, R.; Sette, F. *Phys. Rev. B* **1999**, *60* (21), 14510−14512.
(99) Sainctavit, P.; Petiau, J.; Benfatto, M.; Natoli, C. R. *Physica B (Amsterdam)* **1989**, *158* (1−3), 347−50.
(100) Scholl, A.; Stohr, J.; Luning, J.; Seo, J. W.; Fompeyrine, J.; Siegwart, H.; Locquet, J. P.; Nolting, F.; Anders, S.; Fullerton, E. E.; Scheinfein, M. R.; Padmore, H. A. *Science* **2000**, *287* (5455), 1014−1016.
(101) Stöhr, J. *NEXAFS Spectroscopy*; Springer-Verlag: Berlin, 1992.
(102) Stohr, J.; Scholl, A.; Regan, T. J.; Anders, S.; Luning, J.; Scheinfein, M. R.; Padmore, H. A.; White, R. L. *Phys. Rev. Lett.* **1999**, *83* (9), 1862−1865.
(103) Stöhr, J.; Wu, Y. In *New Directions in Research With Third-Generation Soft X-ray Synchrotron Radiation Sources*; Schlachter, A. S., Wuilleumier, F. J., Eds.; Kluwer: Dordrecht, 1994.
(104) Strange, P.; Durham, P. J.; Gyorffy, B. L. *Phys. Rev. Lett.* **1991**, *67* (25), 3590−3593.
(105) Sugano, S.; Tanabe, Y.; Kamimura, H. *Multiplets of Transition Metal Ions*; Academic Press: New-Yiork, 1970.
(106) Tanaka, S.; Kotani, A. *J. Phys. Soc. Jpn.* **1993**, *62* (2), 464−467.
(107) Thole, B. T.; Carra, P.; Sette, F.; Vanderlaan, G. *Phys. Rev. Lett.* **1992**, *68* (12), 1943−1946.
(108) Thole, B. T.; Durr, H. A.; Vanderlaan, G. *Phys. Rev. Lett.* **1995**, *74* (12), 2371−2374.
(109) Thole, B. T.; van der Laan, G.; Sawatzky, G. A. *Phys. Rev. Lett.* **1985**, *55*, 2086.
(110) Thole, B. T.; Vanderlaan, G.; Butler, P. H. *Chem. Phys. Lett.* **1988**, *14*, 9295.
(111) Tsutsumi, K. *J. Phys. Soc. Jpn.* **1959**, *14*, 1696.
(112) Tsutsumi, K.; Nakamori, H.; Ichikawa, K. *Phys. Rev. B* **1976**, *13*, 929.
(113) Tulkki, J.; Åberg, T. *Res. Rep.−Helsinki Univ. Technol., Lab. Phys.* **1978**, *3*, 2 pp.
(114) Tyson, T. A.; Qian, Q.; Kao, C. C.; Rueff, J. P.; De Groot, F. M. F.; Croft, M.; Cheong, S. W.; Greenblatt, M.; Subramanian, M. A. *Phys. Rev. B* **1999**, *60* (7), 4665−4674.
(115) van der Laan, G.; Zaanen, J.; Sawatzky, G. A.; Karnatak, R.; Esteva, J. M. *Phys. Rev. B* **1986**, *33*, 4253.
(116) Van Elp, J.; Tanaka, A. *Phys. Rev. B: Condens. Matter* **1999**, *60* (8), 5331−5339.
(117) von Barth, U.; Grossmann, G. *Phys. Rev. B* **1982**, *25*, 5150.
(118) Vvdensky, D. D. In *Unoccupied Electronic States*; Fuggle, J. C., Inglesfield, J. E., Eds.; Springer-Verlag: Berlin, 1992.
(119) Wang, X.; Cramer, S. P. *J. Phys. IV* **1997**, *7* (C2), 361−363.
(120) Wang, X.; Randall, C. R.; Peng, G.; Cramer, S. P. *Chem. Phys. Lett.* **1995**, *243* (5−6), 469−473.
(121) Wang, X.; de Groot, F. M. F.; Cramer, S. P. *Phys. Rev. B* **1997**, *56* (8), 4553−4564.
(122) Waychunas, G. A. *Am. Mineral.* **1987**, 7289.
(123) Weissbluth, M. *Atoms and Molecules*; Plenum Press: New York, 1978.
(124) Westre, T. E.; Kennepohl, P.; Dewitt, J. G.; Hedman, B.; Hodgson, K. O.; Solomon, E. I. *J. Am. Chem. Soc.* **1997**, *119* (27), 6297−6314.
(125) Zaanen, J.; Sawatzky, G. A.; Allen, J. W. *Phys. Rev. B* **1985**, *55*, 418.
(126) Zeller, R. In *Unoccupied Eectronic States*; Fuggle, J. C., Inglesfield, J. E., Eds.; Springer-Verlag: Berlin, 1992.

CR9900681